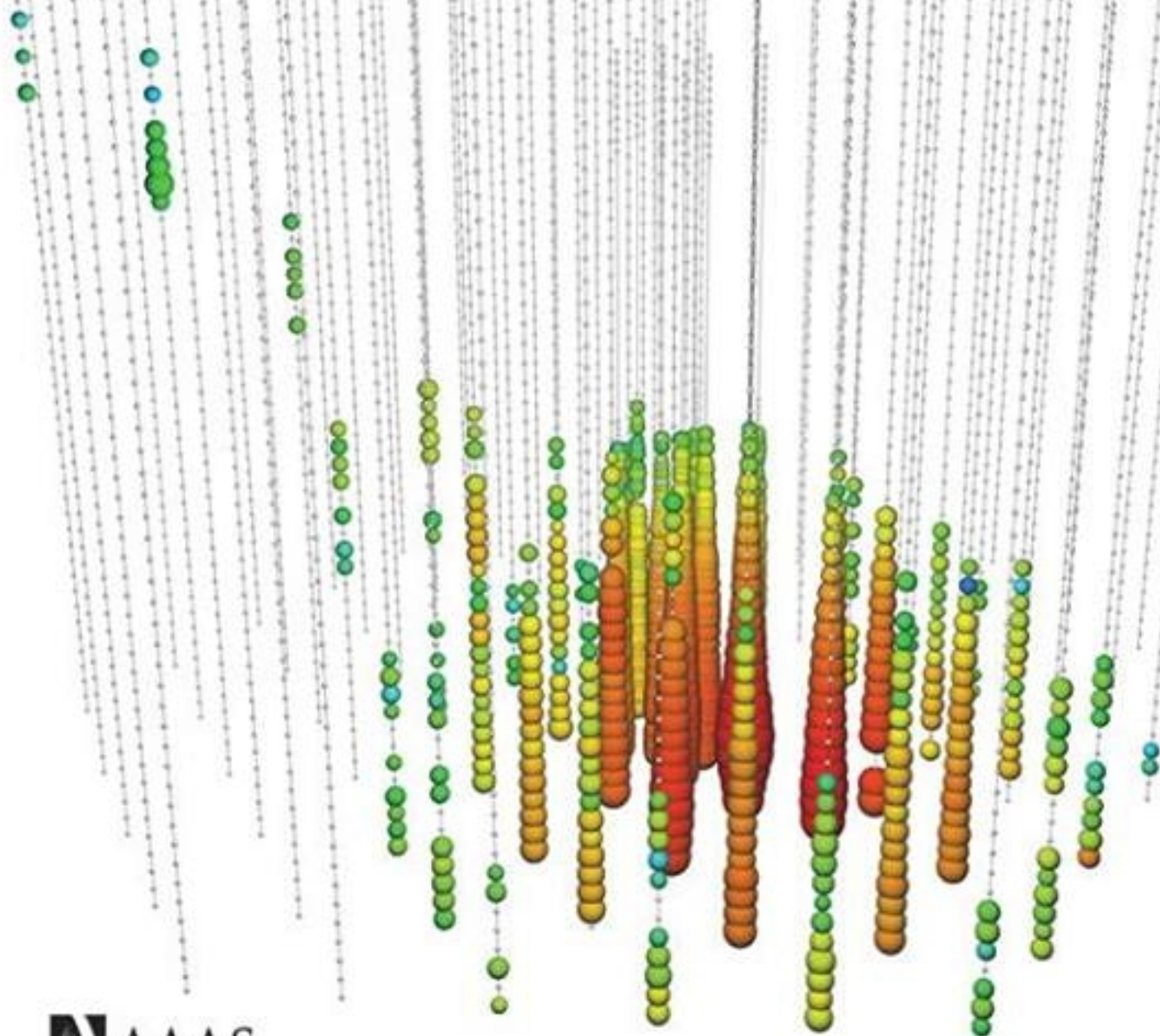


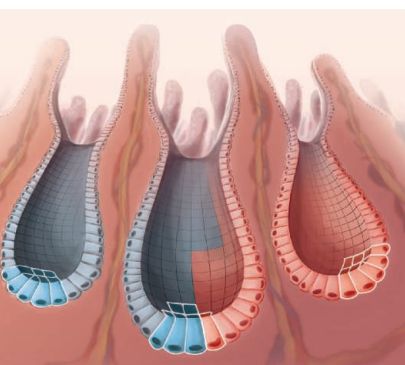
22 November 2013 | \$10

Science

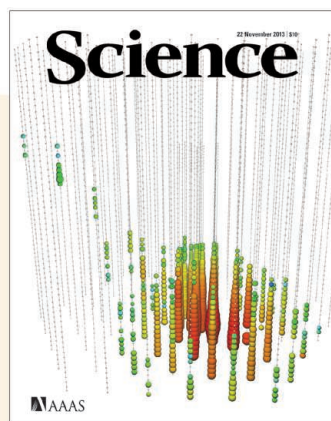




page 926



pages 938 & 995



COVER

Hit distribution (red, early; green, late) of a neutrino interaction with the Antarctic IceCube neutrino detector on 14 July 2011. Light from this transfer of 250 teraelectron volts of energy fills a sphere 600 meters across. This event, among the highest-energy neutrino interactions ever observed, forms part of the first evidence for a high-energy neutrino flux of astrophysical origin. See pages 920 and 947 and <http://dx.doi.org/10.1126/science.1242856>.

Credit: IceCube Collaboration

EDITORIAL

- 909 Bridge or Crutch?
Marcia McNutt

NEWS OF THE WEEK

- 914 A roundup of the week's top stories

NEWS & ANALYSIS

- 917 New Tools Light Up the Intricacies of the Brain
918 Humans Fueled Global Warming Millennia Ago
 >> *Report p. 964*
919 Proposed Tweaks to NSF Peer Review Spur Tensions
920 Physicists Snare a Precious Few Neutrinos From the Cosmos
 >> *Research Article p. 947*
921 Cancer Therapies Use a Little Help From Microbial Friends
 >> *Reports pp. 967 and 971*

NEWS FOCUS

- 922 When Mice Mislead
926 Missing the Mark
 Missile Defense Made Practical
 >> *Science Podcast*

LETTERS

- 930 Atlantic Rainforest's Jaguars in Decline
 M. Galetti et al.
 Capping Progress on Invasive Species?
 C. Carboneras et al.
 Drilling Plans Endanger Yasuni's Biodiversity
 J. J. Alava and N. Calle

- 931 CORRECTIONS AND CLARIFICATIONS

BOOKS ET AL.

- 933 Status Update
 A. E. Marwick, reviewed by W. H. Dutton
934 String Theory and the Scientific Method
 R. Dawid, reviewed by G. Ellis

EDUCATION FORUM

- 935 Instructional Complexity and the Science to Constrain It
 K. R. Koedinger et al.

PERSPECTIVES

- 938 Unwanted Evolution
 I. Bozic and M. A. Nowak
 >> *Report p. 995*
939 Metamaterials Beyond Optics
 M. Wegener
940 Chromosome Capture Brings It All Together
 N. Kleckner et al.
 >> *Research Article p. 948*
942 A View on Energy Transfer Between Cold Atoms
 E. A. Donley
 >> *Report p. 954*
943 Not an Oxidase, But a Peroxidase
 F. M. Raushel
 >> *Report p. 991*
944 Synapses, Language, and Being Human
 P. Lieberman
 >> *Report p. 987*

ON THE WEB THIS WEEK

>> Science Podcast

Listen to stories on the minimum requirements for a Y chromosome, the future of missile defense, details of an extraordinary gamma-ray burst, and more.

>> Find More Online

Check out *Science Express*, our podcast, videos, daily news, our research journals, and *Science Careers* at www.sciencemag.org.

DEPARTMENTS

- 908 This Week in *Science*
910 Editors' Choice
912 *Science Staff*
999 New Products
1000 *Science Careers*

REVIEW

- 946** Beyond Stem Cells: Self-Renewal of Differentiated Macrophages
M. H. Sieweke and J. E. Allen
Review Summary; for full text:
<http://dx.doi.org/10.1126/science.1242974>

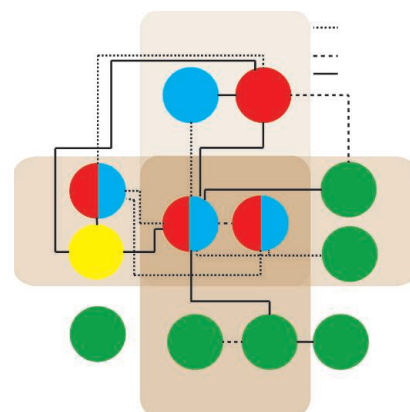
RESEARCH ARTICLES

- 947** Evidence for High-Energy Extraterrestrial Neutrinos at the IceCube Detector
IceCube Collaboration
The IceCube observatory at the South Pole detected neutrinos from outside our solar system.
Research Article Summary; for full text:
<http://dx.doi.org/10.1126/science.1242856>
>> *News story p. 920*
- 948** Organization of the Mitotic Chromosome
N. Naumova et al.
Chromosome conformation changes dramatically during the cell cycle and is unlikely to carry epigenetic information.
>> *Perspective p. 940*

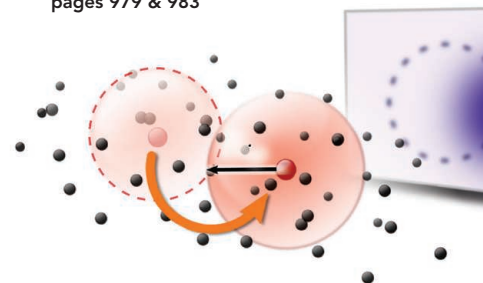
REPORTS

- 954** Observing the Dynamics of Dipole-Mediated Energy Transport by Interaction-Enhanced Imaging
G. Günter et al.
An imaging technique based on a cloud of cold atoms provides a model system to study the coherent transport of energy.
>> *Perspective p. 942*
- 956** Selective C-H Fluorination of Pyridines and Diazines Inspired by a Classic Amination Reaction
P. S. Fier and J. F. Hartwig
A mild fluorination method could help produce compounds of interest in medicinal research.
- 960** Imaging of a Circumsolar Dust Ring Near the Orbit of Venus
M. H. Jones et al.
Imaging data from the STEREO mission indicate the presence of a dust ring around Venus.
- 964** Constraints on the Late Holocene Anthropogenic Contribution to the Atmospheric Methane Budget
L. Mitchell et al.
Records derived from polar ice cores provide constraints on methane emissions during the late preindustrial Holocene.
>> *News story p. 918*

- 967** Commensal Bacteria Control Cancer Response to Therapy by Modulating the Tumor Microenvironment
N. Iida et al.
- 971** The Intestinal Microbiota Modulates the Anticancer Immune Effects of Cyclophosphamide
S. Viaud et al.
The gut microbiota promote the efficacy of several antineoplastic agents in mice.
>> *News story p. 921*
- 976** Substitutions Near the Receptor Binding Site Determine Major Antigenic Change During Influenza Virus Evolution
B. F. Koel et al.
The major antigenic changes of the influenza virus are primarily caused by a single amino acid near the receptor binding site.
- 979** Yeast Reveal a "Druggable" Rsp5/Nedd4 Network that Ameliorates α -Synuclein Toxicity in Neurons
D. F. Tardiff et al.
- 983** Identification and Rescue of α -Synuclein Toxicity in Parkinson Patient-Derived Neurons
C. Y. Chung et al.
Screening in yeast yields an effective therapeutic for Parkinson's patient-derived neuronal stem cells.
- 987** The Human Language-Associated Gene SRPX2 Regulates Synapse Formation and Vocalization in Mice
G. M. Sia et al.
Studies in mice and rats elucidate the function of a protein encoded by a gene that affects language.
>> *Perspective p. 944*
- 991** Evidence that the Fosfomycin-Producing Epoxidase, HppE, Is a Non-Heme-Iron Peroxidase
C. Wang et al.
An iron enzyme previously thought to use O_2 as an oxidant appears to use peroxide instead.
>> *Perspective p. 943*
- 995** Defining Stem Cell Dynamics in Models of Intestinal Tumor Initiation
L. Vermeulen et al.
Common genetic alterations during tumor initiation in the mouse gut reveal clonal advantages.
>> *Perspective p. 938*



pages 979 & 983



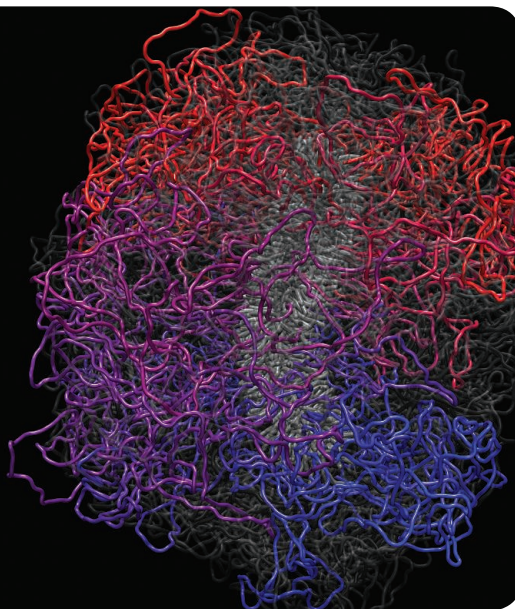
pages 942 & 954

SCIENCE (ISSN 0036-8075) is published weekly on Friday, except the last week in December, by the American Association for the Advancement of Science, 1200 New York Avenue, NW, Washington, DC 20005. Periodicals Mail postage (publication No. 484460) paid at Washington, DC, and additional mailing offices. Copyright © 2013 by the American Association for the Advancement of Science. The title SCIENCE is a registered trademark of the AAAS. Domestic individual membership and subscription (51 issues): \$149 (\$74 allocated to subscription). Domestic institutional subscription (51 issues): \$990; Foreign postage extra: Mexico, Caribbean (surface mail) \$55; other countries (air assist delivery) \$85. First class, airmail, student, and emeritus rates on request. Canadian rates with GST available upon request, GST #1254 88122. Publications Mail Agreement Number 1069624. Printed in the U.S.A.

Change of address: Allow 4 weeks, giving old and new addresses and 8-digit account number. Postmaster: Send change of address to AAAS, P.O. Box 96178, Washington, DC 20090-6178. Single-copy sales: \$10.00 current issue, \$15.00 back issue prepaid includes surface postage; bulk rates on request. Authorization to photocopy material for internal or personal use under circumstances not falling within the fair use provisions of the Copyright Act is granted by AAAS to libraries and other users registered with the Copyright Clearance Center (CCC) Transactional Reporting Service, provided that \$30.00 per article is paid directly to CCC, 222 Rosewood Drive, Danvers, MA 01923. The identification code for Science is 0036-8075. Science is indexed in the Reader's Guide to Periodical Literature and in several specialized indexes.

Chromosome Conundrum >>

The three-dimensional organization of chromosomal DNA within the cell nucleus plays an important role in gene regulation. **Naumova *et al.*** (p. 948, published online 7 November; see the Perspective by **Kleckner *et al.***) used chromosome conformation capture-based methods in human tissue culture cells to analyze the higher order folding of human chromosomes across the cell cycle. During interphase the chromosomes showed locus-specific compartmentalization. In mitotic cells, on the other hand, the chromosome organization was more linear, consistent with arrays of consecutive chromatin loops.



Imaging Excitations

Complex processes such as chemical reactions and photosynthesis involve the transport of energy. The mechanisms of how the energy migrates, the influence of the surrounding environment, or the extent to which quantum mechanics affects the process remain unclear. **Günter *et al.*** (p. 954, published online 7 November; see the Perspective by **Donley**) found that a cloud of cold atoms suitably prepared and decorated with “impurity” Rydberg atoms could be used to image the transport of excitations between excited Rydberg atoms directly. This ability to tune the influence of the background environment may help in the study of the coherent transport of energy in complex many-body systems.

Fluorinating Pyridine

Appending fluorine substituents to carbon centers is commonly used to tune small-molecule properties in pharmaceutical and agrochemical research. However, fluorinations often require the use of corrosive, hazardous reagents. **Fier and Hartwig** (p. 956) present an unusually mild and convenient protocol for fluorinating carbon sites adjacent to nitrogen in pyridines and related nitrogen-bearing arenes. The reaction entails treatment with silver difluoride and proceeds rapidly at room temperature.

Bipolar Signature

Atmospheric methane has increased approximately 2.5-fold since the start of the industrial revolution, a consequence of human activity. However, a smaller and more gradual rise began

around 6000 years ago, near the time when human agriculture began to develop and expand. **Mitchell *et al.*** (p. 964) present two, high-resolution ice core methane records of the past 2500 years, one from each pole. Methane emissions were primarily from the tropics, with secondary contributions from the higher latitudes where most humans lived. Thus, both natural and human sources are needed to explain the late-Holocene atmospheric methane record.

Building Vocalization

The transcription factor FoxP2 (forkhead box P2) affects language acquisition in humans and regulates the protein SRPX2 (sushi repeat-containing protein X-linked 2), which itself also affects language. **Sia *et al.*** (p. 987, published online 31 October; see the Perspective by **Lieberman**) found that in the mouse brain, the FoxP2 transcription factor binds to the *SRPX2* gene. In tissue culture experiments, FoxP2, but not SRPX2, affected dendritic morphology, while both FoxP2 and SRPX2 affected the formation of excitatory synapses. Overexpression of SRPX2 in the mouse brain equivalent of the human brain’s language area affected synapse density and disrupted the ultrasonic vocalizations emitted by mouse pups in search of their mothers.

The Microbiota Makes for Good Therapy

The gut microbiota has been implicated in the development of some cancers, such as colorectal cancer, but—given the important role our intestinal inhabitants play in metabolism—they

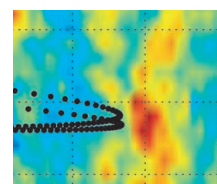
may also modulate the efficacy of certain cancer therapeutics. **Iida *et al.*** (p. 967) evaluated the impact of the microbiota on the efficacy of an immunotherapy [CpG (the cytosine, guanosine, phosphodiester link) oligonucleotides] and oxaliplatin, a platinum compound used as a chemotherapeutic. Both therapies were reduced in efficacy in tumor-bearing mice that lacked microbiota, with the microbiota important for activating the innate immune response against the tumors. **Viaud *et al.*** (p. 971) found a similar effect of the microbiota on tumor-bearing mice treated with cyclophosphamide, but in this case it appeared that the microbiota promoted an adaptive immune response against the tumors.

From Yeast to Therapeutic?

Yeast has shown some promise as a model system to generate lead compounds that could have therapeutic potential for the cellular problems associated with neurodegenerative diseases. Along these lines, **Tardiff *et al.*** (p. 979, published online 24 October) and **Chung *et al.*** (p. 983, published online 24 October) describe the results of multiple screens in yeast that lead to the identification of a potential therapeutic compound to combat the cytotoxic affect of α -synuclein accumulation. The compound was able to reverse the pathological hallmarks of Parkinson’s disease in cultured neurons derived from patients with α -synuclein-induced Parkinson’s disease dementia.

Venus’ Orbit in STEREO

Around Earth’s orbit there is a circumsolar dust ring composed of particles of cometary and asteroidal origin. Tenuous dust rings are believed to be commonly associated with planets, but—other than around Earth—have not been detected. Now, **Jones *et al.*** (p. 960) have used observations from the solar terrestrial relations observatory (STEREO) to map a dust ring associated with the orbit of Venus.



Limiting Tumor Initiation

What is the competitive advantage of cells with frequently occurring mutations during tumor development? **Vermeulen *et al.*** (p. 995; see the Perspective by **Bozic and Nowak**) quantified the advantages of *Apc*-loss, *Kras* activation, and *P53* mutation during tumor initiation in the mouse intestine. The mutations conferred only a limited clonal advantage. Indeed, many mutated stem cells were stochastically replaced by wild-type stem cells, helping to limit tumor initiation.

CREDITS (TOP TO BOTTOM): IMAGES GENERATED BY MAXIM IMAKAEV WITH INPUT FROM GEOFF FUDENBERG AND NATALIA NAUMOVA; JONES ET AL.

Additional summaries

Macrophage Makeover

Macrophages are important immune cells that function in tissue repair during homeostasis and in the innate immune response. Inflammation, which can be triggered by infection, is accompanied by a massive expansion of macrophages in affected tissues. The major source of this increase in resident macrophages has been thought to be hematopoietic stem cells in the bone marrow. However, recent results have shown that the mature differentiated macrophages residing in the affected tissues can themselves proliferate to boost cell numbers. **Sieweke and Allen** (p. 946) review what we know about the origin of macrophages and outline the consequences of local macrophage proliferation for the immune response and tissue homeostasis.

Extraterrestrial Neutrinos

Neutrinos are thought to be produced in astrophysical sources outside our solar system but, up until recently, they had only been observed from one supernova in 1987. **Aartsen et al.** (p. 947; see the cover) report data obtained between 2010 and 2012 with the IceCube neutrino detector that reveal the presence of a high-energy neutrino flux containing the most energetic

neutrinos ever observed, including 28 events at energies between 30 and 1200 TeV. Although the origin of this flux is unknown, the findings are consistent with expectations for a neutrino population with origins outside the solar system.

Flu Drift Limited

Five antigenic sites in the virus surface hemagglutinin protein, which together comprise 131 amino acid positions, are thought to determine the full scope of antigenic drift of influenza A virus.

Koel et al. (p. 976)

show that major antigenic change can be caused by single amino acid substitutions. These single substitutions substantially skew the way the immune system “sees” the virus.

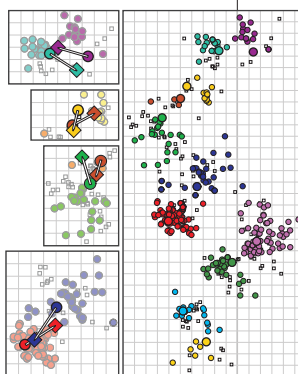
All substitutions of importance are located next to the receptor-binding site in the hemagglutinin. Because there are few positions of importance for

antigenic drift, there are strict biophysical limitations to the substitutions at these positions, which restricts the number of new antigenic drift variants at any point in time. Thus, the evolution of influenza virus may be more predictable than previously thought.

Just Add Peroxide

The HppE enzyme uses iron to catalyze oxidation of an alcohol to an epoxide ring in

the biosynthesis of the antibiotic fosfomycin. Because this process is a two-electron oxidation, it has been unclear how the enzyme reduces its presumed oxidative partner O_2 all the way to water. Where do the two extra electrons come from? **Wang et al.** (p. 991, published 10 October; see the Perspective by **Rauschel**) now show that HppE is actually a peroxidase, and thus reduces H_2O_2 , for which just two electrons are sufficient. The result expands the structural scope of iron-bearing peroxidase enzymes beyond heme motifs.





Marcia McNutt is Editor-in-Chief of *Science*.

Bridge or Crutch?

LAST WEEK, THE U.S. ENERGY INFORMATION ADMINISTRATION (EIA) REPORTED THAT THE COUNTRY produced more crude oil than it imported for the first time in two decades.* Over the past 5 years, the United States has reduced its dependence on imported oil by nearly 50%, largely through the use of hydraulic fracturing (“hydrofracking”) to tap into oil resources in shale rock in the northern Great Plains. The United States is now also the world leader in shale gas production: 39% of domestic gas supplies are derived from this unconventional resource.† Although this change in the nation’s energy portfolio is welcome news, scientists and policy-makers need to be wary of complacency.

The development of home-grown energy has a number of clear benefits. Beyond the obvious positive impacts on the balance of payments, domestic jobs, and reducing national security concerns, inexpensive domestic natural gas is less of an environmental concern than other fossil fuels for electricity generation. For example, by converting coal-fired power plants to ones that run off of natural gas, mercury pollution is avoided. In addition, for the same amount of energy production, natural gas emits less CO₂ when burned than either oil or coal, thus mitigating some global warming.

However, questions remain as to the net impact of the switch to natural gas. Hydrofracking is a consumptive use of water, and the disposal of that water deep underground has been linked to an uptick in small to moderate earthquakes.‡ To truly compare the emissions from burning natural gas to other solutions, one must accurately account for CO₂ gas that is inadvertently released to the atmosphere in the production process. Scientists have been quick to constrain this contribution to climate warming using a variety of approaches, with the conclusion that the gas lost during production is less than 0.5%.§ Although such emissions are not significant enough to change the conclusion that natural gas has a lower CO₂ footprint than coal or oil, the fugitive gas problem should be eliminated with better technology. Furthermore, every shift in the energy marketplace has global reactions. The change to gas at the expense of coal in the United States increases the amount of coal available for export. The important question is, what is the net change in the global load of mercury and CO₂?

It is unknown how long the U.S. gas and oil booms will continue. Wells drilled into discontinuous shale rock formations peak in their production after the first year and then decline rapidly. The formations are not sufficiently permeable to allow free flow of the hydrocarbons through naturally existing pore spaces, and only artificially induced fractures provide access to fluids. Predictions of when this resource will be depleted have been notoriously unreliable, because as technology advances and prices increase, it will be possible to produce fossil fuels that were previously technically or economically not accessible. Alternatively, we could deplete domestic gas rapidly and become dependent for our energy needs on China, ranked number 1 among 41 nations assessed for future technically recoverable shale gas resources (according to the EIA).

Most important, the current energy bonanza should not impede a rapid transition to a renewable energy future. Renewable energy technologies can retain the same benefits of the current gas boom, but they have clear global benefits as well. Some of the renewable technologies under development are distributed and individualized, such as personal solar cells with power storage, which are far more suited to the quarter of the world that has no access to electricity. However, if the developed world does not bring these technologies to market, they will not be available to anyone. Natural gas has been touted as a bridge to our renewable energy future. Let’s make sure it is indeed a bridge and not a crutch.

— Marcia McNutt

10.1126/science.1248348



*www.eia.gov/forecasts/steo/pdf/steo_full.pdf. †www.eia.gov/todayinenergy/detail.cfm?id=13491&src=Natural-b2.

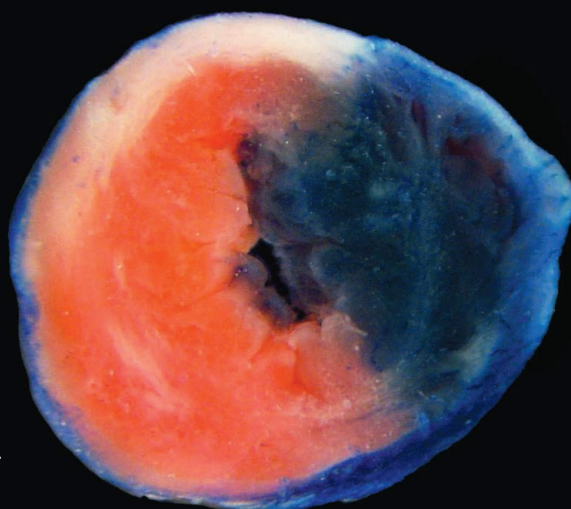
‡W. L. Ellsworth, *Science* **341**, 1225942 (2013); R. D. Vidic *et al.*, *Science* **340**, 1235009 (2013). §D. T. Allen *et al.*, *Proc. Natl. Acad. Sci. U.S.A.* **10.1073/pnas.1304880110** (2013).

BIOMEDICINE

NO Mechanism

Although nitrogen-containing compounds have been used to treat heart failure for well over 1000 years, in many cases their mechanisms of action are unclear. Huang *et al.* now show that agents that increase the production of nitric oxide (NO) can influence heart function through S-nitrosylation of the enzyme GRK2; this protein kinase phosphorylates G protein—coupled receptors, most notably the β -adrenergic receptor, that have critical roles in regulating heart function. They found that GRK2 associates with endothelial NO synthase, the enzyme that produces NO, and nitrosylation of GRK2 inhibits its activity. In a mouse model of heart failure, treatment with agents that increased NO concentrations protected myocytes from cell death, but this effect was lost in animals expressing a mutant form of GRK2 that could not be S-nitrosylated. — LBR

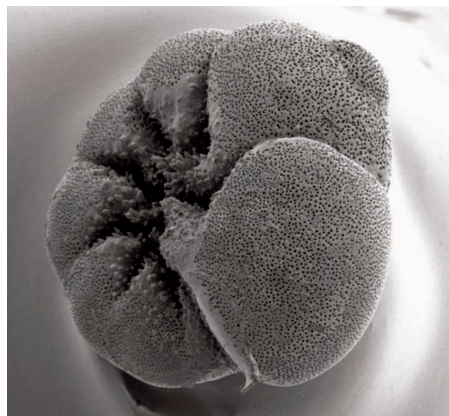
Sci. Signal. 6, ra95 (2013).



GEOLOGY

Uptake Uptick

Foraminifera are tiny aquatic organisms that have mineralized shells composed of calcium carbonate. In marine environments, these structures precipitate from seawater; thus foraminifera shells preserved in the sedimentary record reflect the chemistry and temperature of ancient oceans. However, models of the



uptake of Ca and other trace elements do not entirely explain the concentration and ratio of ions preserved in carbonate shells. Using a combination of isotopic and fluorescent imaging of incubated cultures, Nehrke *et al.* show that passive ion transport is important for trace elements such as Mg and Sr in an extant foraminifera species, but not Ca. Transmembrane transport as the predominant uptake mechanism of Ca helps explain not only the observed

Mg/Ca and Sr/Ca ratios in recently grown shells but also their relation to changes in seawater chemistry, and thus past ocean temperatures. — NW

Biogeosciences 10.5194/bg-10-6759-2013 (2013).

VIROLOGY

Stochastic Reservoir

A major challenge in attempting to eradicate HIV is the virus that remains latent (transcriptionally inactive) in infected cells; current pharmacological therapies focus on inhibiting various steps in the HIV life cycle. It has been thought that the reason latent viruses are inactive is either that they infected T cells that were transitioning to a resting state or that the viruses themselves were defective. The latent reservoir has been measured in the past by one of two methods: forcing all T cells to become active and then measuring viruses that have been induced to replicate (which could lead to underestimates, because not all proviruses have been induced) or identifying all integrated proviral DNA (which may include defective genomes that would never replicate). Ho *et al.* have gone further, by analyzing the viruses that remained inactive after T cell activation. Intact viral genomes were found in nearly 12% of the clones analyzed. When they synthesized a sample of the genomes and reconstructed these viruses, replication occurred with normal growth kinetics, and promoter function appeared normal. The reason for latency was not that the viruses had integrated into heterochromatin, whence transcription would

be suppressed, nor had these noninduced viruses been silenced by CpG methylation. This makes the prospects for a sterilizing cure look somewhat farther away—the authors conclude that the latent reservoir may be as much as 60 times larger than previous estimates. — BJ

Cell 155, 540 (2013).

ECOLOGY

Maternal Choice

Temperature-dependent sex determination (TSD), a phenomenon in which offspring sex is affected by the temperature experienced during embryonic development, occurs in many ectothermic species, such as reptiles and fishes. However, a purely environmental control of sex could lead to evolutionarily unstable sex ratios, suggesting that selection for a maternal behavior, such as the choice of nest sites, could be strong. Mitchell *et al.* used a set of controlled experiments in painted turtles to test whether nest sites selected by females affected sex ratios. That is, they cross-fostered eggs and hatchlings in nest sites that had been chosen by mother turtles, relative to sites selected at random, across both the incubation and hatchling hibernation stages. They found no difference in survival or success between maternally or randomly selected nest sites, but random sites yielded a significant male bias in offspring, with maternal sites—characterized by a more open canopy, more solar radiation, and warmer temperatures in the nest—being more balanced. These results show that maternal influence on sex ratio is probably an important component of reproduction in species with TSD.

Further, the habitats selected by female turtles in this study, specifically warmer sites with less vegetation, indicate the potential for conflict with viability selection in this and other ectothermic species as the climate warms. — SNV

Proc. R. Soc. London Ser. B. **280**, 20132460 (2013).

CHEMISTRY

Water-Splitting Standards

Widespread use of functional electrocatalytic water-splitting systems in conjunction with solar power infrastructure will probably require a composition of Earth-abundant materials that remain stable under the reaction conditions and operate efficiently at minimal overpotential (a measure of how much of the input energy gets stored in the products' chemical bonds for later use when the Sun has set, rather than lost as heat). Numerous reports highlight favorable features of particular experimental catalysts in this context, but cross-comparisons have proven challenging in the absence of established standards for the testing conditions. McCrory *et al.* offer a preliminary framework for making apples-to-apples comparisons of catalysts for the oxygen-evolving half of the couple. They report benchmark tests of nine representative non-precious metal catalysts deposited on glassy carbon electrodes, under standardized acidic (1 M sulfuric acid) and basic (1 M sodium hydroxide) conditions. After first assessing the active surface area for normalization, the authors measured the overpotential necessary to attain a current density of 10 mA/cm² and then tracked performance over 2 hours. None of the tested non-precious metal catalysts were stable in acid, highlighting a priority for further research. In base, the overpotentials across the test set varied relatively little, spanning a range between 350 and 430 mV. — JSY

J. Am. Chem. Soc. **135**,
16977 (2013).

MATERIALS SCIENCE

A Battery for Twos

In theory, Mg batteries can obtain higher energy density and specific energy than Li-based ones, because of the divalent nature of the Mg ion. They may also prove safer than those that rely on Li metal. However, it has been a challenge to find materials that can allow for the fast and reversible insertion of Mg²⁺. Wang *et al.* explore

materials from the Prussian Blue family, which have an open framework and a crystal structure similar to those of ABX₃ perovskites. For their materials, the B sites were occupied with either Ni²⁺ at the N-coordinated sites or Fe³⁺ at the C-coordinated sites, linked together with cyano (CN) groups, which increase the separation distance between the Ni and Fe ions to allow for cation insertion. Nickel hexacyanoferrate was synthesized as nanoparticles and combined with a C cloth as the working electrode. Over 2000 cycles, they were able to reversibly insert and remove Mg²⁺, Ca²⁺, Sr²⁺, and Ba²⁺, when using the appropriate electrolyte. The specific capacity tended to decrease with cycling, but that was probably due to the dissolution of Ni²⁺ into the electrolyte; the capacity loss was eliminated by dissolving Ni²⁺ into the electrolyte before cycling. Changes in the hysteresis seen with increasing charge/discharge rates suggest that there might be a rate-limiting dehydration step during the insertion process. — MSL

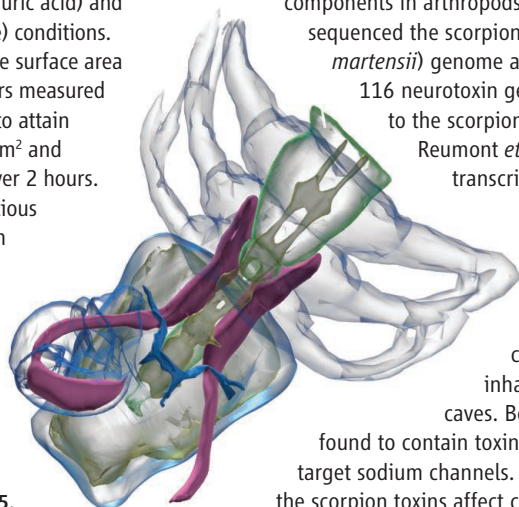
Nano Let. 10.1021/nl403669a (2013).

GENETICS

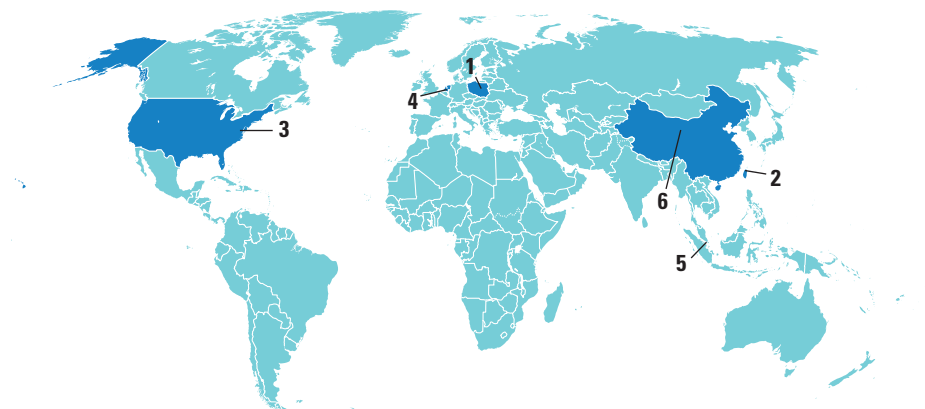
Venom Genetics

Two papers describe the use of genomics in identifying genes encoding venom components in arthropods. Cao *et al.* sequenced the scorpion (*Mesobuthus martensii*) genome and identified 116 neurotoxin genes specific to the scorpion lineage; von Reumont *et al.* profiled the transcriptome of the remipede (*Speleonectes tulumenensis*), which is a blind crustacean that inhabits underwater caves. Both species were found to contain toxins that probably target sodium channels. Additionally, the scorpion toxins affect chloride and potassium channels, whereas the remipede delivers peptidases and chitinases into its victims. A phylogenetic analysis of agatoxins, which are found in this remipede and in venomous spiders, suggests that the remipede neurotoxins evolved independently after gene duplication from a non-venom gland paralog. Similarly, tandem arrays of toxin genes were found in the scorpion, hinting at how gene duplication contributed to the genesis of toxin diversity. — LMZ

Nat. Comm. **4**, 10.1038/ncomms3602 (2013);
Mol. Biol. Evol. **30**, 10.1093/molbev/mst199 (2013).



AROUND THE WORLD



Warsaw 1

Climate Negotiators Pressed About Ocean Acidification

The argument for cutting greenhouse gas emissions often rests on global warming's impact on terra firma. But scientists are increasingly confident that climate change will disrupt the oceans as well. Researchers working with the International Geosphere-Biosphere Programme argued that case this week at a meeting of the United Nations Framework Convention on Climate Change in Poland.

Marine waters are becoming more acidic as they absorb carbon dioxide from the atmosphere, and the researchers warned convention delegates that they had "high con-



Vulnerable. Acidic oceans will likely erode coral reefs faster than they can build up.

fidence" that increasing acidity will erode coral reefs in the tropics faster than they can build up. Mollusks and other shelled creatures will also suffer, although the extent of the economic harm is hard to predict, they further noted in a summary report released at

the meeting. Reducing emissions could slow, but not prevent, the changes.

The meeting, which wraps up 22 November, is intended to help delegates prepare for U.N. negotiations in 2015, which they hope will yield a major climate treaty.

http://scim.ag/_acid

Taipei 2

Yet Another Avian Flu Virus Found in a Human

Scientists in Taiwan have identified the first known human infection with the avian influenza virus subtype H6N1. The female patient, hospitalized in May, suffered moderate but not life-threatening illness and recovered after antiviral drug treatment.

H6N1 is common in wild and domestic birds worldwide and has affected Taiwan's poultry since the 1970s, causing minor symptoms. But it had never before been found in humans—even though the predominant H6N1 strain circulating in poultry in Taiwan since 2000 has a genetic mutation that might allow it to more readily latch on to human lung cells. "It is possible that people have been infected but not recognized due to their mild symptoms," says

Ho-Sheng Wu of Taiwan's Centers for Disease Control in Taipei. The recent patient had had no contact with live poultry, and no close contacts had been infected. If the virus mutates further, it could threaten human health, Wu and his colleagues reported online on 14 November in *The Lancet Respiratory Medicine*.

Washington, D.C. 3

Congress Boosts Chimp Retirement Funding

Congress approved a bill last week that will allow the National Institutes of Health (NIH) to move forward with plans to retire most of its research chimpanzees. NIH decided ear-



Golden years. More NIH research chimpanzees will be heading to Chimp Haven.

lier this year to phase out most NIH-funded invasive studies on chimpanzees and to retire all but 50 of its 360 research chimpanzees. But its spending on the federal chimpanzee sanctuary, housed at Chimp Haven in Keithville, Louisiana, was expected to hit a \$30 million cap, instituted by Congress in 2000, by the end of November.

Both the House of Representatives and the Senate approved a bill to lift the spending cap, allowing NIH to spend up to \$9 million to \$12 million a year over the next 5 years on the federal sanctuary if that is cheaper than keeping NIH's chimpanzees at research facilities (which it should be). The bill has now gone to President Barack Obama for his signature.

http://scim.ag/_chimp

NOTED

>Some planetary scientists last week expressed concern over NASA's 15 November decision to **cancel the Advanced Stirling Radioisotope Generator project**. Dwindling supplies of plutonium-238 had motivated the space agency to invest in a more efficient isotope-based power source for deep space missions, but the U.S. Department of Energy resumed production of the radioactive element this year. Budget constraints also prompted the move, NASA said.

CREDITS (TOP TO BOTTOM): CHIMP HAVEN/NIH; NOAA



'Panda of Indochina' Makes a Camera-Trap Cameo

A last-gasp attempt to save the critically endangered saola may be paying dividends. For the first time since 1999, this antelopelike creature has been spotted in the wild. The new photo documentation—from a camera trap in Vietnam's Annamite Mountains—is a huge morale-booster, says zoologist William Robichaud, coordinator of the International Union for Conservation of Nature's Saola Working Group. It "shows we should never give up hope."

The saola was the first large mammal discovered in half a century when it was described in 1992. But the ungulate gets caught in snares set for civets and deer, and its numbers have dwindled to a few hundred at most.

Over the past few years, Vietnamese villagers have removed more than 30,000 snares from critical saola habitat. The secret spot where the new saola was spotted "will be completely locked down," Robichaud says. <http://scim.ag/Unic0rn>



1895, the London-based ICZN has set rules for naming newly identified species and resolved disputes over names for animals both living and extinct. But the U.K.-based charitable trust that supported ICZN has run out of money. The National University of Singapore (NUS) and the Natural History Museum in London announced on 18 November that they will come to the commission's aid: While the editor of ICZN's *Bulletin of Zoological Nomenclature* will remain at the Natural History Museum, the commission's secretariat, with one full-time staffer coordinating its worldwide activities, will be based at NUS. The arrangement is intended to provide some breathing room so that ICZN can ponder ways to ensure its long-term survival. Vice President Daphne Fautin predicts that if the commission disappeared, the world of nomenclature would fall into "a period of chaos."

http://scim.ag/_ICZN

Zhangye, China 6

City Bans 'Genetic Bombs'

A new round of debate over genetically modified (GM) crops has erupted this month in China after the northwest city of Zhangye on 25 October announced a ban on the sale and use of GM seeds. The ban—



GM cotton

part of the city's regulation to ensure food safety and to support organic crops—makes Zhangye the first city in China to officially outlaw the growing of GM crops.

Environmental groups applauded the move, but it is at odds with a national policy that promotes the production of new GM crops. In defending the decision, Chen Kegong, Zhangye's Communist Party secretary, on 5 November told reporters the city will "unyieldingly uphold" the ban on planting "genetic bombs." >>

The Hague, the Netherlands 4

Dutch Push for Open Access

The Dutch government wants to make all publicly funded research freely accessible within 10 years—and it believes the "gold" model, in which authors pay to be published in freely available online journals, is the way to get there. In a 15 November letter to the Dutch House of Representatives, State Secretary for Education, Culture and Science Sander Dekker announced measures to speed up the transition to open access (OA): The government will host a 2014 roundtable between scientific organizations and academic publishers and will require universities and research organizations to produce annual OA reports. It may make OA compulsory by law in 2016.

Dekker's clear preference for "gold," favored by publishers because it protects their revenues, has irked some OA watchers. The Dutch government "fell for the publishing lobby's nocturnal fantasy," says OA advocate Stevan Harnad, who advocates a bigger role for "green" OA, in which authors can publish in any journal as long as they archive a copy of each paper in a freely accessible electronic archive.

Singapore 5

Zoological Naming Authority Rescued

The International Commission on Zoological Nomenclature (ICZN) has found a new home in Asia and—at least for the moment—some financial security. Since

Random Sample

Epic Sperm Fight Wins 2013 'Dance Your Ph.D.' Contest

The votes are in, and the top prize for the 2013 "Dance Your Ph.D." competition goes to ... Cedric Tan, a postdoc biologist at the University of Oxford in the United Kingdom, who finished his Ph.D. there last year with a thesis titled "Sperm competition between brothers and female choice." His dance interpretation of that research illustrates the chicken mating process using a range of dance styles, from swing and water ballet—yes, in actual water—to modern jazz and what can only be described as cockfighting.

The contest, now in its 6th year, is sponsored by *Science* magazine and AAAS (publisher of *Science*). Based on votes from previous winners

and an independent panel of artists and scientists, Tan won both the biology category and the overall prize: \$1000 and a trip—sponsored by HighWire Press—to screen his video at Stanford University in Palo Alto, California. Tan spent a year on the video, in the midst of a busy field season massaging male chickens to extract their sperm. "I assembled the team, trained them, forced tight skimpy attires on them (they complained a lot), forced them into the freezing cold lake (they hated me for it)," Tan explains by e-mail. According to the judges, this year was the strongest yet. Watch Tan's video, plus the \$500 winners for the chemistry, physics, and social sciences categories at <http://scim.ag/phdance>.



>> AROUND THE WORLD

China grows more than 4 million hectares of GM crops, mostly cotton expressing a pesticide protein, although approval for commercial cultivation of GM corn and rice remains delayed. Luo Yunbo of China Agricultural University says the ban doesn't reflect a broader change in national policy.

NEWSMAKERS

Two Researchers to Round Out DOE Science Team

President Barack Obama has added two academic researchers to his science team at the U.S. Department of Energy (DOE). On 18 November, he nominated chemical engineer **Franklin "Lynn" Orr**, a professor and administrator at Stanford University in California, to fill the newly created position of undersecretary for science and energy. The new post will oversee DOE's Office of Science, as well as fossil, nuclear, and renewable energy research programs and electrical grid and technol-



ogy transfer issues. Orr directs Stanford's Precourt Institute for Energy and served as dean of the School of Earth Sciences from 1994 to 2002. Obama tapped physicist **Marc Kastner** of the Massachusetts Institute of Technology (MIT) in Cambridge to lead the Office of Science. He has served as dean of MIT's School of Science since 2007. "Obama made an inspired choice," MIT President L. Rafael Reif said in a statement, adding that Kastner is "ideally suited" to manage DOE's \$4.6 billion research portfolio. If confirmed by the U.S. Senate, Kastner would replace William Brinkman, who left this past April. <http://scim.ag/DOEteam>

ogy transfer issues. Orr directs Stanford's Precourt Institute for Energy and served as dean of the School of Earth Sciences from 1994 to 2002.

Obama tapped physicist **Marc Kastner** of the Massachusetts Institute of Technology (MIT) in Cambridge to lead the Office of Science. He has served as dean of MIT's School of Science since 2007. "Obama made an inspired choice," MIT President L. Rafael Reif said in a statement, adding that Kastner is "ideally suited" to manage DOE's \$4.6 billion research portfolio. If confirmed by the U.S. Senate, Kastner would replace William Brinkman, who left this past April. <http://scim.ag/DOEteam>

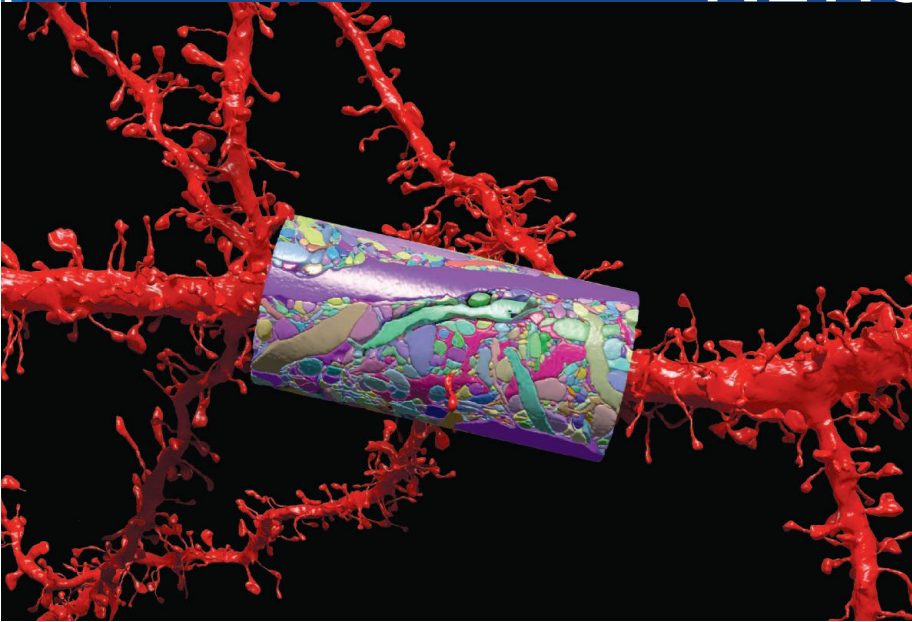
BY THE NUMBERS

62% Portion of Europeans who feel that "science makes our ways of life change too fast," based on a European Commission public opinion survey published last week. <http://scim.ag/Eurpoll>

1 to 2 million Additional babies to be born in China each year as a result of loosening the one-child policy, according to demographers (the present rate: 15 million per year). <http://scim.ag/1China>

Science LIVE

Join us on Thursday, 5 December, at 3 p.m. EST for a live chat with experts on a hot topic in science. <http://scim.ag/science-live>



Fine structure. A composite of artificially colored EM images reveals details within a cylinder of mouse brain tissue, smaller than a grain of sand, that contains 680 nerve fibers and 774 synapses.

NEUROSCIENCE

New Tools Light Up the Intricacies of the Brain

SAN DIEGO, CALIFORNIA—Last week, nearly 5000 of the roughly 30,000 researchers at the Society for Neuroscience conference here crammed into an auditorium to see neuroscientist Jeff Lichtman of Harvard University present a few salt grain–sized chunks of mouse brain. When magnified to fill several large projection screens, a small part of one of these revealed a cylinder of tissue in unprecedented detail: 680 nerve fibers, 79 branched projections called dendrites, and 774 synapses—the junctions where chemical signals jump from neuron to neuron.

Such a precise inventory of the contents of one tiny speck of cortex—just one-billionth of a mouse brain—was unthinkable only a few years ago. But recent advances in high-throughput, automated electron microscopy, from Lichtman's group and others, are “opening a new era” in which investigators study brain circuitry at the level of individual synapses, says Yuan Liu, a program director at the National Institute of Neurological Disorders and Stroke in Bethesda, Maryland, which funds Lichtman's work.

For Liu, Lichtman's talk was a highlight of the meeting because it shows that new technologies and techniques could one day fulfill the promise of President Barack Obama's controversial BRAIN Initiative (*Science*, 1 March, p. 1022), which aims to

speed up the mapping of the human brain's structure and activity. “We cannot afford to give all our money to tech development,” she says, but the value of such investment “really shows” in work such as Lichtman's.

To others, the dizzying complexity of Lichtman's data, assembled from many thousands of 30-nanometer-thin sections over the course of months, was worrisome. Despite producing 100 terabytes of data and some beautiful images, it provided scant new insight into how the brain's complexity is organized, contends neuroscientist Partha Mitra of Cold Spring Harbor Laboratory in New York. Simply describing neural circuitry at this minute level “is far from adequate for anyone wanting to make sense of the brain, and we are not even down to the atomic or molecular scale,” he says. “If you take apart any object around you atom by atom, you will get a mass of complicated detail, but that is not how we have gained insight into the chemical and physical properties of the world.”

Lichtman has heard such skepticism for years as one of the early pioneers in creating detailed wiring diagrams of neural circuits. In 2007, he and colleagues released Brainbow, a method of distinguishing among nerve cells by breeding animals to express random combinations of red, green, and blue fluorescent protein in their neurons.

The technique has aided the mapping of connections in the peripheral system, but has fallen short in distinguishing the densely packed and overlapping neurons of the central nervous system (CNS). New versions of Brainbow that allow more colors, highlight cell membranes rather than cell bodies, and employ fluorescent proteins from different species that allow better antibody labeling have been released this year. Lichtman predicts they will finally start to unravel the CNS connectome, but for now electron microscopy remains the most effective method for tracing its cells, he says.

Mapping the brain at the synaptic level—a resolution 1 trillion times finer than that of a functional magnetic resonance imaging scan—strikes many people as crazy, admits Bobby Kasthuri, one of Lichtman's postdoctoral students. But the detail in the new electron micrographs can be revelatory, Lichtman says. For example, one clear finding from the cortex images is that “you can't just infer synapses” based on where axons and dendrites intersect, he says. “Really seeing what's there gives you a way of framing your ideas better than imagining it,” adds neuroscientist Eve Marder of Brandeis University in Waltham, Massachusetts.

Even as some neuroscientists debated the merits of Lichtman's images, other emerging technologies beckoned in San Diego. A crowd of graduate students buzzed around Stanford University neuroscientist Karl Deisseroth, the inventor of optogenetics, a widely adapted technique for making neurons responsive to light, and CLARITY, a technology that makes brain tissue transparent. Next to him, ghostly fields of firing neurons flickered on a video screen, demonstrating Deisseroth's latest, yet-to-be published brainchild.

Called SWIFT-volume imaging, the technique captures firing of extensive neural circuits in animals whose neurons have been genetically engineered to glow when triggered. To watch the neurons in action, researchers drill a hole into a rodent's skull and employ a microscope that, thanks to new optics and computational techniques, can image and analyze the firing patterns of large, 3D groups of neurons—more than 1000 cells at once, according to Logan Groenick,

a graduate student in the Deisseroth lab who spearheaded the technique. The neurons can be recorded while the animal runs in place on a ball or learns different tasks in a virtual reality environment.

Similarly, in zebrafish, whose nerve cells are visible through largely transparent flesh, the technique allows the activity of individual neurons to be monitored as a fish swims and learns to avoid certain

areas or go to others containing rewards. The technique promises to track real-time activity in major brain structures known to influence behavior, says Mehmet Fatih Yanik, a neuroscientist and engineer at the Massachusetts Institute of Technology in Cambridge. “I think it will be adopted very rapidly by other labs, including my own.”

Warranted or not, enthusiasm for the new techniques is irrepressible. “I won’t

ever stop doing this,” says Kasthuri of his electron microscopy work. “I’m going to try to convince every person I ever meet that this is the way to do this.” The young researchers clustered around Deisseroth’s posters clearly felt similar excitement: At 5 p.m. on Wednesday night, at the tail end of a weeklong conference, security had to shoo them out of the building.

—EMILY UNDERWOOD

CLIMATE CHANGE

Humans Fueled Global Warming Millennia Ago

People were already pumping greenhouse gases into the atmosphere 5000 years before the Industrial Revolution, air bubbles in Antarctic ice suggest. The new evidence—in part from an exceptional record of atmospheric methane freshly cored from the West Antarctic Ice Sheet—supports a paleoclimatologist’s provocative idea that humanity began

of previous glacial periods. But then, about 5000 years ago, methane began to rise in a way that no one could explain.

Delving into the archaeological literature, Ruddiman noted that the methane increase occurred at about the same time as people started cultivating rice in what were essentially manmade, methane-producing wetlands. The

purely natural, so lone ice cores couldn’t give Ruddiman’s hypothesis a rigorous test. Then geochemist Logan Mitchell, now at the University of Utah in Salt Lake City, and colleagues decided to compare the methane trapped over time in two ice cores: one retrieved from Greenland in the 1990s and the other from the West Antarctic Ice Sheet in late 2011—the best record so far from the Southern Hemisphere. Because air circulation tends to be confined within one hemisphere or the other, atmospheric methane produced in one is slow to spread to the other. So methane concentrations can differ between the north and south in ways that reflect the relative sizes and locations of sources.

The results, reported on page 964, show that from 2800 to 600 years ago—the period most easily tested—atmospheric methane rose 17%. Levels started out higher in the Northern Hemisphere, as they are today, but they rose in tandem so that the north-south difference remained unchanged. Natural wetlands could have driven the global rise in the Southern Hemisphere, but Mitchell and his colleagues found a need for a human source—presumably Ruddiman’s expanding rice cultivation—to drive the rise in the Northern Hemisphere.

“Fully one or the other [source] wouldn’t fit the data,” says ice-core paleoclimatologist Eric Wolff of the University of Cambridge in the United Kingdom. “They end up with a bit of both, which is probably okay. It’s reasonably persuasive.”

Ruddiman himself is encouraged. The community’s attitude “is changing slowly,” he says, adding that “it’s in the right direction.” But he notes that modelers have failed to show how natural processes on their own could have boosted methane, much less carbon dioxide, thousands of years ago. Even in the early days of global warming, he thinks, humans must have been the major force.

—RICHARD A. KERR



Closer look. An exceptionally detailed Antarctic ice-core record shows that expanding rice cultivation, plus natural forces, kicked off global warming 5000 years ago.

warming the world early, as methane bubbled out of early rice farmers’ paddies.

Paleoclimatologist William Ruddiman, now a professor emeritus at the University of Virginia in Charlottesville, proposed his early-warming hypothesis 10 years ago after studying ice core records available at the time (*Science*, 16 January 2004, p. 306). Bubbles of ancient air, trapped when fallen snow turned to ice, showed that methane levels declined as the last ice age was ending 10,000 years ago—just as they had done at the end

coincidence suggested humans were behind the rise. And 8000 years ago, another greenhouse gas, carbon dioxide, also began rising suspiciously—perhaps because early farmers were clearing forests for agriculture. Together, Ruddiman calculated, the added greenhouse gases could have warmed the world by 0.8°C, about as much as humans have warmed the world over the past century or two.

Skepticism was widespread in the paleoclimate community. Methane molecules don’t come labeled as human-generated or

Proposed Tweaks to NSF Peer Review Spur Tensions

A yearlong, behind-the-scenes fight between the National Science Foundation (NSF) and congressional Republicans over how to make sure that NSF's vaunted peer-review system is funding research in the national interest finally went public last week.

The venue was a hearing before the House of Representatives science committee on draft legislation that would alter NSF's current practices. And while everyone was on their best behavior, the exchanges between outside scientists and legislators did little to assuage the fears of many researchers that the bill would erode a time-tested system for awarding grants. At the same time, NSF and the committee's chair, Representative Lamar Smith (R-TX), continue to search for common ground.

Smith's bill, not yet formally introduced, is called the Frontiers in Innovation, Research, Science, and Technology (FIRST) Act. It would set priorities for NSF and the National Institute of Standards and Technology as well as for several government-wide programs, including science education, that are coordinated by the White House Office of Science and Technology Policy. The legislation, which would replace a 2010 law that has expired, would not determine any agency's budget; rather, its importance lies in describing how the agencies should operate.

Some FIRST provisions have drawn bipartisan support. One section would help federally funded researchers commercialize research discoveries, for example, and another would strengthen research in high-performance computing. And while a provision to withhold public access to government-funded research papers for up to 3 years differs from the 1-year delay that the White House and most publishers have embraced, lobbyists say those differences can be easily resolved.

For NSF, however, FIRST would mean a significant change in how it does business. One section of the bill would require NSF's director to post online a description of each pending award before it is made, along with the names of the program managers who gave it a green light. Although Smith didn't attend the hearing, he issued a statement saying that the goal is to "increase transparency ... and ensure that American tax dollars are

used effectively and efficiently in funding federal research."

That requirement could sow turmoil, worried Richard Buckius, vice president for research at Purdue University in West Lafayette, Indiana, and a former head of NSF's engineering directorate. "In some of our competitions, we only fund a few out of a hundred proposals," he told lawmakers. "That means there will be 90+ folks who,

the committee's aim by adding a meaningless level of rubber stamping," Daniel Sarewitz of Arizona State University, Tempe, told lawmakers. Instead, Sarewitz suggested the committee ask NSF to discourage applicants from "overhyping" the benefits of their research and to seek reviewers who can give a more realistic assessment. Those changes, he said, would increase the odds that NSF grants would fit FIRST's requirement to be "in the national interest."

The top Democrat on the panel, Representative Eddie Bernice Johnson (D-TX), accused her Republican colleagues of being too negative. "It troubles me that this draft seems to be dominated in both tone and volume by everything that some of my colleagues believe NSF and scientists are doing wrong," Johnson says. She has drafted a bill that would maintain NSF's current review system and expand its programs to attract more women and minorities into science. (On 6 November, the Senate commerce and science committee held a hearing to kick off its process of reauthorizing the 2010 law.)

Smith ignited the current debate in April when he circulated a draft bill with even more prescriptive language about NSF peer review. Although several scientific organizations have complained loudly about the language, Smith maintains that the legislative process is going smoothly. "Significant progress has been made after several months of productive meetings with the National Science Board [NSF's presidentially appointed, policymaking body] and various stakeholders to address the need for NSF to be more accountable," he said last week in a statement to *Science*.

And the dialogue continues. NSF officials said last week they plan to take steps to better document how each award satisfies the agency's current funding criteria and to provide the public with a clearer description of what each grant hopes to achieve. Smith, for his part, was expected to meet privately this week with the science board. "It offers the board a chance to say, 'Here's what we are planning to do,'" says board Chair Dan Arvizu, "and to assure Mr. Smith that we are moving in a productive manner to address his concerns."

—JEFFREY MERVIS

FIRST's Grant Criteria

A House bill would require the NSF director to explain why every grant "is in the national interest" and how it addresses one or more of the following goals:

- Economic competitiveness
- Public health and welfare
- STEM workforce and public literacy
- Academic-industry partnerships
- Scientific progress
- National defense

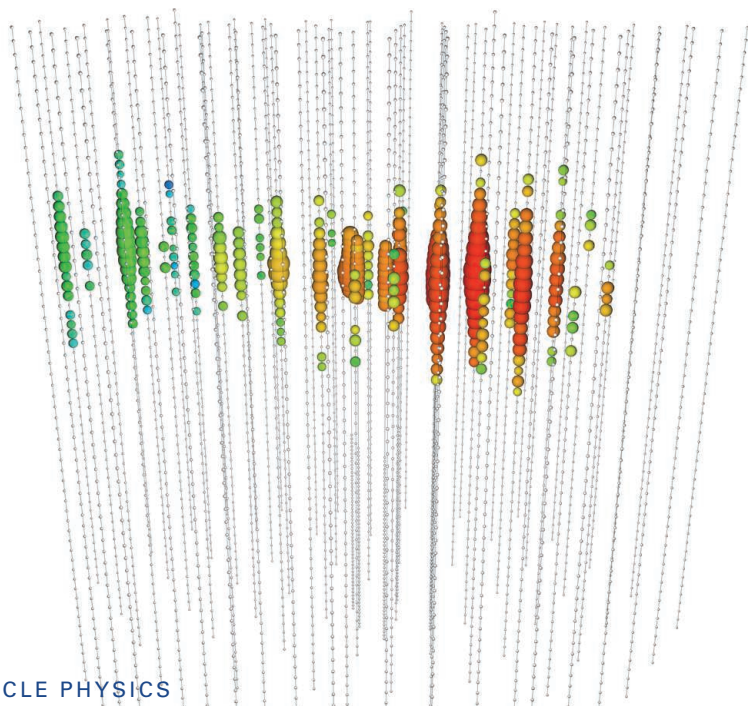
prior to the award, can energize the system and create chaos" by questioning the agency's plans.

Another witness, Tim Killeen, vice chancellor for research for the State University of New York system and a former head of NSF's geosciences directorate, told *Science* that the new policy "could lead to the worst type of grandstanding, with scientists making their case in public for why NSF should have funded their research. It could become a real free-for-all."

Other contentious FIRST language would require the NSF director to certify that every grant will achieve one or more of six national goals (see box). NSF now uses just two criteria—intellectual merit and broader impacts—as yardsticks.

"I do worry about every proposal having to conform to a specified set of criteria," Killeen testified. "Scientific inquiry includes following leads that may not take you anywhere. But yes, the overall portfolio should address all of those statements."

A third witness described a different problem with the language. "This provision is so broad that it could actually act against



Tracer. A rare streaklike event in IceCube's light detectors precisely reveals a neutrino's direction.

energy neutrinos that can come from only far-flung sources.

IceCube's results defied certain expectations. In IceCube, a neutrino can create two types of particle sprays. About one spray in three should contain a streaking particle called a muon, which reveals the neutrino's direction to within a degree. The rest contain only a cascade of particles that peter out quickly, which traces the neutrino far less accurately. Researchers had planned to focus on muon events but found the cosmic signal only when they included cascades, of which they saw 21.

In fact, IceCube may see only a couple of genuine muon events, which is puzzling, says Hawaii's Learned: "Where are all the damned high-energy muons?" The muon shortage may also make spotting sources more difficult, says Chicago's Olinto. "The [search for] point sources is a bit disappointing in that it's not what it was supposed to be," she says, adding that sky mapping may require a thousand events.

However, Francis Halzen, a theorist at the University of Wisconsin, Madison, who dreamed up IceCube in 1988, argues that the event rate is low only because researchers employed stingy criteria to make doubly sure they were seeing cosmic neutrinos. He says he's optimistic the muon technique will soon reveal sources.

Besides, now that physicists have seen something, they can argue for expanding the array, Halzen says. "Five years from now, how successful will we be with this detector?" he says. "That's a question that we may never have to answer because hopefully we'll have an even bigger detector." The IceCube team will propose at least tripling the volume of the array, which cost the National Science Foundation \$272 million, he says. Physicists in Europe hope to build a network of detectors in the Mediterranean Sea with five times IceCube's volume.

But a bigger detector may not suffice, says Eli Waxman, a theorist at the Weizmann Institute of Science in Rehovot, Israel. The rate observed by IceCube matches a prediction he made assuming that cosmic neutrinos come from innumerable sources in distant galaxies, he says. To find sources in that crowd, he says, researchers must assume they go off like firecrackers and look for neutrinos that arrive at the same time conventional telescopes see a flash. It may be years before scientists see stars twinkle in neutrinos.

—ADRIAN CHO

PARTICLE PHYSICS

Physicists Snare a Precious Few Neutrinos From the Cosmos

After 40 years of trying, physicists have detected subatomic particles called neutrinos zinging in at high energies from space. The observation, reported on page 947, comes from a detector called IceCube, built into 1 cubic kilometer of ice at the South Pole, and physicists say it marks the birth of a new field. "I'll bet that 20 years from now we'll look back and say, 'Yeah, this was the start of neutrino astronomy,'" says John Learned of the University of Hawaii, Manoa, who in 1973 proposed building a similar detector in the ocean.

But it may be a while before astronomers paint a picture of the cosmos in neutrinos. IceCube sees high-energy neutrinos at such a low rate that it may not be able to map individual sources of them in the sky, the ultimate goal. That could require an even bigger detector.

Born of nuclear interactions and devoid of charge, neutrinos interact with other matter so feebly that the average neutrino could zip through a light-year of lead. Yet neutrinos are ubiquitous. Trillions of them from the sun pass through each of us every second. Others rain down from the atmosphere, where they're produced by cosmic rays—charged particles from space—striking the air.

High-energy neutrinos also should emanate from supernova explosions and other cosmic fireworks. And unlike charged

particles, which swirl in magnetic fields in space, cosmic neutrinos should point straight back to their sources, which also may be the fonts of the highest energy cosmic rays.

To spot cosmic neutrinos, the IceCube team—276 people from 12 countries—turned part of the polar ice into a particle detector. They melted holes in the ice and lowered 86 strings of light detectors, each spanning the depths from 1450 to 2450 meters. A neutrino striking the ice triggers an avalanche of charged particles, which radiate light. The amount of light reveals the neutrino's energy; the pattern and sequence in which the detectors fire reveal its direction.

From May 2010 to May 2012, IceCube researchers spotted 28 neutrinos with energies above 30 trillion electron volts (TeV)—higher than most atmospheric neutrinos reach—including two above 1000 TeV. Only 11 could be spurious background events caused by atmospheric neutrinos and ordinary cosmic rays, researchers estimate. "It's a great achievement," says Angela Olinto, a physicist at the University of Chicago in Illinois, who does not work on IceCube.

Neutrinos from beyond the solar system have been seen once before. In 1987, detectors around the world spotted a pulse of lower energy neutrinos from a nearby supernova. But IceCube has seen high-

BIOMEDICINE

Cancer Therapies Use a Little Help From Microbial Friends

Outnumbering our own cells more than 10 to one, the microbes thriving peacefully in the human body do more than make up for the warmth and shelter we provide. They make us healthy, helping to tune up our immune systems and keep our digestive systems humming. Now, in two papers on pages 967 and 971, investigators show that our microbial guests may also aid in the treatment of disease.

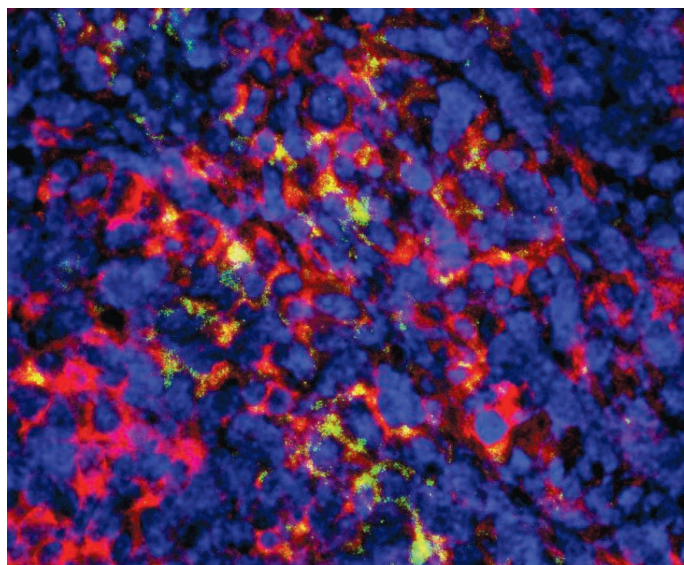
The studies show that in mice, gut bacteria bolster the effects of three antitumor regimens. In each case, when a mouse's microbial residents are missing, the treatments are far less effective. "The bacteria are demonstrated to be critical," says Matthew Redinbo, a structural biologist at the University of North Carolina, Chapel Hill, who in 2010 showed a bacterial enzyme could limit the toxicity of a cancer drug. "[These are] insights that further deepen our appreciation of mammalian-microbial symbiosis."

They could ultimately affect clinical practice, as many cancer patients get antibiotics for infections due to weakened immune systems. "Antibiotic treatments may have adverse effects that weren't predicted previously," suggests Lora Hooper, an immunologist at the University of Texas Southwestern Medical Center in Dallas. Investigators are cautious about applying the mice findings to people, however. The mouse gut bacteria are not the same as those in our own intestines, and the details of how the bacteria collaborate in the destruction of cancer cells are still mysterious.

Some cancer treatments work by stimulating the immune system to deliver a one-two punch. First, cells called macrophages, monocytes, and dendritic cells must be triggered to secrete factors that kill cancer cells. Various cancer drugs have this effect. Next, the adaptive immune system kicks in, generating a more targeted response, as T cells that specifically recognize tumor proteins proliferate and keep the immune system rallied against the tumor.

Curious if gut bacteria influenced the outcome of cancer therapies, immunologists Giorgio Trinchieri and Romina Goldszmid from the National Cancer Institute in Frederick, Maryland, and their colleagues grew

tumors in mice chronically treated with antibiotics and then administered an experimental immunotherapy treatment that included immune-stimulating DNA fragments and antibodies. In these mice, whose microbial communities had been decimated by the antibiotics, the treatment faltered. It failed to elicit the typical spike in a tumor-killing pro-



Microbe-managed. Gut bacteria prime macrophages (red) in a tumor (purple) to convert to cancer killers during anticancer treatments.

tein called tumor necrosis factor, and there was very little tumor cell death. Likewise, mice raised in a sterile environment produced much less tumor necrosis factor than normal in response to the immunotherapy, and tumors stayed intact. Lacking microbes, the "inflammatory response is severely dampened," Trinchieri says.

Antibiotics also dampened the response of macrophages and other immune cells to a different regimen, the researchers found. Cancer drugs such as oxaliplatin work, at least in part, by damaging tumor cells with molecules called reactive oxygen species. But Trinchieri says that in mice taking antibiotics and animals raised to be germ-free, the immune cells made far fewer of the enzymes needed to generate reactive oxygen species. "The gut microbiota have the effect of priming" the immune system, Trinchieri says.

Immunologist Laurence Zitvogel found a role for microbes in the response to a third treatment, cyclophosphamide (CTX), a drug that combats breast cancers, lymphomas, and some brain cancers by increasing the number of a class of immune cells called Th17/Th1.

Zitvogel, who works at the Institut Gustave Roussy in Villejuif, France, noticed that her cancer patients undergoing chemotherapy with CTX often developed digestive system problems. Looking deeper, she and her colleagues found that CTX disrupted the gut lining. Its tiny projections called villi shrank and the wall of the small intestine got leaky.

Certain microbes—a few kinds of Gram-positive bacteria—escaped into the rest of body, the researchers observed. Several, including two *Lactobacillus* species and *Enterococcus hirae*, typically settled into the lymph nodes and spleen.

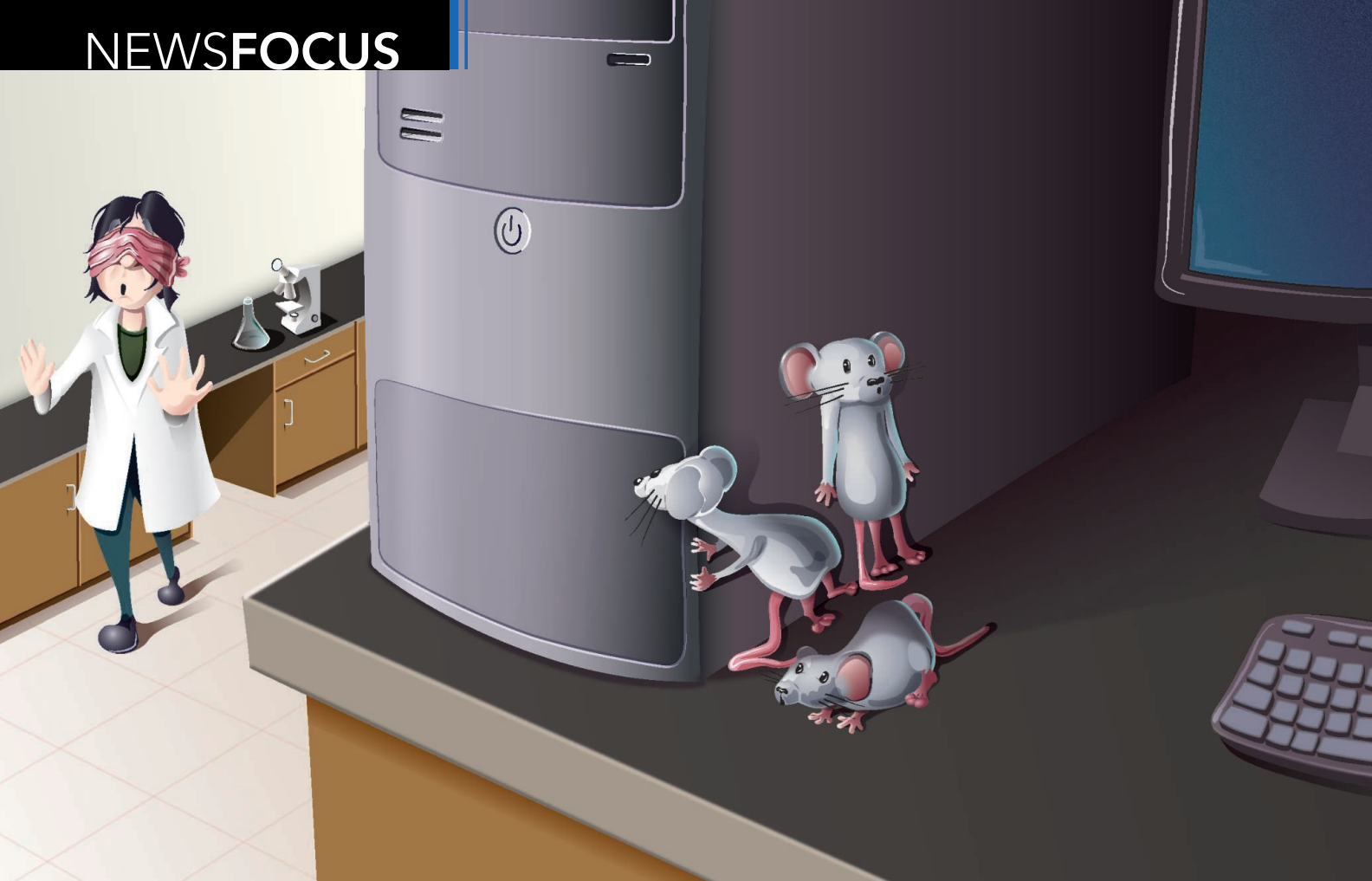
Lab studies showed that this migration may be key to the drug's potency. In a test tube, these so-called Gram-positive bacteria caused immature T cells, such as those found in the spleen and lymph, to turn into Th17 cells, some of which later converted to memory cells that could prolong the immune response to the tumor. Moreover, feeding such bacteria to mice led to an increase in these T cells in the spleen. In contrast, mice bred to be germ-free or treated with a combination

of antibiotics or with just vancomycin, which targets Gram-positive bacteria, showed little to no boost in Th17 cells when given CTX, and their tumors shrank very little.

It's too early to start feeding microbes to cancer patients, investigators say. "You cannot extrapolate these data to humans without first testing in humans," Trinchieri says. He recommends studies of healthy humans to determine how gut microbes affect macrophages and monocytes with and without antibiotic treatment. He would also like to know whether there's any correlation between antibiotic use and chemotherapy treatment success rates.

Nonetheless, the data "illustrate the complex interplay of microbial activity and function with the immune system and therapies," says Jeremy Nicholson, a biochemist at Imperial College London. In the future, doctors who now tissue-type cancer patients' tumors may also assess their gut bacteria to determine the best treatment approach. Zitvogel is already modifying her practice. "We are going to be very careful about prescribing antibiotics during chemotherapy."

—ELIZABETH PENNISI



When Mice Mislead

Tackling a long-standing disconnect between animal and human studies, some charge that animal researchers need stricter safeguards and better statistics to ensure their science is solid

THREE MICE HAD VANISHED. AND ULRICH Dirnagl had a hunch about where they'd ended up: in the metaphorical dustbin housing animals—and there are lots of them—that line up at an experiment's starting line but are discarded before the finish. The paper that Dirnagl, director of the Center for Stroke Research at Charité University Medicine Berlin, was reviewing described how a new drug protected a rodent's brain after a stroke. The authors used 20 mice, half of which got the therapy. But mysteriously, only seven of the 10 treated animals appeared in a graph analyzing the results.

"I wrote to the editor and said, 'I cannot judge this paper, I need to know where the three mice went,'" Dirnagl recalls. For 6 months, radio silence. Then, the editor responded. He'd heard from the authors, he told Dirnagl. The three mice, suffering from massive strokes, had died, and the authors

had simply left them out of the paper. Extra analysis of their stroke drug, however, revealed that those mice had an important message to bear: The therapy harmed the brain rather than helping it.

"This isn't fraud," says Dirnagl, who often works with mice. Dropping animals from a research study for any number of reasons, he explains, is an entrenched, accepted part of the culture. "You look at your data, there are no rules. ... People exclude animals at their whim, they just do it and they don't report it." That bad habit, he believes, is one of several that plague animal studies.

For years, researchers, pharmaceutical companies, drug regulators, and even the general public have lamented how rarely therapies that cure animals do much of anything for humans. Much attention has focused on whether mice with different diseases accurately reflect what happens

in sick people. But Dirnagl and some others suggest there's another equally acute problem. Many animal studies are poorly done, they say, and if conducted with greater rigor they'd be a much more reliable predictor of human biology.

It's hard to generalize, of course: Animal studies cut across a massive swath of biology, tracking everything from the activity of single molecules in a healthy organ to side effects of a new drug poised for human testing. And many who stake their careers on animal studies conduct them with care, judiciously weighing how to structure their experiments and chasing the science wherever their furry subjects take it.

That said, even animal research that has a big effect on human drug studies—like the work Dirnagl reviewed—is governed by far fewer standards than clinical trials in people. There, volunteers are randomly assigned by

CREDIT: V. ALTOUNIAN/SCIENCE

computer to get a new drug or a placebo. Those running a trial are often blinded to who's in what category, preventing clinicians invested in a therapy's success from imagining hints of efficacy in patients they know are getting a new drug. And look up any clinical trial seeking volunteers and you'll see a long list of "inclusion" and "exclusion" criteria governing who can participate. If you have high blood pressure or if your cancer is being treated with a certain drug, you might be out of luck.

Animal studies rarely follow these rules. For ethical and cost reasons, researchers try to use as few animals as possible, which can mean minuscule sample sizes. Unblinded, unrandomized studies are the norm. In Dirnagl's words, "the way we do our research with our animals is stone-age."

From various quarters, there's pressure to change that. High-profile studies showing that preclinical results often cannot be reproduced are driving funders and researchers to seek solutions—as much to mend their public image as to guarantee sound science.

The roots of bias

Dirnagl's concerns were sparked around the same time as a friend and colleague's across the English Channel. A decade ago, Malcolm Macleod, a Scottish neurologist at the University of Edinburgh, went hunting for new stroke therapies. He wanted to find compounds that had looked good in animals but had stalled there and that might be worth testing in people.

Macleod and his colleagues identified 603 drugs tested in animals, 374 of which had helped heal the brain. Of those, 97 had been tried in humans—and only one had worked. And that one, Macleod is quick to point out, wasn't tested because of animal data at all, but because it had already benefitted patients with heart attacks.

Startled by this chasm separating experimental animals and people, Macleod turned his attention to what was going wrong. One possibility, he reasoned, was that the therapy wasn't tested properly in humans—say the dose was too low, or it was given too long after a stroke. Another was that human testing had been appropriate, but the animals were simply a poor model of human stroke. And the third was that the drug wasn't tested properly in animals to begin with.

Macleod dug deeper. What he found alarmed him. Only 36% of the animal studies described randomly assigning animals to stroke treatment or placebo. Only 29% reported blinding. What's more,

studies that didn't report randomizing and blinding—which was most of them—"gave substantially and significantly higher estimates of how good these drugs were," Macleod says. In one case, the effectiveness of a stroke drug was twice as high in the studies that didn't report randomizing as in those that did.

Macleod then turned to other neurological ailments: Alzheimer's, multiple sclerosis, Huntington's disease, Parkinson's, and pain. In animal studies of potential treatments, the situation was, if anything, worse than in stroke, the measures that might dampen bias applied even less often.

Many of these authors likely didn't recognize what Macleod perceived as lack of rigor in their studies because their mentors, and their mentors' mentors, had followed this same approach. "I was trained as an animal researcher," says Lisa Bero, now a health policy expert at the University of California, San Francisco. "Their idea of randomization is, you stick your hand in the cage and whichever one comes up to you, you grab. That is not a random way to select an animal." Some animals might be fearful, or biters, or they might just be curled up in the corner, asleep. None will be chosen. And there, bias begins.

Macleod's work, published in a series of papers beginning in 2004, is complemented by other strands of evidence. A 2008 paper in the journal *Amyotrophic Lateral Sclerosis* described efforts by the nonprofit ALS Therapy Development Institute to retest more than 70 compounds that had eased symptoms in a mouse model of the disease. Not a single one panned out.

It was what the ALS authors did next that was particularly interesting. At the end of their dismal replication efforts, they were

there was a 30% chance that an illusory life expectancy gap would show up. With 10 animals per group, the risk dropped to 10%. "You can imagine 10 labs doing this experiment," says Shai Silberberg, a program director at the National Institute of Neurological Disorders and Stroke (NINDS) in Bethesda, Maryland. "One gets an effect, and they publish it." The other nine are much less likely to submit a paper. Suddenly, the literature is skewed.

The numbers of animals that the ALS researchers used may sound small, but they're grounded in reality. A survey of 76 influential animal studies found that half used five or fewer animals per group.

Bero recently examined animal research of statins for heart disease. At the International Congress on Peer Review and Biomedical Publication in September, she reported that work funded by industry was less likely to endorse the drug in question than work from another funding source, maybe because companies don't want to pour millions of dollars into testing a treatment in people that's unlikely to help them.

Status quo revisited

In Bethesda, Silberberg sits in a position of power, part of a committee advising the NINDS director on which of the most costly studies should be considered. About 3 years ago, Silberberg, who trained as a biophysicist in Israel and later the United States, grew more and more worried that the institute was greenlighting some projects that weren't based on solid science. He decided to do something about that.

There were lots of avenues Silberberg could have followed, and he settled on animals. In part, he was responding to data like Macleod's, with its startling evidence

"The way we do our research with our animals is stone-age."

—ULRICH DIRNAGL, CHARITÉ UNIVERSITY MEDICINE BERLIN

left with a treasure trove of data on 2241 control animals—mice that hadn't gotten any active drug. The researchers randomly assigned mice to two groups, matched for sex, litter size, and other variables. Then they looked for differences in mean life expectancy—something they shouldn't see, because the two groups were essentially the same.

What they found was telling. If the two groups contained just four animals each,

of what he saw as entrenched biases in animal research. A slice of NINDS's budget is funneled to translating animal studies to people. Among other things, Silberberg worried about "poor patients [who] are exposed to things they shouldn't be."

After lots of agitating and conversation within the National Institutes of Health (NIH), in the summer of 2012 Silberberg and some allies went outside it, convening a workshop in downtown Washington,

D.C. Among the attendees were journal editors, whom he considers critical to raising standards of animal research. “Initially there was a lot of finger-pointing,” he says. “The editors are responsible, the reviewers are responsible, funding agencies are responsible. At the end of the day we said, ‘Look, it’s everyone’s responsibility, can we agree on some core set of issues that need to be reported’” in animal research?

In the months since then, there’s been measurable progress. The scrutiny of animal studies is one piece of an NIH effort to improve openness and reproducibility in all the science it funds. Several institutes are beginning to pilot new approaches to grant review. For an application based on animal results, this might mean requiring that the previous work describe whether blinding, randomization, and calculations about sample size were considered to minimize the risk of bias. “Sometimes the fundamentals get pushed aside—the basics of experimental design, the basics of statistics,” says Lawrence Tabak, principal deputy director of NIH, who is coordinating these efforts.

Another of NIH’s ventures is at the National Institute of Environmental Health



in there.” The Environmental Protection Agency is also reconsidering how it evaluates animal data.

Journals, too, are getting in on the act. In April, *Nature* released a checklist for authors and reviewers, requesting extra detail about scientific methods in life sciences papers. Among other things, the checklist asks whether the animals were randomized and the researchers blinded, and requests the criteria by which animals were dropped from the study—an effort to avoid the three

“I am not pessimistic enough to believe that the entire scientific community is obfuscating results.”

—JOSEPH BASS, NORTHWESTERN UNIVERSITY

Sciences in Research Triangle Park, North Carolina, where toxicologist Kristina Thayer is looking for a way to grade animal studies, in part to guide regulators making recommendations about particular chemicals. For work that examines the hazards of bisphenol A, a compound found in many plastics, Thayer is experimenting with 15 “risk of bias” questions. Among them: Did the researchers randomly allocate animals to treatment groups? Did they know which animals were exposed to chemicals? Were experimental conditions the same across different groups of animals? “When you’re looking at bias, it’s not just yes or no,” she says. “There can be different shades of gray, and there can be scientific judgment

missing mice Dirnagl encountered. *Science Translational Medicine* announced a similar initiative in June, and *Science* is considering the same.

Some in the field consider such requirements uncalled for. “I am not pessimistic enough to believe that the entire scientific community is obfuscating results, or that there’s a systematic bias,” says Joseph Bass, who studies mouse models of obesity and diabetes at Northwestern University in Chicago, Illinois. Although Bass agrees that mouse studies often aren’t reproducible—a problem he takes seriously—he believes that’s not primarily because of statistics. Rather, he suggests the reasons vary by field, even by experiment. For example, results in

Bass’s area, metabolism, can be affected by temperature, to which animals are acutely sensitive. They can also be skewed if a genetic manipulation causes a side effect late in life, and researchers try to use older mice to replicate an effect observed in young animals. Applying blanket requirements across all of animal research, he argues, isn’t realistic.

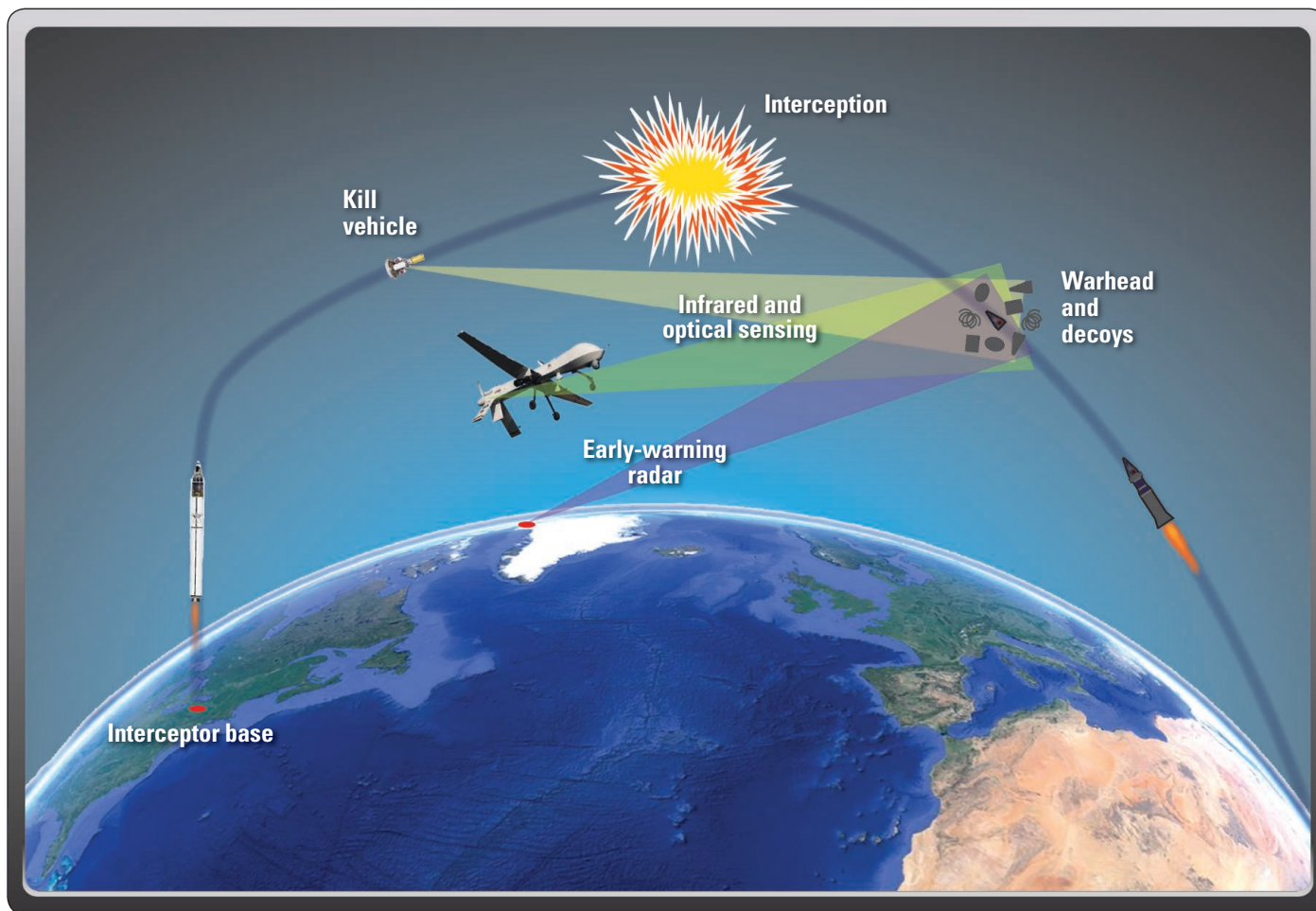
Bass is just as concerned about the undercurrent that scientists aren’t to be trusted. “A lot of what this argument is, is that there’s this ethical flaw across the community, and we’re going to correct it by mandating these laws,” he says.

Dirnagl agrees with this last point, even though he believes that new standards are needed. “A lot of the academic researchers, they are being accused of producing crap, complete crap,” he says. “I think this is overshooting it, and it’s even dangerous. ... We need to properly discuss these quality issues.” More importantly, “we need to teach them to the next generation.” He tries to present his case with optimism, so as not to discourage or alienate his colleagues.

Dirnagl also says he’s cleaned up his own act, something that, for the most part, hasn’t been particularly onerous. He marks the tails of all his animals with numbers and uses a number generator that spits out a list to help him randomly select mice. If during a surgery an animal’s blood pressure drops below a certain level, Dirnagl excludes it, whether it’s getting a new stroke treatment or not. He’s starting to do what clinical trialists have done for years—run multicenter studies, where labs pool their animals to boost the experiment’s reliability with greater numbers.

One open question is whether such adjustments will help animal experiments hold up to scrutiny. “It’s almost certain that we’re not completely right” about what’s worth changing and what’s not, Macleod says, and that will need to be gauged over time. Ultimately, though, he believes better research standards will lead to a renewed trust in mouse models of disease. “I wouldn’t be wasting all my time” on this, he says, if he didn’t have faith that the mice had it in them to be auspicious guides—if only we could figure out the best way to use them.

—JENNIFER COUZIN-FRANKEL



Missing the Mark

The U.S. intercontinental missile defense system faces a crisis as Congress presses for an expansion, interceptors malfunction, and a basic targeting problem remains unsolved

On the morning of 5 July, a long-range missile lifted off from the Marshall Islands in the Pacific and traced an arc into the northern sky. Five minutes later, a U.S. interceptor missile took off from California, 7500 kilometers away, and streaked south toward an encounter far above the atmosphere. When in range, the California-based missile was supposed to release a “kill vehicle” from its nose that would pick out a collision point, maneuver at a closing speed of more than 10 kilometers a second, and slam into the target. That didn’t happen. The kill vehicle failed to detach—and missed.

Similar tests of the U.S. ground-based missile defense system have been under way since 1999, more than one a year on average. According to the Pentagon’s tally, eight have succeeded and eight have failed. But in recent years, the rate of tests has slowed—

there were only three intercept attempts from 2009 to 2013, and all three were failures. The program’s distress has given credibility to skeptics and alarmed some members of Congress, who have asked whether the system can be fixed.

Ambition has always outrun technological reality in the U.S. missile defense system, a legacy of the “Star Wars” push that began 30 years ago for a shield against Soviet attack and is now seen as a defense against a limited or rogue missile strike. In the next 5 weeks, the United States will begin planning an expansion of its ground-based interceptor network, which now has two rocket-launching bases, in California and Alaska. Under pressure from Congress and private groups worried about the threat of a

missile attack from Iran, the Pentagon will pick a location east of the Mississippi and two alternatives to study as a new base for the 18.3-meter interceptors.

Far from welcoming a chance to expand their missile defense system, however, military officials worry about the cost of an Alaska-style base in the east—possibly as much as \$3.5 billion to build, almost half the \$7.7 billion annual budget of the U.S. Missile Defense Agency (MDA). They also worry about the distraction from a pressing problem, unsolved for 50 years: How do you create a system that can reliably single out and hit a target in space?

Navy Vice Admiral James Syring, MDA’s director, has told Congress that the military doesn’t have a “validated” need for a third

Online

sciencemag.org

Podcast interview with author Eliot Marshall (http://scim.ag/pod_6161).

Ground-based defense. U.S. interceptors (*far left*) are designed to hit an incoming warhead in space. Experts worry they won't pick out a real warhead from decoys.

base. He and Secretary of Defense Chuck Hagel have pointed to other items that do need urgent action. One is to learn why the 5 July test failed and work out what a repair will cost. The other is an earlier problem identified after a December 2010 failure of a ground-based interceptor. Until it is fixed, Hagel has said, the military won't acquire 14 new interceptors he promised to buy in March to expand western defenses (*Science*, 29 March, p. 1508). At the moment, the system is in limbo.

But even a string of successful single-target interceptions will not address the system's deeper flaw. In the near vacuum of space, debris and decoys can fly in step with an incoming ballistic warhead, confusing sensors and complicating the job of identifying and destroying the target. Expert reviews have warned repeatedly that target discrimination in space has not been solved or even studied adequately. In testimony to Congress, Syring has identified it as a top priority. But it's not clear that a push to solve this decades-old conundrum can win funding in competition with the cost of fixes, the \$1 billion for Hagel's new interceptors, and calls for a new base.

"The budget implications of the current situation are enormous for MDA," says physicist Philip Coyle, an outspoken critic of the program who was director of operational test and evaluation for the Department of Defense from 1994 to 2001 and former scientific security adviser for the Obama White House. "Given the long list of repairs and upgrades that appear to be needed," he says, "some people think it is a lost cause."

Get a little closer

Even though Congress cut U.S. defense spending overall last year and may do so again this year, it instructed MDA in the 2013 defense authorization bill to start scoping out an East Coast missile base site. The main support for this plan comes from the House of Representatives, where the Republican majority voted to begin construction. But some eastern lawmakers of both parties also relish the federal investment and the new jobs. New York Senator Chuck Schumer, a Democrat, put out a press release in May promoting two upstate New York sites, saying base construction there "could create thousands of jobs and significant revenue in local communities." He added, however, that it was up to the military to decide if a base was needed.

Missile Defense Made Practical

Small is beautiful in missile defense, to judge by recent testing results. In a matchup between a mobile, sea-based system called Aegis, built by the U.S. Navy to knock down short- to medium-range missiles, and the massive backbone of long-range missile defense in Alaska and California (see main story, p. 926), the little Navy one comes out ahead. The Army's mobile interceptor unit called THAAD (Terminal High Altitude Area Defense), designed to protect a relatively small area from medium-range missiles, has also scored well. Weapons analysts advise, however, that none of these systems has ever intercepted an intercontinental-range ballistic warhead, which travels faster than shorter range missiles and may be camouflaged by decoys.

Aegis went through its paces most recently on 4 October near Hawaii, its 34th test since 2001, according to the U.S. Missile Defense Agency (MDA). An Aegis interceptor launched at sea released a kill vehicle that maneuvered toward a medium-range missile target in space and destroyed it. For Aegis, this was the fifth success in a row and the 28th overall. The system, guided by its own radar, is now destined for expanded use ashore in Romania and Poland, where it will serve as a forward sentinel and potential line of defense against missiles fired at Europe. THAAD, for its part, has had 11 hits in 11 trials since 2006, according to the military, and its radars are or will be deployed in Hawaii, Guam, Turkey, Israel, and Japan. In contrast, the big Alaska-California system—the "ground-based midcourse ballistic missile defense"—has failed as often as it has succeeded in tests.

At an appropriations subcommittee hearing on 17 July, Senator Richard Durbin (D-IL) praised Aegis as "reliable" and "proven," and MDA's director Navy Vice Admiral James Syring called it "fantastic." Asked to explain why the Navy system performs so well, Syring said that it was developed slowly with a "systematic, system-engineered approach," whereas the large land-based interceptors were "fielded very quickly for a growing threat" on the assumption that they would be improved later. Syring defended both approaches. But the Government Accountability Office (GAO), Congress's audit agency, has warned many times that to meet a 2004 deadline set by the White House, builders bypassed quality control checkpoints for the big system—allowing "concurrencies" in development and deployment. These, according to an April report by GAO official Cristina Chaplain, caused delays, late failures, and expensive redesigns that have yet to be fully tested.

An enthusiastic supporter of the Aegis system, which is now aboard 27 ships, asked Syring at the July hearing if the Navy system could be stationed off the U.S. East Coast to beef up the ailing land-based system. Syring responded that the answer is classified. Independent experts say that while more Aegis ships would be useful, the system wasn't designed to hit long-range missiles, although it may be modified in an effort to enable it to do so in the future. For the next 5 years, at a minimum, U.S. national defense will rely heavily on the troubled interceptors based in Alaska and California.

—E. M.



Good aim. The Navy's Aegis system, using specialized radar and a small SM-3 missile, has intercepted targets in 28 of 34 tests.

The Senate did not support construction, but agreed last year that candidate sites should be chosen in 2013 and an environmental impact study started as soon as possible.

MDA duly issued a list of five potential sites in September; one of Schumer's was on it, along with others with congressional backing in Maine, Vermont, Ohio, and Michigan. By 31 December, the list will be narrowed to three finalists.

What's to be gained by locating a new base in the east? The short answer, proponents say, is that you get more time to shoot at missiles coming from the Middle East and a chance for better targeting. Basing interceptors closer to Iran, the presumed aggressor in current scenarios, shortens the flight time between the takeoff point in the United States and the earliest contact with a warhead. (The base would add firepower, too—possibly 20 more interceptors.) In theory, the timesaving would allow for an

predict Iran will have a long-range missile by 2015. "We do ourselves a great disservice by having half the country [the east] completely exposed to a potential missile attack," says Jeff Kueter, president of a group that favors putting weapons in space, the George C. Marshall Institute in Washington, D.C. Kueter sees no choice to be made between paying for better interceptors and building a new base: "You need to do both," he says.

A year ago, the U.S. National Academies' National Research Council (NRC) argued for an eastern interceptor base in a report titled *Making Sense of Ballistic Missile Defense*. The chief co-authors of its classified and unclassified sections were missile builder L. David Montague, a former president of the Missile Systems Division of Lockheed Martin, now a consultant in Menlo Park, California; and Washington, D.C., attorney Walter Slocombe, a former defense adviser for several administrations.

out early in its flight, when it is big, slow-moving, and hot. But over the years, schemes for such "boost phase" counterstrikes, including space-based lasers that could punch a hole in a missile's thin skin or fast interceptor rockets based close to a hostile nation, have proved impractical. Intercepting an intercontinental ballistic missile as it arcs through space is the best option left, even though it has its own enormous challenges: targeting and hitting a tiny warhead, separated from its booster, moving faster than a rifle bullet, and potentially surrounded by a cloud of debris or decoys.

Syring has said that his first task is to fix the existing U.S. missile defense system so that it can pass a simple intercept test. He told Congress that a "production quality" flaw in an interceptor caused the first of the three recent failures and a guidance "design issue" caused the second. No report has yet come out on the third.

The next priority, Syring has said in several hearings, is to solve the puzzle of target discrimination. Syring declined a request for an interview, but outside experts have described the problem using unclassified data. Physicist George Lewis of Cornell University was a co-author of an analysis of the challenge posed by decoys, published by the Union of Concerned Scientists in 2000. He notes that a network of satellite-borne infrared sensors and long-range warning radars give an interceptor its first, approximate heading. The early warning radars, operating at 400 to 500 megahertz, aren't capable of pinpointing the warhead by shape or size. They can pick out individual objects from thousands of kilometers away but cannot discriminate among objects less than about 10 to 20 meters long.

High-frequency radars in the 10 gigahertz range, known as X-band, can resolve objects as small as 25 centimeters long, Lewis says, but most existing ones have less than intercontinental range. An exception is a huge system operated from Hawaii, called the Sea-Based X-Band Radar or SBX system, which has observed U.S. tests and missile launches from North Korea. The complex, power-hungry system is costly to use, however, and MDA keeps it idle most of the time, Lewis says. But he predicts that the military will soon get a green light to build a large X-band system on the East Coast, whether or not a new launch base is approved.

No matter how good the tracking information from these external systems is, the kill vehicle must find its own final path to the target using onboard sensors. The device must pick out a warhead roughly

Ground-Based Interceptor Testing Record

Date	Type	Outcome
2 October 1999	Prototype interceptor	Success
19 January 2000	Prototype interceptor	Kill vehicle's infrared sensor malfunctioned
8 July 2000	Prototype interceptor	Kill vehicle did not separate from launcher
14 July 2001	Prototype interceptor	Success
3 December 2001	Prototype interceptor	Success
15 March 2002	Prototype interceptor	Success
14 October 2002	Prototype interceptor	Success
11 December 2002	Prototype interceptor	Kill vehicle did not separate from launcher
15 December 2004	Prototype interceptor	Interceptor failed to launch
14 February 2005	Prototype interceptor	Interceptor failed to launch
1 September 2006	Operational interceptor	Success
28 September 2007	Operational interceptor	Success
5 December 2008	Operational interceptor	Success
31 January 2010	Operational interceptor	Kill vehicle and system performance failures
15 December 2010	Operational interceptor	Kill vehicle guidance error
5 July 2013	Operational interceptor	Failure review under way

efficient "shoot-look-shoot" tactic. After a first interception attempt, radar and other sensors would look to see whether the kill vehicle had hit the target and, if not, call for another. This could improve the aim of successive shots and avoid waste (at a stiff \$75 million per interceptor). Because the California-Alaska system doesn't allow time for a second look at a warhead coming from the east, some say the current strategy is "shoot-shoot-shoot"—send four or more interceptors at each warhead.

Champions of an expanded ground-based defense note that U.S. intelligence reviews

Their panel concluded that the East Coast now is "poorly protected," and their long list of improvements included a new base in New York or Maine. "The key is, you must have shoot-look-shoot capability to increase the size of the battle space" and boost the chance of success, Montague says.

A moving target

The new base is needed, the panel said, because midflight interception is the only workable option for defending against intercontinental missiles. In principle, such a missile would be easiest to target and knock

2 meters long, which may be embedded in a kilometers-wide field of other objects, and slam into it. The latest U.S. kill vehicle, known as the CE-II version, has never achieved this. The older version, CE-I, worked in carefully scripted early tests but now is in doubt, having failed in July.

The NRC report says that the targeting problem can be solved. It recommends that the kill vehicle be capable of reporting back what its own sensors see on the final approach just before a hit or miss. This would provide more precise, close-in views of objects in the “threat package” and sharpen the aim of the next shot, if needed. It would help research, too. The CE-I and CE-II kill vehicles, however, lack a report-back capability, Lewis says, “and apparently that can’t be fixed.” They must be redesigned, flight-tested, and replaced to achieve this, which would take years.

The NRC report also recommends extensive improvements in ground- and sea-based radar. For example, it suggests building five new powerful X-band radars by stacking two copies of an existing Army-Navy radar, AN/TPY-2, and locating them at strategic points in the United States and Europe. This plan also includes an entirely new set of more agile ground-based interceptor launchers.

Others are skeptical that these expensive fixes would suffice, citing many ways in which targeting could still be thrown off. Lewis and Theodore Postol, a physicist at the Massachusetts Institute of Technology in Cambridge, summarized some of them most recently in a 2010 article for the *Arms Control Today* newsletter. Tracking radars could be flooded with signals, they wrote, “[i]f an adversary deployed thousands of wires on slightly different trajectories along with warheads.” Lewis and Postol cite other tricks: A warhead could be enclosed in a reflective balloon to mask its shape; lightweight fake warheads could be released; and the upper stage of the launch vehicle could be cut into bits with explosives to add to the muddle. More powerful radars don’t necessarily help, Lewis argues: “The radar isn’t going to be able to tell you which balloon has the warhead in it. ... They’re all going to just look like balloons.”

IBM physicist Richard Garwin, a defense analyst and arms control advocate who has followed this issue for years and contributed to classified analyses of missile defenses (which he doesn’t discuss), also challenges some conclusions of the NRC report. In a letter to its authors that he made public this year, Garwin says that he’s not convinced they have



Expanded missile defense. A U.S. National Academies study argues that adding a new interceptor base in New York would add to the reach of those based at Fort Greely, Alaska, protecting a wider area with a single shot against warheads from Iran (inside the blue line) and giving time for at least one follow-up shot (within red line).

a solution to the targeting problem, because “[n]either the unclassified nor the classified Report describes how this could be done.”

Not so easy

NRC panel co-chair Montague says it’s “not new news” that U.S. national missile defense is “flawed.” But he thinks critics overstate the ease of deploying decoys. He regards the Union of Concerned Scientists analysis and others as “scholarly and naive,” because “they base their assumptions on first principles, and there’s a lot more than first principles going on.” Take balloons. They’re not so lightweight, Montague says. He’s not sure how you wrap a warhead in a balloon or fix the package to a missile without an attaching part that would become a giveaway “tag” or signature that radars and other sensors could detect. “I’ve been involved in building more missiles than the rest of the free world combined,” he says, “and I know that you cannot make gossamer [decoys or masks] that work.”

MDA officials have cited a few broad themes in their plan to address target discrimination, but declined requests to discuss them. Echoing a recommendation of the NRC panel, they have spoken about combining radar and infrared data from existing sensors to profile and catalog types of real and fake warheads. In testimony, Syring has said MDA is also experimenting with

new infrared and optical sensors that might be placed on high-altitude drone aircraft to provide additional data for sorting out targets and decoys. And MDA is considering a common kill vehicle with new sensors to replace the current 1990s technology aboard both large and small interceptors, Syring has testified. But that’s a long way off.

Even if a fix is feasible, it may not be affordable. MDA’s tab for analyzing this year’s intercept failure, making repairs, and retesting the system could add hundreds of millions of dollars to costs that are already zooming, according to David Best and Cristina Chaplain of the Government Accountability Office. GAO reported in May that unplanned expenses associated with the redesign and testing of the CE-II kill vehicle after a failure in 2010 amount to more than \$1.2 billion—and are still growing. Now, MDA is bracing to hear what it will cost to recover from the CE-I failure.

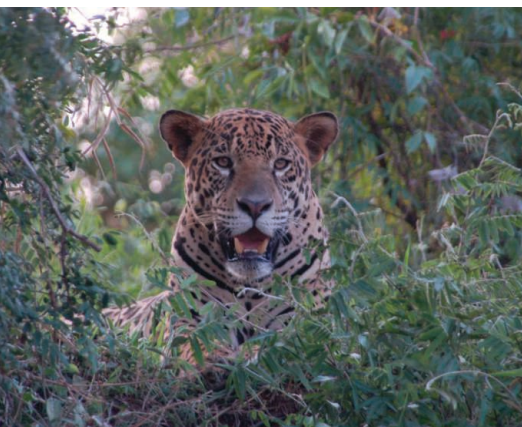
If Congress doesn’t reach an agreement soon on a 2014 budget, automatic cuts enacted in the sequester law could kick in, potentially taking \$700 million out of MDA’s budget. Congress could exempt MDA from the cuts, but only by sacrificing other programs. Syring faces some tough decisions in the next year. But he has made it clear that building a new, multibillion-dollar launch site is not something he wants to add to the must-do list.

—ELIOT MARSHALL

LETTERS

edited by Jennifer Sills

Atlantic Rainforest's Jaguars in Decline



IN HER NEWS FOCUS STORY "PREDATORS IN THE 'hood" (20 September, p. 1332), V. Morell reported that top predator populations are coming back across much of North America. Meanwhile, predators in Brazil continue to decline. A recent meeting of wildlife experts indicated that the Atlantic rainforest that once stretched along the coast of Brazil and parts of Argentina and Paraguay may soon be the first tropical biome to lose its largest top predator, the jaguar (*Panthera onca*). Researchers estimated fewer than 250 mature jaguars alive in the entire biome, distributed in eight isolated populations (1). Even worse, molecular analyses demonstrate that local effective population size (a critical parameter for the maintenance of

genetic diversity) is below 50 animals (2).

Jaguars are persecuted for their potential impact on livestock, and their prey have been overhunted even in large protected areas (3). Jaguars provide a crucial service in controlling herbivores (capibaras, deer, and peccaries) and smaller predators (pumas, ocelots, foxes, and racoons), and their overall extinction will likely disrupt predator-prey interactions with unpredictable effects on ecosystem function (4). The Atlantic rainforest is a highly fragmented biodiversity hotspot, with less than 12% of the original area left (5). Although 24% of the remaining areas are large enough to support jaguars, jaguar populations can be found in only 7% of the rainforest (4).

Population supplementation and reintroduction programs may provide new hope for jaguars, but uncontrolled hunting of jaguars and their prey is still widespread in most protected areas, threatening the persistence of this important top predator. In the absence of effective protection and management, the fate of the largest predator of the Atlantic forests is bleak.

MAURO GALETTI,^{1*} EDUARDO EIZIRIK,^{2,3} BEATRIZ BEISIEGEL,⁴ KÁTIA FERRAZ,⁵ SANDRA CAVALCANTI,³ ANA CAROLINA SRBEK-ARAÚJO,⁶ PETER CRAWSHAW,⁴ AGUSTIN PAVIOLO,⁷ PEDRO MANOEL GALETTI JR.,⁸ MARIA LUISA JORGE,^{1,9} JADER MARINHO-FILHO,¹⁰ UGO VERCILLO,⁴ RONALDO MORATO^{3,4}

¹Departamento de Ecologia, Universidade Estadual Paulista, 13506-900, Rio Claro, SP, Brazil. ²Faculdade de Biociências, PUCRS, Porto Alegre, 90619-900, RS, Brazil. ³Instituto Pró-Carnívoros, 12947-110, Atibaia, SP, Brazil. ⁴Instituto Chico Mendes de Conservação da Biodiversidade, Brasília, 70670-350, DF, Brazil. ⁵Departamento de Ciências Florestais, Universidade de São Paulo, Escola Superior de Agricultura "Luiz de Queiroz," Piracicaba, 13418-900, SP, Brazil. ⁶Universidade Vila Velha, Vila Velha, Espírito Santo, 29102-920, Brazil. ⁷Instituto de Biología Subtropical, CONICET-UN Misiones, Iguazú, N3370AIA, Argentina. ⁸Departamento de Genética e Evolução, Universidade Federal de São Carlos, São Carlos, 13565-905, SP, Brazil. ⁹Vanderbilt University, Nashville, TN 37240, USA. ¹⁰Departamento de Zoologia, Universidade de Brasília, 70910-900, Brasília, DF, Brazil.

*Corresponding author. E-mail: mgaletti@rc.unesp.br

References

1. B. M. Beisiegel, D. A. Sana, E. Moraes Jr., *CatNews Special Issue* **7**, 14 (2012).
2. T. Haag *et al.*, *Mol. Ecol.* **19**, 4906 (2010).
3. F. C. C. de Azevedo, V. A. Conforti, *Mammalia* **72**, 82 (2008).
4. M. L. S. P. Jorge, M. Galetti, M. C. Ribeiro, K. M. P. M. B. Ferraz, *Biol. Conserv.* **163**, 49 (2013).
5. M. C. Ribeiro, J. P. Metzger, A. C. Martensen, F. J. Ponzoni, M. M. Hirota, *Biol. Conserv.* **142**, 1141 (2009).

Capping Progress
on Invasive Species?

THE EUROPEAN COMMISSION RECENTLY PUBLISHED its long-awaited draft legislation on invasive alien species (1). The proposed regulation implements a key target of the European Union Biodiversity Strategy (2), aiming to bring EU policy in line with the Convention on Biological Diversity targets for 2020, which obliges signatories to identify and prioritize invasive alien species and their pathways of invasion, to control or eradicate priority species, and to manage pathways to prevent the introduction and establishment of new invasive alien species (3).

An EU-wide regulation that coordinates a preventative and responsive system across the member states is a welcome step forward. However, one aspect of the draft risks fundamentally compromising its capacity to tackle the issue: The list of species to which the system would apply is strictly capped at a maximum of 50 species, for at least an initial period of 5 years after adoption (realistically, until 2020). This is only 3% of the 1500 invasive alien species already recognized as present and problematic in the European Union (1, 4), which generate a minimum estimated cost of €12.5 billion annually (5, 6).

The justification for capping the number of priority species is "to provide member states with certainty regarding the extent and

Letters to the Editor

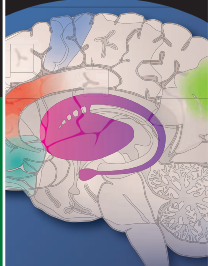
Letters (~300 words) discuss material published in *Science* in the past 3 months or matters of general interest. Letters are not acknowledged upon receipt. Whether published in full or in part, Letters are subject to editing for clarity and space. Letters submitted, published, or posted elsewhere, in print or online, will be disqualified. To submit a Letter, go to www.submit2science.org.

CREDIT: SANDRA CAVALCANTI



Broadening the remit
of metamaterials

939



Synapses and
language

944

costs of the actions they will be expected to take.” Given the recognized long-term cost efficiencies of early action on invasive alien species (7), this economic justification is a short-term one, placing the burden of action and a crushing financial bill on future generations. The system should be flexible, responsive, and able to be updated as frequently as needed. Unless the cap is altered, we risk missing a major opportunity, sacrificing longer-term ecological and economic benefits in the name of minimizing short-term input.

C. CARBONERAS,¹ P. WALTON,² M. VILÀ^{3*}

¹Royal Society for the Protection of Birds, The Lodge, Sandy, Bedfordshire, SG19 2DL, UK. ²Royal Society for the Protection of Birds, Edinburgh Park, Edinburgh, EH12 9DH, UK. ³Estación Biológica de Doñana (EBD-CSIC), E-41092, Sevilla, Spain.

*Corresponding author. E-mail: montse.vila@ebd.csic.es

References

1. “Proposal for a Regulation of the European Parliament and of the Council on the prevention and management of the introduction and spread of invasive alien species” [European Commission, COM(2013) 620 final, Brussels, 2013].
2. “Our life insurance, our natural capital: An EU biodiversity strategy to 2020” [European Commission, COM(2011) 244 final, Brussels, 2011].
3. Convention on Biological Diversity, “Strategic Plan for Biodiversity 2011–2020” (COP 10 Decision X/2, 2010).
4. M. Vilà *et al.*, *Front. Ecol. Environ.* **8**, 135 (2010).
5. C. Shine *et al.*, “Assessment to support continued development of the EU strategy to combat invasive alien species” [Final Report for EC, Institute for European Environmental Policy (IEEP), Brussels, 2010].
6. P. E. Hulme, P. Pyšek, W. Nentwig, M. Vilà, *Science* **324**, 40 (2009).
7. R. P. Keller, D. M. Lodge, D. C. Finnoff, *Proc. Natl. Acad. Sci. U.S.A.* **104**, 203 (2007).

Drilling Plans Endanger Yasuní's Biodiversity

DESPITE BEING ONE OF THE MOST MEGADIVERSE forests and a sanctuary for ancestral indigenous people (1–3), Ecuador's Yasuní National Park has always faced the looming threat of oil exploitation (“Opponents vow to block Amazon drilling,” *News of the Week*, 23 August, p. 827). In 2007, in an effort to protect Yasuní's biodiversity and, more important, mitigate climate change associated with the burning of fossil fuels, Ecuadorian President Rafael Correa promised to keep approximately 850 million barrels of heavy crude oil locked underground to prevent the release of 410 million metric tons of CO₂ into the atmosphere. In exchange, the international community would finance a compensation of US\$3.6 billion (2–5)—about half of the total cost of reducing the CO₂ emissions (US\$7.2 billion) if the oil were to be extracted.

Despite this arrangement, on 15 August 2013, Correa abandoned the moratorium on oil drilling in Yasuní (6). He justified the move by citing inadequate international

CORRECTIONS AND CLARIFICATIONS

Letters: “Response to ‘In defense of WHO's blood donation policy’” by N. Lacetera *et al.* (8 November, p. 692). Due to an editorial error, the corresponding letter author, Neelam Dhingra, was referred to once as “he” instead of “she” and three times as “Dinghra.” The HTML and PDF versions online have been corrected.

Reports: “Structure-based design of a fusion glycoprotein vaccine for respiratory syncytial virus” by J. S. McLellan *et al.* (1 November, p. 592). The senior authors did not contribute equally. The HTML and PDF versions online are correct.

Reports: “Parameter space compression underlies emergent theories and predictive models” by B. B. Machta *et al.* (1 November, p. 604). NSF grant DMR 1312160 should have been included in the Acknowledgments. The HTML and PDF versions online are correct.

News Focus: “Varmus's second act” by J. Kaiser (25 October, p. 416). The article erroneously stated that PubMed Central, NIH's full-text papers archive, will soon add commenting tools. The tools have been added to PubMed, NIH's abstracts database. The HTML and PDF versions online have been corrected.

Reports: “Stress-inducible regulation of heat shock factor 1 by the deacetylase SIRT1” by S. D. Westerheide *et al.* (20 February 2009, p. 1063). The authors inadvertently duplicated lanes from Fig. 2A in the bottom panel of Fig. 2B. The corrected Fig. 2B is provided here and does not alter the conclusions of the experiment. In addition, Fig. 3, A and C, and fig. S7 were affected by an insertion in the construct for the HSF1 K80R mutant, which is described in a correction to the supplementary materials. Experiments with the remade HSF1 K80R construct support our finding that acetylation at HSF1 K80 disrupts DNA binding activity. HSF1 K80R, a mutation that retains the charge of the lysine without allowing acetylation, exhibits DNA binding activity (see corrected Fig. 3A here), whereas the HSF1 K80Q acetylation mimic does not. Also, the HSF1 K80R construct is able to induce *hsp90* and *hsp25* gene expression as potently as HSF1 wild type (WT) when transfected into *hsf1*^{−/−} cells (see corrected Fig. 3C here). Details are in the revised supplementary materials (www.sciencemag.org/cgi/content/full/323/5917/1063/DC1).

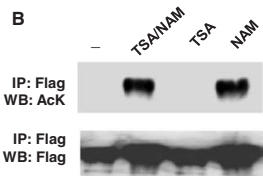


Fig. 2B. Effects of nicotinamide (NAM) and trichostatin A (TSA) on HSF1 acetylation. 293T cells transfected with Flag-HSF1 and p300 were treated with TSA or NAM, or both, and exposed to heat shock, then cell lysates were analyzed by acetylation assay.

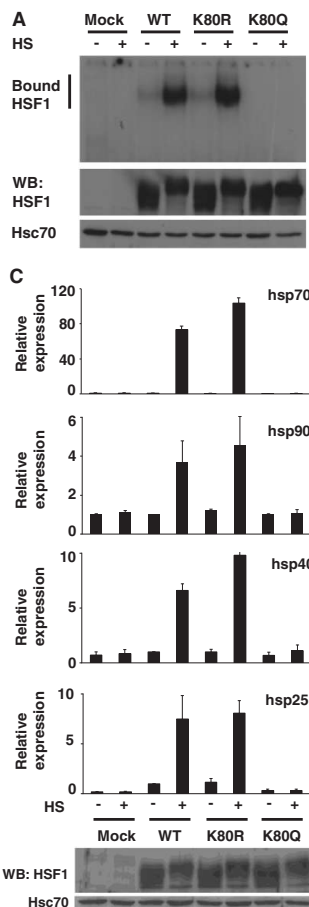


Fig. 3. HSF1 K80Q disrupts the HSR, whereas HSF1 K80R does not. (A) In HSF1, substitution of glutamine at K80 disrupts DNA binding activity, whereas replacement with arginine does not. Electrophoretic mobility shift assay (EMSA) reactions were performed with extracts from *hsf1*^{−/−} cells transfected with the indicated HSF1 constructs treated with or without heat shock (HS) (top). The EMSA probe contains the proximal heat shock element from the human *hsp70* promoter. Western blot analysis was performed on the same samples to show HSF1 and heat shock cognate 70 (Hsc70) levels. (B) Mutation of HSF1 at K80 to arginine rescues the HSR in *hsf1*^{−/−} cells, whereas mutation of HSF1 to glutamine does not. *hsf1*^{−/−} cells were transfected with the indicated versions of human HSF1 and treated with or without heat shock. RNA was quantified using quantitative polymerase chain reaction with primers for the indicated genes. Data are normalized to values obtained for glyceraldehyde 3-phosphate dehydrogenase and are relative to the abundance of each mRNA in WT HSF1 cells treated without heat shock (value set as 1). Experiments in (A) and (C) were performed in triplicate, and error bars indicate \pm SD.

donations from developed nations to protect the park. The presidential decision to exploit Yasuní's oil, estimated to generate \$18 billion, was also portrayed as an opportunity to deal with poverty (6–8). The reality is that poverty was not eradicated during the past four decades of oil exploitation in Ecuador. On the contrary, Big Oil companies (such as Chevron-Texaco) have caused deleterious environmental-social impacts in important areas of Ecuador's Amazon (9), reaching a total liability cost of \$18 billion (10). More than 50% of Ecuador's population disagrees with Correa's decision (6).

The Ecuadorian government should face its responsibility to conserve Yasuní and should implement more sustainable alternatives focused on renewable resources and market diversification (such as ecotourism) to allow for economic growth in the long term. It is not too late for Ecuador to ensure human and environmental rights and keep alive the dream of having a future without oil.

JUAN JOSÉ ALAVA^{1,2*} AND NASTENKA CALLE³

¹School of Resource and Environmental Management, Faculty of Environment, Simon Fraser University, Burnaby, BC V5A 1S6, Canada. ²Fundacion Ecuatoriana para el



Yasuní National Park

Estudio de Mamíferos Marinos, Ecuador. ³Pacific Institute for Climate Solutions, Simon Fraser University, Burnaby, BC V5A 1S6, Canada.

*Corresponding author. E-mail: jalavasa@sfu.ca

References

1. M. S. Bass *et al.*, *PLOS ONE* **5**, e8767 (2010).
2. E. Marx, *Science* **330**, 1170 (2010).
3. S. E. Pappalardo, M. De Marchi, F. Ferrarese, *PLOS ONE* **8**, e66293 (2013).
4. C. Larrea, L. Warnars, *Energy Sustain. Dev.* **13**, 219 (2009).
5. M. Finer, R. Moncel, C. N. Jenkins, *Biotropica* **42**, 63 (2010).
6. El Universo, "Actualidad: El Gobierno pone fin a la iniciativa Yasuní-ITT y avala su explotación," *El Universo* (16 August 2013); www.eluniverso.com/noticias/2013/08/16/nota/1295016/gobierno-pone-fin-iniciativa-yasuni-itt-avala-su-explotacion [in Spanish].
7. "Ecuador's environmental policy: Blame ITT on the West," *The Economist* (16 August 2013); www.economist.com/blogs/americasview/2013/08/ecuadors-environmental-policy.
8. "Oil in Ecuador: It's hard to be green," *The Economist* (28 September 2013); www.economist.com/news/americas/21586825-correa-gets-away-u-turn-its-hard-be-green.
9. M. San Sebastian, A. K. Hurtig, *Pan. Am. J. Publ. Health* **15**, 205 (2004).
10. S. Joseph, *J. Hum. Rights Environ.* **3**, 70 (2012).

CREDIT: GEOFF GALLICE/WIKIMEDIA COMMONS

THE INTERNET

Running in Social Media Circles

William H. Dutton

In 2006, a cover of *Time* announced the magazine's "Person of the Year" to be "You"—because "You control the Information Age" (1). This marked a highpoint in the heady enthusiasm around Web 2.0 innovations such as YouTube, Facebook, and Twitter that enabled Internet users to more easily create, blog, and post content online. Soon called "social media," the new applications not only raised the economic prospects of these startups and Internet industries as a whole in the post-dot-com period but also were seen as heralding the greater empowerment of individuals as producers and users of content. User-generated content and networking would be a democratizing force on the Internet.

That same year, Alice Marwick set out on her dissertation research that led to *Status Update*. Marwick (now at Fordham University) focused on the workers engaged in the San Francisco social media scene. She began following the scene through blogs, tweets, conversations, and then 9 months of participant-observation (2008–09), spending considerable time attending events involving social media firms' members, employees, and their followers. These included tech events, meetups, and mashable parties where members of these social circles valued being seen, such as the famous annual Burning Man gathering in Nevada's Black Rock Desert.

Her study concentrated on how this social media scene functioned rather than, for example, on the production or the use of social media. Nevertheless, she came away from the field with strong conclusions about the social media insiders and their fans—who they are, what they do, and why. In contrast to the democratic empowerment ideology often associated with social media (illustrated by *Time*'s recognition of the user), Marwick found a culture that promoted rather than countered inequality. The culture of the founders, and their social circles, was

hierarchical. These hierarchies were most often dominated by young, white males, but status also accrued to those who worked for the highest-status companies, were most successful as entrepreneurs (the most prized role), or garnered the most attention.

This status hierarchy was not just a local Silicon Valley phenomenon. Marwick saw the founding culture embedded in social

for user status propagates this ideology.

To Marwick, this is nothing less than a betrayal of the counterculture initially associated with the Internet's founding. The Internet may have begun as one of the most successful experiments in socialism in supporting free and open access, but the social media elite and their followers have sold out to a liberal, capitalist ethos of everyone competing for status in the networked society. She notes that to "achieve high status, one must be committed to the entrepreneurial startup culture, engage in self-conscious self-marketing, network continually, or do a combination of all three." More important, social media, from her perspective, have been ideologically produced in ways that reinforce these neoliberal commercial values and interests among users rather than foster a free and open culture of participation.

The book contributes some original insights on the culture of the employees within new social media industries. Silicon Valley and its elite entrepreneurs during the micro-electronics and personal computing eras have been critically examined by academics and journalists, but—despite a major motion picture on Facebook founder Mark Zuckerberg (2)—less work has focused on the social media entrepreneurs. *Status Update* is less about the inner circle of these companies than the social circles of their employees. In fact, the invisibility of the inner circle is one of the book's more frustrating aspects. Likewise, the proverbial user is also under-researched—even though Marwick formulates major

conceptions of the user on the basis of following the social media circles of Silicon Valley and San Francisco. Nonusers and social media users who simply want to share photos or keep in touch with friends remain invisible.

More a journalistic account rather than an ethnography, *Social Update* nevertheless provides a useful critique of a youthful, male cul-



Backyard gathering. Mark Zuckerberg and FriendFeed co-founders.

media applications. Those encourage competition for attention, visibility, and status by design, such as by accumulating "friends," "likes," "followers," retweets, and comments on posts—all various signs of importance within different social media worlds. Rather than enabling democratic empowerment, users are incentivized to think strategically about how to present themselves and their posts online to gain popularity. Improving your status in this world involves strategic self-promotion. Social media are about upgrading your status.

The patterns and themes emerging from Marwick's fieldwork are useful in challenging technologically deterministic views of the Internet. Marwick instead sees social media as socially shaped by the ideology of the founders. They have a neoliberal commitment to "deregulated, free-market economic policies as a means to freedom and prosperity," and the design of social media that brings this self-promotional culture of free competition

Status Update

Celebrity, Publicity, and Branding in the Social Media Age

by Alice E. Marwick

Yale University Press,
New Haven, CT, 2013. 368 pp.
\$27.50, £17.99.
ISBN 9780300176728.

The reviewer is at the Oxford Internet Institute, University of Oxford, 1 St Giles, Oxford OX1 3J5, UK. E-mail: william.dutton@oii.ox.ac.uk

CREDIT: COURTESY OF FACEBOOK

ture of celebrity that pervades the social media scene. The author takes the liberty of addressing topics well beyond her research (such as privacy and surveillance) and speculating on how users think about themselves. However, her research spotlights some key issues. One is the “continued male dominance in the tech industry.” Another, more novel, is how many use social media to market themselves rather than to inform their networks. The author makes a valuable distinction “between making information public and publicizing it.” Marwick sees this not as an accident but as a product of the culture of Silicon Valley’s social media entrepreneurs.

References

1. *Time*, 26 December 2006.
2. D. Fincher, director, *The Social Network* (Columbia Pictures, 2010).

10.1126/science.1245179

PHYSICS

Theories Beyond Testability?

George Ellis

Theoretical physics is often considered the pinnacle of fundamental science, marked by the hallmark of developing strict mathematical theories that lead to empirically testable results confirmed to high accuracy. This is an extraordinary achievement—exemplified by Newton’s theory of gravity, Maxwell’s theory of electromagnetism, Einstein’s theories of special and general relativity, and the standard model of particle physics. Many other disciplines strive to mimic the methods of theoretical physics in order to conform to what is considered the ideal scientific paradigm.

It may come as a surprise then to other scientists that some theoretical physicists are now either explicitly or implicitly pushing for a change in what is required in order that a theory be regarded as scientific. A shift of the balance between empirical and theoretical elements of theory assessment is taking place, with a proposed weakening of the requirement of experimental confirmation of scientific theories. This has arisen because some branches of theoretical physics are dealing with topics that are not merely beyond the reach of current experimental testing: theories are being

offered that will forever be beyond the possibility of testing. Their proponents wish this work to be regarded as solid science, even though its central tenets will never be testable by any practical means.

String theory has been claimed to be the ultimate theory of fundamental physics, unifying all fundamental forces into one and explaining the existence of all fundamental particles as vibrations of two-dimensional objects in 10 or 11 dimensional spacetimes. It thus potentially predicts all the results of standard fundamental physics. However, the energy scales characterizing string theory are so high that it cannot be tested by any particle collider that we can ever hope to construct. The tests that vindicate standard particle physics do not substantiate the string theory claim that extra spacetime dimensions exist, which are invisible to us because they are so small.

If we can’t ever hope to test the theory experimentally, is it really scientific? Richard Dawid’s timely *String Theory and the Scientific Method* provides a carefully written consideration of what kinds of criteria can be used for nonempirical theory assessment, in the absence of direct or even indirect evidence for the theory’s core features. The argument hinges on the concept of limits to underdetermination. Theory is undetermined by the data if various theories can all explain the same evidence, and we have to choose among them. The classic example is the epicycle theory of planetary motion: It can indeed explain the data, given enough epicycles. We reject it because we have a better explanation.

But how do we decide what a better theory is? And what principles can we use to support a theory as scientific, in the absence of evidence? Dawid (a philosopher of science at the University of Vienna) offers three lines of defense for such theories: First, the no alternatives argument (NAA). It is the only scientific theory we can find to explain the phenomena we wish to explain. Second, the argument of unexpected explanatory coherence (UEA). The theory unexpectedly unifies phenomena it was not designed to take into account. Third, the meta-inductive argument (MIA). Theoretical physics has been highly successful in making predictions from unifying theories that have then been confirmed, e.g., the prediction of antiparticles. Therefore we should trust that its new theories would indeed also be confirmed, if some kind of confirmatory experiment was possible.

As regards NAA, people argue that string

theory offers the only available route to a unified theory of fundamental physics, so it must be the correct theory. But that conclusion depends on the key assumption that such a theory exists, which may be incorrect. Although string theory may have a claim as the only ultraviolet completion of quantum field theory, that claim will only be realized when we have a properly defined string theory to consider. As regards UEA, string theory scores well. It points to unexpected mathematical structures relevant to some physics. In this context, however, it is in essence a computational tool rather than a theory regarding the nature of things. As regards MIA, we are asked to believe that past success will necessarily indicate future success. But this need

not be the case. The SU(5) grand unified theory of forces should have worked because it was such a good theory, but proton decay experiments ruled it out.

These arguments add sound support to the theory if we can have experimental evidence of some kind that supports its basic contentions, so

that Bayesian analysis and inference to best explanation can be applied. But do they really allow us to dispense with the need for any directly related evidence at all?

Similar issues arise for claimed scientific theories that support the idea of a multiverse and theories for creation of the universe. Their central claims are not testable by any observation even in principle. (Some associated effects may be predictable, but they have other possible explanations.) In both cases, given the lack of decisive evidence, theoretical arguments are supposed to carry the day. We are faced with extrapolation from tested physics to the unknown. Different extrapolations are possible, depending on what aspect of established theory we regard as most fundamental. But in the contexts considered, the extrapolation is untestable.

Dawid makes what is probably the best possible case that theoretical justification can succeed. The skeptic will remain unconvinced. The rise of the scientific method was crucially based on experimental confirmation of the core aspects of hypothesized theories. The conservative view is that abandoning this gold standard means leaving the realm of science, no matter how well one argues that theory alone will suffice. I applaud the fact that *String Theory and the Scientific Method* explicitly raises these questions and addresses them in a clear and well-considered way.

10.1126/science.1246302

String Theory and the Scientific Method

by Richard Dawid
Cambridge University
Press, Cambridge, 2013.
212 pp. \$95, £60.
ISBN 9781107029712.

The reviewer is at the Department of Mathematics and Applied Mathematics, University of Cape Town, Rondebosch 7700, South Africa. E-mail: george.ellis@uct.ac.za

EDUCATION RESEARCH

Instructional Complexity and the Science to Constrain It

Kenneth R. Koedinger^{1*}, Julie L. Booth², David Klahr¹

Science and technology have had enormous impact on many areas of human endeavor but surprisingly little effect on education. Many large-scale field trials of science-based innovations in education have yielded scant evidence of improvement in student learning (1, 2), although a few have reliable positive outcomes (3, 4). Education involves many important issues, such as cultural questions of values, but we focus on instructional decision-making in the context of determined instructional goals and suggests ways to manage instructional complexity.

Ambiguities and Contexts in Instruction

Many debates about instructional methods suffer from a tendency to apply compelling labels to vaguely described procedures, rather than operational definitions of instructional practices (5, 6). Even when practices are reasonably well defined, there is not a consistent evidential base for deciding which approach is optimal for learning. Empirical investigations of instructional methods, including controlled laboratory experiments in cognitive and educational psychology, often fail to yield consensus. For instance, controversy exists regarding benefits of immediate (7) versus delayed feedback (8), or use of concrete (9) versus abstract materials (10).

Further complicating the picture is that results often vary across content or populations. For example, instruction that is effective for simple skills has been found to be ineffective for more complex skills (11), and techniques such as prompting students to provide explanations (12) may not be universally effective (13). Effectiveness of different approaches is often contingent on student population or level of prior achievement or aptitude. Some approaches, for example, may be particularly effective for low-achieving students (14, 15). Although specific instructional decisions may be useful at the level of the individual student (e.g., will

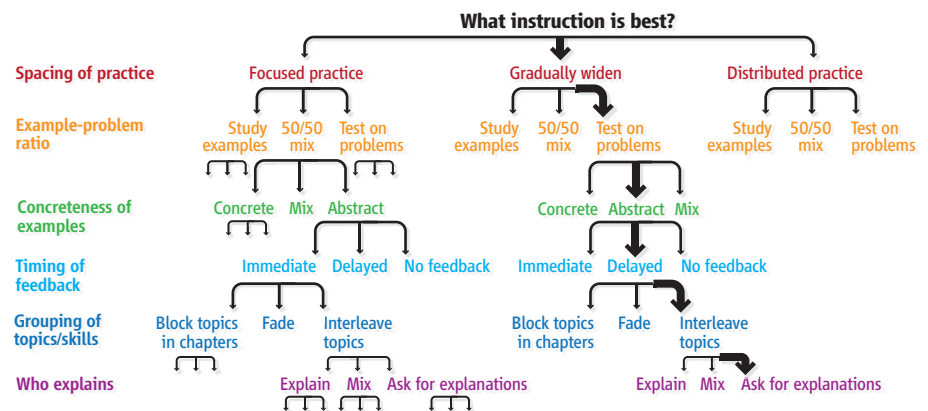
this student learn better right now if I give her feedback or if I let her grapple with the material for a while?), the search for general methods that optimize the effectiveness, efficiency, and level of student engagement is more challenging.

Complexity of Instructional Design

Of the many factors that affect learning in real-world contexts, we describe three of particular importance: instructional technique, dosage, and timing. Independently

School-researcher partnerships and large in vivo experiments help focus on useful, effective, instruction.

Intervention timing. The optimal technique may not be the same early in learning as it is later. Consider how novice students benefit from studying many worked examples in place of many problems, whereas shifting to pure problem-solving practice becomes more effective as students develop expertise (17). Many researchers have suggested that effective instruction should provide more structure or support early in learning or for more difficult or complex ideas and fade that assistance as the learner



Instructional design choices. Different choices along different instructional dimensions can be combined to produce a vast set of instructional options. The path with thicker arrows illustrates one set of choices within a space of trillions of such options.

combining choices on one dimension with choices on other dimensions produces a vast space of reasonable choice options, as shown in the figure.

Instructional techniques. Many lists of learning principles suggest instructional techniques and point to supporting research (12, 16). Each list has between 3 and 25 principles. In-depth synthesis of nine such sources yielded an estimate of 30 independent instructional techniques (see the table and table S1).

Dosage and implementation. Many instructional distinctions have multiple values or are continuous (e.g., the ratio of examples to questions or problems given in an assignment, the spacing of time between related activities). These dimensions are mostly compatible with each other—almost all can be combined with any other.

advances (18, 19).

If we consider just 15 of the 30 instructional techniques we identified, three alternative dosage levels, and the possibility of different dosage choices for early and late instruction, we compute $3^{15 \times 2}$ or 205 trillion options. Some combinations may not be possible or may not make sense in a particular content area, yet other factors add further complexity: Many techniques have more than three possible dosage levels, there may be more than two time points where the instructional optimum changes, different knowledge needs in different domains often require a different optimal combination. For example, it may be optimal to adjust spacing of practice continually for each student on each knowledge component (20). As another example, when the target knowledge is simple facts, requiring

¹Carnegie Mellon University, Pittsburgh, PA 15213, USA.

²Temple University, Philadelphia, PA 19122, USA.

*Corresponding author. koedinger@cmu.edu

recall and use of knowledge produces more robust learning, but for complex problem-solving skills, studying a substantial number of worked examples is better (1).

The vast size of this space reveals that simple two-sided debates about improving learning—in the scientific literature, as well as in the public forum—obscure the complexity that a productive science of instruction must address.

Taming Instructional Complexity

We make five recommendations to advance instructional theory and to maximize its relevance to educational practice.

1. *Searching in the function space.* Following the Knowledge-Learning-Instruction framework (21), we suggest three layers of functions of instruction: (i)

to yield better assessment outcomes that reflect broad and lasting improvements in learner performance, (ii) instruction must change learners' knowledge base or intellectual capacity and (iii) must require that learners' minds execute appropriate learning processes.

We specify different functions to be achieved at each layer. The most distal, but observable, functions of instruction are assessment outcomes: long-term retention, transfer to new contexts, or desire for future learning. More proximal, but unobservable, functions are those that change different kinds of knowledge: facts, procedural skills, principles, learning skills, or learning beliefs and dispositions. The most immediate and unobservable functions support learning processes or mechanisms: memory

and fluency building, induction and refinement, or understanding and sense-making (21, 22).

Functions at each layer suggest more focused questions that reduce the instructional design space (23): Which instructional choices best support memory to increase long-term retention of facts? Which are best for inducing general skills that produce transfer of learning to new situations? Which are best for sense-making processes that produce learning skills and higher learner self-efficacy toward better future learning? We can associate different subsets of the instructional design dimensions with individual learning functions. For example, spacing enhances memory, worked-examples enhance induction, and self-explanation enhances sense-making (see the table). The success of this approach of separating causal functions of instruction depends on partial decomposability (24) and some independence of effects of instructional variables: Designs optimal for one function (e.g., memory) should not be detrimental to another (e.g., induction). To illustrate, consider that facts require memory but not induction; thus, a designer can focus just on the subset of instructional techniques that facilitate memory.

Theoretical work can offer insight into when an instructional choice is dependent on a learning function. Computational models that learn like human students do demonstrate, for instance, that interleaving problems of different kinds functions to improve learning of when to use a principle or procedure (25), whereas blocking similar problems types ("one subgoal at a time") improves learning of how to execute (26).

2. *Experimental tests of instructional function decomposability.* Optimal instructional choices may be function-specific, given variation across studies of instructional techniques where results are dependent on the nature of the knowledge goals. For example, if the instructional goal is long-term retention (an outcome function) of a fact (a knowledge function), then better memory processes (a learning function) are required; more testing than study will optimize these functions. If the instructional goal is transfer (a different outcome function) of a general skill (a different knowledge function), then better induction processes (a different learning function) are required; more worked-example study will optimize these functions. The ideal experiment to test this hypothesis is a two-factor study that varies the knowledge content (fact-learning versus general

Principle		Description of Typical Effect
Memory/Fluency	Spacing	Space practice across time > mass practice all at once
	Scaffolding	Sequence instruction toward higher goals > no sequencing
	Exam expectations	Students expect to be tested > no testing expected
	Testing	Quiz for retrieval practice > study same material
	Segmenting	Present lesson in learner-paced segments > as a continuous unit
	Feedback	Provide feedback during learning > no feedback provided
Induction/Refinement	Pretraining	Practice key prior skills before lesson > jump in
	Worked example	Worked examples + problem-solving practice > practice alone
	Concreteness fading	Concrete to abstract representations > starting with abstract
	Guided attention	Words include cues about organization > no organization cues
	Linking	Integrate instructional components > no integration
	Goldilocks	Instruct at intermediate difficulty level > too hard or too easy
	Activate preconceptions	Cue student's prior knowledge > no prior knowledge cues
	Feedback timing	Immediate feedback on errors > delayed feedback
	Interleaving	Intermix practice on different skills > block practice all at once
	Application	Practice applying new knowledge > no application
Sense-making/Understanding	Variability	Practice with varied instances > similar instances
	Comparison	Compare multiple instances > only one instance
	Multimedia	Graphics + verbal descriptions > verbal descriptions alone
	Modality principle	Verbal descriptions presented in audio > in written form
	Redundancy	Verbal descriptions in audio > both audio & written
	Spatial contiguity	Present description next to image element described > separated
	Temporal contiguity	Present audio & image element at the same time > separated
	Coherence	Extraneous words, pictures, sounds excluded > included
	Anchored learning	Real-world problems > abstract problems
	Metacognition	Metacognition supported > no support for metacognition
	Explanation	Prompt for self-explanation > give explanation > no prompt
	Questioning	Time for reflection & questioning > instruction alone
	Cognitive dissonance	Present incorrect or alternate perspectives > only correct
	Interest	Instruction relevant to student interests > not relevant

Instructional design principles. These address three different functions of instruction: memory, induction, and sense-making (see table S1).

skill) and instructional strategy (example study versus testing). More experiments are needed that differentiate how different instructional techniques enhance different learning functions.

3. Massive online multifactor studies. Massive online experiments involve thousands of participants and vary many factors at once. Such studies (27, 28) can accelerate accumulation of data that can drive instructional theory development. The point is to test hypotheses that identify, in the context of a particular instructional function, what instructional dimensions can or cannot be treated independently.

Past studies have emphasized near-term effects of variations in user-interface features (27, 28). Designing massive online studies that vary multiple instructional techniques is feasible, but convenient access to long-term outcome variables is an unsolved problem. Proximal variables measuring student engagement and local performance are easy to collect (e.g., how long a game or online course is used; proportion correct within it). But measures of students' local performance and their judgments of learning are sometimes unrelated, or even negatively correlated, with desired long-term learning outcomes (29).

4. Learning data infrastructure. Massive instructional experiments are essentially going on all the time in schools and colleges. Because collecting data on such activities is expensive, variations in instructional techniques are rarely tracked and associated with student outcomes. Yet, technology is increasingly providing low-cost instruments to evaluate the learning experience for data collection. Investment is needed in infrastructure to facilitate large-scale data collection, access, and use, particularly in urban and low-income school districts. Two current efforts include LearnLab's huge educational technology data repository (30) and the Gates Foundation's Shared Learning Infrastructure (31).

5. School-researcher partnerships. Ongoing collaborative problem-solving partnerships are needed to facilitate interaction between researchers, practitioners, and school administrators. When school cooperation is well-managed and most or all of an experiment is computer-based, large well-controlled "in vivo" experiments can be run in courses with substantially less effort than an analogous lab study.

A lab-derived principle may not scale to real courses because nonmanipulated variables may change from the lab to a real course, which may change learning results.

In in vivo experiments, these background conditions are not arbitrarily chosen by the researchers but instead are determined by the existing context. Thus, they enable detection of generalization limits more quickly before moving to long, expensive randomized field trials.

School-researcher partnerships are useful not only for facilitating experimentation in real learning contexts but also for designing and implementing new studies that address practitioner needs (32, 33).

In addition to school administrators and practitioners, partnerships must include critical research perspectives, including domain specialists (e.g., biologists and physicists); learning scientists (e.g., psychologists and human-computer interface experts); and education researchers (e.g., physics and math educators). It is important to forge compromises between the control desired by researchers and the flexibility demanded by real-world classrooms. Practitioners and education researchers may involve more domain specialists and psychologists in design-based research, in which iterative changes are made to instruction in a closely observed, natural learning environment in order to examine effects of multiple factors within the classroom (34).

Our recommendations would require reexamination of assumptions about the types of research that are useful. We see promise in sustained science-practice infrastructure funding programs, creation of new learning science programs at universities, and emergence of new fields and professional organizations (35, 36). These and other efforts are needed to bring the full potential of science and technology to bear on optimizing educational outcomes.

References and Notes

1. M. Dynarski et al., Effectiveness of Reading and Mathematics Software Products: Findings from the First Student Cohort [Report provided to Congress by the National Center for Education Evaluation, Institute of Education Sciences (IES), Washington, DC, 2007].
2. Coalition for Evidence-Based Policy, Randomized Controlled Trials Commissioned by the IES since 2002: How Many Found Positive Versus Weak or No Effects; <http://coalition4evidence.org/wp-content/uploads/2013/06/IES-Commissioned-RCTs-positive-vs-weak-or-null-findings-7-2013.pdf>.
3. J. Roschelle et al., *Am. Educ. Res. J.* **47**, 833–878 (2010).
4. J. F. Pane, B. A. Griffin, D. F. McCaffrey, R. Karam, *Effectiveness of Cognitive Tutor Algebra I at Scale* (Working paper, Rand Corp., Alexandria, VA, 2013); www.rand.org/content/dam/rand/pubs/working_papers/WR900/WR984/RAND_WR984.pdf.
5. D. Klahr, J. Li, *J. Sci. Educ. Technol.* **14**, 217–238 (2005).
6. D. Klahr, *Proc. Natl. Acad. Sci. U.S.A.* **110** (suppl. 3), 14075–14080 (2013).
7. A. T. Corbett, J. R. Anderson, *Proceedings of ACM CHI 2001* (ACM Press, New York, 2001), pp. 245–252.

8. R. A. Schmidt, R. A. Bjork, *Psychol. Sci.* **3**, 207–217 (1992).
9. A. Paivio, *J. Verbal Learn. Verbal Behav.* **4**, 32–38 (1965).
10. J. A. Kaminski, V. M. Sloutsky, A. F. Heckler, *Science* **320**, 454–455 (2008).
11. G. Wulf, C. H. Shea, *Psychon. Bull. Rev.* **9**, 185–211 (2002).
12. H. Pashler et al., *Organizing Instruction and Study to Improve Student Learning* (National Center for Education Research 2007–2004, U.S. Department of Education, Washington, DC, 2007).
13. R. Wylie, K. R. Koedinger, T. Mitamura, *Proceedings of the 31st Annual Conference of the Cognitive Science Society (CSS)*, Wheat Ridge, CO, 2009, pp. 1300–1305.
14. R. E. Goska, P. L. Ackerman, *J. Educ. Psychol.* **88**, 249–259 (1996).
15. S. Kalyuga, *Educ. Psychol. Rev.* **19**, 387–399 (2007).
16. K. A. Dunlosky, E. J. Rawson, E. J. Marsh, M. J. Nathan, D. T. Willingham, *Psychol. Sci. Public Interest* **14**, 4–58 (2013).
17. S. Kalyuga, P. Ayres, P. Chandler, J. Sweller, *Educ. Psychol.* **38**, 23–31 (2003).
18. R. L. Goldstone, J. Y. Son, *J. Learn. Sci.* **14**, 69–110 (2005).
19. P. A. Woźniak, E. J. Gorzelańczyk, *Acta Neurobiol. Exp. (Warsz.)* **54**, 59–62 (1994).
20. P. I. Pavlik, J. R. Anderson, *J. Exp. Psychol. Appl.* **14**, 101–117 (2008).
21. K. R. Koedinger, A. T. Corbett, C. Perfetti, *Cogn. Sci.* **36**, 757–798 (2012).
22. L. Resnick, C. Asterhan, S. Clarke, Eds., *Socializing Intelligence through Academic Talk and Dialogue* (American Educational Research Association, Washington, DC, 2013).
23. G. Bradshaw, in *Cognitive Models of Science*, R. Giere and H. Feigl, Eds. (University of Minnesota Press, Minneapolis, 1992), pp. 239–250.
24. H. A. Simon, *Sciences of the Artificial* (MIT Press, Cambridge, MA, 1969).
25. N. Li, W. Cohen, K. Koedinger, *Lect. Notes Comput. Sci.* **7315**, 185–194 (2012).
26. K. VanLehn, *Artif. Intell.* **31**, 1 (1987).
27. D. Lomas, K. Patel, J. Forlizzi, K. R. Koedinger, in *Proceedings of the SIGCHI Conference on Human Factors in Computing Systems* (ACM, New York, 2013), pp. 89–98.
28. E. Andersen, Y. Liu, R. Snider, R. Szeto, Z. Popović, *Proceedings of the SIGCHI Conference on Human Factors in Computing Systems* (ACM, New York, 2011), pp. 1275–1278.
29. R. A. Bjork, J. Dunlosky, N. Kornell, *Annu. Rev. Psychol.* **64**, 417–444 (2013).
30. LearnLab, Pittsburgh Science of Learning Center; www.learnlab.org/technologies/datashop/index.php.
31. InBloom, www.inbloom.org.
32. Strategic Education Research Partnership, www.serpinstiute.org/about/overview.php.
33. IES, U.S. Department of Education, Researcher-Practitioner Partnerships in Education Research, Catalog of Federal Domestic Assistance 84.305H; http://ies.ed.gov/funding/ncer_rfas/partnerships.asp.
34. S. A. Barab, in *Handbook of the Learning Sciences*, K. Sawyer, Ed. (Cambridge Univ. Press, Cambridge, 2006), pp. 153–170.
35. Society for Research on Educational Effectiveness, www.sree.org/.
36. International Educational Data Mining Society, www.educationaldatamining.org/.

Acknowledgments: The authors receive support from NSF grant SBE-0836012 and Department of Education grants R305A100074 and R305A100404. The views expressed are those of the authors and do not represent those of the funders. Thanks to V. Aleven, A. Fisher, N. Newcombe, S. Donovan, and T. Shipley for comments.

Supplementary Materials

www.sciencemag.org/content/342/6161/935/suppl/DC1

10.1126/science.1238056

CANCER

Unwanted Evolution

Ivana Bozic^{1,2} and Martin A. Nowak^{1,2,3}

We mostly think of evolution as a process that has the power to build structures of incredible beauty and functionality, like multicellular organisms, the nervous system, and human language. But evolutionary dynamics can also lead to processes that are not wanted, such as cancer, because they oppose the survival interests of the organism. The somatic evolution of cancer is a consequence of our cells being individual replicators. Upon acquiring mutations, cells can revert to their primitive program of proliferation,

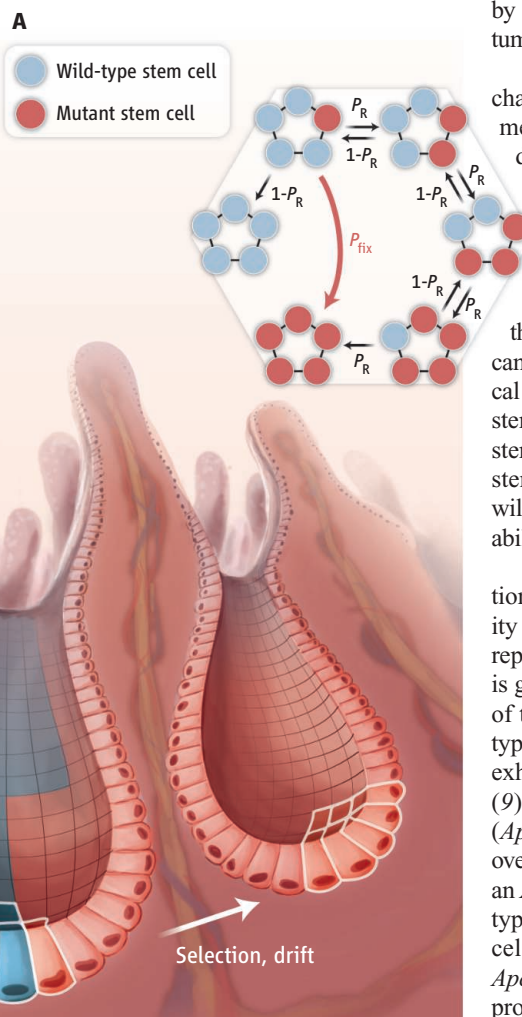
competition for survival, and selection of the fittest. On page 995 of this issue, Vermeulen *et al.* (1) demonstrate how multicellular organisms keep this unwanted evolution in check. By quantifying the effects of mutations that frequently occur during colorectal tumor development, the authors show that intestinal tissue architecture acts as a suppressor of selection.

One way to prevent unwanted evolution is to hold somatic mutation rates low. The mutation rate in healthy human cells is on the order of 10^{-10} to 10^{-9} per nucleotide base pair per cell division (2), perhaps as low as possible given reasonable energy constraints. What about selection—can it be suppressed? There are population structures where this is the case, such as when a large population of differentiated cells is continuously renewed

The dynamics of stem cell replacement at the bottom of the intestinal crypt is visualized and quantified.

¹Program for Evolutionary Dynamics, Harvard University, Cambridge, MA 02138, USA. ²Department of Mathematics, Harvard University, Cambridge, MA 02138, USA. ³Department of Organismic and Evolutionary Biology, Harvard University, Cambridge, MA 02138, USA. E-mail: martin_nowak@harvard.edu

Crypt dynamics. Stem cells reside at the bottom of crypts in the intestine. (A) The number of mutant stem cells (red) increases by 1 with probability P_R and decreases by 1 with probability $1 - P_R$. A single mutant stem cell can be lost by random drift or can take over the compartment with probability P_{fix} (see the equation). (B) The genetic composition of the stem cell compartment (at the base of the crypt) determines the composition of cells (mutant cells shown in red; wild-type cells in blue) in the entire intestinal crypt.



by the asymmetric division of stem cells (3, 4). It has been hypothesized that many epithelial tissues, which are especially susceptible to cancer because of their many cell divisions, are designed to suppress selection (3). Intestinal epithelium is replenished by equipotent stem cells residing at the bottom of crypts. These stem cells are continuously replacing each other in a random fashion (5, 6). Most intestinal tumors are thought to initiate from a transformed (mutated) stem cell, because genomic alterations occurring in differentiated cells would be “flushed out” as a result of the specific tissue architecture (differentiated cells are continuously pushed upward in the crypt and eventually undergo programmed cell death at the top of the crypt) (3, 7). The initiating genetic event in the majority of colorectal cancers is an inactivation of the *APC* tumor suppressor gene, often followed by mutations in the oncogene *KRAS* and the tumor suppressor *P53*, among other genes (8).

To measure the effect of initial genetic changes occurring in colorectal cancer, Vermeulen *et al.* visualized and quantified the dynamics of stem cell replacement in the mouse intestine when one of the stem cells in the crypt contains a particular change, such as an inactivation of one or both copies of *Apc*, activation of *Kras*, or a mutation in *p53*. The authors demonstrate that the evolutionary dynamics of stem cells can be well described by a simple mathematical model that assumes a ring of five to seven stem cells at the base of the crypt. A mutant stem cell replaces its neighboring wild-type stem cell with probability P_R , whereas the wild-type cell replaces the mutant with probability $1 - P_R$ (see the figure).

Vermeulen *et al.* show that *Apc* inactivation and *Kras* activation increase the probability that a stem cell carrying those alterations replaces a neighboring wild-type stem cell. It is generally believed that inactivation of one of the *Apc* alleles does not lead to a phenotypic change, but the authors found that *Apc* exhibits some degree of haploinsufficiency (9): Even a single inactivated *Apc* copy (*Apc*^{+/-}) leads to some selective advantage over wild-type stem cells. The probability that an *Apc*^{+/-} mutant cell replaces an *Apc*^{+/+} wild-type cell is estimated to be $P_R = 0.62$. Stem cells with both copies of *Apc* inactivated, *Apc*^{-/-}, replaced neighboring *Apc*^{+/-} cells with probability $P_R = 0.69$. Activation of *Kras* had

CREDIT: V. ALTOUNIAN/SCIENCE

the most pronounced effect, with a 78% chance of replacing an adjacent wild-type stem cell. The authors also found that *p53* mutations provide a selective advantage, but only in gut affected by inflammation ($P_R = 0.58$) and not in normal conditions ($P_R = 0.48$).

Although mutant stem cells are more likely to replace wild-type stem cells than vice versa, they can nevertheless be lost by random drift (when the frequency of mutant cell in a population decreases until it disappears). The probability that a single mutant stem cell reaches fixation in a crypt (takes over the entire stem cell compartment of the crypt) can be calculated as

$$P_{\text{fix}} = \frac{1 - \left(\frac{1 - P_R}{P_R}\right)}{1 - \left(\frac{1 - P_R}{P_R}\right)^N}$$

in which N is the number of stem cells per crypt. Assuming $N = 5$ stem cells in a crypt and using the experimentally derived values for P_R , the probability for a single *Apc*^{+/-} stem

cell to take over the crypt is 0.42. Similarly, the probability that a single *Apc*^{+/-} cell reaches fixation in an *Apc*^{+/-} background is 0.56. The authors report similar fixation probabilities based on direct measurement.

This detailed quantitative information about the initial steps in the somatic evolution of a solid cancer makes an important connection between theory and experiment. The values for the selective advantage of frequently occurring mutations can provide precise guidelines for future studies of tumor initiation and progression (10–15). As Vermeulen *et al.* point out, a similar approach can be used to investigate the role of chromosomal instability in tumor initiation. Their findings also raise new questions about the events that follow the fixation of a mutation in a single crypt, including quantification of a field cancerization effect and the change in dynamics and tissue morphology caused by the subsequent mutations. Most important, this exciting study opens the door for a quantitative understanding of cancer initiation. One can also envisage the possibility of using

the devised experimental framework for the development and testing of drugs that attack mutated stem cells, thereby preventing the process of cancer initiation.

References

1. L. Vermeulen *et al.*, *Science* **342**, 995 (2013).
2. D. J. Araten *et al.*, *Cancer Res.* **65**, 8111 (2005).
3. M. A. Nowak, F. Michor, Y. Iwasa, *Proc. Natl. Acad. Sci. U.S.A.* **100**, 14966 (2003).
4. E. Lieberman *et al.*, *Nature* **433**, 312 (2005).
5. C. Lopez-Garcia, A. M. Klein, B. D. Simons, D. J. Winton, *Science* **330**, 822 (2010).
6. H. J. Snippert *et al.*, *Cell* **143**, 134 (2010).
7. N. Barker *et al.*, *Nature* **457**, 608 (2009).
8. S. Jones *et al.*, *Proc. Natl. Acad. Sci. U.S.A.* **105**, 4283 (2008).
9. N. L. Solimini *et al.*, *Science* **337**, 104 (2012).
10. R. Meza, J. Jeon, S. H. Moolgavkar, E. G. Luebeck, *Proc. Natl. Acad. Sci. U.S.A.* **105**, 16284 (2008).
11. I. Bozic *et al.*, *Proc. Natl. Acad. Sci. U.S.A.* **107**, 18545 (2010).
12. R. Durrett *et al.*, *Theor. Popul. Biol.* **78**, 54 (2010).
13. C. Tomasetti, B. Vogelstein, G. Parmigiani, *Proc. Natl. Acad. Sci. U.S.A.* **110**, 1999 (2013).
14. B. Vogelstein *et al.*, *Science* **339**, 1546 (2013).
15. D. Wodarz, N. L. Komarova, *Computational Biology of Cancer: Lecture Notes and Mathematical Modeling* (World Scientific, Hackensack, NJ, 2008).

10.1126/science.1247887

MATERIALS SCIENCE

Metamaterials Beyond Optics

Martin Wegener

So far, the field of metamaterials has largely dealt with negative refractive indices in optics and invisibility cloaks (1–3). However, the underlying idea of designing material properties is not that narrow. More broadly, one rationally designs a subwavelength unit cell from existing constituent materials and (periodically) arranges it into an artificial solid. The properties of that solid are then determined by structure rather than chemistry and can be tailored, extreme, or even qualitatively unprecedented. Rational design is the key and makes metamaterials a rather particular class of composite materials.

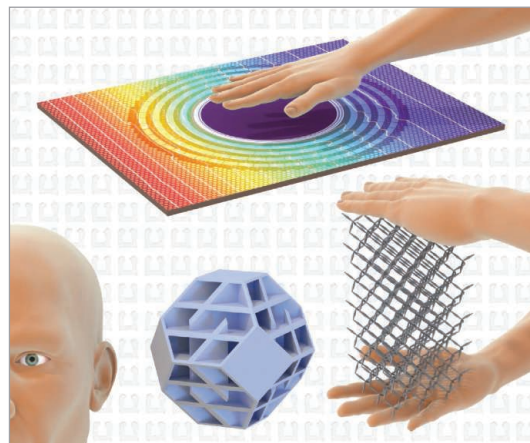
In terms of application, some aspects of metamaterials such as negative phase velocities of light (1, 2), invisibility cloaking (4, 5), or unusual optical nonlinearities (6) are fascinating but are not likely to soon appear in products, because optical absorption (loss) is too high and in part fundamentally

unavoidable. Moreover, the inexpensive manufacturing of complex large-volume three-dimensional optical metamaterials is still a formidable challenge in itself (2).

Why, then, don't we go beyond optics and also consider other material aspects (7) such as thermal, acoustic, elastic, or irreversible nonlinear mechanical properties? The corresponding wavelengths and length scales range from tens of micrometers to centimeters, rather than nanometers in optics. Hence, fabrication limitations are relaxed, thus easing real-world applications. Moreover, one lesson learned from electromagnetism is that off-resonant constituents enable low losses. In the visible spectrum, however, this results in a contrast in refractive index of no more than 3 for available nonabsorbing dielectrics. Some theoretical blueprints demand constituent-material contrasts in the range of tens or hundreds. Such values are accessible in mechanics and thermodynamics (see the figure).

The area of metamaterials may expand to find application in mechanics, acoustics, and thermodynamics.

Consider simple mechanical waves in elastic solids. They exhibit three orthogonal polarizations, one longitudinal (like sound waves in air or water) and two transverse (like electromagnetic waves). This complex



Seeing, hearing, feeling. While optics has been in the foreground of metamaterials research, opportunities arise in other areas such as acoustics, mechanics, and thermodynamics (heat conduction and diffusion). In all of these, larger lattice constants ease the fabrication requirements and losses can be much lower or absent.

Institute of Applied Physics, Institute of Nanotechnology, and DFG Center for Functional Nanostructures, Karlsruhe Institute of Technology, D-76131 Karlsruhe, Germany. E-mail: martin.wegener@kit.edu

elastic behavior gets simpler in so-called pentamode metamaterials, in which the longitudinal polarization dominates because the effective metamaterial shear modulus is small relative to the bulk modulus. Pentamode metamaterials were proposed years ago (8) but have been realized only recently (9). In these materials, wave propagation is scalar, thereby allowing analogies to optics. For example, the elastic counterpart of an optical invisibility cloak becomes possible (7). Such elastic structures would also work in the static limit. One could then mechanically protect or hide sensitive objects within the mechanical cloak.

In more detail, the elastic compressibility plays the same role that electric permittivity plays in electromagnetism; likewise, the mass density plays the role of magnetic permeability (7). Mechanical metamaterials that offer low mass density together with reasonable mechanical stability have been realized (10). Negative mass densities and anisotropic mass-density tensors are well established theoretically (7, 11), and one-dimensional model systems have been demonstrated experimentally (12) as well. Still, experimentalists need feasible blueprints to fabricate three-dimensional microstructures to achieve specific anisotropic mass-density tensors. Progress here would greatly enhance the possibilities in elasticity.

An elastic solid can be viewed as the generalization of a passive reversible linear Hooke spring. But why limit ourselves to this linear mechanical regime? Metamaterial unit cells could be constructed that break or buckle to dissipate mechanical shock energy. We also could work toward active mechanical metamaterials, integrating miniature energy sources together with sensors, actuators, and feedback loops into the individual unit cells. Nonlinear and active mechanical metamaterials are wide open for innovation.

As a second group of examples, consider thermodynamic material properties such as heat conduction or diffusion (7). Much of optical metamaterials is about molding the flow of the Poynting vector—that is, the energy flux per unit time and area. The heat current density in thermodynamics has the same meaning and units. It also follows a related continuity equation, even though waves do not occur in thermodynamics. Material contrast in thermal conductivity can exceed 1000, and thermal metamaterial lattice constants can be made smaller than the thermal diffusion length (the counterpart of the optical wavelength). Losses are absent because heat is at the bottom of

the energy food chain. Consequently, free-space omnidirectional broadband thermal cloaks work nearly perfectly (13). Objects can transiently be protected from overheating while keeping the heat flow in their surroundings as though nothing was there.

Still, the metamaterial cloak needs to be wrapped around the object. It would be yet more stunning and useful if it could rather be spatially separated from the object. Such exterior cloaking is possible and has been demonstrated experimentally in dc electrical conduction using effectively negative electric conductivities (14) of active metamaterials [see also absolute negative mobility (15)]. By analogy, exterior thermal cloaking requires effectively negative metamaterial heat conductivities. Heat would flow from the cold to the hot. The second law of thermodynamics forbids that for passive but not for active materials containing heat sources or sinks. Mathematically, negative heat conductivity is analogous to negative phase velocity in electromagnetism (1, 2).

Yet further opportunities arise in airborne acoustics. Just think more broadly about metamaterials.

References and Notes

1. C. M. Soukoulis, S. Linden, M. Wegener, *Science* **315**, 47 (2007).
2. C. M. Soukoulis, M. Wegener, *Nat. Photonics* **5**, 523 (2011).
3. A. V. Kildishev, A. Boltasseva, V. M. Shalaev, *Science* **339**, 6125 (2013).
4. J. B. Pendry, D. Schurig, D. R. Smith, *Science* **312**, 1780 (2006).
5. U. Leonhardt, *Science* **312**, 1777 (2006).
6. M. Kauranen, A. V. Zayats, *Nat. Photonics* **6**, 737 (2012).
7. M. Kadic, T. Bückmann, R. Schittny, M. Wegener, *Rep. Prog. Phys.* **76**, 126501 (2013).
8. G. W. Milton, A. V. Cherkaev, *J. Eng. Mater. Technol.* **117**, 483 (1995).
9. M. Kadic, T. Bückmann, N. Stenger, M. Thiel, M. Wegener, *Appl. Phys. Lett.* **100**, 191901 (2012).
10. T. A. Schaedler *et al.*, *Science* **334**, 962 (2011).
11. G. W. Milton, M. Briane, J. R. Willis, *New J. Phys.* **8**, 248 (2006).
12. S. H. Lee, C. M. Park, Y. M. Seo, Z. G. Wang, C. K. Kim, *Phys. Rev. Lett.* **104**, 054301 (2010).
13. R. Schittny *et al.*, *Phys. Rev. Lett.* **110**, 195901 (2013).
14. F. Yang *et al.*, *Adv. Funct. Mater.* **23**, 4306 (2013).
15. A. Ros *et al.*, *Nature* **436**, 928 (2005).

Acknowledgments: I thank R. Schittny for preparing the figure and for careful reading of the manuscript, and T. Bückmann, J. Christensen, S. Guenneau, P. Gumbsch, M. Kadic, G. W. Milton, and M. Thiel for discussions. Supported by the DFG Center for Functional Nanostructures and the Karlsruhe School of Optics and Photonics.

10.1126/science.1246545

MOLECULAR BIOLOGY

Chromosome Capture Brings It All Together

Nancy Kleckner,¹ Denise Zickler,² Guillaume Witz¹

A simple, robust model explains higher-order organization of mammalian chromosomes.

The organization and morphogenesis of chromosomes as they prepare to segregate during cell division have fascinated researchers since their first microscopic visualizations. On page 948 of this issue, Naumova *et al.* (1) combine chromosome conformation capture with polymer physics simulations to see inside metaphase chromosomes and elucidate their principles of organization. A new, yet satisfyingly familiar, view emerges.

Electron microscopic visualizations provide compelling evidence that chromosomes are organized as loops (see the figure). Naumova *et al.*'s analysis suggests that chromosome organization is a highly probabilistic

process that, without much specification, yields a robust longitudinal assembly of loop bases running along the length of the chromosome. The model reproduces known properties of mitotic chromosomes, including variable positioning of loci and spatial mixing of regions of intermediate (megabase) size. Although average loop size cannot be determined from chromosome capture data, the loop size necessary for the simulations to match experimental results was 80 kb, very similar to experimental estimates. The proposed model is highly attractive in its simplicity and robustness. A linear array of chromatin loops forms, at consecutive but apparently random positions, and then is longitudinally compressed. These few rules ensure that chromosomes globally always fold into the same shape, without requiring precise specification of either highly conserved genetic loci or specific length scales.

¹Department of Molecular Biology, Harvard University, 52 Oxford Street, Cambridge, MA 01568, USA. ²Institut de Genetique et Microbiologie, Université Paris-Sud, Orsay, France. E-mail: kleckner@fas.harvard.edu

elastic behavior gets simpler in so-called pentamode metamaterials, in which the longitudinal polarization dominates because the effective metamaterial shear modulus is small relative to the bulk modulus. Pentamode metamaterials were proposed years ago (8) but have been realized only recently (9). In these materials, wave propagation is scalar, thereby allowing analogies to optics. For example, the elastic counterpart of an optical invisibility cloak becomes possible (7). Such elastic structures would also work in the static limit. One could then mechanically protect or hide sensitive objects within the mechanical cloak.

In more detail, the elastic compressibility plays the same role that electric permittivity plays in electromagnetism; likewise, the mass density plays the role of magnetic permeability (7). Mechanical metamaterials that offer low mass density together with reasonable mechanical stability have been realized (10). Negative mass densities and anisotropic mass-density tensors are well established theoretically (7, 11), and one-dimensional model systems have been demonstrated experimentally (12) as well. Still, experimentalists need feasible blueprints to fabricate three-dimensional microstructures to achieve specific anisotropic mass-density tensors. Progress here would greatly enhance the possibilities in elasticity.

An elastic solid can be viewed as the generalization of a passive reversible linear Hooke spring. But why limit ourselves to this linear mechanical regime? Metamaterial unit cells could be constructed that break or buckle to dissipate mechanical shock energy. We also could work toward active mechanical metamaterials, integrating miniature energy sources together with sensors, actuators, and feedback loops into the individual unit cells. Nonlinear and active mechanical metamaterials are wide open for innovation.

As a second group of examples, consider thermodynamic material properties such as heat conduction or diffusion (7). Much of optical metamaterials is about molding the flow of the Poynting vector—that is, the energy flux per unit time and area. The heat current density in thermodynamics has the same meaning and units. It also follows a related continuity equation, even though waves do not occur in thermodynamics. Material contrast in thermal conductivity can exceed 1000, and thermal metamaterial lattice constants can be made smaller than the thermal diffusion length (the counterpart of the optical wavelength). Losses are absent because heat is at the bottom of

the energy food chain. Consequently, free-space omnidirectional broadband thermal cloaks work nearly perfectly (13). Objects can transiently be protected from overheating while keeping the heat flow in their surroundings as though nothing was there.

Still, the metamaterial cloak needs to be wrapped around the object. It would be yet more stunning and useful if it could rather be spatially separated from the object. Such exterior cloaking is possible and has been demonstrated experimentally in dc electrical conduction using effectively negative electric conductivities (14) of active metamaterials [see also absolute negative mobility (15)]. By analogy, exterior thermal cloaking requires effectively negative metamaterial heat conductivities. Heat would flow from the cold to the hot. The second law of thermodynamics forbids that for passive but not for active materials containing heat sources or sinks. Mathematically, negative heat conductivity is analogous to negative phase velocity in electromagnetism (1, 2).

Yet further opportunities arise in airborne acoustics. Just think more broadly about metamaterials.

References and Notes

1. C. M. Soukoulis, S. Linden, M. Wegener, *Science* **315**, 47 (2007).
2. C. M. Soukoulis, M. Wegener, *Nat. Photonics* **5**, 523 (2011).
3. A. V. Kildishev, A. Boltasseva, V. M. Shalaev, *Science* **339**, 6125 (2013).
4. J. B. Pendry, D. Schurig, D. R. Smith, *Science* **312**, 1780 (2006).
5. U. Leonhardt, *Science* **312**, 1777 (2006).
6. M. Kauranen, A. V. Zayats, *Nat. Photonics* **6**, 737 (2012).
7. M. Kadic, T. Bückmann, R. Schittny, M. Wegener, *Rep. Prog. Phys.* **76**, 126501 (2013).
8. G. W. Milton, A. V. Cherkaev, *J. Eng. Mater. Technol.* **117**, 483 (1995).
9. M. Kadic, T. Bückmann, N. Stenger, M. Thiel, M. Wegener, *Appl. Phys. Lett.* **100**, 191901 (2012).
10. T. A. Schaedler *et al.*, *Science* **334**, 962 (2011).
11. G. W. Milton, M. Briane, J. R. Willis, *New J. Phys.* **8**, 248 (2006).
12. S. H. Lee, C. M. Park, Y. M. Seo, Z. G. Wang, C. K. Kim, *Phys. Rev. Lett.* **104**, 054301 (2010).
13. R. Schittny *et al.*, *Phys. Rev. Lett.* **110**, 195901 (2013).
14. F. Yang *et al.*, *Adv. Funct. Mater.* **23**, 4306 (2013).
15. A. Ros *et al.*, *Nature* **436**, 928 (2005).

Acknowledgments: I thank R. Schittny for preparing the figure and for careful reading of the manuscript, and T. Bückmann, J. Christensen, S. Guenneau, P. Gumbsch, M. Kadic, G. W. Milton, and M. Thiel for discussions. Supported by the DFG Center for Functional Nanostructures and the Karlsruhe School of Optics and Photonics.

10.1126/science.1246545

MOLECULAR BIOLOGY

Chromosome Capture Brings It All Together

Nancy Kleckner,¹ Denise Zickler,² Guillaume Witz¹

A simple, robust model explains higher-order organization of mammalian chromosomes.

The organization and morphogenesis of chromosomes as they prepare to segregate during cell division have fascinated researchers since their first microscopic visualizations. On page 948 of this issue, Naumova *et al.* (1) combine chromosome conformation capture with polymer physics simulations to see inside metaphase chromosomes and elucidate their principles of organization. A new, yet satisfyingly familiar, view emerges.

Electron microscopic visualizations provide compelling evidence that chromosomes are organized as loops (see the figure). Naumova *et al.*'s analysis suggests that chromosome organization is a highly probabilistic

process that, without much specification, yields a robust longitudinal assembly of loop bases running along the length of the chromosome. The model reproduces known properties of mitotic chromosomes, including variable positioning of loci and spatial mixing of regions of intermediate (megabase) size. Although average loop size cannot be determined from chromosome capture data, the loop size necessary for the simulations to match experimental results was 80 kb, very similar to experimental estimates. The proposed model is highly attractive in its simplicity and robustness. A linear array of chromatin loops forms, at consecutive but apparently random positions, and then is longitudinally compressed. These few rules ensure that chromosomes globally always fold into the same shape, without requiring precise specification of either highly conserved genetic loci or specific length scales.

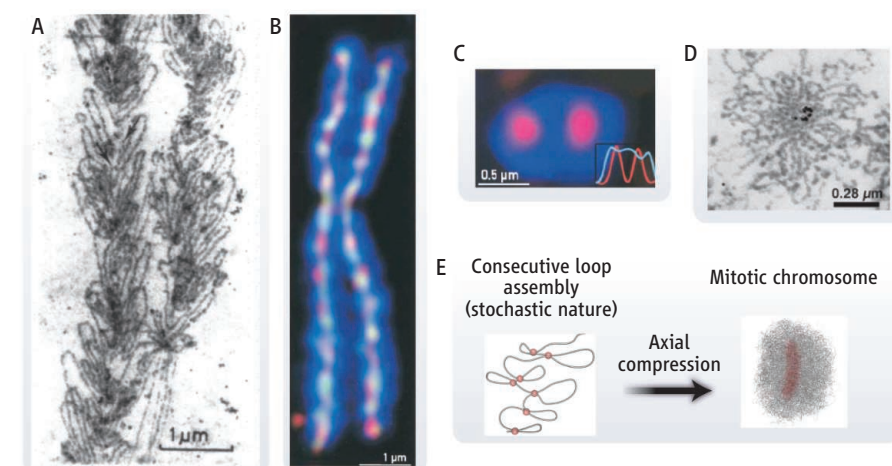
¹Department of Molecular Biology, Harvard University, 52 Oxford Street, Cambridge, MA 01568, USA. ²Institut de Genetique et Microbiologie, Université Paris-Sud, Orsay, France. E-mail: kleckner@fas.harvard.edu

The model of Naumova *et al.* supports the seminal description of Ulrich Laemmli, formulated nearly 40 years ago (2). Laemmli envisioned a constraining protein network located centrally within the chromosome. This “scaffolding” brings segments together into loops, thereby shaping the chromatin to give rodlike chromosomal bodies rather than spherical balls (3). The underlying organization comprises a linearly folded assembly of scaffold associated regions (SARs), rich in the bases adenine (A) and thymine (T), yielding an “AT queue” (3–5). Topoisomerase II, condensin, and AT-hook architectural proteins synergistically collaborate with SARs to give shape (3–5). Compellingly, the AT queue–scaffold model explains classic cytological G/R banding patterns (5). Importantly, in the model of Naumova *et al.*, positioning of loop bases appears random. However, chromosome capture analysis provides a population average description. Different cells may stochastically choose different SARs from a larger array of possibilities. (The common textbook model of a highly ordered scaffold and loops was not Laemmli’s view.)

In Naumova *et al.*’s model, the compressed loop array could run along the chromosome in a straight path or a meandering path. Experimental data define a topoisomerase II–condensin core lying radially within the center of the chromosome and running along its entire length (4, 6). However, the substructure of this scaffold may well be complex (with folds or coils) (4, 5). Laemmli postulated that loops emanate outward radially from the scaffold (7). Naumova *et al.*’s model does not specify a radial array but, similarly, envisions loops emanating out from the central axial feature.

Metaphase chromosome organization has also been proposed to comprise a hierarchical folding of larger domains (8) or connectivity spread uniformly through the chromatin (9). Naumova *et al.* exclude these two models.

At prophase of meiosis, chromosomes comprise linear arrays of loops whose bases are decorated with proteins, including topoisomerase II and condensin (10). In yeast, loop-base sequences are locally AT-rich regions (11). In mammals, loop sizes for meiotic prophase chromosomes are the same as for mitotic metaphase chromosomes (~100 kb). The two cases are obviously related. Remarkably, when a mammalian chromosome segment is introduced into yeast, it acquires the same meiotic prophase organization (loop size and spacing) as the endogenous yeast genome (12). Loop organization is thus clearly determined by probabilistic selection of a subset of available sequences. Also, alterations in structural axis components can



Meiotic and mitotic chromosomes. (A) Meiotic homologs of *Chironomus*, each comprising sister linear loop arrays (14). (B to D) Mitotic metaphase chromosomes in a human cell line. (B and C) Radially central chromosome “barber pole” appearance due to staining for DNA (blue) and associated proteins (red and green) (4). (D) Radial loops of chromatin fibers (15). (E) A model of the two stages of chromosome assembly from Naumova *et al.*

alter, and increase variability of, loop size (13). Maybe loop size is determined in part by “chromatin fiber” persistence length: Loops would form down to the minimum size compatible with fiber stiffness.

In the model of Naumova *et al.*, a linear array of continuous chromatin loops forms and then undergoes longitudinal compression. It will not be surprising if the first stage corresponds to prophase (mitotic and meiotic), while the second stage corresponds to evolution to the metaphase state.

The findings of Naumova *et al.* will reinvigorate discussions of late-stage mitotic chromosome organization and morphogenesis. What is the molecular nature of the final axial compressed loop array? It may comprise a DNA-protein meshwork, as for meiotic prophase chromosome axes (10), rather than a continuous protein-protein structure. Primary components of the metaphase scaffold all mediate DNA-DNA linkages. Most strikingly, if new metaphase chromosomes are treated with deoxyribonuclease, they simply disappear, rather than leaving behind a discrete core (9). Also of interest is how mature mitotic chromosomes can be forcibly extended, allowed to retract, and then extended again for multiple successive cycles. Are protein links metastable? Do they act as “slip-rings”? Does an open DNA-protein meshwork allow reversible deformation without disruption of protein-mediated DNA-DNA links? It is also unclear how sister chromatids acquire their side-by-side metaphase relationship. Perhaps loosely connected sister chromatids become longitudinally organized in parallel, and then further compact, with stress on linkages between sisters promoting their

further removal (5). However, classically, mitotic and meiotic prophase chromosomes appear as morphologically single units, hinting at a more complex situation. Finally, by comparing chromosome capture data for interphase and metaphase, Naumova *et al.* show that mitotic chromosomes lose major features observed previously for interphase stages, e.g., cell type–specific spatial segregation of open domains and closed domains. How epigenetic information for cell type–specific gene expression is retained during the passage through mitosis is unknown. Are relevant elements locally marked? Or are some cell type–specific interactions maintained but invisible at the current level of resolution?

The answers to these questions remain for the future, with imaging, conformation capture, polymer modeling, and genetic analysis all destined to play key roles.

References and Notes

1. N. Naumova *et al.*, *Science* **342**, 948 (2013); 10.1126/science.1236083.
2. U. K. Laemmli *et al.*, *Cold Spring Harb. Symp. Quant. Biol.* **42**, 351 (1978).
3. R. Strick, U. K. Laemmli, *Cell* **83**, 1137 (1995).
4. K. Maeshima, U. K. Laemmli, *Dev. Cell* **4**, 467 (2003).
5. Y. Saitoh, U. K. Laemmli, *Cell* **76**, 609 (1994).
6. T. Ono *et al.*, *Mol. Biol. Cell* **15**, 3296 (2004).
7. M. P. Marsden, U. K. Laemmli, *Cell* **17**, 849 (1979).
8. N. Kireeva *et al.*, *J. Cell Biol.* **166**, 775 (2004).
9. M. G. Poirier, J. F. Marko, *Proc. Natl. Acad. Sci. U.S.A.* **99**, 15393 (2002).
10. N. Kleckner, *Chromosoma* **115**, 175 (2006).
11. Y. Blat, N. Kleckner, *Cell* **98**, 249 (1999).
12. J. Loidl *et al.*, *Chromosoma* **104**, 183 (1995).
13. I. Novak *et al.*, *J. Cell Biol.* **180**, 83 (2008).
14. H. G. Keyl, *Chromosoma* **51**, 75 (1975).
15. K. Maeshima *et al.*, *Chromosoma* **114**, 365 (2005).

Acknowledgments: We thank Z. Liang for important article input. Supported by NIH grants GM025326 and GM044794 to N.K.

10.1126/science.1247514

PHYSICS

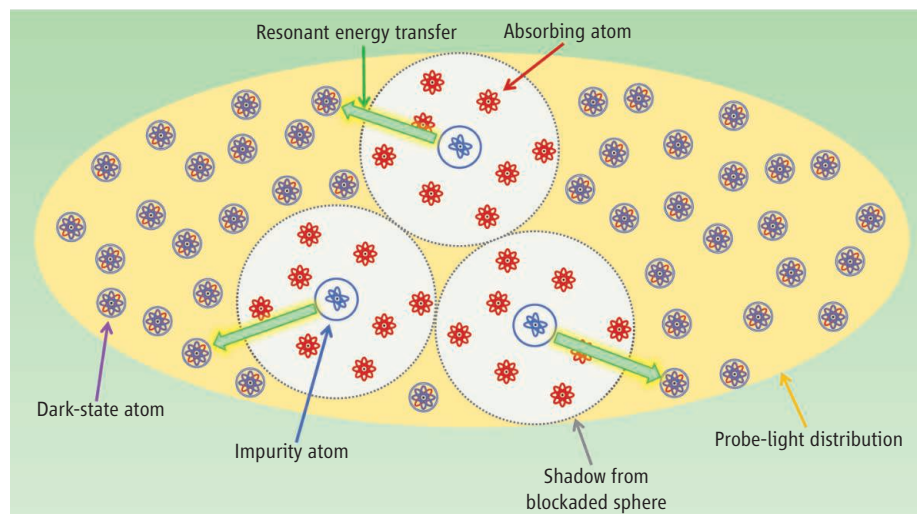
A View on Energy Transfer Between Cold Atoms

Elizabeth A. Donley

Atoms with highly excited electrons—called Rydberg atoms—have many exaggerated properties compared with ordinary ground-state atoms. For example, the loosely bound electrons create large dipoles that lead to long-range interactions between Rydberg atoms that are many orders of magnitude stronger than those between ground-state atoms. Strong interactions between Rydberg atoms can enable energy transport over distances many times the size of the atoms (1). On page 954 of this issue (2), Günter *et al.* describe how they have nondestructively and continuously imaged resonant-energy transfer between cold ^{87}Rb Rydberg atoms with controlled coupling to the environment. Their technique may enable the engineering of open quantum systems for quantum simulation (3), which could lend insight to the transition from classical to quantum energy transport in complex systems. The nature of this transition in a dissipative environment remains an open question and may have relevance to the efficiency of dipole-coupled energy transport in molecular systems such as photosynthetic light-harvesting complexes (4).

Another phenomenon resulting from strong long-range interactions of Rydberg atoms is known as the Rydberg blockade (5). The resonant photoexcitation of one Rydberg atom strongly suppresses the excitation of neighboring atoms because their interactions shift the energy levels of the neighbors out of resonance with the excitation light. This effect limits the density of Rydberg atoms that can be created in an atom cloud.

To directly view distributions of Rydberg atoms, Günter *et al.* developed an imaging technique based on electromagnetically induced transparency (EIT) resonances in blockaded probe atoms that surround “impurity” Rydberg atoms. As an initial demonstration, they created the impurity atoms in the $|50S\rangle$ excited state—highly excited compared with the $|5S\rangle$ ground state for the valence electron of ^{87}Rb . After they created the Rydberg impurities, lasers operating at two different



Imaging energy transfer. Impurity Rydberg atoms (blue) were created by Günter *et al.* in the central region of a cloud of cold rubidium atoms. Their density is limited by the Rydberg blockade effect, and they are surrounded by a blockaded sphere of probe atoms (red). Far from the impurities, the EIT lasers are resonant with the transitions in the probe atoms and the probe atoms go into a “dark state,” which is a quantum superposition of the ground and Rydberg states that transmits the light. Strong interstate Rydberg interactions shift the energy levels for probe atoms around the impurities such that the EIT resonance condition is not met and they absorb probe light, casting shadows on a camera. Hopping of the excitation energy from the impurity atoms to dark-state probe atoms (shown in green) is observed as the shadows diffuse outward. Here, the atom distribution is shown projected onto the camera intensity distribution.

frequencies (a strong coupling laser and a weaker probe) were tuned to an EIT resonance (6) between the ground state and a lower-energy Rydberg state in the remaining probe atoms. The probe atoms near a Rydberg impurity absorbed photons because their energy levels were shifted out of EIT resonance, whereas probe atoms far from a Rydberg atom remained in the transparent EIT “dark state.” Thus, each Rydberg impurity was surrounded by a sphere of absorbing probe atoms marking its position, and shadows appear on camera images around the Rydberg impurities. Many tens of probe atoms per impurity atom can absorb light and amplify the signal from an individual Rydberg atom.

Günter *et al.* used this imaging technique to demonstrate excitation transport between Rydberg impurities and probe atoms. The impurities were now in the $|38S\rangle$ state. The probe atoms were probed with EIT resonant with the $|37S\rangle$ state—close in energy and strongly coupled to the $|38S\rangle$ state through the $|37P\rangle$ state. They first created a sample of impurities in the central region of the cold-

A new method for visualizing energy transfer between highly excited atoms may provide insight into coherent energy transport in molecular systems.

atom cloud and then illuminated a broader portion of the sample with the EIT light. With continuous illumination, the shadow from the absorbing probe atoms near the impurities diffused outward with time and grew to fill the whole region that was illuminated by the EIT light.

A value for the preferred hopping distance for the excitation energy of about $6\ \mu\text{m}$ was determined. This length scale was set by a trade-off between the interstate Rydberg blockade (the density of dark-state probe atoms is appreciable only outside of the blockaded sphere) and the scaling of the dipole-dipole exchange interaction. This energy-hopping distance is about 60 times as great as the radius of the Rydberg atom wave functions. To confirm that the excitation was caused by hopping to probe atoms in the dark state, they did a control experiment in which they initially left the EIT light off and probed the distribution of impurities for a brief period after a variable delay. They confirmed that without the EIT light, energy hopping did not take place and the width of

Time and Frequency Division, National Institute of Standards and Technology, Boulder, CO 80305, USA. E-mail: edonley@boulder.nist.gov

the distribution of impurities did not grow with time. Thus, the environment as controlled by the laser fields had a strong influence on the observed energy transport.

It is likely that in future uses of these techniques, quantum-simulation studies can be performed in open quantum systems with controlled energy hopping and decoherence rates. The ratio of these rates determines whether the energy transport occurs in the classical

or quantum regimes. If the energy hopping rate exceeds the measurement-induced decoherence rate, then quantum coherent energy transport occurs. It may be possible to control and lower the decoherence rate to allow for studies of coherent excitonic behavior, which may bring insights to theories on energy transport in complex molecular systems such as light-emitting organic systems and photosynthetic proteins.

References

1. T. F. Gallagher, P. Pillet, *Adv. At. Mol. Opt. Phys.* **56**, 161 (2008).
2. G. Günter *et al.*, *Science* **342**, 954 (2013).
3. M. Müller, S. Diehl, G. Pupillo, P. Zoller, *Adv. At. Mol. Opt. Phys.* **61**, 1 (2012).
4. E. Collini, *Chem. Soc. Rev.* **42**, 4932 (2013).
5. D. Jaksch, J. I. Cirac, P. Zoller, R. Côté, M. D. Lukin, *Phys. Rev. Lett.* **85**, 2208 (2000).
6. M. Fleischhauer, A. Imamoglu, J. P. Marangos, *Rev. Mod. Phys.* **77**, 633 (2005).

10.1126/science.1247392

BIOCHEMISTRY

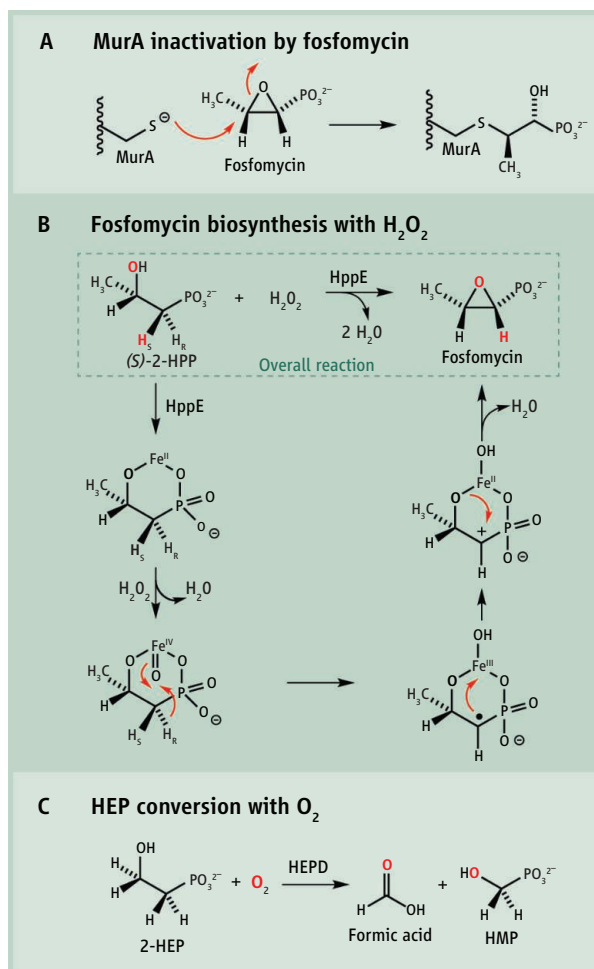
Not an Oxidase, But a Peroxidase

Frank M. Raushel

Fosfomycin (see the figure, panel A) is a deceptively simple antibiotic that is clinically effective for the treatment of gastrointestinal and lower urinary tract infections (1). The biological target of this compound is the bacterial enzyme MurA, which plays a key role in bacterial cell wall biosynthesis. On page 991 of this issue, Wang *et al.* (2) report that a key step in the biosynthesis of fosfomycin requires hydrogen peroxide (H_2O_2) rather than molecular oxygen (O_2). This discovery clarifies how the strained epoxide ring of fosfomycin is synthesized by bacteria and enhances understanding of the catalytic repertoire of iron-activated enzymes.

MurA catalyzes the transfer of the enolpyruvyl group from PEP to UDP-*N*-acetylglucosamine in an essential step of bacterial cell wall biosynthesis. Fosfomycin functions as a structural mimic of PEP. The highly strained epoxide ring of the antibiotic is attacked by a cysteine residue in the MurA active site to generate a covalent enzyme-fosfomycin adduct that renders the enzyme inactive (see the figure, panel A) (3). The pharmacological function of fosfomycin is thus dictated by the structural similarity to PEP and the inherent chemical reactivity of the strained epoxide ring.

In fosfomycin-producing organisms, the antibiotic is constructed in a five-step biosynthetic pathway (4). The epoxide group is assembled in the last step of this pathway from *S*-HPP. During the conversion of *S*-HPP to fosfomycin, catalyzed by the enzyme HppE, two electrons and two hydrogen atoms must be removed from the substrate. O_2 was long thought to be the



A key step in the biosynthesis of the antibiotic fosfomycin requires hydrogen peroxide, rather than molecular oxygen as previously assumed.

Oxidant action. (A) The antibiotic fosfomycin acts by inactivating the enzyme MurA, which plays a key role in bacterial cell wall biosynthesis. (B) It was long thought that fosfomycin biosynthesis, which is catalyzed by the HppE enzyme, requires molecular oxygen (O_2). Wang *et al.* propose an alternative mechanism in which H_2O_2 serves as the oxidant. (C) The HEPD enzyme is structurally similar to HppE yet requires O_2 as the oxidant.

is incorrect. The actual oxidant is H_2O_2 , and HppE is thus a peroxidase rather than an oxidase.

The three-dimensional x-ray structure of HppE shows that the active site is composed of a non-heme iron center (6). When the substrate, HPP, binds to the enzyme, it is coordinated to the iron center by the hydroxyl group and one of the oxygens from the phosphonate moiety (6). Isotopic labeling studies have revealed that one of the hydrogen atoms from the methylene group ($-\text{CH}_2-$) of the substrate is ultimately

ultimate recipient of the two electrons (5), but the reduction of O_2 to two water molecules requires four electrons. Therefore, two additional electrons from nicotinamide or flavin coenzymes were thought to be required for the activation of O_2 . Wang *et al.* now show that this view of the catalytic mechanism of epoxide formation by HppE

found in solvent water and that the epoxide oxygen of fosfomycin derives from the hydroxyl group of the substrate (7, 8).

In the originally proposed reaction mechanism, the iron center of the enzyme-substrate complex bound O_2 (4). This binding event initiated the reduction of O_2 via transfer of electrons from the ferrous

Department of Chemistry, Texas A&M University, College Station, TX 77843, USA. E-mail: raushel@chem.tamu.edu

Glossary

HEP, 2-hydroxyethyl-1-phosphonate

HEPD, HEP dioxygenase

HMP, hydroxymethyl phosphonate

HppE, S-HPP epoxidase

MurA, uridine diphosphate (UDP)-*N*-acetylglucosamine enolpyruvyl transferase

NADH, nicotinamide adenine dinucleotide, H

PEP, phospho(enol)pyruvate

S-HPP, (S)-2-hydroxypropyl-1-phosphonate

UDP, uridine diphosphate

[Fe(II)] iron and externally added NADH to ultimately form the ferryl [Fe(IV)=O] oxidation state (4). However, there are problems with this mechanism. The crystal structure of HppE provided no support for the binding of a companion reductase protein for the transfer of external electrons from either nicotinamide or reduced flavin cofactors (6). Furthermore, the steady-state rate of product formation catalyzed by HppE with O₂ and external reductants is extremely slow (~0.01 s⁻¹). The very slow rate of epoxide formation prompted Wang *et al.* to search for alternative reductants to NADH. They subsequently found that addition of dithionite (S₂O₄²⁻) increased the rate of fosfomycin formation up to 1000 times.

This discovery led to the proposal that the added S₂O₄²⁻ was reducing O₂ to H₂O₂ and that H₂O₂ might be the physiological oxidant for epoxide formation by HppE. This hypothesis proved to be correct. The reduction of H₂O₂ to water requires only two electrons, matching the two-electron requirement for the overall conversion of S-HPP to fosfomycin. With H₂O₂ as the added oxidant, one equivalent of fosfomycin is formed for every H₂O₂ used in the enzyme-catalyzed reaction.

Wang *et al.* propose that the H₂O₂-assisted transformation proceeds via a multistep mechanism that includes an Fe(IV) species and a carbocation intermediate (see the figure, panel B). Experimental support for a carbocation intermediate comes from the observation that HppE catalyzes an unusual 1,2-phosphono migration when R-HPP is used as a substrate during the formation of 1-oxopropan-2-ylphosphonate (9).

Now that it is known that the true oxidant is H₂O₂, proper steady-state and rapid-kinetic studies can be conducted to provide data that will be critical for determination of the rate-limiting steps for this unusual chemical reaction. Thus far, there is no direct spectroscopic evidence for the formation of the ferryl [Fe(IV)=O] intermediate, although recent computational studies are consistent with the formation of this intermediate (10).

It is also unclear how HppE selectively uses H₂O₂ rather than O₂. The enzyme most structurally similar to HppE is HEPD, which converts HEP and O₂ to formate and HMP (see the figure, panel C). The structure of the non-heme iron center and the substrate-bound complex in the active site of HEPD is essentially identical to that of HppE (11). Yet, HEPD does not use H₂O₂ as a cosubstrate, and HppE does not use O₂ as a substrate (5). Further experimental and computational probes are needed to fully understand the structural and dynamic differences between these two enzymes that dictate why one enzyme functions as a peroxidase, whereas the other is a dioxygenase.

References

1. M. E. Falagas, A. C. Kastoris, D. E. Karageorgopoulos, P. I. Rafailidis, *Int. J. Antimicrob. Agents* **34**, 111 (2009).
2. C. Wang *et al.*, *Science* **342**, 991 (2013); 10.1126/science.1240373.
3. J. L. Marquardt *et al.*, *Biochemistry* **33**, 10646 (1994).
4. T. Hidaka *et al.*, *Mol. Gen. Genet.* **249**, 274 (1995).
5. P. Liu *et al.*, *J. Am. Chem. Soc.* **123**, 4619 (2001).
6. L. J. Higgins, F. Yan, P. Liu, H. W. Liu, C. L. Drennan, *Nature* **437**, 838 (2005).
7. F. Hammerschmidt, H. Kählig, *J. Org. Chem.* **56**, 2364 (1991).
8. F. Hammerschmidt, *J. Chem. Soc. Perkin Trans.* **18**, 1993 (1991).
9. W. C. Chang *et al.*, *Nature* **496**, 114 (2013).
10. A. Milaczewska, E. Broclawik, T. Borowski, *Chemistry* **19**, 771 (2013).
11. R. M. Cicchillo *et al.*, *Nature* **459**, 871 (2009).

10.1126/science.1247233

NEUROSCIENCE

Synapses, Language, and Being Human

Philip Lieberman

Humans' ability to cope with the challenges they meet in life is transmitted almost exclusively through the medium of language. We have yet to fully map out the circuits of the human brain, the genes acting on them, and the processes they control that yield this distinct human quality. However, the findings of Sia *et al.* (1), on page 987 of this issue, bring us a step closer. The authors have determined that a secreted protein called sushi repeat-containing protein X-linked 2 (SRPX2) promotes mamma-

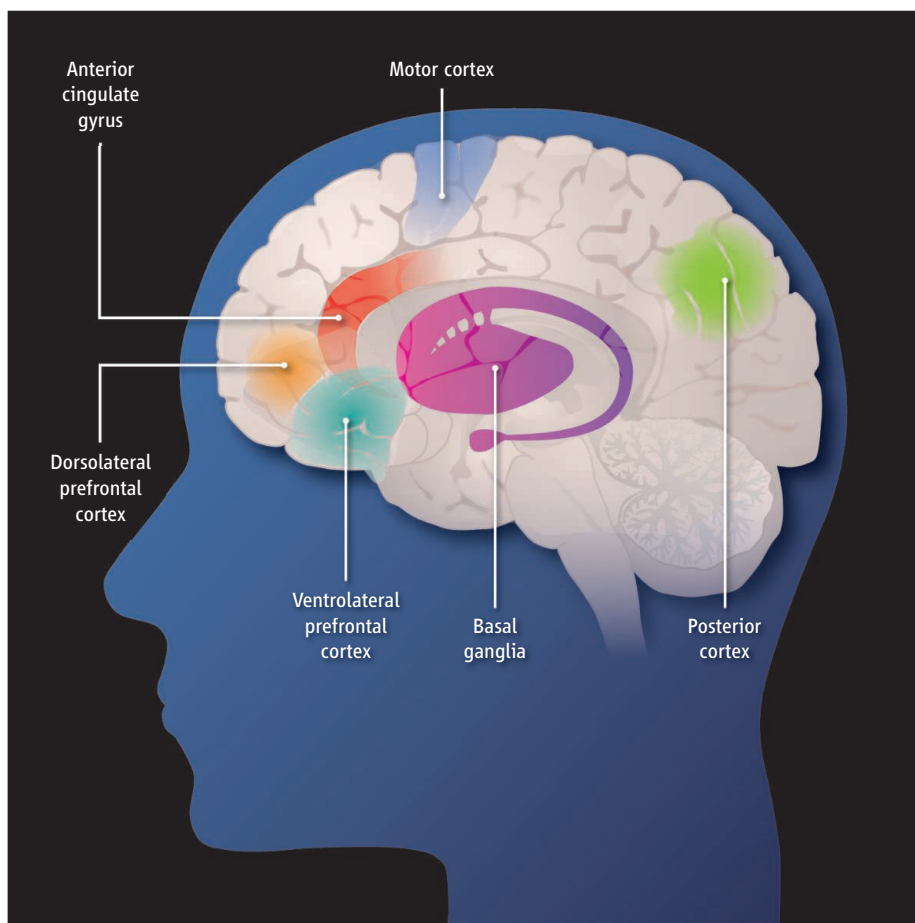
lian vocalization by controlling the formation of synapses in the mouse cerebral cortex. Expression of this protein is known to be repressed by the transcription factor foxhead box protein P2 (FOXP2), which has been implicated in human language acquisition. A link between these two factors and synaptogenesis may have played a role in the evolution of the neural circuits associated with human language and cognition, as well as the pathogenesis of language disorders.

FOXP2 has become a "gene of interest" in the mystery that surrounds the evolution of the human brain. It first came to notice in a study of the behavioral deficits of the members of a large extended family who

Two factors that controls synapse formation in mammalian brain are associated with human language acquisition.

had only one copy of the gene. These individuals had profound difficulties in talking, comprehending, and forming sentences, and had depressed scores on intelligence tests (2). Anomalies in their basal ganglia, subcortical structures deep in the brain, were also noted (3). FOXP2 is one of the few human genes that differ from its chimpanzee version. A series of mutations in FOXP2 has occurred in the last 500,000 years; the most recent one took place about 200,000 years ago, when modern humans appeared in Africa (4). When a form of FOXP2 shared by humans, Neandertals, and Denisovans (another extinct hominin species) was introduced into mouse pups, synaptic plasticity

Cognitive and Linguistic Sciences, Brown University, 190 Thayer Street, Providence, RI 02912, USA. E-mail: phil-ip_lieberman@brown.edu



Language regions. Shown are the many regions of the brain that are required for humans to acquire language. Cortical–basal ganglia circuits are particularly important for this process.

and connections between basal ganglia neurons increased (5). But the mechanisms by which *FOXP2* shapes the neural circuitry associated with language acquisition have not been clear. The *CNTNAP2* gene, for example, also is targeted by *FOXP2* and is linked to language disorders (6).

In the brain, synapses between neurons can be thought of as neural “volume controls” whose settings encode memories, words, and the motor control instructions that enable talking. *SRPX2* is a secreted protein that is mutated in patients with epilepsy and with speech disorders. When Sia *et al.* overexpressed rat or human *SRPX2*-encoding genes in cultured cortical neurons, the density of excitatory synapses increased; the opposite was observed when *SRPX2* expression was decreased using small interfering RNA. These changes were also observed when *SRPX2* expression was similarly modulated in the intact brain (the cerebral cortex) of mouse pups, an animal model used to study human language disorders. Moreover, reducing *SRPX2* expression in the intact brain caused a decrease in vocalization in mouse

pups. Overexpression of *FOXP2* in cultured cortical neurons repressed *SRPX2* expression and decreased excitatory synapses, suggesting that the transcription factor controls synapse density by controlling the amount of *SRPX2* produced.

Although some parts of the brain are specialized for particular functions, such as vision, neural circuits that link activity in different parts of the brain appear to regulate complex aspects of behavior, such as language acquisition and speech (see the figure). Broca’s area of the cortex, for example, is not the brain’s language center, as previously thought. Aphasia—permanent loss of language—never occurs in the absence of subcortical damage (7); it occurs only after damage to the basal ganglia and pathways to them, leaving Broca’s area intact (8, 9). Converging evidence from studies of neural circuitry, lesions localized to the basal ganglia, and Parkinson’s disease (which degrades basal ganglia operations) points to neural circuits that link the basal ganglia with regions of the motor cortex that play a key role in learning and executing complex motor tasks

such as talking. Disrupting basal ganglia circuits to the prefrontal cortex results in a cognitive syndrome in which affected individuals have difficulty in forming and executing new concepts and comprehending distinctions in meaning conveyed by syntax, and experience decrements in short-term “working” memory. Oxygen deficits, which degrade the metabolically active basal ganglia, produce similar deficits (9). Neuroimaging studies support these findings (10, 11). The basal ganglia enter into the process of associative learning by which motor activities such as walking and talking are “automatized” so that they are executed without conscious thought (12). However, associative learning can take place through other neural channels. Synaptic plasticity allows mollusks, which lack basal ganglia, to associate two paired stimuli—shrimp extract and an electrical shock—though it takes hundreds of trials for them to learn to scuttle away (13). And cortical–basal ganglia circuits do not regulate all aspects of human behavior—hundreds of other pathways exist whose functions are unknown.

We do not yet know the full range of genetic events that yielded the human brain, but a mutation at a site near the *FOXP2* amino acid mutations that are unique to humans appears to be responsible for a “selective sweep” that occurred about 200,000 years ago, when modern humans appeared in Africa (14). Such sweeps on genes occur when they enhance the survival of progeny. A process in which *FOXP2* targets the *SRPX2* gene to control the release of a protein that promotes the development of synapses would clearly play a role in that aspect of the evolution of the human brain.

References

1. G. M. Sia, R. L. Clem, R. L. Huganir, *Science* **342**, 987 (2013); 10.1126/science.1245079.
2. F. Vargha-Khadem, K. Watkins, K. Alcock, P. Fletcher, R. Passingham, *Proc. Natl. Acad. Sci. U.S.A.* **92**, 930 (1995).
3. F. Vargha-Khadem *et al.*, *Proc. Natl. Acad. Sci. U.S.A.* **95**, 12695 (1998).
4. T. Maricic *et al.*, *Mol. Biol. Evol.* **30**, 844 (2013).
5. S. Reimers-Kipping *et al.*, *Neuroscience* **175**, 75 (2011).
6. M. Meyer *et al.*, *Science* **338**, 222 (2012).
7. D. T. Stuss, D. F. Benson, *The Frontal Lobes* (Raven, New York, 1986).
8. M. A. Naeser *et al.*, *Arch. Neurol.* **39**, 2 (1982).
9. P. Lieberman, *The Unpredictable Species: What Makes Humans Unique* (Princeton Univ. Press, Princeton, NJ, 2013).
10. O. Monchi, M. Petrides, B. Mejia-Constain, A. P. Strafella, *Brain* **130**, 233 (2007).
11. O. Monchi, M. Petrides, A. P. Strafella, K. J. Worsley, J. Doyon, *Ann. Neurol.* **59**, 257 (2006).
12. A. M. Graybiel, *Curr. Opin. Neurobiol.* **5**, 733 (1995).
13. S. A. Tishkoff *et al.*, *Nat. Genet.* **39**, 31 (2007).
14. M. Smoel, X. Liu, P. Khatovich, *Nat. Rev. Neurosci.* **14**, 119 (2013).

10.1126/science.1247515

Beyond Stem Cells: Self-Renewal of Differentiated Macrophages

Michael H. Sieweke* and Judith E. Allen*

READ THE FULL ARTICLE ONLINE

<http://dx.doi.org/10.1126/science.1242974>



Cite this article as M. H. Sieweke, J. E. Allen, *Science* 342, 1242974 (2013). DOI: 10.1126/science.1242974

Background: Many mature cells of the body are continuously replaced, particularly in tissues that are most exposed to the environment such as cells of the immune system. The need for new cells is driven by cellular turnover during normal tissue homeostasis and is further increased upon infection. Because differentiated cells typically withdraw from the cell cycle, replacement of mature cells is generally thought to depend on differentiation of self-renewing, tissue-specific stem cells. Until recently, tissue macrophages were thought to follow such a pathway, developing from hematopoietic stem cells via bone marrow–progenitor and blood monocyte intermediates. But this view has changed of late with several observations indicating that macrophages can self-renew by local proliferation of mature differentiated cells.

Advances: Recent studies have demonstrated that in macrophages, differentiation and cell cycle withdrawal can be uncoupled by the inactivation of specific transcription factors. These cells can then be expanded indefinitely as functionally differentiated macrophages without tumorigenic transformation. At the same time, it became clear that mature macrophages could also expand massively *in vivo* in response to infections by local proliferation, independently of input from adult hematopoietic stem cells. Furthermore, several populations of tissue macrophages were found to be derived from embryonic progenitors, and macrophages can be self-maintained in adult tissues by local proliferation. Together, these recent data suggest that macrophages are mature differentiated cells that may be endowed with self-renewal capacity akin to that of stem cells.

Outlook: These findings challenge the classical view of tissue maintenance by adult tissue-specific stem cells and indicate that stem cell–like self-renewal mechanisms may be activated in mature differentiated cells. It will be important to determine whether the engaged pathways resemble those active in stem cells and whether they might be activated in other cell types as well. Furthermore, we need to understand how such self-renewal capacity differs from uncontrolled proliferation induced by oncogenic transformation. A first step will be to explore how macrophage proliferation is regulated *in vivo*: How do macrophages adapt their cell numbers to diverse tissue requirements, from near quiescence during homeostasis to massive expansion under challenge? Macrophages are present in nearly every tissue and serve important functions in immunity, cancer, metabolism, and tissue repair. The role of local macrophage proliferation in these processes has remained largely unexplored. It will be important to investigate how the consequences of macrophage accumulation by local proliferation differ from those of monocyte-derived macrophage recruitment under inflammatory conditions. The control of macrophage numbers independent of inflammatory signals may provide new opportunities for therapeutic intervention in many of these areas.

ARTICLE OUTLINE

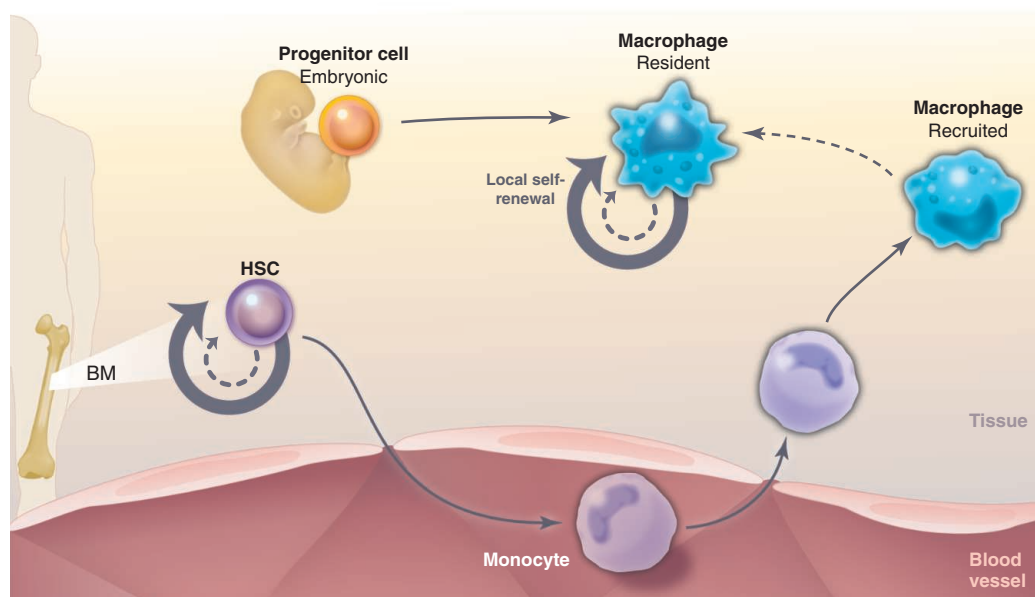
Multiple Pathways to Macrophages

Local Macrophage Proliferation

Mechanisms of Macrophage Self-Renewal

Future Perspectives

Macrophage origin and self-renewal. In the classical view, macrophages develop from self-renewing hematopoietic stem cells (HSC) in the bone marrow (BM) via blood monocyte intermediates. However, new data show that some adult tissue macrophage populations develop from embryonic progenitors independent of HSCs and can self-renew. Local proliferation can assure homeostatic maintenance (dotted arrows) and dramatically increase cell number (solid arrows) upon challenge.



The list of author affiliations is available in the full article online.

*Corresponding author. E-mail: sieweke@ciml.univ-mrs.fr (M.H.S.); j.allen@ed.ad.uk (J.E.A.)

Beyond Stem Cells: Self-Renewal of Differentiated Macrophages

Michael H. Sieweke^{1,2,3,4*} and Judith E. Allen^{5*}

In many mammalian tissues, mature differentiated cells are replaced by self-renewing stem cells, either continuously during homeostasis or in response to challenge and injury. For example, hematopoietic stem cells generate all mature blood cells, including monocytes, which have long been thought to be the major source of tissue macrophages. Recently, major macrophage populations were found to be derived from embryonic progenitors and to renew independently of hematopoietic stem cells. This process may not require progenitors, as mature macrophages can proliferate in response to specific stimuli indefinitely and without transformation or loss of functional differentiation. These findings suggest that macrophages are mature differentiated cells that may have a self-renewal potential similar to that of stem cells.

Faced with constant challenges from the environment and the physiological aging process, the body continuously replaces its cells. This occurs particularly for tissues that are most exposed to the environment, such as the mucosal epithelia, skin, and immune system. Mature differentiated cells from these tissues are continuously lost, and their life span can be very short: just a few days for blood monocytes, for example. Consequently, the turnover of these cells is enormous, even under conditions of normal tissue homeostasis but especially after tissue damage or in the case of the immune system, upon infection. Generally, this need for new cells is sustained by tissue-specific stem cells that are endowed with self-renewal capacity and by transient amplifying progenitor cells that further increase cell numbers during differentiation. Once cells reach full maturity, they typically cease proliferation. Thus, the constant replacement of mature cells normally depends on the input from self-renewing stem cells. One of the best-studied examples of such adult tissue-specific stem cells is hematopoietic stem cells (HSCs) that give rise to all blood cells and immunocytes.

Tissue macrophages serve important roles in the immune response, tissue homeostasis, metabolism, and repair. Because of these multifaceted activities, macrophages have been identified as key players (and targets) in diseases with major importance for public health, such as cancer and cardiovascular, autoimmune, chronic inflammatory, degenerative, and metabolic diseases (*1*). Like

all other leukocytes, macrophages were thought to principally develop from hematopoietic stem cells via bone marrow progenitors and blood monocyte intermediates. This view has recently changed (Fig. 1) with the demonstration that major macrophage populations can be derived from embryonic progenitors in the yolk sac (*2, 3*) or after establishment of definitive hematopoiesis (*4, 5*) and can be maintained long-term, independently of input from adult hematopoietic stem cells (*4, 6, 7*). At the same time, it became clear that macrophages can proliferate and massively expand under challenge conditions, such as infections (*7, 8*), and that genetic inactivation of cell cycle withdrawal mechanisms enables indefinite self-renewal of mature macrophages without transformation or loss of macrophage function (*9*). Together, these recent data suggest that macrophages are mature differentiated cells that may be endowed with a self-renewal capacity akin to that of stem cells.

Multiple Pathways to Macrophages

Monocyte-Derived Macrophages

Before our recent understanding that tissue macrophages can be of embryonic origin, the idea that tissue macrophages originate from the bone marrow via circulating blood monocyte intermediates was textbook knowledge. Arguments to support this view had come mainly from bone marrow transplantation of experimental animals and humans, who received whole-body irradiation or other myelo-ablative treatments, such as cyclophosphamide chemotherapy. Radio-labeled bone marrow cells could be traced to skin implants and the peritoneal cavity of irradiated rats (*10, 11*). In mouse bone marrow chimeras, donor origin of tissue macrophage populations was demonstrated via the use of cytogenetic chromosome (*12*) or haplotype markers (*13*). In human patients receiving sex-mismatched bone marrow transplants, following the Y chromosome demonstrated the donor origin of alveolar macrophages (*14*).

Careful kinetic studies using radio-labeling of highly proliferative bone marrow progenitors and tracing the label to monocytes and macrophages also supported the bone marrow origin of macrophages (*15*). A radiolabeling approach during steroid-induced monocytopenia also provided evidence that monocytes give rise to pulmonary macrophages (*16*) and peritoneal macrophages after sterile inflammation (*17*). Based on this evidence, van Furth and Cohn proposed a model in which tissue macrophages arise from monocyte progenitors in the bone marrow via blood monocyte intermediates (*15*). These early observations were revisited more systematically in studies that demonstrated nearly complete reconstitution of several major tissue macrophage populations in irradiated bone marrow chimeras after 2 to 12 months, with the exception of microglia cells, which showed only a minor but detectable donor contribution at later time points (*18, 19*).

Adoptive transfer and tracing of labeled monocytes have also been employed to study monocyte-derived macrophages. Modern flow cytometry and green fluorescent protein (GFP)–reporter mice have made it possible to clearly characterize monocytes, of which two main subtypes exist: commonly named classical or inflammatory and nonclassical or patrolling monocytes, with a Ly6C^{hi}, CCR2^{hi}, CX3CR1^{lo} or Ly6C^{lo}, CCR2^{lo}, CX3CR1^{hi} surface marker phenotype, respectively (*20*), and a subtype-specific gene-expression profile (*21, 22*). Although monocytes have important functions inside blood vessels in their own right (*21, 23, 24*), these cells also leave the blood to infiltrate tissues and convert into macrophages under diverse challenge conditions such as atherosclerosis (*25*), myocardial infarction (*26*), muscle injury (*27*), or infection and inflammation (*28*). Upon irritation, aseptic wounding, or infection, a massive efflux of monocytes into neighboring tissue occurs within 1 to 2 hours or the first 24 hours, depending on the monocyte subtype (*21*). Consistent with historic carbon-particle-labeling experiments (*29*), modern-day *in vivo* labeling with fluorescent beads (*30, 31*) or transplantation of GFP-expressing monocytes (*22, 32–35*) has demonstrated monocyte infiltration into inflamed skin, the peritoneal cavity, brain, and intestinal lamina propria (*22, 30, 31, 34, 35*) and noninflamed lung and intestines (*22, 30, 32, 33*).

Embryonic Progenitor-Derived Macrophages

Some data have long conflicted with the monocyte-centered view of macrophage origin. For example, the bone-seeking radio-element ⁸⁹Sr, which incorporates close to bone marrow niches and selectively ablates HSC-dependent monopoiesis, did not reduce tissue macrophage populations in the lung, peritoneum (*36*), and liver (*37*). Similarly, CCR2 inactivation severely depletes circulating monocytes without substantially affecting tissue macrophage populations (*7*). Consistent with this observation, many tissue macrophage populations appear to be intact in patients with monocytopenia

¹Centre d'Immunologie de Marseille-Luminy (CIML), Aix-Marseille Université, UM2, Campus de Luminy, Case 906, 13288 Marseille Cedex 09, France. ²Institut National de la Santé et de la Recherche Médicale (INSERM), U1104, Marseille, France. ³Centre National de la Recherche Scientifique (CNRS), UMR7280, Marseille, France. ⁴Max-Delbrück-Centrum für Molekulare Medizin (MDC), Robert-Rössle-Strasse 10, 13125 Berlin, Germany. ⁵Centre for Immunity, Infection and Evolution, and the Institute for Immunology and Infection Research, School of Biological Sciences, University of Edinburgh, Edinburgh EH9 3JT, UK.

*Corresponding author. E-mail: sieweke@ciml.univ-mrs.fr (M.H.S.); j.allen@ed.ac.uk (J.E.A.)

caused by leukemia or certain immune deficiency syndromes (38–40). These observations, however, are not fully conclusive, as increased life span of downstream progeny can compensate for reduced monocyte input (41).

More direct evidence for sources of tissue macrophages, other than bone marrow-derived monocytes, comes from modern lineage-tracing experiments. In these experiments, Cre-recombinase is expressed under the control of a lineage-specific locus to excise a loxP-flanked Stop cassette from a fluorescent protein reporter. Consequently, all progeny of cells that expressed the marker in the past will be labeled, even after expression of the marker itself has ceased. A useful marker is CX3CR1, which is expressed in monocyte dendritic cell progenitors in the bone marrow, but not in many mature macrophage populations. Post-natal induction of Cre led to extensive labeling of monocytes but essentially no labeling of Langerhans cells; Kupffer cells; or peritoneal, alveolar, or splenic macrophages—labeling would be expected if these populations were replaced by monocytes. By contrast, labeled macrophages could be found in the peritoneal cavity after thioglycollate-induced monocyte infiltration (41). Similarly, other lineage-tracing models with strong labeling of monocytes, such as S100a-, Flt3-, and Mx-Cre reporter mice, also showed only limited labeling in lung and spleen macrophages. This finding is supported by studies in parabiotic mice that revealed a poor contribution to lung, spleen, and peritoneal tissue macrophages from partner mouse monocytes (7). Together, these experiments indicate little or no contribution of monocytes to several tissue macrophage populations.

Parallel to these experiments, lineage-tracing experiments identified alternative developmental origins and suggested that many adult macrophage populations are derived from embryonic progenitors (2, 3, 41). Hematopoiesis in the embryo occurs in several waves, with primitive hematopoietic cells first arising in the yolk sac blood islands around embryonic day seven (E7), shifting later to the aorta-gonad-mesonephros region and the fetal liver before it is established in the bone marrow after birth. Yolk sac hematopoiesis produces only macrophages and erythroid cells. Pulse labeling with Runx-Cre ancestry mice at E7.5, before the development of HSCs and thus the establishment of definitive hematopoiesis, marked ~30% of adult brain microglia cells, similar to the proportion of marked yolk sac macrophages and microglia in the embryo (2). This demonstrated that brain microglia cells are derived from such early yolk sac macrophage progenitor cells.

Genetic approaches that selectively disable definitive hematopoiesis now indicate that beyond brain microglia, early yolk sac macrophage progenitors contribute more broadly to tissue macrophage populations in the adult (3). The transcription factor c-Myb is essential for HSC, but its inactivation does not affect yolk sac progenitors and primitive macrophage differentiation (3, 42). Despite the complete absence of definitive HSC-

dependent hematopoiesis, tissue macrophage populations develop in multiple organs of Myb-deficient embryos and display a characteristic macrophage gene and F4/80^{hi} surface-marker expression profile (3). Pulse labeling of cells expressing the macrophage colony-stimulating factor receptor (CSF-1R) at E8.5 in inducible Cre-ancestry mice confirmed that early embryonic progenitor-derived F4/80^{hi} tissue macrophages can persist into adulthood (3). This is consistent with observations that in Myb mutant zebrafish postembryonic tissue, macrophage populations develop in the absence of definitive hematopoiesis (43). Together, these experiments show that early embryonic progenitor-derived macrophages can persist in tissues to adulthood. In addition to yolk sac progenitors, after the onset of definitive hematopoiesis a second wave of embryonic progenitors can contribute to epidermal Langerhans cells (4, 5), which have recently been classified as macrophages on the basis of their dependence on macrophage

colony-stimulating factor (M-CSF, also known as CSF-1) (44). To what extent different populations of yolk sac progenitor-derived macrophages may subsequently be replaced by later embryonic progenitors or monocytes remains a matter of debate (45).

Context-Dependent Macrophage Origin

It is now established that macrophages can be of dual origin from embryonic progenitors or blood monocytes (Fig. 1) and that monocytes contribute only minimally to many tissue macrophage populations under homeostatic conditions (3, 7, 41, 46, 47). However, monocyte contribution can be strongly increased upon inflammation, and it remains an important question to what extent monocyte- and embryo-derived tissue macrophages are distinct and whether under physiological or pathological conditions conversion is possible.

It has been argued that monocytes maintain their own identity, even after entering the tissue, and do not convert into macrophages (7, 46, 48).

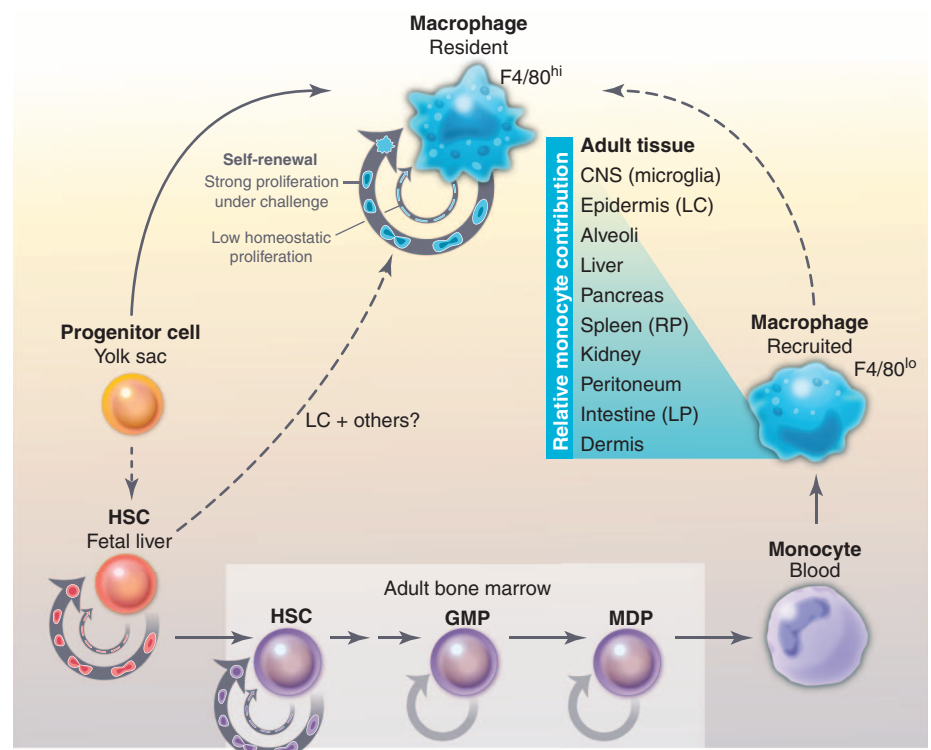


Fig. 1. New view of macrophage origin and self-renewal. Macrophages (blue) can develop from early embryonic progenitors in the yolk sac (and, in some cases, after onset of fetal liver hematopoiesis) to be maintained throughout development and in adult tissues by local self-renewal (top). Similar to stem cells, local self-renewal of macrophages is characterized by low proliferation rates under steady-state conditions (small circular arrows) but strong expansion during development, after depletion, or under challenge (large circular arrows). After hematopoiesis shifts from the yolk sac to the fetal liver and the adult bone marrow, macrophages can also develop from HSCs through transient amplifying myeloid progenitors (large circular arrows) and nonproliferative blood monocytes (bottom). Monocyte-derived macrophages can give rise to resident macrophages under certain conditions, such as bone marrow transplantation after irradiation. More typically, monocyte contribution to resident macrophages is highly tissue-dependent and varies from no contribution for brain microglia and epidermal Langerhans cells to complete monocyte origin for intestinal lamina propria macrophages. Although not a definitive marker, resident macrophages are often F4/80^{hi}, whereas recruited monocyte-derived macrophages are generally F4/80^{lo}. Based on current knowledge, tissues are indicated in increasing order of monocyte contribution to resident macrophage populations (top to bottom). GMP, granulocyte-macrophage progenitor; MDP, macrophage-dendritic progenitor; LC, Langerhans cells; RP, red pulp; LP, lamina propria.

Inflammatory monocyte-derived populations can be phenotypically and functionally distinguished from resident macrophages in many tissues (3, 7, 46, 49–51) and, in some cases, disappear without contributing to the resident pool (49). On the other hand, lineage tracing revealed that thioglycollate-elicited macrophages derived from inflammatory monocytes changed phenotype to integrate into the resident macrophage pool and persisted over time (41). Gene profiling has also indicated that monocytes acquire macrophage gene expression after inflammation-induced tissue infiltration (21, 22, 46). Furthermore, adult Langerhans cells show no monocyte contribution in homeostatic settings (3, 52) but can show substantial replacement from the circulation during inflammation (31, 52), even under mild conditions (53). Monocytes can also fully replace resident macrophages, including F4/80^{hi} populations that are normally embryo-derived, after myelo-ablative conditioning and bone marrow transplantation (7, 18, 19, 47, 52), demonstrating the capacity of monocytes for such an identity change. Monocytes can also contribute to macrophages under noninflamed conditions, but only in a highly tissue-specific manner (Fig. 1). Thus, in models involving no inflammation or irradiation injury,

bone marrow transplantation results in a moderate to major donor contribution to F4/80^{hi} tissue macrophages of the spleen, pancreas, lung, and kidney, but not other tissues (3). Lineage tracing and adoptive transfer also demonstrated a clear monocyte contribution to macrophages of the dermis (46) and intestinal lamina propria (22) but a lack of contribution to many other tissues (3, 7, 41, 46).

Whether the contribution of monocytes to macrophages increases over the life span of the organism, perhaps due to repeated episodes of low-level inflammation, is an interesting question. Nonetheless, it is clear that in most tissues the rate of conversion would be very low and that tissue macrophage populations, irrespective of their yolk sac, embryonic or adult origin, persist over the long term in tissues and self-maintain with no or minimal input from circulating monocytes. This finding indicates that tissue macrophages require mechanisms for local self-renewal to maintain their numbers in homeostasis and under challenge.

Local Macrophage Proliferation

In Homeostasis

Macrophage differentiation from proliferative progenitors involves cell cycle exit, but experimen-

tally, proliferation arrest can be overcome without loss of the differentiated phenotype (9). Macrophages can also be maintained long-term in tissues with little input from HSC-derived progenitors (3–5, 7, 47, 52). This was initially shown for microglia cells and Langerhans cells, two populations that are separated from the circulation by the blood-brain barrier and the basal lamina, respectively, and may thus have more limited access to leukocyte influx. Microglia cells develop from early yolk sac progenitors (54) and enter the developing brain, where they undergo massive proliferative expansion throughout embryonic development (2). In the adult, they remain largely quiescent without input from bone marrow progenitors. Langerhans cells develop from embryonic progenitors before birth (3–5) and are also maintained independently from bone marrow contribution in the adult (52). Directly after birth, they undergo a burst of proliferative expansion and then maintain low levels of homeostatic proliferation (4). Thus, the acquisition and maintenance of the required cell numbers in these two examples appear to be achieved by the proliferation of differentiated macrophages rather than the influx of progenitors. Resident peritoneal macrophages exhibit similar proliferative expansion in newborn mice and maintenance in the adult (50). For alveolar macrophages, historical evidence of cell division came from observations of human biopsies (55) and colony-formation capacity of hamster or human alveolar macrophages (38, 56). Later, ³H-thymidine incorporation analysis led to calculations suggesting that the majority of alveolar macrophages are maintained by local proliferation under steady-state conditions (57). Consistent with this finding, a recent study confirmed a significant proportion of proliferating macrophages (10%) in the steady-state lung (7).

Importantly, proliferation not only sustains macrophage numbers under homeostatic conditions but also mediates their rebound after severe depletion. A strong expansion of resident local macrophages and a several-fold increase in proliferation have been observed for splenic red pulp, bone marrow, and alveolar macrophages using genetic diphtheria toxin and clodronate-depletion models (7). Reestablishment of normal macrophage numbers by local proliferation has also been observed in less artificial settings of macrophage depletion, such as influenza virus infection (7) and inflammation-induced loss of resident peritoneal macrophages (50). Physiological or experimental depletion of Langerhans cells and intestinal macrophages leads to small clonal cell clusters, indicating that cells undergo a few cell divisions before reaching homeostatic numbers (33, 53). Local macrophage expansion appears not to be reliant on a dedicated progenitor population, as during recovery from cytotoxic depletion, a macrophage that had previously divided had the same probability of entering the cell cycle as a cell that had not (7). This suggests that all macrophages are equally capable of proliferation and is consistent with the observation that genetically modified

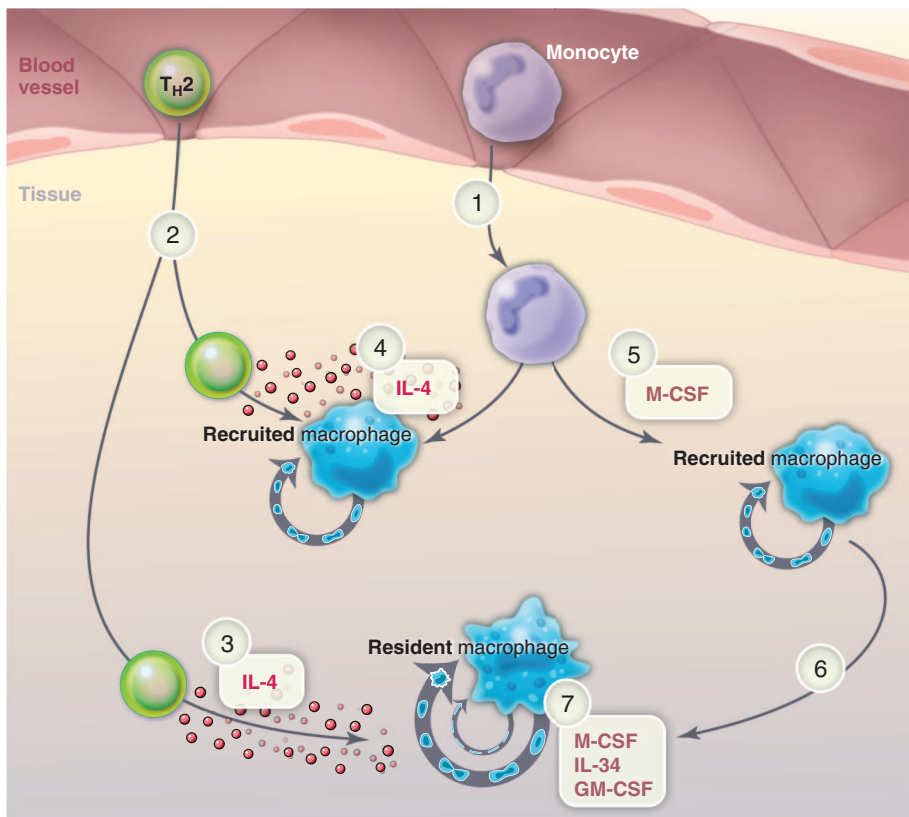


Fig. 2. Cytokine regulation of macrophage self-renewal in different settings. Monocytes are recruited to tissues under classical inflammatory conditions (1). In macroparasite-infected individuals, T_H2 cells release large amounts of IL-4 or IL-13 (2) that lead to massive expansion of resident macrophages (3) and IL-4Rα activation, as well as proliferation of recruited inflammatory macrophages (4). M-CSF can also induce limited proliferation of subsets of recruited macrophages (5), which, under certain conditions and depending on the tissue, can integrate into the resident macrophage pool (6) (see Fig. 1). Self-renewal of resident macrophages (7) during developmental expansion, homeostasis, or insult recovery can be driven by M-CSF or IL-34 in the brain and epidermis and by GM-CSF in the lung.

macrophages with indefinite self-renewal potential can be cloned and recloned with high efficiency and low variation (9). Together, these data indicate that proliferation and expansion of mature differentiated macrophage populations maintain adequate cell numbers during development and homeostasis.

Response to Challenge

The ability of mature macrophages to proliferate becomes particularly evident under stress and challenge conditions that require a large increase in macrophage numbers. Macrophage proliferation is observed in a variety of human pathologies including atherosclerosis, kidney disease, acetaminophen-induced liver failure, and chronic lung inflammation (25, 58–60). Experimentally, injury in the central nervous system or neurodegenerative disease leads to massive microgliosis due to local proliferation of microglia cells (6, 49). Similarly, atopic dermatitis results in proliferative expansion of otherwise largely quiescent Langerhans cells (4). Macrophage proliferation also occurs under nonpathological conditions of stress or challenge. For example, pregnancy leads to a strong increase in uterine macrophage numbers that is largely mediated by local proliferation (61), and wound healing of skeletal muscle is associated with proliferation of previously recruited macrophages (27).

Monocytes are essential for the defense against a broad range of microbial pathogens (28), but their accumulation at an infection site is principally sustained by influx from the blood. Classical early inflammatory signals of microbial infection generally do not permit proliferation of recruited monocyte-derived macrophages, with the notable exception of Ly6B⁺ macrophages in zymosan-induced peritonitis (62). The drastic loss of resident macrophages occurring in the inflammatory process, however, is compensated by local proliferation at later time points (7, 50). Even during classical inflammatory episodes, macrophage numbers may thus be controlled by an early recruitment phase and later proliferative phase, as recently demonstrated for atherosclerotic lesions (25).

In stark contrast to the inflammatory pathways involved in control of microbial pathogens, the response to helminths involves an entirely different cellular network with a central role for the T helper cell 2 (T_H2) cytokines interleukin-4 (IL-4) and IL-13 that signal through the IL-4 receptor α (IL-4R α) (63). Macrophages activated via the IL-4R α are found abundantly at sites of helminth infection and allergic inflammation and yet are typically considered to be anti-inflammatory, raising important questions about their relation to inflammatory monocytes (20). In a murine model of nematode infection that induces a potent T_H2-type immune response, there is a slow accumulation of macrophages in the pleural cavity where the parasites reside. Using bone marrow chimeras in which the pleural cell population was protected from irradiation damage, it was demonstrated that the pleural resident macrophages expanded by

local proliferation, with little contribution from bone marrow-derived cells (8). Proliferation and accumulation were dependent on high levels of IL-4 and/or IL-13 and appear restricted to the infection site (64). The action of IL-4 is not limited to the resident population but also stimulates proliferation of monocyte-derived macrophages (8). Thus, IL-4 and/or IL-13 induced by helminth infection drive the expansion of a noninflammatory resident population or drive proliferation of recruited cells and simultaneously convert them to a less inflammatory macrophage phenotype.

Mechanisms of Macrophage Self-Renewal

Cytokines Inducing Macrophage Proliferation

Several cytokines can drive macrophage proliferation (Fig. 2). The central importance of M-CSF in the maintenance of macrophage numbers is demonstrated by natural M-CSF mutations in mice (op/op) and rats (tl/tl) [reviewed in (65)]. All macrophages express the CSF-1R, but because it is also expressed by progenitors, it is difficult using these mice to distinguish differentiation defects from reduced proliferation of mature cells. However, with the use of blocking antibodies or reconstitution protocols, a specific role for M-CSF in resident macrophage proliferation has been identified in the peritoneal cavity in the

steady state and inflammation (62); during recovery after experimental depletion in the spleen, peritoneal cavity, and lung (7); and in the growing myometrium during pregnancy (61). IL-34, an alternative ligand for CSF-1R produced by brain neurons and keratinocytes, stimulates self-renewal of microglia and Langerhans cells. However, inflammation-induced Langerhans cell repopulation still requires M-CSF (66, 67). CSF-1R signaling is also essential for unlimited self-renewal of MafB- and cMaf-deficient (Maf-DKO) macrophages (9).

Beyond the central role of CSF-1R ligands, granulocyte-macrophage colony-stimulating factor (GM-CSF)/CSF-2 is critical for lung macrophage homeostasis (68) and the ability to repopulate the lung after lethal irradiation (7). GM-CSF also induces proliferation of peritoneal macrophages *in vivo* (69) and can sustain the long-term culture of nontransformed fetal liver-derived macrophage lines (70). Thus, M-CSF, IL-34, and GM-CSF all participate in the process of self-renewal or repopulation, but their contributions are context- and tissue-specific. Furthermore, clear evidence exists for M-CSF-mediated macrophage proliferation in disease settings such as allograft rejection (71), suggesting roles beyond steady-state maintenance.

Recently, a potent proproliferative action of IL-4 on macrophages *in vivo* has also been doc-

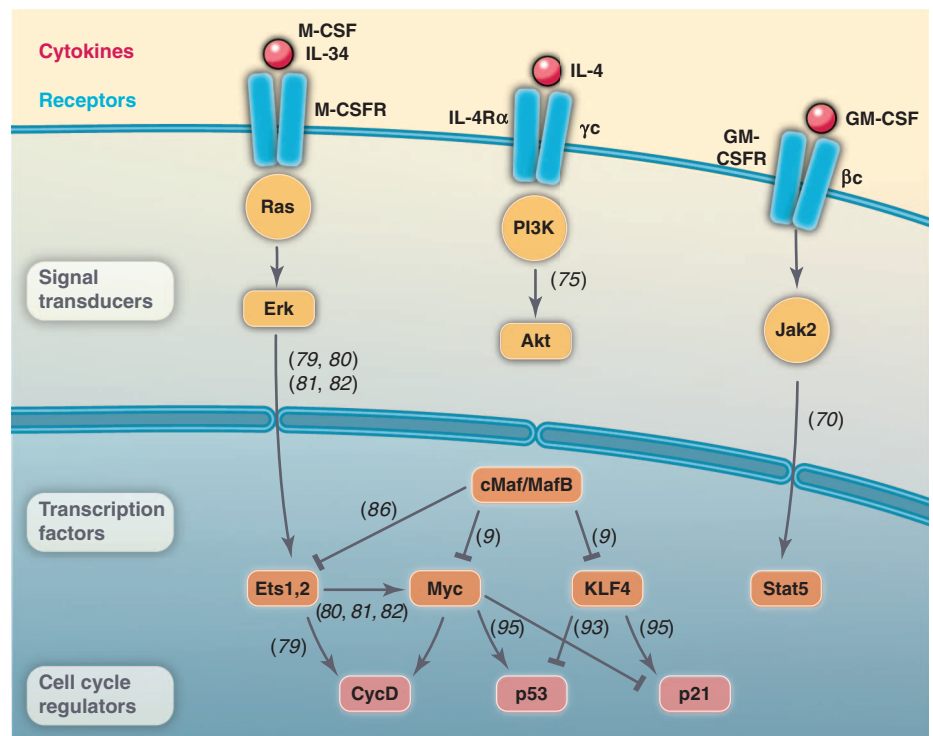


Fig. 3. Intracellular signaling pathways of macrophage self-renewal. M-CSF stimulation of CSF-1R signaling can activate Ets transcription factors via Ras and Erk signaling, which, in turn, can activate D-type cyclins and Myc. MafB and c-Maf repress Ets factors, as well as M-CSF-dependent Myc and KLF4 activation. The cross-antagonistic regulation of p53 and p21 by Myc and KLF4 may be important for balanced cell cycle activation that enables self-renewal without causing tumorigenic transformation. IL-4-induced phosphatidylinositol 3-kinase (PI3K) signaling is important for its proproliferative activity, and Stat5 can mediate GM-CSF-induced macrophage proliferation. Other signaling pathways induced by the cytokines but not documented as involved in proliferation are not pictured. Numbers indicate references on which the figure is based.

umented (8). Injection of IL-4 or IL-13 into the peritoneal cavity of mice induces an almost exclusive expansion of tissue resident macrophages through local proliferation that is not limited to the injection site but drives resident macrophage expansion throughout the body, including the liver and spleen (8, 64). Critically, the IL-4R α is not involved in the steady-state proliferation of tissue resident macrophages (7, 62, 64), and IL-4-mediated macrophage proliferation is independent of the CSF-1R (64). Indeed, IL-4 appears to allow macrophages to divide beyond homeostatic levels maintained by M-CSF (64). With repeated or sustained IL-4 delivery, it is even possible to cause death due to tissue macrophage hyperplasia (72), suggesting that endogenous controls of IL-4-driven proliferation fail in this artificial long-term and high-dose delivery system. IL-4 availability itself may therefore be an important limiting factor in vivo.

Mixed wild-type and IL-4R α -deficient bone marrow chimeras have demonstrated that IL-4 acts directly on macrophages to drive proliferation (64). Surprisingly, however, IL-4 drives minimal macrophage proliferation in culture, suggesting that additional cofactors are required in vivo. Although direct injection of IL-4 into lymphocyte-deficient mice induces macrophage proliferation (8), CD4 helper T cells are required for macrophage expansion during helminth infection (73). This suggests that T cells are an important source of IL-4 in natural settings and that IL-4-driven proliferation may be restricted to adaptive T_H2 environments. It will be critical to determine whether IL-4-mediated macrophage proliferation also occurs in noninfection settings, where there is a growing appreciation that the overarching function of macrophages activated via the IL-4R α is to maintain tissue homeostasis (74).

Intracellular Signaling and Transcription Factors Controlling Macrophage Proliferation

Investigation of the signaling events downstream of the cytokine receptors has been the natural starting point to identify the intracellular mechanisms that mediate macrophage proliferation (Fig. 3). Although most of this work has been done in culture, it has been shown in vivo that AKT signaling is important for IL-4-induced proliferation (75). The IL-4R α can also induce C/EBP β , peroxisome proliferator-activated receptor γ interferon regulatory factor 4, and Stat6 activation (76), but whether the known roles of these transcription factors in the macrophage activation state extend to proliferation is unclear. Dedicated branches of cytokine signaling may exist for differentiation, survival, activation, and proliferation, as has been shown for the CSF-1R (77). Indeed, IL-4 signaling via Stat6 can inhibit M-CSF-stimulated macrophage proliferation (78). In a different context, Stat5 activation is sufficient to mediate extended macrophage proliferation by GM-CSF (70). M-CSF-induced proliferation involves the activation of the Myc, AP-1, and Ets transcription factors (79–81), the latter two of which

respectively activate *c-myc* and *c-myb* (82, 83), two proliferative factors. MafB and c-Maf represent a core module of macrophage transcription factors (48) that are up-regulated during macrophage differentiation and can induce cell cycle arrest (84, 85). In myeloid progenitors, this is mediated by direct inhibition of Myb (84, 85), but because tissue macrophages can develop and proliferate in the absence of Myb (3, 43), this mechanism may not play a role in regulating the proliferation of mature macrophages. Because MafB can also directly bind and inhibit Ets-1 (86), it may rather take part in the inhibition of Ets activity on proliferative genes including c-Myc (80, 81, 82), occurring during cell cycle withdrawal of differentiated macrophages (80). Consistent with this finding, c-Myc is up-regulated in M-CSF- and GM-CSF-induced proliferation (9, 70, 87) and is required for the extended self-renewal capacity of Maf-DKO macrophages (9). It will thus be interesting to determine whether MafB, c-Maf, or their targets are regulated during episodes of physiological or pathological macrophage proliferation in vivo.

Do Macrophages Have Stem Cell-Like Self-Renewal Capacity?

The answer to this question hinges on the definition of self-renewal. Whereas in immunology this term is often relatively loosely employed as replacement of a certain cell population, in stem cell research it is a defining criterion, designating a cell division where at least one of the daughter cells has the same identity as the parental cell (88). Usually the term is thus reserved for stem cells, which can maintain self-renewal divisions over the long term, whereas highly proliferative progenitor cells change their identity as they differentiate. Local proliferation of tissue macrophages may qualify as self-renewal, not only in the loose (immunological) sense but also in the more strict (stem cell) sense, as cell cycle entry appears to occur independently of whether cells divided previously (7), suggesting that it is not restricted to a dedicated progenitor population. Consistent with this observation, Maf-DKO macrophages can divide indefinitely without loss of macrophage identity and can be cloned and re-cloned at the same efficiency (9), indicating that self-renewal in the strict sense, without loss of cellular identity, is possible in macrophages. Other examples in which mature differentiated cells can reenter the cell cycle are hepatocytes (89) and memory cells in the lymphoid system (90).

The notion of true macrophage self-renewal is further supported by the molecular mechanisms involved. Similar to embryonic stem (ES) cells (91, 92), self-renewal in Maf-DKO macrophages depends on Myc and Kruppel-like factor 4 (KLF4) (9). Both Myc and KLF4 are part of the original transcription factor cocktail that can induce reprogramming of somatic cells to pluripotent stem cells (93). However, these transcription factors are not required for the induction of pluripotency and have been suggested to mediate self-

renewal (93). KLF4 does not induce proliferation in macrophages (9) but may mitigate the transforming activity of Myc (94) by opposing its effect on p21 and p53 (93, 95). The balanced activities of Myc and KLF4 may thus be required to enable macrophage self-renewal. Given the similarities in the role of Myc and KLF4 in ES cell and macrophage self-renewal, it will be interesting to determine whether similar signaling and transcription factor networks are employed in the two cell types.

Future Perspectives

We have reviewed the evidence that, irrespective of their origin, tissue macrophages can self-renew by local proliferation without replacement via hematopoietic stem cell-derived monocyte intermediates. It is important to appreciate how completely this concept breaks with the classical view of tissue maintenance by adult tissue-specific stem cells. The observations suggest that macrophages control their numbers independently of stem cells and in intimate relation with the tissue where they reside. It will be important to explore the relative contribution of local proliferation and monocyte recruitment in a range of inflammatory and non-inflammatory settings and how the selective control of local macrophage proliferation versus monocyte recruitment could be turned to therapeutic benefit; for example, in excessive or chronic inflammatory conditions. To achieve this, we will need to understand the signaling pathways and cellular communications that control macrophage proliferation in vivo; in particular, the differences between a long-lived and largely quiescent homeostatic state and high rates of proliferation in response to challenge. It will be valuable to determine whether resident tissue macrophages employ similar signaling pathways and regulatory circuits as stem cells to respond to these divergent demands. It will also be important to understand how macrophage self-renewal differs from transient proliferation or tumorigenic transformation. If this succeeds, macrophages may teach us how to manage nontumorigenic cellular expansion ex vivo and in situ for tissue maintenance and regeneration.

References and Notes

1. T. A. Wynn, A. Chawla, J. W. Pollard, Macrophage biology in development, homeostasis and disease. *Nature* **496**, 445–455 (2013). doi: [10.1038/nature12034](https://doi.org/10.1038/nature12034); pmid: [23619691](https://pubmed.ncbi.nlm.nih.gov/23619691/)
2. F. Ginhoux *et al.*, Fate mapping analysis reveals that adult microglia derive from primitive macrophages. *Science* **330**, 841–845 (2010). doi: [10.1126/science.1194637](https://doi.org/10.1126/science.1194637); pmid: [20966214](https://pubmed.ncbi.nlm.nih.gov/20966214/)
3. C. Schulz *et al.*, A lineage of myeloid cells independent of Myb and hematopoietic stem cells. *Science* **336**, 86–90 (2012). doi: [10.1126/science.1219179](https://doi.org/10.1126/science.1219179); pmid: [22442384](https://pubmed.ncbi.nlm.nih.gov/22442384/)
4. L. Chorro *et al.*, Langerhans cell (LC) proliferation mediates neonatal development, homeostasis, and inflammation-associated expansion of the epidermal LC network. *J. Exp. Med.* **206**, 3089–3100 (2009). doi: [10.1084/jem.20091586](https://doi.org/10.1084/jem.20091586); pmid: [19995948](https://pubmed.ncbi.nlm.nih.gov/19995948/)
5. G. Hoeffel *et al.*, Adult Langerhans cells derive predominantly from embryonic fetal liver monocytes with a minor contribution of yolk sac-derived macrophages. *J. Exp. Med.* **209**, 1167–1181 (2012). doi: [10.1084/jem.20120340](https://doi.org/10.1084/jem.20120340); pmid: [22565823](https://pubmed.ncbi.nlm.nih.gov/22565823/)

6. B. Ajami, J. L. Bennett, C. Krieger, W. Tetzlaff, F. M. Rossi, Local self-renewal can sustain CNS microglia maintenance and function throughout adult life. *Nat. Neurosci.* **10**, 1538–1543 (2007). doi: [10.1038/nn2014](https://doi.org/10.1038/nn2014); pmid: [18026097](https://pubmed.ncbi.nlm.nih.gov/18026097/)
7. D. Hashimoto *et al.*, Tissue-resident macrophages self-maintain locally throughout adult life with minimal contribution from circulating monocytes. *Immunity* **38**, 792–804 (2013). doi: [10.1016/j.immuni.2013.04.004](https://doi.org/10.1016/j.immuni.2013.04.004); pmid: [23601688](https://pubmed.ncbi.nlm.nih.gov/23601688/)
8. S. J. Jenkins *et al.*, Local macrophage proliferation, rather than recruitment from the blood, is a signature of T_H2 inflammation. *Science* **332**, 1284–1288 (2011). doi: [10.1126/science.1204351](https://doi.org/10.1126/science.1204351); pmid: [21566158](https://pubmed.ncbi.nlm.nih.gov/21566158/)
9. A. Aziz, E. Soucie, S. Sarrazin, M. H. Sieweke, MafB/c-Maf deficiency enables self-renewal of differentiated functional macrophages. *Science* **326**, 867–871 (2009). doi: [10.1126/science.1176056](https://doi.org/10.1126/science.1176056); pmid: [19892988](https://pubmed.ncbi.nlm.nih.gov/19892988/)
10. A. Volkman, J. L. Gowans, The origin of macrophages from bone marrow in the rat. *Br. J. Exp. Pathol.* **46**, 62–70 (1965). pmid: [14295560](https://pubmed.ncbi.nlm.nih.gov/14295560/)
11. A. Volkman, The origin and turnover of mononuclear cells in peritoneal exudates in rats. *J. Exp. Med.* **124**, 241–254 (1966). doi: [10.1084/jem.124.2.241](https://doi.org/10.1084/jem.124.2.241); pmid: [5919691](https://pubmed.ncbi.nlm.nih.gov/5919691/)
12. M. Virolainen, Hematopoietic origin of macrophages as studied by chromosome markers in mice. *J. Exp. Med.* **127**, 943–952 (1968). doi: [10.1084/jem.127.5.943](https://doi.org/10.1084/jem.127.5.943); pmid: [5655103](https://pubmed.ncbi.nlm.nih.gov/5655103/)
13. J. J. Godleski, J. D. Brain, The origin of alveolar macrophages in mouse radiation chimeras. *J. Exp. Med.* **136**, 630–643 (1972). doi: [10.1084/jem.136.3.630](https://doi.org/10.1084/jem.136.3.630); pmid: [4559194](https://pubmed.ncbi.nlm.nih.gov/4559194/)
14. E. D. Thomas, R. E. Ramberg, G. E. Sale, R. S. Sparkes, D. W. Golde, Direct evidence for a bone marrow origin of the alveolar macrophage in man. *Science* **192**, 1016–1018 (1976). doi: [10.1126/science.775638](https://doi.org/10.1126/science.775638); pmid: [775638](https://pubmed.ncbi.nlm.nih.gov/775638/)
15. R. van Furth, Z. A. Cohn, The origin and kinetics of mononuclear phagocytes. *J. Exp. Med.* **128**, 415–435 (1968). doi: [10.1084/jem.128.3.415](https://doi.org/10.1084/jem.128.3.415); pmid: [5666958](https://pubmed.ncbi.nlm.nih.gov/5666958/)
16. A. B. van oud Alblas, R. van Furth, Origin, kinetics, and characteristics of pulmonary macrophages in the normal steady state. *J. Exp. Med.* **149**, 1504–1518 (1979). doi: [10.1084/jem.149.6.1504](https://doi.org/10.1084/jem.149.6.1504); pmid: [448291](https://pubmed.ncbi.nlm.nih.gov/448291/)
17. J. Thompson, R. van Furth, The effect of glucocorticosteroids on the kinetics of mononuclear phagocytes. *J. Exp. Med.* **131**, 429–442 (1970). doi: [10.1084/jem.131.3.429](https://doi.org/10.1084/jem.131.3.429); pmid: [5413324](https://pubmed.ncbi.nlm.nih.gov/5413324/)
18. D. W. Kennedy, J. L. Abkowitz, Kinetics of central nervous system microglial and macrophage engraftment: Analysis using a transgenic bone marrow transplantation model. *Blood* **90**, 986–993 (1997). pmid: [9242527](https://pubmed.ncbi.nlm.nih.gov/9242527/)
19. J. Priller *et al.*, Targeting gene-modified hematopoietic cells to the central nervous system: Use of green fluorescent protein uncovers microglial engraftment. *Nat. Med.* **7**, 1356–1361 (2001). doi: [10.1038/nm1201-1356](https://doi.org/10.1038/nm1201-1356); pmid: [11726978](https://pubmed.ncbi.nlm.nih.gov/11726978/)
20. C. Auffray, M. H. Sieweke, F. Geissmann, Blood monocytes: Development, heterogeneity, and relationship with dendritic cells. *Annu. Rev. Immunol.* **27**, 669–692 (2009). doi: [10.1146/annurev.immunol.021908.132557](https://doi.org/10.1146/annurev.immunol.021908.132557); pmid: [19132917](https://pubmed.ncbi.nlm.nih.gov/19132917/)
21. C. Auffray *et al.*, Monitoring of blood vessels and tissues by a population of monocytes with patrolling behavior. *Science* **317**, 666–670 (2007). doi: [10.1126/science.1142883](https://doi.org/10.1126/science.1142883); pmid: [17673663](https://pubmed.ncbi.nlm.nih.gov/17673663/)
22. E. Zigmund *et al.*, Ly6C^{hi} monocytes in the inflamed colon give rise to proinflammatory effector cells and migratory antigen-presenting cells. *Immunity* **37**, 1076–1090 (2012). doi: [10.1016/j.immuni.2012.08.026](https://doi.org/10.1016/j.immuni.2012.08.026); pmid: [23219392](https://pubmed.ncbi.nlm.nih.gov/23219392/)
23. J. Cros *et al.*, Human CD14^{dim} monocytes patrol and sense nucleic acids and viruses via TLR7 and TLR8 receptors. *Immunity* **33**, 375–386 (2010). doi: [10.1016/j.immuni.2010.08.012](https://doi.org/10.1016/j.immuni.2010.08.012); pmid: [20832340](https://pubmed.ncbi.nlm.nih.gov/20832340/)
24. L. M. Carlin *et al.*, Nr4a1-dependent Ly6C^{low} monocytes monitor endothelial cells and orchestrate their disposal. *Cell* **153**, 362–375 (2013). doi: [10.1016/j.cell.2013.03.010](https://doi.org/10.1016/j.cell.2013.03.010); pmid: [23582326](https://pubmed.ncbi.nlm.nih.gov/23582326/)
25. C. S. Robbins *et al.*, Local proliferation dominates lesional macrophage accumulation in atherosclerosis. *Nat. Med.* **19**, 1166–1172 (2013). doi: [10.1038/nm.3258](https://doi.org/10.1038/nm.3258); pmid: [23933982](https://pubmed.ncbi.nlm.nih.gov/23933982/)
26. M. Nahrendorf, M. J. Pittet, F. K. Swirski, Monocytes: Protagonists of infarct inflammation and repair after myocardial infarction. *Circulation* **121**, 2437–2445 (2010). doi: [10.1161/CIRCULATIONAHA.109.916346](https://doi.org/10.1161/CIRCULATIONAHA.109.916346); pmid: [20530020](https://pubmed.ncbi.nlm.nih.gov/20530020/)
27. L. Arnold *et al.*, Inflammatory monocytes recruited after skeletal muscle injury switch into antiinflammatory macrophages to support myogenesis. *J. Exp. Med.* **204**, 1057–1069 (2007). doi: [10.1084/jem.20070075](https://doi.org/10.1084/jem.20070075); pmid: [17485518](https://pubmed.ncbi.nlm.nih.gov/17485518/)
28. C. Shi, E. G. Pamer, Monocyte recruitment during infection and inflammation. *Nat. Rev. Immunol.* **11**, 762–774 (2011). doi: [10.1038/nri3070](https://doi.org/10.1038/nri3070); pmid: [21984070](https://pubmed.ncbi.nlm.nih.gov/21984070/)
29. J. Ungar, G. R. Wilson, Monocytes as a source of alveolar phagocytes. *Am. J. Pathol.* **11**, 681–692.5 (1935). pmid: [19970226](https://pubmed.ncbi.nlm.nih.gov/19970226/)
30. F. Geissmann, S. Jung, D. R. Littman, Blood monocytes consist of two principal subsets with distinct migratory properties. *Immunity* **19**, 71–82 (2003). doi: [10.1016/S1074-7613\(03\)00174-2](https://doi.org/10.1016/S1074-7613(03)00174-2); pmid: [12871640](https://pubmed.ncbi.nlm.nih.gov/12871640/)
31. F. Ginhoux *et al.*, Langerhans cells arise from monocytes in vivo. *Nat. Immunol.* **7**, 265–273 (2006). doi: [10.1038/ni1307](https://doi.org/10.1038/ni1307); pmid: [16444257](https://pubmed.ncbi.nlm.nih.gov/16444257/)
32. L. Landsman, C. Varol, S. Jung, Distinct differentiation potential of blood monocyte subsets in the lung. *J. Immunol.* **178**, 2000–2007 (2007). pmid: [17277103](https://pubmed.ncbi.nlm.nih.gov/17277103/)
33. C. Varol *et al.*, Monocytes give rise to mucosal, but not splenic, conventional dendritic cells. *J. Exp. Med.* **204**, 171–180 (2007). doi: [10.1084/jem.20061011](https://doi.org/10.1084/jem.20061011); pmid: [17190836](https://pubmed.ncbi.nlm.nih.gov/17190836/)
34. A. Mildner *et al.*, Microglia in the adult brain arise from Ly-6C^{hi}CCR2⁺ monocytes only under defined host conditions. *Nat. Neurosci.* **10**, 1544–1553 (2007). doi: [10.1038/nn2015](https://doi.org/10.1038/nn2015); pmid: [18026096](https://pubmed.ncbi.nlm.nih.gov/18026096/)
35. R. Shechter *et al.*, Recruitment of beneficial M2 macrophages to injured spinal cord is orchestrated by remote brain choroid plexus. *Immunity* **38**, 555–569 (2013). doi: [10.1016/j.immuni.2013.02.012](https://doi.org/10.1016/j.immuni.2013.02.012); pmid: [23477737](https://pubmed.ncbi.nlm.nih.gov/23477737/)
36. R. T. Sawyer, P. H. Strausbauch, A. Volkman, Resident macrophage proliferation in mice depleted of blood monocytes by strontium-89. *Lab. Invest.* **46**, 165–170 (1982). pmid: [6174824](https://pubmed.ncbi.nlm.nih.gov/6174824/)
37. M. Yamada, M. Naito, K. Takahashi, Kupffer cell proliferation and glucan-induced granuloma formation in mice depleted of blood monocytes by strontium-89. *J. Leukoc. Biol.* **47**, 195–205 (1990). pmid: [2307905](https://pubmed.ncbi.nlm.nih.gov/2307905/)
38. D. W. Golde, T. N. Finley, M. J. Cline, The pulmonary macrophage in acute leukemia. *N. Engl. J. Med.* **290**, 875–878 (1974). doi: [10.1056/NEJM197404182901603](https://doi.org/10.1056/NEJM197404182901603); pmid: [4522205](https://pubmed.ncbi.nlm.nih.gov/4522205/)
39. S. Hambleton *et al.*, IRF8 mutations and human dendritic-cell immunodeficiency. *N. Engl. J. Med.* **365**, 127–138 (2011). doi: [10.1056/NEJMoa1100066](https://doi.org/10.1056/NEJMoa1100066); pmid: [21524210](https://pubmed.ncbi.nlm.nih.gov/21524210/)
40. V. Bigley *et al.*, The human syndrome of dendritic cell, monocyte, B and NK lymphoid deficiency. *J. Exp. Med.* **208**, 227–234 (2011). doi: [10.1084/jem.20101459](https://doi.org/10.1084/jem.20101459); pmid: [21242295](https://pubmed.ncbi.nlm.nih.gov/21242295/)
41. S. Yona *et al.*, Fate mapping reveals origins and dynamics of monocytes and tissue macrophages under homeostasis. *Immunity* **38**, 79–91 (2013). doi: [10.1016/j.immuni.2012.12.001](https://doi.org/10.1016/j.immuni.2012.12.001); pmid: [23273845](https://pubmed.ncbi.nlm.nih.gov/23273845/)
42. M. L. Mucenski *et al.*, A functional *c-myc* gene is required for normal murine fetal hepatic hematopoiesis. *Cell* **65**, 677–689 (1991). doi: [10.1016/0092-8674\(91\)90099-K](https://doi.org/10.1016/0092-8674(91)90099-K); pmid: [1709592](https://pubmed.ncbi.nlm.nih.gov/1709592/)
43. C. Soza-Ried, I. Hess, N. Netuschil, M. Schorpp, T. Boehm, Essential role of *c-myc* in definitive hematopoiesis is evolutionarily conserved. *Proc. Natl. Acad. Sci. U.S.A.* **107**, 17304–17308 (2010). doi: [10.1073/pnas.1004640107](https://doi.org/10.1073/pnas.1004640107); pmid: [20823231](https://pubmed.ncbi.nlm.nih.gov/20823231/)
44. A. T. Satpathy, X. Wu, J. C. Albring, K. M. Murphy, Re(de)fining the dendritic cell lineage. *Nat. Immunol.* **13**, 1145–1154 (2012). doi: [10.1038/ni.2467](https://doi.org/10.1038/ni.2467); pmid: [23160217](https://pubmed.ncbi.nlm.nih.gov/23160217/)
45. G. J. Randolph, Macrophages in Marseille. *Immunity* **38**, 619–621 (2013). doi: [10.1016/j.immuni.2013.04.002](https://doi.org/10.1016/j.immuni.2013.04.002); pmid: [23601676](https://pubmed.ncbi.nlm.nih.gov/23601676/)
46. C. Jakubczik *et al.*, Minimal differentiation of classical monocytes as they survey steady-state tissues and transport antigen to lymph nodes. *Immunity* **39**, 599–610 (2013). doi: [10.1016/j.immuni.2013.08.007](https://doi.org/10.1016/j.immuni.2013.08.007); pmid: [24012416](https://pubmed.ncbi.nlm.nih.gov/24012416/)
47. J. Murphy, R. Summer, A. A. Wilson, D. N. Kotton, A. Fine, The prolonged life-span of alveolar macrophages. *Am. J. Respir. Cell Mol. Biol.* **38**, 380–385 (2008). doi: [10.1165/rcmb.2007-0224RC](https://doi.org/10.1165/rcmb.2007-0224RC); pmid: [18192503](https://pubmed.ncbi.nlm.nih.gov/18192503/)
48. E. L. Gautier *et al.*, Immunological Genome Consortium, Gene-expression profiles and transcriptional regulatory pathways that underlie the identity and diversity of mouse tissue macrophages. *Nat. Immunol.* **13**, 1118–1128 (2012). doi: [10.1038/ni.2419](https://doi.org/10.1038/ni.2419); pmid: [23023392](https://pubmed.ncbi.nlm.nih.gov/23023392/)
49. B. Ajami, J. L. Bennett, C. Krieger, K. M. McNagny, F. M. Rossi, Infiltrating monocytes trigger EAE progression, but do not contribute to the resident microglia pool. *Nat. Neurosci.* **14**, 1142–1149 (2011). doi: [10.1038/nn.2887](https://doi.org/10.1038/nn.2887); pmid: [21804537](https://pubmed.ncbi.nlm.nih.gov/21804537/)
50. L. C. Davies *et al.*, A quantifiable proliferative burst of tissue macrophages restores homeostatic macrophage populations after acute inflammation. *Eur. J. Immunol.* **41**, 2155–2164 (2011). doi: [10.1002/eji.201141817](https://doi.org/10.1002/eji.201141817); pmid: [21710478](https://pubmed.ncbi.nlm.nih.gov/21710478/)
51. A. Volkman, N. C. Chang, P. H. Strausbauch, P. S. Morahan, Differential effects of chronic monocyte depletion on macrophage populations. *Lab. Invest.* **49**, 291–298 (1983). pmid: [6887784](https://pubmed.ncbi.nlm.nih.gov/6887784/)
52. M. Merad *et al.*, Langerhans cells renew in the skin throughout life under steady-state conditions. *Nat. Immunol.* **3**, 1135–1141 (2002). doi: [10.1038/n852](https://doi.org/10.1038/n852); pmid: [12415265](https://pubmed.ncbi.nlm.nih.gov/12415265/)
53. C. Ghigo *et al.*, Multicolor fate mapping of Langerhans cell homeostasis. *J. Exp. Med.* **210**, 1657–1664 (2013). doi: [10.1084/jem.20130403](https://doi.org/10.1084/jem.20130403); pmid: [23940255](https://pubmed.ncbi.nlm.nih.gov/23940255/)
54. K. Kierdorf *et al.*, Microglia emerge from erythromyeloid precursors via Pu.1- and Irf8-dependent pathways. *Nat. Neurosci.* **16**, 273–280 (2013). doi: [10.1038/nn.3318](https://doi.org/10.1038/nn.3318); pmid: [23334579](https://pubmed.ncbi.nlm.nih.gov/23334579/)
55. D. W. Golde, L. A. Byers, T. N. Finley, Proliferative capacity of human alveolar macrophage. *Nature* **247**, 373–375 (1974). doi: [10.1038/247373a0](https://doi.org/10.1038/247373a0); pmid: [4817856](https://pubmed.ncbi.nlm.nih.gov/4817856/)
56. H. S. Lin, C. Kuhn, T. Kuo, Clonal growth of hamster free alveolar cells in soft agar. *J. Exp. Med.* **142**, 877–886 (1975). doi: [10.1084/jem.142.4.877](https://doi.org/10.1084/jem.142.4.877); pmid: [1080792](https://pubmed.ncbi.nlm.nih.gov/1080792/)
57. J. E. Coggle, J. D. Darling, The proliferation kinetics of pulmonary alveolar macrophages. *J. Leukoc. Biol.* **35**, 317–327 (1984). pmid: [6584524](https://pubmed.ncbi.nlm.nih.gov/6584524/)
58. C. G. Antoniadou *et al.*, Source and characterization of hepatic macrophages in acetaminophen-induced acute liver failure in humans. *Hepatology* **56**, 735–746 (2012). doi: [10.1002/hep.25657](https://doi.org/10.1002/hep.25657); pmid: [22334567](https://pubmed.ncbi.nlm.nih.gov/22334567/)
59. P. B. Bitterman, L. E. Saltzman, S. Adelberg, V. J. Ferrans, R. G. Crystal, Alveolar macrophage replication. One mechanism for the expansion of the mononuclear phagocyte population in the chronically inflamed lung. *J. Clin. Invest.* **74**, 460–469 (1984). doi: [10.1172/JCI111443](https://doi.org/10.1172/JCI111443); pmid: [6746904](https://pubmed.ncbi.nlm.nih.gov/6746904/)
60. N. M. Isbel, D. J. Nikolic-Paterson, P. A. Hill, J. Dowling, R. C. Atkins, Local macrophage proliferation correlates with increased renal M-CSF expression in human glomerulonephritis. *Nephrol. Dial. Transplant.* **16**, 1638–1647 (2001). doi: [10.1093/ndt/16.8.1638](https://doi.org/10.1093/ndt/16.8.1638); pmid: [11477167](https://pubmed.ncbi.nlm.nih.gov/11477167/)
61. E. Tagliani *et al.*, Coordinate regulation of tissue macrophage and dendritic cell population dynamics by CSF-1. *J. Exp. Med.* **208**, 1901–1916 (2011). doi: [10.1084/jem.20110866](https://doi.org/10.1084/jem.20110866); pmid: [21825019](https://pubmed.ncbi.nlm.nih.gov/21825019/)
62. L. C. Davies *et al.*, Distinct bone marrow-derived and tissue-resident macrophage lineages proliferate at key stages during inflammation. *Nat. Commun.* **4**, 1886 (2013). doi: [10.1038/ncomms2877](https://doi.org/10.1038/ncomms2877); pmid: [23695680](https://pubmed.ncbi.nlm.nih.gov/23695680/)
63. J. E. Allen, R. M. Maizels, Diversity and dialogue in immunity to helminths. *Nat. Rev. Immunol.* **11**, 375–388 (2011). doi: [10.1038/nri2992](https://doi.org/10.1038/nri2992); pmid: [21610741](https://pubmed.ncbi.nlm.nih.gov/21610741/)

64. S. J. Jenkins *et al.*, IL-4 directly signals tissue-resident macrophages to proliferate beyond homeostatic levels controlled by CSF-1. *J. Exp. Med.* **210**, 2477–2491 (2013). doi: [10.1084/jem.20121999](#); pmid: [24101381](#)
65. D. A. Hume, K. P. MacDonald, Therapeutic applications of macrophage colony-stimulating factor-1 (CSF-1) and antagonists of CSF-1 receptor (CSF-1R) signaling. *Blood* **119**, 1810–1820 (2012). doi: [10.1182/blood-2011-09-379214](#); pmid: [22186992](#)
66. M. Greter *et al.*, Stroma-derived interleukin-34 controls the development and maintenance of Langerhans cells and the maintenance of microglia. *Immunity* **37**, 1050–1060 (2012). doi: [10.1016/j.immuni.2012.11.001](#); pmid: [23177320](#)
67. Y. Wang *et al.*, IL-34 is a tissue-restricted ligand of CSF1R required for the development of Langerhans cells and microglia. *Nat. Immunol.* **13**, 753–760 (2012). doi: [10.1038/ni.2360](#); pmid: [22729249](#)
68. Y. Shibata *et al.*, GM-CSF regulates alveolar macrophage differentiation and innate immunity in the lung through PU.1. *Immunity* **15**, 557–567 (2001). doi: [10.1016/S1074-7613\(01\)00218-7](#); pmid: [11672538](#)
69. H. J. Koenen *et al.*, Effect of intraperitoneal administration of granulocyte/macrophage-colony-stimulating factor in rats on omental milky-spot composition and tumoricidal activity in vivo and in vitro. *Cancer Immunol. Immunother.* **42**, 310–316 (1996). doi: [10.1007/s002620050288](#); pmid: [8706054](#)
70. G. Fejer *et al.*, Nontransformed, GM-CSF-dependent macrophage lines are a unique model to study tissue macrophage functions. *Proc. Natl. Acad. Sci. U.S.A.* **110**, E2191–E2198 (2013). doi: [10.1073/pnas.1302877110](#); pmid: [23708119](#)
71. M. D. Jose, Y. Le Meur, R. C. Atkins, S. J. Chadban, Blockade of macrophage colony-stimulating factor reduces macrophage proliferation and accumulation in renal allograft rejection. *Am. J. Transplant.* **3**, 294–300 (2003). doi: [10.1034/j.1600-6143.2003.00068.x](#); pmid: [12614284](#)
72. J. D. Milner *et al.*, Sustained IL-4 exposure leads to a novel pathway for hemophagocytosis, inflammation, and tissue macrophage accumulation. *Blood* **116**, 2476–2483 (2010). doi: [10.1182/blood-2009-11-255174](#); pmid: [20570861](#)
73. P. Loke *et al.*, Alternative activation is an innate response to injury that requires CD4⁺ T cells to be sustained during chronic infection. *J. Immunol.* **179**, 3926–3936 (2007). pmid: [17785830](#)
74. C. L. Karp, P. J. Murray, Non-canonical alternatives: What a macrophage is 4. *J. Exp. Med.* **209**, 427–431 (2012). doi: [10.1084/jem.20120295](#); pmid: [22412174](#)
75. D. Rückert *et al.*, Induction of IL-4R α -dependent microRNAs identifies PI3K/Akt signaling as essential for IL-4-driven murine macrophage proliferation in vivo. *Blood* **120**, 2307–2316 (2012). doi: [10.1182/blood-2012-02-408252](#); pmid: [22855601](#)
76. T. Lawrence, G. Natoli, Transcriptional regulation of macrophage polarization: Enabling diversity with identity. *Nat. Rev. Immunol.* **11**, 750–761 (2011). doi: [10.1038/nri3088](#); pmid: [22025054](#)
77. F. J. Pixley, E. R. Stanley, CSF-1 regulation of the wandering macrophage: Complexity in action. *Trends Cell Biol.* **14**, 628–638 (2004). doi: [10.1016/j.tcb.2004.09.016](#); pmid: [15519852](#)
78. L. Arpa, A. F. Valledor, J. Lloberas, A. Celada, IL-4 blocks M-CSF-dependent macrophage proliferation by inducing p21^{Waf1} in a STAT6-dependent way. *Eur. J. Immunol.* **39**, 514–526 (2009). doi: [10.1002/eji.200838283](#); pmid: [19130475](#)
79. M. F. Roussel, Signal transduction by the macrophage-colony-stimulating factor receptor (CSF-1R). *J. Cell Sci. Suppl.* **1994** (suppl. 18), 105–108 (1994). doi: [10.1242/jcs.1994.Supplement_18.15](#); pmid: [7883784](#)
80. G. W. Klappacher *et al.*, An induced Ets repressor complex regulates growth arrest during terminal macrophage differentiation. *Cell* **109**, 169–180 (2002). doi: [10.1016/S0092-8674\(02\)00714-6](#); pmid: [12007404](#)
81. S. J. Langer, D. M. Bortner, M. F. Roussel, C. J. Sherr, M. C. Ostrowski, Mitogenic signaling by colony-stimulating factor 1 and ras is suppressed by the ets-2 DNA-binding domain and restored by myc overexpression. *Mol. Cell. Biol.* **12**, 5355–5362 (1992). pmid: [1448070](#)
82. M. F. Roussel, J. N. Davis, J. L. Cleveland, J. Ghysdael, S. W. Hiebert, Dual control of myc expression through a single DNA binding site targeted by ets family proteins and E2F-1. *Oncogene* **9**, 405–415 (1994). pmid: [8290253](#)
83. J. Sullivan, B. Feeley, J. Guerra, L. M. Boxer, Identification of the major positive regulators of *c-myc* expression in hematopoietic cells of different lineages. *J. Biol. Chem.* **272**, 1943–1949 (1997). doi: [10.1074/jbc.272.3.1943](#); pmid: [8999884](#)
84. S. P. Hedge, A. Kumar, C. Kurschner, L. H. Shapiro, c-Maf interacts with c-Myb to regulate transcription of an early myeloid gene during differentiation. *Mol. Cell. Biol.* **18**, 2729–2737 (1998). pmid: [9566892](#)
85. S. Tillmanns *et al.*, SUMO modification regulates MafB-driven macrophage differentiation by enabling Myb-dependent transcriptional repression. *Mol. Cell. Biol.* **27**, 5554–5564 (2007). doi: [10.1128/MCB.01811-06](#); pmid: [17548468](#)
86. M. H. Sieweke, H. Tekotte, J. Frampton, T. Graf, MafB is an interaction partner and repressor of Ets-1 that inhibits erythroid differentiation. *Cell* **85**, 49–60 (1996). doi: [10.1016/S0092-8674\(00\)81081-8](#); pmid: [8620536](#)
87. M. Cheng, D. Wang, M. F. Roussel, Expression of c-Myc in response to colony-stimulating factor-1 requires mitogen-activated protein kinase kinase-1. *J. Biol. Chem.* **274**, 6553–6558 (1999). doi: [10.1074/jbc.274.10.6553](#); pmid: [10037749](#)
88. S. He, D. Nakada, S. J. Morrison, Mechanisms of stem cell self-renewal. *Annu. Rev. Cell Dev. Biol.* **25**, 377–406 (2009). doi: [10.1146/annurev.cellbio.042308.113248](#); pmid: [19575646](#)
89. N. Fausto, J. S. Campbell, The role of hepatocytes and oval cells in liver regeneration and repopulation. *Mech. Dev.* **120**, 117–130 (2003). doi: [10.1016/S0925-4773\(02\)00338-6](#); pmid: [12490302](#)
90. K. S. Schluns, L. Lefrançois, Cytokine control of memory T-cell development and survival. *Nat. Rev. Immunol.* **3**, 269–279 (2003). doi: [10.1038/nri1052](#); pmid: [12669018](#)
91. P. Cartwright *et al.*, LIF/STAT3 controls ES cell self-renewal and pluripotency by a Myc-dependent mechanism. *Development* **132**, 885–896 (2005). doi: [10.1242/dev.01670](#); pmid: [15673569](#)
92. J. Jiang *et al.*, A core Klf circuitry regulates self-renewal of embryonic stem cells. *Nat. Cell Biol.* **10**, 353–360 (2008). doi: [10.1038/ncb1698](#); pmid: [18264089](#)
93. S. Yamanaka, Strategies and new developments in the generation of patient-specific pluripotent stem cells. *Cell Stem Cell* **1**, 39–49 (2007). doi: [10.1016/j.stem.2007.05.012](#); pmid: [18371333](#)
94. W. R. Baumbach, E. J. Keath, M. D. Cole, A mouse c-myc retrovirus transforms established fibroblast lines in vitro and induces monocyte-macrophage tumors in vivo. *J. Virol.* **59**, 276–283 (1986). pmid: [3016297](#)
95. B. D. Rowland, D. S. Peepler, KLF4, p21 and context-dependent opposing forces in cancer. *Nat. Rev. Cancer* **6**, 11–23 (2006). doi: [10.1038/nrc1780](#); pmid: [16372018](#)

Acknowledgments: M.H.S. was supported by the Agence Nationale de la Recherche (ANR-11-BSV3-0026) and is a Fondation pour la Recherche Médicale (DEq. 20071210559 and DEq. 20110421320) and INSERM-Helmholtz group leader. J.A. received funding from the Medical Research Council UK (MR/K01207X1 and MR/J001929/1), the Wellcome Trust, and European Union FP7 Health-2009-4.3.1-1, 242131 (E PIAF).

10.1126/science.1242974

Evidence for High-Energy Extraterrestrial Neutrinos at the IceCube Detector

IceCube Collaboration*

READ THE FULL ARTICLE ONLINE

<http://dx.doi.org/10.1126/science.1242856>



Cite this article as IceCube Collaboration, *Science* **342**, 1242856 (2013). DOI: 10.1126/science.1242856

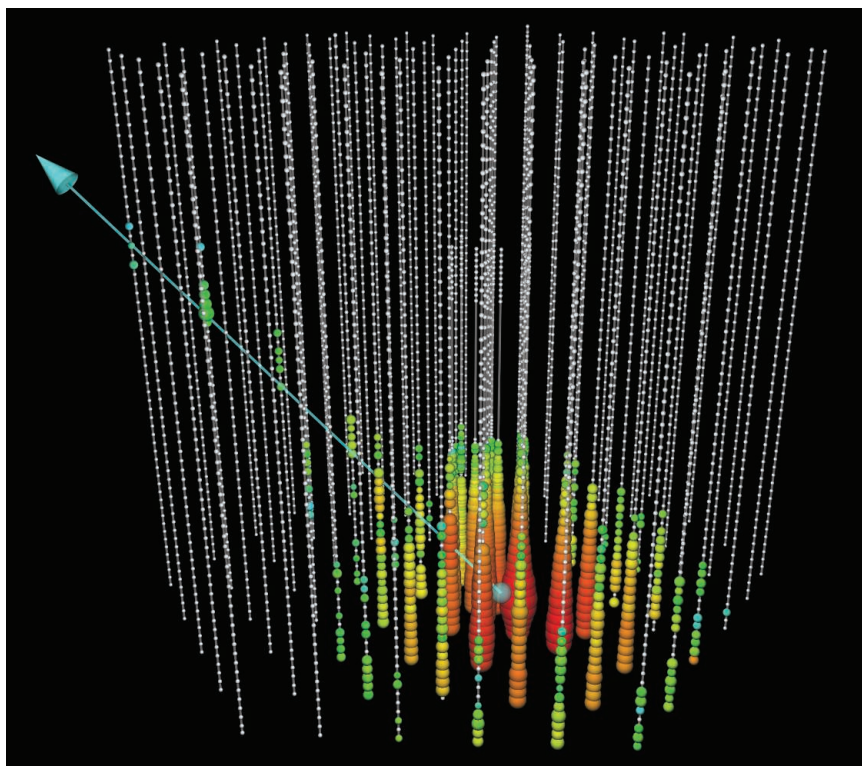
Introduction: Neutrino observations are a unique probe of the universe's highest-energy phenomena: Neutrinos are able to escape from dense astrophysical environments that photons cannot and are unambiguous tracers of cosmic ray acceleration. As protons and nuclei are accelerated, they interact with gas and background light near the source to produce subatomic particles such as charged pions and kaons, which then decay, emitting neutrinos. We report on results of an all-sky search for these neutrinos at energies above 30 TeV in the cubic kilometer Antarctic IceCube observatory between May 2010 and May 2012.

Methods: We have isolated a sample of neutrinos by rejecting background muons from cosmic ray showers in the atmosphere, selecting only those neutrino candidates that are first observed in the detector interior rather than on the detector boundary. This search is primarily sensitive to neutrinos from all directions above 60 TeV, at which the lower-energy background atmospheric neutrinos become rare, with some sensitivity down to energies of 30 TeV. Penetrating muon backgrounds were evaluated using an in-data control sample, with atmospheric neutrino predictions based on theoretical modeling and extrapolation from previous lower-energy measurements.

Results: We observed 28 neutrino candidate events (two previously reported), substantially more than the $10.6^{+5.0}_{-3.6}$ expected from atmospheric backgrounds, and ranging in energy from 30 to 1200 TeV. With the current level of statistics, we did not observe significant clustering of these events in time or space, preventing the identification of their sources at this time.

Discussion: The data contain a mixture of neutrino flavors compatible with flavor equipartition, originate primarily from the Southern Hemisphere where high-energy neutrinos are not absorbed by Earth, and have a hard energy spectrum compatible with that expected from cosmic ray accelerators. Within our present knowledge, the directions, energies, and topologies of these events are not compatible with expectations for terrestrial processes, deviating at the 4σ level from standard assumptions for the atmospheric background. These properties, in particular the north-south asymmetry, generically disfavor any purely atmospheric explanation for the data. Although not compatible with an atmospheric explanation, the data do match expectations for an origin in unidentified high-energy galactic or extragalactic neutrino accelerators.

A 250 TeV neutrino interaction in IceCube. At the neutrino interaction point (bottom), a large particle shower is visible, with a muon produced in the interaction leaving up and to the left. The direction of the muon indicates the direction of the original neutrino.



FIGURES IN THE FULL ARTICLE

Fig. 1. Drawing of the IceCube array.

Fig. 2. Distribution of best-fit deposited energies and declinations.

Fig. 3. Coordinates of the first detected light from each event in the final sample.

Fig. 4. Distributions of the deposited energies and declination angles of the observed events compared to model predictions.

Fig. 5. Sky map in equatorial coordinates of the TS value from the maximum likelihood point source analysis.

Fig. 6. Distribution of deposited PMT charges (Q_{tot}).

Fig. 7. Neutrino effective area and volume.

SUPPLEMENTARY MATERIALS

Materials and Methods

Event Displays 1 to 28

Neutrino Effective Areas

*The list of author affiliations is available in the full article online.

Corresponding authors: C. Kopfer (ckopfer@icecube.wisc.edu); N. Kurahashi (naoko@icecube.wisc.edu); N. Whitehorn (nwhitehorn@icecube.wisc.edu)

Evidence for High-Energy Extraterrestrial Neutrinos at the IceCube Detector

IceCube Collaboration*

We report on results of an all-sky search for high-energy neutrino events interacting within the IceCube neutrino detector conducted between May 2010 and May 2012. The search follows up on the previous detection of two PeV neutrino events, with improved sensitivity and extended energy coverage down to about 30 TeV. Twenty-six additional events were observed, substantially more than expected from atmospheric backgrounds. Combined, both searches reject a purely atmospheric origin for the 28 events at the 4σ level. These 28 events, which include the highest energy neutrinos ever observed, have flavors, directions, and energies inconsistent with those expected from the atmospheric muon and neutrino backgrounds. These properties are, however, consistent with generic predictions for an additional component of extraterrestrial origin.

High-energy neutrino observations can provide insight into the long-standing problem of the origins and acceleration mechanisms of high-energy cosmic rays. As cosmic ray protons and nuclei are accelerated, they interact with gas and background light to produce charged pions and kaons, which then decay, emitting neutrinos with energies proportional to the energies of the high-energy protons that produced them. These neutrinos can be detected on Earth in large underground detectors by the production of secondary leptons and hadronic showers when they interact with the detector material. IceCube, a large-volume Cherenkov detector (*1*) made of 5160 photomultipliers (PMTs) at depths between 1450 and 2450 m in natural Antarctic ice (Fig. 1), has been designed to detect these neutrinos at TeV-PeV energies. Recently, the Fermi collaboration presented evidence for acceleration of low-energy (GeV) cosmic ray protons in supernova remnants (*2*); neutrino observations with IceCube would probe sources of cosmic rays at far higher energies.

A recent IceCube search for neutrinos of EeV (10^6 TeV) energy found two events at energies of 1 PeV (10^3 TeV), above what is generally expected from atmospheric backgrounds and a possible hint of an extraterrestrial source (*3*). Although that analysis had some sensitivity to neutrino events of all flavors above 1 PeV, it was most sensitive to ν_μ events above 10 PeV from the region around the horizon, above which the energy threshold increased sharply to 100 PeV. As a result, it had only limited sensitivity to the type of events found, which were typical of either ν_e or neutral current events and at the bottom of the detectable energy range, preventing a detailed understanding of the population from which they arose and an answer to the question of their origin.

Here, we present a follow-up analysis designed to characterize the flux responsible for these

events by conducting an exploratory search for neutrinos at lower energies with interaction vertices well contained within the detector volume, discarding events containing muon tracks originating outside of IceCube (Fig. 1). This event selection (see Materials and Methods) allows the resulting search to have approximately equal sensitivity to neutrinos of all flavors and from all directions. We obtained nearly full efficiency for interacting neutrinos above several hundred TeV, with some sensitivity extending to neutrino energies as low as 30 TeV (see Materials and Methods). The data-taking period is shared with the earlier

high-energy analysis: Data shown were taken during the first season running with the completed IceCube array (86 strings, between May 2011 and May 2012) and the preceding construction season (79 strings, between May 2010 and May 2011), with a total combined live time of 662 days.

Results

In the 2-year data set, 28 events with in-detector deposited energies between 30 and 1200 TeV were observed (Fig. 2 and Table 1) on an expected background of $10.6^{+5.0}_{-3.6}$ events from atmospheric muons and neutrinos (see Materials and Methods). The two most energetic of these were the previously reported PeV events (*3*). Seven events contained clearly identifiable muon tracks, whereas the remaining 21 were showerlike, consistent with neutrino interactions other than ν_μ charged current. Events containing muon tracks in general have better angular resolution, typically of better than 1 degree (*4*), compared to the 10 to 15 degrees typical of events without visible muons (see Materials and Methods). Four of the low-energy tracklike events started near the detector boundary and were down-going, consistent with the properties of the expected 6.0 ± 3.4 background atmospheric muons, as measured from a control sample of penetrating muons in data. One of these—the only such event in the sample—had hits in the IceTop surface air shower array compatible with its arrival time and direction in IceCube (event 28). The points at which the remaining events were first observed were uniformly distributed throughout the detector (Fig. 3). This is consistent with expectations for neutrino

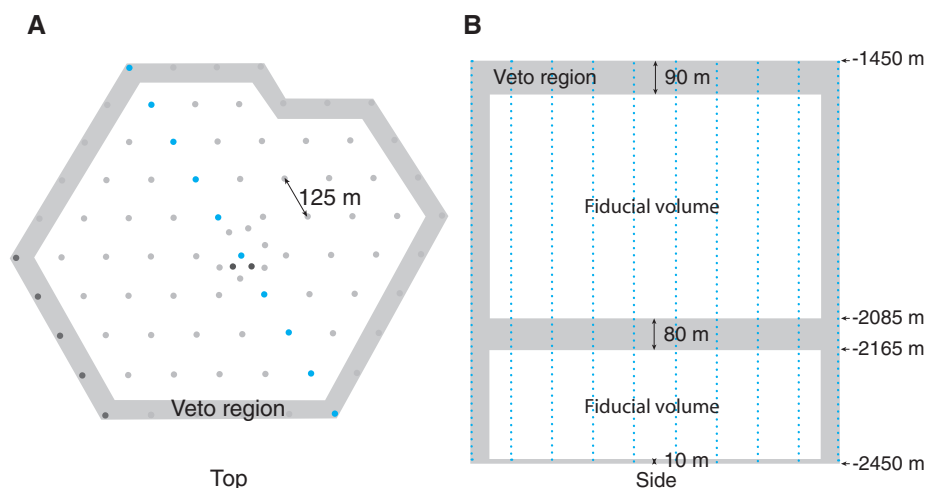


Fig. 1. Drawing of the IceCube array. Results are from the complete pictured detector for 2011 to 2012 and from a partial detector missing the dark gray strings in the bottom left corner for the 2010 to 2011 season. (A and B) The side view (B) shows a cross section of the detector indicated in the top view (A) in blue. Events producing first light in the veto region (shaded area) were discarded as entering tracks (usually from cosmic ray muons entering the detector). Most background events are nearly vertical, requiring a thick veto cap at the top of the detector. The shaded region in the middle contains ice of high dust concentration (*24*). Because of the high degree of light absorption in this region, near horizontal events could have entered here without being tagged at the sides of the detector without a dedicated tagging region.

*Full author list after Acknowledgments.

events and inconsistent with backgrounds from penetrating muons or with detector artifacts, which would have been expected to trace the locations of either the fiducial volume boundary or the positions of the instrumentation.

As part of our blind analysis, we tested a pre-defined fixed atmospheric-only neutrino flux

model (5), including a benchmark charm component (6), reevaluated using current measurements of the cosmic ray spectrum in this energy range (7, 8). This adds an additional 1.5 charm neutrinos to our mean background estimate and predicts, on average, 6.1 (π/K and charm) background neutrinos on top of the 6.0 ± 3.4 back-

ground muon events. Significance was evaluated on the basis of the number of events, the total collected PMT charge of each, and the events' reconstructed energies and directions (see Materials and Methods). Our procedure does not allow us to separately incorporate uncertainties on the various background components. To nevertheless obtain an indication of the range of possible significances, we calculated values relative to background-only hypotheses with charm at the level called "standard" in (6) as a benchmark flux as well as at the level of our current 90% confidence level (CL) experimental bounds (8) (corresponding to 3.8 times standard). To prevent possible confirmation bias, we split the data set into two samples. For the 26 new events reported here, using the benchmark flux, we obtain a significance of 3.3σ (one-sided). Combined using Fisher's method with the 2.8σ observation of the earlier analysis where the two highest energy events were originally reported (3), and which uses the same benchmark atmospheric neutrino flux model, we obtain a final significance for the entire data set of 28 events of 4.1σ . The same calculation performed a posteriori on all 28 events gives 4.8σ . These two final significances would be reduced to

Fig. 2. Distribution of best-fit deposited energies and declinations.

Seven of the events contain muons (crosses) with an angular resolution of about 1° , whereas the remainder are either electromagnetic (EM) or hadronic showers (filled circles) with an energy-dependent resolution of about 15° . Error bars are 68% confidence intervals including both statistical and systematic uncertainties. Energies shown are the energy deposited in the detector, assuming that all light emission is from electromagnetic showers. For ν_e charged-current events, this equals the neutrino energy; otherwise, it is a lower limit on the neutrino energy. The gap in E_{dep} between 300 TeV and 1 PeV does not appear to be significant: Gaps of this size or larger appear in 28% of realizations of the best-fit continuous power-law flux.

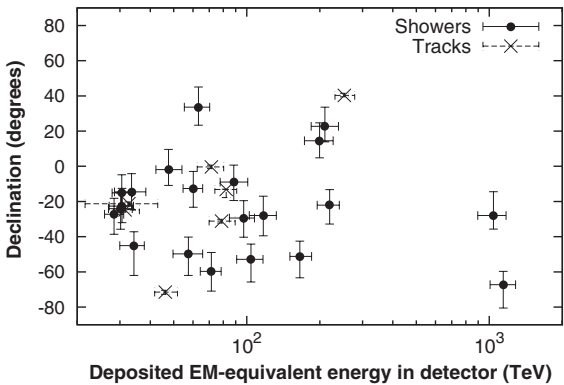


Table 1. Properties of the 28 events. Shown are the deposited electromagnetic-equivalent energy (the energy deposited by the events in IceCube assuming all light was made in electromagnetic showers), as well as the arrival time and direction of each event and its topology (track- or showerlike). The energy shown is equal to the neutrino energy for ν_e charged-current events, within experimental uncertainties, and is otherwise a lower limit on the neutrino energy because

of exiting muons or neutrinos. Errors on energy and the angle include both statistical and systematic effects. Systematic uncertainties on directions for showerlike events were determined on an individual basis; track systematic uncertainties here are equal to 1° , which is an upper limit from studies of the cosmic ray shadow of the moon (4). Additional per-event information, including event displays, can be found in the supplementary materials.

ID	Deposited energy (TeV)	Time (modified Julian date)	Declination (degrees)	Right ascension (degrees)	Median angular error (degrees)	Event type
1	$47.6^{+6.5}_{-5.4}$	55,351	-1.8	35.2	16.3	Shower
2	117^{+15}_{-15}	55,351	-28.0	282.6	25.4	Shower
3	$78.7^{+10.8}_{-8.7}$	55,451	-31.2	127.9	≤ 1.4	Track
4	165^{+20}_{-15}	55,477	-51.2	169.5	7.1	Shower
5	$71.4^{+9.0}_{-9.0}$	55,513	-0.4	110.6	≤ 1.2	Track
6	$28.4^{+2.7}_{-2.5}$	55,568	-27.2	133.9	9.8	Shower
7	$34.3^{+3.5}_{-4.3}$	55,571	-45.1	15.6	24.1	Shower
8	$32.6^{+10.3}_{-11.1}$	55,609	-21.2	182.4	≤ 1.3	Track
9	$63.2^{+7.1}_{-8.0}$	55,686	33.6	151.3	16.5	Shower
10	$97.2^{+10.4}_{-12.4}$	55,695	-29.4	5.0	8.1	Shower
11	$88.4^{+12.5}_{-10.7}$	55,715	-8.9	155.3	16.7	Shower
12	104^{+13}_{-13}	55,739	-52.8	296.1	9.8	Shower
13	253^{+26}_{-22}	55,756	40.3	67.9	≤ 1.2	Track
14	1041^{+132}_{-144}	55,783	-27.9	265.6	13.2	Shower
15	$57.5^{+8.3}_{-7.8}$	55,783	-49.7	287.3	19.7	Shower
16	$30.6^{+3.6}_{-3.5}$	55,799	-22.6	192.1	19.4	Shower
17	200^{+27}_{-27}	55,800	14.5	247.4	11.6	Shower
18	$31.5^{+4.6}_{-3.3}$	55,924	-24.8	345.6	≤ 1.3	Track
19	$71.5^{+7.0}_{-7.2}$	55,926	-59.7	76.9	9.7	Shower
20	1141^{+143}_{-133}	55,929	-67.2	38.3	10.7	Shower
21	$30.2^{+3.5}_{-3.3}$	55,937	-24.0	9.0	20.9	Shower
22	220^{+21}_{-24}	55,942	-22.1	293.7	12.1	Shower
23	$82.2^{+8.6}_{-8.4}$	55,950	-13.2	208.7	≤ 1.9	Track
24	$30.5^{+3.2}_{-2.6}$	55,951	-15.1	282.2	15.5	Shower
25	$33.5^{+4.9}_{-5.0}$	55,967	-14.5	286.0	46.3	Shower
26	210^{+29}_{-26}	55,979	22.7	143.4	11.8	Shower
27	$60.2^{+5.6}_{-5.6}$	56,009	-12.6	121.7	6.6	Shower
28	$46.1^{+5.7}_{-4.4}$	56,049	-71.5	164.8	≤ 1.3	Track

3.6σ and 4.5σ , respectively, using charm at the level of our current 90% CL experimental bound.

Discussion

Although there is some uncertainty in the expected atmospheric background rates, in particular for the contribution from charmed meson decays, the energy spectrum, zenith distribution, and shower to muon track ratio of the observed events strongly constrain the possibility that our events are entirely of atmospheric origin. Almost all of the observed excess is in showers rather than muon tracks, ruling out an increase in penetrating muon background to the level required. Atmo-

spheric neutrinos are a poor fit to the data for a variety of reasons. The observed events are much higher in energy, with a harder spectrum (Fig. 4) than expected from an extrapolation of the well-measured π/K atmospheric background at lower energies (8–10): Nine had reconstructed deposited energies above 100 TeV, with two events above 1 PeV, relative to an expected background from π/K atmospheric neutrinos of about one event above 100 TeV. Raising the normalization of this flux both violates previous limits and, because of ν_μ bias in π and K decay, predicts too many muon tracks in our data (two-thirds of tracks versus one-fourth observed).

Another possibility is that the high-energy events result from charmed meson production in air showers (6, 11). These produce higher-energy events with equal parts ν_e and ν_μ , matching our observed muon track fraction reasonably well. However, our event rates are substantially higher than even optimistic models (11) and the energy spectrum from charm production is too soft to explain the data. Increasing charm production to the level required to explain our observations violates existing experimental bounds (8). Because atmospheric neutrinos produced by any mechanism are made in cosmic ray air showers, down-going atmospheric neutrinos from the southern sky will, in general, be accompanied into IceCube by muons produced in the same parent air shower. These accompanying muons will trigger our muon veto, removing most of these events from the sample and biasing atmospheric neutrinos to the Northern Hemisphere. Most of our events, however, arrive from the south. This places a strong model-independent constraint on any atmospheric neutrino production mechanism as an explanation for our data.

By comparison, a neutrino flux produced in extraterrestrial sources would, like our data, be heavily biased toward showers because neutrino oscillations over astronomical baselines tend to equalize neutrino flavors (12, 13). An equal-flavor E^{-2} neutrino flux, for example, would be expected to produce only one-fifth of track events (see

Fig. 3. Coordinates of the first detected light from each event in the final sample. Penetrating muon events are first detected predominantly at the detector boundaries (top and right sides), where they first make light after crossing the veto layer. Neutrino events should interact uniformly throughout the approximately cylindrical detector volume, forming a uniform distribution in (r^2, z) , with the exception of interactions in the less transparent ice region marked “Dust layer,” which is treated as part of the detector boundary for purposes of our event selection. The observed events are consistent with a uniform distribution.

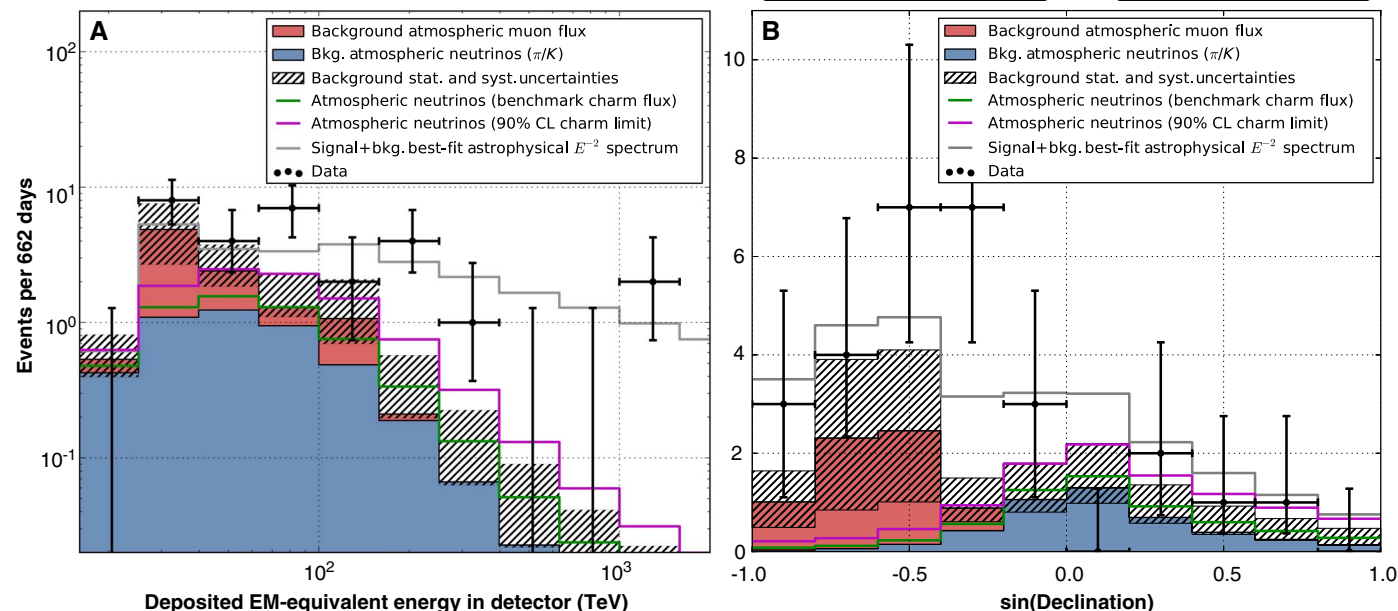
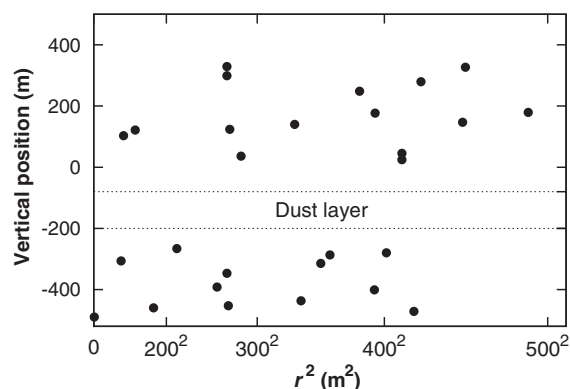


Fig. 4. Distributions of the deposited energies and declination angles of the observed events compared to model predictions. (A and B) Zenith angle entries for data (B) are the best-fit zenith position for each of the 28 events; a small number of events (Table 1) have zenith uncertainties larger than the bin widths in this figure. Energies plotted (A) are reconstructed in-detector visible energies, which are lower limits on the neutrino energy. Note that deposited energy spectra are always harder than the spectrum of the neutrinos that produced them because of the neutrino cross section increasing with energy. The expected rate of atmospheric neutrinos is shown in blue, with

atmospheric muons in red. The green line shows our benchmark atmospheric neutrino flux (see the text), and the magenta line shows the experimental 90% bound. Because of a lack of statistics from data far above our cut threshold, the shape of the distributions from muons in this figure has been determined using Monte Carlo simulations with total rate normalized to the estimate obtained from our in-data control sample. Combined statistical and systematic uncertainties on the sum of backgrounds are indicated with a hatched area. The gray line shows the best-fit E^{-2} astrophysical spectrum with a per-flavor normalization ($1:1:1$) of $E^2\Phi_\nu(E) = 1.2 \times 10^{-8} \text{ GeV cm}^{-2} \text{ s}^{-1} \text{ sr}^{-1}$.

Materials and Methods). The observed zenith distribution is also typical of such a flux: As a result of absorption in Earth above tens of TeV energy, most events (about 60%, depending on the energy spectrum) from even an isotropic high-energy extraterrestrial population would be expected to appear in the Southern Hemisphere. Although the zenith distribution is well explained (Fig. 4) by an isotropic flux, a slight southern excess remains, which could be explained either as a statistical fluctuation or by a source population that is either relatively small or unevenly distributed through the sky.

This discussion can be quantified by a global fit of the data to a combination of the π/K atmospheric neutrino background, atmospheric neutrinos from charmed meson decays, and an isotropic equal-flavor extraterrestrial power-law flux. With the normalizations of all components free to float, this model was fit to the two-dimensional deposited energy and zenith distribution of the data (Fig. 2) in the range of $60 \text{ TeV} < E_{\text{dep}} < 2 \text{ PeV}$, above most of the expected background (Fig. 4). The data are well described in this energy range by an E^{-2} neutrino spectrum with a per-flavor normalization of $E^2\Phi(E) = (1.2 \pm 0.4) \times 10^{-8} \text{ GeV cm}^{-2} \text{ s}^{-1} \text{ sr}^{-1}$. Although it is difficult to substantively constrain the shape of the spectrum with our current limited statistics, a flux at this level would have been expected to generate an additional three to six events in the 2 to 10 PeV range; the lack of such events in the sample may indicate either a softer spectrum (the best fit is $E^{-2.2 \pm 0.4}$) or the presence of a break or cutoff at PeV energies. When limited to only atmospheric neutrinos, the best fit to the data would require a charm flux 4.5 times larger than the current experimental 90% CL upper bounds (8) and even then is disfavored at 4σ with respect to a fit allowing an extraterrestrial contribution.

Search for Neutrino Sources

To search for spatial clustering, indicating possible neutrino sources, we conducted a maximum likelihood point source analysis (14). At each point in the sky, we tested a point source hypothesis based on full-sky uncertainty maps for each event obtained from the reconstruction. This yields a sky map of test statistic values [$\text{TS} = 2\log(L/L_0)$, where L is the maximized likelihood and L_0 is the likelihood under the null hypothesis], which reflects any excess concentration of events relative to a flat background distribution (Fig. 5). To account for trials due to searching the whole sky, we estimate the significance of the highest TS observed by performing the same analysis on the data with the right ascension of the events randomized. The final significance is then the fraction of these randomized maps that have a TS value anywhere in the sky as high or higher than that observed in data. The chance probability calculated this way is independent of Monte Carlo simulation. Therefore, the significance obtained is against the hypothesis that all events in this sample are uniformly distributed in right ascen-

sion, rather than the significance of a cluster of events above predicted backgrounds. Note that because muon tracks have much smaller angular uncertainties than showers, their presence can skew the highest TS values and overshadow clusters of shower events. To correct for this effect, and because muon events are more likely to be atmospheric background, we repeated every clustering analysis described here twice: once with the full 28 events and once with only the 21 shower events.

When using all events, the likelihood map reveals no significant clustering compared to randomized maps. For the shower events, the coordinates with the highest TS are at right ascension = 281° , declination = -23° (galactic longitude $l = +12^\circ$, latitude $b = -9^\circ$). Five events, including the second highest energy event in the sample, contribute to the main part of the excess with two others nearby. The fraction of randomized data sets that yield a similar or higher TS at this exact spot is 0.2%. (At the exact location of the galactic center, the fraction is 5.4%.) The final significance, estimated as the fraction of randomized maps with a similar or higher TS anywhere in the sky, is 8%. This degree of clustering may be compatible with a source or sources in the galactic center region, but the poor angular resolution for showers and the wide distribution of the events do not allow the identification of any sources at this time.

Two other spatial clustering analyses were defined a priori. We performed a galactic plane correlation study using the full directional reconstruction uncertainty for each event to define the degree of overlap with the plane. The plane width was chosen to be $\pm 2.5^\circ$ on the basis of TeV gamma-ray observations (15). A multicluster search using the sum of log-likelihood values at every

local maximum in the likelihood map was also conducted. Neither of these analyses yielded significant results.

In addition to clustering of events in space, we performed two tests for clustering of events in time that calculate significances by comparing the actual arrival times to event times drawn from a random uniform distribution throughout the live time. Because many sources (16–18) are expected to produce neutrinos in bursts, identification of such a time cluster could allow association with a source without reference to the limited angular resolution of most of the observed neutrinos. When using all events, no significant time cluster was observed. Furthermore, each spatial cluster in Fig. 5 containing more than one event was tested individually for evidence of time clustering. Of the eight regions tested, the most significant was a pair that includes the highest energy shower in the sample, but was still compatible with random fluctuations. The five shower events of the densest cluster show no significant overall time clustering.

Materials and Methods

Event Selection

Backgrounds for cosmic neutrino searches arise entirely from interactions of cosmic rays in Earth's atmosphere. These produce secondary muons that penetrate into underground neutrino detectors from above, as well as atmospheric neutrinos that reach the detector from all directions because of the low neutrino cross section, which allows them to penetrate Earth from the opposite hemisphere. These particles are produced in the decays of secondary π and K mesons; at high energies, a flux from the prompt decay of charmed mesons

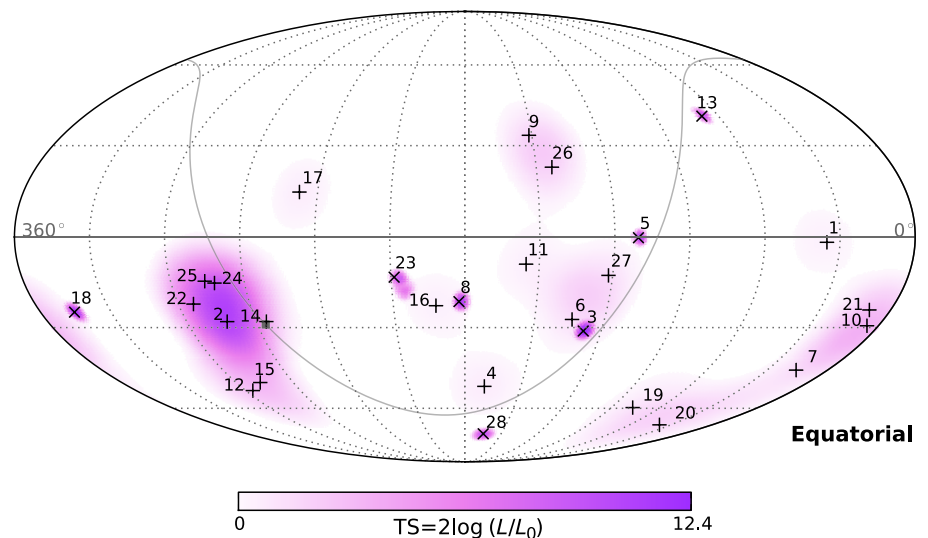


Fig. 5. Sky map in equatorial coordinates of the TS value from the maximum likelihood point source analysis. The most significant cluster consists of five events—all showers and including the second highest energy event in the sample—with a final significance of 8%. This is not sufficient to identify any neutrino sources from the clustering study. The galactic plane is shown as a curved gray line with the galactic center at the bottom left denoted by a filled gray square. Best-fit locations of individual events (listed in Table 1) are indicated with vertical crosses (+) for showers and angled crosses (x) for muon tracks.

(19) has been anticipated, although not yet observed. Cosmic ray muons are the dominant background in IceCube because of their high rate of 3 kHz. These can be removed from the sample either by using only up-going events, by limiting searches to events at very high energies (above ~ 1 PeV) (20, 21), or, as here, by requiring an observation of the neutrino interaction vertex using the detector boundary to detect and veto entering muon tracks.

Neutrino candidates were selected by finding events that originated within the detector interior. Included were those events that produced their first light within the fiducial volume (Fig. 1) and were of sufficiently high energy such that an entering muon track would have been reliably identified if present. In particular, we required that each event have fewer than three of its first 250 observed photoelectrons detected in the veto region. In addition, we required that the event produce at least 6000 photoelectrons overall to

ensure that statistical fluctuations in the light yield were low enough for entering muons to reliably produce light in the veto region. This event selection rejects 99.999% of the muon background above 6000 photoelectrons (Fig. 6) while retaining nearly all neutrino events interacting within the fiducial volume at energies above a few hundred TeV (Fig. 7). This selection is largely independent of neutrino flavor, event topology, or arrival direction. It also removes 70% of atmospheric neutrinos (22) in the Southern Hemisphere, where atmospheric neutrinos are usually accompanied into the detector by muons produced in the same parent air shower. To prevent confirmation bias, we conducted a blind analysis designed on a subsample of 10% of the full data set.

Event Reconstruction

Neutrino interactions in IceCube have two primary topologies: showers and muon tracks. Showers are created by secondary leptons and hadronic

fragmentation in ν_e and ν_τ charged-current interactions and by neutral-current interactions of neutrinos of all flavors. At the relevant energies (≥ 50 TeV), showers, including tracks left by τ leptons, have a length of roughly 10 m in ice and are, to a good approximation, point sources of light (23). Secondary muon tracks are created primarily in ν_μ charged-current interactions along with a hadronic shower at the neutrino interaction vertex, and have a typical range on the order of kilometers, larger than the dimensions of the detector. Note that, for a flux consisting of a mixture of flavors, this implies that showers will be the dominant topology because ν_μ CC represents only a small fraction of the total event rate. For an equally mixed E^{-2} spectrum, about 80% of the observed events would appear as showers.

Although the distribution of hit PMTs in the detector is approximately spherical for shower events, the detailed timing patterns of the photons in the individual PMTs retain the memory of the direction of the primary lepton. Comparison of these distributions with expectations from simulated showers yields a typical median angular resolution of 10° to 15° . Resolution on deposited energy, from the recorded waveform amplitudes, is typically 10 to 15%. In events with a muon track, the extension of the track in the detector provides a much tighter constraint on direction than the shapes of the waveforms alone, improving angular resolution greatly to better than 1° (4). Energy reconstruction only yields a lower limit on neutrino energy as a result of the energy removed from the detector by escaping muons and neutrinos. All quoted directional and energy reconstruction uncertainties are dominated by a systematic component arising from uncertainties in the optical properties of the ice (24) and the optical sensitivity of the PMTs (25).

Atmospheric Muon Background

Remaining atmospheric muon background comes from tracks that produce too little light at the edge of the detector to be vetoed and instead emit their first detected photons in the interior volume, mimicking a starting neutrino. These events usually produce an observable muon track in the detector like that from a ν_μ charged-current event. Much more rarely, catastrophic energy loss processes such as muon bremsstrahlung can create a showerlike signal, especially in the corners of the detector where the exiting muon track may not be observed.

The veto passing rate for throughgoing muons, and therefore the total muon background in the analysis, can be evaluated directly from the data by implementing a two-layer anticoincidence detector. Entering events can be tagged with high efficiency using the outer layer of IceCube; the rate of these tagged events that pass the next veto layer can be used as a control sample to evaluate the rate at which muons are detected by a single detector layer as a function of observed light yield. This per-layer probability can be used to estimate the final background rate after application

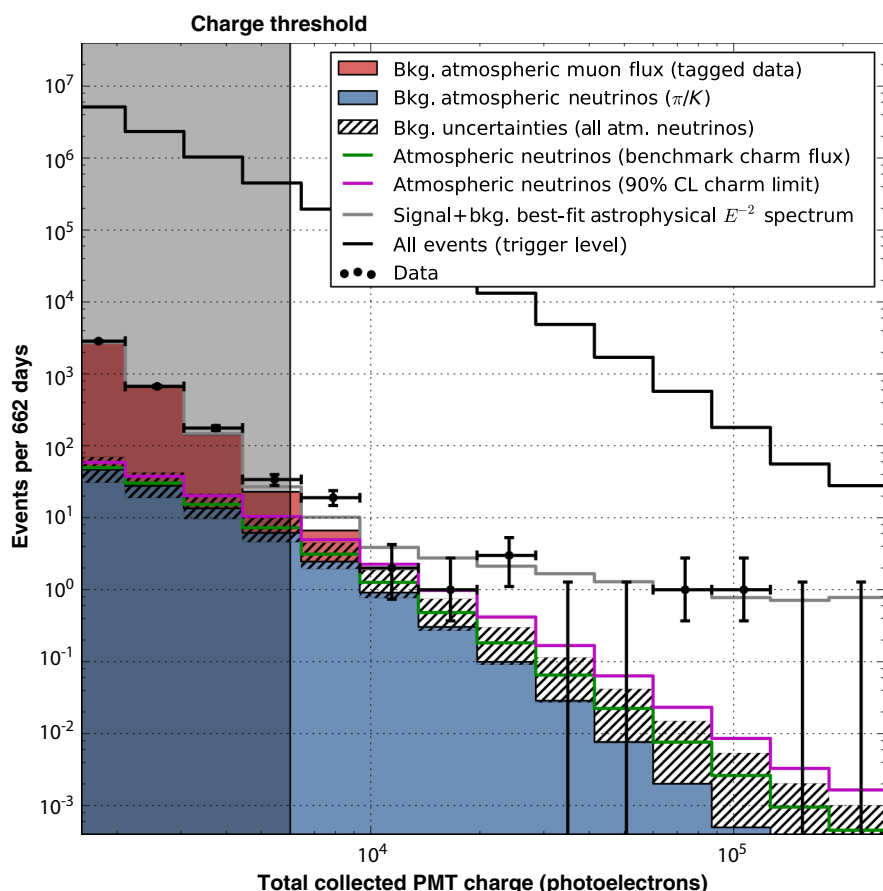


Fig. 6. Distribution of deposited PMT charges (Q_{tot}). Muons at higher total charges are less likely to pass the veto layer undetected, causing the muon background (red, estimated from data) to fall faster than the overall trigger rate (uppermost line). The data events in the unshaded region, at $Q_{\text{tot}} > 6000$, are the events reported in this work, with error bars indicating 68% Feldman-Cousins intervals. The best-fit E^{-2} astrophysical spectrum (gray line) and atmospheric neutrino flux (blue) have been determined using Monte Carlo simulations, with the hatched region showing current experimental uncertainties on the atmospheric neutrino background. The largest of these uncertainties is neutrinos from charmed meson decays, a flux that has yet to be observed and is thus not included in the blue region; the hatched region includes the best experimental 1σ upper limit (8). For scale, two specific charm levels are also shown: a benchmark theoretical model (6) (green line) and the experimental 90% CL upper bound (8) (magenta line).

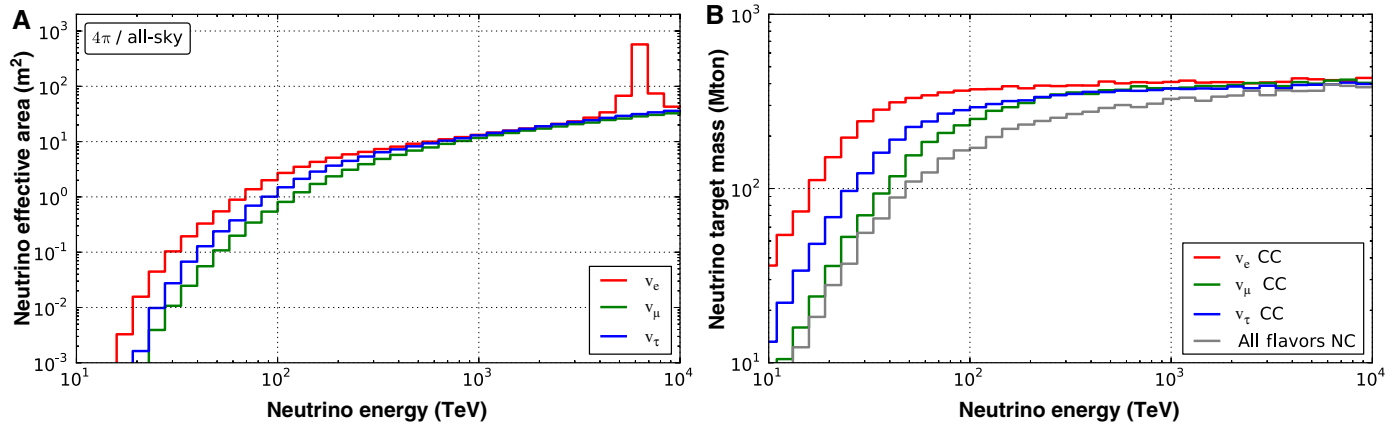


Fig. 7. Neutrino effective area and volume. Event rates can be obtained by multiplying the effective areas by 4π , by the sum of ν and $\bar{\nu}$ fluxes, and by the live time of 662 days. **(A)** Neutrino effective areas for each flavor assuming an equal flux of neutrinos and antineutrinos and averaged over all arrival angles. At 6.3 PeV, resonant W production on atomic electrons increases sensitivity to ν_e . The effective area includes effects from attenuation of

neutrinos in Earth (28), relevant at energies above 100 TeV. **(B)** Effective target mass as a function of energy. The deposited energy threshold in this search causes some flavor bias at low energies because of missing energy in escaping particles from ν_μ and ν_τ charged-current events. For ν_e charged-current events, where all the neutrino energy is visible in the detector, full efficiency is reached above 100 TeV.

of a geometrical correction factor of ~ 2 for the larger size of the analysis fiducial volume compared to the deep interior fiducial volume (after two veto layers). The resulting predicted veto passing rate agrees well with data at low energies, where we expect the event rate to be background-dominated (Fig. 6). In our signal region above 6000 photoelectrons, we observed three tagged events passing the inner veto and so predict 6.0 ± 3.4 veto-penetrating muon events in the 2-year data set.

Atmospheric Neutrinos

Atmospheric neutrino backgrounds, including an as-yet unobserved component from charmed meson decays, were estimated on the basis of a parametrization of the atmospheric neutrino flux (5, 7), consistent with previous IceCube measurements of the Northern Hemisphere muon neutrinos (8). We have also included a suppression of the atmospheric neutrino background from the Southern Hemisphere, resulting from the fact that accompanying high-energy muons produced in the same air shower can trigger our muon veto if they penetrate to the depth of the detector. Here, we have extended previous analytic calculations (22) of this suppression factor using the CORSIKA (26) air shower simulation to determine the fraction of atmospheric neutrinos accompanied at depth by muons above 10 TeV, at which they will be reliably detected by our muon veto. This factor is a strong function of neutrino energy and angle, with the strongest suppression expected at high energies and most downward angles. The suppression factor, bounded above at 90% to cover uncertainties in hadronic interaction models, was then folded with the Northern Hemisphere spectrum to predict the Southern Hemisphere event rate.

This produces an estimate of the atmospheric neutrino background of $4.6^{+3.7}_{-1.2}$ events in the 662-day live time. These events would be concentrated near the energy threshold of the anal-

ysis because of the steeply falling atmospheric neutrino spectrum. Uncertainties in the atmospheric neutrino background are dominated by the flux from charmed meson decays, which is too small to have been observed thus far and is currently bounded above experimentally by a 1σ upper limit of 3.4 events (8). The spectrum and composition of cosmic rays and models of hadronic interactions contribute a rate uncertainty at the relevant energies of $^{+30\%}_{-20\%}$, which dominates the uncertainties in the π/K component of the spectrum (27). The measured 5% uncertainty in the electromagnetic energy scale and detector linearity contributes a proportional $\pm 15\%$ uncertainty to the atmospheric background rates. Given the charge threshold, uncertainty in the light yield of hadronic showers, which is less well constrained, can affect the estimated background neutrino rate. However, the light yield for a hadronic shower is smaller than the well-known light yield for an electromagnetic shower at the same energy, limiting any resulting increase in the background rate to no larger than 30%.

Blind Calculation of Significance

We evaluated the significance of the excess over atmospheric backgrounds on the basis of both the total rate and properties of the observed events. From each event, the total deposited PMT charge, reconstructed energy, and direction were used to compute tail probabilities relative to the atmospheric muon and neutrino backgrounds. Overall significance was computed using the product of the per-event probabilities as a test statistic.

The muon background probability was computed as the fraction of the expected background with deposited charge greater than observed. Above the highest charge event in the control sample, we set an upper limit on the passing rate by assuming a constant veto efficiency. Similarly, the likelihood ratio between an isotropic E^{-2} astrophysical flux and the expected atmospheric neutrino back-

ground in declination and deposited energy was calculated for each event after folding with the observed reconstruction uncertainties, and the probability for an atmospheric neutrino event to have a larger value than observed was computed. Because our control sample of background muon events has limited statistics, we cannot produce a detailed map of the energies and angles of the penetrating muon background. For this reason, the muon and neutrino background probabilities were combined by taking the maximum of the two as the statistic for each event, which will somewhat underestimate the significance of any excess.

References and Notes

1. IceCube Collaboration, First year performance of the IceCube neutrino telescope. *Astropart. Phys.* **26**, 155–173 (2006). doi: [10.1016/j.astropartphys.2006.06.007](https://doi.org/10.1016/j.astropartphys.2006.06.007)
2. Fermi-LAT Collaboration, Detection of the characteristic pion-decay signature in supernova remnants. *Science* **339**, 807–811 (2013). doi: [10.1126/science.1231160](https://doi.org/10.1126/science.1231160); pmid: [23413352](https://pubmed.ncbi.nlm.nih.gov/23413352/)
3. IceCube Collaboration, First observation of PeV-energy neutrinos with IceCube. *Phys. Rev. Lett.* **111**, 021103 (2013). doi: [10.1103/PhysRevLett.111.021103](https://doi.org/10.1103/PhysRevLett.111.021103); pmid: [23889381](https://pubmed.ncbi.nlm.nih.gov/23889381/)
4. IceCube Collaboration, Observation of the cosmic-ray shadow of the Moon with IceCube arXiv:1305.6811 (2013). <http://arxiv.org/abs/1305.6811>
5. M. Honda, T. Kajita, K. Kasahara, S. Midorikawa, T. Sanuki, Calculation of atmospheric neutrino flux using the interaction model calibrated with atmospheric muon data. *Phys. Rev. D* **75**, 043006 (2007). doi: [10.1103/PhysRevD.75.043006](https://doi.org/10.1103/PhysRevD.75.043006)
6. R. Enberg, M. H. Reno, I. Sarcevic, Prompt neutrino fluxes from atmospheric charm. *Phys. Rev. D* **78**, 043005 (2008). doi: [10.1103/PhysRevD.78.043005](https://doi.org/10.1103/PhysRevD.78.043005)
7. T. K. Gaisser, Spectrum of cosmic-ray nucleons, kaon production, and the atmospheric muon charge ratio. *Astropart. Phys.* **35**, 801–806 (2012). doi: [10.1016/j.astropartphys.2012.02.010](https://doi.org/10.1016/j.astropartphys.2012.02.010)
8. IceCube Collaboration, A view of prompt atmospheric neutrinos with IceCube. *Nucl. Phys. B (Proc. Suppl.)* **237–238**, 266–268 (2013). doi: [10.1016/j.nuclphysbs.2013.04.105](https://doi.org/10.1016/j.nuclphysbs.2013.04.105)
9. IceCube Collaboration, Search for a diffuse flux of astrophysical muon neutrinos with the IceCube

- 40-string detector. *Phys. Rev. D* **84**, 082001 (2011). doi: [10.1103/PhysRevD.84.082001](https://doi.org/10.1103/PhysRevD.84.082001)
10. IceCube Collaboration, Measurement of the atmospheric ν_e flux in IceCube. *Phys. Rev. Lett.* **110**, 151105 (2013). doi: [10.1103/PhysRevLett.110.151105](https://doi.org/10.1103/PhysRevLett.110.151105)
 11. E. V. Bugaev, V. A. Naumov, S. I. Sinegovsky, E. S. Zaslavskaya, Prompt leptons in cosmic rays. *Nuov. Cim.* **12**, 41–73 (1989). doi: [10.1007/BF02509070](https://doi.org/10.1007/BF02509070)
 12. S. Choubey, W. Rodejohann, Flavor composition of ultrahigh energy neutrinos at source and at neutrino telescopes. *Phys. Rev. D* **80**, 113006 (2009). doi: [10.1103/PhysRevD.80.113006](https://doi.org/10.1103/PhysRevD.80.113006)
 13. S. Pakvasa, W. Rodejohann, T. J. Weiler, Flavor ratios of astrophysical neutrinos: Implications for precision measurements. *J. High Energy Phys.* **2**, 005 (2008). doi: [10.1088/1126-6708/2008/02/005](https://doi.org/10.1088/1126-6708/2008/02/005)
 14. J. Braun *et al.*, Methods for point source analysis in high energy neutrino telescopes. *Astropart. Phys.* **29**, 299–305 (2008). doi: [10.1016/j.astropartphys.2008.02.007](https://doi.org/10.1016/j.astropartphys.2008.02.007)
 15. A. A. Abdo *et al.*, A measurement of the spatial distribution of diffuse TeV gamma-ray emission from the Galactic plane with Milagro. *Astrophys. J.* **688**, 1078 (2008). doi: [10.1086/592213](https://doi.org/10.1086/592213)
 16. E. Waxman, J. Bahcall, High energy neutrinos from cosmological gamma-ray burst fireballs. *Phys. Rev. Lett.* **78**, 2292–2295 (1997). doi: [10.1103/PhysRevLett.78.2292](https://doi.org/10.1103/PhysRevLett.78.2292)
 17. K. Ioka, S. Razzaque, S. Kobayashi, P. Mészáros, TeV-PeV neutrinos from giant flares of magnetars and the case of SGR 1806–20. *Astrophys. J.* **633**, 1013 (2005). doi: [10.1086/466514](https://doi.org/10.1086/466514)
 18. IceCube Collaboration, Neutrino analysis of the 2010 September Crab Nebula flare and time-integrated constraints on neutrino emission from the Crab using IceCube. *Astrophys. J.* **745**, 45 (2012). doi: [10.1088/0004-637X/745/1/A5](https://doi.org/10.1088/0004-637X/745/1/A5)
 19. T. K. Gaisser, Atmospheric leptons, the search for a prompt component. *High Energy Phys. Phenomenol.* arXiv:1303.1431 (2013). <https://arxiv.org/abs/1303.1431>
 20. IceCube Collaboration, Extending the search for neutrino point sources with IceCube above the horizon. *Phys. Rev. Lett.* **103**, 221102 (2009). doi: [10.1103/PhysRevLett.103.221102](https://doi.org/10.1103/PhysRevLett.103.221102); PMID: 20366087
 21. IceCube Collaboration, Constraints on the extremely-high energy cosmic neutrino flux with the IceCube 2008–2009 data. *Phys. Rev. D* **83**, 092003 (2011). doi: [10.1103/PhysRevD.83.092003](https://doi.org/10.1103/PhysRevD.83.092003)
 22. S. Schönert, T. K. Gaisser, E. Resconi, O. Schulz, Vetoing atmospheric neutrinos in a high energy neutrino telescope. *Phys. Rev. D* **79**, 043009 (2009). doi: [10.1103/PhysRevD.79.043009](https://doi.org/10.1103/PhysRevD.79.043009)
 23. L. Rädcl, C. Wiebusch, Calculation of the Cherenkov light yield from electromagnetic cascades in ice with Geant4. *Astropart. Phys.* **44**, 102–113 (2013). doi: [10.1016/j.astropartphys.2013.01.015](https://doi.org/10.1016/j.astropartphys.2013.01.015)
 24. IceCube Collaboration, Measurement of South Pole ice transparency with the IceCube LED calibration system. *Nucl. Instr. Meth. Phys. Res. A* **711**, 73–89 (2013). doi: [10.1016/j.nima.2013.01.054](https://doi.org/10.1016/j.nima.2013.01.054)
 25. IceCube Collaboration, Calibration and characterization of the IceCube photomultiplier tube. *Nucl. Instr. Meth. Phys. Res. A* **618**, 139–152 (2010). doi: [10.1016/j.nima.2010.03.102](https://doi.org/10.1016/j.nima.2010.03.102)
 26. D. Heck, J. Knapp, J. Capdevielle, G. Schatz, T. Thouw, *CORSIKA: A Monte Carlo Code to Simulate Extensive Air Showers* (Forschungszentrum Karlsruhe GmbH, Karlsruhe, Germany, 1998).
 27. A. Fedynitch, J. Becker Tjus, P. Desiati, Influence of hadronic interaction models and the cosmic ray spectrum on the high energy atmospheric muon and neutrino flux. *Phys. Rev. D* **86**, 114024 (2012). doi: [10.1103/PhysRevD.86.114024](https://doi.org/10.1103/PhysRevD.86.114024)
 28. A. Cooper-Sarkar, S. Sarkar, Predictions for high energy neutrino cross-sections from the ZEUS global PDF fits. *J. High Energy Phys.* **1**, 075 (2008). doi: [10.1088/1126-6708/2008/01/075](https://doi.org/10.1088/1126-6708/2008/01/075)

Acknowledgments: We acknowledge support from the following agencies: U.S. National Science Foundation—Office of Polar Programs, U.S. National Science Foundation—Physics Division, University of Wisconsin Alumni Research Foundation, the Grid Laboratory of Wisconsin (GLOW) grid infrastructure at the University of Wisconsin—Madison, and the Open Science Grid (OSG) grid infrastructure; U.S. Department of Energy, National Energy Research Scientific Computing Center, and the Louisiana Optical Network Initiative (LONI) grid computing resources; Natural Sciences and Engineering Research Council of Canada, WestGrid, and Compute/Calcul Canada; Swedish Research Council, Swedish Polar Research Secretariat, Swedish National Infrastructure for Computing (SNIC), and Knut and Alice Wallenberg Foundation, Sweden; German Ministry for Education and Research (BMBF), Deutsche Forschungsgemeinschaft (DFG), Helmholtz Alliance for Astroparticle Physics (HAP), and Research Department of Plasmas with Complex Interactions (Bochum), Germany; Fund for Scientific Research (FNRS-FWO), FWO Odysseus programme, Flanders Institute to encourage scientific and technological research in industry (IWT), and Belgian Federal Science Policy Office (Belspo); University of Oxford, UK; Marsden Fund, New Zealand; Australian Research Council; Japan Society for Promotion of Science (JSPS); the Swiss National Science Foundation (SNSF), Switzerland; and National Research Foundation of Korea (NRF). Additional data and resources are available in the supplementary materials. These include displays of the neutrino candidate events and list precise arrival times, as well as machine-readable tabular neutrino effective areas (Fig. 7). IceCube data are archived at <http://www.icecube.wisc.edu/science/data>.

IceCube Collaboration:

M. G. Aartsen,² R. Abbasi,²⁷ Y. Abdou,²² M. Ackermann,⁴² J. Adams,¹⁵ J. A. Aguilar,²¹ M. Ahlers,²⁷ D. Altmann,⁹ J. Auffenberg,²⁷ X. Bai,³¹ M. Baker,²⁷ S. W. Barwick,²³ V. Baum,²⁸ R. Bay,⁷ J. J. Beatty,^{17,18} S. Bechet,¹² J. Becker Tjus,¹⁰ K.-H. Becker,⁴¹ M. L. Benaberrahmane,⁴² S. BenZvi,²⁷ P. Berghaus,⁴² D. Berley,¹⁶ E. Bernardini,⁴ A. Bernhard,³⁰ D. Bertrand,¹² D. Z. Besson,²⁵ G. Binder,^{8,7} D. Bindig,⁴¹ M. Bissok,¹ E. Blaufuss,¹⁶ J. Blumenthal,¹ D. J. Boersma,⁴⁰ S. Bokaichuk,²⁰ C. Bohm,³⁴ D. Bose,¹³ S. Böser,¹¹ O. Botner,⁴⁰ L. Brayer,¹³ H.-P. Bretz,⁴² A. M. Brown,¹⁵ R. Bruijn,²⁴ J. Brunner,²² M. Carson,²² J. Casey,⁵ M. Casier,¹³ D. Chirkin,²⁷ A. Christov,²¹ B. Christy,¹⁶ K. Clark,³⁹ F. Clevermann,¹⁹ S. Coenders,⁵ S. Cohen,²⁴ D. F. Cowen,^{39,38} A. H. Cruz Silva,⁴² M. Danninger,³⁴ J. Daughhetee,⁵ J. C. Davis,¹⁷ M. Day,²⁷ C. De Clercq,¹³ S. De Ridder,²² P. Desiati,²⁷ K. D. de Vries,¹³ M. de With,⁹ T. DeYoung,³⁹ J. C. Díaz-Vélez,²⁷ M. Dunkman,³⁹ R. Eagan,³⁹ B. Eberhardt,²⁸ B. Eichmann,¹⁰ J. Eisch,²⁷ R. W. Ellsworth,¹⁶ S. Euler,¹ P. A. Evenson,²¹ O. Fadrian,²⁷ A. R. Fazely,⁶ A. Fedynitch,¹⁰ J. Feintzeig,²⁷ T. Feusels,²² K. Filimonov,⁷ C. Finley,³⁴ T. Fischer-Wasels,⁴¹ S. Flis,³⁴ A. Franckowiak,¹¹ K. Frantzen,²⁷ T. Fuchs,¹⁹ T. K. Gaisser,³¹ J. Gallagher,¹⁶ L. Gerhardt,^{8,7} L. Gladstone,²⁷ T. Glüsenkamp,⁴² A. Goldschmidt,⁸ G. Golup,¹³ J. G. Gonzalez,³¹ J. A. Goodman,¹⁶ D. Góra,⁴² D. T. Grandmont,²⁰ D. Grant,²⁰ A. Groß,³⁰ C. Ha,^{8,7} A. Haj Ismail,²² P. Hallen,¹ A. Hallgren,⁴⁰ F. Halzen,²⁷ K. Hanson,¹² D. Heereman,¹² D. Heinen,¹ K. Helbing,⁴¹ R. Hellauer,¹⁶ S. Hickford,¹⁵ G. C. Hill,² K. D. Hoffman,¹⁶ R. Hoffmann,⁴¹ A. Homeier,¹¹ K. Hoshina,²⁷ W. Huelsnitz,¹⁶ P. O. Hultu,³⁴ K. Hultqvist,³⁴ S. Hussain,³¹ A. Ishihara,¹⁴ E. Jacobi,⁴² J. Jacobsen,²⁷ K. Jagielski,¹ G. S. Japaridze,⁴ K. Jero,²⁷ O. Jlelati,²² B. Kaminsky,⁴² A. Kappes,⁹ T. Karg,⁴² A. Karle,²⁷ J. L. Kelley,²⁷ J. Kiriyluk,³⁵ J. Kläs,⁴³ S. R. Klein,^{8,7} J.-H. Köhne,¹⁹ G. Kohnen,²⁹ H. Kolanoski,⁹ L. Köpke,²⁸ C. Kopper,²⁷ S. Kopper,¹⁹ D. J. Koskinen,³⁹ M. Kowalski,¹¹ M. Krasberg,²⁷ K. Krings,¹ G. Kroll,²⁸ J. Kunnen,¹³ N. Kurahashi,²⁷ T. Kuwabara,³¹ M. Labare,²² H. Landsman,²⁷ M. J. Larson,³⁷ M. Lesiak-Badzak,³⁵ M. Leuermann,¹ J. Leute,³⁰ J. Linemann,²⁸ J. Madsen,³³ G. Maggi,¹³ R. Maruyama,²⁷ K. Mase,¹⁴ H. S. Mattis,⁸ F. McNally,²⁷ K. Meagher,¹⁶ M. Merck,²⁷ T. Meures,¹² S. Miarecki,^{8,7} E. Middell,⁴² N. Milke,¹⁹ J. Miller,¹³ L. Mohrmann,⁴² T. Montaruli,²¹ R. Morse,²⁷ R. Nahnhauser,⁴² U. Naumann,⁴¹ H. Niederhausen,³⁵ S. C. Nowicki,²⁰ D. R. Nygren,⁸ A. Obertacke,⁴¹ S. Odrowski,²⁰ A. Olivas,¹⁶ A. O'Murchadha,¹² L. Paul,¹ J. A. Pepper,³⁷ C. Pérez de los Heros,⁴⁰ C. Pfendner,¹⁹ D. Pieloth,¹⁹ E. Pinat,¹² J. Posselt,¹⁰ P. B. Price,⁷ G. T. Przybylski,⁸ L. Rädcl,¹ M. Rameez,²¹ K. Rawlins,³ P. Redl,¹⁶ R. Reimann,¹ E. Resconi,³⁰ W. Rhode,¹⁹ M. Ribordy,²⁴ M. Richman,¹⁶ B. Riedel,¹⁷ J. P. Rodrigues,²⁸ C. Rott,³⁶ T. Ruhe,¹⁶ B. Ruzybayev,³¹ D. Ryckbosch,²² S. M. Saba,¹⁰ T. Salameh,³⁹ H.-G. Sander,²⁸ M. Santander,²⁷ S. Sarkar,³² K. Schatto,²⁸ F. Scheriau,¹⁹ T. Schmidt,¹⁶ M. Schmitz,¹⁹ S. Schoenen,¹ S. Schöneberg,¹⁰ A. Schönwald,⁴² A. Schukraft,¹ L. Schulte,¹¹ O. Schulz,³⁰ D. Seckel,³¹ Y. Sestayo,³⁰ S. Seunarine,³³ R. Shanidze,⁴² C. Sheremata,²⁰ M. W. E. Smith,³⁹ D. Soldin,⁴¹

G. M. Spiczak,³³ C. Spiering,⁴² M. Stamatikos,¹⁷ T. Stanew,³¹ A. Stasik,¹¹ T. Stezelberger,⁸ R. G. Stokstad,⁸ A. Stößl,⁴² E. A. Strahler,¹³ R. Ström,⁴⁰ G. W. Sullivan,¹⁶ H. Taavola,⁴⁰ I. Taboada,⁵ A. Tamburro,³¹ A. Tepe,⁴¹ S. Ter-Antonyan,⁶ G. Tesić,³⁹ S. Tilav,³⁴ P. A. Toale,³⁷ S. Toscano,²⁷ E. Unger,¹⁰ M. Usner,¹¹ N. van Eijndhoven,¹³ A. Van Overloop,²² J. van Santen,²⁷ M. Vehringer,¹ M. Voge,¹¹ M. Vraeghe,²² C. Walck,³⁴ T. Waldenmaier,⁹ M. Wallraff,¹ Ch. Weaver,²⁷ M. Wellons,²⁷ C. Wendt,²⁷ S. Westerhoff,²⁷ N. Whitehorn,²⁷ K. Wiebe,²⁸ C. H. Wiebusch,¹ D. R. Williams,³⁷ H. Wissing,¹⁶ M. Wolf,³⁴ T. R. Wood,²⁰ K. Woschnagg,⁷ D. L. Xu,³⁷ X. W. Xu,⁶ J. P. Yanez,⁴² G. Yodanis,³⁷ S. Yoshida,³⁴ P. Zarzhitsky,³⁷ J. Ziemann,¹⁹ S. Zierke,¹ M. Zoll³⁴

¹III. Physikalisches Institut, RWTH Aachen University, D-52056 Aachen, Germany. ²School of Chemistry and Physics, University of Adelaide, Adelaide, South Australia 5005, Australia. ³Department of Physics and Astronomy, University of Alaska Anchorage, 3211 Providence Drive, Anchorage, AK 99508, USA. ⁴CITSPS, Clark-Atlanta University, Atlanta, GA 30314, USA. ⁵School of Physics and Center for Relativistic Astrophysics, Georgia Institute of Technology, Atlanta, GA 30332, USA. ⁶Department of Physics, Southern University, Baton Rouge, LA 70813, USA. ⁷Department of Physics, University of California, Berkeley, Berkeley, CA 94720, USA. ⁸Lawrence Berkeley National Laboratory, Berkeley, CA 94720, USA. ⁹Institut für Physik, Humboldt-Universität zu Berlin, D-12489 Berlin, Germany. ¹⁰Fakultät für Physik und Astronomie, Ruhr-Universität Bochum, D-44780 Bochum, Germany. ¹¹Physikalisches Institut, Universität Bonn, Nussallee 12, D-53115 Bonn, Germany. ¹²Université Libre de Bruxelles, Science Faculty CP230, B-1050 Brussels, Belgium. ¹³Vrije Universiteit Brussel, Dienst ELEM, B-1050 Brussels, Belgium. ¹⁴Department of Physics, Chiba University, Chiba 263-8522, Japan. ¹⁵Department of Physics and Astronomy, University of Canterbury, Private Bag 4800, Christchurch, New Zealand. ¹⁶Department of Physics, University of Maryland, College Park, MD 20742, USA. ¹⁷Department of Physics and Center for Cosmology and Astroparticle Physics, Ohio State University, Columbus, OH 43210, USA. ¹⁸Department of Astronomy, Ohio State University, Columbus, OH 43210, USA. ¹⁹Department of Physics, TU Dortmund University, D-44221 Dortmund, Germany. ²⁰Department of Physics, University of Alberta, Edmonton, Alberta T6G 2E1, Canada. ²¹Département de physique nucléaire et corpusculaire, Université de Genève, CH-1211 Genève, Switzerland. ²²Department of Physics and Astronomy, University of Gent, B-9000 Gent, Belgium. ²³Department of Physics and Astronomy, University of California, Irvine, Irvine, CA 92697, USA. ²⁴Laboratory for High Energy Physics, École Polytechnique Fédérale, CH-1015 Lausanne, Switzerland. ²⁵Department of Physics and Astronomy, University of Kansas, Lawrence, KS 66045, USA. ²⁶Department of Astronomy, University of Wisconsin, Madison, WI 53706, USA. ²⁷Department of Physics and Wisconsin IceCube Particle Astrophysics Center, University of Wisconsin, Madison, WI 53706, USA. ²⁸Institute of Physics, University of Mainz, Staudinger Weg 7, D-55099 Mainz, Germany. ²⁹Université de Mons, 7000 Mons, Belgium. ³⁰T.U. Munich, D-85748 Garching, Germany. ³¹Bartol Research Institute and Department of Physics and Astronomy, University of Delaware, Newark, DE 19716, USA. ³²Department of Physics, University of Oxford, 1 Keble Road, Oxford OX1 3NP, UK. ³³Department of Physics, University of Wisconsin, River Falls, WI 54022, USA. ³⁴Oskar Klein Centre and Department of Physics, Stockholm University, SE-10691 Stockholm, Sweden. ³⁵Department of Physics and Astronomy, Stony Brook University, Stony Brook, NY 11794–3800, USA. ³⁶Department of Physics, Sungkyunkwan University, Suwon 440-746, Korea. ³⁷Department of Physics and Astronomy, University of Alabama, Tuscaloosa, AL 35487, USA. ³⁸Department of Astronomy and Astrophysics, Pennsylvania State University, University Park, PA 16802, USA. ³⁹Department of Physics, Pennsylvania State University, University Park, PA 16802, USA. ⁴⁰Department of Physics and Astronomy, Uppsala University, Box 516, S-75120 Uppsala, Sweden. ⁴¹Department of Physics, University of Wuppertal, D-42119 Wuppertal, Germany. ⁴²DESY, D-15735 Zeuthen, Germany.

*Corresponding author. E-mail: ckopper@icecube.wisc.edu (C.K.); naoko@icecube.wisc.edu (N.K.); nwhitehorn@icecube.wisc.edu (N.W.)

Supplementary Materials

www.sciencemag.org/content/342/6161/1242856/suppl/DC1
Event Displays 1 to 28
Neutrino Effective Areas

8 July 2013; accepted 8 October 2013
10.1126/science.1242856

Organization of the Mitotic Chromosome

Natalia Naumova,^{1*} Maxim Imakaev,^{2*} Geoffrey Fudenberg,^{2,3*} Ye Zhan,¹ Bryan R. Lajoie,¹ Leonid A. Mirny,^{2†} Job Dekker^{1†}

Mitotic chromosomes are among the most recognizable structures in the cell, yet for over a century their internal organization remains largely unsolved. We applied chromosome conformation capture methods, 5C and Hi-C, across the cell cycle and revealed two distinct three-dimensional folding states of the human genome. We show that the highly compartmentalized and cell type–specific organization described previously for nonsynchronous cells is restricted to interphase. In metaphase, we identified a homogenous folding state that is locus-independent, common to all chromosomes, and consistent among cell types, suggesting a general principle of metaphase chromosome organization. Using polymer simulations, we found that metaphase Hi-C data are inconsistent with classic hierarchical models and are instead best described by a linearly organized longitudinally compressed array of consecutive chromatin loops.

The three-dimensional (3D) organization of genomes plays critical roles in regulating chromosomal processes, including gene regulation, DNA replication, and genome stability (1–4). During the cell cycle, chromosomes transition between two distinct folding states: interphase and metaphase. Interphase chromosomes are relatively decondensed and acquire a cell type–specific spatial organization. In preparation for cell division, chromosomes undergo exten-

sive spatial reorganization and eventually shut down most transcription. This process culminates in a highly condensed and morphologically reproducible metaphase chromosome state.

Chromosome conformation capture (3C)–based methods extend previous characterizations of interphase chromosomes by detecting physical contact frequencies between pairs of genomic loci (2, 5, 6). During interphase, chromosomes occupy individual territories and are compartmentalized

at several hierarchical levels: large multi-megabase active A- and inactive B-compartments (7), and smaller sub-megabase topologically associating domains (TADs) (8–10). At ~100-kb scales, chromatin looping interactions connect genes to distal regulatory elements, mediating long-range gene regulation (11).

The internal organization of mitotic chromosomes remains enigmatic (12–15). On the basis of studies that have used light microscopy, electron microscopy, tomography, and mechanical measurements, several models of mitotic chromosomes have been proposed. These models can be subdivided into three groups (16, 17): loops-on-a-scaffold models (15, 18, 19), hierarchical models of increasingly thicker coiled or looped fibers (20, 21), and network models, which describe mitotic chromosomes as highly cross-linked

¹Program in Systems Biology, Department of Biochemistry and Molecular Pharmacology, University of Massachusetts Medical School (UMMS), 368 Plantation Street, Worcester, MA 01605–0103, USA. ²Institute for Medical Engineering and Science, and Department of Physics, Massachusetts Institute of Technology (MIT), Cambridge, MA 02139, USA. ³Program in Biophysics, Harvard University, Boston, MA 02115, USA.

*These authors contributed equally to this work.

†Corresponding author. E-mail: job.dekker@umassmed.edu (J.D.); leonid@mit.edu (L.A.M.)

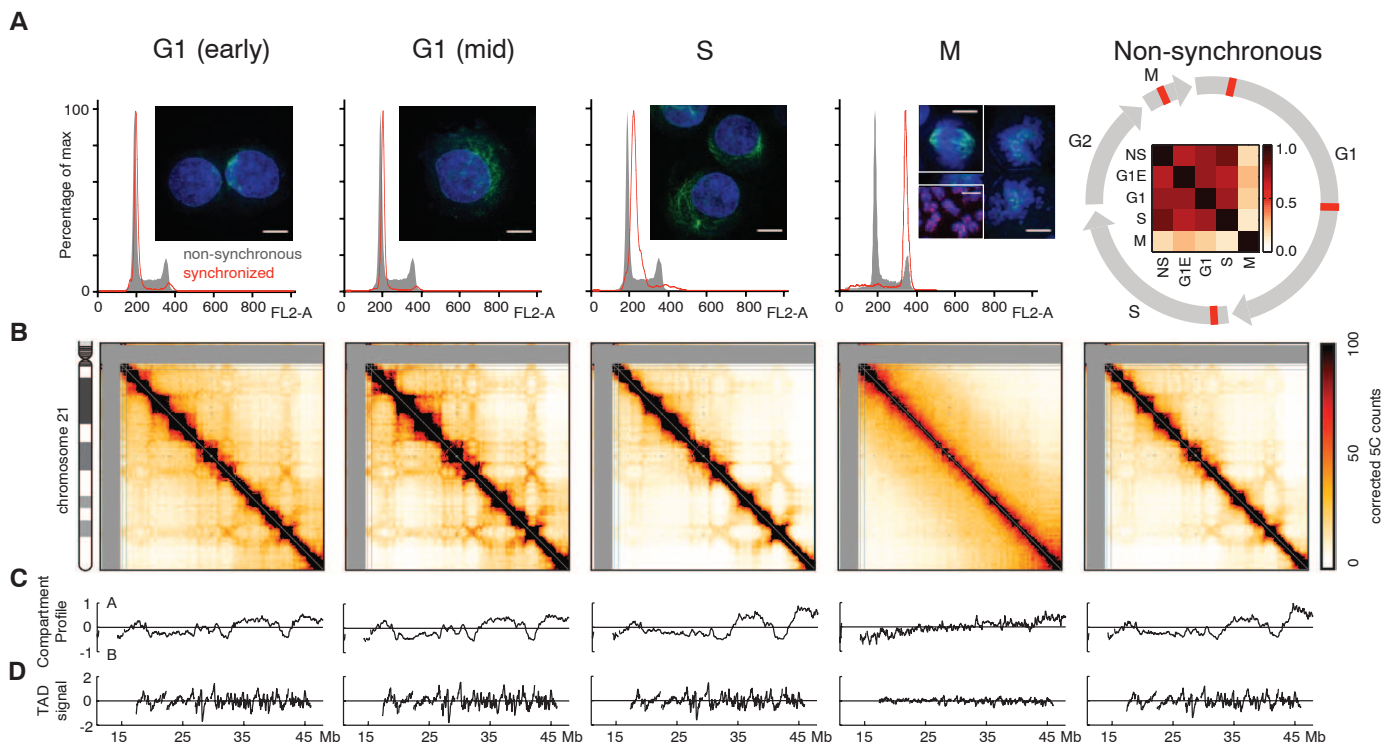


Fig. 1. Organization of chromosome 21 through the cell cycle. (A) Fluorescence-activated cell sorting profiles and microscopy images of cell populations analyzed in this study. Images show 4',6-diamidino-2-phenylindole–stained DNA (blue) and α -tubulin (green). Scale bars, 1 μ m. Image under “M” shows three different pictures: right half, cells arrested in metaphase (12 hours nocodazole); top left inset, control metaphase cells with intact spindle; bottom left inset, nocodazole-arrested chromosomes stained for SMC2, showing separated sister chromatid arms. (Right) Nonsynchronous population consists of a mixture of

all cell-cycle phases. Circular diagram shows cell cycle, with red markers indicating cell-cycle phase of studied synchronization samples. Inside the cell-cycle circle is a correlation matrix between 5C interaction patterns of both nonsynchronous cells and all studied stages of the cell cycle (27). **(B)** Corrected 5C matrices of chromosome 21 for these cell populations; raw 5C data were binned to 250 kb with a 50-kb sliding window and corrected by using ICE. Gray regions are not interrogated in this study. **(C)** A/B compartment profile for each data set. **(D)** TAD signal for each data set.

gels (22, 23), as well as models that combine these different features (24).

We applied chromosome conformation capture carbon copy (5C) (25) and Hi-C (7) to study the spatial organization of human chromosomes during the cell cycle, revealing two distinct folding states. Using polymer simulations, we evaluated existing and new models of metaphase chromosome organization. We propose that metaphase organization can emerge through a two-stage process: linear compaction by consecutive chromatin loops, potentially generated by structural maintenance of chromosomes (SMC) complexes, followed by axial compression.

Results

Changes in Chromosome Organization During the Cell Cycle

For our initial studies, we used HeLa S3 cells because large and homogeneous populations of these cells at various stages of the cell cycle can be obtained relatively easily and efficiently (fig. S1). The HeLa S3 karyotype is complex, but stable. We focused analyses on intra-chromosomal data from six chromosomes that appear normal, as judged by use of spectral karyotyping/multiplex fluorescence in situ hybridization (SKY/M-FISH)

and Hi-C (figs. S2 and S3). Further, our analyses use ICE (iterative correction and eigenvector decomposition) (26), which corrects for biases in sequencing coverage that may arise from copy-number alterations.

We used 5C technology to study the organization of small and un-rearranged chromosome 21 at different time points throughout the cell cycle (Fig. 1). We interrogated long-range interactions using a pool of 5C primers that cover the length of chromosome 21 with an average spacing of 25 kb (27). We studied early-G₁ and mid-G₁ cells, thymidine-arrested early S-phase cells, and nocodazole-arrested prometaphase ("mitotic") cultures (Fig. 1 and figs. S1 and S4) (27). We found that nocodazole treatment up to 12 hours leads to some gradual shortening of mitotic chromosomes, but Hi-C analyses for 3, 7, and 12 hours of incubation yield overall very similar results (fig. S5). Sister chromatid arms are separate and no longer intertwined in nocodazole-arrested cells (Fig. 1A).

The interaction patterns for early-G₁, mid-G₁, and S-phase are highly correlated with each other and with the pattern obtained with nonsynchronous cells [Spearman correlation coefficient (r) > 0.67, $P < 10^{-10}$] (Fig. 1A) (27). For these cell-cycle

phases, the interaction maps display similar plaid patterns of regional enrichment or depletion of long-range interactions (Fig. 1). A similar plaid pattern was previously observed for nonsynchronous cells, which are mainly (97%) in interphase, and has been interpreted to reflect spatial separation of chromosomes in A/B compartments (7).

In mitotic cells, however, the interaction map changes dramatically, and the plaid pattern disappears. The mitotic interaction pattern displays a low correlation with those for all other cell-cycle phases (Spearman $r < 0.27$, $P < 10^{-10}$) (Fig. 1B). Thus, we identify two distinct chromosome folding states in the cell cycle.

Loss of Chromosome Compartments and TADs in Metaphase

Next, we used Hi-C (7) to perform a genome-wide analysis of the mitotic and mid-G₁ states because these represent the two most distinct states of the cell cycle (Fig. 2 and fig. S6). We then used both 5C and Hi-C data to study features of chromosome organization at different levels: compartments at the chromosome scale, and TADs at the sub-megabase scale. Using ICE (26), we obtained compartment profiles. In G₁, an alternating compartment profile (Fig. 2B) and preferential

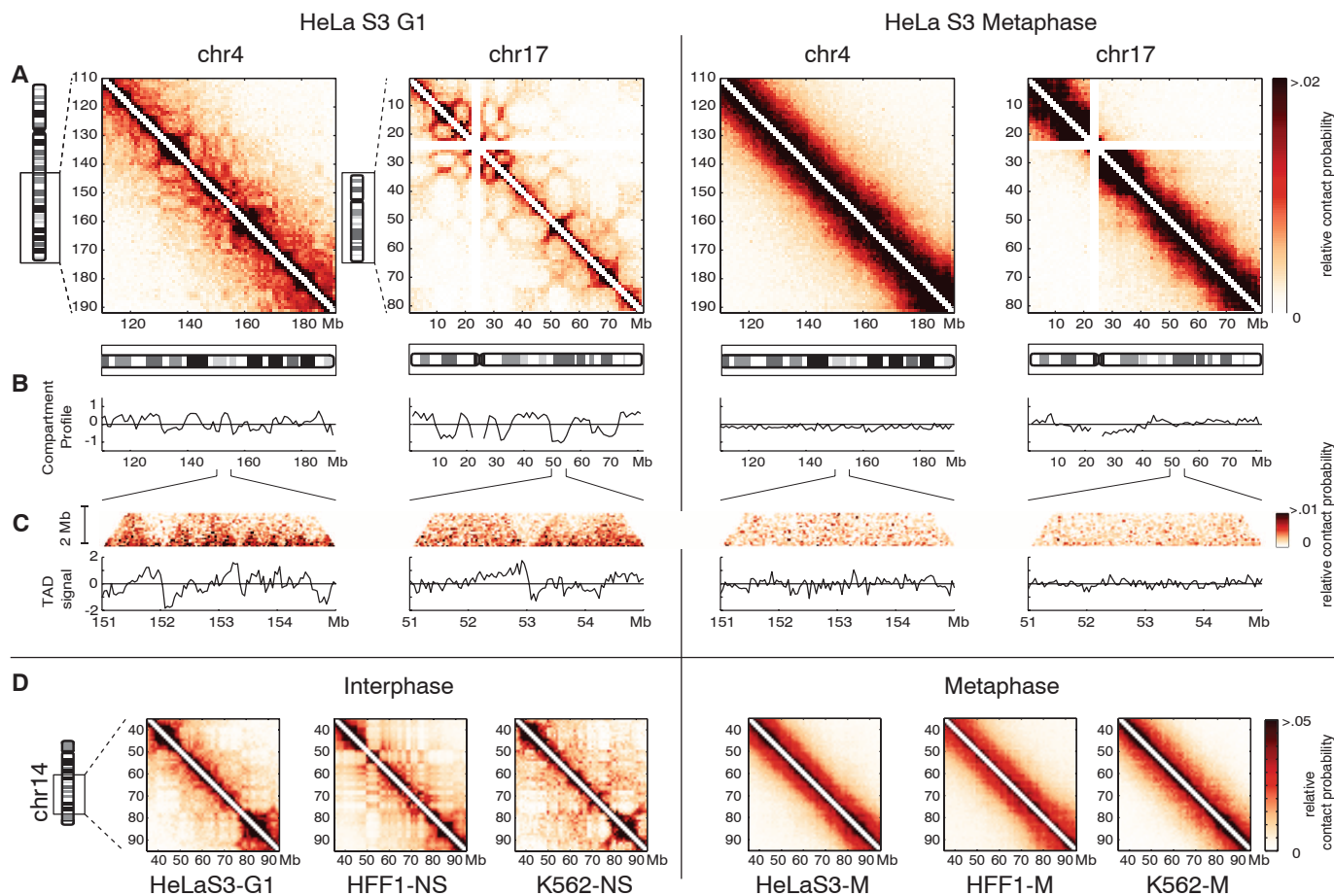


Fig. 2. Hi-C analysis of chromosome organization in G₁ and mitotic cells. (A) Relative Hi-C contact probability maps for chromosome 17 and an equally sized 82-Mb region of chromosome 4, at 1-Mb resolution. M-phase arrest was at 12 hours of nocodazole. (B) A/B compartment profile for these regions. (C) Zoom-in of 4-Mb

subregions. (Top) Region of a contact map at 40-kb resolution. (Bottom) TAD signal for this region. (D) Hi-C contact probability maps for a region of chr14 in interphase and metaphase. Displayed are HeLa-S3-G₁, HFF1-NS (nonsynchronous), and published K562-NS (7) data sets (left) and HeLa-S3-M, HFF1-M, and K562-M data sets (right).

interactions among regions within the same compartment type (fig. S7) were observed, which is in agreement with previous studies on nonsynchronized cells (7, 28). Compartment profiles extracted from 5C agree with Hi-C on chromosome 21 (fig. S8) and are highly correlated in early G₁, mid G₁, and S-phase cells (Spearman $r > 0.85$, $P < 10^{-10}$).

In mitotic cells, Hi-C interaction maps are very similar for all chromosomes, and compartmentalization disappears across the genome (Figs. 1 and 2) because eigenvector decomposition does not detect a compartment profile that alternates along the length of a chromosomal arm. Consistently, preferential interactions between compartments extracted from G₁ Hi-C data, or between regions with similar GC content or similar interphase chromatin marks, are lost in mitosis (fig. S7).

At a sub-megabase scale, chromosomes have been found to be composed of TADs (9, 10). A TAD is a contiguous chromosomal region that largely interacts with itself and is relatively insulated from its direct genomic neighbors. TADs have been identified by their pattern of preferential upstream or downstream interactions: largely downstream at the start of a TAD, and largely upstream at the end (9). We quantify the TAD signal by the log₂-ratio of upstream to downstream interactions of each genomic region. In interphase, the TAD signal is prominent along all chromosomes (Figs. 1 and 2C), which is consistent between Hi-C and 5C on chromosome 21 ($r = 0.73$, $P < 10^{-10}$) and is more prominent in mid-G₁ cells than in early G₁ and S phases.

In mitotic cells, the amplitude of the TAD signal is strongly reduced across all chromosomes; this was confirmed by means of 5C on chromosome 21. The residual variation in the TAD signal in mitotic cells can be explained by the presence of around 15% nonmitotic cells in nocodazole-arrested cultures (fig. S9). A high-synchrony (98%) mitotic data set displays further loss of TADs (fig. S10). Hi-C when performed at fourfold lower formaldehyde concentration (0.25%)

showed similar results, indicating that loss of compartments and TADs is not due to over-cross-linking of condensed chromosomes (figs. S11 and S12). We conclude that large-scale compartments and sub-megabase TADs are mostly lost in metaphase.

We repeated the analysis of interphase and metaphase chromosome conformation in two additional cell types: erythroid K562 cells and primary human foreskin fibroblasts (HFF1) (Fig. 2D and figs. S13 and S14). In interphase, all three cell types display A/B compartments, but their locations are different (fig. S15). In contrast, the Hi-C data for mitotic chromosomes are strikingly similar for all three cell types, showing loss of compartments and TADs, leading to virtually identical homogeneous interaction maps for all chromosomes. Thus, during the cell cycle chromosomes alternate between cell type-specific and locus-specific interphase organizations and a universal cell-type and locus invariant mitotic conformation.

Two Levels of Organization of Mitotic Chromosomes

Because chromosomes can be understood as long polymers, we examined how the contact probability $P(s)$ derived from Hi-C maps depends on genomic distance, s , between a pair of loci in each chromosomal arm (Fig. 3). This dependence is informative of the underlying polymer state (29–31). $P(s)$ for interphase and mitotic chromosomes are strikingly different while being highly consistent among cell types (Fig. 3A). In contrast to interphase, mitotic chromosomes display a slow decrease in contact probability $P(s) \sim s^{-0.5}$ from 100 kb to 10 Mb, followed by a rapid fall-off at ~10 Mb. These features are observed for all chromosomes irrespective of their lengths (Fig. 3B) and are robust to details of a Hi-C experiment and methods used to compute $P(s)$ (fig. S16).

The two regimes in metaphase $P(s)$ suggest that chromatin is organized differently above and below 10 Mb. Regions separated by more than 10 Mb rarely contact each other and thus occupy distinct spatial positions; this is consistent

with the known linear organization of mitotic chromosomes, in which consecutive regions occupy consecutive longitudinal positions. In contrast, loci within any continuous 10-Mb region frequently contact each other. Thus, mitotic chromosomes can be considered as a linearly ordered structure above 10 Mb consisting of spatially mixed layers of ~10 Mb (Fig. 3B).

To understand mitotic chromosome organization within a 10-Mb layer, we compared the observed $P(s)$ with that of the equilibrium globule and fractal globule polymer states. A fractal globule state has $P(s) \sim s^{-1}$ and is characterized by spatial segregation of different regions (Fig. 3C). Conversely, the equilibrium globule state exhibits a plateau in $P(s)$ [$P(s) \sim s^0$] and is characterized by a high degree of mixing between different regions of the polymer. The observed $P(s) \sim s^{-0.5}$ in metaphase falls in between $P(s)$ for these two states, indicating an intermediate level of spatial mixing. Thus, although previous work found that a fractal globule state was consistent with interphase $P(s)$ from 500 kb to 7 Mb (7), a different polymer model is needed to account for the greatly different $P(s)$ for mitotic chromosomes.

Polymer Modeling of Mitotic Chromosome Organization

We next developed and tested polymer models of the final folded state of a mitotic chromosome. Because details of the folding pathway and initial conformations are unknown, we studied equilibrium polymer models (27). For each model, we generated an ensemble of conformations, simulated Hi-C experiments of this ensemble, and evaluated its ability to reproduce the main features of the Hi-C data: the observed $P(s)$ (Fig. 3B) and a homogeneous ensemble-average interaction map (Figs. 1 and 2 and fig. S17). We additionally required that models have the known cylindrical chromosome geometry, chromatin-packing density [~70 Mb per 1 μ m of chromatid (32)], and linear organization of mitotic chromatids (33). We modeled 77 Mb of chromatin

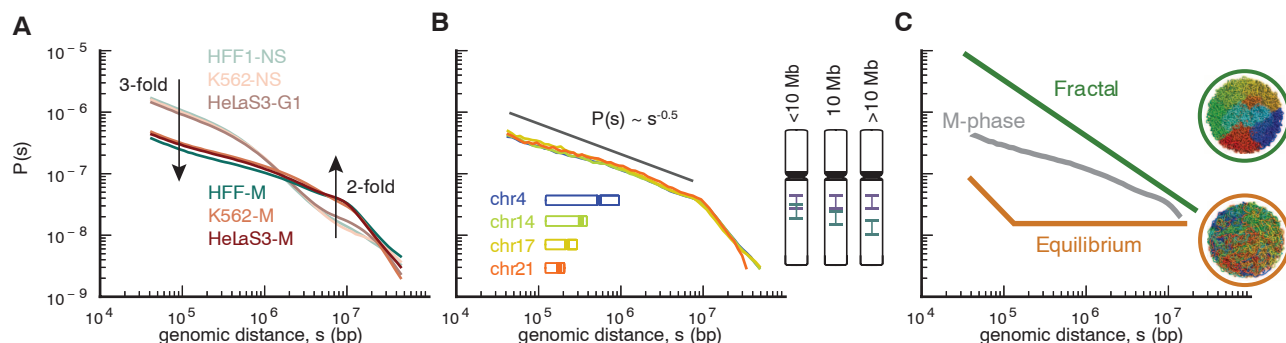


Fig. 3. Contact probability as a function of genomic distance. To compare experiments with different numbers of reads, here and below all $P(s)$ plots are normalized to integrate to one. (A) Contact probability for interphase and mitotic cells averaged over all chromosomes; data sets are as in Fig. 2D. Arrows indicate fold-change from interphase to metaphase. (B) Contact probability for individual HeLa S3 mitotic chromosomes, compared with $P(s) \sim s^{-0.5}$. Diagrams on the right illustrate that loci separated by fewer than 10 Mb occupy overlapping longitudinal

positions, whereas loci separated by more than 10 Mb rarely overlap. (C) Mitotic $P(s)$ below 10 Mb plotted against schematic $P(s)$ for fractal and equilibrium globule states. Insets show spatial organization of simulated polymer fibers for each state, in which fibers (here and below) are colored from blue to red along their lengths. Observed $P(s)$ for mitotic chromosomes falls in between that of an equilibrium globule, in which regions of the polymer are highly mixed, and a fractal globule, in which different regions are spatially segregated.

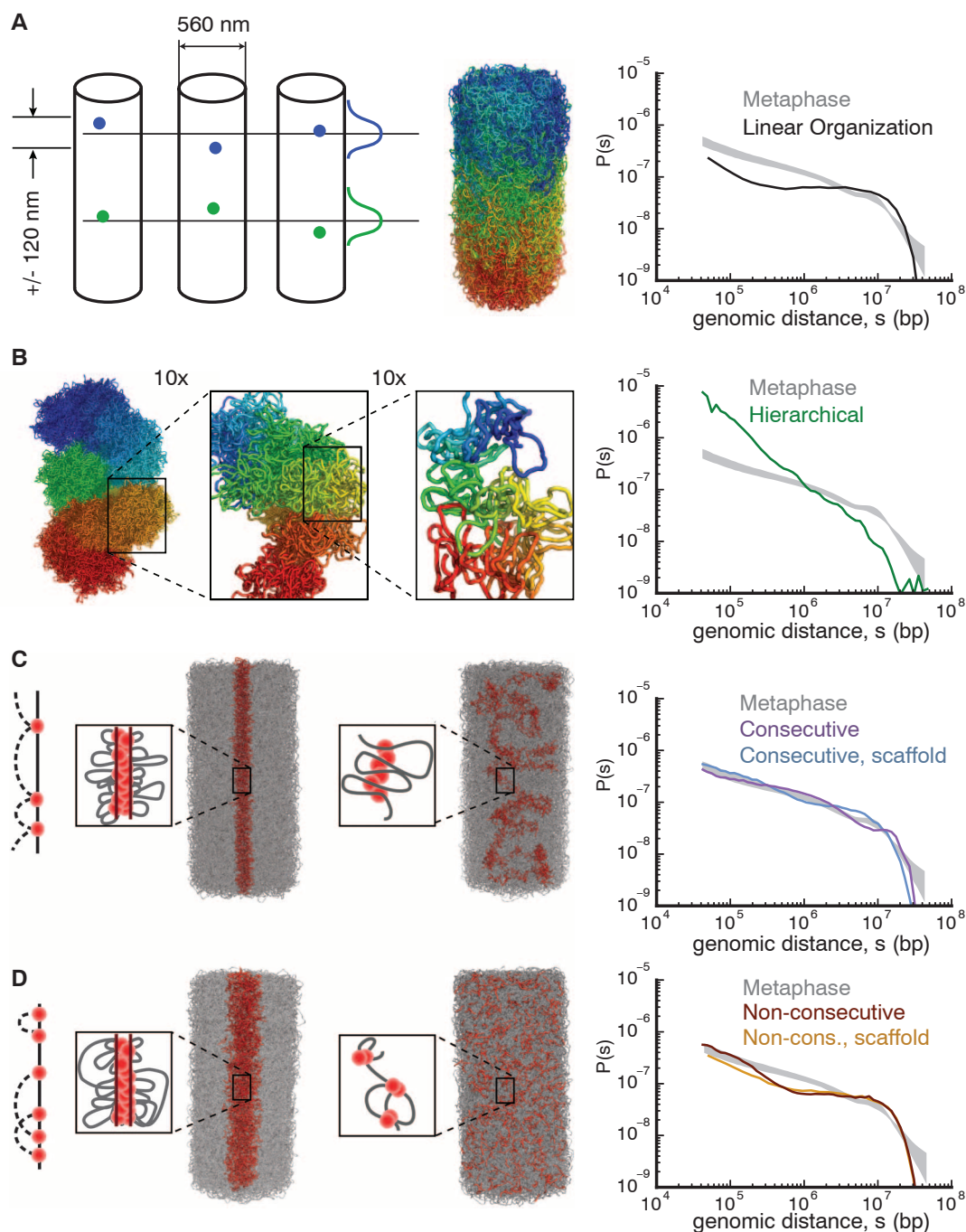
(approximately equivalent to chromosome 17, which is 1 μm long and 0.5 μm in diameter) as a polymer of 128,000 monomers, each representing three nucleosomes (~ 600 bp), with a diameter of 10 nm and a persistence length of 4 monomers (10 to 12 nucleosomes) (34). We chose these parameters to best represent a 10-nm fiber (27) because the pervasiveness of the 30-nm fiber in vivo has become increasingly contested (22, 35, 36). Further simulations have shown that our main results hold for a 30-nm fiber, as well as for a more flexible 10-nm fiber (fig. S18), and our results are relatively insensitive to the local structure of the chromatin fiber. Polymer models were simulated

by using Langevin dynamics, with interactions and constraints specific to each model. We account for topoisomerase II activity (37, 38) by allowing chromatin fibers to occasionally pass through each other and thus change the topological state of a chromosome (27, 39); this was accomplished by setting a finite energy cost for two monomers to occupy the same volume.

First, we tested whether an equilibrium model with a combination of cylindrical geometry and linear organization is sufficient to reproduce the observed $P(s)$ (Fig. 4A and fig. S19). This model imposes linear organization by constraining monomers to have reproducible mean longitudinal

positions with a 120-nm standard deviation (SD) along the longitudinal axis of the chromosome, as observed with microscopy (33). Simulations of this model generate a layered chromosome conformation in which the fall-off in contact probability $P(s)$ naturally emerges at ~ 10 Mb, demonstrating that linear organization and a fall-off in contact probability are connected (fig. S19 and movie S1). However, in contrast to the Hi-C data, models constrained only by cylindrical geometry and linear organization produce $P(s)$ with a plateau from 200 kb to 10 Mb (Fig. 4A) and are highly mixed within a layer, similar to an equilibrium globule (Fig. 3C and fig. S20).

Fig. 4. Polymer models of mitotic chromosome organization (left) and their corresponding $P(s)$ (right). Experimental $P(s)$ in metaphase (gray shaded area) is bounded by minimum and maximum $P(s)$ calculated from six independent Hi-C data sets (three cell lines). (A) Linear organization model. Each monomer is constrained to have reproducible mean longitudinal positions with 120 nm SD (illustrated in the diagram, next to an example of a polymer conformation for this model). (B) Hierarchical model formed by successively folding the fiber into a next-level fiber, here by using loops with average length of 9 kb, 240 kb, and 4.8 Mb; conformation is colored from blue to red at each level of magnification (figs. S21 and S22). (C) Models with consecutive loops, cylindrical geometry, and linear organization. Bases of the loops (red) are either attracted to a central scaffold (left) or free (middle). For optimal loop sizes, $P(s)$ curves for these models approach experimental $P(s)$. (D) Models with nonconsecutive loops, cylindrical geometry, and linear organization, either attracted to a central scaffold (left) or free (middle). Nonconsecutive loops are obtained by randomizing positions of consecutive loop bases while maintaining loop lengths. Models with nonconsecutive loops have worse agreement with metaphase $P(s)$ than that of models with consecutive loops (fig. S24).



We evaluated two major classes of models for mitotic chromosomes: hierarchical models (20, 21) and loops/scaffold models (15, 18, 19). In hierarchical models, the chromatin fiber is successively folded into a thicker fiber at each hierarchical level. Models with both looping and solenoidal twisting at each level were implemented by use of constraints on distances and angles between subsets of monomers (Fig. 4B and figs. S21 and S22). We found that although hierarchical folding can produce chromosomes with the correct geometry and linear organization, the contact probability for these models decreased much more sharply than was observed in Hi-C (Fig. 4B and fig. S22). This indicates that hierarchical models overly constrain the chromatin fiber because most of the contacts occur locally, within the first- and second-level fibers.

To study models with loops emanating from a scaffold (17, 18), we induced formation of consecutive loops, attracted their bases to a central scaffold, and imposed linear ordering and cylindrical geometry (Fig. 4C and movie S2). To form consecutive loops, we chose a random subset of genomic positions as loop bases; each loop base was then connected by harmonic bonds to immediately preceding and subsequent loop bases along the chromosome (27). This process forms an array of consecutive nonoverlapping loops with an exponential distribution of loop lengths. For each average loop length, we equilibrated the system (fig. S23) and found that chromosome models with 80 kb average loop size closely reproduce experimental $P(s)$ (Fig. 4C and fig. S18) and yield moderately mixed chromatin organization within layers (fig. S20 and movies S3 and S4). Surprisingly, a scaffold-free model with consecutive 120-kb loops still achieved good agreement with experimental $P(s)$ (Fig. 4C and fig. S18). This stems from the spatial proximity of neighboring consecutive loops and explains how short-range interactions (~100 kb) can increase contact probabilities over much longer ranges (~5 Mb) (fig. S24). Loop sizes for our best-fitting models closely agree with earlier measurements: 80 kb (40), 30 to 90 kb (18), and 83 ± 29 kb (41).

Models with only attraction to a scaffold (fig. S19), or with nonconsecutive loops (Fig. 4D), are inconsistent with experimental $P(s)$. Additionally, cell-to-cell variability in loop positions and sizes is required to reproduce the homogeneous population-averaged Hi-C maps (fig. S17). Taken together, stochastic arrays of consecutive loops, either on or off the scaffold, are essential for agreement with Hi-C data.

A Two-Step Process for Mitotic Chromosome Folding

In our polymer models, mitotic chromosome organization is described by two main features: arrays of consecutive 80- to 120-kb loops and linear ordering of loci separated by more than 10 Mb. Consecutive loops could be formed by linear compaction of the chromatin fiber (42) by loop-extruding, SMC-containing complexes

in early prophase—for example, as proposed by Alipour and Marko (43). Arrays of loops have also been proposed for mitotic and meiotic chromosome organization on the basis of cytological and molecular considerations (44). Chromosomes with consecutive loops resemble a polymer bottle-brush model (Fig. 5 and fig. S24), which has previously been suggested as a model for condensed chromosomes (34). The second feature, linear ordering above 10 Mb, was imposed in our consecutive-loop models of the final folded state (Fig. 4C) but could emerge naturally from axial compression of long prophase chromosomes (19, 38, 42, 44). Compression cannot be accomplished by increased chromatin-chromatin affinity alone because this would lead to condensation into a globular ge-

ometry (17, 34, 43). However, mechanisms that locally compress the backbone formed by loop bases naturally allow for active anisotropic compression into a shorter and thicker chromosome, with the same width regardless of chromosome length (14). Additionally, differences in the duration or efficiency of the first and second stages of chromosomal condensation provide a natural mechanism for condensation-related proteins to separately affect mitotic chromosome length and width (23).

These considerations led us to propose a model in which mitotic chromosomes are formed by a two-stage process (Fig. 5): First, an interphase chromosome is linearly compacted into an array of consecutive loops, forming a prophaselike chromatid of ~5 μm in length and ~1 μm in di-

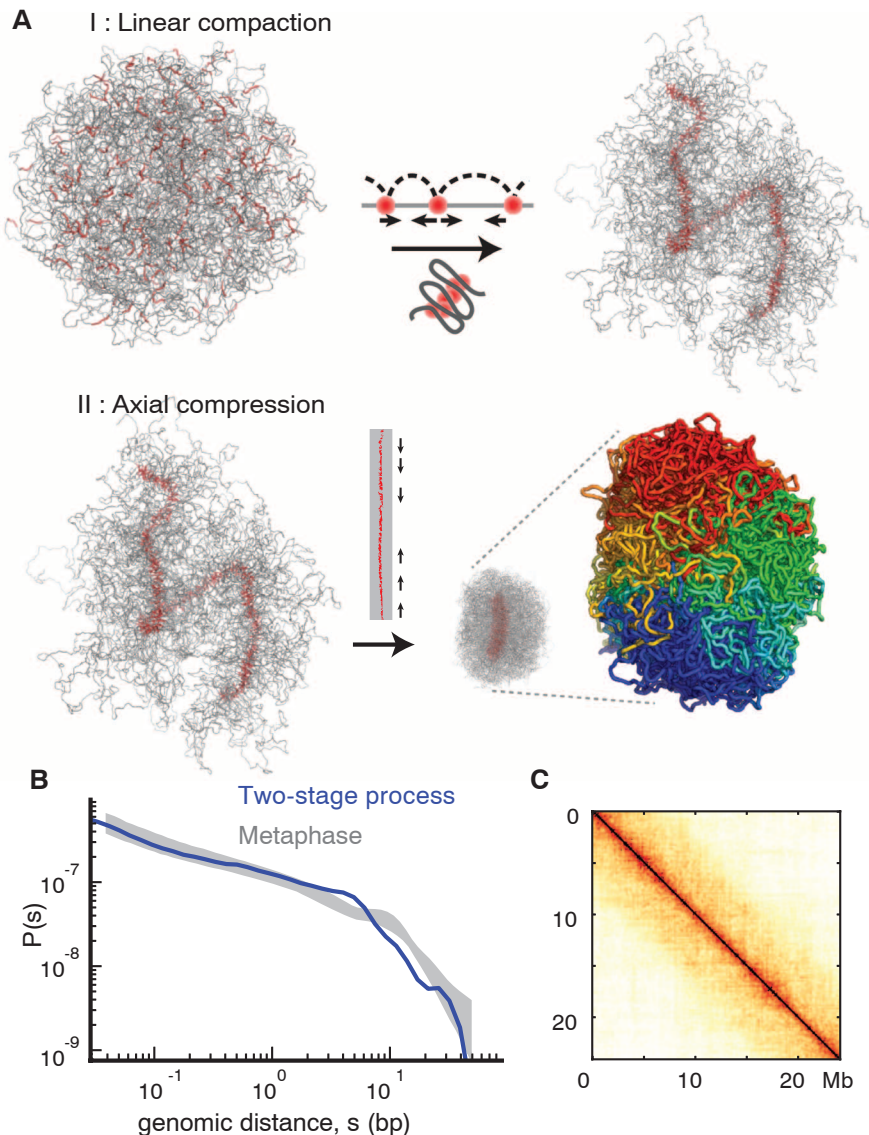


Fig. 5. A two-stage process of mitotic chromosome folding. (A). Stage I: Linear compaction by formation of consecutive chromosomal loops leads to the formation of a fiber of loop bases. Stage II: Homogeneous axial compression of the fiber's backbone leads to the formation of a dense chromosome. This two-stage process produces a chromosome with the appropriate cylindrical geometry and linear organization (genomic position is indicated by the coloring from blue to red). (B) Contact probability $P(s)$ for the two-stage process compared with observed $P(s)$ (gray shaded area, as in Fig. 4). (C). Average contact map for chromosomes folded by the two-stage process.

ameter. Second, this chromatid undergoes homogeneous axial compression (27).

We simulated the first state by creating an array of consecutive loops, without explicitly modeling loop extrusion. To simulate the second stage, we imposed interactions between nearby loop bases and concomitantly condensed loops using poor solvent conditions. The resulting conformations naturally acquire cylindrical chromosomal geometry and linear ordering and demonstrate good agreement with experimental Hi-C and microscopy data (Fig. 5, fig. S20, and movies S5 and S6).

Discussion

The interphase and mitotic states represent two functionally distinct 3D organizations of the genome. We found that mitotic chromosomes preserve few if any of the structural features that define interphase chromosomes. We also found that metaphase chromosomes acquire a similar organization in different cell types. This raises the question of how epigenetic information is inherited through mitosis, when transcription largely ceases and many proteins, including RNA polymerase, dissociate from chromosomes. Current models of epigenetic memory involve retention of key transcription factors and chromatin architectural proteins at specific loci [“bookmarking” (45)], but roles of higher-order chromatin folding have also been proposed (46). In mitotic chromosomes, we not only found that the large-scale spatial segregation into cell type-specific A/B compartments is lost, but that locally folded TADs that are conserved between cell types are also largely absent. Additionally, the homogeneous mitotic interaction maps show no evidence for the emergence of new compartments, including a lack of preferential interactions within chromosomal bands. These observations imply that higher-order chromatin structures have to form de novo in early G₁ and do not themselves carry epigenetic memory. It is possible that their reemergence in early G₁ is driven by histone marks, DNA methylation, and protein complexes that remain on DNA through mitosis, such as at TAD boundaries (47) or at key gene regulatory elements (48).

Our proposed model of a metaphase chromosome as a compressed array of consecutive loops (Fig. 4C) is supported by several previously described structural features. Imaging studies have shown that individual loci do not occupy reproducible radial positions (33). Additionally, contiguous chromosomal regions of <1 Mb do not fill a full radial cross-section of the chromosome, whereas regions of several megabase do (49). Reproduced by our model, these features are consistent with incomplete mixing within a 10-Mb layer (fig. S20). Average loop lengths of 80 to 120 kb, which best reproduce experimental $P(s)$ in our models, agree with previous estimations of loop lengths (18, 40, 41). We remain agnostic about the role of a scaffold because models with compact, diffuse, or no scaffold agree equally well with Hi-C data (fig. S26). Further, the loops in our models are irregular and would form a

uniform density “melt,” which is consistent with recent electron microscopy and small-angle x-ray scattering studies (fig. S20) (22, 50).

One aspect makes our proposed model of the mitotic chromosome different from earlier proposals. Several classical models assumed a highly structured folding, with regular solenoids, loops of fixed length, or distinct hierarchical levels. Our model achieves agreement with earlier experiments and our Hi-C data by incorporating variability at all levels of assembly: cell-to-cell differences in loop positions and lengths and substantial mixing within a 10-Mb layer. Moreover, classical models of solenoidal and hierarchical folding would require machinery able to manipulate chromatin at the micrometer and multi-megabase scales; similarly, a recently proposed polymer model (51) implies a mechanism to control the formation of long-range loops. Our model, on the contrary, proposes largely local loop formation followed by a linear compression of the resulting backbone of loop bases, allowing the rest of the chromatin fiber to stay in a largely disordered ensemble. The use of local folding mechanisms and the lack of strict sequence-driven control makes this two-stage folding mechanism robust with respect to chromosome sizes, compositions, and genomic rearrangements. However, the current resolution of our data does not rule out the use of different subsets from a large set of specific sequence elements as loop bases in different cells.

Future studies performed at higher resolution—for example, through deeper sequencing of Hi-C libraries, single-cell Hi-C, and at multiple time points through prophase and telophase-early G₁—may lead to insights into the finer-scale organization of chromosomes and the intricate folding pathways that connect interphase and mitotic chromosome structures.

References and Notes

1. J. Dekker, *Science* **319**, 1793–1794 (2008).
2. P. Fraser, W. Bickmore, *Nature* **447**, 413–417 (2007).
3. G. Fudenberg, G. Getz, M. Meyerson, L. A. Mirny, *Nat. Biotechnol.* **29**, 1109–1113 (2011).
4. Y. Zhang et al., *Cell* **148**, 908–921 (2012).
5. M. R. Hübner, D. L. Spector, *Annu. Rev. Biophys.* **39**, 471–489 (2010).
6. J. Dekker, K. Rippe, M. Dekker, N. Kleckner, *Science* **295**, 1306–1311 (2002).
7. E. Lieberman-Aiden et al., *Science* **326**, 289–293 (2009).
8. Y. Markaki et al., *Cold Spring Harb. Symp. Quant. Biol.* **75**, 475–492 (2010).
9. J. R. Dixon et al., *Nature* **485**, 376–380 (2012).
10. E. P. Nora et al., *Nature* **485**, 381–385 (2012).
11. A. Sanyal, B. R. Lajoie, G. Jain, J. Dekker, *Nature* **489**, 109–113 (2012).
12. W. Flemming, *Schriften des Naturwissenschaftlichen Vereins für Schleswig-Holstein* **3**, 23 (1878).
13. E. J. DuPraw, *Nature* **209**, 577–581 (1966).
14. A. L. Bak, J. Zeuthen, F. H. Crick, *Proc. Natl. Acad. Sci. U.S.A.* **74**, 1595–1599 (1977).
15. M. P. Marsden, U. K. Laemmli, *Cell* **17**, 849–858 (1979).
16. J. R. Swedlow, T. Hirano, *Mol. Cell* **11**, 557–569 (2003).
17. K. Maeshima, M. Eltsov, *J. Biochem.* **143**, 145–153 (2008).
18. J. R. Paulson, U. K. Laemmli, *Cell* **12**, 817–828 (1977).
19. K. Maeshima, U. K. Laemmli, *Dev. Cell* **4**, 467–480 (2003).
20. J. Sedat, L. Manuelidis, *Cold Spring Harb. Symp. Quant. Biol.* **42**, 331–350 (1978).

21. A. S. Belmont, J. W. Sedat, D. A. Agard, *J. Cell Biol.* **105**, 77–92 (1987).
22. Y. Nishino et al., *EMBO J.* **31**, 1644–1653 (2012).
23. J. F. Marko, *Chromosome Res.* **16**, 469–497 (2008).
24. N. Kireeva, M. Lakonishok, I. Kireev, T. Hirano, A. S. Belmont, *J. Cell Biol.* **166**, 775–785 (2004).
25. J. Dostie et al., *Genome Res.* **16**, 1299–1309 (2006).
26. M. Imakaev et al., *Nat. Methods* **9**, 999–1003 (2012).
27. Materials and methods are available as supplementary materials on Science Online.
28. M. Simonis et al., *Nat. Genet.* **38**, 1348–1354 (2006).
29. G. Fudenberg, L. A. Mirny, *Curr. Opin. Genet. Dev.* **22**, 115–124 (2012).
30. A. Rosa, N. B. Becker, R. Everaers, *Biophys. J.* **98**, 2410–2419 (2010).
31. R. Lua, A. L. Borovinskiy, A. Y. Grosberg, *Polymer (Guildf.)* **45**, 717–731 (2004).
32. G. Li, G. Sudlow, A. S. Belmont, *J. Cell Biol.* **140**, 975–989 (1998).
33. Y. G. Strukov, A. S. Belmont, *Biophys. J.* **96**, 1617–1628 (2009).
34. J. F. Marko, E. D. Siggia, *Mol. Biol. Cell* **8**, 2217–2231 (1997).
35. E. Fussner et al., *EMBO Rep.* **13**, 992 (2012).
36. K. Maeshima, S. Hihara, H. Takata, *Cold Spring Harb. Symp. Quant. Biol.* **75**, 439–444 (2010).
37. Y. Adachi, M. Luke, U. K. Laemmli, *Cell* **64**, 137–148 (1991).
38. K. Samejima et al., *J. Cell Biol.* **199**, 755–770 (2012).
39. J. L. Sikorav, G. Jannink, *Biophys. J.* **66**, 827–837 (1994).
40. D. A. Jackson, P. Dickinson, P. R. Cook, *EMBO J.* **9**, 567–571 (1990).
41. W. C. Earnshaw, U. K. Laemmli, *J. Cell Biol.* **96**, 84–93 (1983).
42. T. Hirota, D. Gerlich, B. Koch, J. Ellenberg, J. M. Peters, *J. Cell Sci.* **117**, 6435–6445 (2004).
43. E. Alipour, J. F. Marko, *Nucleic Acids Res.* **40**, 11202–11212 (2012).
44. N. Kleckner et al., *Proc. Natl. Acad. Sci. U.S.A.* **101**, 12592–12597 (2004).
45. K. D. Sarge, O. K. Park-Sarge, *Trends Biochem. Sci.* **30**, 605–610 (2005).
46. W. Deng, G. A. Blobel, *Curr. Opin. Genet. Dev.* **20**, 548–554 (2010).
47. N. E. Follmer, A. H. Wani, N. J. Francis, *PLOS Genet.* **8**, e1003135 (2012).
48. S. Kadake et al., *Cell* **150**, 725–737 (2012).
49. Y. G. Strukov, Y. Wang, A. S. Belmont, *J. Cell Biol.* **162**, 23–35 (2003).
50. P. König, M. B. Braunfeld, J. W. Sedat, D. A. Agard, *Chromosoma* **116**, 349–372 (2007).
51. Y. Zhang, D. W. Heermann, *PLOS ONE* **6**, e29225 (2011).

Acknowledgments: All data will be made publicly available through the Gene Expression Omnibus. This work was supported by grants from the National Cancer Institute (Physical Sciences–Oncology Center at MIT U54CA143874 to L.A.M.) and the National Human Genome Research Institute (HG003143 to J.D.), the Human Frontier Science Program (to J.D.), and a W. M. Keck Foundation distinguished young scholar in medical research grant (to J.D.). We thank J. A. Stamatoyannopoulos and R. Humbert for designing part of the 5C primers; C. Smith and A. Hawkins for technical help; J. Benanti for providing HFF1 cell stock and discussion; M. Walhout, Dekker lab, and Mirny lab members for discussions; and the UMMS deep sequencing core for sequencing 5C and Hi-C libraries. The data are available at ArrayExpress database www.ebi.ac.uk/arrayexpress, accession no. E-MTAB-1948. Information about Gene Expression Omnibus accession nos. can be found in the supplementary materials. Data visualizations can also be found at <http://hic.umassmed.edu> and <http://mirnylab.mit.edu>.

Supplementary Materials

www.sciencemag.org/content/342/6161/948/suppl/DC1
Materials and Methods

Figs. S1 to S26

Tables S1 to S3

References

Movies S1 to S6

4 February 2013; accepted 17 October 2013

Published online 7 November 2013;

10.1126/science.1236083

Observing the Dynamics of Dipole-Mediated Energy Transport by Interaction-Enhanced Imaging

G. Günter,¹ H. Schempp,¹ M. Robert-de-Saint-Vincent,¹ V. Gavryusev,¹ S. Helmrich,¹ C. S. Hofmann,¹ S. Whitlock,^{1*} M. Weidemüller^{1,2*}

Electronically highly excited (Rydberg) atoms experience quantum state-changing interactions similar to Förster processes found in complex molecules, offering a model system to study the nature of dipole-mediated energy transport under the influence of a controlled environment. We demonstrate a nondestructive imaging method to monitor the migration of electronic excitations with high time and spatial resolution, using electromagnetically induced transparency on a background gas acting as an amplifier. The continuous spatial projection of the electronic quantum state under observation determines the many-body dynamics of the energy transport.

Watching a many-body quantum system evolve under the influence of well-controlled interactions is the essence of Feynman's vision for a quantum simulator (1–3), which could be used to address fundamental questions about coherent quantum and open-system dynamics in diverse settings (4, 5). One such question is the nature of energy transfer in real physical systems, such as complex chemical reactions, excitonic transport in organic semiconductors (6) and molecular aggregates (7), or photosynthetic light-harvesting complexes (8). Both disorder and environment play crucial roles in the transport dynamics. In particular, it is unclear to what extent quantum mechanical effects may enhance or reduce the transport efficiency (9). The simulation of random walks in the quantum regime has recently been rendered accessible using manipulation techniques for single atoms (10, 11) and photons (12).

Ultracold gases of highly excited (Rydberg) atoms, which possess exceptionally large dipole moments and long-range quantum state-changing interactions, represent a unique model system (13, 14) for the study of dipole-induced energy transport in a many-body environment. Evidence of Rydberg energy exchange has been deduced from spectroscopic properties of optical Rydberg excitation (15–18) and from the macroscopic transfer of Rydberg state populations (19, 20). So far, however, the direct microscopic observation of Rydberg energy transport has remained out of reach because of the difficulty in spatially following the migration of Rydberg excitations in real time. The first images of Rydberg atoms were recently obtained by means of destructive methods such as field-ion microscopy (21), optical pumping of Rydberg atoms back to the

ground state followed by high-resolution fluorescence imaging (22), or core electron absorption in two-electron Rydberg atoms (23). Here, we realize a nondestructive and state-selective optical imaging technique, as proposed in (24, 25), for the investigation of Rydberg energy transport

under continuous observation. Each Rydberg impurity locally triggers strong absorption by many neighboring background atoms, allowing one to image small numbers of otherwise invisible impurities. We observe and control transport dynamics on micrometer length scales with microsecond resolution. We show that the dynamics are affected by the back-action of the continuous non-destructive measurement process, which induces a transition to quasi-classical diffusive transport. Furthermore, the Rydberg blockade effect, in which the presence of a single Rydberg atom strongly suppresses subsequent excitation of additional atoms (13), introduces a characteristic length scale to the transport dynamics, similar to that of self-assembling systems.

The basic idea of our imaging method (24) is to exploit the strong interactions between impurity atoms in the Rydberg state $|i\rangle$ with a bath of surrounding atoms, each optically coupled to a probe Rydberg state $|p\rangle$. Impurity-probe interactions cause a level shift of the $|p\rangle$ states in the vicinity of each impurity; this shift is mapped onto the light field by means of an electromagnetically induced transparency (EIT) resonance (26–28). Recording the probe laser transmission

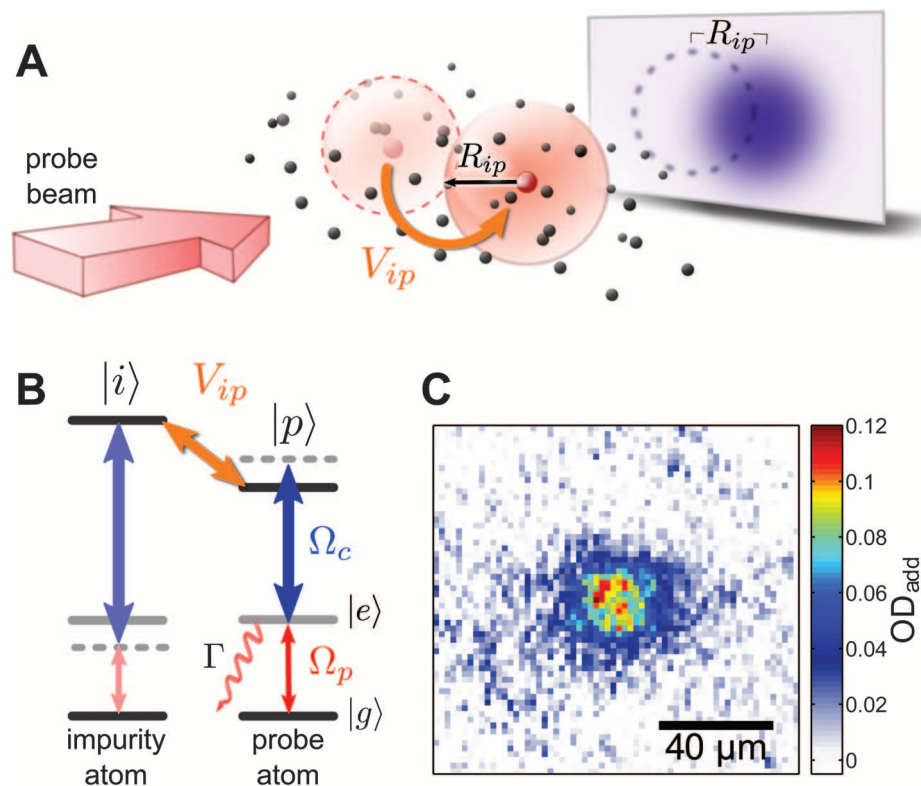


Fig. 1. Interaction-enhanced imaging scheme for studying transport dynamics. (A) Each impurity (red dot) breaks the EIT condition for probe atoms within a volume characterized by R_{ip} because of the interaction-induced level shift on an auxiliary Rydberg state $|p\rangle$ of the probe atoms. These atoms therefore strongly absorb the probe beam, casting a shadow in the images. State-exchange interactions with strength V_{ip} lead to impurity transport. (B) Simplified level diagram showing the involved states in the excitation of the Rydberg impurities $|i\rangle$ as well as the states involved in the EIT ladder scheme, which is used to probe the level shift on the state $|p\rangle$. (C) Averaged optical density image of an impurity distribution for approximately 100 impurities.

¹Physikalisches Institut, Universität Heidelberg, 69120 Heidelberg, Germany. ²University of Science and Technology of China, Hefei, Anhui 230026, China.

*Corresponding author. E-mail: whitlock@physi.uni-heidelberg.de (S.W.); weidemuller@uni-heidelberg.de (M.W.)

with a charge-coupled device (CCD) camera produces an absorption image of the distribution of impurities (Fig. 1A). The ultracold atomic gas is dressed by a strong coupling laser field (with Rabi frequency Ω_c) and a weaker probe laser field (Ω_p). The intermediate state $|e\rangle$ is short-lived, with a spontaneous scattering rate Γ . Destructive interference between excitation pathways decouples the atoms from the probe laser (29), except in the vicinity of an impurity atom where the EIT condition is broken, causing the surrounding probe atoms to become strongly absorbing.

The radius of the absorbing spot around each impurity is given by the interstate blockade radius R_{ip} , corresponding to the distance at which the EIT spectral half width ($\Omega_c^2/2\Gamma$ in the weak probe limit neglecting laser linewidths) equals the interaction-induced level shift (Fig. 1B). Thus, each impurity is effectively accompanied by a sphere of absorbing atoms, which enables us to monitor its location and dynamics. Strong impurity-

probe interactions are achieved using resonant Rydberg-Rydberg interactions (Förster resonance) (13). The Rydberg blockade introduces another important length scale to the system: the impurity-impurity blockade radius R_{ii} , which is the closest distance between two impurities after laser excitation. By choosing appropriate states or by using modest electric fields to tune the Förster resonance, it is possible to independently vary R_{ii} and R_{ip} .

To demonstrate the essential features of the imaging method, we excited Rydberg impurities in state $|i = 50S\rangle$ in a small central region of the cloud (30). The excitation pulse was followed by the acquisition of the probe absorption image under EIT conditions, using separate lasers coupled to the probe state $|p = 37S\rangle$. For sufficiently weak probe light, blockade effects between the probe atoms, which would lead to a reduced transparency, can be neglected (24). From comparison with an image without impurities, we could deter-

mine the additional optical density OD_{add} due to the presence of impurities, from which we extracted the number of additional two-level absorbers N_{add} . A typical image of approximately 100 impurity atoms (averaged over 100 shots) is shown in Fig. 1C. In Fig. 2, we show the number of additional absorbers as a function of the number of impurity atoms N_{imp} measured by field ionization detection for a higher density of ground-state atoms and a smaller excitation volume. For low numbers of impurities, a linear dependence is observed because each impurity blocks roughly the same number of probe atoms. From the slope, we determine an amplification factor of $A = N_{\text{add}}/N_{\text{imp}} = 19 \pm 2$.

The optical depth per interstate blockade sphere is ~ 0.5 , which suggests that our images might be sensitive to single impurities. At present, however, we are limited by our optical resolution, which is larger than both R_{ip} and R_{ii} , allowing us to clearly detect as few as five impurities in a single shot with approximate time resolution of 5 μs . By improving the optical resolution below R_{ip} , it will ultimately be possible to follow the evolution of individual impurities in real time. For increasing numbers of impurities (~ 10), we observed a saturation of the number of additional absorbers (Fig. 2). This is a manifestation of the Rydberg blockade effect resulting in a saturation of the density of impurities. For stronger excitation, the number of impurities increases further because of excitation in the low-density wings of the cloud, but the number of additional absorbers is only slightly increased. To study transport of the kind

$$|i\rangle \otimes |p\rangle \rightleftharpoons |p\rangle \otimes |i\rangle \quad (1)$$

we switch to states that possess strong dipolar state-exchange interactions. The effects of the Rydberg blockade and the continuous optical observation lead to interesting new features. In particular, the spatial correlations due to the Rydberg blockade and the dissipation induced by the scattering of probe light, which acts as a controlled environment, have a strong impact on the intrinsically coherent transfer mechanism. In a simplified picture, we consider coherent state exchange of an atom in state $|i\rangle$ with all of the surrounding atoms. The hopping frequency $\omega_{\text{hop}}(r) \approx 2\rho_{\text{pp}}(r)V_{\text{dd}}(r)$ between an impurity and an atom at distance r depends on the dipole-dipole exchange interaction $V_{\text{dd}}(r) = C_3/r^3$ (where C_3 is the dipole-dipole coupling strength) and on the population $\rho_{\text{pp}}(r)$ of the $|p\rangle$ state. Through the dependence of ρ_{pp} on the laser fields and the blockade effect, it is possible to control the hopping dynamics. Light scattering by probe atoms causes a measurement-induced environmental decoherence rate $\gamma_{\text{env}} \approx \Omega_p^2/\Gamma$. Through the density or varying Ω_p , this can be controlled independently of ω_{hop} . For our parameters, we estimate that γ_{env} is typically 150 times the peak value of ω_{hop} . Therefore, we expect classical hopping to dominate with a rate $\Gamma_{\text{hop}}(r) \approx \omega_{\text{hop}}^2(r)/\gamma_{\text{env}}$ to each of the neighboring atoms. Because of the competition between the interstate Rydberg blockade and the $1/r^3$ scaling of V_{dd} ,

Fig. 2. Dependence of the number of additional absorbers on the number of impurities. For small numbers of impurities, the number of additional absorbers grows linearly. The black line is a fit used to determine the amplification factor. For large numbers of impurities, the additional absorbers and the blocked fraction saturate as a result of the Rydberg blockade effect. In this regime, the additional impurities are excited only in the low-density wings of the cloud and therefore do not significantly increase the number of additional absorbers.

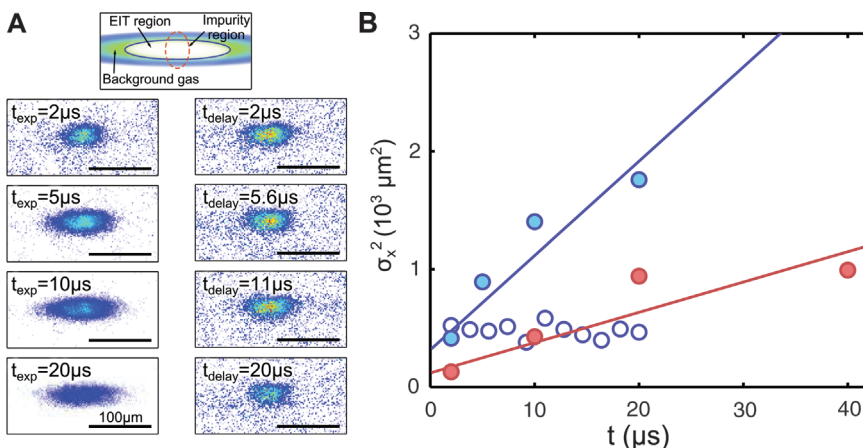
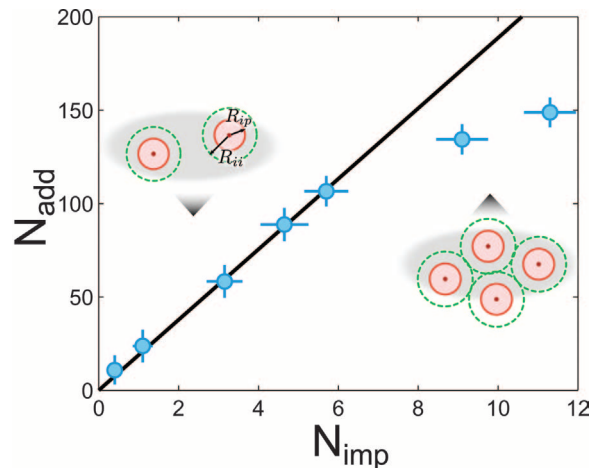


Fig. 3. Diffusion of Rydberg impurities. (A) The strong exchange interactions between impurities and probe atoms lead to an expansion of the Rydberg distribution in time in the presence of the imaging light. The top sketch shows the experimental geometry; the following images show the additional optical depth for different exposure times (left column) or different delay times (right column), with fixed color scale (on the Förster resonance). (B) The squared width of the distribution σ_x^2 increases approximately linearly with time. On the Förster resonance (solid blue circles), the expansion is faster than off resonance (solid red circles). For comparison, open blue circles show σ_x^2 on resonance for fixed exposure time (2 μs), but with varying delay between the excitation and the illumination of the atoms with imaging light.

there is a preferred hopping distance $r_{\text{hop}} \approx R_{ip}$. This introduces an intrinsic scale into the transport dynamics, similar to that of self-assembled systems. We expect the width of the impurity distribution in each direction $\sigma(t)$ to grow as $\sigma^2(t) = \sigma^2(0) + 2Dt$, with $D \approx (5/18)R_{ip}^2\Omega_p^2/\Gamma$ (see supplementary text).

To investigate these dynamics, we excited impurities in the $|i = 38S\rangle$ state and performed EIT with the $|p = 37S\rangle$ state. The pair state $|38S\rangle \otimes |37S\rangle$ couples to the exchange-symmetric pair state $|37P\rangle \otimes |37P\rangle$. Therefore, energy transport can occur as a result of $|38S\rangle \rightleftharpoons |37S\rangle$ exchange. The coupling $C_3 = 2\pi \times 1.6 \text{ GHz}\cdot\mu\text{m}^3$ gives $R_{ip} = 6.3 \pm 0.5 \mu\text{m}$. Figure 3A (left column) shows images of the impurity distribution for different exposure times. The distribution is seen to expand horizontally as a function of imaging exposure time. Expansion in the vertical direction was not observed because of the smaller size of the EIT coupling beam in this direction. In addition to the growing width, we observed a slight decay of N_{add} that can be attributed to the lifetime of the $|38S\rangle$ Rydberg state ($\sim 30 \mu\text{s}$). To perform a quantitative analysis of the dynamics, we extracted the second central moment σ_x^2 of the imaged distributions as a function of the exposure time. As shown in Fig. 3B for different conditions, σ_x^2 grows approximately linearly. On the Förster resonance and including the effect of time integration during the exposure pulse (see supplementary materials), we find $D = 80 \pm 13 \mu\text{m}^2/\mu\text{s}$. From the simple scaling discussed above, $D_{\text{expect}} = 55 \pm 23 \mu\text{m}^2/\mu\text{s}$, which agrees with the measurements.

To verify the role of the environment in the observed dynamics, we also recorded images with a fixed short exposure time of $2 \mu\text{s}$ (Fig. 3A, right column), but with different times between impurity excitation and image acquisition (while $\Omega_p = 0$). We observed no diffusion, thus confirming that impurity-probe interactions are responsible for the dynamics and that the dynamics can indeed be controlled by modifying the environment via the laser fields. Additionally, this result demonstrates that mechanical forces between impurity atoms do not play a role.

Finally, we studied transport in the regime of off-resonant exchange interactions. Earlier experiments under these conditions observed spectral broadening and rapid dephasing of coherent state transfer (*15–17*), which was too high to be explained by the process in Eq. 1 alone. This was attributed to secondary processes resulting in enhanced spatial diffusion, which we can now directly observe. By setting the electric field to zero, we tune the Förster defect to 100 MHz . Here, we expect weaker impurity-probe exchange interactions and a change in the character of the interactions to van der Waals type ($1/r^6$ scaling), resulting in a much smaller r_{hop} .

In this case, we measured slower diffusion with $D = 26 \pm 6 \mu\text{m}^2/\mu\text{s}$ (Fig. 3B). However, this is still almost an order of magnitude faster than can be expected from the above model, including the slightly different experimental parameters (see sup-

plementary text). Our observation thus reveals that the diffusion involves additional processes (such as the always resonant secondary process $|37S\rangle \otimes |37P\rangle \rightleftharpoons |37P\rangle \otimes |37S\rangle$) and that spatial diffusion of secondary $|nP\rangle$ excitations plays an important role for Rydberg-state dynamics and energy transfer.

Future experiments may be able to investigate the transition to coherent quantum dynamics in many-body systems. By detuning the EIT lasers from the intermediate state, decoherence via photon scattering can be suppressed while maintaining the preferred distance for hopping given by the blockade radius. This will allow for the study of excitonic behavior, in which impurities evolve as delocalized superposition states. In this regime, completely different transport behavior is expected, such as localization or enhanced transport, depending on dimensionality, degree of disorder, and dissipation in the system. By switching back to resonant probing, this evolution could be observed. This provides an ideal platform for benchmarking current theories used to explain energy transport in complex systems such as light-harvesting complexes, where the competition between mechanical and excitonic transport and the role of interactions are still open questions (*8*).

References and Notes

1. R. Feynman, *Int. J. Theor. Phys.* **21**, 467–488 (1982).
2. I. Bloch, J. Dalibard, S. Nascimbène, *Nat. Phys.* **8**, 267–276 (2012).
3. J. I. Cirac, P. Zoller, *Nat. Phys.* **8**, 264–266 (2012).
4. J. T. Barreiro *et al.*, *Nature* **470**, 486–491 (2011).
5. H. Weimer, M. Müller, I. Lesanovsky, P. Zoller, H. P. Büchler, *Nat. Phys.* **6**, 382–388 (2010).
6. H. Najafav, B. Lee, Q. Zhou, L. C. Feldman, V. Podzorov, *Nat. Mater.* **9**, 938–943 (2010).
7. A. M. van Oijen, M. Ketelaars, J. Köhler, T. J. Aartsma, J. Schmidt, *Science* **285**, 400–402 (1999).
8. E. Collini, *Chem. Soc. Rev.* **42**, 4932–4947 (2013).
9. M. Sarovar, A. Ishizaki, G. R. Fleming, K. B. Whaley, *Nat. Phys.* **6**, 462–467 (2010).

10. M. Karski *et al.*, *Science* **325**, 174–177 (2009).
11. C. Weitenberg *et al.*, *Nature* **471**, 319–324 (2011).
12. A. Peruzzo *et al.*, *Science* **329**, 1500–1503 (2010).
13. T. F. Gallagher, P. Pillet, *Adv. At. Mol. Opt. Phys.* **56**, 161–218 (2008).
14. O. Mülken *et al.*, *Phys. Rev. Lett.* **99**, 090601 (2007).
15. W. R. Anderson, J. R. Veale, T. F. Gallagher, *Phys. Rev. Lett.* **80**, 249–252 (1998).
16. I. Mourachko *et al.*, *Phys. Rev. Lett.* **80**, 253–256 (1998).
17. W. R. Anderson, M. P. Robinson, J. D. D. Martin, T. F. Gallagher, *Phys. Rev. A* **65**, 063404 (2002).
18. J. Nipper *et al.*, *Phys. Rev. Lett.* **108**, 113001 (2012).
19. S. Westermann *et al.*, *Eur. Phys. J. D* **40**, 37–43 (2006).
20. C. S. E. van Ditzhuijzen *et al.*, *Phys. Rev. Lett.* **100**, 243201 (2008).
21. A. Schwarzkopf, R. E. Sapiro, G. Raithe, *Phys. Rev. Lett.* **107**, 103001 (2011).
22. P. Schauß *et al.*, *Nature* **491**, 87–91 (2012).
23. P. McQuillen, X. Zhang, T. Strickler, F. B. Dunning, T. C. Killian, *Phys. Rev. A* **87**, 013407 (2013).
24. G. Günter *et al.*, *Phys. Rev. Lett.* **108**, 013002 (2012).
25. B. Olmos, W. Li, S. Hofferberth, I. Lesanovsky, *Phys. Rev. A* **84**, 041607 (2011).
26. J. D. Pritchard *et al.*, *Phys. Rev. Lett.* **105**, 193603 (2010).
27. C. S. Hofmann *et al.*, *Phys. Rev. Lett.* **110**, 203601 (2013).
28. T. Peyronel *et al.*, *Nature* **488**, 57–60 (2012).
29. M. Fleischhauer, A. Imamoglu, J. P. Marangos, *Rev. Mod. Phys.* **77**, 633–673 (2005).
30. See supplementary materials on Science Online.

Acknowledgments: We thank S. Wüster, T. Pohl, I. Bloch, M. Höning, and M. Fleischhauer for fruitful discussions. Supported by Studienstiftung des deutschen Volkes (G.G. and C.S.H.), Landesgraduierten Akademie (H.S.), EU Marie-Curie program grants FP7-PEOPLE-2011-IEF-300870 (M.R.d.S.V.) and PERG08-GA-2010-277017 (S.W.), EU Marie-Curie program ITN COHERENCE grant FP7-PEOPLE-2010-ITN-265031 (V.G.), the Heidelberg Center for Quantum Dynamics, and Deutsche Forschungsgemeinschaft grant WE2661/10.2.

Supplementary Materials

www.sciencemag.org/content/342/6161/954/suppl/DC1
Materials and Methods
Supplementary Text
Fig. S1
References

19 August 2013; accepted 16 October 2013
10.1126/science.1244843

Selective C-H Fluorination of Pyridines and Diazines Inspired by a Classic Amination Reaction

Patrick S. Fier and John F. Hartwig*

Fluorinated heterocycles are prevalent in pharmaceuticals, agrochemicals, and materials. However, reactions that incorporate fluorine into heteroarenes are limited in scope and can be hazardous. We present a broadly applicable and safe method for the site-selective fluorination of a single carbon-hydrogen bond in pyridines and diazines using commercially available silver(II) fluoride. The reactions occur at ambient temperature within 1 hour with exclusive selectivity for fluorination adjacent to nitrogen. The mild conditions allow access to fluorinated derivatives of medically important compounds, as well as a range of 2-substituted pyridines prepared by subsequent nucleophilic displacement of fluoride. Mechanistic studies demonstrate that the pathway of a classic pyridine amination can be adapted for selective fluorination of a broad range of nitrogen heterocycles.

The selective introduction of fluorine into small molecules can lead to subtle or profound effects on the pK_a (acid dissociation

constant), conformation, solubility, and stability compared to the nonfluorinated counterpart. In particular, the introduction of fluorine into a basic

heterocycle can modulate the basicity and binding properties with only a small change in the steric environment (1–3). These effects are especially prevalent in 2-fluoropyridines where fluorine and nitrogen are juxtaposed. For example, the 2-fluoropyridyl-containing anticancer compound BMS-754807 has higher potency, cell activity, and selectivity than the nonfluorinated analog (4).

A valuable strategy for creating molecular diversity is to form a synthetic intermediate by C–H bond cleavage that can be converted to a variety of products. Because many nucleophiles react with 2-fluoropyridines and related 2-fluoroazines to form products containing new carbon–heteroatom or carbon–carbon bonds, a conversion of heteroarenes to 2-fluoroheteroarenes would create a valuable platform for the preparation of an array of functionalized products. Substitution reactions of 2-fluoroazines occur under milder reaction conditions than the substitution reactions of other 2-haloazines because of the strong electron-withdrawing properties of fluorine.

Although 2-fluoropyridines and -azines have favorable physical properties and are valuable synthetic intermediates, they are difficult to prepare when the heterocycle contains functional groups. The direct fluorination of pyridines and diazines with F_2 is known, but F_2 gas is too hazardous for use in most laboratories, and the reactions with F_2 occur in low yield, even with very simple pyridines and diazines (5–7). Alternative routes to these products include the Balz–Schiemann reaction and nucleophilic aromatic substitution of 2-chloro or 2-nitroazines with anhydrous fluoride. However, the Balz–Schiemann reaction involves strongly acidic and oxidizing conditions to form a diazonium salt intermediate. This potentially explosive species is then heated in anhydrous HF or as an isolated tetrafluoroborate salt to induce fluorination (Fig. 1) (8). Nucleophilic aromatic substitution (9–11) is limited because it occurs in high yields only with strongly electron-deficient heteroarenes. Moreover, both reaction classes require prefunctionalized substrates, which may be inaccessible directly from a complex molecule.

Thus, a method to form 2-fluoropyridines and 2-fluorodiazines directly from pyridines and diazines containing additional functional groups under mild conditions with simple reagents would provide an important tool for synthetic and medicinal chemistry. Here, we report a mild C–H bond fluorination reaction of a broad range of pyridines and diazines with a single, commercially available reagent. The fluorination of several medically important compounds and the application of this fluorination reaction to the synthesis of a range of 2-pyridyl compounds via 2-fluoropyridines are demonstrated.

Our design of a direct fluorination of pyridines and diazines was based on the mechanism

of a classic reaction of pyridines, the Chichibabin reaction. In this reaction, pyridines react with $NaNH_2$ to form 2-aminopyridines (Fig. 1B) (12) by initial coordination of pyridine to the sodium cation, followed by dearomative nucleophilic addition of the amide to the 2-position and subsequent loss of hydride. We considered that a similar reaction could be developed for the fluorination of pyridine C–H bonds if a reagent or set of reagents could be identified having (i) a sufficiently Lewis acidic site to bind the pyridine, thereby increasing the electrophilicity of the adjacent carbon atom; (ii) a sufficiently nucleophilic fluoride to add to the activated carbon of the pyridine; and (iii) the oxidizing potential to aromatize the intermediate σ adduct.

With these considerations in mind, we investigated reactions with commercially available AgF_2 . AgF_2 is an attractive fluorinating agent because it is commercially available in multigram-to-kilogram quantities and is cheaper than many common fluorinating reagents (13). Many years ago, AgF_2 was reported to react with an excess of benzene in refluxing hexane, but a mixture of fluorinated products formed (14). Even earlier, AgF_2 was reported to react with 2,4,6-trifluoropyrimidine, but this reaction occurred in low yield, required high temperature, and has not been investigated since (15). We sought to determine if reactions of AgF_2 with heteroarenes would occur in a milder and more controlled fashion by a pathway analogous to that of the Chichibabin reaction. To do so, we studied the fluorination of 2-phenylpyridine. Reactions with this substrate would show whether AgF_2 is selective for fluorination of the heteroarene over fluorination of an arene and whether fluorination of the heteroarene would be regioselective for the 2-position, as we envisioned.

These studies (summarized in table S1) showed that the reaction between 2-phenylpyridine and two equivalents of AgF_2 in acetonitrile (MeCN) at room temperature formed 2-fluoro-6-phenylpyridine in 56% yield as the only fluorinated product detectable by ^{19}F nuclear magnetic resonance (NMR) spectroscopy. The only organic material detected by gas chromatography was the starting 2-phenylpyridine and 2-fluoro-6-phenylpyridine.

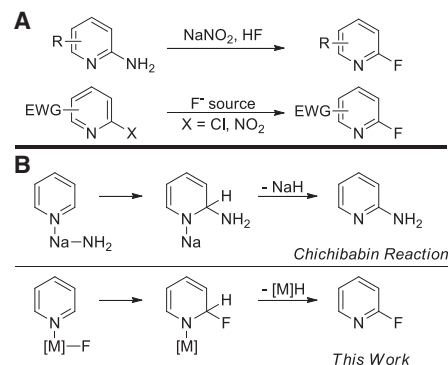


Fig. 1. Toward a milder pyridine fluorination. (A) Conventional syntheses of 2-fluoropyridines. EWG, electron-withdrawing group. (B) The Chichibabin reaction and proposed fluorination reaction.

Reactions performed in solvents other than MeCN did not afford the fluorinated product in appreciable amounts. During the course of the reaction, AgF_2 is reduced to form the yellow solid AgF , which was characterized by ^{19}F NMR spectroscopy (16). The addition of an additional equivalent of AgF_2 at the beginning of the reaction increased the yield of the fluorinated product to 88% (table S1). Although only two equivalents of AgF_2 are present in the balanced equation, some of the silver reagent is consumed through unproductive reactions with the solvent. Even though HF is formally generated as a stoichiometric byproduct in the reaction, and one might envision that this side product would interfere with the reaction or react with auxiliary functional groups, the yield and scope of the reaction was not altered by the addition of base. Likewise, the reactions with AgF_2 are insensitive to light.

The fluorination of a broad range of substituted pyridines occurs with AgF_2 (Fig. 2). Both electron-donating and electron-withdrawing groups at each position of the ring are tolerated. Pyridines containing ketones, esters, amides, acetals, protected alcohols and amines, nitriles, alkyl tosylates, and enolizable carbonyls underwent the fluorination in good yield (17). Notably, bromide and chloride substituents in the 2-position of the pyridine, which are susceptible to nucleophilic displacement, remained intact during the reaction. Carboxylic acids and aldehydes were transformed to the corresponding acyl fluorides without formation of the 2-fluoropyridine products.

The reactions with pyridines containing functional groups in the 3-positions formed the 2-fluoro-3-functionalized pyridine products preferentially. In some cases, a mixture of 2,3 and 2,5 functionalized products were formed, but these products were separable by silica gel chromatography. The C–H fluorination reaction also proceeded with several pyridines containing more than one substituent to form valuable disubstituted fluoropyridines **2ab** to **2ah** suitable for multiple further derivatizations (see below). The fluorination reaction also occurred with **1ai**, the precursor to the well-known drug Prilosec (omeprazole), in high yield to form the fully substituted fluoropyridine **2ai**.

The reaction conditions developed for the fluorination of pyridines led to the fluorination of a range of other types of six-membered nitrogen heterocycles. As shown in Fig. 3, quinolines, pyrazines, pyrimidines, and pyridazines reacted to afford monofluorinated products. Pyrimidines containing an alkyl, aryl, oxygen, or nitrogen group in the 2-position reacted to form the corresponding 4-fluoropyrimidines in good yield. In contrast, AgF_2 reacted with the π -excessive five-membered aromatic heterocycles to form complex mixtures of products (18).

Isolated yields of the reactions performed with 0.5 mmol of substrate were comparable to the yields determined by ^{19}F NMR spectroscopy for reactions performed on a 0.1-mmol scale. The volatility of some products prevented

their isolation in high yield; in these cases, the yields determined by ^{19}F NMR spectroscopy are reported. In each reaction, only the monofluorination product is observed. Furthermore, the organic material in these reactions consists solely of the monofluorinated product and unreacted starting material (as determined by thin-layer chromatography and gas chromatography–mass spectrometry). Because the presence of fluorine adjacent to nitrogen decreases the basicity and polarity of the products, relative to the starting material, the products are easily purified by silica gel chromatography or acid/base extractions.

To demonstrate the utility of these reactions for medicinal chemistry, we performed the fluorination reactions on several medically relevant compounds (Fig. 2B). The fluorination of acetyl-Mydriacyl (tropicamide, **1aj**), an anticholinergic drug containing a base-sensitive acetate and an acidic α -phenyl amide, proceeded with AgF_2 to form **2aj** in 74% isolated yield. Compound **1ak**, containing a 1-(piperidin-4-yl)-1H-imidazo[4,5-b]pyridin-2-(3H)-one core found in more than 1000 calcitonin gene-related peptide (CGRP) receptor antagonists (**19**), also reacted smoothly to form **2ak** in high yield. Finally, **1al** reacted with AgF_2 to form a 2-fluorinated analog of Daliresp (roflumilast), a drug used to treat chronic obstructive pulmonary disease. These results demonstrate that the fluorination chemistry described herein can be used for the late-stage fluorination of medically important compounds.

The ability to conduct the fluorination reaction on a multigram scale was assessed. The fluorination of 2,5-disubstituted pyridine **1am** on a 5-mmol scale (Fig. 4A) gave 1.34 g of pure **2am** in 83% yield. The product of this reaction was then converted in one step to a fluorinated analog of the antidiabetic drug Actos (pioglitazone).

As noted in the introduction, a fluorine atom in the 2-position of pyridines and diazines allows several transformations to be conducted that cannot be conducted on the parent heteroarene or derivatives of it. For example, 2-fluoropyridines undergo selective lithiation in the 3-position of the ring with lithium diisopropylamide, and the resulting 3-pyridyl anion can be quenched with a variety of electrophiles (**20–22**). 2-Fluoropyridines also undergo acid-catalyzed hydrolysis to 2-pyridones (**23**).

However, the most common reactions of 2-fluoropyridines are nucleophilic substitutions with a range of carbon and heteroatom nucleophiles (**24–28**). Fluoroarenes are known to be more reactive than the other haloarenes toward nucleophilic aromatic substitution. With a mild method to prepare 2-fluoropyridines, a range of 2-pyridyl compounds can now be synthesized from a readily available intermediate. To demonstrate the utility of 2-fluoropyridines in studies of structure-reactivity relationships, we performed the C-H fluorination reaction to prepare a model compound containing a benzyl-protected 2-pyridyl alcohol and a morpholine-derived amide (Fig. 4B). This 2-fluoropyridine reacted under mild condi-

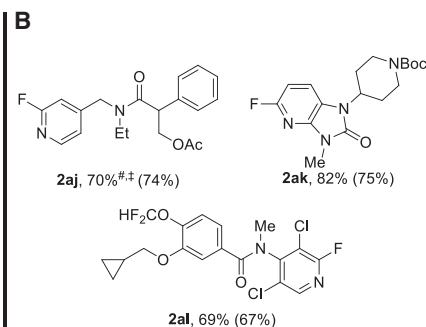
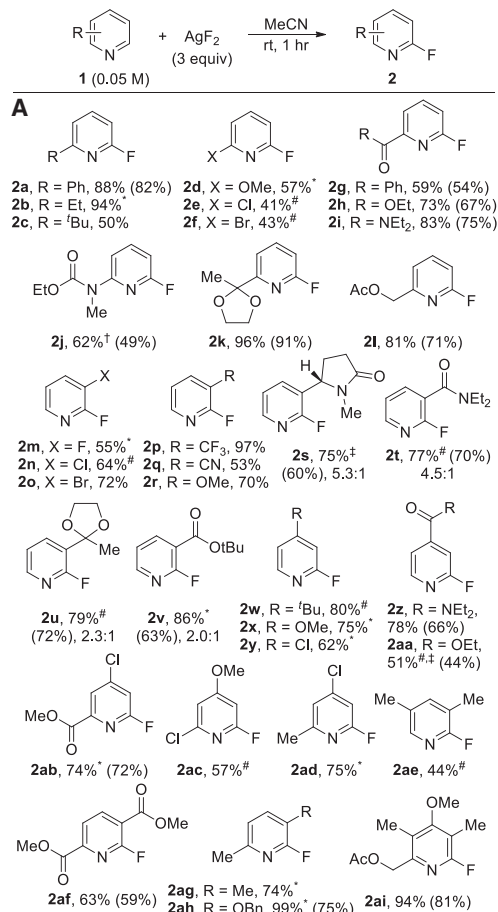


Fig. 2. Fluorination of pyridines with AgF_2 . (A) General substrate scope. (B) Fluorination of medically relevant compounds. Reactions were performed with 0.1 mmol of pyridine to determine yields by ^{19}F NMR spectroscopy with PhCF_3 as an internal standard. Isolated yields for reactions performed on a 0.5-mmol scale are shown in parentheses; rt, room temperature. *Reactions performed at 0.1 M. [‡]Reactions performed at 0.025 M. [†]Reactions performed for 2 hours. [‡]Reactions performed at 50°C.

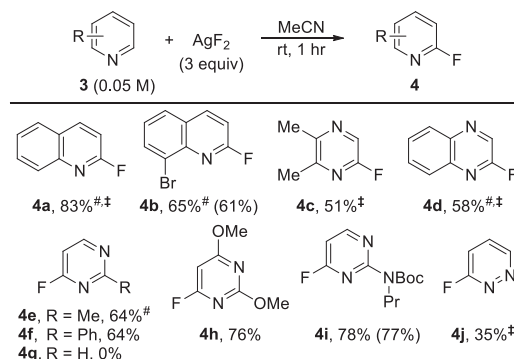


Fig. 3. Fluorination of quinolines and diazines with AgF_2 . *Reactions performed at 0.025 M. [‡]Reactions performed at 50°C.

tions with oxygen, nitrogen, and carbon nucleophiles in good yields. This sequence of C-H bond fluorination and substitution can be valuable for late-stage diversification of lead compounds.

A series of experiments were performed to gain insight into the mechanism of the reactions between pyridines and AgF_2 . The insolubility and paramagnetism of AgF_2 prevented our gaining detailed data from NMR spectroscopic experiments. However, the ^1H NMR resonances of Me_3py did shift downfield in the presence of three equivalents of AgF_2 (**29**), suggesting that pyridines bind to AgF_2 .

A kinetic isotope effect (KIE) was measured to assess the reversibility of the C-H bond cleav-

age process. The reaction of AgF_2 with equivalent amounts of pyridine and pyridine- d_5 revealed a KIE of 2.9 ± 0.1 after 27% conversion (Fig. 4C).

An *N*-fluoropyridinium salt could be an intermediate in the reaction because *N*-fluoropyridinium fluoride, which is formed by the reaction of pyridine with F_2 , rearranges to 2-fluoropyridine at low temperature (**30**). Isolated *N*-fluoropyridinium salts also undergo base-induced rearrangement to 2-fluoropyridines at ambient temperature (**31, 32**). Particularly relevant to our results, 2-fluoro-3-substituted pyridines are formed preferentially from 3-substituted *N*-fluoropyridinium salts. This selectivity mirrors that of our reactions of 3-substituted pyridines with AgF_2 .

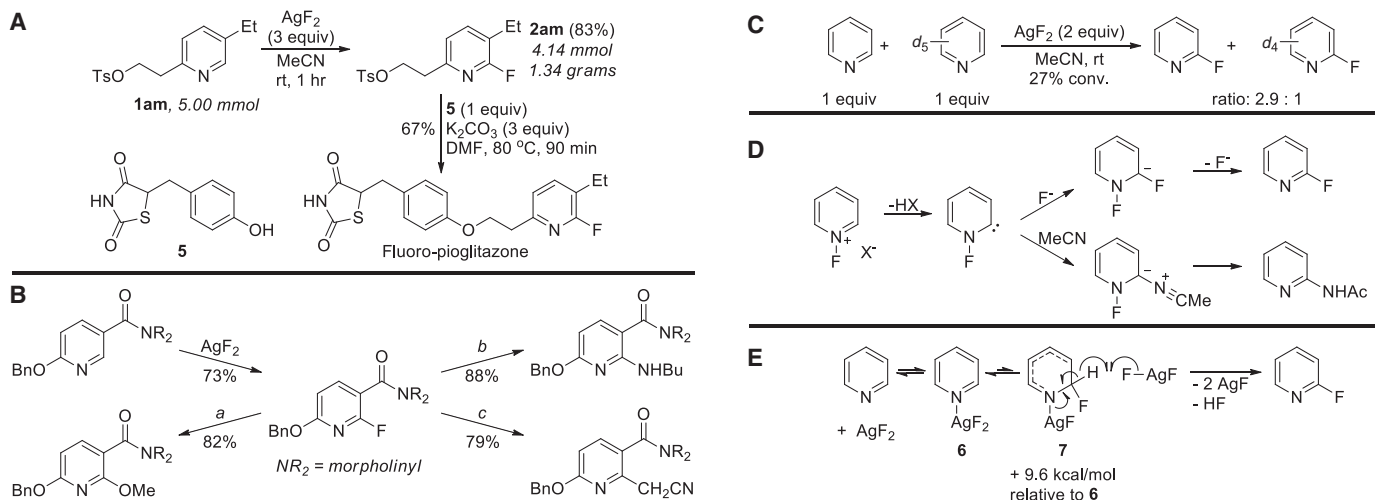


Fig. 4. Scale-up of the fluorination reaction, synthetic utility of the products, and mechanistic considerations. (A) Gram-scale fluorination with AgF₂ and the synthesis of fluoro-pioglitazone. (B) Nucleophilic substitution reactions of a 2-fluoropyridine (isolated yields). Reaction conditions: (a) KO^tBu (5 equivalents), MeOH, 65°C, 2.5 hours. (b) ⁿBuNH₂, rt,

45 min. (c) Potassium hexamethyldisilazide (KHMDs, 3 equivalents), MeCN (1.5 equivalents), PhMe, 0°C to rt, 7 hours. (C) Competition experiment between pyridine and pyridine-d₅. (D) Reactivity of *N*-fluoropyridinium salts. (E) Proposed mechanism for the fluorination of pyridines with AgF₂.

However, the base-induced rearrangements of isolated *N*-fluoropyridinium salts occur through electrophilic carbene intermediates (Fig. 4D) (31, 32), which react rapidly with MeCN to form pyridyl acetamides after hydrolysis (33, 34). Because our fluorination reactions are performed in MeCN, it is unlikely that a similar mechanism occurs for the reactions with AgF₂. Furthermore, reactions with AgF₂ in the presence of added base or fluoride occurred in yields that were similar to those obtained in the absence of these additives (table S1). The base and fluoride should increase the rate of formation of the carbene intermediate and of the subsequent reaction with fluoride, respectively. Taken together, these results are inconsistent with the reactions of AgF₂ occurring through the intermediacy of an *N*-fluoropyridinium cation.

An alternative mechanism involves addition of a fluorine radical from AgF₂ to the pyridine to form a delocalized radical and AgF. However, several pieces of data are inconsistent with such a pathway. First, the exclusive selectivity for fluorination at the 2-position of pyridines contrasts with the mixture of isomeric products formed in varying amounts, depending on the steric and electronic properties of the reactants, for the addition of alkyl, aryl, and fluoroalkyl radicals to pyridines (35–38). Second, if the fluorine radical is nucleophilic, then the reaction would be expected to proceed in higher yield with more electron-deficient azines, and if the radical is electrophilic, then fluorination of benzo-fused or free aryl rings would be expected to compete with fluorination of the heteroarene, and neither prediction is observed. Third, 2,6-dimethylpyridine does not undergo fluorination, and a radical should add to the 3- or 4-position. Finally, the observed KIE of 2.9 would require reversible transfer of the fluorine radical from silver to the heteroarene,

and the transfer of a fluorine radical from the arene to silver most likely has an inaccessibly high kinetic barrier and must occur faster than a more typical hydrogen-atom abstraction.

Instead, we propose that the fluorination occurs by a mechanism similar to that of the Chichibabin reaction (see above). This mechanism would involve initial coordination of AgF₂ to pyridine, followed by addition of the [Ag]-F bond across the π system of the pyridine to form an amido-silver(II)-fluoride complex (Fig. 4E, 7). Subsequent hydrogen-atom abstraction by a second equivalent of AgF₂ from 7 would then form two equivalents of AgF and one equivalent of HF (39). Alkyl and allyl, acyl, silyl, and amido complexes of several metal complexes are known to add across the C=N bond of pyridines, including those of Ni and Cu (40–43) at or below room temperature. To determine if the analogous product from reaction of pyridine with AgF₂ lies at an accessible energy, we computed the relative ground-state energies of the pyridine-AgF₂ coordination complex (Fig. 4E, 6) and the addition product (7) in an acetonitrile solvent continuum by density functional theory methods (44). Compound 7 was calculated to lie only 9.6 kcal/mol higher in free energy at room temperature in acetonitrile than the pyridine-AgF₂ coordination complex 6. These results imply that the proposed intermediate is accessible at room temperature. To account for the observed KIE of 2.9 and an overall barrier commensurate with the reaction times and temperatures, we propose that the coordination of pyridine to AgF₂ and the addition step are reversible; the transition state for hydrogen-atom abstraction would then lie at the highest energy along the reaction coordinate. In this case, the regioselectivity observed with 3-substituted pyridines would be controlled by the relative concentrations of the isomeric ad-

dition products and the relative rates of reaction of these two isomers with a second equivalent of AgF₂. The same trend in regioselectivity is observed in the Chichibabin reaction (12).

The halogenation of arenes and heteroarenes is a classic reaction in organic chemistry, but the fluorination of these reagents has required multiple steps. Even for laboratories equipped to use fluorine gas, the fluorination of functionalized pyridines occurs in low yields. Thus, the mild conditions, fast reaction times, broad scope, high tolerance for auxiliary functionality, and commercial availability of the reagent for the fluorination that we report create the ability to generate fluorinated pyridines and diazines. Considering the high interest in generating fluorinated drug and agrochemical candidates and the high utility of fluorinated heteroarenes as synthetic intermediates, we anticipate that synthetic chemists will rapidly adopt this class of halogenation reaction (45, 46).

References and Notes

1. A. W. Erian, *J. Heterocycl. Chem.* **38**, 793–808 (2001).
2. P. Kirsch, *Modern Fluoroorganic Chemistry: Synthesis, Reactivity, Applications* (Wiley-VCH, Weinheim, Germany, 2004).
3. J.-P. Bégue, D. Bonnet-Delpon, *Bioorganic and Medicinal Chemistry of Fluorine* (Wiley, Hoboken, NJ, 2008).
4. M. D. Wittman et al., *J. Med. Chem.* **52**, 7360–7363 (2009).
5. J. H. Simons, U.S. Patent 2,447,717 (1948).
6. M. Van Der Puy, *Tetrahedron Lett.* **28**, 255–258 (1987).
7. R. D. Chambers et al., *J. Chem. Soc. Perkin Trans. 1*, 803–810 (1999).
8. T. Fukuhara, N. Yoneda, A. Suzuki, *J. Fluor. Chem.* **38**, 435–438 (1988).
9. D. J. Adams, J. H. Clark, *Chem. Soc. Rev.* **28**, 225–231 (1999).
10. H. Sun, S. G. DiMaggio, *Angew. Chem. Int. Ed.* **45**, 2720–2725 (2006).
11. S. D. Kuduk, R. M. DiPardo, M. G. Bock, *Org. Lett.* **7**, 577–579 (2005).
12. C. K. McGill, A. Rappa, *Adv. Heterocycl. Chem.* **44**, 1–79 (1988).
13. The cost of AgF₂ is \$1.83/mmol compared to \$2.41/mmol for Selectfluor, the cheapest and most commonly used electrophilic fluorinating reagent in a typical laboratory setting. Prices are based on the 2013 Sigma-Aldrich catalog prices for 10 g of reagent.

14. A. Zweig, R. G. Fischer, J. E. Lancaster, *J. Org. Chem.* **45**, 3597–3603 (1980).
15. H. Schroeder *et al.*, *J. Org. Chem.* **27**, 2580–2584 (1962).
16. Commercial AgF₂ is a black crystalline solid.
17. The direct fluorination of pyridines with F₂ gas has been reported to occur in 31 to 70% yields with alkyl, chloro, and ester substituted pyridines. The direct fluorination of pyridines containing benzyl acyl, or bromo substituents with F₂ gas resulted in less than 30% yield. See (5–7).
18. The presence of five-membered aromatic heterocycles is not tolerated in the fluorination of pyridines.
19. D. K. Leahy *et al.*, *Org. Process Res. Dev.* **16**, 244–249 (2012).
20. T. Güngör, F. Marsais, G. Queguiner, *J. Organomet. Chem.* **215**, 139–150 (1981).
21. L. Estel, F. Marsais, G. Queguiner, *J. Org. Chem.* **53**, 2740–2744 (1988).
22. C. Bobbio, M. Schlosser, *J. Org. Chem.* **70**, 3039–3045 (2005).
23. H. I. Bradlow, C. A. Vanderwerf, *J. Org. Chem.* **14**, 509–515 (1949).
24. Y. H. Cherng, *Tetrahedron* **58**, 4931–4935 (2002).
25. A. Kling *et al.*, *Bioorg. Med. Chem.* **11**, 1319–1341 (2003).
26. S. Thomas, S. Roberts, L. Pasumansky, S. Gamsey, B. Singaram, *Org. Lett.* **5**, 3867–3870 (2003).
27. T. Kauffmann, A. Mitschker, A. Woltermann, *Chem. Ber.* **116**, 992–1000 (1983).
28. A. Loupy, N. Philippon, P. Pigeon, H. Galons, *Heterocycles* **32**, 1947 (1991).
29. In CD₃CN; ¹H resonances for Me₃py: δ 6.83, 2.38, and 2.23 ppm. ¹H resonances for Me₃py + AgF₂: δ 7.10, 2.59, and 2.32 ppm.
30. H. Meinert, *Z. Chem.* **5**, 64 (1965).
31. T. Umemoto, G. Tomizawa, *Tetrahedron Lett.* **28**, 2705–2708 (1987).
32. T. Umemoto, G. Tomizawa, *J. Org. Chem.* **54**, 1726–1731 (1989).
33. T. Umemoto, G. Tomizawa, H. Hachisuka, M. Kitano, *J. Fluor. Chem.* **77**, 161–168 (1996).
34. A. S. Kiselyov, L. Strekowski, *Synth. Commun.* **24**, 2387–2392 (1994).
35. F. Minisci, E. Vismara, F. Fontana, *Heterocycles* **28**, 489 (1989).
36. F. O'Hara, D. G. Blackmond, P. S. Baran, *J. Am. Chem. Soc.* **135**, 12122–12134 (2013).
37. Y. Fujiwara *et al.*, *Nature* **492**, 95–99 (2012).
38. D. A. Nagib, D. W. C. MacMillan, *Nature* **480**, 224–228 (2011).
39. It is likely that AgF combines with the liberated HF to form silver bifluoride (AgHF₂).
40. E. Piers, M. Soucy, *Can. J. Chem.* **52**, 3563–3564 (1974).
41. P. B. Kraikivskii *et al.*, *J. Organomet. Chem.* **694**, 3912–3917 (2009).
42. P. B. Kraikivskii, H. F. Klein, V. V. Saraev, N. E. Schlörer, V. V. Bocharova, *J. Organomet. Chem.* **696**, 3376–3383 (2011).
43. P. B. Kraikivskii *et al.*, *J. Organomet. Chem.* **715**, 43–47 (2012).
44. D. Andrae, U. Häussermann, M. Dolg, H. Stoll, H. Preuss, *Theor. Chim. Acta* **77**, 123 (1990).
45. T. W. Bell, L. Y. Hu, S. V. Patel, *J. Org. Chem.* **52**, 3847–3850 (1987).
46. T. Honda, H. Namiki, M. Kudoh, H. Nagase, H. Mizutani, *Heterocycles* **59**, 169 (2003).

Acknowledgments: We thank the NIH (R37GM-55382) for support of this work and Chevron for a fellowship to P.S.F. A provisional patent application has been filed on this reaction.

Supporting Online Material

www.sciencemag.org/content/342/6161/956/suppl/DC1

Materials and Methods

Table S1

References (47–56)

25 July 2013; accepted 22 October 2013

10.1126/science.1243759

Imaging of a Circumsolar Dust Ring Near the Orbit of Venus

M. H. Jones,^{1*} D. Bewsher,² D. S. Brown²

The gravitational interaction of dust in the zodiacal cloud with individual planets is expected to give rise to ringlike features: Such a circumsolar ring has been observed associated with Earth, but such resonance rings have not been confirmed to exist for other planets. Here, we report on sensitive photometric observations, based on imaging from the STEREO mission, that confirm the existence of a dust ring at the orbit of Venus. The maximum overdensity of dust in this ring, compared to the zodiacal cloud, is ~10%. The radial density profile of this ring differs from the model used to describe Earth's ring in that it has two distinct steplike components, with one step being interior and the other exterior to the orbit of Venus.

A circumsolar dust ring is known to exist around the orbit of Earth (1, 2). It arises from the trapping of interplanetary dust grains, primarily of asteroidal and cometary origin (3–5), into orbits that are resonant with Earth's orbit. Dust grains of sizes from 1 to 100 μm are subject to Poynting-Robertson (P-R) drag and to a lesser extent solar wind drag, which results in a gradual decay of their orbits [about 10⁴ years for a 10-μm particle at 1 astronomical unit (AU)] (6). As a dust grain slowly spirals inward toward the orbit of the Earth, it successively passes into locations in which it may be trapped temporarily (for time scales of 10⁴ to 10⁵ years) into a particular orbital resonance (1, 7–9). Dust in individual resonances will cluster into periodic patterns around the orbit, and, when multiple resonances combine to form a real dust ring, these underlying structures result in the azimuthal distribution of the ring being nonuniform (1).

Searches for resonance structures around the orbits of Mars and Jupiter have not yet been successful (10). The situation at Venus is more complex. A detection of enhanced scattering was reported (11) from Venera 9 and 10 but is attributed to circumplanetary rather than circumsolar dust. On the basis of a reanalysis of photometry from the Helios mission, data consistent with a dust ring just outside the orbit of Venus have been presented (12), but the existence of such a ring could not be confirmed beyond doubt.

A circumsolar dust ring at Venus would provide observational data, which should lead to improved understanding of the factors affecting the formation of resonance rings, such as (P-R and solar wind) drag forces, an elliptical planetary orbit, and gravitational perturbation by an exterior planet (1, 7, 8). Furthermore, understanding of circumstellar dust rings is important in the context of exoplanetary systems (13). Not only are they an important consideration in proposed space-based interferometric imaging of exoplanets (14), large scale rings have been imaged directly, as in the case of Fomalhaut (15). Here, we describe a search for a ring at the

orbit of Venus based on photometry from an exterior viewpoint.

The STEREO mission (16), launched in October 2006, uses two nearly identical spacecraft, A and B, to provide synoptic observations of the Sun and the heliosphere interior to 1 AU. Each spacecraft carries a Heliospheric Imager instrument (17), HI-2, both of which continuously monitor the inner zodiacal cloud. These HI-2A and HI-2B instruments have a field of view of about 70° centered on ecliptic latitude β ≈ 0° at heliocentric longitude |λ'| = 53.7°. In searching for a dust ring at the orbit of Venus, the lines of sight that are of interest are close to the ecliptic plane and have 40° < |λ'| < 50° (depending on the location of the spacecraft) (Fig. 1).

In normal science operations, the HI-2 instrument generates a 1024 pixel-by-1024 pixel image with ≈4-arc min resolution every 2 hours. Further processing, including positional calibration (18), results in the level-1 data used here. The instrument is sensitive to wavelengths of 400 to 1000 nm, and the dominant diffuse source in HI-2 images is solar radiation scattered by dust grains [with radii of 10 to 100 μm (19)] in the zodiacal cloud. The typical surface brightness at (λ' ≈ 45°, β ≈ 0°) is ≈8 DN s⁻¹ pixel⁻¹ [DN is data number, 1 DN ≈ 15 photoelectrons is the default unit used by the instrument team (17)]. The HI-2 instrument was designed (17) to monitor coronal mass ejections having a surface brightness of about 1% of that of the zodiacal light. By combining ~100 HI-2 level-1 images, photometry on the zodiacal cloud to an accuracy of order 0.1% can be extracted. A major limitation is the presence of systematic errors that compromise this photometry. These arise from various sources: saturation stripes, ghosting caused by bright objects, and the presence of the galactic plane within 30° of the region of interest. To avoid contamination, data containing these features were not used in our analysis.

Photometry of HI-2 data involved combining level-1 images from 10 consecutive days (i.e., up to

¹Department of Physical Sciences, The Open University, Walton Hall, Milton Keynes, Buckinghamshire MK7 6AA, UK. ²Jeremiah Horrocks Institute, University of Central Lancashire, Preston, Lancashire PR1 2HE, UK.

*Corresponding author. E-mail: m.h.jones@open.ac.uk

120 images, with an integrated exposure time of ≈ 8 days). Surface brightnesses were determined over a grid with extent $|\beta| < 8.5^\circ$ and $35.0^\circ < \lambda' <$

60.0° (HI-2A) or $-60.0^\circ < \lambda' < -35.0^\circ$ (HI-2B), with cell size of 0.5° in λ' and 1.0° in β . For each cell, the cumulative probability distribution of

Fig. 1. The viewing geometry (from ecliptic north) of a circumsolar dust ring at Venus from STEREO-B. Planet and STEREO spacecraft (A and B) positions are for 12 June 2008. A ring at the orbit of Venus (thick gray band) is viewed tangentially from B along a line of sight passing through T. The range of helioecliptic longitude λ' mapped is indicated (pale gray). Crosses indicate the locations of T in the observations presented here. The start dates of the STEREO-A data sets are (a1) 9 June 2009, (a2) 29 June 2009, (a3) 19 July 2009, and (a4) 12 November 2008. There are 10 consecutive sets of STEREO-B data: (b1) 18 April to (b10) 17 July 2008.

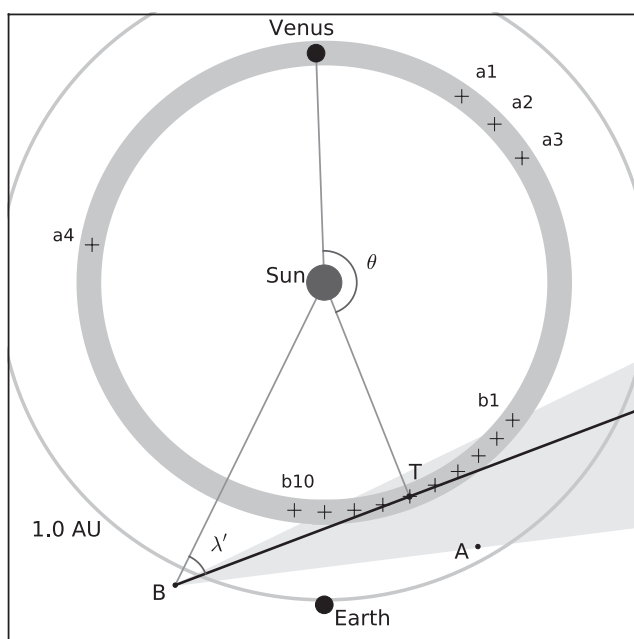
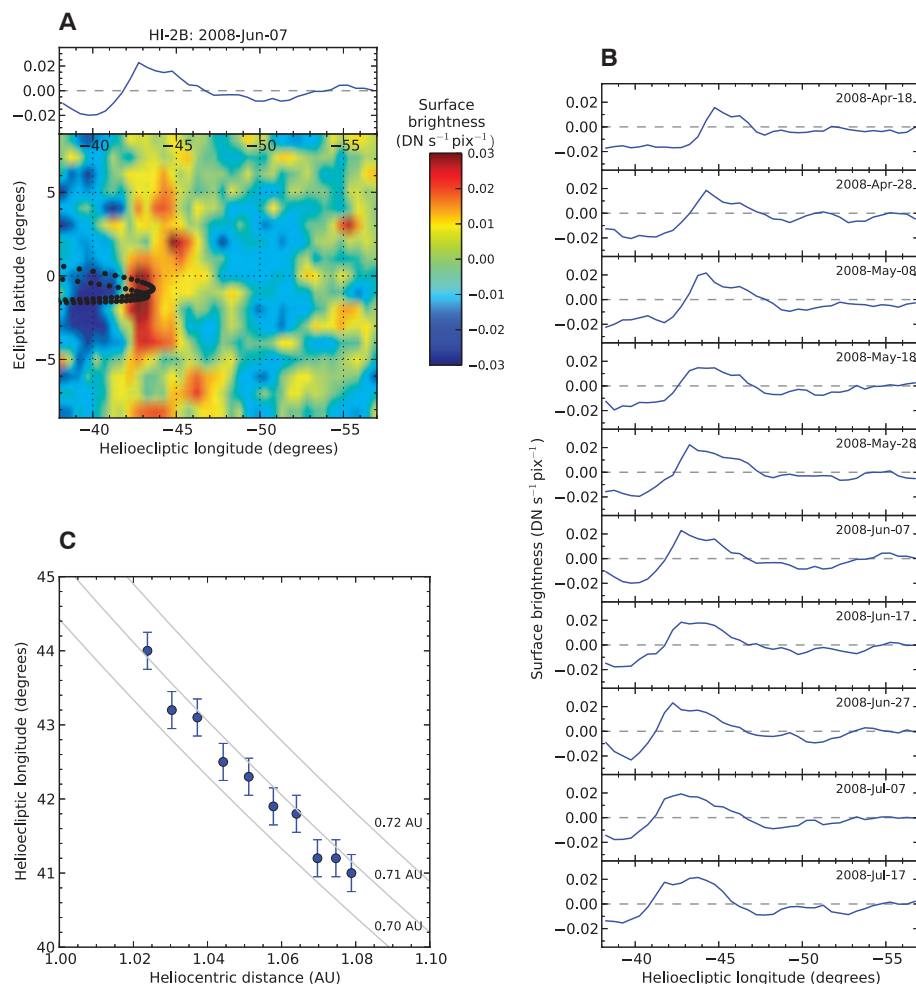


Fig. 2. A bright feature and its change of position with varying heliocentric distance of the STEREO-B spacecraft. (A) The surface brightness map (bottom) and mean scan (top) of a 10-day integration of HI-2B data starting on 7 June 2009 00:00 UTC. The orbit of Venus as viewed from STEREO-B at the start and the end of the integration time is shown by black dots. Surface brightness is expressed in $\text{DN s}^{-1} \text{pixel}^{-1}$ [pixels are those of the charge-coupled device (CCD) of the HI-2 instrument]. (B) Surface brightness mean scans for a sequence of 10 10-day periods (b1 to b10 in Fig. 1) starting on 18 April 2008 00:00 UTC. (C) The helioecliptic longitude of the midrise point on the sunward side of the peaks in (B) against the heliocentric distance of STEREO-B. The gray curves show the expected behavior if the feature is associated with a physical ring at the indicated radii. Error bars indicate $1\text{-}\sigma$ measurement uncertainties.



surface brightness was determined by using the image pixels within that cell (typically $\approx 14,000$ values). The surface brightness of each cell was estimated as that corresponding to a probability of 0.45 (a value slightly lower than the median is expected due to the presence of point sources). This grid was treated as a series of independent scans at constant β , which were fitted to a power law, $k|\lambda'|^{-n}$ (20). Each scan was detrended by using a box-car filter of width 6.5° (i.e., 13 cells of 0.5° width), followed by subtraction of the result of applying the filter to the best-fitting power law for that scan. The resultant scans are used in two ways: as a map of extent $38.0^\circ \leq |\lambda'| \leq 57.0^\circ$ and $|\beta| \leq 8.5^\circ$ and as a mean scan along the ecliptic plane (covering $38.0^\circ \leq |\lambda'| \leq 57.0^\circ$) by averaging over $|\beta| \leq 4.5^\circ$.

An example map from a 10-day observation period of HI-2B data starting on 7 June 2008 00:00 UTC (all data sets are referred to by their starting date) shows a bright feature coincident with the tangent to the orbit of Venus (Fig. 2A). This is as expected for a dust ring along a line of sight where the dust column density is maximized (Fig. 1; the position of the tangent point with respect to Venus is given by the azimuthal angle θ). Given the sensitivity of these maps to systematic errors, this is in itself insufficient to

demonstrate beyond doubt the existence of such a ring. However, when the same detrending method is applied to a region ($-67.0^\circ \leq \lambda' \leq -48.0^\circ$) that does not contain the orbit of Venus, no such bright feature is detected (fig. S1).

Furthermore, this data set is just one from a 100-day interval (starting 18 April 2008) from

which 10 consecutive data sets (b1 to b10 in Fig. 1) could be analyzed. In the mean scans of this sequence (Fig. 2B), the helioelectric longitude of the feature decreases with time. Because of the spacecraft orbit, the heliocentric distance, r , of STEREO-B varied from 1.02 to 1.08 AU over this interval. The view of a physical feature would be

expected to change with viewing position, with $|\lambda'|$ decreasing as r increases. The position of the feature was determined (to an accuracy of $\approx 0.25^\circ$) by reference to the point at which the surface brightness is midway between the peak and minimum value on the sunward side. Figure 2C shows these positions against r . The behavior is

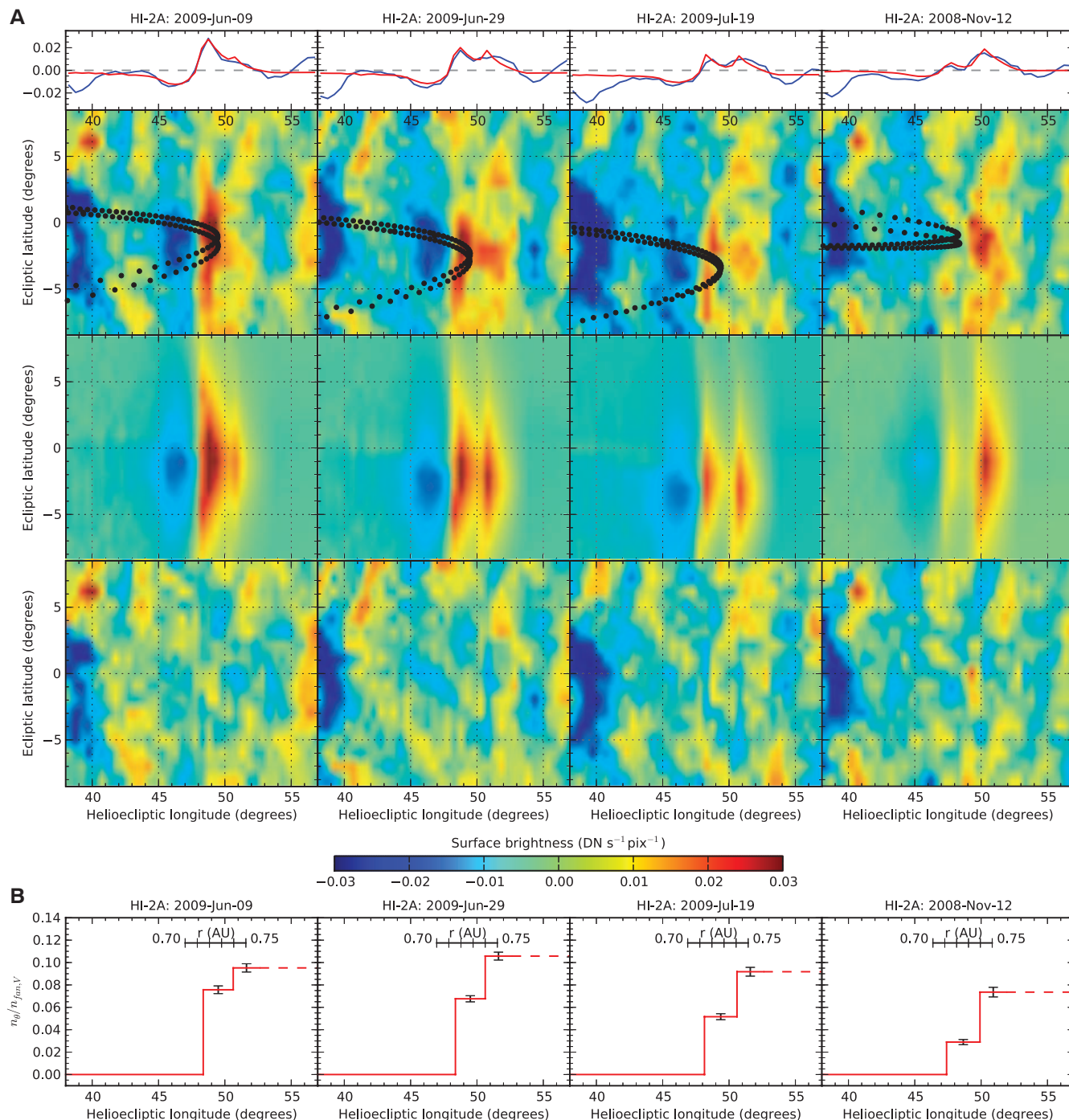


Fig. 3. Surface brightness mean scans and maps and model radial density profiles for HI-2A data sets starting at 00:00 UTC on 9 June, 29 June, and 19 July 2009 and 12 November 2008. (A) From the top downward: top, mean scans (blue) with best-fitting models (red); second row, maps from the data; third row, maps of the best-fitting models;

bottom row, residual (data minus model) maps. Units are as in Fig. 2A. **(B)** The fitted radial density profiles for the two-step density model shown in (A). The profile is plotted against the helioelectric longitude of the tangent point of a ring with heliocentric radius (r). Density is expressed in terms of $n_{\text{H}}/n_{\text{fan},V}$. Error bars show the 1- σ uncertainties of the fitted densities.

as expected for a physical ring located close to the orbit of Venus. Last, there are observations from STEREO-A that view the same tangent point ($\theta = 170^\circ$) as the 17 July 2008 data. Again, an extended feature is observed close to the orbit of Venus (fig. S2), further supporting the view that it arises from a physical structure at this location.

In the sequence of mean scans (Fig. 2B), θ changes by $\approx 60^\circ$; hence, the feature appears to be an arc occupying a substantial fraction of the orbit. In conjunction with further HI-2A data that also show a bright feature near the orbit of Venus (Fig. 3A) but that are $\approx 120^\circ$ away in θ from the HI-2B data (Fig. 1), these data are indicative of a ring (or a series of arcs) that is associated with the orbit of Venus.

The mean scans in Fig. 2B allow some inferences to be made about the underlying dust density distribution. The bright feature is asymmetric, with a steeper decline on the sunward side than its other side. This rules out models in which the variation of dust density with r is symmetric around some fixed radius [as in the Gaussian model (21) of Earth's ring], which would exhibit a peak with the shallower decline on its sunward side.

The majority of the mean scans (Fig. 2B) show evidence of a double-peak structure (e.g., 8 May 2008), but there are mean scans from HI-2A data (Fig. 3A) that more clearly reveal the existence of two components to the peak profile. The data from 9 June 2009 display a strong sharp peak slightly interior to the orbit of Venus but with a shallow decline exterior to the orbit. By 29 June 2009, the sharp peak has reduced in intensity, whereas the gradual decline has changed into a second peak. By 19 July 2009, there are two very distinct peaks in the mean scan profile. An earlier observation, 12 November 2008, shows that the interior peak can be weak, whereas the exterior peak is relatively strong. Therefore, there appear to be two distinct components to the ring, one just inside and one exterior to the orbit of Venus. Furthermore, the absolute and relative intensities of these two components show considerable variation with θ .

To characterize this observed behavior, we adopted a simple parametric model to describe the dust density distribution (22). The model is defined in terms of coordinates (r, z, θ), in which z is the vertical distance from the plane of the ring. The vertical behavior is modeled as an exponential distribution with scale height σ_z (21). The radial dependence is one in which the density changes in two sharp steps (at r_0 and r_1), so the dust density in the ring is $n_\theta(r)e^{-|z|/\sigma_z}$, where

$$n_\theta(r) = \begin{cases} 0, & r < r_0 \\ n_{0,\theta}, & r_0 < r < r_1 \\ n_{1,\theta}, & r_1 < r \end{cases} \quad (1)$$

A limitation of this model is that the ring density should drop to zero as r increases beyond r_1 . Such a decline cannot be discerned in the maps because of the spatial filtering used. Accepting this limitation, this two-step model was

adopted because it provides an indication of the sharp density changes that appear to be present.

The ring is assumed to be coplanar with the orbit of Venus, and a phase function for optical scattering (23) is adopted. In fitting this model to the maps, the variable parameters were $n_{0,\theta}$, $n_{1,\theta}$, r_0 , and r_1 (table S1). The scale height was fixed at the weighted mean (of the HI-2A observations) value of $\sigma_z = 0.055$ AU, noting that genuine variation in σ_z with θ cannot be ruled out.

The two-step model provides an adequate description of the data as shown (Fig. 3A) in the data, model, and residual (compare with the no-signal map of fig. S1) maps. There are some discrepancies, most notably that the outer step in the model has a sharper peak than is observed, but overall the model reproduces the range of observed behavior by variation of a small number of parameters.

Overall, the ring densities are up to $\sim 10\%$ of the density $n_{\text{fan},V}$ of the smooth cloud (at its symmetry plane) (24). The difference in profiles between 9 June 2009 and 19 July 2009 can be explained in the two-step model by the variation of the relative difference between the first and second density steps. The profile with a very sharp interior peak (9 June 2009) has $n_{0,\theta} \approx 0.8 n_{1,\theta}$. As the sequence of observations progresses, $n_{0,\theta}/n_{1,\theta}$ decreases to ≈ 0.57 , resulting in a double-peak profile by 19 July 2009. The data from 12 November 2008, in which the inner component was weak, has $n_{0,\theta} \approx 0.4 n_{1,\theta}$. Furthermore, the absolute densities show variation between this observation and the 2009 June and July observations: $n_{1,\theta} = 0.074 n_{\text{fan},V}$ for the former, whereas $n_{1,\theta} \approx 0.10 n_{\text{fan},V}$ for the latter. This is in qualitative agreement with the prediction (1) that the greater drag experienced by dust at the orbit of Venus and the higher orbital speeds should result in a ring that is less pronounced than Earth's ring [which has an overdensity of about 0.16 (21)]. Also, the data of 2009 June and July represent small (negative) values of θ (-38° to -59°) (25), and the relatively high values of $n_{0,\theta}$ and $n_{1,\theta}$ may reflect a density enhancement similar to the so-called trailing blob observed in Earth's ring (21, 26).

The radii r_0 and r_1 are well constrained and do not exhibit much variation between different data sets. r_0 is not only interior to the semimajor axis of the orbit of Venus (0.7233 AU), it is also interior to the perihelion distance of Venus (0.7184 AU). Likewise, the location of the second step, r_1 , is exterior to the aphelion distance of Venus (0.7282 AU). Numerical simulations (14) of resonance rings in exozodiacal clouds predict a sharp change in ring surface density interior to the planetary orbit. In particular, where the ring density contrast exceeds 30% (which admittedly is not the case for the Venus ring), the inner edge is at ≈ 0.83 of the semimajor axis of the planetary orbit (14). Applied to Venus, this implies $r_0 \approx 0.60$ AU—smaller than observed here. Additionally, a sharp increase in surface density at a radius exterior to the planetary orbit is apparent

in some ring simulations [see catalog (27) linked to (14)].

References and Notes

- S. F. Dermott, S. Jayaraman, Y. L. Xu, B. Å. S. Gustafson, J. C. Liou, *Nature* **369**, 719–723 (1994).
- W. T. Reach *et al.*, *Nature* **374**, 521–523 (1995).
- J. M. Hahn, H. A. Zook, B. Cooper, B. Sunkara, *Icarus* **158**, 360–378 (2002).
- D. Nesvorný *et al.*, *Astrophys. J.* **713**, 816–836 (2010).
- M. Rowan-Robinson, B. May, *Mon. Not. R. Astron. Soc.* **429**, 2894–2902 (2013).
- J. A. Burns, P. L. Lamy, S. Soter, *Icarus* **40**, 1–48 (1979).
- A. A. Jackson, H. A. Zook, *Nature* **337**, 629–631 (1989).
- S. J. Weidenschilling, A. A. Jackson, *Icarus* **104**, 244–254 (1993).
- A. J. Mustill, M. C. Wyatt, *Mon. Not. R. Astron. Soc.* **413**, 554–572 (2011).
- M. J. Kushner, W. T. Reach, M. E. Brown, *Icarus* **145**, 44–52 (2000).
- V. A. Krasnopolsky, A. A. Krysko, *Planet. Space Sci.* **27**, 951–957 (1979).
- C. Leinert, B. Moser, *Astron. Astrophys.* **472**, 335–340 (2007).
- M. J. Kushner, M. J. Holman, *Astrophys. J.* **588**, 1110–1120 (2003).
- C. C. Stark, M. J. Kushner, *Astrophys. J.* **686**, 637–648 (2008).
- P. Kalas, J. R. Graham, M. Clavin, *Nature* **435**, 1067–1070 (2005).
- M. L. Kaiser *et al.*, *Space Sci. Rev.* **136**, 5–16 (2008).
- C. Eyles *et al.*, *Sol. Phys.* **254**, 387–445 (2009).
- D. S. Brown, D. Bewsher, C. J. Eyles, *Sol. Phys.* **254**, 185–225 (2009).
- E. Grün, H. A. Zook, H. Fechtig, R. H. Giese, *Icarus* **62**, 244–272 (1985).
- S. Kouchmy, P. L. Lamy, in *Properties and Interactions of Interplanetary Dust*, R. H. Giese, P. Lamy, Eds. (Reidel, Dordrecht, Netherlands, 1985), pp. 63–74.
- T. Kelsall *et al.*, *Astrophys. J.* **508**, 44–73 (1998).
- Materials and methods are available as supplementary materials on Science Online.
- S. S. Hong, *Astron. Astrophys.* **146**, 67–75 (1985).
- $n_{\text{fan},V}$ was found using a modified fan model (21) with optical scattering (23) and scaled to match the mean surface brightness of the 9 June 2009 data.
- The presence of Venus in the field of view precludes observations with $|\theta| < 38^\circ$.
- W. T. Reach, *Icarus* **209**, 848–850 (2010).
- <http://asd.gsfc.nasa.gov/Christopher.Stark/catalog.php>.

Acknowledgments: The HI instrument was developed by a collaboration that included the Rutherford Appleton Laboratory and the University of Birmingham, both in the United Kingdom; the Centre Spatial de Liège (CSL), Belgium; and the U.S. Naval Research Laboratory (NRL), Washington, DC. The STEREO/SECCHI (Sun Earth Connection Coronal and Heliospheric Investigation) project is an international consortium of the NRL (USA), Lockheed Martin Solar and Astrophysics Lab (USA), NASA Goddard Space Flight Center (USA), Rutherford Appleton Laboratory (UK), University of Birmingham (UK), Max-Planck-Institut für Sonnen-system-forschung (Germany), CSL (Belgium), Institut d'Optique Théorique et Appliquée (France), and Institut d'Astrophysique Spatiale (France). The HI-2 level-1 science data used in this study are available from www.ukssdc.ac.uk/solar/stereo/data.html.

Supplementary Materials

www.sciencemag.org/content/342/6161/960/suppl/DC1
Materials and Methods
Supplementary Text
Figs. S1 and S2
Table S1
References

15 July 2013; accepted 28 October 2013
10.1126/science.1243194

Constraints on the Late Holocene Anthropogenic Contribution to the Atmospheric Methane Budget

Logan Mitchell,^{1*} Ed Brook,¹ James E. Lee,¹ Christo Buizert,¹ Todd Sowers²

The origin of the late preindustrial Holocene (LPIH) increase in atmospheric methane concentrations has been much debated. Hypotheses invoking changes in solely anthropogenic sources or solely natural sources have been proposed to explain the increase in concentrations. Here two high-resolution, high-precision ice core methane concentration records from Greenland and Antarctica are presented and are used to construct a high-resolution record of the methane inter-polar difference (IPD). The IPD record constrains the latitudinal distribution of emissions and shows that LPIH emissions increased primarily in the tropics, with secondary increases in the subtropical Northern Hemisphere. Anthropogenic and natural sources have different latitudinal characteristics, which are exploited to demonstrate that both anthropogenic and natural sources are needed to explain LPIH changes in methane concentration.

The 2.5-fold increase in the concentration of atmospheric methane (CH_4) since the start of the Industrial Revolution has accounted for ~20% of the total increase in radiative forcing over that time and motivated efforts to understand both natural CH_4 biogeochemistry and anthropogenic impacts on CH_4 sources and sinks (1). There has been a lively debate about the impact of early human activities on the global CH_4 budget, stimulated by the observation that atmospheric CH_4 levels generally follow 30°N summer solar insolation over the past 800,000 years, but in the mid-Holocene [~5000 years ago (ka)] there is a divergence, with CH_4 increasing and insolation decreasing. The “early anthropogenic hypothesis” postulates that human activities were responsible for the increase in CH_4 since the mid-Holocene (and CO_2 increases since ~7 ka) (2), but others argue that the increase originates from natural sources (3). Archaeological evidence supports the hypothesis about early anthropogenic emissions, particularly from rice agriculture (4, 5), although the magnitude of those emissions is debated (3, 6).

One tool for understanding CH_4 budget changes is the CH_4 Inter-Polar Difference (IPD) (7–9), which can be reconstructed from polar ice cores. The IPD is a function of the latitudinal distribution of sources and sinks, as well as the interhemispheric mixing time. The prevalence of Northern Hemisphere (NH) sources leads to a positive IPD, with higher CH_4 levels recorded in Greenland ice cores than in Antarctic ones. Recent work has shown that the main CH_4 sink (OH) is stable on a range of time scales (10–12), and we have assumed that there have been no changes in the spatial distribution of OH in the late preindustrial Holocene (LPIH). Because interhemispheric transport has a second-order effect on the IPD

(13), source changes are left as the dominant control on IPD variation. Because ~95% of humans lived in the NH tropics and subtropics (0° to 60°N) during the LPIH (14), the fingerprint of anthropogenic emissions would have been an increased IPD relative to the natural background. Indeed, NH anthropogenic emissions in the industrial age have increased the IPD to ~125 parts per billion (ppb) (~7.5% of the mean global concentration), far above the 42 ppb preindustrial background (~6.4% of the mean global concentration). Here we present decadal resolved ice core CH_4 records from the West Antarctic Ice Sheet (WAIS) Divide and the Greenland Ice Sheet Project 2 (GISP2) ice cores, which we use to reconstruct the IPD from 800 B.C.E. to 1800 C.E. (Fig. 1), thus providing data-driven constraints on the early anthropogenic hypothesis.

Our high-precision CH_4 measurements [pooled standard deviation ($\text{SD} \pm 2.4$ ppb) (15)] reproduce multidecadal-scale variability observed in a shallow core (WDC05A) (16) and in the Law Dome ice core (15, 17, 18). We used the WAIS Divide layer-counted ice chronology (19) and a dynamic firm densification model to construct a gas-age chronology. A Monte Carlo correlation technique using the multidecadal variations was then used to create a GISP2 gas-age chronology synchronized with the WAIS Divide chronology (15). When the synchronized GISP2 chronology was compared to one constructed independently with a firm densification model and a layer-counted ice chronology, we found a difference of 0 ± 11 years, demonstrating that our chronology is robust (15). The IPD was calculated by subtracting the WAIS Divide from the GISP2 CH_4 concentration after linear interpolation to annual spacing. Uncertainty bands (1σ) were computed with a Monte Carlo technique incorporating measurement precision and timescale uncertainties (15).

The IPD remains essentially constant (781 B.C.E. to 1803 C.E. mean, 41.6 ppb; trend 0.9 ± 0.3 ppb/ka) throughout the LPIH despite a 115-ppb (17%) increase in the global concentration, which is broadly consistent with previous low-resolution

estimates (fig. S4) (8, 17, 20). The IPD record shows small (~5 ppb) centennial-scale variations, with a minimum around 250 B.C.E. and maximum around 1100 C.E.

We used an Eight Box Atmospheric CH_4 Model (EBAMM) after (21) to examine hypothesized CH_4 emission scenarios and to compare modeled concentrations with the ice core records (15). The model has six tropospheric boxes covering 30° latitude each and one stratospheric box per hemisphere. We refer to these boxes as the tropical (0° to 30°), mid-latitude (30° to 60°), and high-latitude (60° to 90°) boxes. The distribution of CH_4 sources is fundamentally under-constrained by concentration data from just the two poles (22). However, the modern source distribution provides additional constraints on the relatively small emissions from the 30° to 90°S and 60° to 90°N regions (15). With these constraints, our data can be used in conjunction with EBAMM to solve for the source strength of two latitudinal bands at a time [fig. S8 (15)]. We constructed three “latitudinal” emission scenarios (L1, L2, and L3) that balance the global budget and represent the range of realistic emissions. While keeping emissions outside the zonal bands of interest constant, we solved for emissions in the Southern Hemisphere (SH) versus NH tropics (L1), tropical (30°S to 30°N) versus mid-latitude NH (L2), and tropical versus mid- to high-latitude NH (L3, Fig. 1). Whenever two EBAMM boxes fell within a latitudinal band, we assumed a fixed emission ratio between them. L3 is equivalent to a simpler three-box model (fig. S9) (8, 15). Next, we calculated the net change in emissions between 800 B.C.E. and 1400 C.E. in each latitudinal band, using linear regression (Table 1). We focused on the time period from 800 B.C.E. to 1400 C.E. to avoid the exponential population increase after 1500 C.E. and potential natural emission reductions related to the Little Ice Age. Assuming an atmospheric lifetime of 10 years (12), our latitudinal scenarios show that global sources increased by ~24 Tg/year between 800 B.C.E. and 1400 C.E., with the majority of that increase coming from tropical sources (Fig. 1). Varying the CH_4 lifetime from 8 to 12 years (12) caused the increase in global emissions to change by ± 5 Tg/year but did not affect the latitudinal distribution of CH_4 emissions over the LPIH (15).

There are two published model-based scenarios of natural wetland CH_4 emission changes during the LPIH (N1 and N2 in Table 1, and Fig. 2). Scenario N1 is based on TRENCH (Transient Emissions of Natural CH_4), a coarse-grid transient model forced by global ice volume, greenhouse gases, and insolation (23). Scenario N2 used output from a fine-grid CH_4 emissions module tied to a dynamic vegetation model, using the climate from the HadCM3 (Hadley Centre Coupled Model, version 3) general circulation model (3). These models suggest that global natural CH_4 emissions changed between ~2 and 10 Tg/year between 800 B.C.E. and 1400 C.E. for the N1 and N2 scenarios, respectively. Neither indicates large

¹College of Earth, Ocean, and Atmospheric Sciences, Oregon State University, Corvallis, OR 97331, USA. ²Department of Geosciences and Earth and Environmental Systems Institute, Pennsylvania State University, University Park, PA 16802, USA.

*Corresponding author. E-mail: logan.e.mitchell@gmail.com

decreases in natural CH₄ emissions during the late Holocene in response to declining NH insolation, as proposed by the early anthropogenic hypothesis. However, neither model can explain the global increase in CH₄ emissions of ~24 Tg/year, suggesting that either these models are deficient in some way or some amount of anthropogenic emissions is needed to explain the full LPIH CH₄ increase.

Scenarios A1 and A2 use two published estimates of anthropogenic emissions for the LPIH, while leaving natural emissions constant (to isolate the anthropogenic impact). Scenario A1 uses anthropogenic emission estimates from Houweling *et al.* (24) (anthropogenic emissions = 20 Tg/year at 1500 C.E.), and A2 uses estimates from Ruddiman (25) (anthropogenic emissions =

43 Tg/year at 1500 C.E.). To estimate time-dependent anthropogenic emissions, we binned global population from the HYDE 3.1 database (14) into the EBAMM boxes and defined per-capita emissions based on estimates of emissions and population in 1500 C.E. Scenarios A1 and A2 assume constant per-capita emissions; scenarios involving changes in per-capita emissions from rice agriculture with time are considered below. The latitudinal distribution of CH₄ emissions from rice agriculture was calculated using population from the rice-producing region of Asia (60° to 140°E and 10°S to 50°N) (4, 5). If anthropogenic biomass burning emissions are also scaled on a per-capita basis, the ¹³CH₄ isotopic budget increases with time, which is inconsistent with the isotopic observations (15, 26). We there-

fore kept all biomass burning emissions (natural and anthropogenic) constant; although some small variations are expected based on $\delta^{13}\text{CH}_4$ observations (26), these lack a long-term trend and cannot be systematically tied to population changes on a per-capita basis (27). A1 and A2 yield an increase in emissions of 12 Tg/year and 24 Tg/year from 800 B.C.E. to 1400 C.E., respectively. Because most of the increase in emissions occurred in the NH (Table 1), both scenarios cause the IPD to increase through time, which is not observed in the IPD record (Fig. 2). However, increases in global population followed by losses from the Mongol invasion and the spread of the Black Plague in the rice-producing portion of Asia (fig. S12) create a maximum in the modeled IPD from ~1000 to 1400 C.E., which is observed in the IPD record lending support to the hypothesis that some of the LPIH increases in emissions were anthropogenic in origin and that variability in population is responsible for some of the variations in the CH₄ record (16).

The contribution of natural versus anthropogenic emissions can be distinguished from their latitudinal distribution (Table 1). Comparing anthropogenic emissions to the emissions in the latitudinal scenarios, it is clear that scenarios A1 and A2 both have moderate NH emissions similar to those of L1, L2, and L3, whereas N1 and N2 do not. This suggests that most of the increase in NH emissions is anthropogenic in origin, particularly in the tropical NH (N2 suggests that a small fraction of the mid-latitude NH increase could be natural). In the SH, A1 and A2 show small increases in emissions, because there are minimal population increases in the SH. However, the primary source increase in scenario N2 is SH tropical wetlands, which is consistent with reconstructed increases in the South American monsoon strength (28). Because natural wetlands represent the only sizeable source of SH tropical emissions in any of our scenarios, it follows that they are responsible for the majority of the SH emissions identified by our latitudinal scenarios. Scenario N1 does not show tropical SH increases, possibly because N1 has a lower spatial resolution and simplified climate.

Based on these results, we examined scenarios with combined natural and anthropogenic emissions, as well as the impact of allowing per-capita emissions from rice agriculture to change through time (29, 30). If per-capita emissions from rice agriculture were constant through time, then the best fit to the concentration data is a combination of N2 and A1. However, if we assume that the per-capita emissions from rice agriculture decreased linearly by 50% over the LPIH, then the larger anthropogenic emissions of A2 combined with N2 provide the best fit (Fig. 2). Larger reductions in per-capita emissions from rice agriculture do not fit the concentration data when using our modeling framework (15).

Given the current understanding of past population trends and the dependence of CH₄ emissions on climate, our results suggest that increases in both SH natural wetland emissions and a

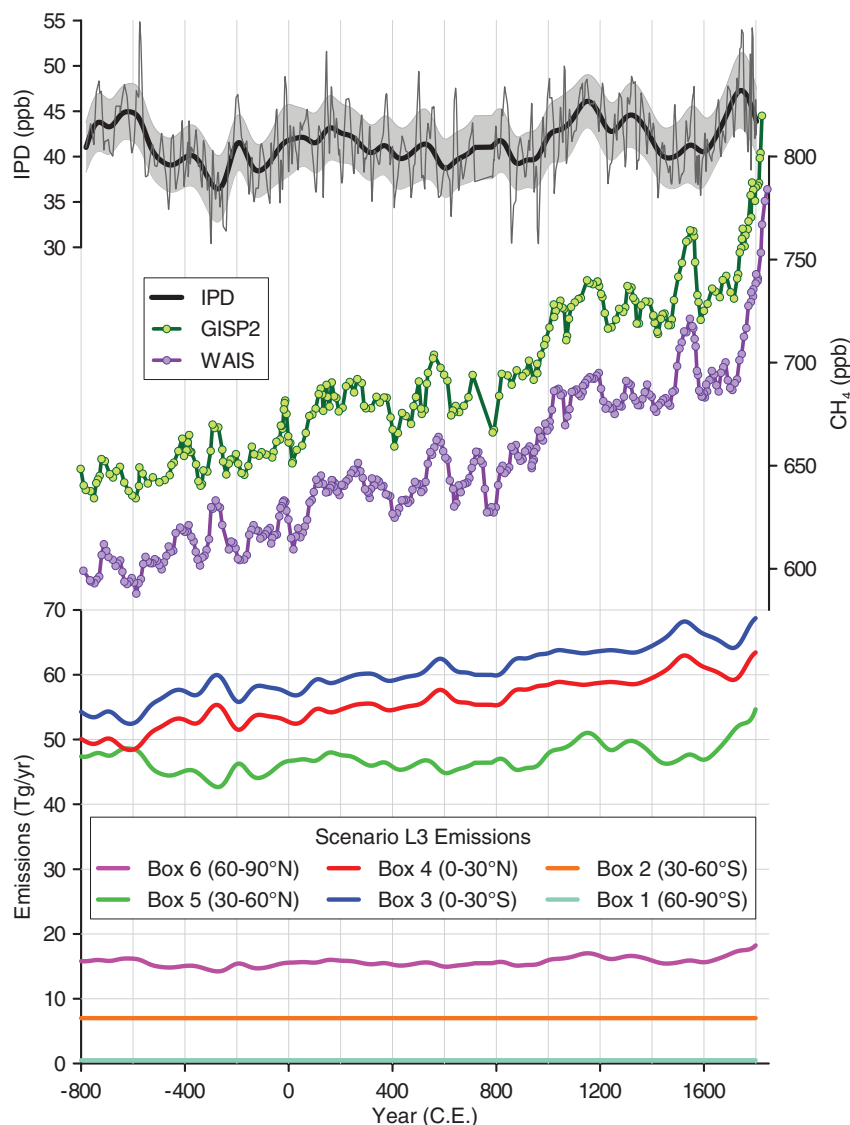


Fig. 1. IPD (top), ice core CH₄ records (middle), and calculated emissions from scenario L3 (bottom). CH₄ data points show the mean concentration from replicate samples measured at that depth. The thin IPD line shows the IPD obtained by linear interpolation between ice core measurements at an annual spacing, and the thick line was computed using a 20-year low-pass filter. The IPD 1 σ error bands were obtained using a Monte Carlo procedure accounting for analytical uncertainty of the measurements and chronologic uncertainty of the tie points (15).

Table 1. Modeled change in zonal CH₄ emissions between 800 B.C.E. and 1400 C.E. (Tg/year), assuming a 10-year CH₄ lifetime. Model scenario labels are as follows: L1, L2, and L3 solve for total emissions in selected zonal regions indicated by the bold and italic numbers. N1 and N2 have changes in natural emissions only. A1 and A2 have changes in anthropogenic emissions only. The combined scenarios (N2+A1 and N2+A2 with −50% per capita) have changes in both natural and anthropogenic emissions.

EBAMM box (latitude band)	L1*	L2*	L3*	N1	N2	A1	A2	N2+A1	N2+A2 with −50% per capita
6 (60° to 90°N)	0	0	1 ± 1	0	−1	0	0	0	0
5 (30° to 60°N)	0	6 ± 6	3 ± 3	−1	3	4	8	7	6
4 (0° to 30°N)	18 ± 9	9 ± 3	9 ± 2	−1	1	7	15	7	10
3 (0° to 30°S)	<i>6 ± 7</i>	<i>9 ± 3</i>	<i>10 ± 2</i>	0	7	1	1	8	8
2 (30° to 60°S)	0	0	0	0	0	0	0	0	0
1 (60° to 90°S)	0	0	0	0	0	0	0	0	0
Total change	24 ± 4	24 ± 4	23 ± 4	(−2)	10	12	24	22	24
CH ₄ increase (ppb)	93	92	92	(−6)	41	43	92	84	94

*The difference in the zonal CH₄ emissions between 800 B.C.E. and 1400 C.E. (±2 times the 1σ SD of the prediction interval) after calculating the linear regression of emissions from the global CH₄ budget solved for tropical and subtropical NH emissions. In L1 to L3, we solved for the zonal bands indicated by the bold and italic numbers; when there were two boxes within a band, we assumed a fixed emission ratio between them. See the supplementary materials for details.

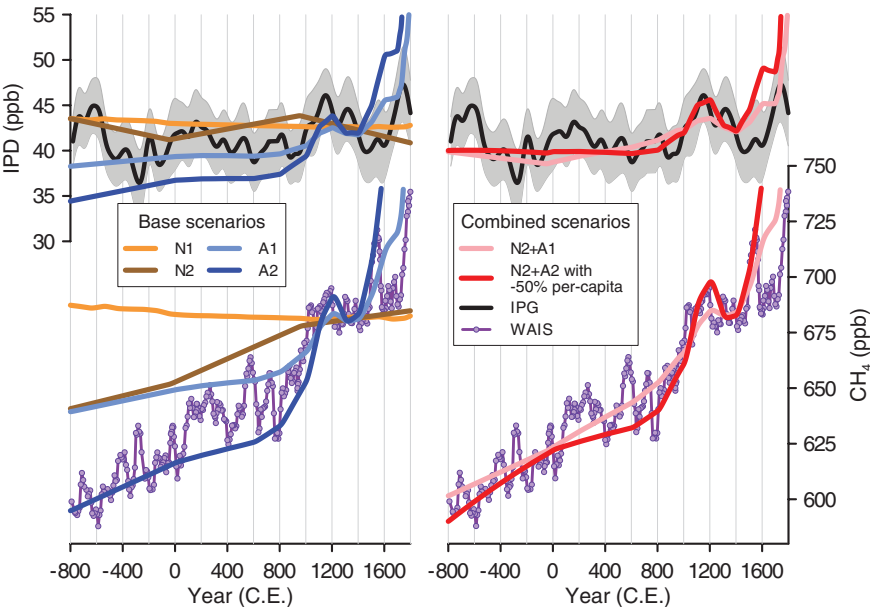


Fig. 2. Modeled CH₄ concentrations from the IPD (top) and box 1 (60° to 90°S, bottom) for scenarios N1, N2, A1, and A2 (left), as well as the combined scenarios A1+N2, and A2+N2 with a 50% reduction in per-capita rice agriculture emissions (right). All scenarios are tuned to match the concentration and IPD at ~1400 C.E. The emission histories used to produce these scenarios are shown in fig. S10. Model concentrations from box 6 (60° to 90°N) and Greenland concentration data are omitted for clarity.

moderate amount of NH anthropogenic emissions are needed to close the LPIH global CH₄ budget. Our concentration data set provides a constraint for future CH₄ budget modeling efforts focusing on constraining natural and anthropogenic emissions.

References and Notes

1. P. Forster et al., in *Climate Change 2007: The Physical Science Basis. Contribution of Working Group I to the Fourth Assessment Report of the Intergovernmental Panel on Climate Change*, S. Solomon et al., Eds. (Cambridge Univ. Press, Cambridge, 2007), pp. 131–234.
2. W. F. Ruddiman, *Clim. Change* **61**, 261–293 (2003).

3. J. S. Singarayer, P. J. Valdes, P. Friedlingstein, S. Nelson, D. J. Beerling, *Nature* **470**, 82–85 (2011).
4. D. Q. Fuller et al., *Holocene* **21**, 743–759 (2011).
5. W. F. Ruddiman, Z. T. Guo, X. Zhou, H. B. Wu, Y. Y. Yu, *Quat. Sci. Rev.* **27**, 1291–1295 (2008).
6. W. F. Ruddiman, J. E. Kutzbach, S. J. Vavrus, *Holocene* **21**, 865–8879 (2011).
7. I. Funget al., *J. Geophys. Res. Atmos.* **96**, 13033 (1991).
8. J. Chappellaz et al., *J. Geophys. Res. Atmos.* **102**, 15987 (1997).
9. E. J. Brook, S. Harder, J. Severinghaus, E. J. Steig, C. M. Sucher, *Global Biogeochem. Cycles* **14**, 559–572 (2000).
10. K. R. Lassey, D. M. Etheridge, D. C. Lowe, A. M. Smith, D. F. Ferretti, *Atmos. Chem. Phys.* **7**, 2119–2139 (2007).

11. S. A. Montzka et al., *Science* **331**, 67–69 (2011).
12. V. Naik et al., *Atmos. Chem. Phys.* **13**, 5277–5298 (2013).
13. E. J. Dlugokencky et al., *Geophys. Res. Lett.* **36**, L18803 (2009).
14. K. K. Goldewijk, A. Beusen, P. Janssen, *Holocene* **20**, 565–573 (2010).
15. Materials and methods are available as supplementary materials on Science Online.
16. L. E. Mitchell, E. J. Brook, T. Sowers, J. R. McConnell, K. Taylor, *J. Geophys. Res. Biogeosci.* **116**, G02007 (2011).
17. D. M. Etheridge, L. P. Steele, R. J. Francey, R. L. Langenfelds, *J. Geophys. Res. Atmos.* **103**, 15979 (1998).
18. C. MacFarling Meure et al., *Geophys. Res. Lett.* **33**, L14810 (2006).
19. T. J. Fudge et al., *Nature* **500**, 440–444 (2013).
20. T. Nakazawa et al., *Geophys. Res. Lett.* **20**, 943–946 (1993).
21. T. Marik, thesis, University of Heidelberg, Heidelberg, Germany (1998).
22. M. A. K. Khalil, R. A. Rasmussen, *J. Geophys. Res. Oceans* **88**, 5131 (1983).
23. T. Y. M. Konijnendijk, S. L. Weber, E. Tuenter, M. van Weele, *Clim. Past* **7**, 635–648 (2011).
24. S. Houweling, F. Dentener, J. Lelieveld, *J. Geophys. Res. Atmos.* **105**, 17243 (2000).
25. W. F. Ruddiman, *Rev. Geophys.* **45**, RG4001 (2007).
26. C. J. Sapart et al., *Nature* **490**, 85–88 (2012).
27. O. Pechony, D. T. Shindell, *Proc. Natl. Acad. Sci. U.S.A.* **107**, 19167–19170 (2010).
28. X. F. Wang et al., *Quat. Sci. Rev.* **25**, 3391–3403 (2006).
29. W. F. Ruddiman, E. C. Ellis, *Quat. Sci. Rev.* **28**, 3011–3015 (2009).
30. J. O. Kaplan et al., *Holocene* **21**, 775–791 (2011).
31. L. E. Mitchell, thesis, Oregon State University, Corvallis, OR (2013).

Acknowledgments: This work was supported by NSF Office of Polar Programs (OPP) grants 0538578, 0520523, 0944584, and 0538538; and by NASA/Oregon Space Grant Consortium grant NNG05GJ85H and the NOAA Climate and Global Change Fellowship Program, administered by the University Corporation for Atmospheric Research (C.B.). We thank two anonymous reviewers whose comments greatly improved the manuscript; B. Markle, A. Morin, B. Williams, and J. Edwards for assisting in sample preparation and analysis; T. Marik, who provided the original eight-box model code (BOSCAGE); J. Severinghaus and G. Etiope, who contributed preliminary results from their work; T. Konijnendijk, J. Van Etten, and J. Singarayer, who provided model data from their published works; the WAIS Divide Science Coordination Office at the Desert Research Institute, Reno, NV for the collection and distribution of the WAIS Divide ice core (K. Taylor, NSF grants 0230396, 0440817, 0944348, and 0944266–University of New Hampshire); NSF OPP, which funds the Ice Drilling Program Office and Ice Drilling Design and Operations group for coring activities; NSF, which funds the National Ice Core Laboratory, which curated and processed the core; Raytheon Polar Services, which provided logistics support in Antarctica; and the 109th New York Air National Guard for airlift in Antarctica. Data and description can be downloaded from the NOAA National Climate Data Center (www.ncdc.noaa.gov/paleo/paleo.html). EBAMM model code is archived with L.E.M.’s thesis (31), available online at <http://ir.library.oregonstate.edu/xmlui/handle/1957/37906>.

Supplementary Materials

www.sciencemag.org/content/342/6161/964/suppl/DC1
Materials and Methods
Figs. S1 to S17
Tables S1 and S2
References

9 April 2013; accepted 23 October 2013
10.1126/science.1238920

Commensal Bacteria Control Cancer Response to Therapy by Modulating the Tumor Microenvironment

Noriho Iida,^{1*} Amiran Dzutsev,^{1,2*} C. Andrew Stewart,^{1*} Loretta Smith,¹ Nicolas Bouladoux,³ Rebecca A. Weingarten,⁴ Daniel A. Molina,⁵ Rosalba Salcedo,¹ Timothy Back,¹ Sarah Cramer,¹ Ren-Ming Dai,^{1,2} Hiu Kiu,¹ Marco Cardone,¹ Shruti Naik,³ Anil K. Patri,⁶ Ena Wang,⁷ Francesco M. Marincola,^{7,8} Karen M. Frank,⁴ Yasmine Belkaid,³ Giorgio Trinchieri,^{1†‡} Romina S. Goldszmid^{1†‡}

The gut microbiota influences both local and systemic inflammation. Inflammation contributes to development, progression, and treatment of cancer, but it remains unclear whether commensal bacteria affect inflammation in the sterile tumor microenvironment. Here, we show that disruption of the microbiota impairs the response of subcutaneous tumors to CpG-oligonucleotide immunotherapy and platinum chemotherapy. In antibiotics-treated or germ-free mice, tumor-infiltrating myeloid-derived cells responded poorly to therapy, resulting in lower cytokine production and tumor necrosis after CpG-oligonucleotide treatment and deficient production of reactive oxygen species and cytotoxicity after chemotherapy. Thus, optimal responses to cancer therapy require an intact commensal microbiota that mediates its effects by modulating myeloid-derived cell functions in the tumor microenvironment. These findings underscore the importance of the microbiota in the outcome of disease treatment.

The commensal microbiota influences metabolism, tissue development, inflammation, and immunity (1). The gut microbiota affects inflammation and immunity not only locally at the mucosal level but also systemically (2–5), raising the question of whether the microbiota affects inflammatory processes that contribute to cancer and its therapy. Tumor-associated

inflammatory cells promote cancer cell proliferation and suppress antitumor immunity (6). Anti-cancer treatments alter this microenvironment and may evoke tumor-destructive immune responses (7–9), but whether commensal organisms affect this process is unexplored.

To investigate whether commensal bacteria alter inflammation in the tumor microenviron-

ment, mice received an antibiotic cocktail (ABX) of vancomycin, imipenem, and neomycin in drinking water starting 3 weeks before tumor inoculation and continuing throughout the experiment. To analyze tumors of comparable stages of progression in both wild-type (WT) and genetically altered mice, three C57Bl/6 mouse transplantable tumors were selected based on susceptibility to therapy: EL4 lymphoma, MC38 colon carcinoma, and B16 melanoma. Tumor cells were injected subcutaneously, and mice were analyzed or treated when the tumors reached a diameter of ≥ 4 mm. Gene expression analysis of pretherapy MC38 and EL4 tumors revealed down-regulation of genes related to inflammation, phagocytosis, antigen presentation, and adaptive immune responses in ABX-treated mice but up-regulation of genes related to tissue development, cancer, and metabolism

¹Cancer and Inflammation Program, National Cancer Institute, Frederick, MD 21702, USA. ²Leidos Biomedical Research, Inc., Frederick National Laboratory, Frederick, MD 21702, USA. ³Mucosal Immunology Section, Laboratory of Parasitic Diseases, National Institute of Allergy and Infectious Diseases, Bethesda, MD 20892, USA. ⁴Microbiology Service, Department of Laboratory Medicine, Clinical Center, National Institutes of Health, Bethesda, MD 20892, USA. ⁵Technical Resources International, Inc., Bethesda, MD 20817, USA. ⁶Nanotechnology Characterization Laboratory, Advanced Technology Program, Leidos Biomedical Research, Inc., Frederick National Laboratory, Frederick, MD 21702, USA. ⁷Department of Transfusion Medicine, Clinical Center, National Institutes of Health, Bethesda, MD 20892, USA. ⁸Sidra Medical and Research Centre, Doha, Qatar.

*These authors contributed equally to this work.

†These authors contributed equally to this work.

‡Corresponding author. E-mail: trinchig@mail.nih.gov (G.T.); rgoldszmid@mail.nih.gov (R.S.G.)

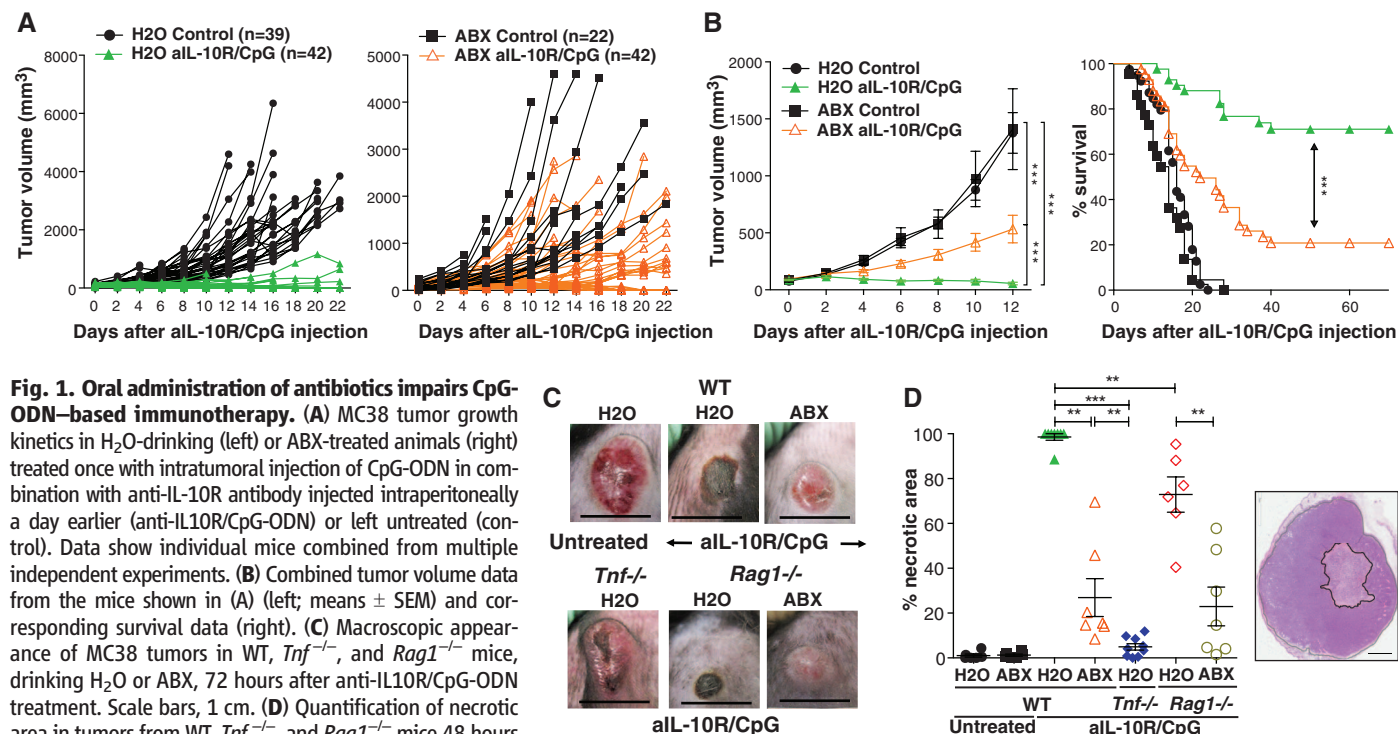


(fig. S1, A and B). ABX lowered the frequency of monocyte-derived Ly6C⁺ MHC class II⁺ cells in EL4 and MC38 tumors and the spleen of MC38 tumor-bearing mice. ABX also decreased Ly6G^{high} neutrophil frequency in MC38 tumors (fig. S2).

To determine whether ABX affect tumor immunotherapy, MC38 and B16 tumor-bearing mice were treated with a combination of intratumoral CpG-oligodeoxynucleotides (ODN), a ligand of Toll-like receptor 9 (TLR9), and inhibitory interleukin-10 (IL-10) receptor antibodies (anti-IL-10R) (10). This immunotherapy retards tumor growth and prolongs survival by rapidly inducing hemorrhagic necrosis dependent on tumor necrosis factor (TNF) production by tumor-associated myeloid cells followed by a CD8 T cell response required for tumor eradication (11). ABX impaired therapy efficacy to retard tumor growth and lengthen survival (Fig. 1, A and B, and fig. S3A). Anti-IL-10R/CpG-ODN treatment induced MC38 tumor necrosis in control mice that was greatly reduced both macroscopically and histologically in ABX-treated animals (Fig. 1, C and D). Similar observations in immunodeficient *Rag1*^{-/-} mice demonstrated that ABX regulate the response to anti-IL-10R/CpG-ODN independently of adaptive immunity (Fig. 1D). However, in *Tnf*^{-/-} mice, anti-IL-10R/CpG-ODN induced minimal necrosis and had no effect on tumor growth in either control or ABX-treated mice (Fig. 1, C and D, and fig. S3B).

ABX significantly impaired CpG-ODN-induced *Tnf* expression and frequencies of TNF-positive leukocytes in MC38 tumors at 3 hours (Fig. 2, A and B). ABX decreased the frequencies of TNF-producing cells and the amount of cytokine per cell in Ly6C⁺ MHC-II⁺ monocytes, Ly6C⁺ F4/80^{hi} macrophages, CD11c^{hi} MHC-II⁺ dendritic cells (DC), and Ly6C⁺ F4/80^{int} MHC-II⁺ monocyte-derived cells (fig. S4, A to C). ABX also decreased CD86 expression and IL-12B production in tumor-associated DC (fig. S4, D and E). After anti-IL-10R/CpG-ODN, tumors from ABX-treated mice also displayed diminished expression of pro-inflammatory *Il1a*, *Il1b*, *Il12b*, and *Cxcl10*, but not of anti-inflammatory *Il10*, *Il1rn*, and *Socs3* or *Nos2* genes (fig. S5). To determine whether the ABX effect was dependent on decreased bacteria load, germ-free (GF) or specific pathogen-free (SPF) mice bearing MC38 tumors received anti-IL-10R/CpG-ODN treatment. Tumors of GF as compared to SPF control mice produced significantly lower amounts of TNF and IL-12B (Fig. 2, C to E). Thus, commensal microbiota primes tumor-associated innate myeloid cells for inflammatory cytokine production in response to anti-IL-10R/CpG-ODN, and ABX or the GF status of the mice attenuates this response and the TNF-dependent early tumor necrosis.

Gavage administration thrice weekly of bacterial lipopolysaccharide (LPS) largely restored *Tnf* expression and frequency of TNF-producing leukocytes in tumors of ABX-treated WT mice but not *Tlr4*^{-/-} mice [lacking the Toll-like receptor 4 (TLR4) receptor for LPS] (Fig. 2F and fig. S6A). Conversely, *Tlr4* deficiency led to lower

induction of *Tnf* and reduced tumor regression after immunotherapy (Fig. 2, F and G), whereas *Tlr2* deficiency had no effect (fig. S6B). Overall, these findings suggest that bacterial products, in part through TLR4 activation, directly or indirectly prime tumor-associated myeloid cells for TLR9-dependent response to CpG-ODN. The ability of oral ABX treatment to reduce gastrointestinal but not skin bacterial load, combined with an absence of bacterial DNA in tumors and the restorative effect of gastrointestinal LPS administration, suggest that intestinal bacteria regulate the inflammatory response in the tumor microenvironment.

To determine how individual bacterial species affect the antitumor response, we correlated fecal microbiota composition with TNF production. Principal-component analysis of natural variation in microbiota composition versus TNF production suggested a codependence (fig. S7). Two experimental microbiota perturbations were used: (i) three-week ABX treatment followed by a 1- to 4-week recovery, and (ii) three-week single-antibiotic treatments. Bacterial abundance was restored to pretreatment levels 1 week after ABX cessation (Fig. 3A); bacterial diversity (fig. S8) and composition gradually increased, although neither reached the pre-ABX condition (Fig. 3, B and C, and figs. S9 and S10). *Tnf* expression did not recover until week 4 post-ABX (Fig. 3D). All the single antibiotics tested increased variability

in *Tnf* expression, whereas only imipenem consistently reduced total bacterial abundance (fig. S11, A to D, and fig. S12). The different perturbations resulted in different bacteria being present. Thus, partially overlapping genera were identified that positively or negatively correlated with *Tnf* expression (figs. S13 and S14A). Among the positive correlates were Gram-negative genera [e.g., *Alistipes* (figs. S13 and S14A)], consistent with a role for TLR4 in priming TNF production. However, Gram-positive genera also showed positive correlation, suggesting that recognition pathways other than TLR4 were also involved. Identification of the same genera in different data sets increased the confidence in the validity of the correlation. Particularly, one genus (*Lactobacillus*) negatively and one (*Ruminococcus*) positively correlated with TNF expression in all three analyses (fig. S13). The *Lactobacillus* genus included *L. murinum*, *L. intestinalis*, and *L. fermentum*, the latter previously identified to have anti-inflammatory effects (12, 13). The *Ruminococcus* genus was represented by a single unclassified operational taxonomic unit (OTU) and the *Alistipes* genus by the single *A. shahii* species. *Lactobacillus* species recovered quickly after ABX withdrawal, whereas recovery of *Ruminococcus* and *Alistipes* species was delayed and coincided with restoration of the TNF response (fig. S14B). Administration of cultured *A. shahii* by gavage to mice preexposed

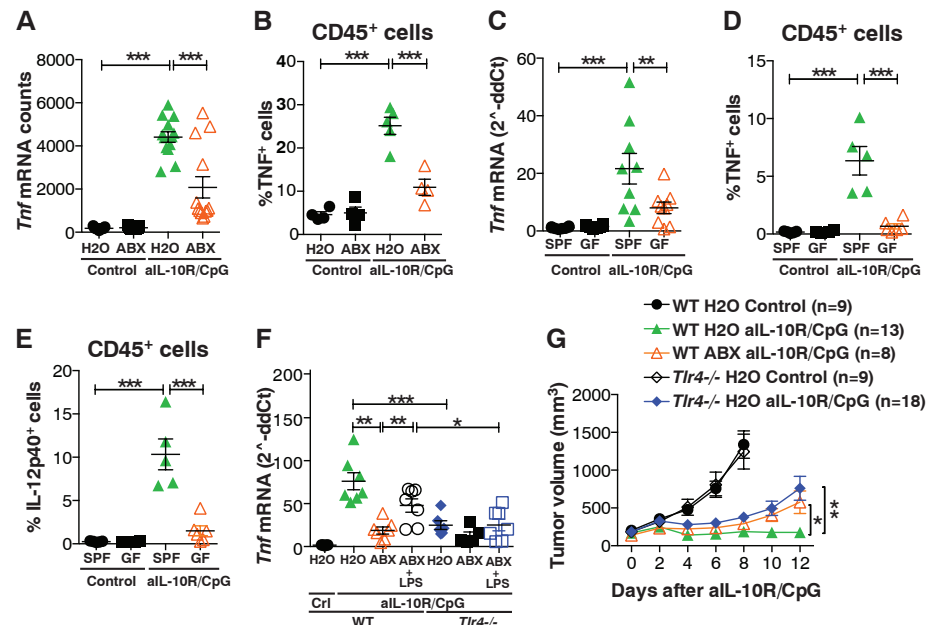


Fig. 2. Commensal bacteria and TLR4 are necessary for optimal TNF production by tumor myeloid cells after anti-IL-10R/CpG treatment. (A) *Tnf* mRNA (Nanostring nCounter) in MC38 tumors from H₂O- or ABX-treated mice exposed or not to anti-IL-10R/CpG-ODN therapy. (B) TNF-producing MC38 tumor infiltrating CD45⁺ cells in H₂O- or ABX-treated mice. (C to E) *Tnf* mRNA [real-time polymerase chain reaction (RT-PCR)] (C) and percentage TNF- (D) or IL-12p40- (E) producing CD45⁺ cells (flow cytometry) in MC38 tumors from SPF or GF mice. (F) MC38 tumor *Tnf* mRNA in WT mice or in *Tlr4*^{-/-} mice orally gavaged or not with LPS (25 mg per kg of weight, three times per week, 2 weeks before and 1 week after tumor injection). (G) MC38 tumor growth in H₂O- or ABX-treated WT mice or *Tlr4*^{-/-} mice treated or not with anti-IL-10R/CpG-ODN. Data show individual mice [(A) to (F)] or means ± SEM (G). **P* < 0.05, ***P* < 0.01, and ****P* < 0.001.

to ABX reconstituted the ability of tumor-associated myeloid cells to produce TNF (Fig. 3E and fig. S15A). Conversely, administration of *L. fermentum* to intact mice attenuated the response (fig. S15B). These association experiments validate the results of the correlation analysis and confirm the ability of these species to influence the tumor response to CpG-ODN.

To determine whether the microbiota also affects cancer treatments not considered to be directly dependent on inflammation processes, we next examined the response to agents used in human cancer chemotherapy. The platinum compounds oxaliplatin and cisplatin cause tumor cytotoxicity by forming platinum DNA adducts and intrastrand cross-links (14). Reactive oxygen species (ROS) are important for DNA damage and apoptosis in response to platinum compounds (15). Oxaliplatin, unlike cisplatin, also induces immunogenic cell death that drives antitumor T cell immunity (9, 16). Oxaliplatin eradicated most subcutaneous EL4 tumors and prolonged survival in control mice, but ABX-treated animals displayed significantly reduced tumor regression and survival (Fig. 4A

and fig. S16A). GF animals similarly failed to respond to oxaliplatin treatment (fig. S16B). The therapeutic effects of oxaliplatin on a different tumor (MC38) and of cisplatin on EL4 tumors were also significantly reduced in ABX-treated mice (fig. S16, C and D).

The effect of ABX was observed as early as day 2 after treatment with oxaliplatin (Fig. 4A), suggesting suppression of early cytotoxicity rather than of inflammation/immunity after immunogenic cell death. Indeed, ABX attenuated most gene expression changes observed in EL4 tumors 18 hours after oxaliplatin treatment (Fig. 4B). The genes inhibited by ABX were related to monocyte differentiation, activation, and function, whereas the genes that were increased in ABX-treated mice were related to cellular functions such as metabolism, transcription, translation, and DNA replication (fig. S17). Gene expression analysis using the Nanostring nCounter technology confirmed the expression changes of selected genes (fig. S18).

Gene expression analysis revealed that after oxaliplatin treatment the induction of pro-

inflammatory genes was decreased in the absence of microbiota, suggesting that inflammation was important for the antitumor effect of the drug. However, unlike anti-IL-10R/CpG-ODN, oxaliplatin antitumor effects were independent of TNF (fig. S19A). The observation that ABX treatment attenuated the induction of *Nox1* and *Cybb* encoding ROS-generating NADPH (reduced nicotinamide adenine dinucleotide phosphate) oxidase 2 (NOX2) and of the ROS-responsive *Nos2*, *Sod1*, and *Sod2* after oxaliplatin led us to examine oxaliplatin-induced ROS production. Oxaliplatin induced ROS in tumors from control but not ABX-treated mice, as detected in vivo by bioluminescence (fig. 4C). Induction of ROS was dependent on NOX2 encoded by the *Cybb* gene (Fig. 4C). Because NOX2 is expressed in phagocytic cells (17), we examined ROS production in tumor-infiltrating hematopoietic cells ex vivo. The fluorescence intensity of the ROS probe in tumor-infiltrating CD11b⁺Gr-1^{hi} neutrophils and in F4/80⁺ Gr-1^{int} macrophage-like cells increased after oxaliplatin treatment in control mice, but this response was impaired in ABX-treated or *Cybb*^{-/-} animals (Fig. 4D). ROS inhibition by the antioxidant N-acetyl cysteine (NAC) was previously shown to block oxaliplatin-induced apoptosis of cancer cell lines in vitro and inhibit the effectiveness of oxaliplatin therapy of mouse tumor cell lines in vivo (18, 19). We found that inhibition of ROS by either *Cybb* deficiency or NAC impaired oxaliplatin-induced EL4 tumor regression as early as day 2 and decreased overall survival at an extent comparable to that of ABX (Fig. 4E and fig. S19B). Depletion of myeloid cells by Gr-1 antibody impaired the ability of oxaliplatin to induce tumor regression and to increase survival (Fig. 4F and fig. S19C). These data suggest that the reduced effect of oxaliplatin in ABX-treated or GF mice is partially due to reduced myeloid-cell ROS production. To investigate whether gut commensals prime these cells by release of TLR agonists, we studied *Thr4*^{-/-} and *Myd88*^{-/-} mice. (Myd88 is the adaptor protein that signals downstream of IL-1 family receptors and most TLRs.) *Myd88*, but not *Thr4*, deficiency impaired the early antitumor effect of oxaliplatin, although *Thr4* deficiency had a partial effect on long-term tumor growth and survival (fig. S19D). *Il1r* or *Il18r* deficiency did not impair the response (fig. S19D), suggesting that the commensal effect was related to microbial product sensing.

The levels of tumor DNA-bound platinum were similar in control and ABX-treated mice, although tumors from ABX-treated mice showed reduced DNA damage (fig. S20). These data suggest that ABX prevent oxaliplatin-induced DNA damage and apoptosis after DNA adduct formation in part by decreasing ROS production (15, 18, 19). In ABX-treated mice, the decreased induction of the DNA damage response gene *Atr* and of the p53 downstream genes *Bax*, *Fas*, *Cdkn1a*, and *Rb1* is compatible with reduced tumor DNA damage and p53-dependent activation of apoptosis. Although tumor-cell-produced ROS were previously reported to be required for the

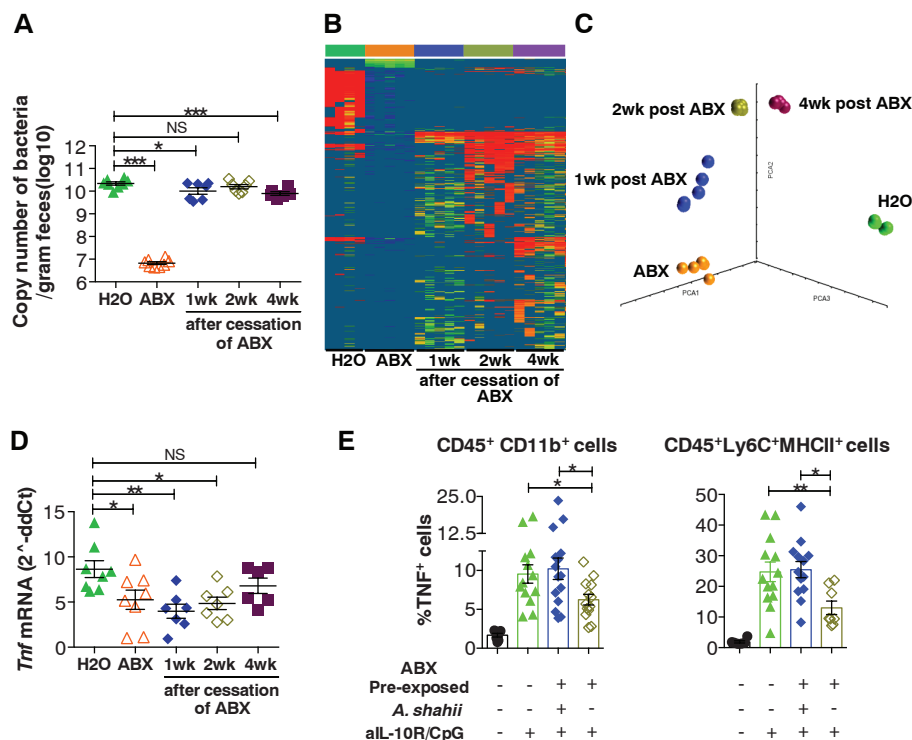


Fig. 3. Commensal microbiota composition correlates with tumor TNF response. (A and B) MC38 tumors were subcutaneously implanted 1, 2, or 4 weeks after the cessation of a 3-week ABX treatment. Control mice continuously drinking H₂O or ABX were included. (A) Eubacteria 16S ribosomal RNA gene copy number in feces was determined by RT-PCR. (B) 16S-sequence frequencies were analyzed by pyrosequencing in fecal microbiota. Data are shown as heat map of OTUs (97% similarity) normalized to copy number of 16S per gram of feces (OTUs represented by <0.1% of total reads were removed from the analysis). (C) Principal-component analysis of unweighted Unifrac distances. (D) Tumor *Tnf* mRNA expression 3 hours after anti-IL-10R/CpG-ODN treatment was determined by RT-PCR. (E) Control H₂O-drinking mice or 1 week after cessation of ABX treatment were exposed to anti-IL-10R/CpG-ODN therapy. A group of ABX pre-exposed mice was subjected to oral gavage with *A. shahii*. Mice were killed 3 hours after CpG-ODN treatment, and intracellular TNF was measured in the indicated tumor-associated myeloid cell subsets. Data show individual mice and means \pm SEM from one representative experiment out of two performed [(A) and (D)] or combined data from two experiments (E).

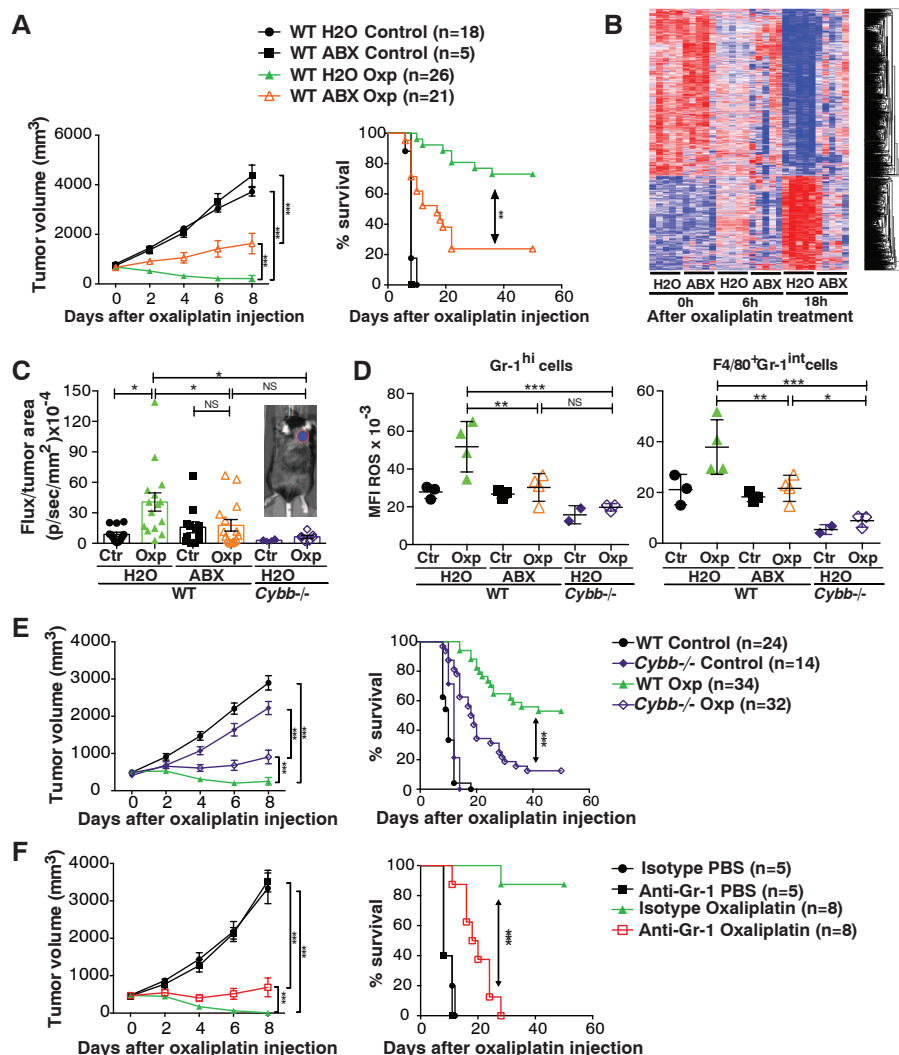


Fig. 4. Commensal bacteria control oxaliplatin therapy response by modulating ROS production. (A) Subcutaneous EL4 tumor-bearing H₂O- or ABX-treated mice were treated with oxaliplatin (10 mg per kg of weight); tumor growth (top) and survival (bottom) are shown. (B) Global gene expression ($q < 0.1$, >2 -fold change compared to time 0, two-way analysis of variance analysis) in tumors from H₂O- and ABX-treated mice before (0 hours) and after (6 and 18 hours) oxaliplatin treatment. (C and D) ROS production 24 hours after oxaliplatin injection in subcutaneous EL4 tumors from H₂O- or ABX-treated WT mice and *Cybb*^{-/-} mice was measured in vivo by bioluminescence (probe L-012) [inset in (C) shows a representative mouse with tumor area marked in red] and ex vivo in tumor-infiltrating cells (D, fluorescent probe, flow cytometry). (E and F) EL4-bearing WT and *Cybb*^{-/-} mice (E) and Gr-1 antibody- or immunoglobulin G isotype-treated mice (F) were treated with oxaliplatin. (A), (C), and (E) show data combined from several independent experiments; (D) and (F) show a representative experiment out of two.

cytotoxic effect of platinum compounds in vitro, our data indicate that the ROS required for oxaliplatin genotoxicity in vivo are mostly derived from tumor-associated inflammatory cells. Because ABX treatment affected tumor cytotoxicity shortly after chemotherapy, and this effect was observed using both oxaliplatin and its relative cisplatin that is unable to trigger immunogenic cell death, the data suggest that commensal bacteria modulate the genotoxicity of platinum compounds independently of immunity elicited by immunogenic cell death. However, DC activation and adaptive antitumor immune responses after oxaliplatin

may also require a commensal-dependent inflammatory response.

Besides platinum complexes, drugs such as anthracyclines, alkylating agents, podophyllotoxins, and camptothecine induce ROS as part of their anticancer activity and may be similarly regulated (15, 20–22). Mechanisms by which the gut microbiota affects the systemic inflammatory tone are only now being uncovered (23, 24). In a different setting, total body irradiation was shown to increase the efficacy of adoptively transferred tumor-specific CD8⁺ T cells in part by inducing microbial translocation (25). Our study indicates

that commensal bacteria differentially affect the type of inflammatory tone required for response to different therapeutic protocols and highlights the potential to improve cancer treatment by manipulating human gut microbiota.

References and Notes

- Y. K. Lee, S. K. Mazmanian, *Science* **330**, 1768–1773 (2010).
- J. C. Clemente, L. K. Ursell, L. W. Parfrey, R. Knight, *Cell* **148**, 1258–1270 (2012).
- J. P. McAleer, J. K. Kolls, *Immunity* **37**, 10–12 (2012).
- M. C. Abt et al., *Immunity* **37**, 158–170 (2012).
- T. Ichinohe et al., *Proc. Natl. Acad. Sci. U.S.A.* **108**, 5354–5359 (2011).
- S. I. Grivennikov, F. R. Greten, M. Karin, *Cell* **140**, 883–899 (2010).
- Y. Shirota, H. Shirota, D. M. Klinman, *J. Immunol.* **188**, 1592–1599 (2012).
- L. Zitvogel, O. Kepp, G. Kroemer, *Cell* **140**, 798–804 (2010).
- L. Apetoh et al., *Nat. Med.* **13**, 1050–1059 (2007).
- A. P. Vicari et al., *J. Exp. Med.* **196**, 541–549 (2002).
- C. Guiducci, A. P. Vicari, S. Sangaletti, G. Trinchieri, M. P. Colombo, *Cancer Res.* **65**, 3437–3446 (2005).
- R. R. Jenq et al., *J. Exp. Med.* **209**, 903–911 (2012).
- L. Peran et al., *Br. J. Nutr.* **97**, 96–103 (2007).
- Z. H. Siddik, *Oncogene* **22**, 7265–7279 (2003).
- T. Ozben, *J. Pharm. Sci.* **96**, 2181–2196 (2007).
- F. Ghiringhelli et al., *Nat. Med.* **15**, 1170–1178 (2009).
- G. R. Drummond, S. Selemidis, K. K. Griendling, C. G. Sobey, *Nat. Rev. Drug Discov.* **10**, 453–471 (2011).
- S. Kim, T. J. Lee, J. W. Park, T. K. Kwon, *J. Cell. Biochem.* **105**, 971–979 (2008).
- A. Laurent et al., *Cancer Res.* **65**, 948–956 (2005).
- K. A. Conklin, *Integr. Cancer Ther.* **3**, 294–300 (2004).
- J. Fang, H. Nakamura, A. K. Iyer, *J. Drug Target.* **15**, 475–486 (2007).
- S. Simizu, M. Takada, K. Umezawa, M. Imoto, *J. Biol. Chem.* **273**, 26900–26907 (1998).
- S. C. Ganai et al., *Immunity* **37**, 171–186 (2012).
- Y. Huang et al., *Genes Immun.* **13**, 311–320 (2012).
- C. M. Paulos et al., *J. Clin. Invest.* **117**, 2197–2204 (2007).

Acknowledgments: We greatly appreciate the support of D. Trageser-Cessler and A. Cesar in the NIAID germ-free facility; H. Zhou in the NIH Center for Human Immunology; T. Plona and K. Pike in the Laboratory of Molecular Technology, Leidos Biomedical Research, Inc.; and R. Winkler-Pickett, M. Karwan, and D. Zhao in the Cancer and Inflammation Program, CCR/NCI. We thank D. Klinman and A. Hurwitz for advice and R. Germain for critically reviewing the manuscript. The data presented in this manuscript are tabulated in the main paper and in the supplementary materials. This research was supported by the Intramural Research Program of the NIH (NCI, Center for Cancer Research, and NIAID) and the Japanese Society for Promotion of Science (JSPS) Research Fellowship for Japanese Biomedical and Behavioral Researchers at NIH. The 16S sequences were deposited in the Sequence Read Archive (SRA) under accession PRJNA221649. Array data were deposited at the Gene Expression Omnibus (GEO) with accession no. GSE51414.

Supplementary Materials

www.sciencemag.org/content/342/6161/967/suppl/DC1
Materials and Methods
Figs. S1 to S20
References (26–36)

15 May 2013; accepted 15 October 2013
10.1126/science.1240527

The Intestinal Microbiota Modulates the Anticancer Immune Effects of Cyclophosphamide

Sophie Viaud,^{1,3} Fabiana Saccheri,¹ Grégoire Mignot,^{4,5} Takahiro Yamazaki,¹ Romain Daillère,^{1,3} Dalil Hannani,¹ David P. Enot,^{7,8} Christina Pfirschke,⁹ Camilla Engblom,⁹ Mikael J. Pittet,⁹ Andreas Schlitzer,¹⁰ Florent Ginhoux,¹⁰ Lionel Apetoh,^{4,5} Elisabeth Chachaty,¹¹ Paul-Louis Woerther,¹¹ Gérard Eberl,¹² Marion Bérard,¹³ Chantal Ecobichon,^{14,15} Dominique Clermont,¹⁶ Chantal Bizet,¹⁶ Valérie Gaboriau-Routhiau,^{17,18} Nadine Cerf-Bensussan,^{17,18} Paule Opolon,^{19,20} Nadia Yessaad,^{21,22,23,24} Eric Vivier,^{21,22,23,24} Bernhard Ryffel,²⁵ Charles O. Elson,²⁶ Joël Doré,^{17,27} Guido Kroemer,^{7,8,28,29,30} Patricia Lepage,^{17,27} Ivo Gomperts Boneca,^{14,15} François Ghiringhelli,^{4,5,6*} Laurence Zitvogel^{1,2,3*†}

Cyclophosphamide is one of several clinically important cancer drugs whose therapeutic efficacy is due in part to their ability to stimulate antitumor immune responses. Studying mouse models, we demonstrate that cyclophosphamide alters the composition of microbiota in the small intestine and induces the translocation of selected species of Gram-positive bacteria into secondary lymphoid organs. There, these bacteria stimulate the generation of a specific subset of "pathogenic" T helper 17 (pT_H17) cells and memory T_H1 immune responses. Tumor-bearing mice that were germ-free or that had been treated with antibiotics to kill Gram-positive bacteria showed a reduction in pT_H17 responses, and their tumors were resistant to cyclophosphamide. Adoptive transfer of pT_H17 cells partially restored the antitumor efficacy of cyclophosphamide. These results suggest that the gut microbiota help shape the anticancer immune response.

It is well established that gut commensal bacteria profoundly shape mammalian immunity (1). Intestinal dysbiosis, which constitutes a disequilibrium in the bacterial ecosystem, can lead to overrepresentation of some bacteria able to promote colon carcinogenesis by favoring chronic inflammation or local immunosuppression (2, 3). However, the effects of microbial dysbiosis on nongastrointestinal cancers are unknown. Anticancer chemotherapeutics often cause mucositis (a debilitating mucosal barrier injury associated with bacterial translocation) and neutropenia, two complications that require treatment with antibiotics, which in turn can result in dysbiosis (4, 5). Some antineoplastic agents mediate part of their anticancer activity by stimulating anticancer immune responses (6). Cyclophosphamide (CTX), a prominent alkylating anticancer agent, induces immunogenic cancer cell death (7, 8), subverts immunosuppressive T cells (9), and promotes T_H1 and T_H17 cells controlling cancer outgrowth (10). Here, we investigated the impact of CTX on the small intestine microbiota and its ensuing effects on the antitumor immune response.

We characterized the inflammatory status of the gut epithelial barrier 48 hours after therapy with nonmyeloablative doses of CTX or the anthracycline doxorubicin in naïve mice. Both drugs caused shortening of small intestinal villi, discontinuities of the epithelial barrier, interstitial edema, and focal accumulation of mononuclear cells in the lamina propria (LP) (Fig. 1, A and B). After chemotherapy, the numbers of goblet cells and Paneth cells were increased in villi (Fig. 1C) and crypts (Fig. 1D), respectively. The antibac-

terial enzyme lysozyme (but not the microbicide peptide RegIIIγ) was up-regulated in the duodenum of CTX-treated mice (Fig. 1E). Orally administered fluorescein isothiocyanate (FITC)-dextran became detectable in the blood (11) 18 hours after CTX treatment, confirming an increase in intestinal permeability (Fig. 1F). Disruption of the intestinal barrier was accompanied by a significant translocation of commensal bacteria in >50% mice into mesenteric lymph nodes and spleens that was readily detectable 48 hours after CTX treatment, and less so after doxorubicin treatment (Fig. 2A). Several Gram-positive bacterial species, including *Lactobacillus johnsonii* (growing in >40% cases), *Lactobacillus murinus*, and *Enterococcus hirae*, could be cultured from these lymphoid organs (Fig. 2B).

Next, we analyzed the overall composition of the gut microbiota by high-throughput 454 pyrosequencing, followed by quantitative polymerase chain reaction (QPCR) targeting the domain bacteria and specific bacterial groups. Although CTX failed to cause a major dysbiosis at early time points (24 to 48 hours, fig. S1), CTX significantly altered the microbial composition of the small intestine (but not of the caecum) in mice bearing subcutaneous cancers (namely, metastasizing B16F10 melanomas and nonmetastasizing MCA205 sarcomas) 1 week after its administration (Fig. 2C and fig. S2). Consistent with previous reports on fecal samples from patients (12), CTX induced a reduction in bacterial species of the *Firmicutes* phylum (fig. S2) distributed within four genera and groups (*Clostridium* cluster XIVa, *Roseburia*, unclassified *Lachnospiraceae*, *Coprococcus*; table S1) in the mucosa of CTX-

treated animals. QPCR was applied to determine the relative abundance (as compared to all bacteria) of targeted groups of bacteria (*Lactobacillus*, *Enterococcus*, cluster IV of the *Clostridium leptum* group) in the small intestine mucosa from CTX-versus vehicle-treated naïve and tumor-bearing mice. In tumor bearers, the total bacterial load of the small intestine at 7 days after CTX treatment, as well as the bacterial counts of the *Clostridium leptum*, was not affected (Fig. 2D). However, CTX treatment led to a reduction in the abundance of lactobacilli and enterococci (Fig. 2D). Together, these data reveal the capacity of CTX to provoke the selective translocation of distinct Gram-positive bacterial species followed by notable changes in the small intestinal microbiome.

Coinciding with dysbiosis 7 days after CTX administration, the frequencies of CD103⁺CD11b⁺ dendritic cells (fig. S3A) and T cell receptor αβ (TCRαβ)⁺CD3⁺ T cells expressing the transcription factor RORγt (fig. S3B) were significantly decreased in the LP of the small intestine (but not the colon), as revealed by flow cytometry of dissociated tissues (fig. S3B) and in situ immunofluorescence staining (fig. S3C). RORγt is required for the generation of T_H17 cells [which produce

¹Institut National de la Santé et de la Recherche Médicale, U1015, Equipe labellisée Ligue Nationale Contre le Cancer, Institut Gustave Roussy, Villejuif, France. ²Centre d'Investigation Clinique Biothérapie CICBT 507, Institut Gustave Roussy, Villejuif, France. ³Université Paris-Sud, Kremlin Bicêtre, France. ⁴Institut National de la Santé et de la Recherche Médicale, U866, Centre Georges François Leclerc, Dijon, France. ⁵Institut National de la Santé et de la Recherche Médicale, Group Avenir, Dijon, France. ⁶Faculté de Médecine, Université de Bourgogne, Dijon, France. ⁷Institut National de la Santé et de la Recherche Médicale, U848, Institut Gustave Roussy, Villejuif, France. ⁸Metabolomics and Cell Biology Platforms, Institut Gustave Roussy, Villejuif, France. ⁹Center for Systems Biology, Massachusetts General Hospital and Harvard Medical School, Boston, MA, USA. ¹⁰Singapore Immunology Network (SiGN), Agency for Science, Technology and Research (A*STAR), Singapore. ¹¹Service de Microbiologie, Institut Gustave Roussy, Villejuif, France. ¹²Lymphoid Tissue Development Unit, Institut Pasteur, Paris, France. ¹³Nimale Centrale, Institut Pasteur, Paris, France. ¹⁴Institut Pasteur, Unit Biology and Genetics of the Bacterial Cell Wall, Paris, France. ¹⁵Institut National de la Santé et de la Recherche Médicale, Group Avenir, Paris, France. ¹⁶Institut Pasteur, Collection de l'Institut Pasteur, Paris, France. ¹⁷Institut National de la Recherche Agronomique, Micalis-UMR1319, 78350 Jouy-en-Josas, France. ¹⁸Institut National de la Santé et de la Recherche Médicale U989, Université Paris Descartes, 75730 Paris, France. ¹⁹Institut Gustave Roussy, IFR54, Villejuif, France. ²⁰Institut Gustave Roussy, Institut de Recherche en Cancérologie Intégrée de Villejuif (IRCIV), Laboratoire de Pathologie Expérimentale, Villejuif, France. ²¹Centre d'Immunologie de Marseille-Luminy, Aix-Marseille Université UM2, Marseille, France. ²²Institut National de la Santé et de la Recherche Médicale, UMR 1104, Marseille, France. ²³Centre National de la Recherche Scientifique, Unité Mixte de Recherche 7280, Marseille, France. ²⁴Assistance Publique des Hôpitaux de Marseille, Hôpital de la Conception, Marseille, France. ²⁵Laboratory of Molecular and Experimental Immunology and Neurogenetics, UMR 7355, CNRS-University of Orleans, Orleans, France. ²⁶University of Alabama at Birmingham, Birmingham, AL, USA. ²⁷AgroParisTech, Micalis-UMR1319, 78350 Jouy-en-Josas, France. ²⁸Equipe 11 labellisée Ligue contre le Cancer, Centre de Recherche des Cordeliers, Paris, France. ²⁹Pôle de Biologie, Hôpital Européen Georges Pompidou, Assistance Publique-Hôpitaux de Paris, Paris, France. ³⁰Université Paris Descartes, Paris, France.

*Joint senior authors.

†Corresponding author. E-mail: laurence.zitvogel@gustaveroussy.fr

interleukin-17 (IL-17)], and strong links between gut-residing and systemic T_H17 responses have been established in the context of autoimmune diseases affecting joints, the brain, or the pancreas (13–15). Confirming previous work (9, 10), CTX induced the polarization of splenic $CD4^+$ T cells toward a T_H1 [interferon- γ (IFN- γ)–producing] and T_H17 pattern (Fig. 3A and fig. S3D). This effect was specific for CTX and was not found for doxorubicin (fig. S4). The gut microbiota was indispensable for driving the conversion of naïve $CD4^+$ T cells into IL-17 producers in response to CTX. Indeed, the ex vivo IL-17 release by TCR-stimulated splenocytes increased upon CTX treatment of specific-pathogen-free (SPF) mice, yet failed to do so in germ-free (GF) mice (Fig. 3A, left panel). Sterilization of the gut by broad-spectrum antibiotics (ATB, a combination of colistin, ampicillin, and streptomycin; fig. S5) also suppressed the CTX-stimulated secretion of IL-17 (Fig. 3A, right panel) and IFN γ by TCR-stimulated splenocytes (fig. S3D). Treatment of mice with vancomycin, an antibiotic spe-

cific for Gram-positive bacteria (16), also reduced the CTX-induced T_H17 conversion (Fig. 3A, right panel). In conventional SPF mice, the counts of lactobacilli and SFB measured in small intestine mucosa (Fig. 2D) positively correlated with the T_H1 and T_H17 polarization of splenocytes (Fig. 3B and fig. S3E), whereas that of *Clostridium* group IV did not (Fig. 3B). Together, these results point to a specific association between particular microbial components present in the gut lumen (and occasionally in lymphoid organs) and the polarity of T_H responses induced by CTX treatment.

CTX increased the frequency of “pathogenic” T_H17 (p T_H17) cells, which share hallmarks of T_H1 cells (nuclear expression of the transcription factor T-bet, cytoplasmic expression of IFN- γ , and surface exposure of the chemokine receptor CXCR3) and T_H17 cells (expression of ROR γ t, IL-17 and CCR6) (17, 18), within the spleen (fig. S3F and Fig. 3C). Again, this response depended on the gut microbiota (Fig. 3C). Moreover, the increase in p T_H17 cells required expression of

myeloid differentiation primary response gene 88 (*MyD88*), which signals downstream of toll-like receptors (fig. S6A) and is required for the therapeutic success of anticancer chemotherapies in several tumor models (19). In contrast, the two pattern recognition receptors, nucleotide-binding oligomerization domain-containing 1 (Nod1) and Nod2, were dispensable for the CTX-induced raise in splenic p T_H17 cells and for the tumor growth-retarding effects of CTX (fig. S6B). These results establish the capacity of CTX to stimulate p T_H17 cells through a complex circuitry that involves intestinal bacteria and MyD88, correlating with its anticancer effects. Beyond its general effect on the frequency of p T_H17 cells, CTX induced TCR-restricted, antigen-specific immune responses against commensal bacteria (fig. S7). Hence, we addressed whether Gram-positive bacterial species that translocated into secondary lymphoid organs in response to CTX (Fig. 2A) could polarize naïve $CD4^+$ T cells toward a T_H1 or T_H17 pattern. Both *L. johnsonii* and *E. hirae* stimulated the differentiation of naïve $CD4^+$ T cells into T_H1

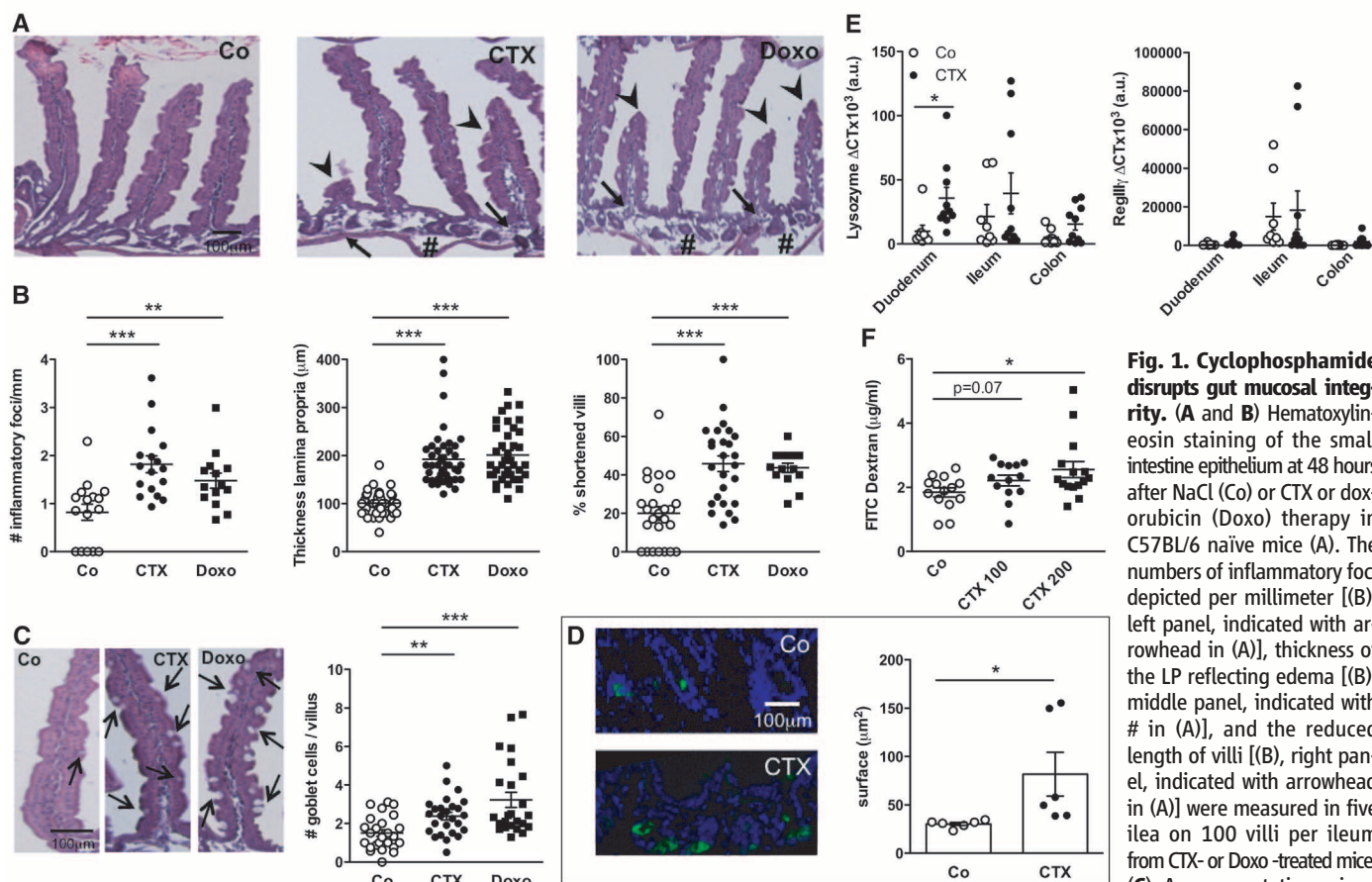


Fig. 1. Cyclophosphamide disrupts gut mucosal integrity.

(A and B) Hematoxylin-eosin staining of the small intestine epithelium at 48 hours after NaCl (Co) or CTX or doxorubicin (Doxo) therapy in C57BL/6 naïve mice (A). The numbers of inflammatory foci depicted per millimeter [(B), left panel, indicated with arrowhead in (A)], thickness of the LP reflecting edema [(B), middle panel, indicated with # in (A)], and the reduced length of villi [(B), right panel, indicated with arrowhead in (A)] were measured in five ilea on 100 villi per ileum from CTX- or Doxo-treated mice. (C) A representative micrograph of an ileal villus containing typical mucin-containing goblet cells is shown in vehicle- and CTX- or Doxo-treated mice (left panels). The number of goblet cells per villus was enumerated in the right panel for both chemotherapy agents. (D) Specific staining of Paneth cells is shown in two representative immunofluorescence micrographs (left panels). The number of Paneth cells was quantified by measuring the average area of the lysozyme-positive clusters in six ilea harvested from mice treated with NaCl (Co) or CTX at 24 to 48 hours (right panel). (E) QPCR analyses of lysozyme M and RegIIIγ transcription levels in duodenum and ileum LP cells from mice treated with CTX at 18 hours. Means \pm SEM of normalized Δ CT of three to four mice per group pooled from three independent experiments. (F) In vivo intestinal permeability assays measuring 4-kD FITC-dextran plasma accumulation at 18 hours after CTX treatment at two doses. Graph shows all data from four independent experiments, with each symbol representing one mouse ($n = 13$ to 15 mice). Data were analyzed with the Student's t test. * $P < 0.05$, ** $P < 0.01$, *** $P < 0.001$.

and T_H17 cells in vitro, in the presence of bone marrow–derived dendritic cells, whereas toll-like receptor 4–activating purified bacterial lipopolysaccharide (LPS) or *Escherichia coli* both had a minor effect (fig. S8). Moreover, orally fed *L. johnsonii* and *E. hirae*, but neither *L. plantarum* (a bacterium that was not detected in translocation experiments, Fig. 2B) nor *L. reuteri*, facilitated the reconstitution of the pool of pT_H17 cells in the spleen of ATB-treated SPF mice (Fig. 3D). T_H1 memory responses against *L. johnsonii* were consistently detected in 50% of mice receiving CTX (Fig. 3E) but not in control mice, after in vitro restimulation of CD4⁺ T cells with bone marrow–derived dendritic cells loaded with *L. johnsonii* (and to a lesser extent *E. hirae*, but not with other commensals or pathobionts). Taking into account that CTX-induced dysbiosis peaks at late time points (day 7), we postulate that the translocation of a specific set of Gram-positive commensal bacteria is necessary and sufficient to mediate the CTX-driven accumulation of pT_H17 cells and T_H1 bacteria-specific memory T cell responses.

Because commensal bacteria modulate intestinal and systemic immunity after CTX treatment, we further investigated the effect of antibiotics on CTX-mediated tumor growth inhibition. Long-term treatment with broad-spectrum ATB reduced the capacity of CTX to cure P815 mastocytomas established in syngenic DBA2 mice (Fig. 4A and fig. S9A). Moreover, the antitumor effects mediated by CTX against MCA205 sarcomas were reduced in GF compared with SPF mice (Fig. 4B, left and middle panels). Driven by the observations that CTX mostly induced the translocation of Gram-positive bacteria and that Gram-positive bacteria correlated with splenic T_H1/T_H17 polarization, we compared the capacity of several ATB regimens: namely, vancomycin (depleting Gram-positive bacteria) and colistin (depleting most Gram-negative bacteria) to interfere with the tumor growth–inhibitory effects of CTX. Vancomycin, and to a lesser extent colistin, compromised the antitumor efficacy of CTX against MCA205 sarcoma (Fig. 4C and fig. S9B). Using a transgenic tumor model of autochthonous lung carcinogenesis driven by oncogenic K-Ras coupled

to conditional p53 deletion (20), we confirmed the inhibitory role of vancomycin on the anticancer efficacy of a CTX-based chemotherapeutic regimen (Fig. 4D). Vancomycin also prevented the CTX-induced accumulation of pT_H17 in the spleen (Fig. 4E) and reduced the frequencies of tumor-infiltrating CD3⁺ T cells and T_H1 cells (Fig. 4F).

Although the feces of most SPF mice treated with ATB usually were free of cultivable bacteria (fig. S5), some mice occasionally experienced the outgrowth of *Parabacteroides distasonis*, a species reported to maintain part of the intestinal regulatory T cell repertoire and to mediate local anti-inflammatory effects (21–23). This bacterial contamination was associated with the failure of an immunogenic chemotherapy (doxorubicin) against established MCA205 sarcomas (fig. S10A). Moreover, experimental recolonization of ATB-sterilized mice with *P. distasonis* compromised the anticancer effects of doxorubicin (fig. S10B), demonstrating that gut microbial dysbiosis abrogates anticancer therapy. Finally, monoassociation of tumor-bearing GF mice with SFB, which promotes

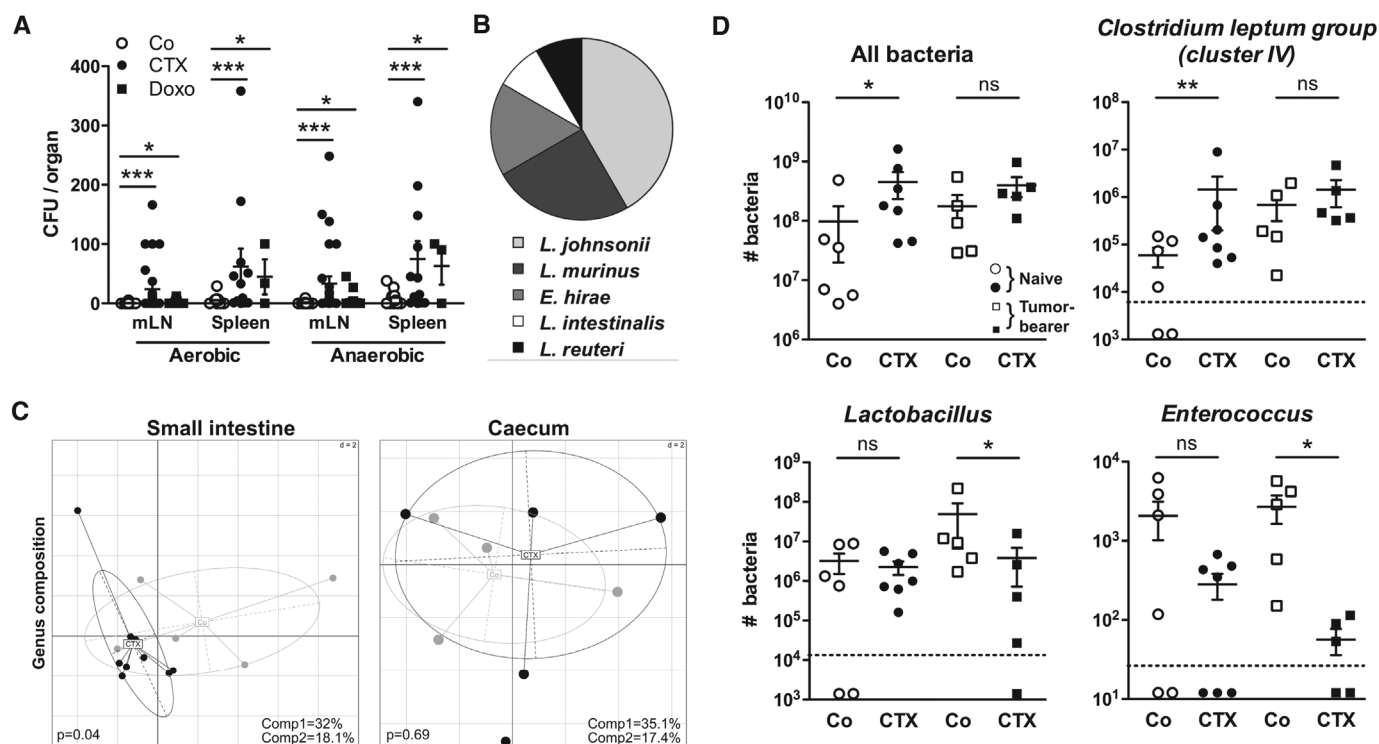


Fig. 2. Cyclophosphamide induces mucosa-associated microbial dysbiosis and bacterial translocation in secondary lymphoid organs. (A and B) At 48 hours after CTX or Doxo treatment, mesenteric lymph node (mLN) and spleen cells from naïve mice were cultivated in aerobic and anaerobic conditions, and colonies were enumerated (A) from each mouse treated with NaCl (Co) ($n = 10$ to 16 mice), CTX ($n = 12$ to 27 mice), or Doxo ($n = 3$ to 17 mice) (three to four experiments) and identified by mass spectrometry (B). In NaCl controls, attempts at bacterial identification mostly failed and yielded 67% *L. murinus* (not shown). Data were analyzed with the Student's t test. (C) The microbial composition (genus level) was analyzed by 454 pyrosequencing of the 16S ribosomal RNA gene from ilea and caeca of naïve mice and B16F10 tumor bearers. Principal-component analyses highlighted specific clustering of mice

microbiota (each circle represents one mouse) depending on the treatment (NaCl: Co, gray circles; CTX-treated, black circles). A Monte Carlo rank test was applied to assess the significance of these clusterings. (D) QPCR analyses of various bacterial groups associated with small intestine mucosa were performed on CTX- or NaCl (Co)-treated, naïve, or MCA205 tumor-bearing mice. Absolute values were calculated for total bacteria, *Lactobacilli*, *Enterococci*, and *Clostridium* group IV and normalized by the dilution and weight of the sample. Standard curves were generated from serial dilutions of a known concentration of genomic DNA from each bacterial group and by plotting threshold cycles (Ct) versus bacterial quantity (colony-forming units). Points below the dotted lines were under the detection threshold. Data were analyzed with the linear model or generalized linear model. * $P < 0.05$, ** $P < 0.01$, *** $P < 0.001$; ns, not significant.

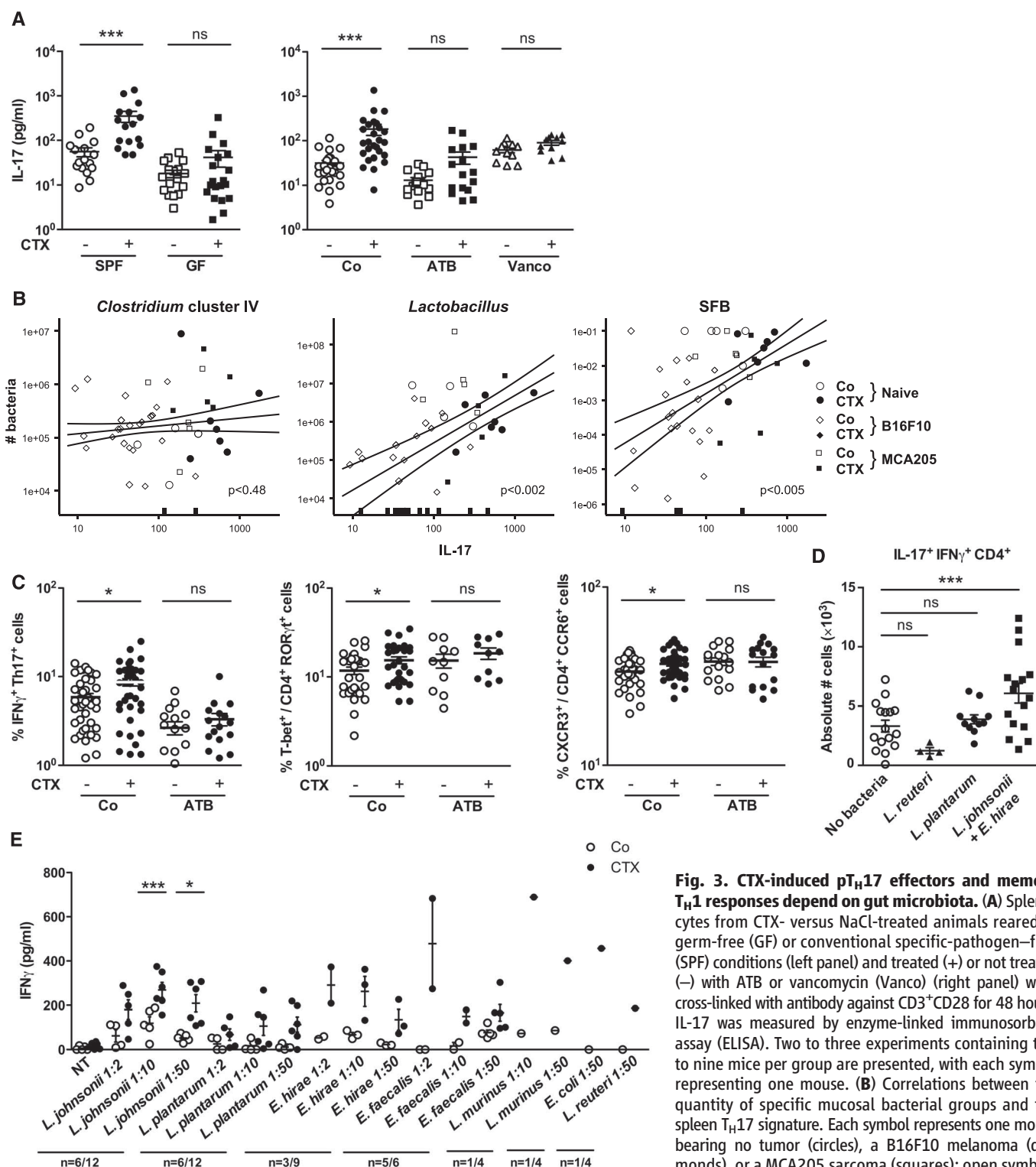


Fig. 3. CTX-induced pTH17 effectors and memory TH1 responses depend on gut microbiota. (A) Splenocytes from CTX- versus NaCl-treated animals reared in germ-free (GF) or conventional specific-pathogen-free (SPF) conditions (left panel) and treated (+) or not treated (−) with ATB or vancomycin (Vanco) (right panel) were cross-linked with antibody against CD3⁺CD28 for 48 hours. IL-17 was measured by enzyme-linked immunosorbent assay (ELISA). Two to three experiments containing two to nine mice per group are presented, with each symbol representing one mouse. (B) Correlations between the quantity of specific mucosal bacterial groups and the spleen TH17 signature. Each symbol represents one mouse bearing no tumor (circles), a B16F10 melanoma (diamonds), or a MCA205 sarcoma (squares); open symbols denote NaCl-treated mice and filled symbols indicate CTX-treated animals. (C) Intracellular analyses of splenocytes harvested from non-tumor-bearing mice after 7 days of either NaCl or CTX treatment, under a regimen of ATB or with water as control. Means \pm SEM of percentages of IFN- γ ⁺ TH17⁺ cells, T-bet⁺ cells among ROR γ t⁺ CD4⁺ T cells, and CXCR3⁺ cells among CCR6⁺CD4⁺ T cells in two to eight independent experiments, with each circle representing one mouse. (D) Intracellular staining of total splenocytes harvested 7 days after CTX treatment from naïve mice orally reconstituted with the indicated bacterial species after ATB treatment. (E) Seven days after CTX or NaCl (Co) treatment, splenic CD4⁺ T cells were restimulated ex vivo with bone-marrow dendritic cells loaded with decreasing amounts of bacteria for 24 hours. IFN- γ release, monitored by ELISA, is shown. The numbers of responder mice (based on the NaCl baseline threshold) out of the total number of mice tested is indicated (n). Statistical comparisons were based on the paired *t* test. Data were analyzed with either beta regression or linear model and correlation analyses from modified Kendall tau. **P* < 0.05, ****P* < 0.001; ns, not significant.

cytes harvested from non-tumor-bearing mice after 7 days of either NaCl or CTX treatment, under a regimen of ATB or with water as control. Means \pm SEM of percentages of IFN- γ ⁺ TH17⁺ cells, T-bet⁺ cells among ROR γ t⁺ CD4⁺ T cells, and CXCR3⁺ cells among CCR6⁺CD4⁺ T cells in two to eight independent experiments, with each circle representing one mouse. (D) Intracellular staining of total splenocytes harvested 7 days after CTX treatment from naïve mice orally reconstituted with the indicated bacterial species after ATB treatment. (E) Seven days after CTX or NaCl (Co) treatment, splenic CD4⁺ T cells were restimulated ex vivo with bone-marrow dendritic cells loaded with decreasing amounts of bacteria for 24 hours. IFN- γ release, monitored by ELISA, is shown. The numbers of responder mice (based on the NaCl baseline threshold) out of the total number of mice tested is indicated (n). Statistical comparisons were based on the paired *t* test. Data were analyzed with either beta regression or linear model and correlation analyses from modified Kendall tau. **P* < 0.05, ****P* < 0.001; ns, not significant.

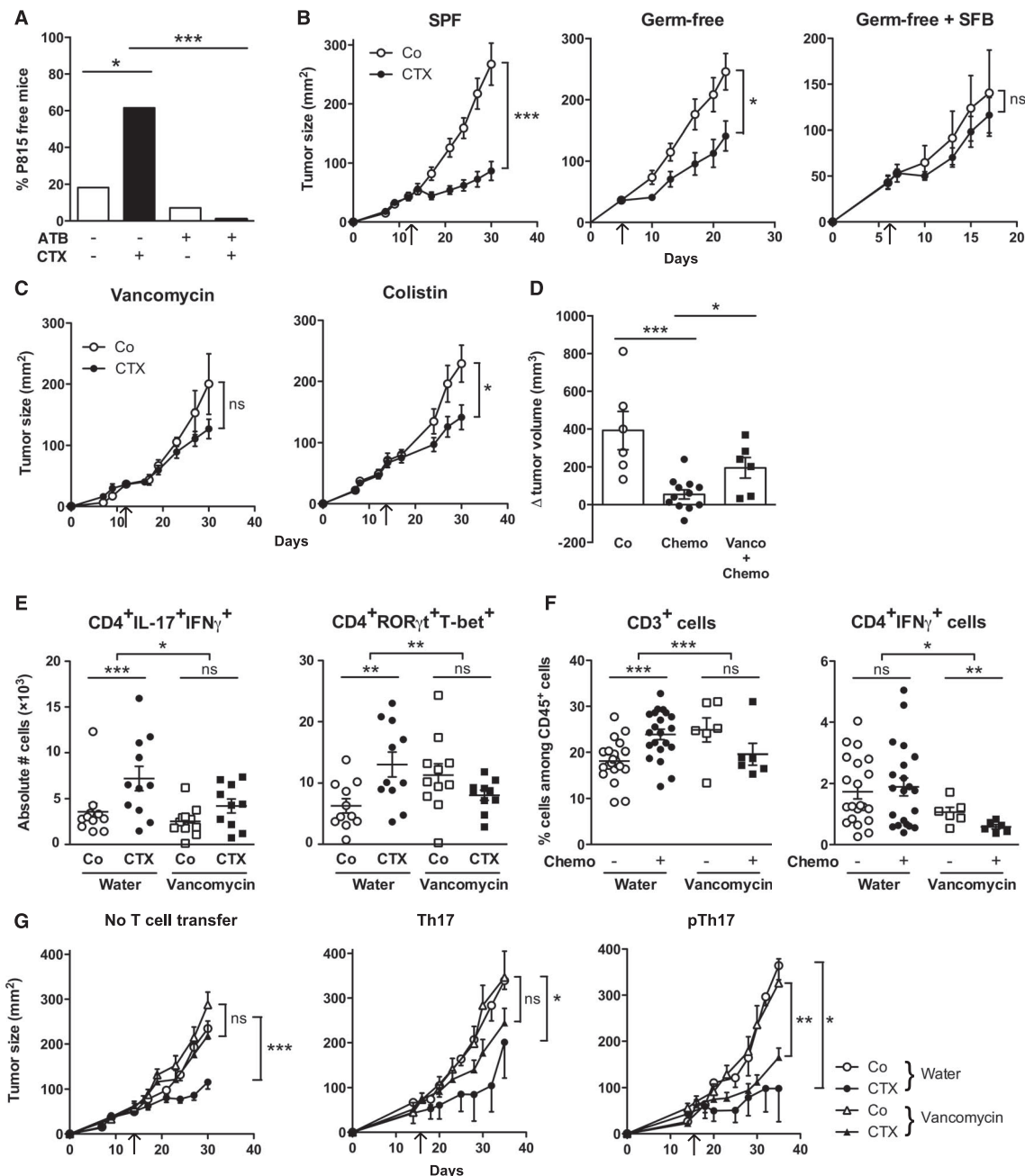
T_H17 cell differentiation in the LP (1, 13, 14), also had a detrimental impact on the tumor growth-inhibitory effect of CTX (Fig. 4B, right panel).

The aforementioned results highlight the association between specific CTX-induced alterations in gut microbiota, the accumulation of pT_H17

cells in the spleen, and the success of chemotherapy. To establish a direct causal link between these phenomena, we adoptively transferred T_H17

Fig. 4. Vancomycin blunts CTX-induced pT_H17 differentiation, which is mandatory for the tumoricidal activity of chemotherapy.

(A) After a 3-week-long pretreatment with broad-spectrum ATB, DBA2 mice were inoculated with P815 mastocytomas (day 0) and treated at day 6 with CTX, and tumor growth was monitored. Tumor growth kinetics are shown in fig. S9A, and percentages of tumor-free mice at the time mice were killed are depicted for two experiments of 11 to 14 mice per group. (B) MCA205 sarcomas were inoculated at day 0 in specific-pathogen-free (SPF) or germ-free (GF) mice that were optionally mono-associated with segmented filamentous bacteria (SFB), treated with CTX (arrow), and monitored for growth kinetics (means \pm SEM). One representative experiment ($n = 5$ to 8 mice per group) out of two or three is shown for GF mice and two pooled experiments ($n = 14$ mice per group) for SPF mice. (C) After a 3-week conditioning with vancomycin or colistin, C57BL/6 mice were inoculated with MCA205 sarcomas (day 0) and treated at day 12 to 15 with CTX (arrow), and tumor growth was monitored. Pooled data ($n = 15$ to 20 mice per group) from two independent experiments are shown for colistin treatment and one representative experiment ($n = 6$ mice per group) for vancomycin treatment. (D) Eight-week-old KP (*Kras*^{LSL-G12D/WT}; *p53*^{Flox/Flox}) mice received an adenovirus expressing the Cre recombinase (AdCre) by intranasal instillation to initiate lung adenocarcinoma (day 0). Vancomycin was started for a subgroup of mice (Chemo + Vanco) on day 77 after AdCre treatment. One week after the start of vancomycin, CTX-based chemotherapy was applied intraperitoneally to mice that received only chemotherapy (Chemo) or that received in parallel vancomycin (Chemo + Vanco). Mice received chemotherapy on days 84, 91, and 98. A control group was left untreated (Co). Data show the evolution of total lung tumor volumes (mean \pm SEM) assessed by noninvasive imaging between days 73 and 100 in 6 to 12 mice per group. (E) As in Fig. 3C, we determined the number of pT_H17 cells in spleens from untreated or vancomycin-



treated mice bearing established (15 to 17 days) MCA205 tumors, 7 days after CTX treatment. Each symbol represents one mouse from two pooled experiments. (F) Flow cytometric analyses of CD3⁺ and CD4⁺IFN- γ ⁺ T cells were performed by gating on CD45⁺ live tumor-infiltrating lymphocytes extracted from day 18 established MCA205 tumors (8 days after CTX treatment) in water- or vancomycin-treated mice. Each symbol represents one mouse from up to four pooled experiments. (G) MCA205 tumors established in wild-type mice pretreated for 3 weeks with water or vancomycin were injected with CTX (arrow), and tumor growth was monitored. At day 7 after CTX treatment, 3 million ex vivo generated T_H17 or pT_H17 CD4⁺ T cells were injected intravenously. Up to three experiments with 2 to 10 mice per group were pooled. Data were analyzed with either the *t* test, linear model, or generalized linear model. **P* < 0.5, ***P* < 0.1, ****P* < 0.001; ns, not significant.

or pT_H17 populations into vancomycin-treated mice and evaluated their capacity to reestablish the CTX-mediated tumor growth retardation. Ex vivo propagated pT_H17 exhibited a pattern of gene expression similar to that expressed by CTX-induced splenic CD4⁺ T cells in vivo (fig. S11). Only pT_H17, but not T_H17 cells, could rescue the negative impact of vancomycin on the CTX-mediated therapeutic effect (Fig. 4G). These results emphasize the importance of pT_H17 cells for CTX-mediated anticancer immune responses.

Although much of the detailed molecular mechanisms governing the complex interplay between epithelial cells, gut microbiota, and intestinal immunity remain to be deciphered, the present study unveils the unsuspected impact of the intestinal flora on chemotherapy-elicited anticancer immune responses. Our data underscore new risks associated with antibiotic medication during cancer treatments, as well as the potential therapeutic utility of manipulating the gut microbiota.

References and Notes

1. L. V. Hooper, D. R. Littman, A. J. Macpherson, *Science* **336**, 1268–1273 (2012).
2. S. I. Grivennikov et al., *Nature* **491**, 254–258 (2012).
3. S. Wu et al., *Nat. Med.* **15**, 1016–1022 (2009).
4. M. J. van Vliet, H. J. Harmsen, E. S. de Bont, W. J. Tissing, *PLoS Pathog.* **6**, e1000879 (2010).
5. C. Ubeda et al., *J. Clin. Invest.* **120**, 4332–4341 (2010).
6. G. Kroemer, L. Galluzzi, O. Kepp, L. Zitvogel, *Annu. Rev. Immunol.* **31**, 51–72 (2013).
7. A. Sistigu et al., *Semin. Immunopathol.* **33**, 369–383 (2011).
8. G. Schiavoni et al., *Cancer Res.* **71**, 768–778 (2011).
9. F. Ghiringhelli et al., *Eur. J. Immunol.* **34**, 336–344 (2004).
10. S. Viaud et al., *Cancer Res.* **71**, 661–665 (2011).
11. J. Yang, K. X. Liu, J. M. Qu, X. D. Wang, *Eur. J. Pharmacol.* **714**, 120–124 (2013).
12. J. Zwieler et al., *PLoS ONE* **6**, e28654 (2011).
13. H. J. Wu et al., *Immunity* **32**, 815–827 (2010).
14. Y. K. Lee, J. S. Menezes, Y. Umesaki, S. K. Mazmanian, *Proc. Natl. Acad. Sci. U.S.A.* **108** (suppl. 1), 4615–4622 (2011).
15. L. Wen et al., *Nature* **455**, 1109–1113 (2008).
16. L. B. Rice, *Am. J. Infect. Control* **34** (suppl. 1), S11–S19, discussion S64–S73 (2006).
17. Y. Lee et al., *Nat. Immunol.* **13**, 991–999 (2012).
18. K. Ghoreschi et al., *Nature* **467**, 967–971 (2010).
19. L. Apetoh et al., *Nat. Med.* **13**, 1050–1059 (2007).

20. V. Cortez-Retamozo et al., *Proc. Natl. Acad. Sci. U.S.A.* **109**, 2491–2496 (2012).
21. M. Kverka et al., *Clin. Exp. Immunol.* **163**, 250–259 (2011).
22. S. K. Lathrop et al., *Nature* **478**, 250–254 (2011).
23. M. B. Geuking et al., *Immunity* **34**, 794–806 (2011).

Acknowledgments: We thank T. Angélique (Institut Pasteur), C. Flament, M. Vétizou (Gustave Roussy), and K. LeRoux (INRA) for technical assistance. The data reported in this manuscript are tabulated in the main paper and in the supplementary materials. This work was supported by Institut National du Cancer (INCa), la Ligue contre le cancer (LIGUE), labelisée, L.Z., G.K.), SIRIC Socrates, LABEX, and PACRI Onco-Immunology, European Research Council Advanced Grant (to G.K.), and European Research Council starting grant (PGNfromSHAPEtoVIR no. 202283 to I.G.B.), and partially supported by NIH grant P01DK071176 (C.O.E.).

Supplementary Materials

www.sciencemag.org/content/342/6161/971/suppl/DC1
Materials and Methods
Supplementary Text
Figs. S1 to S12
Table S1
References (24–42)

16 September 2013; accepted 16 October 2013
10.1126/science.1240537

Substitutions Near the Receptor Binding Site Determine Major Antigenic Change During Influenza Virus Evolution

Björn F. Koel,¹ David F. Burke,^{2,3} Theo M. Bestebroer,¹ Stefan van der Vliet,¹ Gerben C. M. Zondag,^{4,5} Gaby Vervaet,¹ Eugene Skepner,^{2,3} Nicola S. Lewis,^{2,3} Monique I. J. Spronken,¹ Colin A. Russell,^{3,6} Mikhail Y. Eropkin,⁷ Aeron C. Hurt,⁸ Ian G. Barr,⁸ Jan C. de Jong,¹ Guus F. Rimmelzwaan,¹ Albert D. M. E. Osterhaus,¹ Ron A. M. Fouchier,^{1,*} Derek J. Smith^{1,2,3,9*}

The molecular basis of antigenic drift was determined for the hemagglutinin (HA) of human influenza A/H3N2 virus. From 1968 to 2003, antigenic change was caused mainly by single amino acid substitutions, which occurred at only seven positions in HA immediately adjacent to the receptor binding site. Most of these substitutions were involved in antigenic change more than once. Equivalent positions were responsible for the recent antigenic changes of influenza B and A/H1N1 viruses. Substitution of a single amino acid at one of these positions substantially changed the virus-specific antibody response in infected ferrets. These findings have potentially far-reaching consequences for understanding the evolutionary mechanisms that govern influenza viruses.

Influenza A/H3N2 virus is a major cause of morbidity and mortality in humans and poses a considerable economic burden (1, 2). Vac-

cination is the primary method to reduce this public health impact. The hemagglutinin (HA) surface glycoprotein is the main component of influenza vaccines, and antibodies to HA can prevent serious illnesses (3). However, influenza viruses can escape from antibody-mediated neutralization by accumulating mutations in HA in a process called antigenic drift, and as a consequence influenza vaccines require frequent updates. Several recent studies have focused on the identification of conserved domains of HA as targets of virus-neutralizing antibodies to circumvent this problem (4–7). Other recent work has focused on identifying the mechanisms of antigenic drift (8, 9) and on sequence-based prediction to identify positively selected codons (10–13). This research has been restricted by our limited

fundamental insight into the molecular basis of antigenic evolution.

Seminal work in the 1980s identified 131 amino acid positions in five antigenic sites (A to E) on the globular head of HA as main targets for specific antibodies and suggested that antigenic drift is caused by accumulation of amino acid substitutions in these sites (14, 15). This work led to the widely used heuristic that it takes at least four amino acid substitutions, spread between two or more different antigenic sites, to cause substantial antigenic change. Smith *et al.* (16) showed that 11 antigenic clusters of viruses emerged during the 35-year period that followed the introduction of the A/H3N2 virus in humans in 1968, each of which was subsequently replaced by viruses with distinct antigenic properties. Between 1 and 13 amino acid substitutions were associated with each of the antigenic cluster transitions. Almost all of these cluster-difference substitutions were in the antigenic sites (16). Here, we investigated which of these substitutions actually caused the antigenic change.

We selected a representative virus from each antigenic cluster. The HA1 subunit amino acid sequence, which comprises the globular head domain of HA including the receptor binding site (RBS), of each representative virus was identical to the consensus sequence for all strains from the respective cluster (17). The consensus HA genes, representing natural circulating viruses, were used to make recombinant viruses in the context of the A/Puerto Rico/8/1934 reference virus (18). We also produced chimeric viruses with the full HA1 or with HA1 positions 109 to 301 of each antigenic cluster consensus strain in the context of HA of the Sichuan 1987 cluster consensus virus (fig. S1). The antigenic properties of all viruses were analyzed in hemagglutination inhibition (HI) assays using a panel of 8 to 16 ferret antisera raised against A/H3N2 viruses between 1968 and 2006 (table S1). The wild-type, recombinant, and chi-

¹Department of Viroscience, Erasmus MC, 3015GE Rotterdam, Netherlands. ²Center for Pathogen Evolution, Department of Zoology, University of Cambridge, Cambridge CB2 3EJ, UK. ³WHO Collaborating Centre for Modeling Evolution and Control of Emerging Infectious Diseases, University of Cambridge, Cambridge CB2 3EJ, UK. ⁴BaseClear B.V., 2333CC Leiden, Netherlands. ⁵Luris, Leiden University, 2333AA Leiden, Netherlands. ⁶Department of Veterinary Medicine, University of Cambridge, Cambridge CB3 0ES, UK. ⁷Research Institute of Influenza, 197376 St. Petersburg, Russia. ⁸WHO Collaborating Centre for Reference and Research on Influenza, VIDRL, Melbourne, Victoria 3051, Australia. ⁹Fogarty International Center, National Institutes of Health, Bethesda, MD 20892, USA.

*Corresponding author. E-mail: dsmith@zoo.cam.ac.uk (D.J.S.); r.fouchier@erasmusmc.nl (R.A.M.F.)

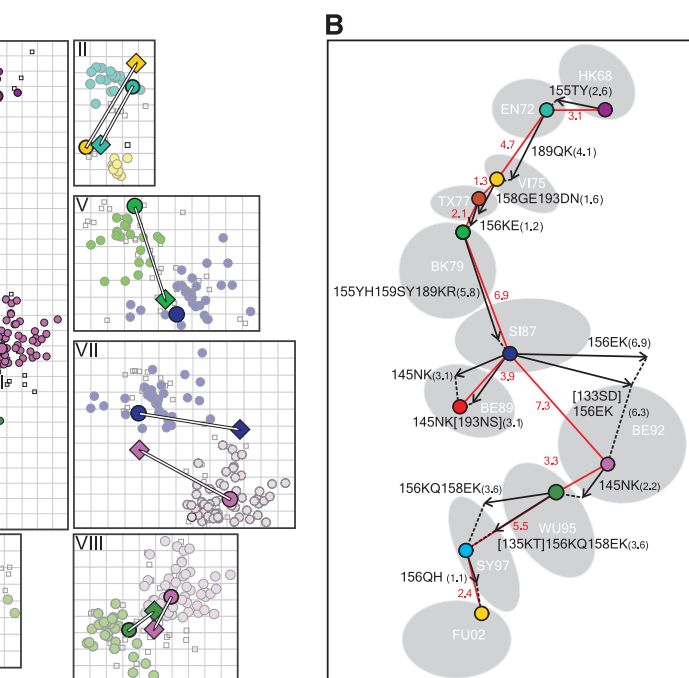
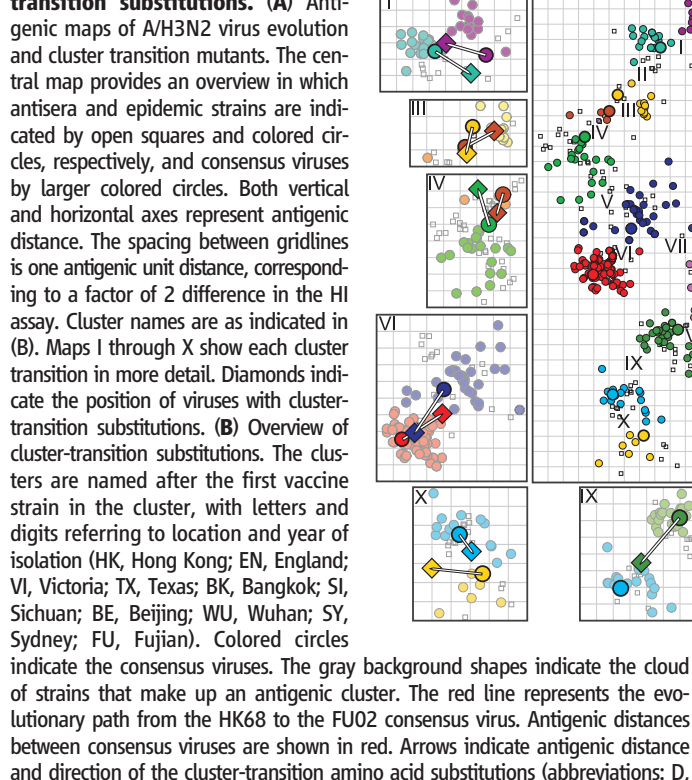
meric viruses all had similar antigenic properties in the HI assay (figs. S2 and S3). Thus, HA1 positions 109 to 301 determined the antigenic phenotype of representative A/H3N2 strains circulating between 1968 and 2003.

Each of the 54 cluster-difference substitutions within positions 109 to 301 of the HA1 region (table S2) was introduced independently into the corresponding consensus HA and tested for antigenic effect. If no single substitution induced the antigenic change to the subsequent cluster, combinations of substitutions were tested. We call the subset of cluster-difference substitutions that were

responsible for the major antigenic change between clusters “cluster-transition” substitutions. The cluster-transition substitutions were also tested in reverse. For example, each of the 11 cluster-difference substitutions between the EN72 and VI75 clusters were introduced individually in the EN72 consensus virus. We found that substitution 189QK alone caused the change in antigenic phenotype from EN72-like to VI75-like. The reverse substitution 189KQ was then introduced into the VI75 consensus HA and resulted in reversion of the antigenic phenotype to EN72-like (fig. S4B).

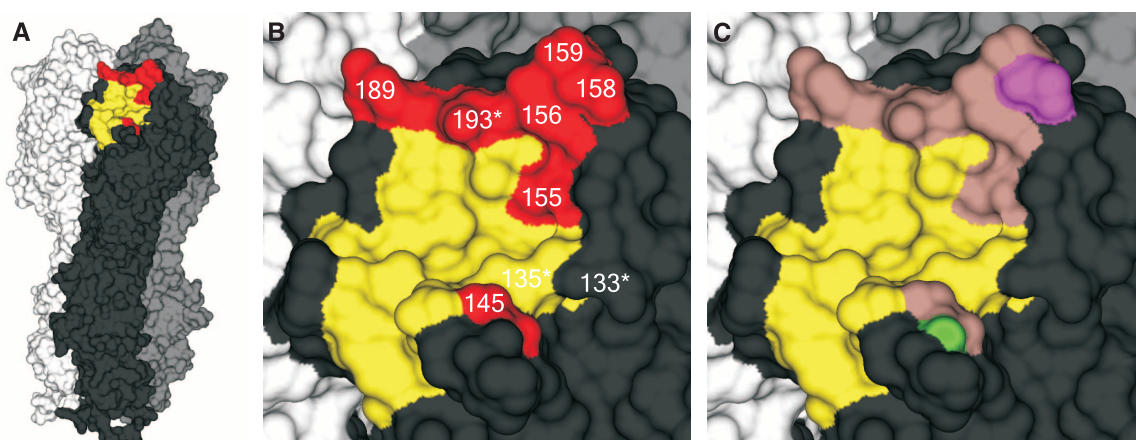
Surprisingly, 7 of the 10 cluster transitions were caused by only a single amino acid substitution (Fig. 1 and table S3). Two cluster transitions were caused by two substitutions, and one by three substitutions. In two of the three cluster transitions for which more than one substitution was required for the full antigenic change, one substitution was responsible for the majority of the antigenic change and the additional substitution(s) had a relatively modest effect on the antigenic phenotype (Fig. 1; fig. S4, C and E; and table S2). For the remaining transition, the effect caused by the single substitution could not be determined

Fig. 1. Antigenic effect of cluster-transition substitutions. (A) Anti-



Asp; E, Glu; G, Gly; H, His; K, Lys; N, Asn; Q, Gln; R, Arg; S, Ser; T, Thr; Y, Tyr). Antigenic distance between the mutant and consensus virus is indicated in parentheses. Substitutions between square brackets are accessory substitutions, which changed direction toward the subsequent cluster (Fig. 2, figs. S6 and S10, and table S3) and did not significantly add to the antigenic distance.

Fig. 2. Positions of the cluster-transition amino acid substitutions indicated on an A/Aichi/2/



substitutions responsible for antigenic change of influenza A/H1N1 and B virus are shown in green and magenta, respectively. The positions responsible for cluster transitions of A/H3N2 virus are shown in light brown.

(fig. S4I). We further tested the results for all cluster transitions using virus neutralization assays and obtained similar results (figs. S5 and S6 and table S2). In summary, we found that at least 9 of 10 A/H3N2 cluster transitions over the 35-year period were predominantly caused by single amino acid substitutions.

Strikingly, all the cluster-transition substitutions occurred at only seven positions, immediately adjacent to the RBS (Fig. 2). Six of seven positions align to form an antigenic ridge on the periphery of the RBS; the other, at position 145, is located on a loop that is partly involved in receptor binding. Five of seven key positions were involved in a cluster transition at least twice (Fig. 1 and table S3).

Substitutions responsible for major antigenic change were located exclusively in antigenic sites A (position 145) and B (positions 155, 156, 158, 159, 189, and 193), with none in sites C, D, or E. Our results do not contradict the studies that found 131 positions that can cause antigenic change and that define sites A to E (14, 15). Rather, we show that nature has, during 35 years of A/H3N2 virus circulation in humans, selected for the substantial antigenic changes caused by substitutions at only seven of these 131 positions; this is an important change in our understanding of the antigenic evolution of seasonal influenza viruses. Even though antibodies have been found to bind many regions of the HA, the location of the key positions for antigenic change on the periphery of the RBS suggests that RBS region-specific antibodies play the critical role in neutralizing influenza A/H3N2 viruses.

To test the surprising finding that the antigenic phenotype was determined by the amino acids at just seven positions, we attempted to change the phenotype of the HK68 consensus virus to become FU02-like by introducing only the five cluster-transition substitutions that differ between the HK68 and FU02 antigenic clusters (table S4). This test compares the effect of substitutions at just five positions (HK68+5) to the 54 substitutions that occurred over 35 years between HK68 and FU02, 47 of which were in antigenic sites. Remarkably, we found that the HK68+5 mutant was FU02-like antigenically; it had an HI titer a factor of 3 lower than that of the FU02 consensus virus to a FU02 antiserum (fig. S7 and table S4). Although HK68+5 had a substantially (factor of 20) reduced titer with the HK68 antiserum (by a factor of 20), it retained some residual low reactivity with the HK68 serum. In a similar experiment, we incrementally introduced cluster-transition substitutions into the HK68 consensus virus. The antigenic properties of the mutants matched those of the consensus viruses from subsequent clusters other than in their HI titers to one of the two HK68 sera. After introduction of all cluster-transition substitutions between the first five clusters, we were unable to rescue the mutant virus. In summary, even for highly divergent strains with as many as 54 substitutions and 35 years of evolution between them, only the amino acid substitutions

at key positions determined the majority of the antigenic phenotype.

We next tested the effect of a cluster-transition substitution in HA on the antibody response in an infected host. Two groups of three ferrets each were inoculated with either the wild-type HK68 consensus virus or HK68 containing cluster-transition substitution 155TY, and antisera were collected 2 weeks later. Each antiserum was titrated in the HI assay to 31 viruses belonging to the HK68, EN72, or V175 antigenic clusters (16). Relative to its reactivity with HK68-like viruses, antisera to the HK68 consensus virus had a factor of 25 (4.6 \log_2) reduction in reactivity to EN72-like strains and had no reactivity to the majority of the V175-like viruses. In contrast, antisera to HK68 155TY had only a factor of 4 (2.1 \log_2) reduction in titers to EN72-like strains but had substantial titers to the viruses from the V175 cluster (Fig. 3 and fig. S9). Thus, a single cluster-transition substitution can also substantially increase reactivity of the antiserum raised to the mutant virus to strains from subsequent antigenic clusters while maintaining reactivity to the antigenic cluster of origin.

The identification of key influential positions in HA and single amino acid substitutions responsible for major antigenic changes provides a plausible explanation for the previously described punctuated nature of the antigenic evolution of influenza A/H3N2 virus (16): 9 out of 10 cluster transitions were predominantly caused by a single amino acid substitution.

Although we found that almost 90% of HA substitutions associated with cluster transitions had little or no measurable antigenic effect, these findings do not imply that substitutions away from the RBS are phenotypically neutral. Some may be neutral hitchhikers carried along by chance, but others may collectively add to the decreased recognition by antibodies raised to a strain in an earlier cluster (Fig. 3 and figs. S7 and S8), or they may be compensatory mutations necessary to retain function.

Given the high mutation rate of influenza virus and the observation that single amino acid substitutions are sufficient to cause antigenic cluster transitions, it is surprising that new antigenic clusters appear as slowly as they do—on average every 3.3 years (16). One hypothesis is that antigenic change has an intrinsic fitness cost that slows down the antigenic evolution of the virus. We found that several mutant viruses with substitutions near the RBS could not be rescued (fig. S4, E and I, and fig. S8). These results suggest that introduction of mutations on the periphery of the RBS can affect HA function and that co-mutations may be crucial to retain viral fitness. The requirement for co-mutations that offset the fitness cost of antigenic evolution could provide an explanation for the paradox of high mutation rate and slow antigenic evolution.

Almost all substitutions responsible for cluster transitions resulted in substantial changes in

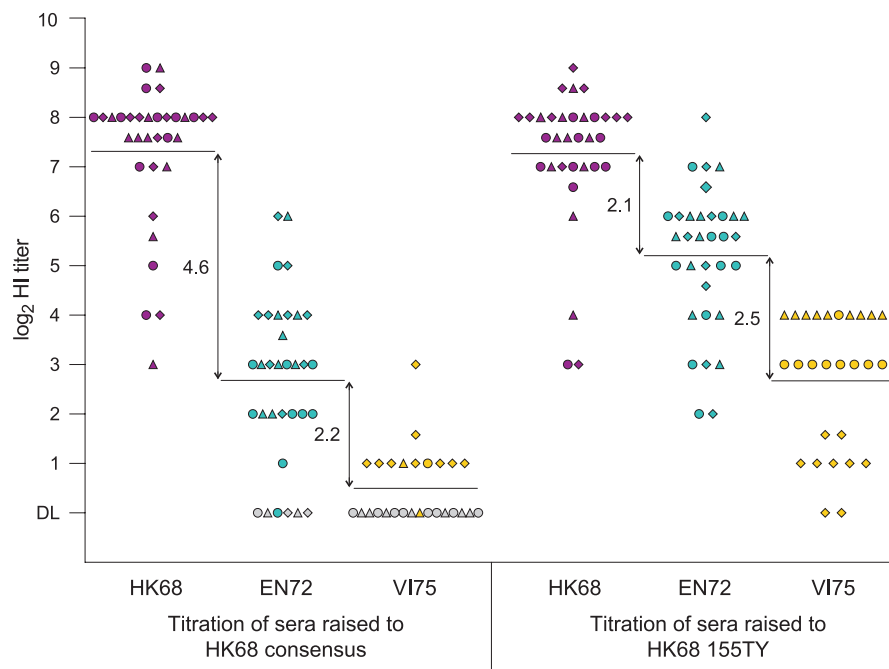


Fig. 3. Effect of a cluster-transition substitution on the antibody response of ferrets. Groups of three ferrets were inoculated with HK68 consensus virus or HK68+155TY, and antisera were tested to strains from the HK68 (purple), EN72 (cyan), or V175 (yellow) clusters of Fig. 1. Circles, triangles, and diamonds mark the three individual antisera. Black horizontal lines show the mean \log_2 HI titer. DL indicates the detection limit of the HI assay at the starting dilution (1/20) we used. Reactivity below detection was set to the value of the detection limit to calculate the means; these points are indicated in gray. The \log_2 reduction in mean reactivity to the different strains is indicated between the groups.

the biophysical properties of the amino acids involved. For instance, in nine cluster transitions at least one charge change was involved, and substantial volume changes were involved in three transitions (table S5). The amino acid composition of the key positions seems limited by their exposed nature. Hydrophobic amino acids are typically located on the interior of a protein, where they can be shielded from solvent access. Tyrosine, which is only partially hydrophobic because of the hydroxyl group on its aromatic ring, was the only hydrophobic amino acid observed on the key positions. The necessity for maintaining a functional HA structure as well as escape from neutralizing antibodies may have restricted the range of possible amino acids.

The number of potential glycosylation sites on the A/H3N2 virus HA has steadily increased since 1968 (19), and the presence of carbohydrate side chains has been associated with shielding of antibody epitopes (20, 21). A total of 14 HA positions are associated with glycosylation of the A/H3N2 viruses that circulated between 1968 and 2003. Two positions, 133 and 144, are located adjacent to the RBS. However, changes in glycosylation did not coincide with cluster transitions, and viruses belonging to the same antigenic cluster often had different glycosylation states (22). In agreement with these observations, the cluster-transition substitutions neither introduced nor deleted any glycosylation sites, and glycosylation was therefore not directly involved in the antigenic changes between the clusters. The location of the majority of the potential glycosylation sites away from the RBS could be the reason why changes in glycosylation have not played a major role in the antigenic change of A/H3N2 viruses.

To further expand these results, we examined the most recent antigenic cluster transitions in the other human seasonal influenza viruses: the B/Yamagata and B/Victoria lineages of the B viruses, and the pre-2009 A/H1N1 viruses (the current A/H1N1pdm09 viruses are yet to undergo a cluster transition). We found the same results as for the A/H3N2 viruses: The major antigenic change was caused by a single amino acid substitution in the corresponding region close to the RBS (Fig. 2C and figs. S11 to S13).

We find that although human A/H3N2 seasonal influenza viruses have fixed amino acid substitutions at 54 positions in antigenic sites, substitutions at only seven of these locations have been responsible for the major antigenic changes in these viruses to date. Moreover, these locations are all near the RBS of the HA, which suggests the mechanism for slowing the antigenic evolution of these viruses could be a reduction in receptor binding function. This small number of critical positions, and the restricted amino acid usage involved in antigenic cluster transitions, suggests that possibilities for important antigenic change of seasonal influenza viruses may be more restricted than previously thought, with potentially far-reaching consequences for understanding the

underlying evolutionary mechanisms governing such viruses.

References and Notes

1. M. Akazawa, J. L. Sindelar, A. D. Paltiel, *Value Health* **6**, 107–115 (2003).
2. K. Stöhr, *Lancet Infect. Dis.* **2**, 517 (2002).
3. J. L. Virelizier, *J. Immunol.* **115**, 434–439 (1975).
4. J. Sui *et al.*, *Nat. Struct. Mol. Biol.* **16**, 265–273 (2009).
5. T. T. Wang *et al.*, *PLOS Pathog.* **6**, e1000796 (2010).
6. J. Steel *et al.*, *MBio* **1**, e00018-10 (2010).
7. D. C. Ekiert *et al.*, *Science* **333**, 843–850 (2011).
8. K. Koelle, S. Cobey, B. Grenfell, M. Pascual, *Science* **314**, 1898–1903 (2006).
9. S. E. Hensley *et al.*, *Science* **326**, 734–736 (2009).
10. W. M. Fitch, R. M. Bush, C. A. Bender, N. J. Cox, *Proc. Natl. Acad. Sci. U.S.A.* **94**, 7712–7718 (1997).
11. R. M. Bush, C. A. Bender, K. Subbarao, N. J. Cox, W. M. Fitch, *Science* **286**, 1921–1925 (1999).
12. W. Zhai, M. Slatkin, R. Nielsen, *J. Mol. Evol.* **65**, 340–348 (2007).
13. S. L. Kosakovsky Pond, A. F. Poon, A. J. Leigh Brown, S. D. Frost, *Mol. Biol. Evol.* **25**, 1809–1824 (2008).
14. D. C. Wiley, I. A. Wilson, J. J. Skehel, *Nature* **289**, 373–378 (1981).
15. I. A. Wilson, N. J. Cox, *Annu. Rev. Immunol.* **8**, 737–787 (1990).
16. D. J. Smith *et al.*, *Science* **305**, 371–376 (2004).
17. See supplementary materials on Science Online.
18. E. de Wit *et al.*, *J. Gen. Virol.* **88**, 1281–1287 (2007).
19. J. J. Skehel, D. C. Wiley, *Annu. Rev. Biochem.* **69**, 531–569 (2000).
20. J. J. Skehel *et al.*, *Proc. Natl. Acad. Sci. U.S.A.* **81**, 1779–1783 (1984).

21. Y. Abe *et al.*, *J. Virol.* **78**, 9605–9611 (2004).
22. B. P. Blackburne, A. J. Hay, R. A. Goldstein, *PLOS Pathog.* **4**, e1000058 (2008).

Acknowledgments: We thank M. Aban, G. van Amerongen, C. Baas, R. van Beek, M. de Graaf, S. Herfst, S. James, M. Linster, K. Sutherland-Cash, and C. Whittleston for excellent technical assistance and discussions. D.F.B. and D.J.S. acknowledge the use of the CamGrid distributed computing resource. Supported by an NWO VICI grant, National Institute of Allergy and Infectious Diseases contract HHSN266200700010C, NIH Director's Pioneer Award DP1-OD000490-01, European Union FP7 program EMPIRE (223498), European Union FP7 program ANTIGONE (278976), and program grant P0050/2008 from the Human Frontier Science Program. The Melbourne WHO Collaborating Centre for Reference and Research on Influenza is supported by the Australian Government Department of Health and Aging. A.D.M.E.O. (on behalf of Viroclinics Biosciences B.V.) has advisory affiliations with GSK, Novartis, and Roche. A.D.M.E.O. and G.F.R. are consultants for Viroclinics Biosciences B.V. A/H3N2 virus sequences were previously published by Smith *et al.* (16). The sequences of the influenza A/H1N1 and B viruses used in this study are available from the GISAID EpiFlu Database (www.gisaid.org) and are listed in table S6.

Supplementary Materials

www.sciencemag.org/content/342/6161/976/suppl/DC1
Materials and Methods
Figs. S1 to S13
Tables S1 to S6
References (23–29)

15 August 2013; accepted 17 October 2013
10.1126/science.1244730

Yeast Reveal a “Druggable” Rsp5/Nedd4 Network that Ameliorates α -Synuclein Toxicity in Neurons

Daniel F. Tardiff,¹ Nathan T. Jui,² Vikram Khurana,^{1,3} Mitali A. Tambe,⁴ Michelle L. Thompson,^{5*} Chee Yeun Chung,¹ Hari B. Kamadurai,⁶ Hyoung Tae Kim,⁷ Alex K. Lancaster,^{1†} Kim A. Caldwell,⁵ Guy A. Caldwell,⁵ Jean-Christophe Rochet,⁴ Stephen L. Buchwald,² Susan Lindquist^{1,8‡}

α -Synuclein (α -syn) is a small lipid-binding protein implicated in several neurodegenerative diseases, including Parkinson's disease, whose pathobiology is conserved from yeast to man. There are no therapies targeting these underlying cellular pathologies, or indeed those of any major neurodegenerative disease. Using unbiased phenotypic screens as an alternative to target-based approaches, we discovered an *N*-aryl benzimidazole (NAB) that strongly and selectively protected diverse cell types from α -syn toxicity. Three chemical genetic screens in wild-type yeast cells established that NAB promoted endosomal transport events dependent on the E3 ubiquitin ligase Rsp5/Nedd4. These same steps were perturbed by α -syn itself. Thus, NAB identifies a druggable node in the biology of α -syn that can correct multiple aspects of its underlying pathology, including dysfunctional endosomal and endoplasmic reticulum-to-Golgi vesicle trafficking.

Phenotypic cell-based drug screens are a powerful yet underused approach to identify lead compounds and probe the underlying cellular pathologies that cause human disease (1). Such unbiased screens may be particularly helpful for neurodegenerative diseases (NDs), such as Parkinson's disease (PD) and Alzheimer's disease (AD), for which the molecular underpinnings of disease remain unclear. However, establishing robust neuronal phenotypes amenable to high-throughput screening and subsequent target identification

remains a challenge. To bridge this gap, we exploited yeast cells that express ND-causing proteins to recapitulate salient cellular pathologies. α -Synuclein (α -syn), for example, causes derangements in vesicle trafficking, metal ion homeostasis, and mitochondrial function that are associated with α -synucleinopathies, such as PD (2). The resulting growth inhibition greatly facilitates robust high-throughput screening.

We recently screened ~190,000 compounds for their ability to restore the growth of cells

the biophysical properties of the amino acids involved. For instance, in nine cluster transitions at least one charge change was involved, and substantial volume changes were involved in three transitions (table S5). The amino acid composition of the key positions seems limited by their exposed nature. Hydrophobic amino acids are typically located on the interior of a protein, where they can be shielded from solvent access. Tyrosine, which is only partially hydrophobic because of the hydroxyl group on its aromatic ring, was the only hydrophobic amino acid observed on the key positions. The necessity for maintaining a functional HA structure as well as escape from neutralizing antibodies may have restricted the range of possible amino acids.

The number of potential glycosylation sites on the A/H3N2 virus HA has steadily increased since 1968 (19), and the presence of carbohydrate side chains has been associated with shielding of antibody epitopes (20, 21). A total of 14 HA positions are associated with glycosylation of the A/H3N2 viruses that circulated between 1968 and 2003. Two positions, 133 and 144, are located adjacent to the RBS. However, changes in glycosylation did not coincide with cluster transitions, and viruses belonging to the same antigenic cluster often had different glycosylation states (22). In agreement with these observations, the cluster-transition substitutions neither introduced nor deleted any glycosylation sites, and glycosylation was therefore not directly involved in the antigenic changes between the clusters. The location of the majority of the potential glycosylation sites away from the RBS could be the reason why changes in glycosylation have not played a major role in the antigenic change of A/H3N2 viruses.

To further expand these results, we examined the most recent antigenic cluster transitions in the other human seasonal influenza viruses: the B/Yamagata and B/Victoria lineages of the B viruses, and the pre-2009 A/H1N1 viruses (the current A/H1N1pdm09 viruses are yet to undergo a cluster transition). We found the same results as for the A/H3N2 viruses: The major antigenic change was caused by a single amino acid substitution in the corresponding region close to the RBS (Fig. 2C and figs. S11 to S13).

We find that although human A/H3N2 seasonal influenza viruses have fixed amino acid substitutions at 54 positions in antigenic sites, substitutions at only seven of these locations have been responsible for the major antigenic changes in these viruses to date. Moreover, these locations are all near the RBS of the HA, which suggests the mechanism for slowing the antigenic evolution of these viruses could be a reduction in receptor binding function. This small number of critical positions, and the restricted amino acid usage involved in antigenic cluster transitions, suggests that possibilities for important antigenic change of seasonal influenza viruses may be more restricted than previously thought, with potentially far-reaching consequences for understanding the

underlying evolutionary mechanisms governing such viruses.

References and Notes

1. M. Akazawa, J. L. Sindelar, A. D. Paltiel, *Value Health* **6**, 107–115 (2003).
2. K. Stöhr, *Lancet Infect. Dis.* **2**, 517 (2002).
3. J. L. Virelizier, *J. Immunol.* **115**, 434–439 (1975).
4. J. Sui *et al.*, *Nat. Struct. Mol. Biol.* **16**, 265–273 (2009).
5. T. T. Wang *et al.*, *PLOS Pathog.* **6**, e1000796 (2010).
6. J. Steel *et al.*, *MBio* **1**, e00018-10 (2010).
7. D. C. Ekiert *et al.*, *Science* **333**, 843–850 (2011).
8. K. Koelle, S. Cobey, B. Grenfell, M. Pascual, *Science* **314**, 1898–1903 (2006).
9. S. E. Hensley *et al.*, *Science* **326**, 734–736 (2009).
10. W. M. Fitch, R. M. Bush, C. A. Bender, N. J. Cox, *Proc. Natl. Acad. Sci. U.S.A.* **94**, 7712–7718 (1997).
11. R. M. Bush, C. A. Bender, K. Subbarao, N. J. Cox, W. M. Fitch, *Science* **286**, 1921–1925 (1999).
12. W. Zhai, M. Slatkin, R. Nielsen, *J. Mol. Evol.* **65**, 340–348 (2007).
13. S. L. Kosakovsky Pond, A. F. Poon, A. J. Leigh Brown, S. D. Frost, *Mol. Biol. Evol.* **25**, 1809–1824 (2008).
14. D. C. Wiley, I. A. Wilson, J. J. Skehel, *Nature* **289**, 373–378 (1981).
15. I. A. Wilson, N. J. Cox, *Annu. Rev. Immunol.* **8**, 737–787 (1990).
16. D. J. Smith *et al.*, *Science* **305**, 371–376 (2004).
17. See supplementary materials on Science Online.
18. E. de Wit *et al.*, *J. Gen. Virol.* **88**, 1281–1287 (2007).
19. J. J. Skehel, D. C. Wiley, *Annu. Rev. Biochem.* **69**, 531–569 (2000).
20. J. J. Skehel *et al.*, *Proc. Natl. Acad. Sci. U.S.A.* **81**, 1779–1783 (1984).

21. Y. Abe *et al.*, *J. Virol.* **78**, 9605–9611 (2004).
22. B. P. Blackburne, A. J. Hay, R. A. Goldstein, *PLOS Pathog.* **4**, e1000058 (2008).

Acknowledgments: We thank M. Aban, G. van Amerongen, C. Baas, R. van Beek, M. de Graaf, S. Herfst, S. James, M. Linster, K. Sutherland-Cash, and C. Whittleston for excellent technical assistance and discussions. D.F.B. and D.J.S. acknowledge the use of the CamGrid distributed computing resource. Supported by an NWO VICI grant, National Institute of Allergy and Infectious Diseases contract HHSN266200700010C, NIH Director's Pioneer Award DP1-OD000490-01, European Union FP7 program EMPIRE (223498), European Union FP7 program ANTIGONE (278976), and program grant P0050/2008 from the Human Frontier Science Program. The Melbourne WHO Collaborating Centre for Reference and Research on Influenza is supported by the Australian Government Department of Health and Aging. A.D.M.E.O. (on behalf of Viroclinics Biosciences B.V.) has advisory affiliations with GSK, Novartis, and Roche. A.D.M.E.O. and G.F.R. are consultants for Viroclinics Biosciences BV. A/H3N2 virus sequences were previously published by Smith *et al.* (16). The sequences of the influenza A/H1N1 and B viruses used in this study are available from the GISAID EpiFlu Database (www.gisaid.org) and are listed in table S6.

Supplementary Materials

www.sciencemag.org/content/342/6161/976/suppl/DC1
Materials and Methods
Figs. S1 to S13
Tables S1 to S6
References (23–29)

15 August 2013; accepted 17 October 2013
10.1126/science.1244730

Yeast Reveal a “Druggable” Rsp5/Nedd4 Network that Ameliorates α -Synuclein Toxicity in Neurons

Daniel F. Tardiff,¹ Nathan T. Jui,² Vikram Khurana,^{1,3} Mitali A. Tambe,⁴ Michelle L. Thompson,^{5*} Chee Yeun Chung,¹ Hari B. Kamadurai,⁶ Hyoung Tae Kim,⁷ Alex K. Lancaster,^{1†} Kim A. Caldwell,⁵ Guy A. Caldwell,⁵ Jean-Christophe Rochet,⁴ Stephen L. Buchwald,² Susan Lindquist^{1,8‡}

α -Synuclein (α -syn) is a small lipid-binding protein implicated in several neurodegenerative diseases, including Parkinson's disease, whose pathobiology is conserved from yeast to man. There are no therapies targeting these underlying cellular pathologies, or indeed those of any major neurodegenerative disease. Using unbiased phenotypic screens as an alternative to target-based approaches, we discovered an *N*-aryl benzimidazole (NAB) that strongly and selectively protected diverse cell types from α -syn toxicity. Three chemical genetic screens in wild-type yeast cells established that NAB promoted endosomal transport events dependent on the E3 ubiquitin ligase Rsp5/Nedd4. These same steps were perturbed by α -syn itself. Thus, NAB identifies a druggable node in the biology of α -syn that can correct multiple aspects of its underlying pathology, including dysfunctional endosomal and endoplasmic reticulum-to-Golgi vesicle trafficking.

Phenotypic cell-based drug screens are a powerful yet underused approach to identify lead compounds and probe the underlying cellular pathologies that cause human disease (1). Such unbiased screens may be particularly helpful for neurodegenerative diseases (NDs), such as Parkinson's disease (PD) and Alzheimer's disease (AD), for which the molecular underpinnings of disease remain unclear. However, establishing robust neuronal phenotypes amenable to high-throughput screening and subsequent target identification

remains a challenge. To bridge this gap, we exploited yeast cells that express ND-causing proteins to recapitulate salient cellular pathologies. α -Synuclein (α -syn), for example, causes derangements in vesicle trafficking, metal ion homeostasis, and mitochondrial function that are associated with α -synucleinopathies, such as PD (2). The resulting growth inhibition greatly facilitates robust high-throughput screening.

We recently screened ~190,000 compounds for their ability to restore the growth of cells

expressing toxic levels of TDP-43 (3), a protein associated with diverse NDs. A weak hit from that screen, an N-aryl benzimidazole (NAB) (Fig. 1A), proved more potent and effective against α -syn toxicity (Fig. 1B). NAB reversed diverse phenotypes caused by α -syn (4–7), including the accumulation of vesicular α -syn foci (Fig. 1C) (8, 9), the generation of reactive oxygen species (Fig. 1D), the block of endoplasmic reticulum (ER)–Golgi trafficking (Fig. 1E), and the nitration of proteins (6). The toxicity of α -syn is extremely dependent on expression levels (7, 10); however, NAB did not reduce α -syn accumulation (Fig. 1E).

¹Whitehead Institute for Biomedical Research (WIBR), Cambridge, MA 02142, USA. ²Department of Chemistry, Massachusetts Institute of Technology (MIT), Cambridge, MA 02139, USA. ³Department of Neurology, Massachusetts General Hospital and Harvard Medical School, Boston, MA 02114, USA. ⁴Department of Medicinal Chemistry and Molecular Pharmacology, Purdue University, West Lafayette, IN 47907, USA. ⁵Department of Biological Sciences, University of Alabama, Tuscaloosa, AL 35487, USA. ⁶Department of Structural Biology, St. Jude Children's Research Hospital, Memphis, TN 38018, USA. ⁷Department of Cell Biology, Harvard Medical School, Boston, MA 02115, USA. ⁸Howard Hughes Medical Institute (HHMI), Department of Biology, MIT, Cambridge, MA 02139, USA.

*Present address: Department of Pharmacology, University of Arizona, 1501 North Campbell Avenue, Tucson, AZ 85716, USA.

†Present address: Department of Pathology, Beth Israel Deaconess Medical Center, 330 Brookline Avenue, Boston, MA 02215, USA; and Center for Biomedical Informatics, Harvard Medical School, 10 Shattuck Street, Boston, MA 02115, USA. ‡Corresponding author. E-mail: lindquist_admin@wi.mit.edu

We next asked whether the protective activity of NAB was conserved in neurons. First, we tested a nematode model in which PD-relevant dopaminergic (DA) neurons degenerate in an age-dependent manner in response to human α -syn expression (5). Second, we tested rat primary neuronal cultures in which adenoviral expression of a familial α -syn mutation (A53T) causes selective loss of DA neurons: Tyrosine-hydroxylase (TH)–positive cells are lost, and neuronal processes retract (4, 5). Third, we tested cortical neurons differentiated from PD-patient induced pluripotent stem cells (iPSCs) carrying either the A53T α -syn mutation or an α -syn triplication, both of which caused protein trafficking defects and nitrosative stress (6). In each case, NAB reversed α -syn toxicity or pathology, suggesting that the compound's target and mechanisms of action (MOA) were conserved from yeast to human cells (Fig. 1, F and G, and fig. S1) (6).

Yeast screens can reveal the target space for small molecules that suppress growth by identifying genetic alterations that restore it (11). At concentrations higher than those that rescued α -syn toxicity, NAB inhibited the growth of wild-type (WT) cells. To test whether α -syn rescue and growth inhibition had related MOA, we synthesized 29 NAB analogs (fig. S2). Compounds inactive in rescuing α -syn did not reverse α -syn foci formation or rescue ER-to-Golgi trafficking (fig. S3). Compounds that potently rescued α -syn also more potently inhibited growth in WT cells

(Fig. 2A, fig. S2, and supplementary text). This allowed us to use genetic screens in WT cells to investigate NAB's MOA. Although NAB inhibited growth, cells retained full viability (Fig. 2B).

Using our most potent analog, NAB2, we selected for genetic alterations that allowed growth at high concentrations. We used three approaches: (i) a library of overexpression strains covering most genes in the yeast genome (~5800 genes), (ii) a library of ~300,000 random transposon-insertions (12), and (iii) spontaneous genomic point mutations arising from ~2 million cells (fig. S4). A small number of hits were recovered and formed a highly connected network of functionally related genes (Fig. 2C). These were an E3 ubiquitin ligase that promotes endosomal transport (*RSP5*), endocytic proteins (*SLA1*, *VRP1*), a multivesicular body sorting deubiquitinase (*DOA4*), an Rsp5 adaptor (*BUL1*), two proteins that can deubiquitinate Rsp5 substrates (*UBP7* and *UBP11*), known and potential Rsp5 substrates (*BAP2*, *BAP3*, and *MMP1*), and *VPS23*, which directs Rsp5 substrates for degradation in the vacuole (Fig. 2C). Analogs ineffective against α -syn did not exhibit dosage sensitivity with NAB network genes (fig. S5), supporting a related MOA between α -syn rescue and growth inhibition of WT cells.

The network topology of screen hits, and the nature of their altered dosage-sensitivity to NAB2 (figs. S6 to S8), suggested that NAB acts on Rsp5 to promote ubiquitin-mediated endosomal transport. With the exception of *RSP5*, which is es-

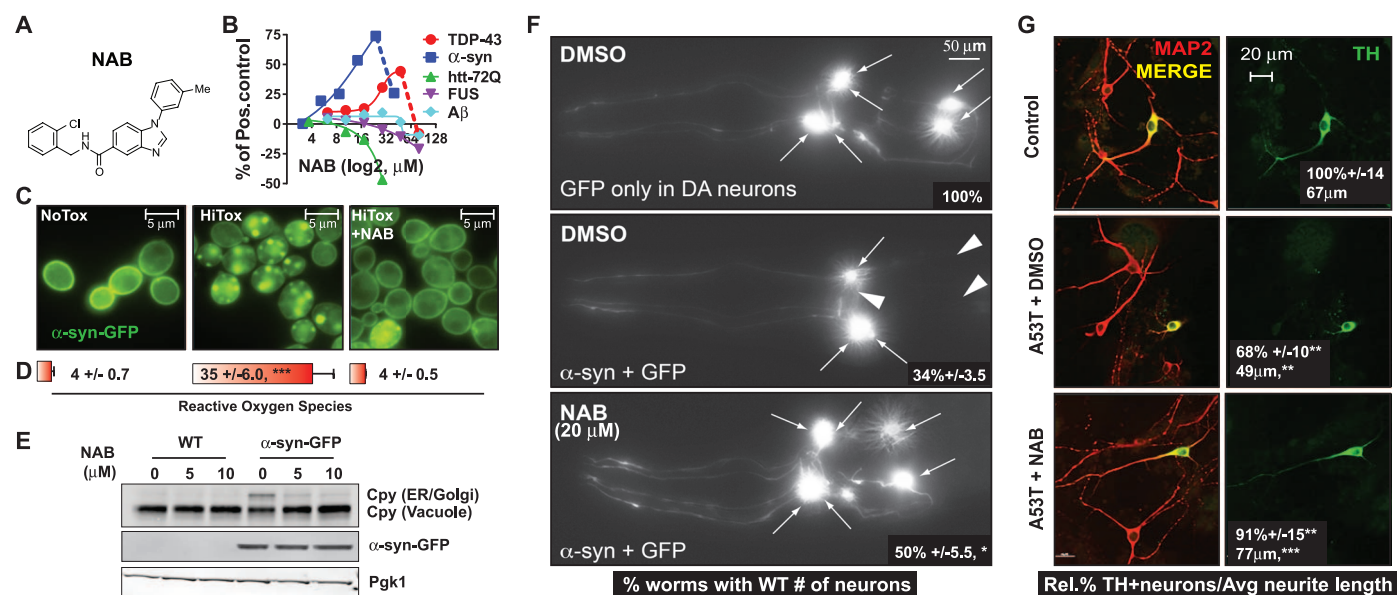


Fig. 1. NAB protects yeast and neurons from α -syn toxicity. (A) NAB structure. (B) Dose-response curves for NAB in yeast proteinopathy models. (C) α -syn-GFP localization in NoTox, HiTox, and HiTox/10 μ M NAB. (D) Percent of reactive oxygen species–positive cells under same conditions as (C). Values are mean \pm SD; $n = 3$ independent trials. (E) Immunoblot of Cpy showing ER–Golgi trafficking defect and α -syn protein levels in WT and HiTox cells treated with NAB. (F) Fluorescence microscopy of the six anterior DA neurons in representative *C. elegans* expressing either GFP or human α -syn and GFP after treatment with dimethyl sulfoxide (DMSO) or NAB. Arrows indicate intact DA

neuron cell bodies and arrowheads indicate regions where these cells have degenerated. Inlaid values reflect mean \pm SD; $n = 3$ independent trials. (G) Representative images of DA-enriched cultures established from embryonic rat midbrains. Control, untransduced; A53T, transduced with A53T α -syn virus; red, MAP2 (neuronal tubulin); green, TH-positive neurons. Inlaid values reflect mean with control set to 100% and \pm SD; $n = 3$ independent trials for percent TH-positive neurons and mean \pm SEM, $n = \sim 75$ neurons for neurite length. For all data: * $P < 0.05$; ** $P < 0.01$; *** $P < 0.001$ using one-way analysis of variance (ANOVA) and a Tukey's test.

essential, every other gene in our network could be deleted. But no deletion (including a double deletion of *UBP7* and *UBP11*) conferred more than partial resistance to NAB2. Thus, although these other proteins are involved in NAB2 activity, they cannot themselves be its target. Indeed, the effects of altering *RSP5* gene dosage indicate that it is the central node: Increased *RSP5* dosage increased sensitivity to NAB2, and decreased *RSP5* dosage decreased sensitivity to NAB2 (Fig. 2D). Furthermore, in otherwise isogenic cells a single amino acid substitution in the ~1000-amino-acid protein (*rsp5*^{G747E}) conferred resistance to NAB2 (Fig. 2D and fig. S7).

Rsp5 is the single yeast member of the highly conserved mammalian family of HECT domain Nedd4 E3 ligases. These proteins catalyze K63 linkages of ubiquitin to diverse membrane proteins and thereby regulate endosomal trafficking, not proteasomal degradation (13, 14). HECT domain ubiquitin ligases contain multiple protein-

protein interaction domains that bind diverse adaptor proteins and substrates. Calcium, lipid binding, and autoinhibitory conformations regulate substrate specificity and endosomal transport from either the plasma membrane or Golgi to the vacuole/lysosome. Most aspects of these complex modes of Rsp5 regulation have not been recapitulated in vitro.

Therefore, to further investigate NAB2 activities we monitored, in WT cells, its effects on three proteins whose trafficking depends on Rsp5: Mup1 (15), Sna3 (16), and Bap2 (17). NAB2 (i) promoted the Rsp5-dependent endocytosis and vacuolar delivery of the methionine permease, Mup1 (Fig. 2E and fig. S9); (ii) promoted the Rsp5-dependent Golgi-to-vacuole trafficking of the adaptor protein Sna3 (Fig. 2F and fig. S9); and (iii) promoted the Rsp5-dependent degradation of the leucine permease Bap2 (fig. S10). (This affected leucine-dependent growth, explaining its recovery in our overexpression screen.)

We further established the relevance of the NAB/Rsp5 network by genetically altering screen hits in the context of α -syn. Indeed, most but not all genetic manipulations that antagonized NAB2 activities in WT cells antagonized its activities against α -syn toxicity. For example, deleting Δ *sla1* and Δ *vps23*, or overexpressing the deubiquitinases *UBP7* and *UBP11*, all partially compromised the ability of NAB2 to rescue α -syn toxicity (Fig. 3A and fig. S11). Deleting Δ *ubp7* and Δ *ubp11*, either singly or in combination, had no effect on NAB2's rescue of α -syn toxicity (fig. S11).

The spontaneous point mutation recovered in our screen, *rsp5*^{G747E}, which compromised Rsp5 activity (Fig. 2, E and F, and fig. S7) and conferred resistance to NAB2 in WT cells, shifted the dose of NAB2 required for α -syn rescue in a complementary fashion (Fig. 3A). Consistent with this, *rsp5*^{G747E} prevented NAB2 from fully reverting the formation of α -syn foci (Fig. 3B) and from restoring ER-to-Golgi trafficking (Fig. 3C)

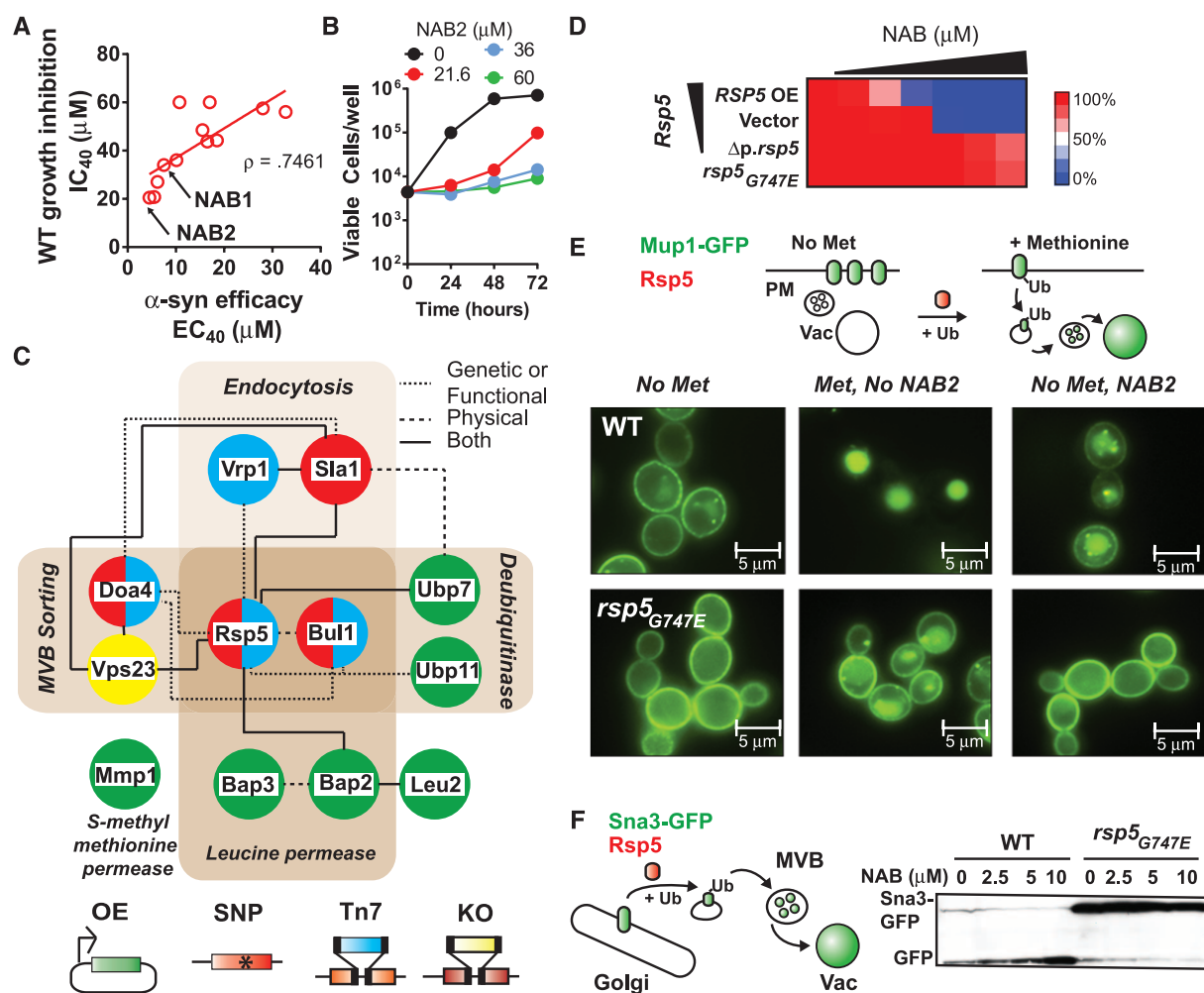


Fig. 2. Chemical genetic screens of NAB2 reveal a network centered on the E3 ligase, Rsp5. (A) Efficacy (EC_{40}) in α -syn cells versus growth inhibition (IC_{40}) in WT cells for active analogs. NAB1 is the screen hit, and NAB2 is the most potent analog. (B) Viable cells recovered after prolonged NAB2 treatment. (C) NAB2 interaction network. Node color reflects screen of origin indicated below. Edges are interactions (legend, top right) according to String database and literature. *VPS23* was deleted after identification of other hits.

(D) Heat map of *RSP5* variant cell growth in response to increasing NAB2 compared with untreated cells. Mutants include *rsp5*^{G747E} and the hypomorphic allele, Δ *p.rsp5*. (E) (Top) Methionine- and Rsp5-dependent Mup1-GFP endocytosis. (Bottom) Mup1-GFP localization in WT and *rsp5*^{G747E} strains under indicated conditions. (F) (Left) Schematic of Sna3-GFP endosomal trafficking to the vacuole, where GFP is cleaved. (Right) Immunoblot analysis of Sna3-GFP in WT and *rsp5*^{G747E} cells treated with NAB2.

phenotypes. Together, these analyses established Rsp5 as the central node and only potential protein target within the NAB network.

Rsp5's importance in modifying α -syn toxicity was highlighted by integrating the NAB/Rsp5 and α -syn genetic networks (table S3) (4, 18).

These interactions connected our NAB network to nearly 30% of the previously established genetic modifiers of α -syn toxicity, including those that function in Golgi/vesicular transport, endosomal transport, lipid metabolism, protein catabolism, and tubulin assembly (Fig. 3D and fig. S12).

Next, we tested α -syn's effect on Mup1-green fluorescent protein (GFP) and Sna3-GFP trafficking. Indeed, α -syn expression impeded both the methionine-induced transport of Mup1-GFP from the plasma membrane to the vacuole (Fig. 4A) and the constitutive trafficking of Sna3-

Fig. 3. NAB/Rsp5 network directly affects rescue of α -syn toxicity. (A) Heat map of NAB2 dose-response in WT and modified α -syn strains. Rescue is relative to EC₁₀₀ for NAB2 in WT α -syn cells. (B) α -syn-GFP localization in WT or *rsp5*^{G747E} α -syn cells under indicated conditions. Inlaid values indicate percent of cells with large α -syn foci (mean \pm SD, *n* = 3 independent trials). (C) Immunoblot of Cpy trafficking defect α -syn cells with DMSO or NAB2. **P* < 0.05 using one-way ANOVA. (D) Interaction network of α -syn and NAB2 genetic modifiers. α -syn nodes, purple; NAB2 nodes are color-coded according to screen of origin (Fig. 2C). *RSP5*, *UBP7*, and *UBP11* are larger because they both suppress NAB2 growth inhibition and enhance α -syn toxicity (4). Edges between nodes depict physical or genetic interactions. Thicker lines indicate both genetic and physical interactions. Red edges link node interactions between α -syn and NAB2 networks. Remaining α -syn edges are blue.

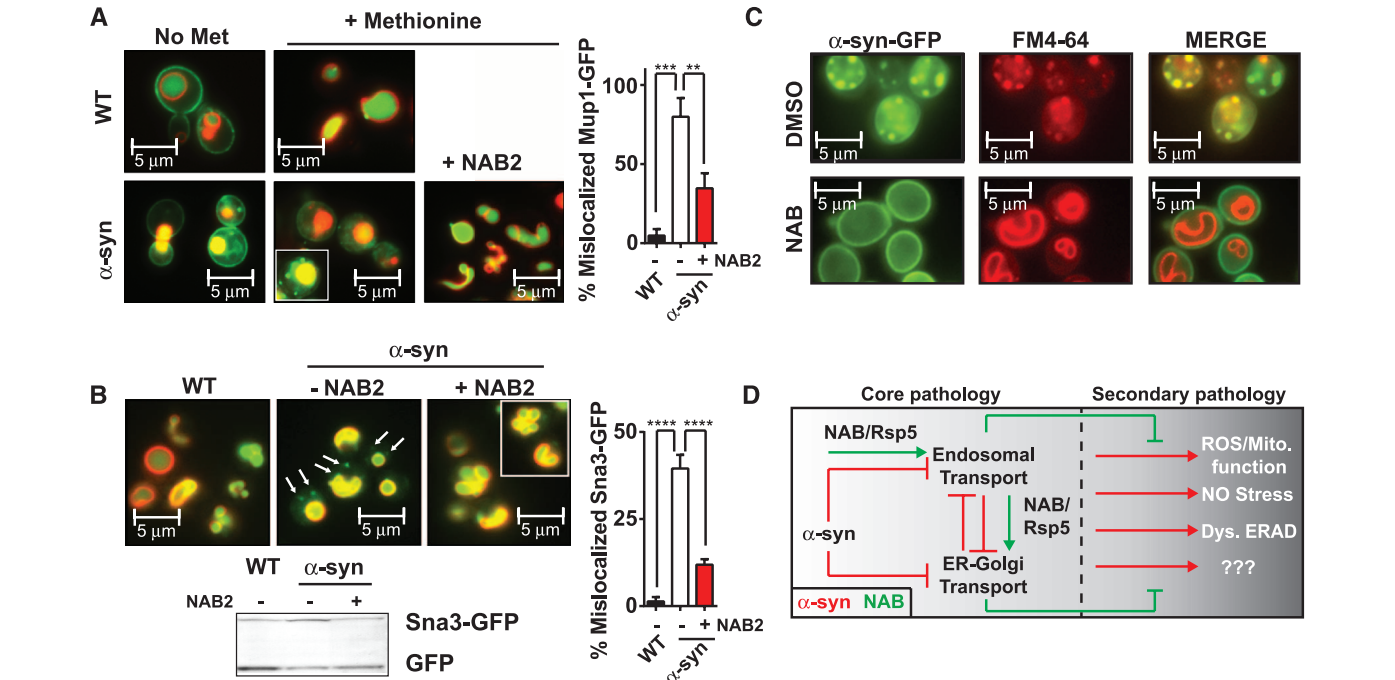
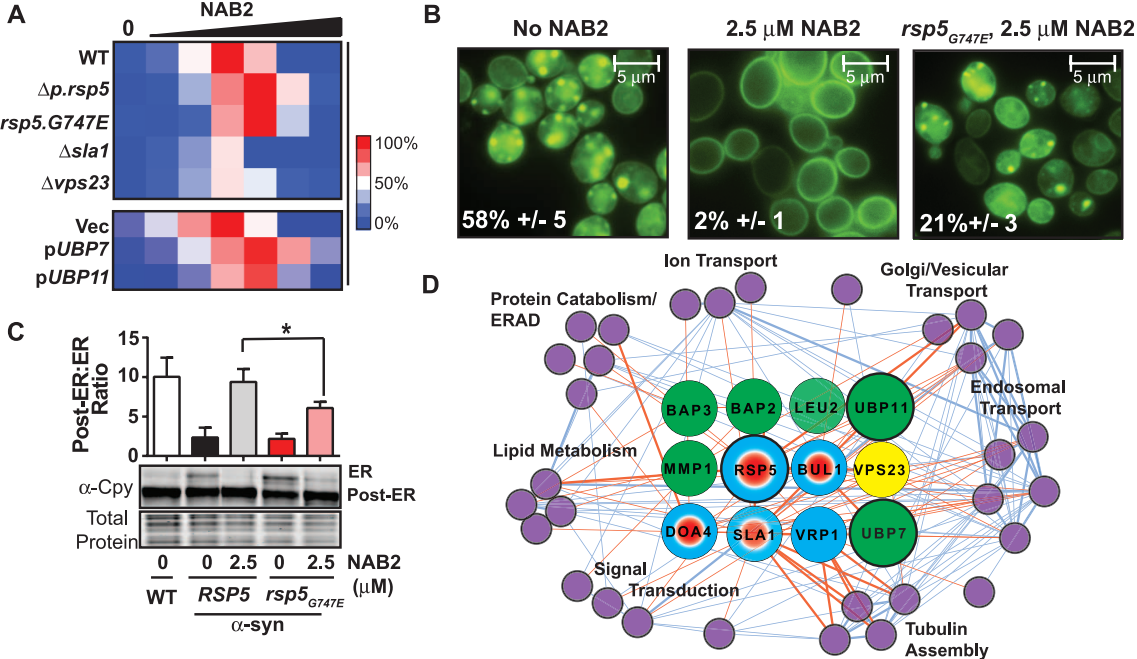


Fig. 4. NAB2 directly antagonizes α -syn-induced endosomal defects. (A) Methionine-stimulated Mup1-GFP endocytosis in WT or untagged α -syn strains with DMSO or NAB2. Pulse-labeling cells with FM4-64 during the first hour of α -syn expression marked the vacuole. (B) Effects of α -syn on Sna3-GFP localization. Immunoblot shows Sna3-GFP cleavage in response

to α -syn and NAB. FM4-64 labeling is as in (A). Arrows indicate stalled endosomal vesicles containing Sna3-GFP. (C) Pulse-labeling of FM4-64 of α -syn cells after 4 hours of expression in the presence or absence of NAB2. (D) Schematic of NAB2 mechanism in antagonizing core and secondary α -syn pathologies.

GFP from the Golgi and the vacuole (Fig. 4B). Further, in the presence of α -syn, NAB2 restored trafficking of both substrates (Fig. 4, A and B).

In addition to specific substrates, bulk endosomal transport from the plasma membrane to the vacuole was perturbed by α -syn (Fig. 4C) (7–9, 19). When FM4-64 was used to pulse-label the endosomal pathway, after prolonged α -syn expression the dye strongly colocalized with α -syn inclusions and failed to reach the vacuole (Fig. 4C). NAB2 fully restored endocytosis and concomitantly reduced α -syn inclusions (Fig. 4C, bottom). Thus, the ability of NAB to promote Rsp5-dependent processes directly restored diverse cellular pathologies caused by α -syn, including both ER-to-Golgi and endosomal trafficking (Fig. 4D and fig. S8).

Rsp5/Nedd4 can ubiquitinate α -syn, and Nedd4 localizes to Lewy Bodies in brain samples from PD patients (20). However, α -syn levels were not altered by NAB2 in vivo (Fig. 1E). And when tested in vitro, NAB2 did not affect the ubiquitination of α -syn and Sn3 by Rsp5 (fig. S13). As noted, however, most of the complexities of Rsp5 in vivo activities have yet to be recapitulated in vitro. Thus, NAB2 exemplifies the ability of unbiased in vivo phenotypic screens to uncover chemical probes that cannot be discovered through simple target-based in vitro approaches. Likewise, NAB2 chemical genetics identify a deeply rooted biological node, Rsp5, that had not been identified in previous overexpression or deletion screens. Despite their central role in protein homeostasis and several human diseases, to date E3 ubiquitin ligases are virtually untouched by biological probes, let alone therapeutics.

The vesicular trafficking processes perturbed by α -syn and promoted by NAB are fundamental to all eukaryotic cells yet are particularly important to neurons that rely heavily on efficient synaptic vesicle dynamics and regulated neurotransmitter release. Indeed, dysfunctional endosomal transport is emerging as a contributing factor in α -syn pathology in human neurons. Altered cell biology, post mortem pathology, and human genetic risk factors all implicate altered vesicular trafficking (4, 7–9, 19, 21–25). The ability of NAB to promote endosomal trafficking through Rsp5/Nedd4 and thus “reset” vesicle trafficking homeostasis, in turn, rescued several other, seemingly disparate, α -syn phenotypes. Identifying such deeply rooted pathways that ramify to affect multiple aspects of protein-folding pathology may be critical for developing disease-modifying therapies.

References and Notes

1. D. C. Swinney, J. Anthony, *Nat. Rev. Drug Discov.* **10**, 507–519 (2011).
2. V. Khurana, S. Lindquist, *Nat. Rev. Neurosci.* **11**, 436–449 (2010).
3. D. F. Tardiff, M. L. Tucci, K. A. Caldwell, G. A. Caldwell, S. Lindquist, *J. Biol. Chem.* **287**, 4107–4120 (2012).
4. A. A. Cooper et al., *Science* **313**, 324–328 (2006).
5. L. J. Su et al., *Dis. Model. Mech.* **3**, 194–208 (2010).
6. C. Y. Chung et al., *Science* **342**, XXX (2013).
7. T. F. Outeiro, S. Lindquist, *Science* **302**, 1772–1775 (2003).

8. A. D. Gitler et al., *Proc. Natl. Acad. Sci. U.S.A.* **105**, 145–150 (2008).
9. J. H. Soper, V. Kehm, C. G. Burd, V. A. Bankaitis, V. M. Lee, *J. Mol. Neurosci.* **43**, 391–405 (2011).
10. A. B. Singleton et al., *Science* **302**, 841 (2003).
11. A. M. Smith, R. Ammar, C. Nislow, G. Gaefer, *Pharmacol. Ther.* **127**, 156–164 (2010).
12. A. Kumar, *Methods Mol. Biol.* **416**, 117–129 (2008).
13. D. Rotin, S. Kumar, *Nat. Rev. Mol. Cell Biol.* **10**, 398–409 (2009).
14. E. Lauwers, Z. Erpapazoglou, R. Haguenaer-Tsapis, B. André, *Trends Cell Biol.* **20**, 196–204 (2010).
15. A. Menant, R. Barbey, D. Thomas, *EMBO J.* **25**, 4436–4447 (2006).
16. C. MacDonald, D. K. Stringer, R. C. Piper, *Traffic* **13**, 586–598 (2012).
17. F. Omura, Y. Kodama, T. Ashikari, *FEMS Microbiol. Lett.* **194**, 207–214 (2001).
18. E. Yeger-Lotem et al., *Nat. Genet.* **41**, 316–323 (2009).
19. V. Sancken et al., *Hum. Mol. Genet.* **21**, 2432–2449 (2012).
20. G. K. Tofaris et al., *Proc. Natl. Acad. Sci. U.S.A.* **108**, 17004–17009 (2011).
21. G. Esposito, F. Ana Clara, P. Verstreken, *Dev. Neurobiol.* **72**, 134–144 (2012).
22. D. A. MacLeod et al., *Neuron* **77**, 425–439 (2013).
23. C. Vilariño-Güell et al., *Am. J. Hum. Genet.* **89**, 162–167 (2011).
24. A. Zimprich et al., *Am. J. Hum. Genet.* **89**, 168–175 (2011).
25. P. Zabrocki et al., *Biochim. Biophys. Acta* **1783**, 1767–1780 (2008).

Acknowledgments: We thank A. Kumar for providing the plasmid Tn7 library; B. Wendland and L. Hicke for the Rsp5 antibody; the WIBR Genome Technology Core for Illumina Sequencing; B. Schulman (B. Schulman and H.B.K. were funded

by NIH grant 5R01GM069530) and A. Goldberg for help with in vitro ubiquitination assays; T. DiCesare for graphics support; and members of the Lindquist Lab for helpful comments on the manuscript. S.L. is an investigator for HHMI. D.F.T. was funded by a National Research Service Award (NRSA) fellowship F32NS061419 and research supported by the JPB Foundation (D.F.T. and S.L.), the Eleanor Schwartz Charitable Foundation, and an HHMI Collaborative Innovation Award (D.F.T., V.K., C.Y.C., and S.L.; G.A.C., K.A.C., and M.L.T.; and J.-C.R. and M.A.T.). N.T.J. was funded by a NRSA fellowship (F32GM099817), and N.T.J. and S.L.B. were funded by NIH grant GM58160. H.T.K. was funded by the Bachmann-Strauss Dystonia & Parkinson Foundation. Genome sequencing data are deposited in the National Center for Biotechnology Information under BioProject accession number PRJNA222476. WIBR and MIT have filed a patent application, on which D.F.T., N.T.J., S.L.B., and S.L. are inventors, relating to use of compounds described here in treatment of neurodegenerative diseases. In addition, S.L. is an inventor on patents and patent applications filed by the University of Chicago relating to methods of screening for compounds that decrease α -syn-associated toxicity using yeast that express α -syn. All the yeast plasmids and strains and NAB are available under a Uniform Biological Material Transfer Agreement from the Whitehead Institute.

Supplementary Materials

www.sciencemag.org/content/342/6161/979/suppl/DC1
Materials and Methods
Supplementary Text
Figs. S1 to S13
Tables S1 to S3
References (26–50)

29 August 2013; accepted 16 October 2013
Published online 24 October 2013;
10.1126/science.1245321

Identification and Rescue of α -Synuclein Toxicity in Parkinson Patient–Derived Neurons

Chee Yeun Chung,^{1*} Vikram Khurana,^{1,2*} Pavan K. Auluck,^{1,3} Daniel F. Tardiff,¹ Joseph R. Mazzulli,² Frank Soldner,¹ Valeriya Baru,^{1,4} Yali Lou,^{1,4} Yelena Freyzon,¹ Sukhee Cho,⁵ Alison E. Mungenast,⁵ Julien Muffat,¹ Maisam Mitalipova,¹ Michael D. Pluth,⁶ Nathan T. Jui,⁶ Birgitt Schüle,⁷ Stephen J. Lippard,⁶ Li-Huei Tsai,^{4,5} Dimitri Krainc,² Stephen L. Buchwald,⁶ Rudolf Jaenisch,^{1,8} Susan Lindquist^{1,4,8†}

The induced pluripotent stem (iPS) cell field holds promise for in vitro disease modeling. However, identifying innate cellular pathologies, particularly for age-related neurodegenerative diseases, has been challenging. Here, we exploited mutation correction of iPS cells and conserved proteotoxic mechanisms from yeast to humans to discover and reverse phenotypic responses to α -synuclein (α syn), a key protein involved in Parkinson’s disease (PD). We generated cortical neurons from iPS cells of patients harboring α syn mutations, who are at high risk of developing PD dementia. Genetic modifiers from unbiased screens in a yeast model of α syn toxicity led to identification of early pathogenic phenotypes in patient neurons. These included nitrosative stress, accumulation of endoplasmic reticulum (ER)–associated degradation substrates, and ER stress. A small molecule identified in a yeast screen (NAB2), and the ubiquitin ligase Nedd4 it affects, reversed pathologic phenotypes in these neurons.

Neurodegenerative dementias are devastating and incurable diseases for which we need tractable cellular models to investigate pathologies and discover therapeutics. Parkinson’s disease dementia (PDD), a debilitating nonmotor manifestation of Parkinson’s disease (PD), affects as many as 80% of patients (1). The best pathological correlate of PDD is neuron loss and pathological aggregation of α -synuclein (α syn) within

deep layers of the cerebral cortex (1). Contursi kindred patients, who harbor an autosomal dominant and highly penetrant Ala⁵³→Thr⁵³ (A53T) mutation in α syn, manifest prominent PD and dementia (2, 3). Induced pluripotent stem (iPS) cells from a female member of this kindred (table S1) have recently been mutation-corrected to control for genetic background effects (4). To establish a model for cortical synucleinopathy, we differentiated

two pairs of subclones from these lines (fig. S1) into cortical neurons (see supplementary materials and methods and figs. S2 and S3).

Over 12 weeks of differentiation, cultures consisted primarily of excitatory glutamatergic neurons mixed with glia (figs. S2, C to E, and S3). To identify neurons, we infected neural precursors before differentiation with lentiviruses expressing enhanced yellow fluorescent protein or red fluorescent protein (RFP) under the control of the synapsin promoter (fig. S2G). When cocultured, A53T and corrected neurons were electrically active at 8 weeks of differentiation. They exhibited similar calcium fluxes and electrophysiology (fig. S2, H and I). The majority of neurons were immunopositive for Tbr1, a transcription factor indicating developing deep cortical layers (fig. S2E) (5). α syn was robustly expressed, but only after neuronal differentiation (fig. S2, C to F). In neuronal processes, α syn was both cytoplasmic and punctate (fig. S2, C to E). Thus, these cells provide a relevant substrate for examining early α syn-related cortical pathologies.

It has been difficult to establish neurodegenerative phenotypes in iPS cell-derived neurons that can be solely attributable to disease-causing genetic mutations. Previous studies accelerated degenerative phenotypes with toxins such as oxidative stressors (6–8). In addition, inconsistent differentiation precludes these cells from being used in high-throughput screening. To address these problems, we turned to a yeast platform in which α syn-expression results in toxicity (9, 10) and disease-relevant phenotypes, including focal accumulation of α syn, mitochondrial dysfunction, α syn-mediated vesicle trafficking defects, links to genetic and environmental risk factors, and sensitivity to α syn dosage (9–12). We reasoned that unbiased genetic analysis in this system could guide discovery of innate pathological phenotypes.

Previous unbiased yeast genetic screens, encompassing 85% of the yeast proteome, identified robust modifiers of α syn toxicity (9, 12). We first tested Fzf1, a transcriptional regulator of nitrosative stress responses (13) that suppressed α syn toxicity in yeast (Fig. 1A). Nitrosative stress is caused by nitric oxide (NO) and related redox forms. Though it is not known if there is a direct causal connection between nitrosative stress and

α syn toxicity, the nitration of tyrosine residues is increased in postmortem brain samples from synucleinopathy patients (14, 15).

To determine if nitritative damage occurs to yeast proteins in direct response to α syn, we took advantage of an antibody to nitrotyrosine. In yeast, this antibody exhibited minimal background in control strains, allowing us to detect intense protein nitration that was tightly dependent on α syn dosage (Fig. 1B). Nitration was a highly specific response to α syn toxicity and was not observed with other neurodegenerative disease proteins expressed at equally toxic levels, including amyloid β peptide, TDP-43, polyQ-expanded Huntingtin, and Fus (Fig. 1B).

Expression of Fzf1 strongly decreased protein nitration induced by α syn (Fig. 1C). Next, we asked if α syn toxicity could be tuned by altering the production of NO. In yeast, NO levels are regulated by switching between distinct isoforms of mitochondrial cytochrome c oxidase (COX5): Deletion of COX5A increases NO; deletion of COX5B decreases it (16). Indeed, these manipulations increased and decreased nitrotyrosine levels in response to α syn (Fig. 1D). Toxicity increased and decreased commensurately (Fig. 1E). Thus, in yeast, nitrosative stress is not simply a consequence of α syn toxicity but also contributes to toxicity.

To investigate a connection between α syn and nitrosative stress in neurons, we employed FL2, a copper and fluorescein-based NO sensor (17). We optimized the use of FL2 with rat primary cortical cultures (fig. S4), a neuronal synucleinopathy model. Overexpression of α syn increased the FL2 signal, with a perinuclear distribution in the cell body (Fig. 2A, top) that partially colocalized with the endoplasmic reticulum (ER) (Fig. 2A, bottom). High density of processes and mixed cell types hindered intensity measurements outside of well-defined neuronal cell bodies.

Having optimized the FL2 assay in rat neurons, we turned to our Parkinson patient-derived cortical neurons at 8 weeks of differentiation. Two isogenic pairs of A53T and mutation-corrected neurons were differentiated in parallel and labeled with synapsin-RFP (fig. S2G). Intraneuronal FL2 signals increased in A53T neurons relative to corrected neurons, again most readily visualized in the cell body (Fig. 2B, top). As in rodent neurons, we observed partial colocalization of this signal with an ER marker (Fig. 2B, bottom). Cytoplasmic nitrotyrosine staining also accumulated in mutant neurons compared with corrected neurons (Fig. 2C). Similarly, cytoplasmic nitrotyrosine staining was prominent in neurons and neuropil of the postmortem frontal cortex from another patient

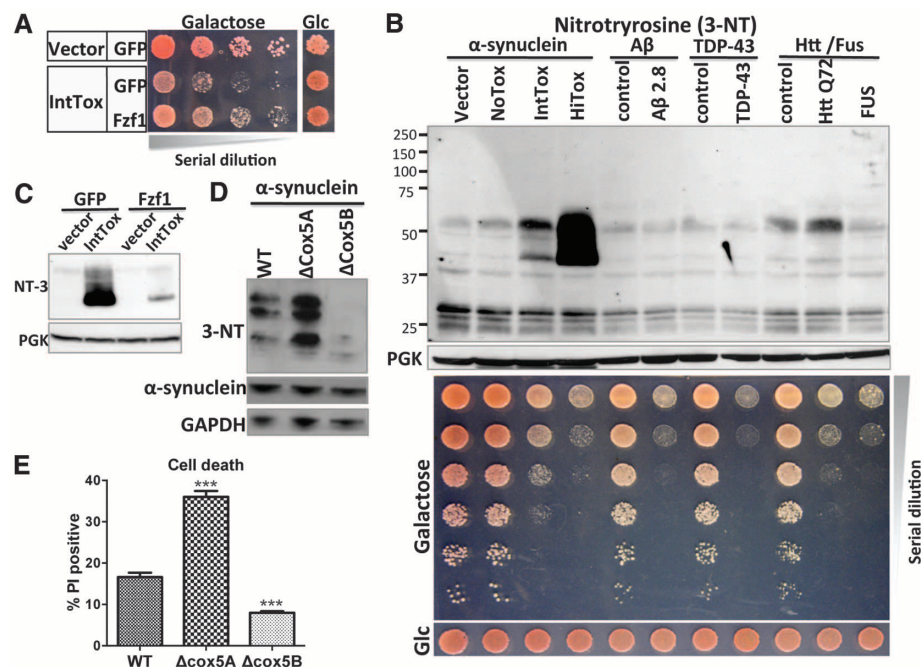


Fig. 1. A specific link between α syn toxicity and nitrosative stress is identified in yeast. (A) Fzf1 overexpression reduces α syn toxicity in yeast (IntTox), measured by growth of serially diluted yeast. GFP, green fluorescent protein; Glc, glucose. (B) Protein nitration levels were measured by immunoblotting for 3-nitrotyrosine (3-NT). Strains expressing low (NoTox), intermediate (IntTox), and high (HiTox) levels of α syn were analyzed (11). Neurodegeneration-related models with equivalent toxicity [expressing A β (β -amyloid peptide), Htt72Q (Huntingtin exon 1 with 72 glutamines), or Fus] were not similarly affected. PGK, phosphoglycerate kinase. (C) Fzf1 expression reduced α syn-induced increase in nitration. (D and E) NO-increasing deletion of Cox5A (Δ Cox5A) increased protein nitration levels, whereas the NO-decreasing Cox5B deletion (Δ Cox5B) reduced protein nitration levels (D). Toxicity was determined by flow cytometry with propidium iodide (PI)-stained cells (E). Data are represented as mean \pm SEM (error bars). *** P < 0.001 [one-way analysis of variance (ANOVA) with Bonferroni post hoc test]. WT, wild type.

¹Whitehead Institute for Biomedical Research, Cambridge, MA 02142, USA. ²Department of Neurology, Massachusetts General Hospital and Harvard Medical School, Boston, MA 02114, USA. ³Department of Pathology (Neuropathology), Massachusetts General Hospital and Harvard Medical School, Boston, MA 02114, USA. ⁴Howard Hughes Medical Institute, Department of Biology, Massachusetts Institute of Technology, Cambridge, MA, USA. ⁵The Picower Institute for Learning and Memory, Department of Brain and Cognitive Sciences, Massachusetts Institute of Technology, Cambridge, MA 02139, USA. ⁶Department of Chemistry, Massachusetts Institute of Technology, Cambridge, MA 02139, USA. ⁷The Parkinson's Institute, Sunnyvale, CA 94085, USA. ⁸Department of Biology, Massachusetts Institute of Technology, Cambridge, MA, USA.

*These authors contributed equally to this work.

†Corresponding author. E-mail: lindquist_admin@wi.mit.edu

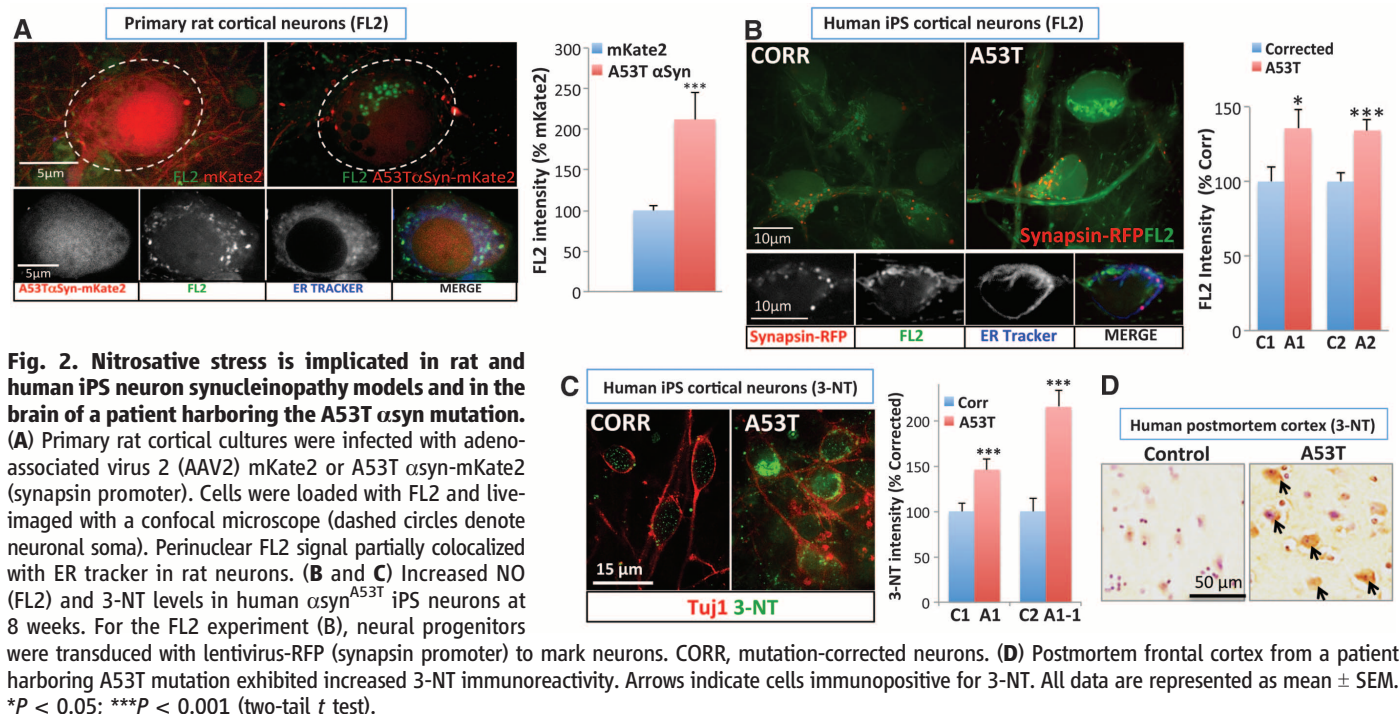


Fig. 2. Nitrosative stress is implicated in rat and human iPS neuron synucleinopathy models and in the brain of a patient harboring the A53T α syn mutation. (A) Primary rat cortical cultures were infected with adeno-associated virus 2 (AAV2) mKate2 or A53T α syn-mKate2 (synapsin promoter). Cells were loaded with FL2 and live-imaged with a confocal microscope (dashed circles denote neuronal soma). Perinuclear FL2 signal partially colocalized with ER tracker in rat neurons. (B and C) Increased NO (FL2) and 3-NT levels in human α syn^{A53T} iPS neurons at 8 weeks. For the FL2 experiment (B), neural progenitors were transduced with lentivirus-RFP (synapsin promoter) to mark neurons. CORR, mutation-corrected neurons. (D) Postmortem frontal cortex from a patient harboring A53T mutation exhibited increased 3-NT immunoreactivity. Arrows indicate cells immunopositive for 3-NT. All data are represented as mean \pm SEM. * P < 0.05; *** P < 0.001 (two-tail t test).

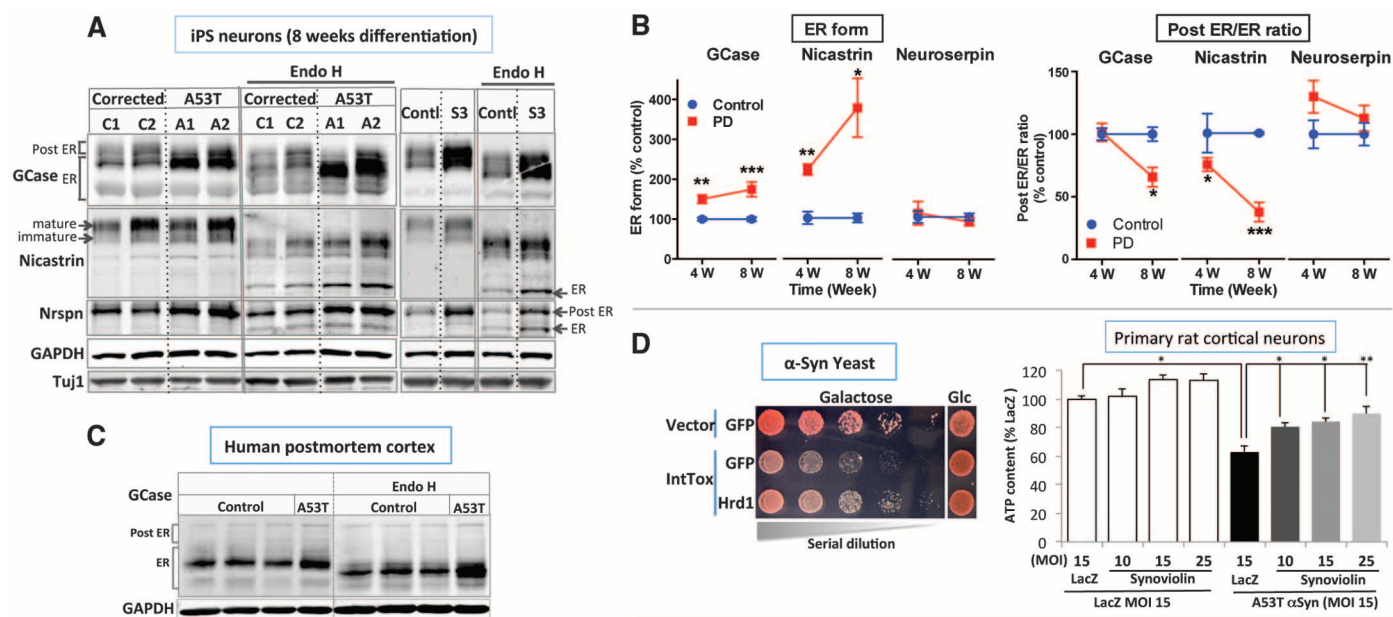


Fig. 3. Accumulation of ERAD substrates in patient cortical neurons is reversed by synoviolin. (A and B) Cortical iPS neurons from α syn^{A53T} (A1, A2), α syn^{corrected} (C1, C2), and α syn^{triplication} (S3) patients and a male human embryonic stem cell line (BGO1) were harvested at 8 to 12 weeks. ER or post-ER forms were distinguished on the basis of sensitivity to endoglycosidase H (Endo H) in GCase, nicastrin, and neuroserpin (Nrsn) [n = 4 to 6 replicates, two-tail t test compared with control (Cont1) samples at each time point]. GAPDH, glyceraldehyde-3-phosphate dehydrogenase. (C) ER forms of GCase also accumulated in the postmortem cortex from the A53T patient. (D) Coexpression of Hrd1 or its mammalian homolog, synoviolin, reduced α syn toxicity in yeast and rat cortical neurons. Rat cultures were transduced by lentivirus encoding synoviolin with varying multiplicity of infection (MOI) and cotransduced with lenti- α syn^{A53T} or lenti-LacZ. Cellular adenosine triphosphate (ATP) content was measured (one-way ANOVA with Bonferroni post hoc test). (E) Lentiviral transduction of synoviolin

reduced accumulation of ER forms of GCase and nicastrin in α syn^{A53T} iPS cortical neurons at 8 to 12 weeks. Baseline PD levels were equated to the percentage of control established in Fig. 3 to depict biological importance of the change. All data are represented as mean \pm SEM. * P < 0.05; ** P < 0.01; *** P < 0.001.

in the same kindred (18), but not in control brain samples (Fig. 2D).

The yeast synucleinopathy model exhibits ER stress, ER-associated degradation (ERAD) substrate accumulation, and defective trafficking from the ER to Golgi (12). ER stress has also been described in a mouse synucleinopathy model (19). Because NO was visualized in the vicinity of the ER in neurons (Fig. 2), we asked whether modulating NO levels modulates ER stress. Indeed, manipulating COX5 isoforms to increase and decrease NO levels commensurately altered the unfolded protein response (fig. S5A) and the ER accumulation of carboxypeptidase Y (CPY) (fig. S5B), a well-characterized ERAD substrate that traffics between the ER and vacuole (12). This required the presence of α syn (fig. S5A), implying a connection between nitrosative and ER stress in the context of α syn toxicity. Correspondingly, two hallmarks of ER stress—protein disulfide isomerase and binding immunoglobulin protein—increased at 12 weeks of differentiation in the A53T neurons compared with control cells (fig. S5C). Levels of CHOP (CCAAT enhancer-binding protein homologous protein), a component of ER stress-induced apoptosis, did not change (fig. S5C), indicating that cellular pathology was still at an early stage.

Next, we assessed the accumulation and trafficking of three ERAD substrates implicated in neurodegeneration: glucocerebrosidase (GCase), neuroserpin, and nicastrin (20). GCase mutations are common risk factors for PD and confer risk for cognitive impairment in this disease (21).

GCase accumulates in the ER of cultured cells overexpressing α syn (22). ER forms of GCase and nicastrin accumulated, and the ratio of post-ER-to-ER forms declined in A53T compared with mutation-corrected patient neurons starting at 4 weeks (Fig. 3, A and B, and fig. S6, A to C). Neuroserpin was not affected at the time points we examined (Fig. 3, A and B, and fig. S6, A to C). Levels of neuron-specific markers were unaffected (Fig. 3A and fig. S6C). These findings were consistent in multiple rounds of differentiation and robust-to-distinct differentiation protocols (fig. S6C). Phenotypes were not present in the undifferentiated iPS cell lines (fig. S6D). Thus, ERAD dysfunction is an early and progressive cellular phenotype in response to mutated α syn in patient neurons.

The increase in the ER form of GCase and the decrease in the post-ER-to-ER ratio were recapitulated in the brain of an A53T patient (Fig. 3C and fig. S7B). Cortices from sporadic PD samples exhibited the same trend (fig. S7). We also analyzed cortical neurons generated from the iPS cells of a male patient of the Iowa kindred. This patient harbored a triplication of the wild-type α syn gene and manifested aggressive dementia, in addition to parkinsonism (table S1). Aged cortical neurons generated from the male human embryonic stem cell line BG01 (23) served as a control. ERAD substrates accumulated (Fig. 3A and fig. S6B) and ER stress increased (fig. S5C) in neurons from this patient, closely phenocopying A53T cells.

Another suppressor of α syn toxicity recovered in the yeast screen was Hrd1 (Fig. 3D, left) (9).

Hrd1 is a highly conserved E3 ubiquitin ligase (synoviolin-1 or Syvn1 in humans) that plays a critical role in ERAD from yeast to human. In primary rat cortical neurons, lentiviral expression of Syvn1 rescued α syn toxicity in a dose-dependent manner (Fig. 3D, right). Syvn1 also reduced nicastrin and GCase accumulation in the ER of the A53T patient cortical neurons (Fig. 3E).

Next, we tested the ability of NAB2 (24) to rescue the pathological phenotypes we discovered here in both yeast cells and PD neurons. NAB2, an *N*-arylbenzimidazole, was recovered in a yeast screen of more than 180,000 small molecules and rescues α syn toxicity in yeast by activating the Rsp5-Nedd4 pathway (24). This protein is another highly conserved ubiquitin ligase and plays a key role in regulating vesicle trafficking (25, 26). NAB2 reduced protein nitration in the yeast synucleinopathy model (Fig. 4A) and decreased NO levels in A53T patient neurons (Fig. 4B). Moreover, NAB2 reduced the accumulation of immature ER forms of CPY in yeast (Fig. 4A). This molecule increased the post-ER forms and decreased the immature forms of nicastrin and GCase in PD patient neurons (Fig. 4C and fig. S8). Furthermore, NAB2 analogs that were inactive in yeast (24) were also inactive in human neurons (fig. S9). Connecting NAB2 back to the ubiquitin ligase, we used a lentivirus to overexpress Nedd4. This phenocopied the effects of the compound, increasing the mature forms of nicastrin and GCase (Fig. 4D).

Conserved biology in a cross-species cellular discovery platform, as described here, enabled the

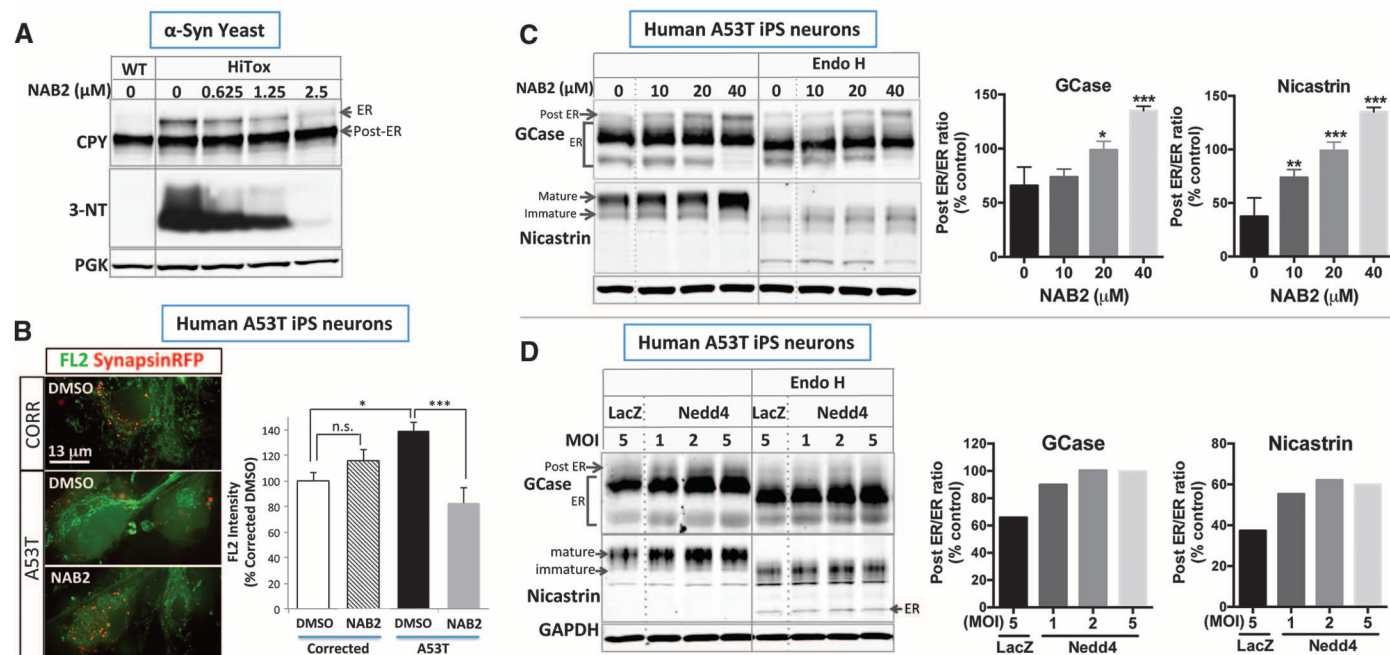


Fig. 4. A small-molecule modifier, identified in an unbiased yeast screen, and its target correct analogous defects in yeast and patient neurons. (A) NAB2 ameliorates α syn-induced ER accumulation of CPY and nitrosative stress in the yeast model. (B) NAB2 (5 μ M) decreases nitric oxide (FL2) levels in α syn^{A53T} iPS neurons labeled with synapsin-RFP. DMSO, dimethyl sulfoxide. (C) NAB2 increases post-ER forms of and ameliorates the ER accu-

mulation of GCase and nicastrin in α syn^{A53T} iPS neurons. (D) Lentiviral delivery of Nedd4 phenocopies the NAB2 treatment, increasing mature forms of GCase and nicastrin. Baseline PD levels were equated to the percentage of control established in Fig. 3. All data are represented as mean \pm SEM; n.s., not significant. * P < 0.05; ** P < 0.01; *** P < 0.001 (two-tail t test compared with control condition).

discovery of innate pathologic phenotypes in neurons derived from patients with PD. It also enabled the identification of genes and small molecules that reverted these phenotypes (24) (fig. S10). A similar approach might be useful in the study of other PD-relevant phenotypes identified in yeast, including mitochondrial dysfunction and perturbed metal-ion homeostasis (9, 11). The existence of other yeast models of neurodegenerative diseases suggests that this approach may also be generalizable to other diseases (11, 27, 28).

References and Notes

1. D. J. Irwin *et al.*, *Ann. Neurol.* **72**, 587–598 (2012).
2. P. J. Spira, D. M. Sharpe, G. Halliday, J. Cavanagh, G. A. Nicholson, *Ann. Neurol.* **49**, 313–319 (2001).
3. K. Markopoulou *et al.*, *Acta Neuropathol.* **116**, 25–35 (2008).
4. F. Soldner *et al.*, *Cell* **146**, 318–331 (2011).
5. T. Saito *et al.*, *Cereb. Cortex* **21**, 588–596 (2011).
6. H. N. Nguyen *et al.*, *Cell Stem Cell* **8**, 267–280 (2011).
7. B. Byers *et al.*, *PLOS ONE* **6**, e26159 (2011).
8. O. Cooper *et al.*, *Sci. Transl. Med.* **4**, 141ra90 (2012).
9. A. D. Gitler *et al.*, *Nat. Genet.* **41**, 308–315 (2009).
10. T. F. Outeiro, S. Lindquist, *Science* **302**, 1772–1775 (2003).
11. V. Khurana, S. Lindquist, *Nat. Rev. Neurosci.* **11**, 436–449 (2010).
12. A. A. Cooper *et al.*, *Science* **313**, 324–328 (2006).
13. A. Sarver, J. DeRisi, *Mol. Biol. Cell* **16**, 4781–4791 (2005).
14. B. I. Giasson *et al.*, *Science* **290**, 985–989 (2000).
15. E. Gómez-Tortosa *et al.*, *Acta Neuropathol.* **103**, 495–500 (2002).
16. P. R. Castello *et al.*, *Proc. Natl. Acad. Sci. U.S.A.* **105**, 8203–8208 (2008).
17. M. D. Pluth, E. Tomat, S. J. Lippard, *Annu. Rev. Biochem.* **80**, 333–355 (2011).
18. P. T. Kotzbauer *et al.*, *Exp. Neurol.* **187**, 279–288 (2004).
19. E. Colla *et al.*, *J. Neurosci.* **32**, 3306–3320 (2012).
20. K. Tabuchi, G. Chen, T. C. Südhof, J. Shen, *J. Neurosci.* **29**, 7290–7301 (2009).
21. R. N. Alcalay *et al.*, *Neurology* **78**, 1434–1440 (2012).
22. J. R. Mazzulli *et al.*, *Cell* **146**, 37–52 (2011).
23. M. Mitalipova *et al.*, *Stem Cells* **21**, 521–526 (2003).
24. D. F. Tardiff *et al.*, *Science* **342**, 979–983 (2013).
25. C. M. Haynes, S. Caldwell, A. A. Cooper, *J. Cell Biol.* **158**, 91–102 (2002).
26. P. Donovan, P. Poronnik, *Int. J. Biochem. Cell Biol.* **45**, 706–710 (2013).
27. A. C. Elden *et al.*, *Nature* **466**, 1069–1075 (2010).
28. S. Treusch *et al.*, *Science* **334**, 1241–1245 (2011).

Acknowledgments: We thank D. Dickson, L. Golbe, and J. Trojanowski for postmortem tissue or data; D. Pincus for the UPR reporter; I. Cheeseman, J. Kim, J. Pruszk, P. Wisniewski, and W. Salmon for important technical advice; R. Alagappan, T. Lungiangwa, and P. Xu for superb technical assistance; and S. Santagata, L. Whitesell, M. Feany, D. Landgraf, and L. Clayton for fruitful discussion and critical comments on the manuscript. Grant support was provided by a Howard Hughes Medical Institute Collaborative Innovation Award (S.L.), JPB Foundation grants (S.L.), NIH/National Institute on Aging grant K01 AG038546 (C.Y.C.), an American Brain Foundation and Parkinson's Disease Foundation Clinician-Scientist Development Award (V.K.), NIH grant 5 R01CA084198 (R.J.), and the NSF (S.J.L.). Whitehead Institute for Biomedical Research has filed a patent application, on which authors V.K., C.Y.C., and S.L. are inventors, relating to the use of yeast- and iPS cell-based models of synucleinopathies and

associated phenotypes for identifying compounds. In addition, author S.L. is an inventor on patents and patent applications filed by The University of Chicago relating to methods of screening for compounds that decrease α -synuclein-associated toxicity using yeast that expresses α -synuclein. All the yeast plasmids and strains and NAB2 are available under a Uniform Biological Material Transfer Agreement from the Whitehead Institute. Author contributions: C.Y.C., V.K., and S.L. conceptualized the study, designed the experiments, and wrote the paper. V.K. developed the human iPS cell-derived cortical synucleinopathy model, assisted by Y.L. Pluripotent cell lines, advice on experimental design, and technical expertise were provided by F.S., J.R.M., J.M., M.M., and R.J. F.S. reprogrammed the WIBR-IP5-SYN^{TRPL} line from fibroblasts provided by B.S. C.Y.C. developed the rat cortical synucleinopathy model, assisted by V.B. The mKate2-tagged constructs were generated by Y.F. C.Y.C. and V.K. performed all experiments except Fig. 1, D and E, Fig. 2E, and fig. S5, A and B (P.K.A.); Fig. 4A (D.F.T.); Fig. 4C and fig. S6C (J.R.M./D.K.); fig. S2, H and I (A.E.M./S.C./L.-H.T.); and fig. S1 (Y.F./Y.L.). The small molecule NAB2 was synthesized by N.T.J. and S.L.B., based on a yeast screen performed by D.F.T. FL2 dye synthesis and technical advice were provided by M.D.P. and S.J.L.

Supplementary Materials

www.sciencemag.org/content/342/6161/983/suppl/DC1
Materials and Methods
Figs. S1 to S10
Table S1
References (29–40)

29 August 2013; accepted 16 October 2013
Published online 24 October 2013;
10.1126/science.1245296

The Human Language–Associated Gene SRPX2 Regulates Synapse Formation and Vocalization in Mice

G. M. Sia,^{1,2} R. L. Clem,³ R. L. Huganir^{1,2*}

Synapse formation in the developing brain depends on the coordinated activity of synaptogenic proteins, some of which have been implicated in a number of neurodevelopmental disorders. Here, we show that the sushi repeat–containing protein X-linked 2 (*SRPX2*) gene encodes a protein that promotes synaptogenesis in the cerebral cortex. In humans, *SRPX2* is an epilepsy- and language-associated gene that is a target of the foxhead box protein P2 (*FoxP2*) transcription factor. We also show that *FoxP2* modulates synapse formation through regulating *SRPX2* levels and that *SRPX2* reduction impairs development of ultrasonic vocalization in mice. Our results suggest *FoxP2* modulates the development of neural circuits through regulating synaptogenesis and that *SRPX2* is a synaptogenic factor that plays a role in the pathogenesis of language disorders.

Synapse formation is an essential process during brain development that is coordinated by many membrane and secreted proteins (1–5). Proper development of neural circuitry is required for brain function, and mutations in synaptogenic genes have been linked to many cog-

nitive diseases, including autism, schizophrenia, and mental retardation (6–8). Although a number of proteins have been shown to modulate synaptogenesis, no single gene knockout has been shown to completely ablate the formation of any major class of synapses, suggesting that the brain may use many proteins to regulate this process. To search for synaptogenic factors, we embarked on a high-throughput overexpression screen for human genes encoding membrane and secreted proteins that mediate synaptogenesis in the central nervous system. We identified sushi repeat–containing protein X-linked (*SRPX2*) as a secreted protein that modulates synapse density in dissociated hippo-

campal neurons. The *SRPX2* gene is mutated in human patients suffering from rolandic (sylvian) epilepsy with associated oral and speech dyspraxia (9) and is a target of the *FoxP2* gene (10), suggesting that *SRPX2* may be involved in neural connectivity and language in humans. Although sushi domain proteins, also known as complement control protein (CCP) domain proteins, function as regulators of the immune system in vertebrates (11), they also regulate neuronal development in *C. elegans* (12) and *Drosophila* (13, 14). We therefore decided to further examine the role of *SRPX2* in synapse formation.

To verify that *SRPX2* controls synapse density, we overexpressed rat and human *SRPX2* genes in dissociated rat cortical cells. Overexpression of *SRPX2* caused an increase in the density of vesicular glutamate transporter 1 (VGLUT1) and PSD-95 puncta on the neurons while leaving the density of inhibitory synaptic markers vesicular γ -aminobutyric acid (GABA) transporter (VGAT) and gephyrin unchanged (Fig. 1, A and B). Dendritic morphology was unaffected by *SRPX2* overexpression (fig. S3A). Both human and rat *SRPX2* genes are capable of increasing spine density when overexpressed (Fig. 1C). Thus, *SRPX2* overexpression increases the density of excitatory synapses and spines in vitro without an effect on inhibitory synapse formation.

SRPX2 mRNA is found in neurons in multiple brain regions, including the cerebral cortex and hippocampus (9, 15). To further characterize the expression and localization of *SRPX2* at the protein level, we generated an antibody against *SRPX2* and used it to perform immunocytochemistry on

¹Howard Hughes Medical Institute, Johns Hopkins University School of Medicine, 725 North Wolfe Street, Baltimore, MD 21205, USA. ²Department of Neuroscience, Johns Hopkins University School of Medicine, 725 North Wolfe Street, Baltimore, MD 21205, USA. ³Friedman Brain Institute, Mount Sinai School of Medicine, 1425 Madison Avenue, New York, NY 10029, USA.

*Corresponding author. E-mail: rhuganir@jhmi.edu

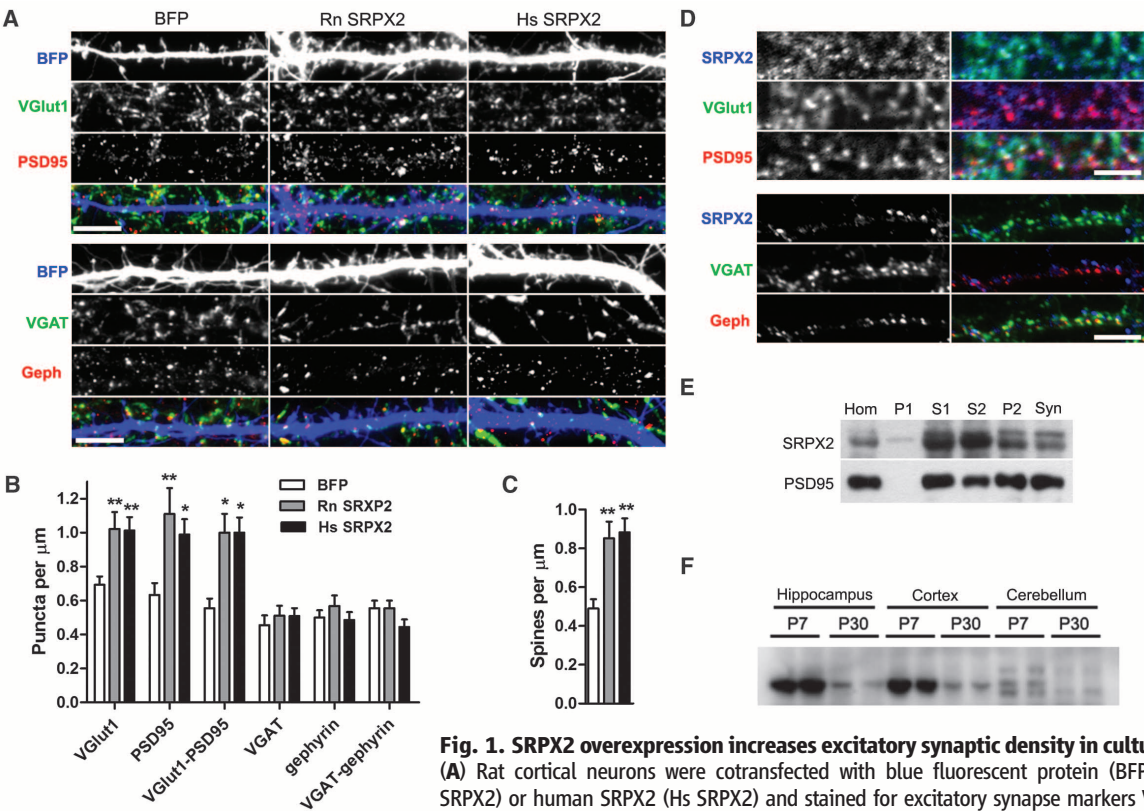
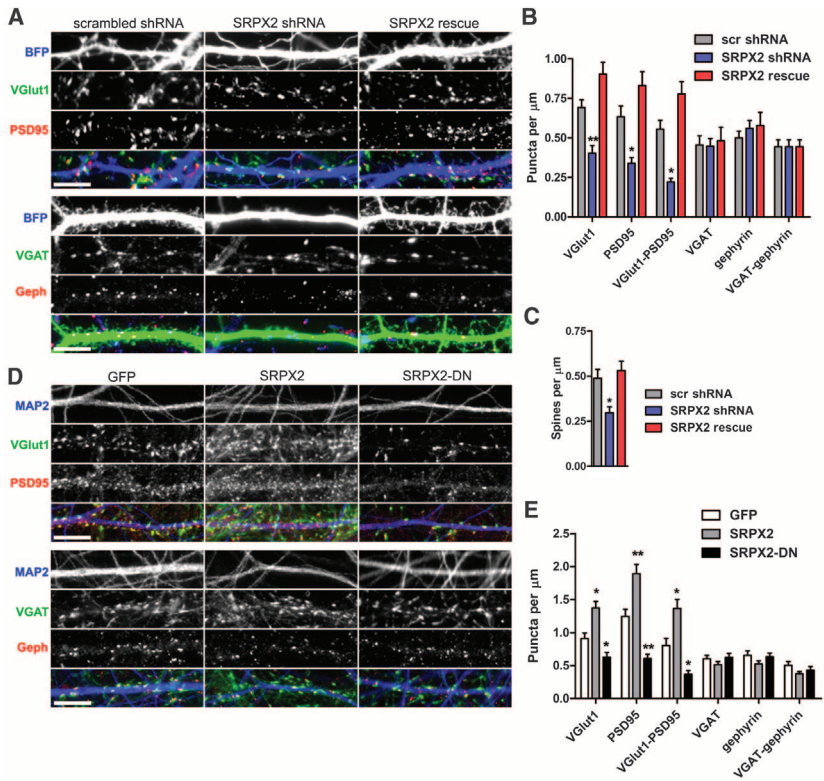


Fig. 1. SRPX2 overexpression increases excitatory synaptic density in cultured neurons. (A) Rat cortical neurons were cotransfected with blue fluorescent protein (BFP) and rat (Rn SRPX2) or human SRPX2 (Hs SRPX2) and stained for excitatory synapse markers VGLUT1 (green) and PSD95 (red), as well as for inhibitory synaptic markers VGAT (green) and gephyrin (red). Scale bars, 5 μm . (B) Quantification of synapse density shown in (A). (Means \pm SEM, $n = 13$ to 35 neurons, $*P < 0.05$, $**P < 0.01$). (C) Quantification of spine density shown in (A). (Means \pm SEM, $n = 25$ to 35 neurons, $**P < 0.01$). (D) DIV 21 dissociated rat cortical neurons were surface-stained for SRPX2 and then permeabilized and stained for excitatory and inhibitory synaptic markers. Scale bars, 3.5 μm . (E) Synaptosome preparation was immunoblotted for SRPX2 and PSD95. Fractions are crude homogenate (Hom), P1 pellet (P1), S1 supernatant (S1), S2 supernatant (S2), P2 pellet (P2), and synaptosomes (Syn). (F) Western blot analysis of SRPX2 levels in the cerebral cortex, hippocampus, and cerebellum of P7 and P30 mice.

Fig. 2. Reduction of endogenous SRPX2 and secretion of dominant negative SRPX2 decrease excitatory synaptic density in cultured neurons. (A) Rat cortical neurons were cotransfected with BFP and scrambled shRNA, SRPX2 shRNA, or SRPX2 shRNA and rescue construct (SRPX2 rescue) and then stained for excitatory or inhibitory synaptic markers. Scale bar, 5 μm . (B) Quantitation of synapse density shown in (A). (Means \pm SEM, $n = 12$ to 35 neurons, $*P < 0.05$, $**P < 0.01$). (C) Quantitation of spine density shown in (A). (Means \pm SEM, $n = 22$ to 35 neurons, $*P < 0.05$). (D) Rat cortical neurons were incubated with medium conditioned by human embryonic kidney-293 cells overexpressing GFP, SRPX2, or SRPX2-DN and immunostained for the dendritic marker MAP2, and excitatory or inhibitory synaptic markers. Scale bar, 5 μm . (E) Quantitation of synapse density shown in (D). (Means \pm SEM, $n = 12$ to 21 neurons, $*P < 0.05$, $**P < 0.01$).



rat cortical cultures. We verified that the antibody is specific for SRPX2 and does not recognize the closely related SRPX protein (fig. S1). We observed that SRPX2 staining is largely colocalized with VGlut1 and PSD-95 puncta and excluded from VGAT and gephyrin puncta (Fig. 1D), which is consistent with its effect on excitatory synapses. Immunoblots of synaptosome preparations showed that SRPX2 is partially retained on synaptic membranes (Fig. 1E), and staining of the heterologous and neuronal cells overexpressing SRPX2 also showed large puncta

of SRPX2 on the surface of cells (fig. S2A), suggesting that SRPX2 is largely oligomerized and deposited close to the site of secretion. To investigate whether SRPX2 forms oligomers, we performed coimmunoprecipitations from culture medium of heterologous cells coexpressing SRPX2–green fluorescent protein (GFP) and SRPX2–Flag and found that SRPX2 binds to itself, but not to the closely related family member SRPX (fig. S2B). We also tested the properties of a dominant negative SRPX2 bearing a mutation associated with epilepsy and language disorders in

human patients (9) and found that SRPX2-DN is secreted into the medium and retains binding to native SRPX2 (fig. S2B). In rat cerebral cortex lysates, SRPX2 is more highly expressed in juvenile as compared with adult rats (Fig. 1F), coinciding with the period of elevated synapse formation. Thus, the spatial and temporal expression patterns of SRPX2 are consistent with a role in excitatory synaptogenesis.

To investigate whether endogenous SRPX2 regulates synapse formation, we generated a small hairpin RNA (shRNA) that efficiently knocks down SRPX2 (fig. S1, B and C). When dissociated neurons were transfected with the SRPX2-directed shRNA, a reduction of excitatory synapse and spine density (Fig. 2, A, B, and C) was observed, without a change in inhibitory synaptic density (Fig. 2, A and B) and dendritic morphology (fig. S3B). To control for off-target effects of the shRNA, we also generated a rescue shRNA-resistant SRPX2 construct bearing a silent mutation and confirmed that the rescue construct is not knocked down by the shRNA (fig. S1D). Coexpression of the rescue construct with SRPX2-shRNA in dissociated neurons results in the reversal of the deficits in excitatory synapse and spine formation with no effect on inhibitory synapse formation (Fig. 2, A to C). This data demonstrates that endogenous SRPX2 is critical for excitatory synapse formation. To examine whether secreted SRPX2 can cause changes in synapse density, we cultured cortical neurons with conditioned medium taken from heterologous cells overexpressing GFP, SRPX2, or SRPX2-DN. We found that cortical neurons cultured with SRPX2-conditioned medium showed an increased excitatory synapse density without a change in inhibitory synapse density (Fig. 2, D and E). Neurons cultured with SRPX2-DN-conditioned medium showed a decrease in excitatory synapse density (Fig. 2, D and E). All conditioned media had no effect on dendritic morphology (fig. S2C). Taken together, these results suggest that SRPX2 expression levels can bidirectionally regulate the density of excitatory synapses in neurons, and that secreted dominant negative SRPX2 impairs excitatory synapse formation.

Because SRPX2 expression is repressed by FoxP2 in heterologous cells (10), we further investigated the effect of FoxP2 on synaptogenesis. To verify that SRPX2 is regulated by FoxP2 in rat cortical neurons, we electroporated dissociated neurons with FoxP2 or GFP before plating and blotted for SRPX2 levels after 4 to 7 days of culture (Fig. 3A). We found that FoxP2-transfected cortical neurons contain a lower amount of SRPX2 as compared with that of GFP-transfected neurons (Fig. 3B), suggesting that FoxP2 represses SRPX2 expression in cortical cultures. To confirm that FoxP2 directly represses the SRPX2 gene in neuronal cells, we performed chromatin immunoprecipitation (ChIP) of FoxP2 from P0 C57BL/6J mouse cortices and found that FoxP2 binds to the promoter of the SRPX2 gene *in vivo* (Fig. 3C). Next, to assess FoxP2's effect on synaptic density

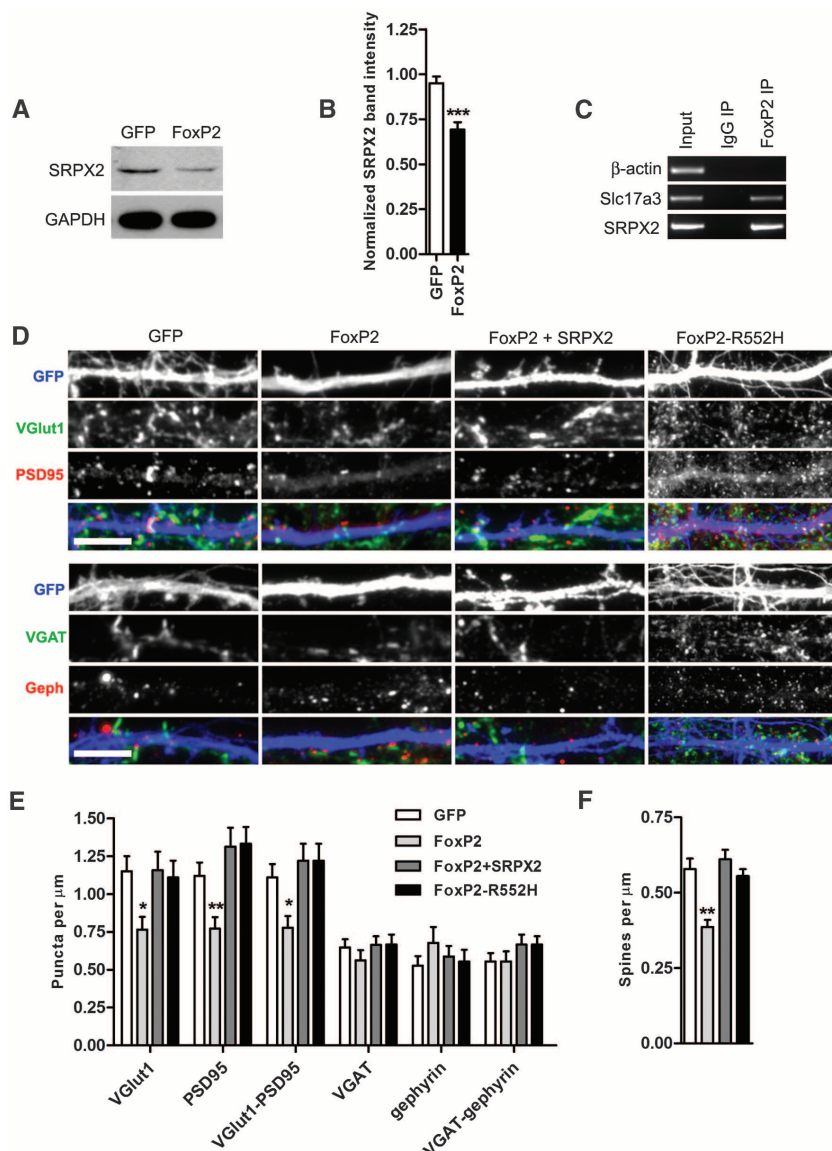


Fig. 3. FoxP2 regulates excitatory synapse density through SRPX2. (A) Western blot analysis of SRPX2 levels in cortical neurons electroporated with GFP or FoxP2 at plating and cultured for 4 days. (B) Quantitation of SRPX2 levels shown in (A). (Means \pm SEM, $n = 6$ to 7 blots, *** $P < 0.001$.) (C) ChIP assay of FoxP2 in cortices of P0 C57BL/6J mice. FoxP2 does not bind to the β -actin promoter but does bind the promoter of the previously identified FoxP2 target gene *Slc17a3* (32) and the promoter of the SRPX2 gene. (D) Rat cortical neurons were cotransfected with GFP and FoxP2, FoxP2 and SRPX2, or FoxP2-R552H and immunostained for excitatory and inhibitory synaptic markers. Scale bars, 5 μ m. (E) Quantitation of synapse density shown in (D). (Means \pm SEM, $n = 15$ to 17 neurons, * $P < 0.05$, ** $P < 0.01$.) (F) Quantitation of spine density shown in (D). (Means \pm SEM, $n = 32$ to 36 neurons, ** $P < 0.01$.)

we overexpressed FoxP2 in a small subset of DIV 4 neurons using liposome transfection and stained for synaptic markers 7 days after transfection. We found that neurons transfected with FoxP2 showed a lower density of excitatory synaptic markers and spines, without a change in the density of inhibitory synapses (Fig. 3, D to F). In addition, expression of FoxP2-R552H, containing a human mutation that abolishes FoxP2 transcriptional activity, does not cause a change in synaptic density (Fig. 3E), indicating that FoxP2 transcriptional activity is required for its effects of synaptic density. To determine whether FoxP2's effect on synapse formation may be due to decreases in SRPX2 expression, we coexpressed SRPX2 with FoxP2 in cortical neurons and found that this rescued the reduction of excitatory synapses and spines caused by FoxP2 (Fig. 3, D to F). In addition, overexpression of FoxP2 in cortical neurons caused a decrease in the number of primary dendrites and a concomitant decrease in total dendritic length (fig. S2D), an effect that is not rescued by SRPX2 coexpression. This suggests that FoxP2 has additional effectors that regulate dendritic morphology in cortical neurons, and that SRPX2's effect is specific to synapse formation. These results, together with data above showing that SRPX2 levels modulate synapse density bidirectionally, suggest that FoxP2 regulates synapse density through controlling SRPX2 levels.

To investigate the effects of SRPX2 *in vivo*, we electroporated C57BL/6J mice at E12.5 (embryonic day 12.5) in utero, targeting layers V/VI cortical neurons in a region spanning the motor and somatosensory cortices in the mouse cerebral cortex (Fig. 4A). This region of the brain was chosen because it is analogous to the language area in the human cortex, which displays cytoarchitectural defects in human patients bearing SRPX2 mutations (9). Layers V/VI neurons were chosen for their expression of the FoxP2 gene, as well as the presence of a long apical dendrite that is well suited for morphological assays. Neurons transfected with SRPX2-directed shRNA showed a decrease in the density of dendritic spines on the apical dendrite of layer V/VI neurons (Fig. 4, B and C), an effect that is reversed by cotransfection of the shRNA-resistant SRPX2 construct. Neurons transfected with the dominant negative human SRPX2-DN construct also showed a decrease in dendritic spine density (Fig. 4, B and C), indicating that SRPX2 mutations regulate apical dendritic spine density *in vivo*. Next, to test whether the spine density changes were reflected in electrophysiological measures of synapse density, we recorded miniature excitatory postsynaptic currents (mEPSCs) from electroporated layer V/VI neurons at P17–20 in whole-cell voltage clamp configuration. When compared with scrambled shRNA transfected control neurons, both SRPX2 shRNA-transfected and SRPX2-DN-transfected neurons showed a significant reduction in mEPSC frequency, whereas neurons cotransfected with SRPX2 shRNA and the SRPX2 rescue plasmid showed no difference in frequency (Fig. 4, D and

E). In addition, there was a small decrease in the mEPSC amplitude of SRPX2-DN-transfected neurons (Fig. 4E) and a small increase in the decay time constant (fig. S4A). These results suggest that SRPX2 can regulate excitatory synapse number in the intact mouse brain.

Because humans who bear mutated SRPX2 alleles suffer from electrical and morphological developmental defects in the language cortex that impair language acquisition, we wanted to examine whether SRPX2 knockdown can cause a similar defect in mice. When separated from their mothers, infant mouse pups emit ultrasonic vocalizations that elicit a search-and-retrieve behavior in nearby dams (16, 17). The isolation-induced infant pup ultrasonic vocalization task has been widely used to characterize mouse models of human language, social, and arousal disorders, including mice containing FoxP2 mutations (18–22). We observed that pups electroporated with SRPX2 shRNA showed a decreased vocalization frequency as compared with that of pups electroporated with scrambled shRNA or GFP controls (Fig. 4F and fig. S4B), and this defect is reversed by cotransfection of the rescue shRNA-resistant SRPX2 construct. Moreover, electroporation of SRPX2-DN also decreased ultrasonic vocalization frequency. Hence, we show that dysregulation of SRPX2

results in impaired ultrasonic vocalization in infant mice.

We have shown that SRPX2 is a sushi domain protein involved in synapse formation. In invertebrates, sushi domain proteins have been shown to cluster AChRs at synapses in *C. elegans* (12) and is localized to the nascent synaptic cleft in *Drosophila* (13, 14). In vertebrates, sushi domain proteins are primarily studied as regulators of the classical complement cascade (11). Our results suggest that sushi domain proteins may also play roles in regulating synaptic development and organization in vertebrates. In addition, because genes of the classical complement cascade have been shown to regulate synapse elimination (23), we speculate that SRPX2 may act through modulation of components of the complement cascade.

To date, FoxP2 is the only gene that has been shown to be involved in a human monogenic language disorder (24), although the cellular mechanisms involved remain obscure. Previous studies have suggested that FoxP2 may regulate neurite growth (25), dendritic morphology, and synaptic physiology of basal ganglia neurons (26, 27). We show here that FoxP2 can regulate synaptogenesis of excitatory synapses in cortical neurons through SRPX2. Although activity-regulated transcription factors have been shown to regulate

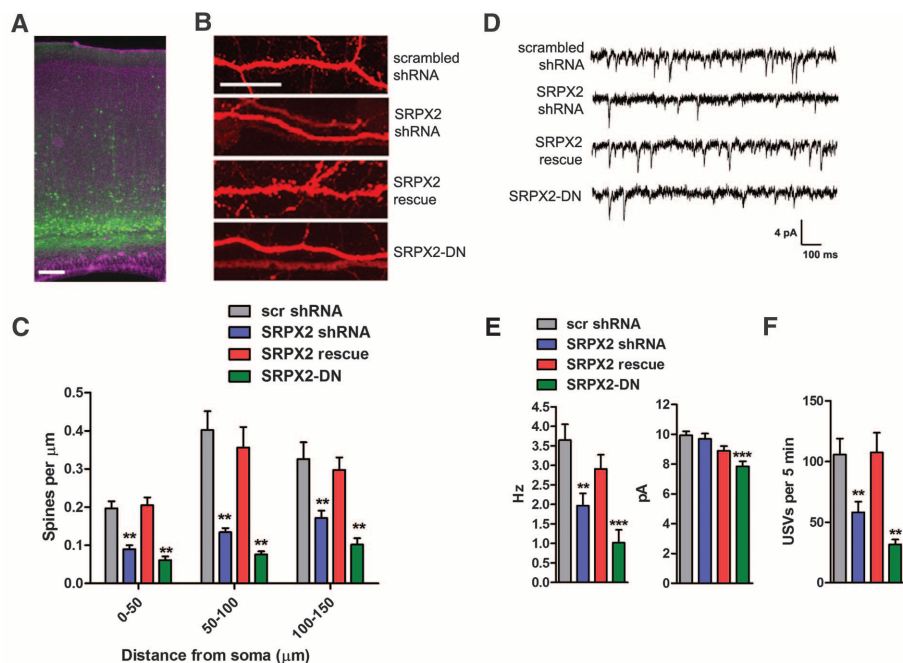


Fig. 4. SRPX2 regulates excitatory synapse density and ultrasonic vocalization *in vivo*. (A) Low-magnification micrograph of electroporated layer V/VI neurons in cortices of P21 C57BL/6J mice. (B) Representative micrographs of apical dendrites of cortical neurons electroporated in utero with scrambled shRNA, SRPX2 shRNA, SRPX2 shRNA and rescue construct, or SRPX2 dominant negative construct. Scale bar, 10 μm. (C) Quantitation of spine density on apical dendrite of layer V/VI neurons electroporated with various constructs. (Means ± SEM, $n = 16$ to 49 neurons, $**P < 0.01$). (D) Representative traces of mEPSC recordings from layer V/VI cortical neurons electroporated with scrambled shRNA, SRPX2 shRNA, SRPX2 shRNA and rescue construct, and SRPX2 dominant negative construct. (E) Average frequency and amplitude of mEPSC recordings. (Means ± SEM, $n = 8$ to 11 neurons, $**P < 0.01$, $***P < 0.001$). (F) Average number of ultrasonic vocalizations emitted in 5 min by P7 mouse pups electroporated with various SRPX2 constructs. (Means ± SEM, $n = 22$ to 46 mice, $**P < 0.01$).

synaptogenesis (28, 29), developmental synapse formation can occur in the complete absence of activity (30, 31), and it is unclear whether such synapse formation is also regulated by activity-independent transcription factors. We show here that FoxP2 is an activity-independent transcription factor that regulates synaptogenesis through SRPX2. Our study suggests that FoxP2 can affect the development of language-related neural circuitry through regulating synaptogenesis, and that SRPX2 may be involved in the pathogenesis of language disorders.

References and Notes

- P. Scheiffele, J. Fan, J. Choih, R. Fetter, T. Serafini, *Cell* **101**, 657–669 (2000).
- E. R. Graf, X. Zhang, S. X. Jin, M. W. Linhoff, A. M. Craig, *Cell* **119**, 1013–1026 (2004).
- T. Biederer et al., *Science* **297**, 1525–1531 (2002).
- J. Ko et al., *Neuron* **50**, 233–245 (2006).
- J. de Wit et al., *Neuron* **64**, 799–806 (2009).
- P. Szatmari et al., *Nat. Genet.* **39**, 319–328 (2007).
- T. Walsh et al., *Science* **320**, 539–543 (2008).
- F. Laumonnier et al., *Am. J. Hum. Genet.* **74**, 552–557 (2004).
- P. Roll et al., *Hum. Mol. Genet.* **15**, 1195–1207 (2006).
- P. Roll et al., *Hum. Mol. Genet.* **19**, 4848–4860 (2010).
- M. D. Kirkitadze, P. N. Barlow, *Immunol. Rev.* **180**, 146–161 (2001).
- M. Gendrel, G. Rapti, J. E. Richmond, J.-L. Bessereau, *Nature* **461**, 992–996 (2009).
- M. Hoshino, F. Matsuzaki, Y. Nabeshima, C. Hama, *Neuron* **10**, 395–407 (1993).
- M. Hoshino, E. Suzuki, Y. Nabeshima, C. Hama, *Development* **122**, 589–597 (1996).
- E. S. Lein et al., *Nature* **445**, 168–176 (2007).
- J. Fischer, K. Hammerschmidt, *Genes Brain Behav.* **10**, 17–27 (2011).
- J. N. Crawley, *Brain Pathol.* **17**, 448–459 (2007).
- W. Shu et al., *Proc. Natl. Acad. Sci. U.S.A.* **102**, 9643–9648 (2005).
- E. Fujita et al., *Proc. Natl. Acad. Sci. U.S.A.* **105**, 3117–3122 (2008).
- M. Groszer et al., *Curr. Biol.* **18**, 354–362 (2008).
- S. Gaub, M. Groszer, S. E. Fisher, G. Ehret, *Genes Brain Behav.* **9**, 390–401 (2010).
- C. A. French et al., *Genesis* **45**, 440–446 (2007).
- B. Stevens et al., *Cell* **131**, 1164–1178 (2007).
- C. S. Lai, S. E. Fisher, J. A. Hurst, F. Vargha-Khadem, A. P. Monaco, *Nature* **413**, 519–523 (2001).
- S. C. Vernes et al., *PLoS Genet.* **7**, e1002145 (2011).
- W. Enard et al., *Cell* **137**, 961–971 (2009).
- S. Reimers-Kipping, W. Hevers, S. Pääbo, W. Enard, *Neuroscience* **175**, 75–84 (2011).
- S. W. Flavell et al., *Science* **311**, 1008–1012 (2006).
- Y. Lin et al., *Nature* **455**, 1198–1204 (2008).
- M. Verhage et al., *Science* **287**, 864–869 (2000).
- F. Varoqueaux et al., *Proc. Natl. Acad. Sci. U.S.A.* **99**, 9037–9042 (2002).
- S. C. Vernes et al., *Am. J. Hum. Genet.* **81**, 1232–1250 (2007).

Acknowledgments: We thank M. Pletnikov and J. Yocum of the Behavioral Core Facility and M. Pucak of the Multiphoton/Electrophysiology Core Facility. We also thank H. Vega, S. Yang, N. O'Sullivan, and X. Wang for technical assistance. This study was supported by National Institutes of Health grant P50MH084020 to R.L.H. and grant NS050274 to the Multiphoton Core Facility. Under a licensing agreement between Millipore and the Johns Hopkins University, R.L.H. is entitled to a share of royalties received by the University on sales of products described in this article. R.L.H. is a paid consultant to Millipore. The terms of this arrangement are being managed by the Johns Hopkins University in accordance with its conflict-of-interest policies.

Supplementary Materials

www.sciencemag.org/content/342/6161/987/suppl/DC1
Materials and Methods
Figs. S1 to S4
References (33–37)

22 August 2013; accepted 11 October 2013

Published online 31 October 2013;

10.1126/science.1245079

Evidence that the Fosfomycin-Producing Epoxidase, HppE, Is a Non-Heme-Iron Peroxidase

Chen Wang,¹ Wei-chen Chang,² Yisong Guo,² Hui Huang,³ Spencer C. Peck,⁴ Maria E. Pandelia,² Geng-min Lin,³ Hung-wen Liu,^{3*} Carsten Krebs,^{1,2*} J. Martin Bollinger Jr.^{1,2*}

The iron-dependent epoxidase HppE converts (S)-2-hydroxypropyl-1-phosphonate (S-HPP) to the antibiotic fosfomycin [(1R,2S)-epoxypropylphosphonate] in an unusual 1,3-dehydrogenation of a secondary alcohol to an epoxide. HppE has been classified as an oxidase, with proposed mechanisms differing primarily in the identity of the O₂-derived iron complex that abstracts hydrogen (H•) from C1 of S-HPP to initiate epoxide ring closure. We show here that the preferred cosubstrate is actually H₂O₂ and that HppE therefore almost certainly uses an iron(IV)-oxo complex as the H• abstractor. Reaction with H₂O₂ is accelerated by bound substrate and produces fosfomycin catalytically with a stoichiometry of unity. The ability of catalase to suppress the HppE activity previously attributed to its direct utilization of O₂ implies that reduction of O₂ and utilization of the resultant H₂O₂ were actually operant.

The drug fosfomycin [(1R,2S)-epoxypropylphosphonate, Fos; see Fig. 1 for structure] kills pathogenic bacteria by inactivating uridine diphosphate (UDP)-N-acetylglucosamine enolpyruvyl transferase (MurA) and thereby blocking synthesis of peptidoglycan, which constitutes

the backbone of the cell wall (1, 2). The chemical “warhead” of Fos is its strained epoxide ring, which is opened upon attack by a cysteine residue in the active site of MurA, resulting in an inactivating covalent modification (1, 2). The epoxide of Fos is installed in the last step of its biosynthesis by the non-heme-iron(II) enzyme (S)-2-hydroxypropyl-1-phosphonate (S-HPP) epoxidase (HppE), which mediates an unusual 1,3-dehydrogenation of the secondary alcohol in the substrate to form the new carbon-oxygen bond of the three-membered ring (3).

HppE has been described as an oxidase, i.e., purported to use O₂ as its oxidizing cosubstrate (Fig. 1A, reaction I) (3). This formulation of the epoxidation reaction would require that two electrons, in addition to the two provided by S-HPP

in forming the epoxide, be transferred to the HppE active site to achieve redox balance in the four-electron reduction of O₂. The source of these electrons and the manner in which they might be delivered have remained unclear, as published structures of the enzyme do not reveal an obvious reductase domain (4–6), and gene clusters specifying the Fos-biosynthetic enzyme machinery do not encode a readily identifiable, dedicated reductase protein (7, 8). In vitro investigations of the HppE reaction have relied on either a heterologous reductase protein (called E₃) from the 3,6-dideoxyhexose biosynthetic pathway of *Yersinia pseudotuberculosis* with its reducing cosubstrate nicotinamide adenine dinucleotide (E₃/NADH) or the combination of the biochemical reductants NADH and flavin mononucleotide (NADH/FMN) (3, 9). That these reducing systems support only very slow Fos production (~1 min⁻¹) has reinforced the notion that additional components (e.g., the natural reducing system) might remain to be identified (9).

By contrast to simpler chemical and enzymatic epoxidation reactions involving addition of an oxygen atom (e.g., from a high-valent metal-oxo complex) to a carbon-carbon double bond (10, 11), the HppE reaction involves cleavage of a carbon-hydrogen bond of S-HPP (the *pro-R* C1–H bond) and formation of a new carbon-oxygen single bond to C1. In the product, the epoxide oxygen takes up the position on C1 originally occupied by the *pro-S* rather than the abstracted *pro-R* hydrogen, implying that C1 is inverted in the ring-closure step (3, 12). Although the mechanisms by which the C1–H bond is cleaved and the new C1–O bond is formed remain unknown, the observation by x-ray crystallography that S-HPP chelates the Fe^{II} cofactor via the C2 hydroxyl and the phosphonate

¹Department of Biochemistry and Molecular Biology, The Pennsylvania State University, University Park, PA, USA. ²Department of Chemistry, The Pennsylvania State University, University Park, PA, USA. ³Division of Medicinal Chemistry, College of Pharmacy, and Department of Chemistry and Biochemistry, The University of Texas at Austin, Austin, TX, USA. ⁴Department of Chemistry and the Howard Hughes Medical Institute, and Institute for Genomic Biology, University of Illinois at Urbana-Champaign, Urbana, IL, USA.

*Corresponding author. E-mail: h.w.liu@mail.utexas.edu (H.-w.L.); ckrebs@psu.edu (C.K.); jmb21@psu.edu (J.M.B.)

(5) and precedent from studies on other O_2 -activating iron enzymes (13, 14) led to the suggestion of three alternative pathways (Fig. 1B, blue arrow) (4, 15). These hypothetical O_2 -dependent mechanisms are distinguished by the nature of the C1–H–cleaving iron complex and the order of bond-breaking, bond-forming, and electron-injection steps.

As depicted in Fig. 1B, abstraction of the *pro-R* hydrogen atom (H^\bullet) from C1 could be mediated by a Fe^{III} -superoxo ($Fe^{III}-O_2^\bullet$) complex formed by simple addition of O_2 to the Fe^{II} cofactor (pathway I, beige arrows); a Fe^{III} -hydroperoxo complex, formed by addition of O_2 , an electron, and a proton to the cofactor (pathway II, green arrows); or a Fe^{IV} -oxo (ferryl) complex, formed by addition of O_2 , transfer of two electrons and two protons, and cleavage of the O–O bond (pathway III, red arrows). Of these possibilities, a ferryl complex was favored in a recent computational study (16). The mechanism of epoxide-ring closure after formation of the C1 radical is equally uncertain. The most straightforward possibility, suggested by studies on other iron enzymes that mediate formation of new carbon-heteroatom bonds, would be a radical group transfer of the Fe-coordinated C2–O atom to the C1 radical (17–22). However, the inversion of C1 remains challenging to explain according to this mechanism. On the basis of a remarkable oxidative 1,2-phosphonate migration mediated by HppE upon the substrate analog, (*R*)-1-hydroxypropyl-1-phosphate (Fig. 1, A and C, reactions II), a recent study posited a different ring-closure mechanism, involving formation of a C1 carbocation by electron transfer from the C1 radical to the iron cofactor and subsequent nucleophilic capture of the C1 carbocation by the C2 alkoxide (Fig. 1C, reaction I) (23). In this mechanism, neighboring group participation (anchimeric assistance) by the phosphonate (with retention of the C1 stereochemistry, dashed red line) could promote formation of the formal carbocation and then also dictate the net inversion of C1 after subsequent attack by the C2–O.

Precedent suggests that the H^\bullet -abstracting complex might be identified by use of rapid-kinetic and spectroscopic methods to detect it and demonstrate a kinetic isotope effect on its decay upon use of $[1,1\text{-}^2H_2]\text{-S-HPP}$ as the substrate (24). However, related O_2 -activating iron oxidases and oxygenases have catalytic rate constants typically in the range of 1 to 100 s^{-1} (24, 25). Therefore, if generation of the C1–H–cleaving intermediate requires one or two electrons, a reductant considerably more efficient than the reported E_3/NADH and NADH/FMN systems [which support maximum turnover rates of $\sim 0.01\text{ s}^{-1}$ (9)] might be required to gain entry into the reaction sequence fast enough to accumulate the C1–H–cleaving complex (24). In seeking a more suitable reductant, we determined that sodium dithionite ($\text{Na}_2\text{S}_2\text{O}_4$) can support multiple turnovers at rates more than a thousand times greater (10 to 100 s^{-1}) than those supported by the NADH -based re-

ducing systems. Dithionite is itself reactive toward O_2 on this same time scale (26), creating a conundrum as to how it could deliver electrons to HppE without first being oxidized by O_2 . Closer examination of the reaction led to the new hypothesis that dithionite might actually function by reducing O_2 directly rather than donating electrons to the HppE active site during an O_2 -initiated catalytic cycle. We therefore evaluated whether the expected O_2 -reduction product, H_2O_2 , can serve as the oxidant for Fos production by HppE.

To test this hypothesis, we added varying quantities of H_2O_2 slowly to solutions of Fe^{II} -HppE, L-ascorbate, and $[2,3,3,3\text{-}^2H_4]\text{-(S)-2-hydroxypropyl-1-phosphonate}$ ($d_4\text{-S-HPP}$), remotely labeled to distinguish the enzymatic product ($[2,3,3,3\text{-}^2H_4]\text{-(1R,2S)-epoxypropyl-1-phosphonate}$; $d_4\text{-Fos}$) from the commercially available Fos standard. Reaction

samples were analyzed by liquid chromatography with mass-spectrometric detection (LC-MS). As shown in fig. S1, the intensity of the peak arising from the $d_4\text{-S-HPP}$ substrate at a mass/charge ratio (m/z) of 143 (negative-ion mode) with an elution time of ~ 3 min is diminished (A), and a new peak at $m/z = 141$ (consistent with the mass of the $d_4\text{-Fos}$ product) coeluting at ~ 2 min with the commercial Fos ($m/z = 137$; dotted orange trace) grows (B) as more H_2O_2 is added. The identity of the new product was established to be Fos by 1H -nuclear magnetic resonance (1H -NMR) analysis of a reaction sample to which H_2O_2 was added to a final 1:1 molar ratio with respect to the unlabeled *S*-HPP substrate (Fig. 2). Although line broadening, possibly arising from the presence of iron from the enzyme in the NMR sample, is evident, comparison of the spectrum of the reaction product (spectrum B) to that of com-

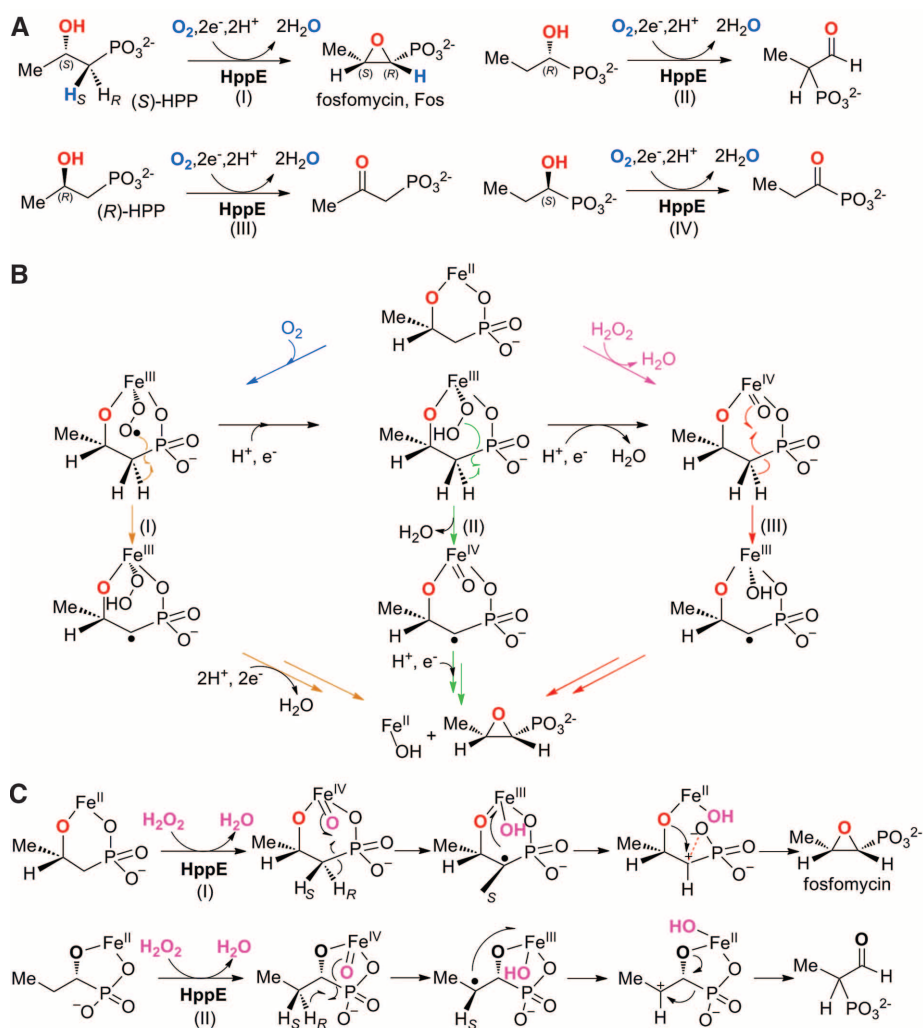


Fig. 1. Proposed and demonstrated reactions of HppE and their possible mechanisms. (A) Putatively O_2 -dependent reactions purportedly catalyzed by HppE on *S*-HPP (I) and its stereo- and structural isomers (II to IV). (B) Mechanisms previously proposed for the putatively O_2 -dependent fosfomycin-generating epoxidation reaction (blue arrow) and the mechanism indicated by the finding that H_2O_2 rather than O_2 is the oxidizing co-substrate (magenta and red arrows). (C) Proposed mechanisms for H_2O_2 -driven (I) epoxide ring closure to produce fosfomycin and (II) phosphonate migration with the (*R*)-1-hydroxypropyl-1-phosphonate analog (23).

mercial Fos (spectrum A) reveals features with the proper chemical shifts and integrated intensities at ~ 3.05 parts per million (ppm) (multiplet from C2-H), ~ 2.62 ppm (doublet of doublets from C1-H), and ~ 1.25 ppm (doublet from C2-Me). None of these features is present in the spectrum of the S-HPP starting material (spectrum C). Additional minor features at ~ 2.72 , ~ 2.66 , and ~ 2.43 ppm in the spectrum of the product sample (B) arise from the 2-keto oxidation product known to be generated by HppE from the (*R*)-2-hydroxypropyl-1-phosphonate (*R*-HPP) enantiomer (27), which is present as a minor ($\sim 6\%$) contaminant in our synthetic S-HPP substrate.

The nearly complete consumption of S-HPP by one molar equivalent of H_2O_2 evident in the NMR spectra implies an experimental Fos: H_2O_2

stoichiometry close to the predicted value of unity. The experimental stoichiometry was accurately determined by LC-MS with commercial Fos as an internal standard (Fig. 3A, gray traces) to quantify the d_4 -Fos product from the HppE peroxidase reaction (black traces). The stoichiometry was determined to be 1.00 ± 0.05 (Fig. 3B). Coupling between H_2O_2 reduction and Fos production is thus extremely tight.

The requirements for the productive HppE peroxidase reaction were defined and its catalytic nature verified by analysis of reactions carried out with high H_2O_2 /HppE ratios from which individual reaction components were serially omitted (fig. S2 and associated text). With all components present, the enzyme could effect at least 50 turnovers. The kinetics of a single turnover of H_2O_2 -

driven Fos production were then determined at 4°C . With 0.096 mM HppE $\cdot\text{Fe}^{\text{II}}$, 0.050 mM H_2O_2 , and 0.50 mM d_4 -S-HPP, d_4 -Fos production was complete in ~ 0.1 s (Fig. 4). Simulation of the kinetic data requires a second-order rate constant of at least $1.2 \times 10^5 \text{ M}^{-1} \text{ s}^{-1}$ for reaction of the HppE $\cdot\text{Fe}^{\text{II}}$ -S-HPP complex with H_2O_2 (—), and the data are simulated best with a value of $4.8 \times 10^5 \text{ M}^{-1} \text{ s}^{-1}$ for this rate constant (—). It is possible that the first-order steps after addition of H_2O_2 to the enzyme could be slower than the addition step itself; in this case, the second-order rate constant for H_2O_2 addition could be underestimated by the analysis. Regardless, the determined rate constant is only a factor of 10 to 100 less than the value of k_{cat}/K_M reported for bovine liver catalase, an enzyme for which H_2O_2 is the established physiological substrate and which is often touted as having evolved almost to catalytic perfection (i.e., to operate at the diffusion limit) (28). Quantitative assessment of the ability of commercial bovine liver catalase to compete with HppE for reaction with added H_2O_2 yielded an estimate of $5 \times 10^5 \text{ M}^{-1} \text{ s}^{-1}$ for the k_{cat}/K_M (H_2O_2) of HppE at 21°C (fig. S3 and associated text). It is likely that the experimental error in the rate constants obtained at 4° and 21°C (we estimate a factor of 2 for each) coincidentally obscures the actual temperature dependence of the reaction rate.

Both reducing systems used in previous in vitro studies on HppE (E_3/NADH and NADH/FMN)

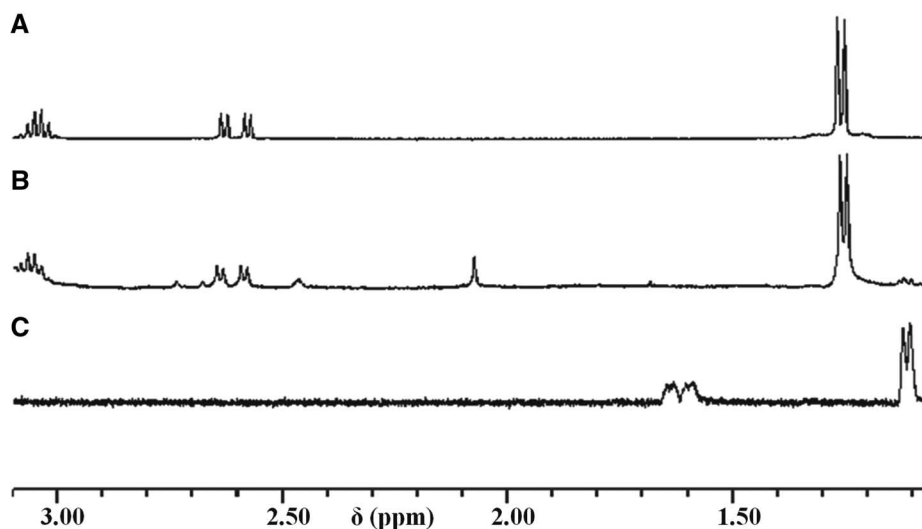


Fig. 2. ^1H -NMR spectra demonstrating production of Fos by HppE upon its reaction with H_2O_2 . (A) Commercial Fos standard. (B) Products after slow addition of H_2O_2 (final concentration of 5.0 mM) to a solution of HppE (final concentration of 0.10 mM), Fe^{II} (0.080 mM), S-HPP (5.0 mM), and L-ascorbic acid (4.0 mM). The reaction was carried out at 21°C in the absence of O_2 . (C) The S-HPP substrate. Details of sample preparation in (B) and spectral acquisition are provided in the supplementary materials.

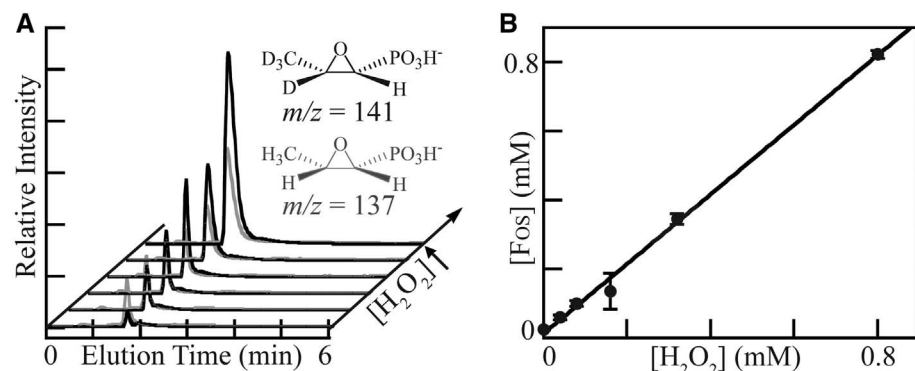


Fig. 3. Determination of the Fos: H_2O_2 reaction stoichiometry. (A) LC-MS chromatograms monitoring $m/z = 141$ for the HppE-generated d_4 -Fos product (black) and $m/z = 137$ for the commercial Fos internal standard (gray). (B) Quantity of d_4 -Fos produced by HppE as a function of $[\text{H}_2\text{O}_2]$ added. The error bars are the standard deviations from the mean values of six measurements at each concentration. The slope gives the Fos: H_2O_2 reaction stoichiometry (1.00 ± 0.05). Reaction conditions were the same as in Fig. 2, with the exception of the $[\text{H}_2\text{O}_2]$ added.

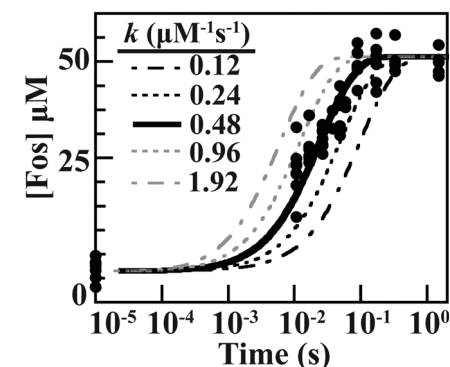


Fig. 4. Kinetics of d_4 -Fos production in a single turnover with limiting H_2O_2 . Samples were prepared by mixing a solution containing 0.24 mM HppE, 0.19 mM Fe^{II} , and 1.0 mM d_4 -S-HPP with an equal volume of 0.10 mM H_2O_2 and allowing the reaction to proceed at 4°C for the indicated time before terminating by mixing the reaction solution with an equal volume of the quench solution (80% isopropanol/20% acetic acid on a volume basis). All data points from three independent trials, with duplicate points in each trial, are shown. A quench time of 5 ms has been assumed. The points at zero reaction time, which represent samples of the reactant complex that were quenched without exposure to H_2O_2 , are plotted with an x value of 10^{-5} s for display on the logarithmic time axis. The traces are simulations with the second-order rate constants given in the legend.

generate H_2O_2 from O_2 (29, 30). The demonstration that HppE is an efficient peroxidase therefore raises the possibility that its reported oxidase activity in the presence of the NADH-based reducing systems might actually have resulted from reduction of O_2 by the reducing system and utilization of the resultant H_2O_2 by HppE. As a test of this possibility, HppE reactions with O_2 and one of the two reducing systems were carried out in the presence of varying concentrations of catalase. As shown in fig. S3, increasing the concentration of catalase diminishes the Fos yield in these reactions with catalase-concentration ([catalase]) dependencies (blue and green points) essentially identical to that for the direct reaction with H_2O_2 (red). These data strongly suggest that the Fos production previously attributed to HppE oxidase activity actually reflects its peroxidase activity. Consistent with this conclusion, use of $\text{H}_2^{18}\text{O}_2$ as oxidant and H_2^{18}O -enriched solvent does not result in incorporation of a detectable quantity of ^{18}O into the Fos product. This observation confirms that the epoxide is formed from the oxygen atom already present in the substrate, as previously demonstrated when the reaction was thought to involve O_2 . In addition, when added directly, H_2O_2 also supports the alternative oxidations of substrate analogs that were previously attributed to O_2 , including the aforementioned oxidative 1,2-phosphonate migration with (*R*)-1-hydroxypropyl-1-phosphonate [Fig. 1A, reaction II (23)] and the C2 dehydrogenation of (*R*)-2-hydroxypropyl-1-phosphonate to the corresponding ketone [Fig. 1A, reaction III (27)]. The observations suggest that all HppE activities reported in previous studies arose from the enzyme's reaction with H_2O_2 generated by the reducing systems rather than its reaction directly with O_2 .

Additional evidence that HppE is not an oxidase is the failure of the $\text{Fe}^{\text{III}}\text{-O}_2^{\cdot-}$ complex that should result from addition of O_2 to its Fe^{II} cofactor (17, 31–34) to accumulate in the absence of a reducing system. Freeze-quench Mössbauer spectroscopic experiments using an efficient enzymatic O_2 -generation system that can drive formation of even dissociable O_2 adducts (35) revealed that O_2 adds either very slowly or with low affinity (or both) to the HppE cofactor, irrespective of the presence of bound substrate (fig. S4 and associated text). The apparent failure of substrate binding to promote O_2 addition contrasts with the behavior of most proven oxidases and oxygenases that use non-heme-iron cofactors (24, 36–40). It also contrasts with the behavior of HppE toward H_2O_2 : Reaction of the substrate-free enzyme with H_2O_2 was found to be about a factor of 50 slower (fig. S5 and associated text) than the productive reaction in the presence of *S*-HPP, implying that substrate binding does indeed promote reaction with H_2O_2 . Conversely, the inability of 2-hydroxyethyl-1-phosphonate (HEP) dioxygenase (HEPD), the non-heme-iron enzyme that is structurally most similar to HppE (fig. S6) (41), to use H_2O_2 also

suggests that the peroxidase activity seen with HppE reflects its natural function (fig. S7 and associated text). HppE and HEPD share the ability to oxidize HEP (fig. S7A, blue bars and fig. S7B, green bars) [also *R*-HPP (42)], but HEPD unequivocally uses O_2 as its cosubstrate for this oxidation (41). It does not use H_2O_2 for catalytic oxidation of HEP (fig. S7A, green bars) under the conditions that support efficient consumption of *S*-HPP by HppE (red bars). Even in its cross-reactivity toward HEP, HppE is still an efficient peroxidase (blue bars) but has no activity with O_2 as the oxidant in the absence of a reducing system to first convert the O_2 to H_2O_2 (fig. S7B, blue bars). The enzymes' nearly orthogonal use of the oxidants, despite their very similar structures and overlapping substrate profiles, further supports the hypothesis that HppE is an authentic peroxidase rather than an oxidase capable of an adventitious "peroxide-shunt" reaction.

Unlike the previously postulated O_2 -dependent epoxidation reaction, in which the iron complex responsible for the crucial abstraction of the *pro-R* H• from C1 of *S*-HPP could potentially have been in any of three different overall oxidation states (the three pathways in Fig. 1B), reaction of the Fe^{II} cofactor with H_2O_2 is redox balanced to bypass the first two oxidation states and proceed directly to a Fe^{IV} -oxo (ferryl) complex (magenta and red arrows). Formation of inorganic ferryl complexes from Fe^{II} precursors and H_2O_2 is well precedented [e.g., (43, 44)], and the abstraction of H• by a ferryl complex has been demonstrated in the reactions of other non-heme-iron enzymes (13, 18, 38, 40, 45–47). The use of H_2O_2 , the literature precedents, and the recent computational study (16) all point to a ferryl complex as the most likely initiator of the HppE reaction.

The conclusion that HppE uses a ferryl complex generated directly from H_2O_2 rather than O_2 to initiate its epoxidation reaction suggests that the Fos-biosynthetic machinery should not require a specific HppE reductase. Instead, the epoxidation could be supported by any endogenous or exogenous reaction that generates H_2O_2 . Conceivably, Fos-synthesizing *Streptomyces* might encounter H_2O_2 in their environments, turning a general toxin produced by competing organisms to their advantage by using it to produce a counter toxin of their own. Such a scenario would add to the growing list of known uses of H_2O_2 , which had previously been considered primarily as a metabolic toxin, in productive physiological reactions related to intercellular interactions (48, 49).

References and Notes

1. J. L. Marquardt *et al.*, *Biochemistry* **33**, 10646–10651 (1994).
2. D. H. Kim *et al.*, *Biochemistry* **35**, 4923–4928 (1996).
3. P. Liu *et al.*, *J. Am. Chem. Soc.* **123**, 4619–4620 (2001).
4. J. W. Munos *et al.*, *Biochemistry* **47**, 8726–8735 (2008).
5. L. J. Higgins, F. Yan, P. Liu, H. W. Liu, C. L. Drennan, *Nature* **437**, 838–844 (2005).
6. D. Yun *et al.*, *J. Am. Chem. Soc.* **133**, 11262–11269 (2011).
7. T. Hidaka *et al.*, *Mol. Gen. Genet.* **249**, 274–280 (1995).
8. S. Y. Kim *et al.*, *Antimicrob. Agents Chemother.* **56**, 4175–4183 (2012).
9. F. Yan, J. W. Munos, P. Liu, H.-w. Liu, *Biochemistry* **45**, 11473–11481 (2006).
10. G. De Faveri, G. Ilyashenko, M. Watkinson, *Chem. Soc. Rev.* **40**, 1722–1760 (2011).
11. C. J. Thibodeaux, W.-c. Chang, H.-w. Liu, *Chem. Rev.* **112**, 1681–1709 (2012).
12. F. Hammerschmidt, *J. Chem. Soc. Perkin Trans. 1*, 1993 (1991).
13. C. Krebs, D. Galonić Fujimori, C. T. Walsh, J. M. Bollinger Jr., *Acc. Chem. Res.* **40**, 484–492 (2007).
14. W. A. van der Donk, C. Krebs, J. M. Bollinger Jr., *Curr. Opin. Struct. Biol.* **20**, 673–683 (2010).
15. N. Lehnert, F. Neese, R. Y. N. Ho, L. Que Jr., E. I. Solomon, *J. Am. Chem. Soc.* **124**, 10810–10822 (2002).
16. A. Miłaczewska, E. Broclawik, T. Borowski, *Chemistry* **19**, 771–781 (2013).
17. S. Ye *et al.*, *Chemistry* **18**, 6555–6567 (2012).
18. M. L. Matthews *et al.*, *Proc. Natl. Acad. Sci. U.S.A.* **106**, 17723–17728 (2009).
19. P. L. Roach *et al.*, *Nature* **387**, 827–830 (1997).
20. M. Lundberg, P. E. M. Siegbahn, K. Morokuma, *Biochemistry* **47**, 1031–1042 (2008).
21. T. Borowski, H. Noack, M. Radoń, K. Zych, P. E. M. Siegbahn, *J. Am. Chem. Soc.* **132**, 12887–12898 (2010).
22. H. M. Hanauske-Abel, V. Günzler, *J. Theor. Biol.* **94**, 421–455 (1982).
23. W.-c. Chang *et al.*, *Nature* **496**, 114–118 (2013).
24. J. M. Bollinger Jr., C. Krebs, *J. Inorg. Biochem.* **100**, 586–605 (2006).
25. C. Krebs *et al.*, *Coord. Chem. Rev.* **257**, 234–243 (2013).
26. J. A. Morello, M. R. Craw, H. P. Constantine, R. E. Forster, *J. Appl. Physiol.* **19**, 522–525 (1964).
27. Z. Zhao *et al.*, *Angew. Chem. Int. Ed. Engl.* **41**, 4529–4532 (2002).
28. J. Switala, P. C. Loewen, *Arch. Biochem. Biophys.* **401**, 145–154 (2002).
29. V. Massey, *J. Biol. Chem.* **269**, 22459–22462 (1994).
30. V. P. Miller, J. S. Thorson, O. Ploux, S. F. Lo, H.-w. Liu, *Biochemistry* **32**, 11934–11942 (1993).
31. C. D. Brown, M. L. Neidig, M. B. Neibergall, J. D. Lipscomb, E. I. Solomon, *J. Am. Chem. Soc.* **129**, 7427–7438 (2007).
32. M. M. Mbughuni *et al.*, *Proc. Natl. Acad. Sci. U.S.A.* **107**, 16788–16793 (2010).
33. G. J. Christian, S. Ye, F. Neese, *Chem. Sci.* **3**, 1600 (2012).
34. E. I. Solomon *et al.*, *Chem. Rev.* **100**, 235–350 (2000).
35. L. M. K. Dassama *et al.*, *Biochemistry* **51**, 1607–1616 (2012).
36. M. Tarasev, F. Rhames, D. P. Ballou, *Biochemistry* **43**, 12799–12808 (2004).
37. J. A. Broadwater, C. Achim, E. Münck, B. G. Fox, *Biochemistry* **38**, 12197–12204 (1999).
38. L. M. Hoffart, E. W. Barr, R. B. Guyer, J. M. Bollinger Jr., C. Krebs, *Proc. Natl. Acad. Sci. U.S.A.* **103**, 14738–14743 (2006).
39. J. C. Price, E. W. Barr, L. M. Hoffart, C. Krebs, J. M. Bollinger Jr., *Biochemistry* **44**, 8138–8147 (2005).
40. M. L. Matthews *et al.*, *Biochemistry* **48**, 4331–4343 (2009).
41. R. M. Cicchillo *et al.*, *Nature* **459**, 871–874 (2009).
42. J. T. Whitteck, R. M. Cicchillo, W. A. van der Donk, *J. Am. Chem. Soc.* **131**, 16225–16232 (2009).
43. F. Li, J. England, L. Que Jr., *J. Am. Chem. Soc.* **132**, 2134–2135 (2010).
44. H. Hirao, F. Li, L. Que Jr., K. Morokuma, *Inorg. Chem.* **50**, 6637–6648 (2011).
45. J. C. Price, E. W. Barr, B. Tirupati, J. M. Bollinger Jr., C. Krebs, *Biochemistry* **42**, 7497–7508 (2003).
46. D. P. Galonić, E. W. Barr, C. T. Walsh, J. M. Bollinger Jr., C. Krebs, *Nat. Chem. Biol.* **3**, 113–116 (2007).
47. D. G. Fujimori *et al.*, *J. Am. Chem. Soc.* **129**, 13408–13409 (2007).

48. E. W. Miller, O. Tulyathan, E. Y. Isacoff, C. J. Chang, *Nat. Chem. Biol.* **3**, 263–267 (2007).
 49. E. A. Veal, A. M. Day, B. A. Morgan, *Mol. Cell* **26**, 1–14 (2007).

Acknowledgments: This work was supported by grants from the NIH (GM 040541 to H.-w.L. and GM 069657 to C.K.

and J.M.B.), the Welch Foundation (F-1511 to H.-w.L.), and the NSF (MCB-0642058 to C.K. and J.M.B.). We thank M. T. Green for helpful discussions.

Supplementary Materials

www.sciencemag.org/content/342/6161/991/suppl/DC1
 Materials and Methods

Figs. S1 to S7
 References (50–67)

10 May 2013; accepted 1 October 2013
 Published online 10 October 2013;
 10.1126/science.1240373

Defining Stem Cell Dynamics in Models of Intestinal Tumor Initiation

Louis Vermeulen,^{1,2,*} Edward Morrissey,^{1*} Maartje van der Heijden,^{1,2} Anna M. Nicholson,¹ Andrea Sottoriva,³ Simon Buczacki,¹ Richard Kemp,¹ Simon Tavaré,^{1,4} Douglas J. Winton¹

Cancer is a disease in which cells accumulate genetic aberrations that are believed to confer a clonal advantage over cells in the surrounding tissue. However, the quantitative benefit of frequently occurring mutations during tumor development remains unknown. We quantified the competitive advantage of *Apc* loss, *Kras* activation, and *P53* mutations in the mouse intestine. Our findings indicate that the fate conferred by these mutations is not deterministic, and many mutated stem cells are replaced by wild-type stem cells after biased, but still stochastic events. Furthermore, *P53* mutations display a condition-dependent advantage, and especially in colitis-affected intestines, clones harboring mutations in this gene are favored. Our work confirms the previously theoretical notion that the tissue architecture of the intestine suppresses the accumulation of mutated lineages.

Cancer development involves competition between normal and deviant cell lineages, ultimately resulting in disruptive tissue overgrowth (1). The cellular effects of mutations can increase proliferation or impair response to cell death-inducing signals (2). However, only very limited quantitative data exist on the net effects of oncogenic alterations at the cell population level. In the intestine, cancer arises from an initial transformation event occurring primarily, but not exclusively, in the stem cell compartment (3, 4). Because normal intestinal crypt homeostasis is characterized by competition between equipotent stem cells that continuously replace each other in a random fashion (Fig. 1A) (5, 6), oncogenic mutations may confer an advantage on the clone in which they arise by acting on these dynamics. We confirmed and used this assumption to quantify the competitive benefit of mutations frequently occurring in colorectal cancer (CRC).

To track the fate of wild-type (WT) and mutated cell lineages, we induced low-level intestinal recombination either specifically in the crypt base using *Lgr5*-EGFP-*Cre*^{ER} mice or more generally in *AhCre*^{ER} mice, both crossed to the R26-

Lox-STOP-Lox-*tdTomato* (tdTom^{fl/fl}) reporter strain. Clones were visualized and quantified at the bottom of the crypt, allowing robust clone size quantification around the circumference of the crypt (fig. S1). We observed that on average, clones expand, and the number of fixed clones (i.e., crypts within which the whole epithelium is tdTom⁺) increases with time (Fig. 1, B to E). By quantitative analysis of the clone size distributions using the stochastic master equation and Bayesian inference, we confirmed earlier studies that continuous, one-dimensional neutral replacements govern intestinal stem cell dynamics (figs. S2 and S3) (5, 6). This process is fully defined by only two parameters: the number of functional stem cells per crypt (*N*) and the rate at which these replace each other (λ). Because of the high-quality clone size distribution data we obtained, we can directly infer both *N* and λ with considerable precision (fig. S2). For the proximal small intestine (SI), we find that *N* = 5 and λ = 0.1 replacements per stem cell per day (figs. S2 and S3). This inferred number of stem cells is considerably lower than the number of *Lgr5*⁺ cells (~16) per crypt (5) but agrees with a functional marker-free estimate of stem cell numbers (7). In fact, we directly confirmed a previous suggestion that a sizable fraction of *Lgr5*⁺ cells are actually more committed progenitor cells and do not function as stem cells in homeostasis (8) (fig. S4).

Next, we crossed *AhCre*^{ER}/tdTom^{fl/fl} mice with *Kras*-G12D^{fl} and *Apc*^{fl/fl} mice. Recombination in these mice will result in activation of an oncogenic *Kras* variant or inactivation of one or both copies of the negative Wnt regulator *Apc*, in addition to tdTom expression. We confirmed that tdTom expression is tightly matched to on-

cogenic recombination events (fig. S5). Furthermore, our analysis was facilitated by the fact that the low-level clone induction of pre-neoplastic lineages does not substantially alter tissue morphology, as has been reported before (9, 10) (Fig. 1B and fig. S6). We found that activated *KRAS* confers an evident clonal advantage as the *Kras*^{G12D} harboring clones expand and become fixed more rapidly than the WT lineages (Fig. 1, B to E). In order to express this effect quantitatively, we introduced an additional variable to the one-dimensional drift model to capture the biased drift properties: *P_R* signifies the chance that a tdTom⁺ stem cell replaces its nonlabeled neighbor; conversely, 1-*P_R* represents the chance that the nonlabeled stem cell replaces the tdTom⁺ neighboring stem cell. The neutral version of the model is described by unbiased stochastic replacements, and as expected, using the inference method in combination with the neutral clone size distribution data we find *P_R*(WT versus WT) = 0.50 [0.48 to 0.52, 95% confidence interval (CI)] (Fig. 1F), indicating that two adjacent stem cells have equal probability to replace each other. Applying this inference strategy to the biased drift data of *Kras* mutant clones, we found a well-demarcated posterior probability peak: *P_R*(*Kras*^{G12D} versus WT) = 0.78 (0.75 to 0.81, 95% CI) (Fig. 1G). This implies that for replacement events occurring at the interface of a *Kras*^{G12D} and a WT clone, the *Kras* mutant stem cell replaces the WT stem cell in ~80% of the cases, and conversely that the WT stem cell replaces the mutant stem cell in ~20% of the replacement events. Thus, interpreting the altered size distribution of clones in terms of individual stem cell fates provides an intuitive estimate of the potency of oncogenic mutations in the context of a stochastic model, by integrating the effects of proliferation rate, cell death frequencies, and self-renewal properties into a single parameter (*P_R*).

Because human CRCs arise in the majority of cases after the inactivation of *APC*, we determined the clonal advantage of lineages harboring either heterozygous or homozygous inactivating mutations within this gene. *Apc*^{+/-} lineages display only a limited, but significant, benefit over WT clones, whereas *Apc*^{-/-} lineages have a more marked clonal benefit already at 4 days, making it unlikely that secondary effects of *Apc* loss [such as chromosomal instability (CIN)] are involved (Fig. 2, A to C). After applying the inference strategy to this data to determine *P_R*, we found that *P_R*(*Apc*^{+/-} versus WT) = 0.62 (0.58 to 0.66, 95% CI) and *P_R*(*Apc*^{-/-} versus WT) = 0.79 (0.75 to 0.82, 95% CI) (Fig. 2, D and E). In reality, *Apc*^{-/-}

¹Cancer Research UK, Cambridge Institute, University of Cambridge, Robinson Way, Cambridge CB2 0RE, UK. ²Laboratory for Experimental Oncology and Radiobiology, Center for Experimental Molecular Medicine, Academic Medical Center, Meibergdreef 9, 1105 AZ, Amsterdam, Netherlands. ³Department of Preventive Medicine, Keck School of Medicine, University of Southern California, Los Angeles, CA, USA. ⁴Department of Biological Sciences, University of Southern California, Los Angeles, CA, USA.

*These authors contributed equally to this work.

†Corresponding author. E-mail: l.vermeulen@amc.uva.nl

Fig. 1. Quantifying the clonal benefit of *Kras*^{G12D}. (A) Intestinal stem cells are equipotent and continuously replace each other in a stochastic fashion. (B) Confocal images of SI crypt bottoms of *AhCre*^{ER}/tdTom^{+/fl} mice (WT) and *AhCre*^{ER}/tdTom^{+/fl}/*Kras*-G12D^{fl} (*Kras*^{G12D}) at the indicated time points after clone induction. Clone sizes are indicated as fractions (in eighths) of the crypt circumference. Blue, nuclear stain (DAPI); red, tdTom expression; scale bars represent 30 μm. (C) Heat maps depict the relative frequency of clones of the indicated size (columns) at various time points (rows) for both WT and *Kras*^{G12D}. (D and E) Graph displays the average size (D) or the percentage of fixed clones (E) of WT and *Kras*^{G12D} clones at different time points after induction. Error bars indicate the SEM. [(C) to (E)] *N* = 5 mice for each group; for each time point and condition, >200 clones were analyzed. (F and G) Bayesian inference of the biased drift parameter *P_R* for WT versus WT (F) and *Kras*^{G12D} versus WT (G) clones. The vertical axis indicates the probability density; the horizontal axis indicates the *P_R* values. The higher the probability density value, the more likely this *P_R* value underlies the observed biased drift. *P_R* = 0.5 indicates neutral drift. The cartoons summarize the replacement properties (with color coding as in the graphs).

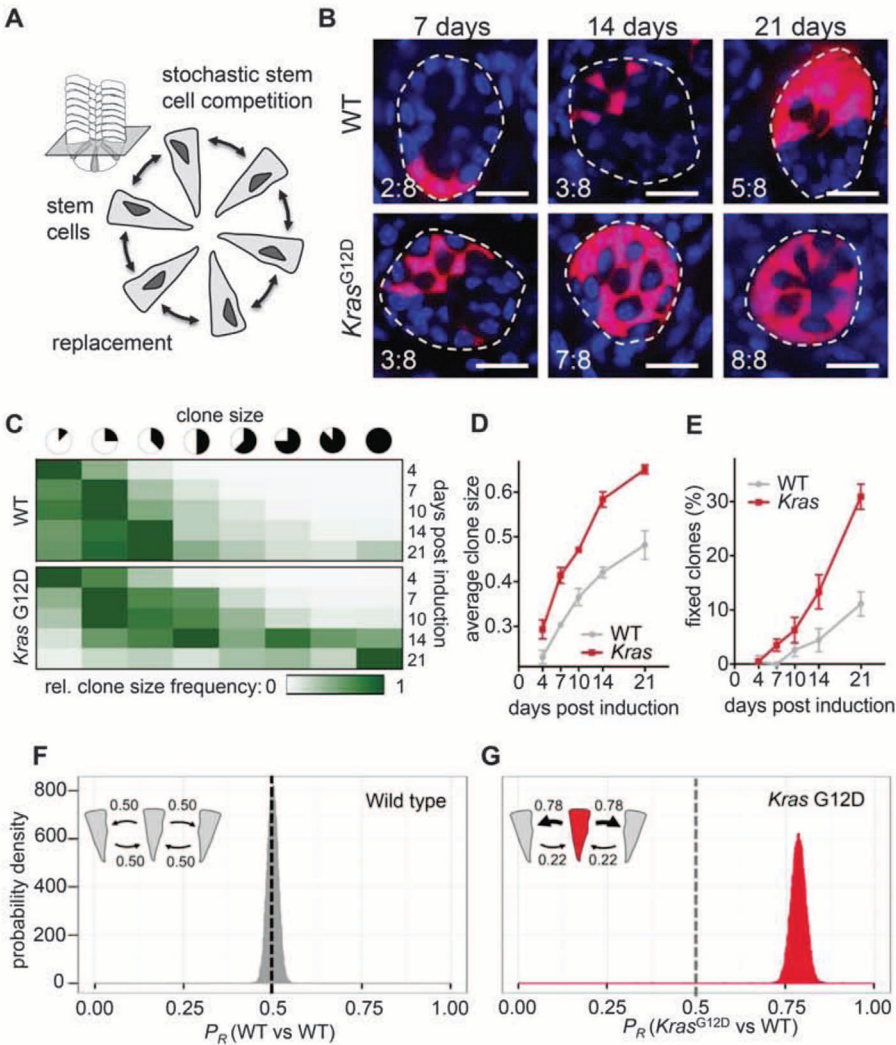
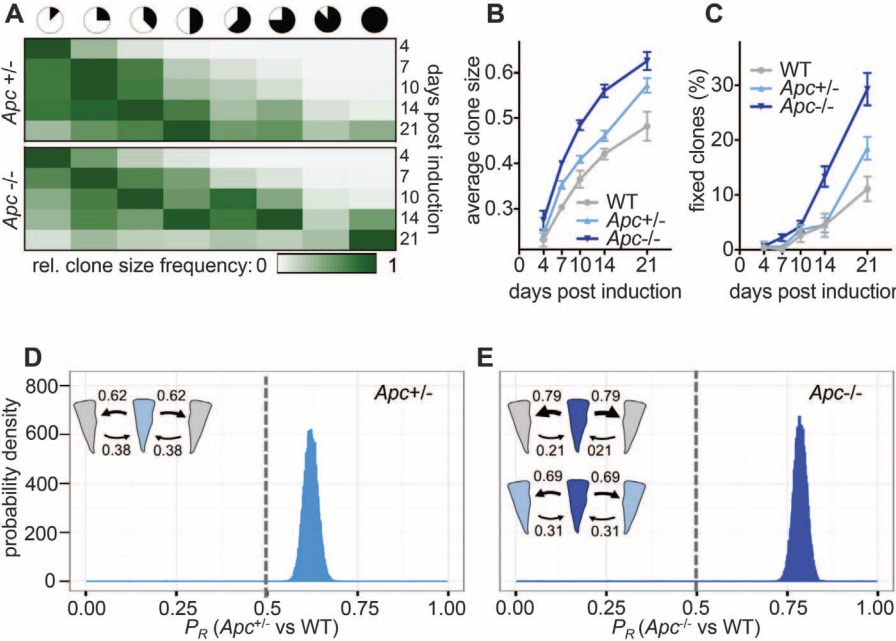


Fig. 2. Quantifying the clonal benefit of *Apc* loss. (A) Heat maps depict the relative frequency of clones of the indicated size (columns) at various time points (rows) for *Apc*^{+/-} and *Apc*^{-/-}. (B and C) Graph displays the average size (B) or the percentage of fixed clones (C) of WT, *Apc*^{+/-}, and *Apc*^{-/-} clones at different time points after induction. Error bars indicate the SEM. WT is as in Fig. 1. [(A) to (C)] *N* = 5 mice for each group; for each time point and condition, >200 clones were analyzed. (D and E) Bayesian inference of the biased drift parameter *P_R* for *Apc*^{+/-} versus WT (D) and *Apc*^{-/-} versus WT (E).



mutations usually occur in a clone of $Apc^{+/-}$ cells because of loss of heterozygosity (LOH) or an independent additional mutation (10); therefore, we also calculated the benefit of $Apc^{+/-}$ stem cells over $Apc^{+/+}$ stem cells: $P_R(Apc^{+/-}$ versus $Apc^{+/+}) = 0.69$ (0.65 to 0.72, 95% CI) (Fig. 2E). Both in the case of $Kras^{G12D}$ and in the case of the inactivation of Apc , the inferred values for P_R result in clone size distributions in accordance with the measured data (fig. S7). A further confirmation of the validity of the model comes from the observation that tdTom⁺ clones induced in Apc^{Min} mice, which are characterized by a heterozygous germline Apc mutation, display similar dynamics to neutral clones in a WT background [$P_R(Apc^{Min}$ versus $Apc^{Min}) = 0.48$ (0.46 to 0.51, 95% CI)],

indicating neutral competition between $Apc^{+/-}$ lineages, although clones holding this mutation clearly have an advantage over WT clones (fig. S8).

Our findings reveal that although $Kras^{G12D}$ mutations or the inactivation of Apc result in a marked competitive advantage of the respective cell lineage, this does not mean that the clone will become deterministically fixed. Mutated stem cells are commonly replaced by WT stem cells, thereby evading the accumulation of further mutations. By using the inferred parameters of the biased drift model (N , λ , P_R) and the adapted stochastic master equations, we calculated the proportion of mutant clones that reach fixation at a particular clone age (Fig. 3A). This analysis reveals that the majority of stem cells acquiring an $Apc^{+/-}$ muta-

tion will be stochastically replaced by WT stem cells, and these mutant lineages will disappear from the tissue. In addition only ~55% of $Apc^{+/-}$ mutant stem cells within an $Apc^{+/-}$ background will reach fixation. These findings reveal that the accumulation of mutations in the intestinal tissue is an inefficient process because of the particular tissue architecture and the continuous stochastic replacements of stem cells. To illustrate the inefficiency of the process, we determined the contribution of different mutational trajectories in the formation of aberrant crypt foci (ACF); i.e., a crypt with a fixed $Apc^{+/-}$ clone (Fig. 3B). Only 22% of the ACFs result from two subsequent Apc hits (or LOH), and a large proportion of ACFs arise in crypts in which multiple Apc hits have

Fig. 3. Mutational trajectories. (A) Graph depicts the likelihood of the indicated clone types reaching fixation in a crypt over time. Shaded areas indicate 95% CI. (B) Cartoon summarizes the most direct way to reach the stage of a fixed $Apc^{+/-}$ clone. The fixation probabilities are indicated in the figure [value at 100 days in (A)]. The graph depicts the proportion of fixed $Apc^{+/-}$ clones (vertical axis) that arise after the total number of Apc hits, indicated at the horizontal axis.

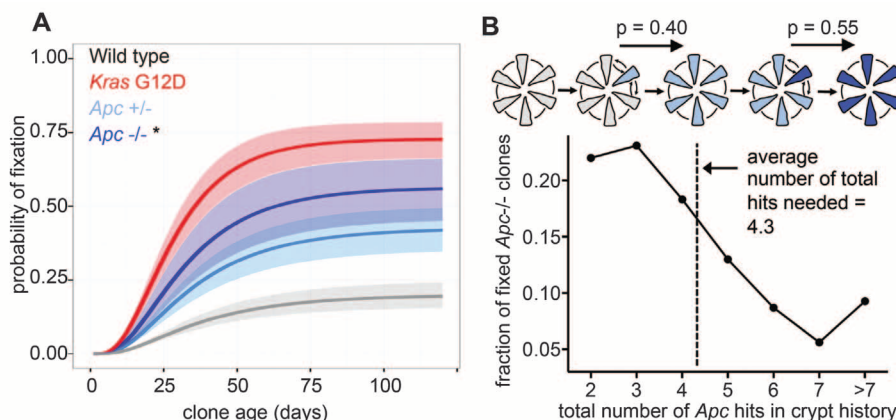
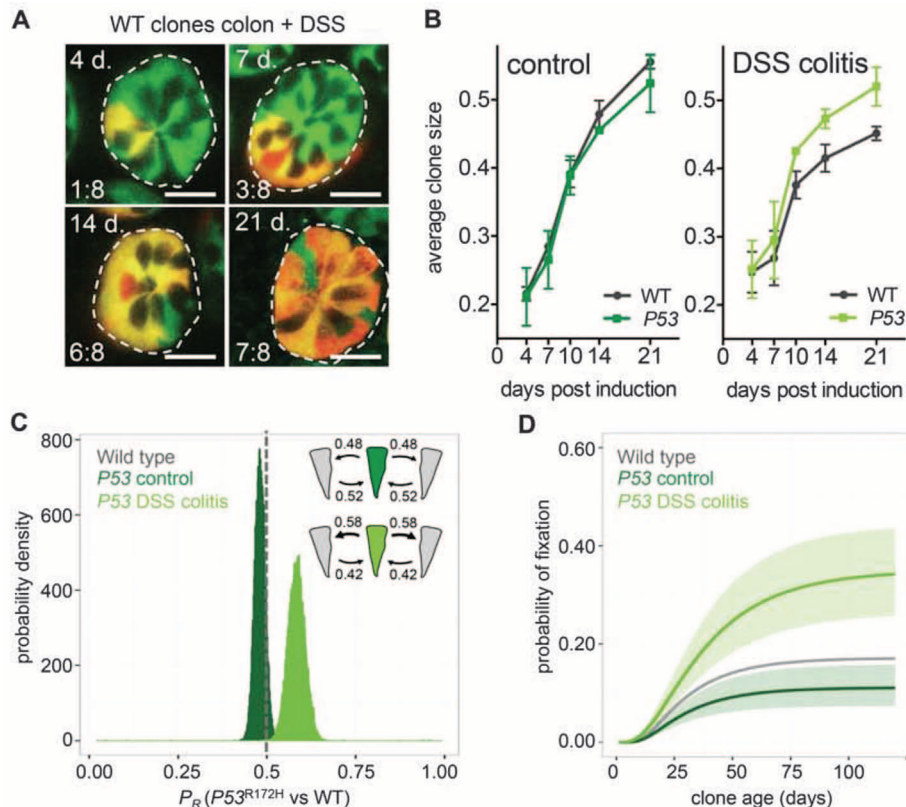


Fig. 4. P53 mutations confer a condition-dependent clonal advantage. (A) Confocal images of colonic crypt bottoms of DSS-treated $Lgr5$ -Cre^{ER}/tdTom^{+/+} mice at the indicated time points after clone induction. Clone sizes are indicated in eighths of the crypt circumference. Green, $Lgr5$ -GFP; red, tdTom; scale bars represent 30 μ m. (B) Graph depicts the average size of WT or $P53^{R172H}$ clones at different time points after induction in a control (left) and colitis (right) setting. Error bars indicate the SEM, $N = 5$ mice for each group; for each time point and condition, >150 clones were analyzed. (C) Bayesian inference of the biased drift parameter P_R for $P53^{R172H}$ versus WT in control animals and DSS-treated animals (colitis). (D) Graph depicts the likelihood of $P53^{R172H}$ clones to reach fixation in homeostasis and in colitis. Shaded areas indicate 95% CI.



taken place, the majority of which have been eliminated through the stochastic loss of mutant stem cells (Fig. 3B and fig. S9). Incorporating the inefficiency of fixation of the earliest events in CRC into a simple model describing the population incidence of this disease (11) highlights how these values could be used in future studies to link them to cancer frequencies in the human population (fig. S9).

Because *TP53* mutations are often seen in patients with CRC (2), we next investigated the effect of the dominant-negative hotspot mutation *P53*^{R172H}. However, no significant benefit of this mutation could be detected in the SI (fig. S8). Because *TP53* is reported to be of particular importance in colitis-associated CRC formation (12), we also studied *P53* mutations in a chronic colitis model (Fig. 4). Colitis was induced by feeding mice dextran sodium sulfate (DSS) starting a week before clone induction and was maintained until analysis of clone size distributions (Fig. 4, A and B, and fig. S10). Colitis induces a shift in stem cell dynamics in the colon, mainly by reducing the replacement rate (fig. S2), and although *P53*^{R172H} did not confer a benefit to colon stem cells under normal conditions, in colitis, it significantly increases fitness: P_R (*P53*^{R172H} versus WT) = 0.48 (0.45 to 0.51, 95% CI) and P_R (*P53*^{R172H} versus WT) = 0.58, (0.54 to 0.63, 95% CI), respectively (Fig. 4C). Therefore, *P53* mutated clones have an increased likelihood to become fixed in a gut affected by inflammation (Fig. 4D). This presumably reflects the benefit of *P53*-mutated cells in dealing with colitis-associated reactive oxygen species formation (13). More generally, this result demonstrates that the competitive benefit of mutations

during tumor initiation is dependent on the context in which they arise.

Our work presents a quantification of the effects of relevant mutations on stem cell dynamics during the initiation of a solid malignancy. A limited competitive advantage of common mutations in CRC is revealed, and many mutations that occur are lost from the population because of stochastic, albeit biased, replacement by neighboring WT lineages. This finding supports the accepted but so far theoretical notion that the tissue architecture and the features of the “evolutionary graph” representing the intestinal stem cell population prevent deterministic fixation of mutated lineages (14–16). The values now placed on the clonal advantages conferred by common mutations can be used in future modeling studies of tumor initiation in the intestine that so far have not used experimentally derived values for the benefits of individual mutations (17). This will help to assess other phenomena associated with CRC development, such as CIN (18). Furthermore, our work reveals that the potential competitive benefits of mutations are dependent on the environment in which they arise and provides a compelling explanation of why *TP53* mutations are found frequently and already at early stages in colitis-associated CRC (12). The method used here provides a powerful tool to investigate therapeutic strategies to specifically eradicate (pre-) neoplastic stem cells while preserving their normal counterparts.

References and Notes

1. P. C. Nowell, *Science* **194**, 23–28 (1976).
2. E. R. Fearon, B. Vogelstein, *Cell* **61**, 759–767 (1990).

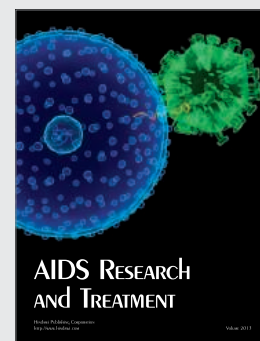
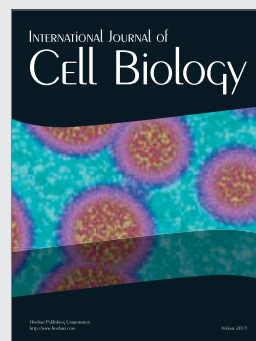
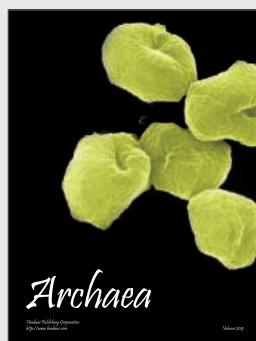
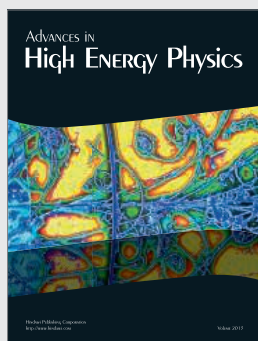
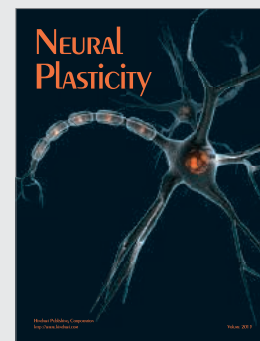
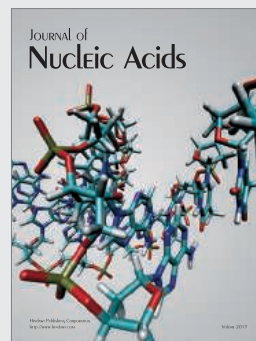
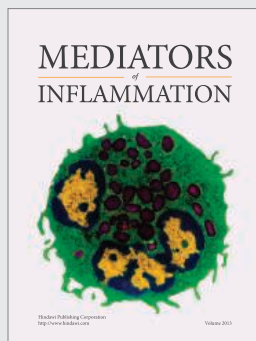
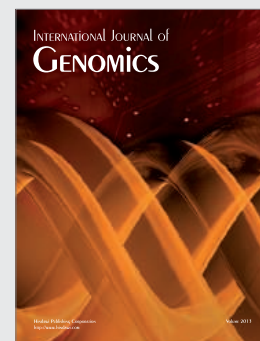
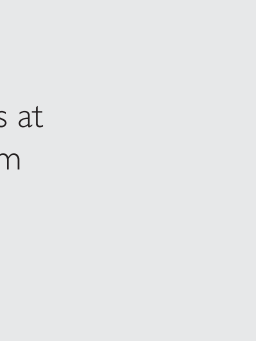
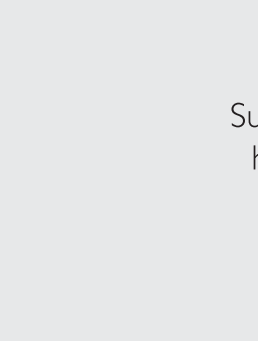
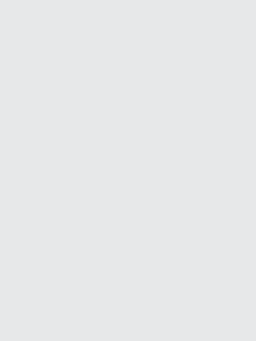
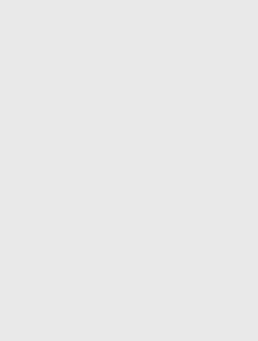
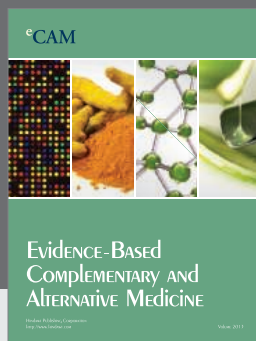
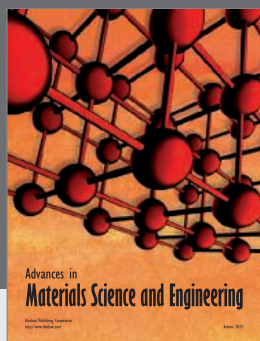
3. N. Barker *et al.*, *Nature* **457**, 608–611 (2009).
4. S. Schmitalla *et al.*, *Cell* **152**, 25–38 (2013).
5. H. J. Snippet *et al.*, *Cell* **143**, 134–144 (2010).
6. C. Lopez-Garcia, A. M. Klein, B. D. Simons, D. J. Winton, *Science* **330**, 822–825 (2010).
7. S. Kozar *et al.*, *Cell Stem Cell* **13**, 626–633 (2013).
8. S. J. Buczacck *et al.*, *Nature* **495**, 65–69 (2013).
9. O. J. Sansom *et al.*, *Proc. Natl. Acad. Sci. U.S.A.* **103**, 14122–14127 (2006).
10. J. M. Fischer, A. J. Miller, D. Shibata, R. M. Liskay, *Oncogene* **31**, 2028–2038 (2012).
11. P. Calabrese, S. Tavaré, D. Shibata, *Am. J. Pathol.* **164**, 1337–1346 (2004).
12. S. J. Leedham *et al.*, *Gastroenterology* **136**, 542, e6 (2009).
13. L. B. Meira *et al.*, *J. Clin. Invest.* **118**, 2516–2525 (2008).
14. M. A. Nowak, F. Michor, Y. Iwasa, *Proc. Natl. Acad. Sci. U.S.A.* **100**, 14966–14969 (2003).
15. F. Michor, Y. Iwasa, H. Rajagopalan, C. Lengauer, M. A. Nowak, *Cell Cycle* **3**, 358–362 (2004).
16. E. Lieberman, C. Hauert, M. A. Nowak, *Nature* **433**, 312–316 (2005).
17. I. Bozic *et al.*, *Proc. Natl. Acad. Sci. U.S.A.* **107**, 18545–18550 (2010).
18. M. A. Nowak *et al.*, *Proc. Natl. Acad. Sci. U.S.A.* **99**, 16226–16231 (2002).

Acknowledgments: We thank the Cambridge Institute Biological Resource Unit for animal husbandry and F. De Sousa E Melo, J. P. Medema, and P. Calabrese for useful discussion. This work was supported by Cancer Research UK; L.V. received a fellowship from the Koningin Wilhelmina Fonds (KWF, Dutch Cancer Society). We declare no competing financial interests.

Supplementary Materials

www.sciencemag.org/content/342/6161/995/suppl/DC1
Materials and Methods
Figs. S1 to S10
References (19–40)

12 July 2013; accepted 22 October 2013
10.1126/science.1243148



Hindawi

Submit your manuscripts at
<http://www.hindawi.com>

4 NEW WAYS ACS IS

OPEN

The American Chemical Society announces a bold and comprehensive program of Open Access initiatives:



ACS Central Science

A new, highly selective peer-reviewed journal covering the broad spectrum of chemical sciences—free to readers and authors—to be introduced during 2014.



ACS Editors' Choice

Free public access to new research of importance to the global community—one article every day—starting January 2014.



ACS Author Rewards

Corresponding Authors receive credits for each article published in 2014, which they can use to fund any ACS open access option in the next three years.



ACS AuthorChoice

Lets authors facilitate open access for a one-time fee—expanded in 2014 to include Creative Commons licenses and more.

For details go to www.acsopenaccess.org



ACS Publications
Most Trusted. Most Cited. Most Read.

Better results — on any sequencing platform

Get the most from your NGS

Discover new and innovative solutions,
dedicated for use with any NGS workflow

Streamline your next-generation sequencing (NGS) workflow and achieve high-quality results you can rely on.

- **Highly specific and selective nucleic acid purification and target enrichment**
- **Unbiased whole genome amplification from a single cell**
- **High DNA library yields using optimized workflows that allow ~50% time-savings**
- **Outstanding results on any sequencing platform**
- **Intuitive, knowledge-based data interpretation for deeper insight into NGS results**

Visit www.qiagen.com/goto/NGS to learn more!



Sample & Assay Technologies

Science Translational Medicine

Integrating Science, Engineering, and Medicine



Publishing results that harness the basic sciences to advance human health in all areas of medicine

Submit your research

ScienceTranslationalMedicine.org

Recommend to your library

ScienceOnline.org/recommend

Join the ranks of high-profile papers published in *Science Translational Medicine*:

NEUROLOGY

A Theoretically Based Index of Consciousness Independent of Sensory Processing and Behavior

A. G. Casali *et al.* (M. Massimini), *Sci. Transl. Med.* **5** 198ra105 (2013)

IMMUNOLOGY

TGF β Receptor Mutations Impose a Strong Predisposition for Human Allergic Disease

P.A. Frischmeyer-Guerrero *et al.* (H. Dietz), *Sci. Transl. Med.* **5** 195ra94 (2013)

BIOENGINEERING

A Human Disease Model of Drug Toxicity-Induced Pulmonary Edema in a Lung-on-a-Chip Microdevice

D. Huh *et al.* (D. Ingber), *Sci. Transl. Med.* **5** 159ra147 (2012)

CANCER

Genome-Wide Mutational Signatures of Aristolochic Acid and its Application as a Screening Tool

S.L. Poon *et al.* (B. T. Teh), *Sci. Transl. Med.* **5** 197ra101 (2013)

TISSUE ENGINEERING

Human Cartilage Repair with a Photoreactive Adhesive-Hydrogel Composite

B. Sharma *et al.* (J.J. Elisseeff), *Sci. Transl. Med.* **5** 167 ra6 (2013)

Chief Scientific Advisors

Elazer Edelman, M.D., Ph.D.

Massachusetts Institute of Technology

Garret FitzGerald, M.D.

University of Pennsylvania

Editor

Katrina L. Kelner, Ph.D.

AAAS, Washington, DC



scitranslmededitors@aaas.org



The New Legend

Eppendorf Reference® 2

»Reference« stands for extraordinary precision and accuracy, a long service life, and an ergonomic design. The new Reference 2 boasts these proven Premium characteristics and this operating philosophy with its innovative state-of-the-art technology; making it a reliable partner for you and your demanding work.

- > Single-button operation enables ergonomic handling with reduced operating effort
- > High precision and accuracy providing reliable pipetting results
- > Quick and secure volume setting, incl. volume lock
- > RFID chip contains all relevant data regarding the pipette



www.eppendorf.com/reference

Eppendorf®, the Eppendorf logo, Eppendorf PhysioCare Concept® and Eppendorf Reference® are registered Trademarks of Eppendorf AG, Germany. All right reserved, including graphics and images. Copyright © 2013 by Eppendorf AG.

CNV AND LOH ARRAY

The new CytoSure Consortium Cancer +SNP array (4x180k) allows the simultaneous detection of copy number variation (CNV) and loss of heterozygosity (LOH), with a SNP resolution that enables reporting of LOH at 10Mb. Focusing on content recommended by the CCMC, an international organization of clinical cytogeneticists, molecular cytogeneticists, and molecular pathologists, this targeted array covers over 500 cancer genes and 130 cancer-associated genomic regions for haematological malignancies and solid tumours. The CCMC-approved standardized array design is intended to improve clinical research quality and promotes collaboration and communication between cancer cytogenomics laboratories. The new array will be the latest addition to a range of OGT microarrays specifically designed for detecting CNV and LOH on a single array for cancer research. Due to the unique design of OGT's SNP probes, there are no changes to the standard aCGH protocol, no restriction digest is required, and any reference sample can be used.

Oxford Gene Technology

For info: +44-(0)-1865-856826 | www.ogt.com



LAB SAFETY SHIELD

The Lab Safety Shield has been designed to neatly fit around popular brands of stirrer hotplate to provide protection for chemists from draughts, splashes, aerosols, and spills. Ideal for use where fumehood space is at a premium, the compact and highly affordable Lab Safety Shield provides additional protection to chemists undertaking applications such as heated parallel reactions in tubes. The device also beneficially shields reactions from the cooling effect of fumehood ventilation, particularly important when consistent and reproducible heating to parallel experiments is required. Manufactured from robust 5 mm polycarbonate, the Lab Safety Shield is resistant to a wide range of laboratory solvents and is temperature-resistant to 170°C. Designed with a small footprint (29.5 x 16 x 17 cm) to minimize use of valuable fumehood space, the shield maintains access to hotplate controls and gives good all-round visibility of the reaction or process.

Asynt

For info: +44-(0)-1638-781709 | www.asynt.com

SEMICONDUCTOR CHIPS

The Ion PGM solution now significantly exceeds its competitor on the major performance metrics for benchtop sequencing. The performance gains are the result of upfront sample prep automation, new Ion PGM semiconductor chips that deliver up to 10-fold greater throughput, and improved variant calling with Torrent Suite Software v3.6. Combined with Ion AmpliSeq technology, targeted DNA and RNA sequencing using the Ion PGM solution is superior. The Ion PGM solution offers the fastest and simplest workflow—single-day assay, from sample to annotated variants; highest sensitivity for basic and clinical research applications; and lowest cost per sample. Ion Torrent semiconductor sequencing makes high-quality, next generation sequencing affordable with the Ion PGM System at a fraction of the cost of the alternative.

Life Technologies

For info: 800-955-6288 | www.lifetechnologies.com

DIGITAL PCR SYSTEM

The QX200 Droplet Digital PCR (ddPCR) system is the only digital polymerase chain reaction (PCR) system that works with EvaGreen and TaqMan hydrolysis probes (reagents that are used with the instrument) to provide users more flexibility in the design of their digital PCR experiments. The new system can be used with the company's recently launched 75 Droplet Digital PCR-validated assays (tests) for cancer mutation detection and genomic variations (gene copy number) to make running an experiment easier. Digital PCR provides researchers a tool for the detection of rare mutations (including distinguishing rare sequences in tumors), precise measurement of copy number variation, and absolute quantification of gene expression. ddPCR has been widely embraced, demonstrating a level of sensitivity and simplicity not available by any other means.

Bio-Rad

For info: 800-424-6723 | www.bio-rad.com

LIQUID DISTRIBUTION

The Calibrex organo 525 and the Calibrex solutae 530 smoothly dispense exact volumes of liquid reagents directly from bottle or flask. With its ground glass plunger, the organo 525 is ideal for dispensing organic liquids and noncrystallizing solutions. The solutae 530 has a PFA-coated plunger that is resistant to salt solutions, weak and strong acids, and bases, which prevents the plunger and barrel from seizing together. Scientists can check continuously updated chemical compatibility data by scanning the QR code imprinted on each unit. Precise dispensing volumes up to 25 mL, 50 mL, and 100 mL are easily set with one hand using the spring loaded sliding cursor, or by using a classic screw button supplied with each dispenser. No tools are required for cleaning and maintenance—users can calibrate the dispensers using the integrated key located under the plunger cap. Calibrex dispensers can be autoclaved fully assembled at 121°C/250°F.

Wheaton

For info: 800-225-1437 | www.wheaton.com

Electronically submit your new product description or product literature information! Go to www.sciencemag.org/products/newproducts.dtl for more information.

Newly offered instrumentation, apparatus, and laboratory materials of interest to researchers in all disciplines in academic, industrial, and governmental organizations are featured in this space. Emphasis is given to purpose, chief characteristics, and availability of products and materials. Endorsement by *Science* or AAAS of any products or materials mentioned is not implied. Additional information may be obtained from the manufacturer or supplier.

Polish-American Scientific Award 2014

call for nominations

The American Association for the Advancement of Science (AAAS) and the Foundation for Polish Science (FNP) are pleased to announce an opening call for nominations in the first edition of the Polish-American Scientific Award.

The award addresses outstanding scientific achievements in any field of science accomplished in American-Polish scientific cooperation and is granted jointly to two researchers on the basis of a competition. The Award amounts to \$5000 for each of the researchers.

All active members of the Polish and American scientific community holding a doctoral degree, or working as a researcher or research administrator at a university or other R&D institution (including the industrial sector) are eligible to nominate candidates for the Award. Self-nominations shall be also considered.

Each nomination shall refer jointly to a team of research collaborators, one member working in Poland and one member working in the United States, regardless of their nationality.

Nominations should contain the following:

- Acknowledgement of the joint scientific achievement made by collaborations between the two candidates in the sense of the award
- Curricula vitae of both scientists and a list of publications relevant to the joint achievement
- One letter of support for the nominees (in case of self-nominations - two)- the author of which should not be the nominator nor the nominees.

Nominations shall be submitted in English either in paper or electronic version by the closing date of **15th December, 2013** to one of the following addresses:

Linda Stroud, American Association for the Advancement of Science, 1200 New York Avenue, NW, Washington, DC 2005, USA, lstroud@aaas.org.

Kinga Slominska, Foundation for Polish Science, ul. Gzazyny 11, 02-548 Warszawa, POLAND, kinga.slominska@fnp.org.pl

The contest is carried out by a joint committee of AAAS and FNP including external members. The award ceremony will take place in a ceremonial setting. AAAS and FNP will invite the laureates for a honorary lecture in their respective countries.

For more information please address:

Kinga Slominska at FNP: +48 22 424 0252;

Vaughan Turekian at AAAS: +1 202 326 6655

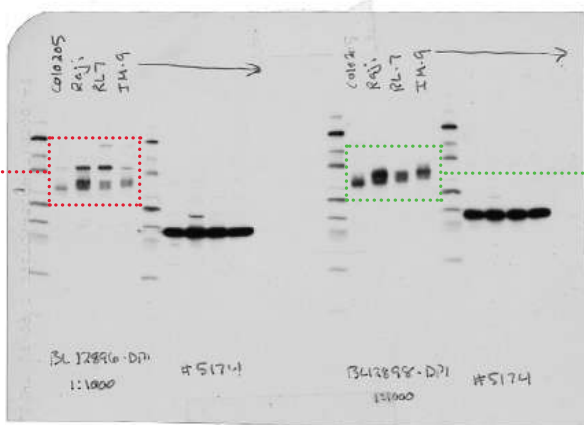
You've carefully designed your experiment.

Taylor Ngo started at CST 8 years ago and is currently in the Molecular Biology group.

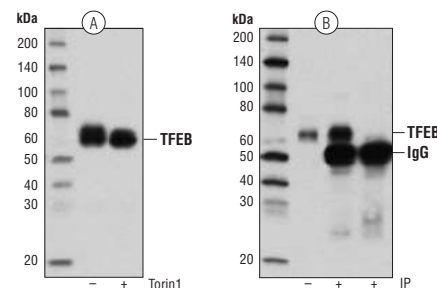
Does your antibody measure up?

We validate all our antibodies in-house. If it's not specific, it doesn't ship.

REJECTED
Extra Band
Weak Signal



CST APPROVED
Clean Band
Strong Signal



TFEB Antibody #4240: (A) WB analysis of Raji cell extracts, untreated (-) or Torin1-treated, using #4240 (Torin1 treatment induces dephosphorylation). **(B)** IP of TFEB from COLO 205 cells using #4240 (lane 2) or Normal Rabbit IgG #2729 (lane 3). Lane 1 is 10% input.

WB analysis of various cell extracts using two development samples at 1:1000 dilution. GAPDH (D16H11) XP® Rabbit mAb #5174 was used as a loading control.

Please visit our website to request a copy of our new white paper – *A Guide to Successful Western Blotting*.

www.cellsignaling.com/successfulWB

© 2013 Cell Signaling Technology, Inc. Cell Signaling Technology® and XP® are trademarks of Cell Signaling Technology, Inc.



Cell Signaling
TECHNOLOGY®

There's only one

Science



Science Careers Advertising

For full advertising details, go to ScienceCareers.org and click For Employers, or call one of our representatives.

Tracy Holmes

Worldwide Associate Director
Science Careers
Phone: +44 (0) 1223 326525

THE AMERICAS

E-mail: advertise@sciencecareers.org
Fax: 202-289-6742

Tina Burks

East Coast/West Coast/South America
Phone: 202-326-6577

Marci Gallun

Midwest/Canada
Phone: 202-326-6582

Candice Nulsen

Corporate
Phone: 202-256-1528

Online Job Posting Questions

Phone: 202-312-6375

EUROPE / INDIA / AUSTRALIA / NEW ZEALAND / REST OF WORLD

E-mail: ads@science-int.co.uk
Fax: +44 (0) 1223 326532

Axel Gesatzki

Phone: +44 (0)1223 326529

Sarah Lelarge

Phone: +44 (0) 1223 326527

Kelly Grace

Phone: +44 (0) 1223 326528

JAPAN

Yuri Kobayashi

Phone: +81-(0)90-9110-1719
E-mail: ykobayas@aaas.org

CHINA / KOREA / SINGAPORE / TAIWAN / THAILAND

Ruolei Wu

Phone: +86-1367-1015-294
E-mail: rwu@aaas.org

All ads submitted for publication must comply with applicable U.S. and non-U.S. laws. *Science* reserves the right to refuse any advertisement at its sole discretion for any reason, including without limitation for offensive language or inappropriate content, and all advertising is subject to publisher approval. *Science* encourages our readers to alert us to any ads that they feel may be discriminatory or offensive.

Science Careers

From the journal *Science*



ScienceCareers.org

For recruitment in science, there's only one

Science

Science



Breakthrough of the Year

Special Editorial Feature:

December 20, 2013

Reserve ads by December 3 to guarantee space*

*Ads accepted until December 16 if space is still available.

**This December, reach an additional
25,000 scientists at no extra cost!**

Each year, the *Science* editorial team reviews the most exciting discoveries of the past 12 months in the "Breakthrough of the Year" issue. You'll not only reach 129,551 *Science* subscribers and our 570,400 worldwide readers, but also a special group of 25,000 scientists at no extra cost. These scientists are carefully selected for their demographic similarities to *Science*'s current audience.

**Book space in this issue and reach nearly
600,000 potential employees!**

To Book Your Ad:

E-mail: advertise@sciencecareers.org

Or telephone us:

US/Canada/South America:

202-326-6582

Europe/India/Australia/New Zealand/

Rest of World: +44 (0) 1223 326500

Japan: +81-(0)90-9110-1719

China/Korea/Singapore/Taiwan/

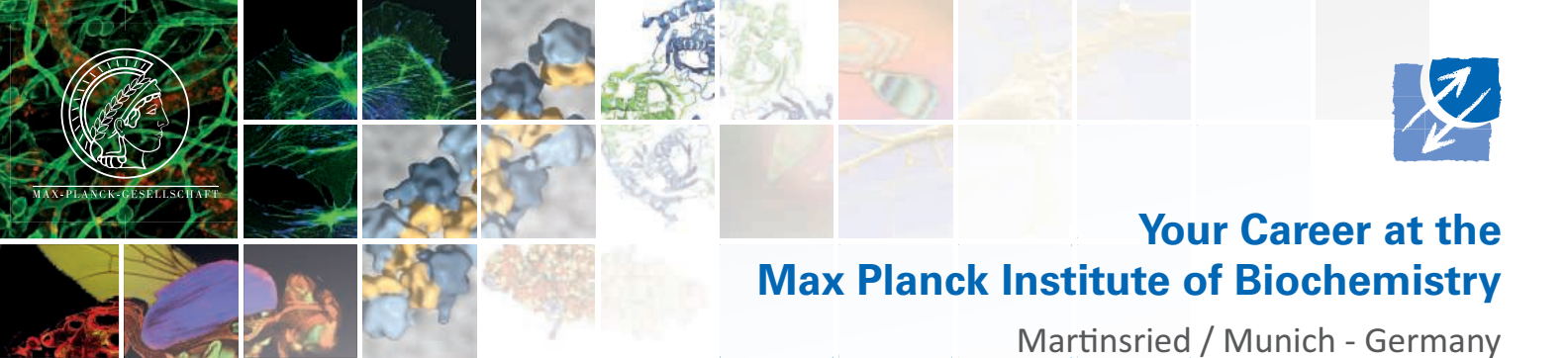
Thailand: +86-1367-1015-294

Science Careers

From the journal *Science*



ScienceCareers.org



Your Career at the Max Planck Institute of Biochemistry

Martinsried / Munich - Germany

About the Institute

The Max Planck Society for the Advancement of Science is an independent non-profit research organization which promotes groundbreaking basic research. The Max Planck Institute of Biochemistry (MPIB) is one of the largest biomedical research institutes within the Max Planck Society. Currently, it consists of 26 groups conducting cutting-edge research in the molecular life sciences. Further details are listed on the right side of the advertisement. The world-leading MPIB houses state-of-the-art facilities with a lively and highly international atmosphere that offers exceptional opportunities to scientists at every stage of their career. It is located on the thriving life science campus of Martinsried, in the south-west of Munich, together with the MPI of Neurobiology, the Ludwig Maximilians University, the Helmholtz Zentrum Munich and the Innovation and Startup Centers for Biotechnology.

Open Position: Director of Department

The MPI of Biochemistry is currently seeking to fill one of its Max Planck Director positions to complement its existing departments headed by Directors Wolfgang Baumeister, Elena Conti, Reinhard Fässler, F-Ulrich Hartl, Stefan Jentsch, Matthias Mann, Petra Schwillle and Axel Ullrich. The position is equivalent to that of a tenured Full-Professor and is without teaching commitments. The offer includes a highly competitive package with substantial core funding (personnel, consumables, investments) and generous lab space. We are seeking candidates who study the molecular mechanisms of fundamental biological problems. In particular, they should use **biochemistry, chemical biology, bioinformatics/systems biology** or **cell biology** in fields complementing existing research areas at the Institute. Candidates are expected to have a strong track record and several years of experience as a PI.

Applicants should send their CV, list of publications and a brief summary of past and current research to the office of the Managing Board of Directors by email (gl@biochem.mpg.de).

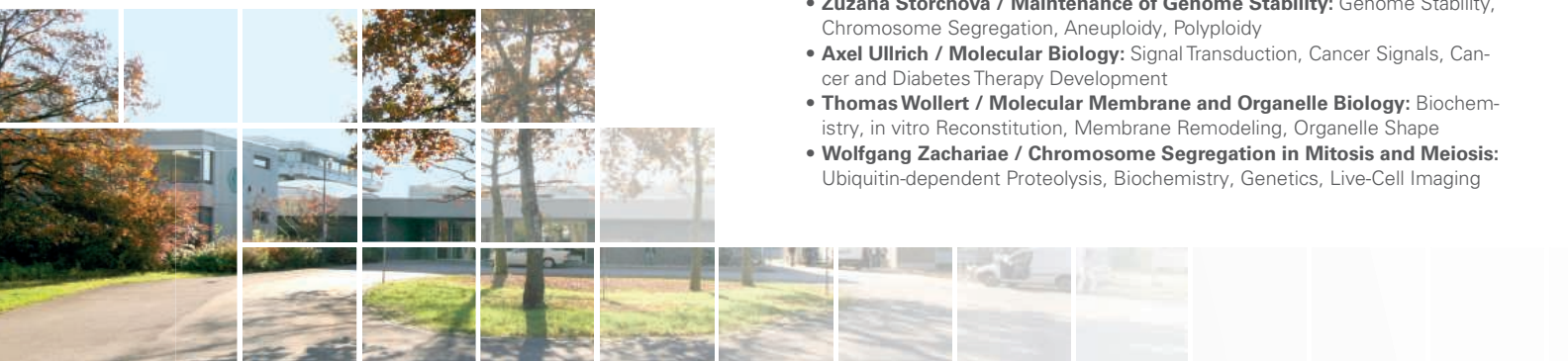
For further information about the MPIB, please visit www.biochem.mpg.de.

The Max Planck Society is committed to employing more disabled individuals and especially encourages them to apply. The Max Planck Society seeks to increase the number of women in those areas where they are underrepresented and therefore explicitly encourages women to apply.

The deadline for application is **December 31, 2013**.

Research Groups

- **Wolfgang Baumeister / Molecular and Cellular Structural Biology:** Cryo-electron Microscopy, Hybrid Methods, Protein Degradation
- **Christian Biertümpfel / Molecular Mechanisms of DNA Repair:** Structural Biology, DNA Damage, DNA Repair, DNA Replication, Protein-DNA Interactions
- **Julia von Blume / Molecular Basis of Protein Trafficking:** Membrane Trafficking, Protein Sorting and Secretion, Golgi Apparatus, Ca²⁺, ADF/cofilin, Hailey Hailey disease
- **Elena Conti / Structural Cell Biology:** Structural Studies, RNA Transport, RNA Surveillance, RNA Degradation
- **Reinhard Fässler / Molecular Medicine:** Integrin, Adhesion Signalling, Mouse Genetics
- **Friedrich Förster / Modeling of Protein Complexes:** Cryoelectron Microscopy, Modeling, Ubiquitin Proteasome Pathway, ER-translocation
- **Carsten Grashoff / Molecular Mechanotransduction:** Cell Biology, Mechano-transduction, Biosensors
- **Stephan Gruber / Chromosome Organization and Dynamics:** Bacterial Cell Biology, Biochemistry, Chromosome Segregation, Condensin Complexes
- **Bianca Habermann / Computational Biology:** Genome Analysis, Systems Biology, Sequence Analysis, NGS Data Analysis
- **F-Ulrich Hartl / Cellular Biochemistry:** Molecular Chaperones, Protein Folding, Proteostasis, Aging and Neurodegenerative Diseases
- **Manajit Hayer-Hartl / Chaperonin-assisted Protein Folding:** Protein Folding and Assembly, Rubisco, GroEL and GroES, Mass Spectrometry
- **Stefan Jentsch / Molecular Cell Biology:** Ubiquitin and Ubiquitin-Like Proteins, Protein Degradation, DNA Transactions and Chromatin Biology
- **Esben Lorentzen / Intraflagellar Transport:** Cilia, Intraflagellar Transport, X-ray Crystallography, Protein Complexes
- **Matthias Mann / Proteolytics and Signal Transduction:** Mass Spectrometry, Systems Biology, Bioinformatics, Cancer
- **Naoko Mizuno / Cellular and Membrane Trafficking:** Structural Biology, Cryo Electron Microscopy, Biophysics, Membrane Trafficking, Membrane Curvature
- **Jürg Müller / Chromatin Biology:** Genetics and Biochemistry of Chromatin, Transcription, Histone Modifications, Drosophila Development
- **Inaam Nakchbandi / Translational Medicine:** Fibronectin, Integrin, Bone, Disease
- **Boris Pfander / DNA Replication and Genome Integrity:** DNA Replication, Checkpoints, DNA Damage, Posttranslational Modifications, Yeast
- **Andreas Pichlmair / Innate Immunity:** Host-Pathogen Interactions, Viruses, Proteomics, Perturbation of Immune Signaling
- **Marc Schmidt-Supprian / Molecular Immunology and Signal Transduction:** Immunology, Mouse Genetics, Signal Transduction, Immune Diseases
- **Frank Schnorrer / Muscle Dynamics:** Drosophila Muscle Development, Sarcomere, Cell Migration, Muscle Patterning
- **Petra Schwillle / Cellular and Molecular Biophysics:** Single Molecule Techniques, Membranes, Synthetic Biology
- **Zuzana Storchova / Maintenance of Genome Stability:** Genome Stability, Chromosome Segregation, Aneuploidy, Polyploidy
- **Axel Ullrich / Molecular Biology:** Signal Transduction, Cancer Signals, Cancer and Diabetes Therapy Development
- **Thomas Wollert / Molecular Membrane and Organelle Biology:** Biochemistry, in vitro Reconstitution, Membrane Remodeling, Organelle Shape
- **Wolfgang Zachariae / Chromosome Segregation in Mitosis and Meiosis:** Ubiquitin-dependent Proteolysis, Biochemistry, Genetics, Live-Cell Imaging





MARSHALL UNIVERSITY RESEARCH CORPORATION
Marshall University
Joan C. Edwards School of Medicine
Three Post-Doctoral Positions

Duties: Study the pathophysiology of metabolic syndrome and obesity, using pharmacological and genetic approaches. Studies will be carried out in both animal and stem cell culture models to define the molecular basis of cellular obesity and signaling molecules.

Requires M.D. or Ph.D. in Medicine/Physiology or related field. Candidates should be knowledgeable of arachidonic acid metabolisms, cyclooxygenase, epoxigenase and soluble epoxide hydrolase SIGNALING PATHWAY. Candidates should have experience in small animal handling, molecular biology techniques, biochemical assays and in conducting cell culture studies. The candidate will be involved in the design of experimental protocols; collection, analysis and interpretation of data; preparation of oral and written scientific reports, such as presentation of results at local, state, and national meetings; composition of scientific manuscripts for submission to journals and writing grant applications.

He/she will also participate in interdepartmental seminars, journal clubs and local and national scientific societies. It is also expected that he/she will incorporate previous skills and knowledge into the evolution of data interpretations.

Work in an excellent learning and teaching environment, with opportunity for growth and the pursuit of an independent career. Excellent salary compensation and positions are available immediately and will remain open until filled.

Contact: Send a curriculum vitae and a cover letter describing research interests and experience to: **Nader G. Abraham, PhD** at Abrahamn@Marshall.edu.



南京大學
NANJING UNIVERSITY

Nanjing, CHINA

Founded in 1902, Nanjing University is one of the oldest and most prestigious institutions of higher learning in China. As a key comprehensive university with an array of outstanding faculty members, it has enjoyed coordinated development in humanities, social sciences, natural sciences, technological sciences, life sciences, modern engineering and management and so on. With the motto of "Sincerity with Aspiration, Perseverance and Integrity," Nanjing University carries the spirit of constant striving for educational and academic excellence. Today's Nanjing University invites outstanding scholars of all nationalities to join us in the mission to build this university into a world-class comprehensive research university with a global vision.

Position: Distinguished Professor

Offered by Thousand Talents Program/ Chang Jiang Scholars Program/ Deng Feng Scholar Program A

- The applicant should hold a professorship/associate professorship (or an equivalent position) in a prominent overseas university (or research institutes)
- The applicant demonstrates outstanding capabilities in scientific innovation, whose research capabilities and achievements are recognized by peers as at leading level.

Position: Young Talents Professor

Offered by Thousand Young Talents Program/Deng Feng Scholar Program B

- The applicant should hold an assistant professorship (or an equivalent position)/research fellowship in a prominent overseas university (or research institutes)
- The applicant should have been a top talent among peers and shown a strong potential to be a future leader in his/her area.

The position offers adequate scientific resources, abundant research funding, attractive salary and generous reallocation package, including the opportunity to buy an apartment in an inter price rate and subsidy.

Interested candidates please visit <http://rczp.nju.edu.cn/>



Research without Borders
All posts based near Vienna, Austria

The International Institute for Applied Systems Analysis (IIASA) has a world-class reputation for delivering scientific insight to policymakers worldwide. IIASA is expanding to meet the growing demand for international and interdisciplinary research in the global problem areas of Energy & Climate Change, Food & Water, Poverty & Equity. To this end, we are recruiting:

Program Leader, Risk, Policy, and Vulnerability Program:

You will lead a team of over 30 multinational researchers using quantitative and qualitative methods for assessing risk and vulnerability, and analyzing policy options designed to cope with global change.

Program Leader, Advanced Systems Analysis Program:

You will lead a team of over 25 multinational researchers to develop new, more sophisticated methodologies for systems analysis so that better solutions to global problems can be found.

Senior Science Officers (2 posts):

You will work within the IIASA Directorate together with IIASA's Internal Research Committee and Research Programs to strengthen and facilitate collaboration among IIASA Research Programs.

For more information and to apply for any of the above roles, please visit: www.iiasa.ac.at/vacancies

Postdoctoral Researchers:

Every year a number of postdoctoral scholarships are available for research on topics related to the IIASA research agenda. For further details, please visit: www.iiasa.ac.at/postdoc



TEXAS BIOMEDICAL
RESEARCH INSTITUTE



SNPRC
Southwest National
Primate Research
Center

STEM CELL REGENERATIVE MEDICINE
FACULTY POSITIONS

Southwest National Primate Research Center (SNPRC)

The SNPRC at the Texas Biomedical Research Institute invites applications and nominations for two faculty positions in stem cell regenerative medicine. Applicants and nominees are expected to have an interest in, and preferably experience with, nonhuman primate models. Major strengths of the SNPRC are in genetics and genomics, metabolic disorders, and infectious diseases. Several primate models of human diseases developed at SNPRC are ideally suited for translational research on stem cell regenerative medicine. The SNPRC has an outstanding diversity of primate resources, including large colonies of baboons, rhesus monkeys, common marmosets, and chimpanzees.

The SNPRC has close associations with the University of Texas Health Science Center at San Antonio and the University of Texas at San Antonio, including opportunities for roles in graduate education. A critical mass of stem cell regenerative medicine researchers exists at those institutions, together with the developing stem cell regenerative medicine program at the SNPRC. The SNPRC has a strong tradition in postdoctoral training.

Rank and salary will be nationally competitive and commensurate with experience. The laboratories and offices of the successful candidates will be located in the new SNPRC laboratory and administration facility, which is now under construction and expected to be ready for occupancy in March 2014.

Applications and nominations should be sent to the **Chair, SNPRC Regenerative Medicine Search Committee, c/o Human Resources Office, P. O. Box 760549, San Antonio, TX 78245-0549**, and should include a letter outlining qualifications and research interests. Applications, but not nominations, must also include a CV, and the names and contact information for at least three references. Additional information about the SNPRC can be found at www.snprc.org. Additional information about Texas Biomed can be found at www.txbiomed.org. *EOE*



Hiring Vice President at South University of Science and Technology (SUSTC) Shenzhen, China

The South University of Science and Technology, China (SUSTC) invites applications and nominations for Vice President (Academic Affairs) and Vice President (Education). SUSTC is committed to **excellence in teaching and research**; therefore, it offers internationally competitive salaries, fringe benefits, retirement and housing subsidy to the Vice Presidents. The modern campus also offers pleasant working conditions.

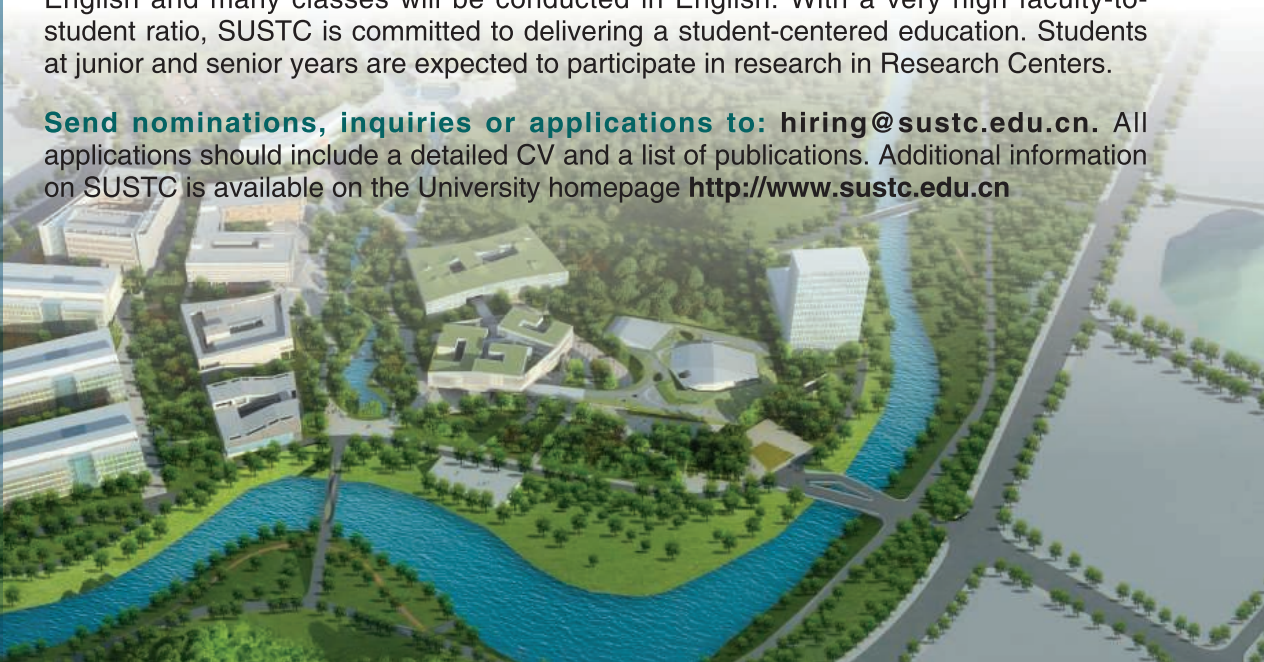
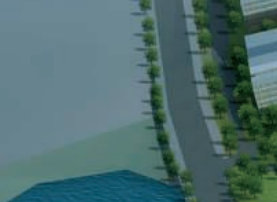
About SUSTC

SUSTC is a public institution funded by the municipal of Shenzhen, a special economic zone city in southern China. The University receives full financial support from the municipal. Set on five hundred acres of wooded landscape in the picturesque Nanshan (South Mountain) area, the campus offers an idyllic environment suitable for learning and scholarship. SUSTC engages in basic and problem-solving research of lasting impact to benefit society and mankind. Key research areas of the university include but not limited to: *Neural and Cognitive Sciences, Biology and Gene Engineering, Modern Physics, Control and Modification of Materials, Nanoscience and Nanotechnology, Mathematics and Applied Mathematics, Molecular Chemistry and Catalysis, Large-Scale Computational Research, Robotics and Artificial Intelligence, Information Systems and Electronic Engineering, Modern Cities and future developments, Energy Sciences and technology, Environmental Sciences, Financial Mathematics and Engineering.*

The Vice President (Academic Affairs, VPAA) and Vice President (Education, VPE) report directly to the president. The **VPAA** provides strategic leadership in the development and implementation of academic and research programs. The **VPE** provides strategic leadership in student education and whole person development. Successful candidates are expected to be internationally renowned scholars with administrative experience and good communication skills. Excellent leadership and organizational skills are also important.

The teaching language at SUSTC is English or Putonghua. As we expect an international faculty, the majority of teaching materials and reference books will be in English and many classes will be conducted in English. With a very high faculty-to-student ratio, SUSTC is committed to delivering a student-centered education. Students at junior and senior years are expected to participate in research in Research Centers.

Send nominations, inquiries or applications to: hire@sustc.edu.cn. All applications should include a detailed CV and a list of publications. Additional information on SUSTC is available on the University homepage <http://www.sustc.edu.cn>





TEXAS BIOMEDICAL RESEARCH INSTITUTE

Associate Scientific Director

Applications are invited for the position of Associate Scientific Director at Texas Biomedical Research Institute, www.txbiomed.org, located in San Antonio, TX. The Associate Scientific Director assists the Chief Scientific Officer in the scientific administration of the Institute and may conduct investigator-initiated research. The individual is responsible for providing administrative support and oversight for the Institutional Animal Care and Use Committee, the Biohazards and Safety Committee, and the Recombinant DNA Committee. Additional regulatory compliance duties include administering the Institute's Misconduct in Science Policy as the Research Integrity Officer, administering human subject research compliance as the Human Protections Administrator for the Texas Biomed HHS Federal Wide Assurance and as the Texas Biomed liaison to the University of Texas Health Science Center Institutional Review Board, and serving as the Authorized Signing Official for Texas Biomed requests for access to the National Center for Biotechnology Information Genotypes and Phenotypes Database. The position also provides administrative supervision of scientific support services that include the Office of Sponsored Programs (Director + 3 FTE), the Northrup Library (Director + 1 FTE), Information Systems (Director + 4 FTE), Quality Assurance/Quality Control for GLP and Animal Rule studies compliance (4 FTE), Technical Publications (2 FTE) and Print Shop (2 FTE). Applicants should have a doctoral degree and at least 10 years of job-specific experience. They should be qualified to provide administrative oversight for institutional compliance with the Animal Welfare Act and USDA Animal Welfare Regulations, the Public Health Service Policy on the Humane Care and Use of Laboratory Animals, the NIH Policy and Guidance on Human Subjects Research, PHS policies on Research Misconduct (42 CFR part 93), NIH Grants Policy, and FDA regulations for Good Laboratory Practice for Nonclinical Laboratory Studies (21 CFR part 58). A history of NIH grant support is desired.

Apply online at <http://www.txbiomed.org/about/employment/job-opportunities> or mail your application to the **Director of Human Resources, Texas Biomedical Research Institute, P.O. Box 760549, San Antonio, TX 78245-0549**. Applications must also include a CV and the names and contact information for at least three references. *EOE*

Science Careers is the forum
that answers questions.



Science Careers is dedicated to opening new doors and providing timely answers to the career questions that matter to you.



Science Careers Forum:

Your Future Awaits.

- » Relevant Career Topics
- » Timely Advice and Answers
- » Community, Connections, and More!

Visit the forum and join the conversation today!



ScienceCareers.org



Postdoctoral Research Scientists

We are looking for two or three self-motivated postdoctoral research scientists to join Dr. So Iwata's group at the SPring-8 Angstrom Compact Free Electron Laser Facility (SACLA) RIKEN in Japan. The SACLA Science Research Group is now developing a data collection system for the serial femtosecond crystallography (SFX) and is constructing a system to determine the structure of drug-target proteins. Successful candidates will have experience in protein crystallography using synchrotron radiation or XFEL including protein production, crystallization, beam-line technologies and/or software development.

Application deadline is **31 January 2014** and the start date is **1 April 2014** (negotiable).

Details about the positions and the research center can be found at http://www.riken.jp/en/careers/researchers/20131025_2/

Contact:

Dr. So Iwata
SACLA Science Research Group
Photon Science Research Division
RIKEN SPring-8 Center,
1-1-1 Kouto, Sayo, Hyogo 679-5148 Japan

Email:

s.iwata@spring8.or.jp
rie.tanaka.hw@riken.jp



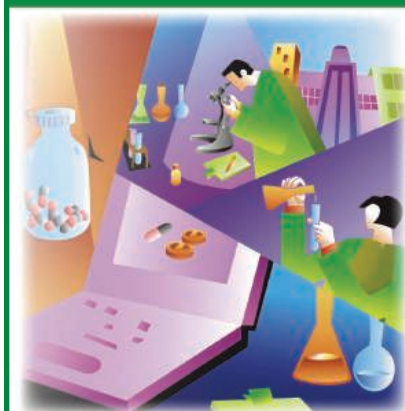
JOHNS HOPKINS
BLOOMBERG
SCHOOL of PUBLIC HEALTH

Faculty Position Biochemistry and Molecular Biology

The Department of Biochemistry and Molecular Biology at the Bloomberg School of Public Health of Johns Hopkins University invites applications for a tenure-track faculty position, preferably at the Assistant Professor level. We seek outstanding applicants with a demonstrated ability to study problems of major public health relevance at the cellular, molecular, and/or structural level. Areas of highest priority for this search include DNA repair and genome integrity. Applicants interested in stress response biology, chronic diseases and cancer biology should also apply. Successful applicants will be expected to establish an outstanding research program, be strongly committed to graduate level training and education, and contribute to the success of the department and school. Visit <http://www.jhsph.edu/departments/biochemistry-and-molecular-biology/faculty-openings/> for information about the application process and recent faculty hires. Applications will be accepted until **January 15, 2014**.

We actively encourage applications from women and minority candidates. The Johns Hopkins University is an Equal Opportunity/Affirmative Action Employer.

**CAREER
TRENDS** Running
Your Lab



Download your free copy today at
ScienceCareers.org/booklets

Science Careers

From the journal Science AAAS

Brought to you by the
AAAS/Science Business Office



ENGINEERING AT ILLINOIS

DRIVE YOUR VISION

ENDOWED CHAIRS AND PROFESSORSHIPS IN BIOENGINEERING

Bioengineering is revolutionizing 21st century healthcare worldwide. But to have the greatest impact, the best minds have to work together across a variety of fields. At the University of Illinois, that interdisciplinary attitude and the desire to deliver safe, effective, affordable medical technologies drive us. They've led to breakaway work in imaging, biosensing, cellular mechanics, and biophysics. Now we're expanding our team. Thanks to the \$100 million Grainger Engineering Breakthroughs Initiative, we're creating more than 35 new endowed professorships and chairs in Bioengineering and other fields. If you're ready to drive the future of Bioengineering, Illinois is the place for you.

GraingerInitiative.engineering.illinois.edu



Illinois is an Affirmative Action/Equal Opportunity Employer. www.inclusiveillinois.illinois.edu.
Full consideration will be given to applications and nominations received by December 16, 2013.

There's only one GALILEO GALILEI

Born in 1564, Galileo Galilei once contemplated a career in the priesthood. It's perhaps fortunate for science that upon the urging of his father, he instead decided to enroll at the University of Pisa. His career in science began with medicine and from there he subsequently went on to become a philosopher, physicist, mathematician, and astronomer, for which he is perhaps best known. His astronomical observations and subsequent improvements to telescopes built his reputation as a leading scientist of his time, but also led him to probe subject matter counter to prevailing dogma. His expressed views on the Earth's movement around the sun caused him to be declared suspect of heresy, which for some time led to a ban on the reprinting of his works.

Galileo's career changed science for all of us and he was without doubt a leading light in the scientific revolution, which is perhaps why Albert Einstein called him the father of modern science.

Want to challenge the status quo and make the Earth move? At *Science* we are here to help you in your own scientific career with expert career advice, forums, job postings, and more — all for free. For your career in science, there's only one *Science*. Visit ScienceCareers.org today.



For your career in science, there's only one **Science**

AAAS

ScienceCareers.org

Research Opportunities in Luxembourg. See what's behind it.



PEARL LUXEMBOURG'S RESEARCH PROGRAMME FOR INTERNATIONALLY RECOGNISED SENIOR RESEARCHERS

- Interested in establishing a high-profile research programme? Through our research programme PEARL (financial contribution up to EUR 5 million) we give you the opportunity to transfer your research programme to a research institution in Luxembourg.



ATTRACT LUXEMBOURG'S RESEARCH PROGRAMME FOR OUTSTANDING YOUNG RESEARCHERS FROM ALL OVER THE WORLD

Interested in doing scientific research at a high level in an international environment? Our research programme ATTRACT will allow you to set up your independent research team within a research institution in Luxembourg which will offer you attractive career opportunities. Funding up to EUR 2.5 million.



More information about ATTRACT and PEARL as well as the other funding opportunities offered by the National Research Fund Luxembourg can be found on the FNR's website.

Go and see what's behind on www.fnr.lu/pearl and www.fnr.lu/attract

For an overview on research in Luxembourg, have a look at www.innovation.public.lu



INVESTIGATING FUTURE CHALLENGES



UNIL | Université de Lausanne

Faculty of Biology and Medicine

| le savoir vivant |

THE FACULTY OF BIOLOGY AND MEDICINE OF THE UNIVERSITY OF LAUSANNE, SWITZERLAND, INVITES APPLICATIONS FOR TWO OPEN POSITIONS AS:

ASSOCIATE OR FULL PROFESSOR AND TENURE-TRACK ASSISTANT PROFESSOR TOWARDS ASSOCIATE PROFESSOR AT THE DEPARTMENT OF FUNDAMENTAL MICROBIOLOGY

Envisioned starting date: August/September, 2014.

The Department of Fundamental Microbiology (<http://www.unil.ch/dmf>) wishes to strengthen its activities in the fields of molecular microbiology and host-microbiome interactions. Depending on the experience of the candidates, the positions can be filled at the level of tenure-track assistant professor, associate or full professor.

Successful candidates are expected to develop an internationally recognized research programme funded by external sources, and must have a record of outstanding research achievements and successful funding applications.

The Department has excellent experimental facilities and access to the latest imaging, proteomics and genomics platforms on campus. A start-up package as well as a yearly research allowance for positions and consumables will be available within a dynamic research environment.

Pre-existing knowledge of French is not required but the selected candidates are expected to be able to teach in French after 2 years. They will supervise Masters and PhD students, and participate in teaching activities by the Department. Candidates at associate/full professor level will also share administrative responsibilities in the management of the Department.

More detailed job descriptions are available on the Internet site <http://www.unil.ch/fbm/page64812.html>.

Further information may be obtained from Prof. Hernandez (Nouria.Hernandez@unil.ch), chairwoman of the search committee.

Applications must be formulated in English and should include a motivation letter, the curriculum vitae, a list of publications highlighting the five most significant ones, a brief statement of the past and future research programmes, and teaching experience, as well as names and contact information of three references. They should be submitted online by January 31st, 2014 as a single pdf file to www.unil.ch/iafbm/application.



Seeking to promote an equitable representation of women and men among its staff, the University encourages applications from women.



Oakland University Department of Biological Sciences Tenure-Track Assistant Professor Position In Microbiology

The Department of Biological Sciences at Oakland University invites applications for a tenure-track position in Microbiology at the Assistant Professor level. We seek an outstanding individual that investigates cutting-edge questions relevant to prokaryotic organisms. Preference will be given to candidates with an applied research focus in areas such as biotechnology, translational medicine, or environmental biology. Qualified investigators in other specialties will also be given consideration and are encouraged to apply. The successful candidate is expected to develop an innovative, extramurally funded research program, to teach at the undergraduate and graduate levels, to mentor undergraduate and graduate students (MS and PhD), and to participate in service activities.

All applicants must have a PhD and relevant post-doctoral experience. Applicants are expected to demonstrate an excellent record of research productivity as evidenced by publications and a defined plan to obtain extramural funding. Laboratory space, a competitive startup package, and full access to Departmental and University-subsidized research facilities will be provided.

The Search Committee will review applications starting January 6, 2014 and will continue until the position is filled. Applications should include a cover letter, curriculum vitae and detailed statement of research plans and teaching philosophy as well as 3 reference letters. Application material excluding reference letters must be submitted online at: <http://academicjobs.oakland.edu/postings/816>. Reference letters are to be sent directly to Dr. Gerard Madlambayan (microsearch@oakland.edu). Inquiries should be addressed to: **Dr. Arik Dvir, Chair, Department of Biological Sciences** (dvir@oakland.edu).

Oakland University is an Equal Opportunity Employer and encourages applications from women and minorities.



AAAS is here – helping scientists achieve career success.

Every month, over 400,000 students and scientists visit ScienceCareers.org in search of the information, advice, and opportunities they need to take the next step in their careers.

A complete career resource, free to the public, *Science* Careers offers a suite of tools and services developed specifically for scientists. With hundreds of career development articles, webinars and downloadable booklets filled with practical advice, a community forum providing answers to career questions, and thousands of job listings in academia, government, and industry, *Science* Careers has helped countless individuals prepare themselves for successful careers.

As a AAAS member, your dues help AAAS make this service freely available to the scientific community. If you're not a member, join us. Together we can make a difference.

To learn more, visit aaas.org/plusyou/sciencecareers





AAAS is here – promoting universal science literacy.

In 1985, AAAS founded Project 2061 with the goal of helping all Americans become literate in science, mathematics, and technology. With its landmark publications *Science for All Americans* and *Benchmarks for Science Literacy*, Project 2061 set out recommendations for what all students should know and be able to do in science, mathematics, and technology by the time they graduate from high school. Today, many of the state standards in the United States have drawn their content from Project 2061.

Every day Project 2061 staff use their expertise as teachers, researchers, and scientists to evaluate textbooks and assessments, create conceptual strand maps for educators, produce groundbreaking research and innovative books, CD-ROMs, and professional development workshops for educators, all in the service of achieving our goal of universal science literacy.

As a AAAS member, your dues help support Project 2061 as it works to improve science education. If you are not yet a AAAS member, join us. Together we can make a difference.

To learn more, visit aaas.org/plusyou/project2061



POSITIONS OPEN

DEPARTMENT OF EXERCISE SCIENCE Arnold School of Public Health

The Department of Exercise Science in the Arnold School of Public Health at the University of South Carolina invites applications for a tenure-track/tenured position at the **ASSISTANT** or **ASSOCIATE PROFESSOR** level to begin in August 2014. Priority given to candidates with interests in inflammation and/or cancer research, who have or will develop a collaborative, multidisciplinary research program that complements the Department's current strengths in physical activity and nutrition. Incumbent expected to interact with a network of researchers in the Arnold School of Public Health ([website: http://sph.sc.edu](http://sph.sc.edu)), the Center for Colon Cancer Research ([website: http://ccr.sc.edu](http://ccr.sc.edu)) and the Center on Dietary Supplements and Inflammation ([website: http://cobre.med.sc.edu](http://cobre.med.sc.edu)). Research approaches can be basic or applied, making use of in vitro, small animal, or human models, and can include clinical trials, epidemiology and/or community engagement methodology. Doctorate in relevant health sciences field with potential for excellence in research and teaching required. For full description of position and application instructions, please visit: [website: http://sph.sc.edu/exsc/pdf/EXSC-tenure-track-11-2014.pdf](http://sph.sc.edu/exsc/pdf/EXSC-tenure-track-11-2014.pdf).

An Affirmative Action/Equal Employment Opportunity Employer.

TENURE-TRACK FACULTY POSITIONS Available at the NIH-funded Center of Biomedical Research Excellence (COBRE) in Inflammation and Dietary

Supplements at the University of South Carolina

The University of South Carolina (USC) invites applications for several tenure-track **ASSISTANT PROFESSOR** positions in Inflammation and Dietary Supplements. Outstanding applicants working in the area of inflammation and willing to incorporate dietary supplements research are encouraged to apply. Current areas of research are highlighted at the following websites: <http://cobre.med.sc.edu/> and <http://camcenter.med.sc.edu/>. The successful candidates will be recruited, based on research experience and interest, in a department at any of the participating schools/colleges, namely the School of Medicine, School of Public Health, School of Pharmacy, College of Engineering, School of Nursing and College of Arts and Sciences. The candidates must have Ph.D. or equivalent, and postdoctoral research experience. The recruits will be eligible to apply for funds from the NIH COBRE grant at USC. However, recruits with major independent funding, current or past, such as NIH R01 or K99/R00 are not eligible to apply for COBRE funding. Furthermore, recruits with NIH R03, R21 or smaller grants are eligible to apply for COBRE funding. Successful candidates are expected to develop a strong extramurally funded (such as NIH R01) research program. They must participate in the teaching and service mission of the respective departments. Competitive salary and startup funds are available. The candidates will also receive excellent mentoring by senior faculty to pursue successful independent careers. Please submit curriculum vitae, statement of research plans and three letters of recommendation to: Dr. Mitzi Nagarkatti, Chair, Department of Pathology, Microbiology, and Immunology, University of South Carolina School of Medicine, Columbia, SC 29208 through e-mail: cobre@uscm.edu. The search will start immediately and continue until the positions are filled. *USC Columbia is an Equal Opportunity/Affirmative Action Employer and encourages applications from women and minorities and is responsive to the needs of dual career couples.*

University of Vermont Department of Animal Science seeks a tenure-track **ASSISTANT PROFESSOR** in Animal Health. Evaluation of applicants begins January 15, 2014. For full position description, see [website: http://uvmjobs.com](http://uvmjobs.com). *The University of Vermont is an Affirmative Action/Equal Opportunity Institution.*

POSITIONS OPEN



The University of Maryland is recruiting for a **RESEARCH ASSOCIATE** to join our dynamic group of NIH-funded translational pain scientists. Our primary focus is on the role for neurotrophin signaling in the development and persistence of neuropathic pain. We also utilize transcriptomic and genetic analyses to identify new candidate pathways that, when perturbed, reduce pain. Preferred skills include expertise in single cell electrophysiology, whole cell patch clamp and familiarity with, or experience with, optogenetic techniques. Candidates should have a Ph.D. in neuroscience or related field with at least four years of postdoctoral experience. Applicants should submit a letter of interest, résumé, and the names of three professional references to **Susan G. Dorsey** (e-mail: sdorsey@son.umaryland.edu).

The University of Maryland is an Equal Opportunity/Affirmative Action/ADA Employer.

FISH BIOLOGIST Tenure-Track Faculty Position

The Department of Biological Sciences and the Environmental Studies Program at Western Michigan University (WMU) seek applications for a jointly appointed tenure-track position with specialization in Fish Biology at the rank of **ASSISTANT PROFESSOR** beginning in fall 2014, pending budgetary approval. A Ph.D. and relevant postdoctoral experience are required. The successful candidate will participate in a new interdisciplinary undergraduate Freshwater Science and Sustainability major, establish an extramurally funded research program, participate in the training of Master's and Ph.D. students, and serve on departmental and university committees. Some teaching in an online or hybrid format will be required in collaboration with the Great Lakes Water Studies Institute at Northwestern Michigan College in Traverse City, Michigan ([website: https://www.nmc.edu/resources/water-studies/](https://www.nmc.edu/resources/water-studies/)). The Institute has excellent research facilities on Lake Michigan available to the candidate.

Information concerning the Biological Sciences Department's and the Environmental Studies Program's faculty and programs can be obtained at [websites: http://www.wmich.edu/biology/](http://www.wmich.edu/biology/) and <http://www.wmich.edu/environment>, respectively. Western Michigan University is a learner centered, discovery driven and globally engaged research institution and a U.S. News and World Report top 100 public university, with a growing graduate program that offers a unique opportunity for individuals seeking a balanced research and teaching career. The Carnegie Foundation for the Advancement of Teaching has placed WMU among the 139 public institutions in the nation designated as research universities with high research activity.

Applicants should visit [website: http://www.wmujobs.org/applicants/Central?quickFind=53580](http://www.wmujobs.org/applicants/Central?quickFind=53580) to apply. To apply please send letter of application, curriculum vitae, statements of research interests and teaching philosophy, and have three letters of reference sent to: Maarten Vonhof, Ph.D., Fish Biologist Search Committee, Department of Biological Sciences, Room 3441 Wood Hall, Western Michigan University, Kalamazoo, MI 49008-5410. Applications are due November 30, 2013, but will be considered until position is filled.

WMU is an Affirmative Action/Equal Opportunity Employer consistent with applicable federal and state law. All qualified applicants are encouraged to apply.

Stop searching for a job;
start your career.
www.ScienceCareers.org

POSITIONS OPEN

Missouri State University: August 11, 2014 opening for **ASSISTANT PROFESSOR** in Developmental Biology.

Requirements: Ph.D. in Biology or related area, peer-reviewed publications in Developmental Biology, and excellent communication skills. Duties: teach Introductory and Developmental Biology, and specialty area; advisement; externally funded research. Submit: letter of application (including commitment to diverse student populations), curriculum vitae, three references, teaching/interest statement, and copies of all transcripts at [website: https://jobs.missouristate.edu](https://jobs.missouristate.edu).

Employment will require a criminal background check at University Expense. Application review begins December 15, 2013 and continues until filled. Direct queries to e-mail: kkim@missouristate.edu.

Equal Opportunity/Affirmative Action Employer.

Your
career
is our
cause.

Get help
from the
experts.

www.sciencecareers.org

- Job Postings
- Job Alerts
- Resume/CV Database
- Career Advice
- Career Forum

Science Careers

From the journal *Science*



✓ More
scientists agree—
we are the most
useful website.

Science Careers

From the journal *Science*



www.ScienceCareers.org